

AGARD-CP-355

DTIC FILE COPY

AD-A134 058

AGARD-CP-355

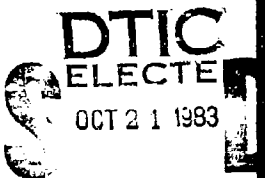
AGARD

ADVISORY GROUP FOR AEROSPACE RESEARCH & DEVELOPMENT

7 RUE ANCELLE 92200 NEUILLY SUR SEINE FRANCE

AGARD CONFERENCE PROCEEDINGS No. 355

**Characterization, Analysis and
Significance of Defects in
Composite Materials**



NORTH ATLANTIC TREATY ORGANIZATION



DISTRIBUTION AND AVAILABILITY
ON BACK COVER

83 10 19 106

AGARD-CP-355

NORTH ATLANTIC TREATY ORGANIZATION
ADVISORY GROUP FOR AEROSPACE RESEARCH AND DEVELOPMENT
(ORGANISATION DU TRAITE DE L'ATLANTIQUE NORD)

AGARD Conference Proceedings No.355
CHARACTERIZATION, ANALYSIS AND SIGNIFICANCE OF
DEFECTS IN COMPOSITE MATERIALS

Accession For	
NTIS GRAFI	
DTIC TAB	
Unnumbered	<input type="checkbox"/>
Justification	
By	
Distribution/	
Availability Codes	
Dist	Avoid and/or Special

A

OTIO
COPY
INSPECTED

Papers presented at the 56th Meeting of the Structures and Materials Panel
in London, United Kingdom on 12-14 April 1983.

THE MISSION OF AGARD

The mission of AGARD is to bring together the leading personalities of the NATO nations in the fields of science and technology relating to aerospace for the following purposes:

- Exchanging of scientific and technical information;
- Continuously stimulating advances in the aerospace sciences relevant to strengthening the common defence posture;
- Improving the co-operation among member nations in aerospace research and development;
- Providing scientific and technical advice and assistance to the North Atlantic Military Committee in the field of aerospace research and development;
- Rendering scientific and technical assistance, as requested, to other NATO bodies and to member nations in connection with research and development problems in the aerospace field;
- Providing assistance to member nations for the purpose of increasing their scientific and technical potential;
- Recommending effective ways for the member nations to use their research and development capabilities for the common benefit of the NATO community.

The highest authority within AGARD is the National Delegates Board consisting of officially appointed senior representatives from each member nation. The mission of AGARD is carried out through the Panels which are composed of experts appointed by the National Delegates, the Consultant and Exchange Programme and the Aerospace Applications Studies Programme. The results of AGARD work are reported to the member nations and the NATO Authorities through the AGARD series of publications of which this is one.

Participation in AGARD activities is by invitation only and is normally limited to citizens of the NATO nations.

The content of this publication has been reproduced
directly from material supplied by AGARD or the authors.

Published July 1983

Copyright © AGARD 1983
All Rights Reserved

ISBN 92-835-0333-3



Printed by Specialised Printing Services Limited
40 Chigwell Lane, Loughton, Essex IG10 3TZ

PREFACE

Les matériaux composites sont caractérisés par des propriétés physiques exceptionnelles qui justifient le développement rapide de leur application dans les véhicules aériens et spatiaux, auquel on assiste actuellement.

Cependant, comme n'importe quel matériau de structure, ils ne sont pas à l'abri de certains défauts d'intégrité pouvant intervenir aussi bien au cours du cycle de fabrication que comme conséquence des conditions de service.

Les technologies actuelles de contrôle non destructif sont capables, en général, de révéler la présence de ces anomalies, mais l'expérience est encore faible qui devrait permettre d'en apprécier les conséquences éventuelles et de décider du sort de l'élément en cause:

- laisser voler tel quel
- réparer
- réformer.

L'attitude actuelle des producteurs autant que des exploitants d'éléments en composite est d'éviter la difficulté en exerçant une politique d'extrême sévérité, conduisant au rejet et au rebut de la plupart des pièces suspectes, souvent bien au-dessous du niveau de risque raisonnable.

Il est hors de doute que cette coûteuse pratique ne peut favoriser la popularité des matériaux composites et ne peut manquer, à terme, d'handicaper leur développement.

L'objet de la présente Conférence de Spécialistes était donc de préciser les critères et tolérance d'acceptation des composites défectueux, par un approfondissement de la connaissance des conséquences des dommages.

Si le but final, qui devrait être un véritable règlement des conditions d'acceptation, ne peut encore être considéré comme atteint, les différents exposés ont mis en évidence ou confirmé un certain nombre d'acquisitions. Ainsi, l'importance de la porosité dont les seuils admissibles peuvent désormais être fixés.

Une très importante constatation que ressort des exposés est le caractère non pernicieux et la faible tendance à l'aggravation des dommages. Ceci constitue pour le composite un avantage que l'on appréciera, par rapport aux métaux.

On peut regretter qu'il n'ait pas été rapporté davantage de résultats d'expérience en service d'éléments endommagés. Ceci est tout naturellement l'illustration et la conséquence de la politique sévère d'acceptation évoquée plus haut, laquelle enferme actuellement le problème dans un processus circulaire qu'il est grand temps de rompre.

GEORGES JURE
Chairman, Sub-Committee on
Defects in Composite Materials

CONTENTS

	Page
PREFACE	iii
	Reference
<u>SESSION I - CHARACTERIZATION AND ANALYSIS OF DEFECTS</u>	
✓ FRACTOGRAPHIC ANALYSIS OF FAILURES IN CFRP by D.Parslow	1
✓ NDE TECHNIQUES FOR COMPOSITE LAMINATES by G.P.Sendeckyj	2
✓ MONITORING OF DEFECT PROGRESSION BY ACOUSTIC EMISSION; by J.Block	3
LA DISSECTION DES PIECES COMPOSITES: UNE AIDE PRECIEUSE A LA CONCEPTION ET AU CONTROLE NON DESTRUCTIF par M.Bourgeon	4
GROWTH OF DELAMINATIONS UNDER FATIGUE LOADING; by R.Prinz	5
EXPERIMENTAL INVESTIGATION OF DELAMINATIONS IN CARBON FIBRE COMPOSITE by W.Geier, J.Vilsmeier and D.Weisgerber	6
CHARACTERIZATION OF CUMULATIVE DAMAGE IN COMPOSITES DURING SERVICE; by M.E.Roylance, W.W.Houghton, G.E.Foley, R.J.Shuford and G.R.Thomas	7
✓ AN EMPIRICAL APPRAISAL OF DEFECTS IN COMPOSITES by N.B.Parslow	8
<u>SESSION II - SIGNIFICANCE OF DEFECTS</u>	
CORRELATION BETWEEN NON-DESTRUCTIVE INSPECTION RESULTS AND PERFORMANCE OF GRAPHITE/EPOXY STRUCTURAL PARTS; by F.Cipri	9
THE EFFECT OF DAMAGE ON THE TENSILE AND COMPRESSIVE PERFORMANCE OF CARBON FIBRE LAMINATES by S.M.Bishop and G.Dorey	10
BEHAVIOUR OF IDEALIZED DISCONTINUITIES AND IMPACT DAMAGES IN CFRP UNDER FATIGUE LOADING; by R.M.Aoki	11
INFLUENCE DE DEFAUTS DE FABRICATION SUR LE COMPORTEMENT STATIQUE ET DYNAMIQUE DES STRUCTURES EN COMPOSITE CARBONE-RESINE par J.Cuny et G.Briens	12
ADVANCED N.D. TECHNIQUES FOR COMPOSITE PRIMARY STRUCTURES; by M.Farioli, F.Perto, G.Samanni and V.Wagner	13
COMPUTATION OF INFLUENCE OF DEFECTS ON STATIC AND FATIGUE STRENGTH OF COMPOSITES by R.C.Tennyson, J.S.Hansen, G.R.Hepple, G.Mabson, G.Wharram and K.N.Street	14
FRACTURE MECHANICS OF SUBLAMINATE CRACKS IN COMPOSITE LAMINATES by A.S.D.Wang	15

Reference

Paper No.16 Withdrawn

- | | |
|---|----|
| THE SIGNIFICANCE OF DEFECTS AND DAMAGE IN COMPOSITE STRUCTURES
by R.T.Potter | 17 |
| IN-SERVICE NDI OF COMPOSITE STRUCTURES: AN ASSESSMENT OF CURRENT
REQUIREMENTS AND CAPABILITIES
by D.E.W.Stone and B.Clarke | 18 |
| EFFECT OF DEFECTS ON AIRCRAFT COMPOSITE STRUCTURES
by R.A.Garrett | 19 |
| THE ENGINEERING SIGNIFICANCE OF DEFECTS IN COMPOSITE STRUCTURES
by D.J.Wilkins | 20 |
| DEFECT OCCURRENCES IN THE MANUFACTURE OF LARGE CFC STRUCTURES
AND WORK ASSOCIATED WITH DEFECTS, DAMAGE AND REPAIR OF CFC
COMPONENTS
by C.S.Francis and G.Jackson | 21 |
| DELAMINATION GROWTH IN COMPOSITE STRUCTURES UNDER INPLANE
COMPRESSION LOADING
by D.Y.Konishi | 22 |

AD P001940

1-1

FRACTOGRAPHIC ANALYSIS OF FAILURES IN CFRP

by

D Purslow
Royal Aircraft Establishment
Materials and Structures Department
FARNBOROUGH, UK

SUMMARY

A wide-ranging fractographic research programme, from the fundamental characterisation of test coupon fractures to the failure analysis of full-scale aerospace components, has been undertaken in Materials and Structures Department, RAE.

This paper describes work on unidirectional CFRP test coupons in which a known mode of failure had been produced, the modes being longitudinal and transverse tension, compression and shear. From a fundamental understanding of the character of the different modes and of the mechanisms of fracture propagation it is shown how the qualitative significance of "micro-defects" occurring in good quality laminates may be assessed. The defects considered are fibre faults, fibre-matrix bond strength, fibre distribution, fibre alignment and voids and inclusions; these are illustrated and their individual and collective significance discussed.

1 INTRODUCTION

Microscopic examination of the fracture surfaces of CFRP test coupons in which a known mode of failure had been produced has provided the basis for a wide-ranging fractographic research programme. This basis has led beyond the ability to recognise significant characteristic features in each mode of failure to a detailed understanding of the fracture processes involved. From this knowledge it is possible to make qualitative assessments of the significance of defects on fracture initiation and propagation.

As an introduction to the topic this paper briefly describes the characteristics and fracture processes in several static modes of failure in unidirectional laminates and illustrates the occurrence of some manufacturing defects in the failure of good quality laminates. The influence and significance of the defects in unidirectional CFRP and their relevance to multidirectional laminates is discussed. The modes of failure analysed are longitudinal tension, transverse tension, compression and shear; the defects considered are fibre faults, fibre-matrix bond strength, fibre distribution, fibre alignment, voids and inclusions. Two resin systems are considered, one a plasticised epoxy (manufactured in 1982) in which the plasticiser separates into an array of microscopic spheroids and a brittle epoxy (manufactured in 1977) which shows more clearly some fractographic features masked by the spheroids in the first system. Apart from two optical micrographs, all the illustrations are taken from gold plated specimens in a scanning electron microscope.

2 TYPES OF DEFECT

The 2 mm thick unidirectional laminates were fabricated from prepreg sheet and cured in an autoclave. They were of good quality and the defects considered are those which might be dubbed "micro-defects" and are likely to occur in all current laminates.

Fibre Faults. These are formed during manufacture of the fibres and may occur as flaws or voids either on the surface or internally as illustrated in Fig 1. Additionally, large diameter fibres of unknown properties are found which may or may not be hollow, Fig 2.

Fibre-Matrix Bond. For a given, consistent fibre-matrix system the bond strength should not vary. However, experience has shown that small changes such as minor variations in fibre surface treatment may produce significant changes in the fibre-matrix bond strength and consequent alteration in CFRP properties. Fig 3 illustrates a well-bonded, brittle composite where in places the propagating transverse tensile crack has broken the fibres rather than the bond. Such bonds frequently show evidence of chemical changes in the resin around the fibre resulting in fractures within the matrix, with thin concentric films of resin remaining on the fibres. With the plasticised resin a high bond strength may result in preferential breaking of the plasticiser - epoxy interface, all the fibres remaining covered in epoxy as shown in Fig 4. Poor fibre-matrix bond strength will naturally result in fibre surfaces devoid of resin, Fig 5; but clean fibre surfaces do not necessarily imply poor bond strength.

Fibre Distribution. The variation in fibre distribution is best illustrated by an optical micrograph such as Fig 6. The average fibre content is about 65% by volume but, as can be seen, within a small area varies from the very high volume fraction hexagonal array at A to very low at a ply boundary, B.

Fibre Misalignment. At the boundaries of the prepreg laminates numbers of highly misaligned fibres occur as in Fig 7. In addition, significant misalignment may arise throughout the laminate thickness due usually to twisting of the individual fibre tows Fig 8.

Voids and Inclusions. In a high quality laminate the void content is less than 0.5% by volume and those voids which do arise are usually very small ($c.10 \mu\text{m}$), Fig 9.

Large voids occasionally form in the resin rich areas associated with interply misaligned fibres, Fig 10. Particles, such as the unreacted hardener, Fig 11, which make no bond with the resin may, because of moisture absorption, etc, be more significant than voids of the same magnitude.

3 LONGITUDINAL TENSION

A longitudinal tension failure in a brittle composite is shown in Fig 12. Radiating lines called "radials" can be detected originating at the relatively smooth area. These radials are formed as the fracture propagates along different radii at gradually diverging axial positions causing lines of hills and valleys of increasing magnitude. Frequently individual fibres exhibit similar radials, Fig 13, which may originate at a fault in the fibre or at a point on the surface close to an adjacent fibre. In the case of fibres in close proximity, these radials may indicate that the failure of one fibre is directly attributable to the prior failure of its neighbour - these are referred to as Directly Attributable Fibre Failures (DAFF) and are illustrated in Fig 14 where fibre A has caused the failures of fibres B and C and subsequently D and E. Note the preference for the failure to progress from fibre to fibre (C→D→E) rather than cross the resin rich area adjacent to B, C and E. Within the matrix fracture, particularly in brittle composites, lines may also develop due to the failure propagating in slightly different planes. These lines may take the form of radials, Fig 15, which radiate in the direction of propagation and tend to die out as the lines diverge or more usually, "rivers", Fig 16 which converge in the direction of propagation, the plane separation becoming greater as the lines converge.

These features make it possible to chart the progression of a tensile fracture from fibre to fibre over a large proportion of a failure surface even in non-brittle composites, frequently enabling the exact origin of failure to be determined.

Thus it is also possible to assess the effect of defects on the failure process. From the preceding discussion of the failure of the plasticised composite illustrated in Fig 14, it becomes clear immediately that the fibre distribution affects the fracture propagation. Where the fibres are closely spaced the fracture takes on a brittle nature and travels from fibre to fibre as DAFF. Where the fibres are well spaced the failure may progress across the matrix or, more likely, along individual fibre surfaces producing a less brittle fracture with considerable fibre pull-out.

In a brittle composite the same preference for the failure to progress as DAFF occurs as shown in Fig 17.

Figures 18, 19 and 20 are taken from different areas of the same non-brittle specimen. Failure of individual fibres at a fault may result in fibre pull-out as shown in Fig 18. Where the fibres are more closely spaced, breakage at a fibre fault may merely cause the axial position of the fracture plane to differ slightly from neighbouring fibres - one of the prime causes of the hill-and-valley radials Fig 19. Where the fibres are touching the failure again propagates from fibre to fibre as DAFF and the presence of a fibre fault has no effect as in Fig 20.

Weakening of the fibre-matrix bond causes the failure to become less brittle (eg compare Figs 12 and 18) with more fibre pull-out and consequently much less sensitivity to impact under load.

Fibre misalignment can be seen to cause delamination where it occurs at a ply boundary, Fig 21, or pull-out of blocks of fibres where it is due to twisting of the fibre tows, Fig 8. In a brittle composite misalignment may well cause premature failure locally or even total failure in a small test coupon as is illustrated in Fig 22.

Small voids in the quantities accepted in good material rarely occur in longitudinal tensile fracture surfaces since when they are seen they have had negligible effect on the tensile crack propagation. However, occasional large inclusions may have more serious consequences locally, even in recent non-brittle material as shown in Fig 23, where the inclusion is the origin of the local tensile failure and the cause of the subsequent delamination. It should be noted that the processes involved in both brittle and non-brittle failures are identical, it is merely their relative importance which differs.

4 COMPRESSION

In the case of compression the main fractographic problem is the obliteration of most of the microscopic features during post-failure abrasion of the adjacent surfaces. Nevertheless, detailed investigation shows that in the current plasticised composite, failure commences as in-phase fibre microbuckling which may extend over the whole surface as shown in Figs 24-26. In earlier, brittle composites, failure was by shearing of the fibres at a higher compressive ultimate stress. The term microbuckling is used to describe the buckling of the fibres over a wavelength of about 10 fibre diameters or less. In the upper area of Fig 24 the microstructure has been destroyed by post failure abrasion. On the lower fracture plane the fibres show clearly the characteristics of microbuckling as in the enlargement Fig 25. In the upper plane of Fig 25, the fibres have broken in-phase in flexure, the upper and lower halves of each fibre fracture being tensile and compressive failures respectively. In the lower plane, although more damaged, evidence of flexural failure is in the opposite direction as would be expected with fractures occurring at the antinodes of a buckle. The buckle axis, roughly horizontal in Fig 25, is usually perpendicular to the direction of compressive failure propagation. If therefore the larger area shown in Fig 26 is examined, it can be seen that, looking along the upper boundary of the micrograph from left to right, the buckle axis changes angle from positive to negative indicating that the local compression failure started in the lower central region of the area depicted.

Because most of the fibres are constrained to fail in a given buckling plane, fibre faults and small voids are rarely seen, indicating they have little effect on the compressive failure. In addition, movement of the fibres both during and after failure make minor fibre misalignment and variations in fibre distribution impossible to detect. Highly misaligned fibres and their associated resin rich areas induce premature delamination and ultimate failure, as illustrated in Fig 27. General fibre misalignment due to twisted tows causes axial cracking and rapid changes in the failure plane effecting an overall reduction in compressive strength.

The change of mode between fibre shear and fibre micro-buckling in brittle and non-brittle CFRP compression failures in these examples is due to the change in matrix characteristics - a further weakening of the matrix or fibre-matrix bond would produce a reduction in fibre stability and a further reduction in compressive strength.

5 TRANSVERSE TENSION

The tensile stress in this case is in the plane of the laminate and perpendicular to the fibres. Part of a brittle transverse tensile failure which originates at a fibre fault is shown in Fig 28. The failure surface is naturally constrained to be roughly planar by the fibres themselves. However, minor radials do develop in the surface due to slight changes in plane as the fracture propagates. The plane changes are the result of fibre breakage and the radials therefore take the form of broken fibre ends. For example, in Fig 28, the failure propagating from the faulty fibre at O causes the radials OA, OB, OC, OD etc to occur. Similarly oriented radials and rivers develop in the matrix as described in paragraph 3. In plasticised composites, identical features arise in transverse tension but are masked by the cellular nature of the fractured matrix. Fig 29 shows a typical failure in the plasticised composite occurring at a pair of misaligned fibres A-A, the stress concentration due to the misalignment and associated resin richness causing failure to commence in this area.

A similar phenomenon has occurred in the failure illustrated in Fig 4 where fracture has commenced at the resin rich area at the top left hand corner of the picture. At higher magnification, Fig 30 the various failure surfaces are clearly visible, the fairly smooth fibrillar surface at B is that of a fibre and at C, that of the resin at a fibre-matrix bond failure. Note the non-cellular nature of the resin close to the fibre surface at D and the tendency for the epoxy phase to part from the spheroids of plasticiser as at E. Observe also that the imprints of the spheroids are roughly circular - noticeably different from the imprints left on a shear fracture.

Voids and inclusions such as illustrated in Fig 11 tend to reduce the strength of the failure plane but since they occur uniformly throughout the composite, removal of one such defect from which failure originated would merely cause fracture to commence at an adjacent defect at a negligibly higher stress. However, large voids, Fig 10, large fibres, Fig 28, or a group of badly aligned fibres, Fig 29, may cause premature failure as already discussed in this paragraph.

Reduction of the fibre-matrix bond strength below the strength of the matrix naturally causes a corresponding reduction in transverse tensile strength.

6 SHEAR

The various stages of shear failure are illustrated in a brittle composite in Fig 31. Ultimate failure due to an applied shear stress normally commences as failure in the matrix perpendicular to the tensile component of the resolved shear stress. Because of the presence of the relatively stiff fibres, fracture cannot originate at a point source and propagate as is the case in tension. Increasing shear stress causes some tensile failures to occur in the matrix as at A, Fig 31. A further increase in shear stress does not cause these to propagate out of the incipient fracture plane but increases the number of such tensile failures as in plane B. Shear failure finally occurs when these 45° tensile failures turn over to form the characteristic 'S' shapes and ultimately coalesce over the whole plane as at C. Fig 32 shows a shear failure in the plasticised composite. The characteristic "cups" formed by ultimate failure along the planes of 45° tensile cracks are seen at D and indicate the relative movement of the mating surface as arrowed. Again, as was seen in the case of transverse tension, the preference of the matrix to fail at the interphase boundary rather than at the fibre surface is evident. Looking more closely, Fig 33, the imprints of the spheroids in the epoxy layer round the fibre E are not completely circular, as in tensile fractures, but semicircular the right hand semicircle having been removed by the relative movement of the two surfaces at failure and in the same directions as shown in Fig 32. Similarly, as illustrated in Fig 34, the same relative movement causes those fibres which cross the failure plane to break in tension at F and compression at G. Hence the resin cusps, spheroid imprints and fibre failure modes are all diagnostic of a shear failure and of the directions of applied stress.

Micro-defects such as voids, faulty or misaligned fibres shown in Figs 35 and 36 do not individually precipitate fracture, as may be the case in tension, but serve to weaken a given shear plane and make it more susceptible to overall premature failure.

Although weakening of the fibre-matrix bond will encourage separation of the matrix from fibres in places before the 45° tensile failures described earlier, final fracture will still take place as described and be dictated by the overall strength of that plane, albeit at a reduced stress.

7 GENERAL SIGNIFICANCE OF MICRO-DEFECTS

It has been shown in the preceding fractographic analyses that micro-defects occur in even the best CFRP laminates and do affect the failure mechanisms. Nevertheless, it may be concluded from the description of the occurrence of micro defects in good quality composites and their influence on the fracture processes that, apart from local perturbances which affect only small coupons, unless all the

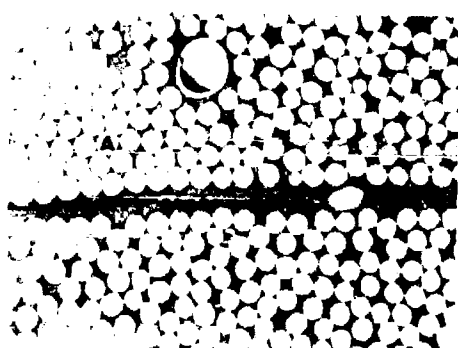
defects can be removed, their presence may be regarded as a material property. That is to say, for instance, that unless all fibre faults are eliminated, removal of one particular fibre fault from which a longitudinal tension failure originates would merely cause failure to commence at an adjacent defect at a negligibly higher stress. However, large weak fibres, inclusions or misalignment may have more significant local effects on the transverse tensile and shear strengths.

The strength of the fibre-matrix bond has been shown to affect all four failure modes considered. If quality control were adequate, then the compromise necessary between the high shear and compressive strengths obtainable with high bond strength and the toughness associated with a weaker bond could be determined and adhered to. In practice, variations in bond strength occur all too frequently and permeate the whole of the laminate, a weakened bond lowering the transverse tensile, shear and compressive strengths making the composite more susceptible to delamination but at the same time increasing its toughness, particularly when subjected to impact under tensile stress.

The fibre distribution varies rapidly from place to place within a composite and has been shown, for instance, to locally increase the brittleness of a longitudinal tension failure where the packing is high. Similarly, fibre misalignment, voids and inclusions will cause stress concentrations and thus may locally lower the ultimate strengths in all four modes. Unless such variations could be completely eliminated, the most significant aspect, apart from the overall effect on composite properties, is the consequent increase in variability of small strength test coupons.

The scope of this paper does not allow a fractographic description of failures in multi-directional laminates but the work has shown that the significance of the defects discussed in unidirectional material applies similarly.

Thus, in the case of static failures, the existence of micro-defects in good quality laminates, whilst causing a general lowering of strength, may be regarded as a material property and allowed for in design. In full-scale composite aerospace structures such defects therefore have little significance. However, one exception may be the variation in fibre-matrix bond strength, but this should be detected by testing each batch of prepreg. It should also be stated that improvements such as better general fibre alignment in the prepreg would provide a welcome improvement in composite properties.

FIG 1 FIBRE FLAW ($\times 8000$)FIG 2 HOLLOW FIBRE ($\times 1500$)FIG 3 TRANSVERSE TENSILE FAILURE ($\times 2000$)FIG 4 FAILURE AT EPOXY-PLASTICISER INTERFACE ($\times 1000$)FIG 5 FAILURE AT FIBRE-MATRIX INTERFACE ($\times 750$)FIG 6 FIBRE DISTRIBUTION ($\times 500$)

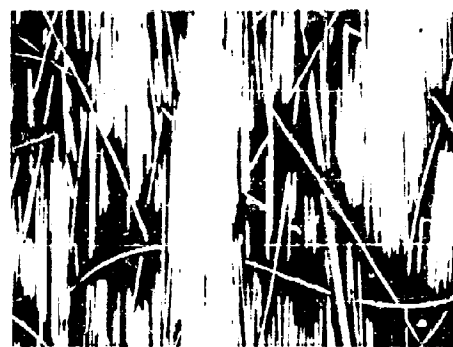
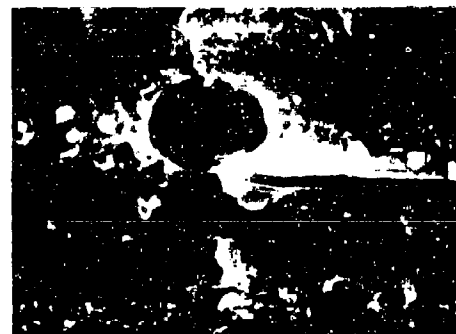
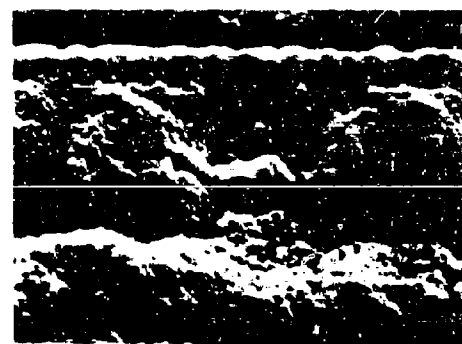
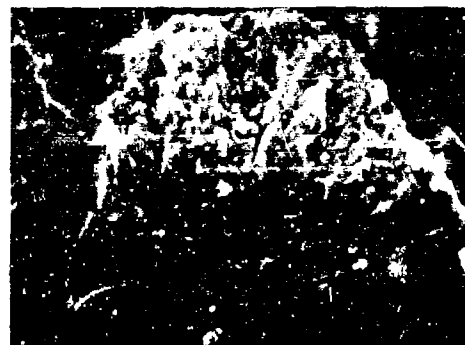
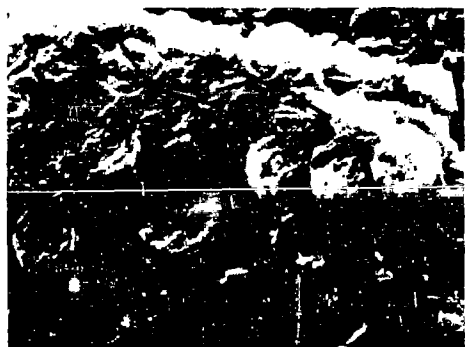
FIG 7 FIBRE MISALIGNMENT AT A PLY BOUNDARY ($\times 100$)FIG 8 FIBRE MISALIGNMENT WITHIN A TWM ($\times 300$)FIG 9 SMALL VOID ($c.10\mu\text{m}$ DIAMETER)FIG 10 LARGE VOID WITH MISALIGNED FIBRES ($\times 100$)FIG 11 PARTICLE INCLUSION ($\times 1000$)

FIG 12 BRITTLE LONGITUDINAL TENSILE FAILURE ($\times 50$)FIG 13 FIBRE FRACTURE ($\times 7000$)FIG 14 FIBRE-FIBRE FRACTURE PROPAGATION ($\times 3500$)FIG 15 RADIAL MATRIX FRACTURE ($\times 3000$)FIG 16 MATRIX RIVERS ($\times 2000$)FIG 17 DAFF PROPAGATION IN A BRITTLE COMPOSITE ($\times 1200$)

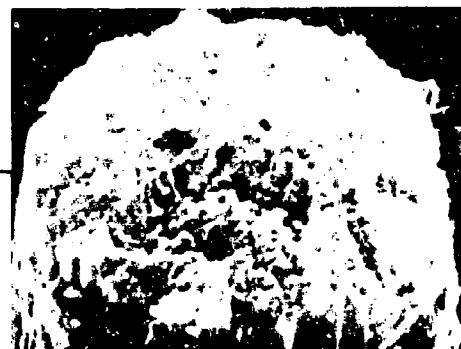


FIG 18 NON-BRITTLE LONGITUDINAL TENSILE FAILURE ($\times 300$) ($\times 10000$)



FIG 19 HILL-VALLEY FORMATION
DUE TO FIBRE FAULT ($\times 400$)

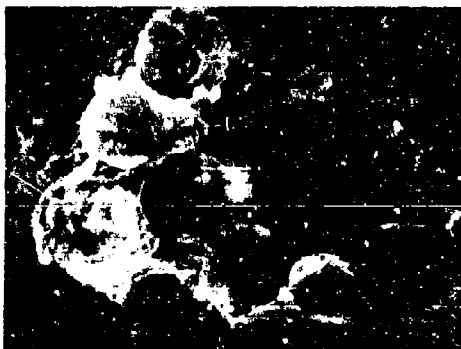


FIG 20 DAFF UNINFLUENCED BY FIBRE FAULT ($\times 2000$)

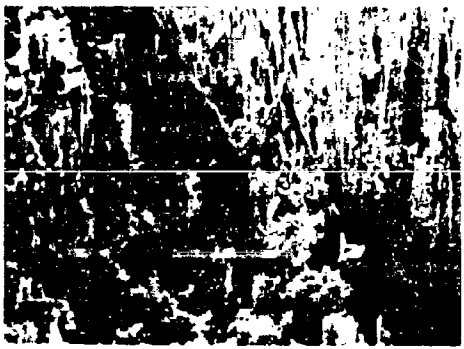


FIG 21 DELAMINATION DUE TO
FIBRE MISALIGNMENT ($\times 75$)

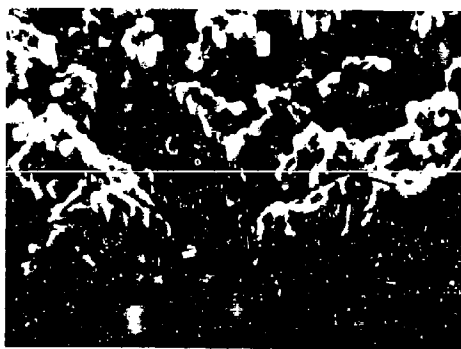


FIG 22 FAILURE INITIATION AT
MISALIGNED FIBRES ($\times 250$)



FIG 23 FAILURE INITIATION AND DELAMINATION AT AN INCLUSION ($\times 100$)



FIG 24 MICRO-BUCKLING COMPRESSIVE FAILURE ($\times 100$)



FIG 25 FIBRE MICROBUCKLING ($\times 750$)

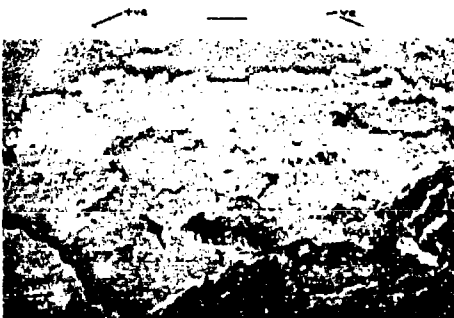


FIG 26 ROTATION OF BUCKLE AXIS AROUND FAILURE ORIGIN (. . 50)



FIG 27 COMPRESSIVE DELAMINATION DUE TO MISALIGNED FIBRE ($\times 50$) ($\times 200$)



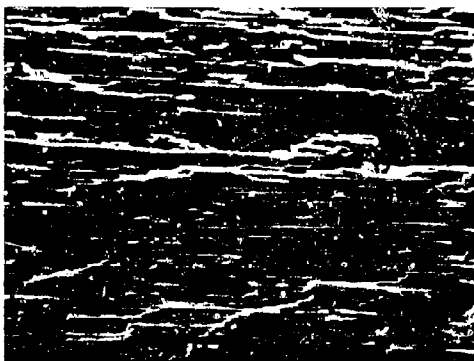


FIG 28 BRITTLE TRANSVERSE TENSILE FAILURE ($\times 50$)

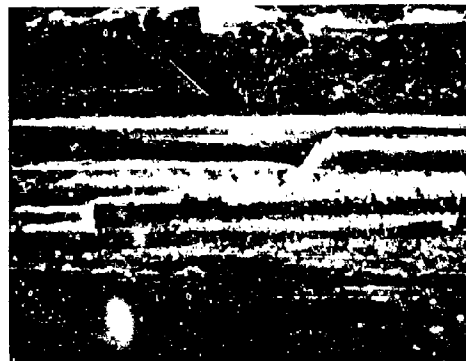


FIG 29 NON-BRITTLE TRANSVERSE
TENSILE FAILURE ($\times 50$)



FIG 30 STRUCTURE OF PLASTICISED MATRIX ($\times 2500$)



FIG 31 INITIATION OF SHEAR FAILURE ($\times 750$) ($\times 2000$)

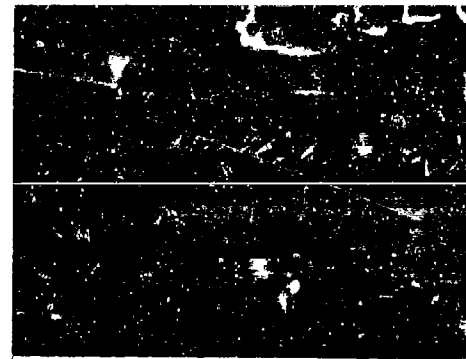




FIG 32 CUSPS IN SHEAR FAILURE ($\times 1500$)

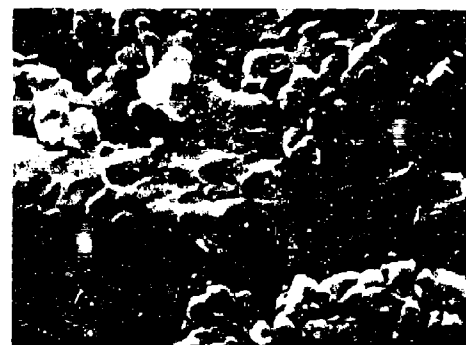


FIG 33 SHEAR FAILURE OF
PLASTICIZED MATRIX ($\times 4000$)



FIG 34 FIBRE FRACTURES IN
SHEAR FAILURE ($\times 500$)



FIG 35 MISALIGNED FIBRES ($\times 400$)



FIG 36 FIBRE FAULT ($\times 200$)

✓

AD P001911

2-1

NDE TECHNIQUES FOR COMPOSITE LAMINATES

George P. Sendeckyj
Aerospace Engineer

Air Force Wright Aeronautical Laboratories (FIBEC)
Wright-Patterson AFB, Ohio 45433, USA

SUMMARY

Destructive and nondestructive evaluation (NDE) techniques for documenting defects and damage in resin-matrix composite materials are described and assessed from the viewpoint of a researcher studying the damage accumulation process. The results show that deplying, a destructive evaluation technique, provides the most detailed information on the spatial distribution of damage in resin-matrix composite materials. Of the NDE techniques, penetrant enhanced stereo x-ray radiography is the best one. Ultrasonic, holographic, and edge replication NDE techniques provide much less information than x-ray radiography. Acoustic emission, thermographic and stiffness change monitoring provide valuable information on when to conduct more thorough evaluations using one of the other NDE techniques.

1. INTRODUCTION

Nondestructive evaluation (NDE) techniques have been primarily developed to assess the quality of materials. Since only the presence of flaws (manufacturing defects and damage) and not their accurate description is of interest when performing quality assurance inspections, emphasis was placed on developing NDE methods for rapid evaluation of the quality of large structural components. This emphasis resulted in the development of powerful NDE techniques that are in every day use on the production line and in-service. Unfortunately, these NDE methods do not have the capability to provide the accurate description of defects and damage that is required by the researcher investigating the damage accumulation process in composite materials.

A number of NDE methods that have been used in studying damage accumulation in composite materials are reviewed herein. Emphasis is placed on the ability of the NDE techniques to provide a detailed and accurate description of the damage. With this emphasis in mind, the review is organized into four major sections. Destructive inspection methods that can serve as the standard of comparison for the NDE methods are discussed in Section 2. Various NDE methods are described and examples of the type of damage features that can be documented by their use are given in Section 3. A comparison of the NDE techniques, based on their ability to serve as a research tool in damage accumulation studies, is given in Section 4. Finally, recommendations for improving the 'best' NDE method are made in the last section.

2. DESTRUCTIVE INSPECTION METHODS

The following two distinct destructive inspection methods have been successfully used to document the state of damage in composite laminates.

2.1 Sectioning

A fairly accurate description of damage in resin-matrix composite laminates can be obtained by sectioning of properly prepared samples (Refs. 1-2). In this method, the sample is treated with a penetrant and then sectioned by dry grinding away of material. For glass-epoxy laminates, any penetrant can be used. For boron-epoxy and graphite-epoxy composites, a penetrant (such as Zy glo) that can be observed under ultraviolet light has to be used. This technique is tedious to use and requires special care if damage details are to be accurately documented. It can find matrix cracks and delaminations, but not fiber fractures.

2.2 Deplying

Delying (Refs. 3-6) is a recently developed destructive inspection technique for accurately documenting the state of damage in resin-matrix composite laminates. It is relatively easy to use and provides extremely accurate information on matrix cracking, delaminations, and fiber fractures. The deplying technique consists of the following steps:

(a) The sample to be depried is first treated with a gold chloride diethylether solution (containing 9.6% gold by weight) for approximately 30 minutes. After the gold chloride diethylether solution has saturated the sample, the surfaces of the sample are wiped with acetone moistened cotton to remove the penetrant from the surface. The sample is then heated to approximately 65 C to remove the diethylether before proceeding with the deplying.

(b) The treated sample is placed into a stainless steel wire mesh holder and the

holder is inserted into a furnace maintained at 420 to 425 C for 70 to 100 minutes. An inert gas, such as argon, may be used to purge the furnace (Ref. 6). The resin is partially pyrolyzed during this heat treatment. Upon completion of the partial pyrolysis, the holder containing the sample is removed from the furnace and allowed to cool to room temperature.

(c) After cooling, the partially pyrolyzed sample is carefully removed from the holder and individual laminae are unstacked. The unstacking is done by applying adhesive tape to the surface of the top lamina to reinforce it and lifting the top lamina from the sample. The delplied laminae is then attached to a work sheet to ease handling during examination and photography.

(d) The delpled laminae are examined with a stereo microscope at a magnification of 8X to 50X. The laminae is illuminated with light from a fluorescent lamp impinged at 90 degrees to the fiber direction for examination for fiber fractures. Under this illumination, the gold residue on the delpled surface is not visible. A high intensity light source impinging the laminae surface parallel to the fiber direction is used to locate delaminations and matrix cracks. Under this illumination, the gold residue is visible and can be distinguished from the fibers and resin residue.

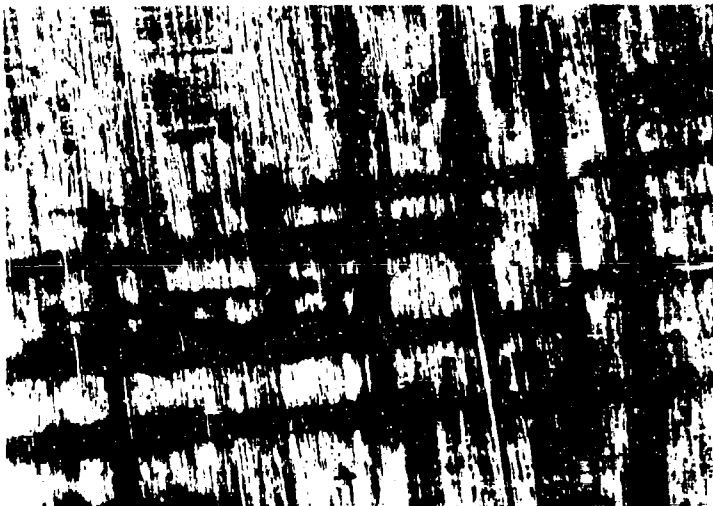
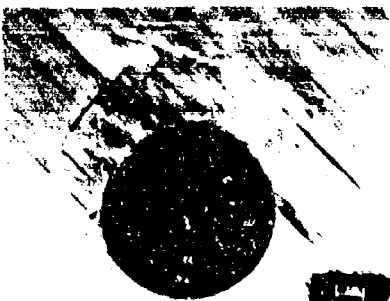


Fig. 1. Network porosity between adjacent laminae in graphite-epoxy laminate (Courtesy of S. M. Freeman).

Typical results obtained by the delpling method are shown in Figs. 1 to 3. Figure 1 shows a magnified view of network porosity between two adjacent laminae in a graphite-epoxy laminate. The network porosity has the appearance of interconnected dark bands running in and perpendicular to the fiber direction. The fibers appear as fine light lines. Residual resin appears as dark gray regions (see the lower left-hand side of the figure). Figures 2 and 3 show typical damage in a 24 ply ($\pm 45/0/90/\pm 45/0/90/\pm 45/0/90$) member of a graphite-epoxy mechanical joint loaded to 87.7% of its ultimate strength. Figures 2 and 3 show the damage indications on the 10th (-45 degree) and 11th (0 degree) lamina from the top surface, respectively. Illumination for observing fiber fractures and delaminations was used in making the left and right-hand photographs, respectively. As can be seen from the left-hand views in Figs. 2 and 3, extensive fiber fracturing has occurred. The fiber fractures in the 0 degree lamina appear as jagged lines running in the -45 and 90 degree directions. Similarly, the fiber fractures in the -45 degree lamina run in the 45 degree direction. This implies that matrix cracking and delamination was a factor in causing the compressive failure of the fibers. As can be seen from the right-hand views in the figures, considerable delamination has occurred between the 45 and -45, and -45 and 0 degree laminae. The delaminations appear as light colored patterns in the figures. They are bounded by fiber fractures and matrix cracks.

As can be seen from these examples, delpling provides extremely detailed information on the nature of damage in resin-matrix composite materials. By careful probing and scanning electron microscope examination of the delpled laminae, detailed documentation of the number of broken fibers and the spatial distribution of fiber breaks can be obtained. This information cannot be easily obtained by any other method.



DEPLY - FIBER FRACTURES



DEPLY - DELAMINATIONS (GOLD)

Fig. 2. Depiled -45 lamina in $(\pm 45/0/90/\mp 45/0/90/\pm 45/0/90)_S$ graphite-epoxy laminate (Courtesy of S. M. Freeman).



DEPLY - FIBER FRACTURES



DEPLY - DELAMINATIONS (GOLD)

Fig. 3. Depiled 0 lamina in $(\pm 45/0/90/\mp 45/0/90/\pm 45/0/90)_S$ graphite-epoxy laminate (Courtesy of S. M. Freeman).

3. NONDESTRUCTIVE EVALUATION METHODS

A large number of nondestructive evaluation methods have been used to document manufacturing defects and the damage accumulation process in resin-matrix composite materials. The methods have different limitations and detail resolution capabilities. They are reviewed herein from the viewpoint of a researcher interested in obtaining detailed information on the damage accumulation process in resin-matrix composite materials.

3.1 Conventional and Stereo X-Ray Radiography

Conventional and stereo radiography are well established x-ray inspection procedures, described in reference books (Refs. 7-9). Since the procedure for making conventional radiographs is used in making stereo radiographs, it will not be dwelt on separately. The standard stereo radiography procedure consists of making two x-ray radiographs of an object from slightly different orientations. This can be done by translating the x-ray source relative to the object/film combination by moving either the x-ray source or the film and object. In either case, the amount of permissible translation is limited by the characteristics of the cone of x-rays emanating from the x-ray tube. To overcome this limitation, we have used a different procedure (Ref. 10). Instead of translating the object/film combination relative to the x-ray source, we rotate it through a small angle. This has the advantage of keeping the object/film combination centered within the cone of x-rays emanating from the x-ray source. The fixture that we designed for this purpose is described in Ref. 10.

The procedure for making radiographs of defects and damage in resin-matrix com-

posite materials differs from the conventional ones in that an x-ray opaque penetrant is used to bring out details of the damage. The penetrant is necessary to provide sufficient contrast between the damage and the composite so that the damage can be observed. Various penetrants have been developed and used for this purpose. Tetrabromoethane (TBE) was the first penetrant to be successfully used (Refs. 11-13). Since it is a carcinogen, extreme care must be taken when using it. A penetrant that was developed to replace it is diiodobutane (DIB). It is safer to use than TBE, but it is still dangerous because it is an organic halide (Refs. 14-15). The best penetrant is zinc iodide in an alcohol solution (Refs. 14-15). This penetrant is safe to use and no special precautions must be taken. The formulation of the zinc iodide solution is:

Zinc iodide (ZnI_2) - 60 grams
 Water (H_2O) - 10 milliliters
 Isopropyl alcohol ($CH_3CH(OH)CH_3$) - 10 milliliters
 Kodak "Photo Flo 600" (as a wetting agent) - 1 milliliter.

The selected penetrant is applied to the surfaces of the specimen for a sufficiently long time (approximately 30 minutes) for it to penetrate into all of the damage. After it has completely saturated the specimen, excess penetrant is removed from the surfaces with absorbent towels. The specimen is then placed on a sheet of x-ray film (making sure that it is intimate contact with the film) and the specimen/film combination is positioned under the x-ray source. The film is exposed with the specimen in one position relative to the x-ray source. The film is removed. A new sheet of film is used to make another exposure with the specimen/film combination rotated through a small angle (approximately 15 degrees) relative to the x-ray source.

Various x-ray films can be used. Our experience has been that a high resolution, single-coat x-ray film like Kodak Type R single-coat industrial x-ray film gives best results. Double-coat films that require shorter exposure times are not satisfactory because the x-ray images on the two emulsions are slightly displaced, resulting in a double image on the film. This leads to loss of resolution in the stereo image constructed from the stereo pairs.

Similarly various x-ray units can be used, but x-ray units emitting soft x-rays give the best results. The recommended unit is one that has a small focal spot and can be operated at voltages between 15 and 25 kV and high currents. The low operating voltage produces soft x-rays that provide resolution of structural details in the laminate, such as porosity and fiber spacing irregularities. This increases the amount of information contained in the x-ray negatives.

The optimum exposure times are those that give a negative from which high magnification prints can be made. These are shorter than the exposure times used in making normal x-ray negatives intended for direct viewing. Once the stereo x-ray negatives are made, high magnification prints are made and these are viewed using one of several possible viewing arrangements (Ref. 10).

A typical sequence of penetrant enhanced stereo x-ray photographs of fatigue loading induced damage in a 25.4 mm wide ($0/\pm 45/90$)_{S2} graphite-epoxy specimen containing a 4.75 mm diameter hole is shown in Figs. 4 through 12. The specimen was alternately subjected to cyclic loading and NDE. The loading consisted of an initial static tensile loading to 13.3 kN followed by successive blocks of constant amplitude fatigue loading at 5 Hz using a sinusoidal waveform. The maximum and minimum cyclic loads were 13.3 and 1.33 kN, respectively.

The figures show artifacts that can be interpreted as damage. The interpretation of these artifacts as particular types of damage requires understanding how the penetrant affects the x-ray beam and how it enters the damaged specimen. The penetrant absorbs x-rays preventing them from reaching and exposing the film. Thus, regions containing penetrant appear darker in the photographs than regions containing no penetrant. Regions containing no penetrant have a uniform grayness level that depends on the x-ray absorption characteristics of the composite specimen being examined. The hole appears as a clear white region in the photographs since all x-rays reach the film. The regions containing penetrant range from the background gray to black depending on the amount of penetrant present.

The penetrant can enter the damaged specimen by being absorbed into the resin and by capillary action (penetration) into the regions of damage. The absorbed penetrant, entering the matrix by diffusion, causes a slight change in the background density of the image. The penetrant entering the specimen by capillary action causes large changes in grayness of the negative. The change in density of the negative depends on the amount of penetrant inside the damaged regions, which in turn depends on the "thickness" of the damage. The thicker the damage, the darker it appears in the photographs. With these preliminaries out of the way, the artifacts in the figures can be interpreted. Matrix cracks are narrow and long in the plane of the specimen and relatively thick in the depthwise direction. Their thickness corresponds to the thickness of the lamina. Hence, if penetrant gets into the matrix cracks, they appear as long narrow dark lines in the photographs. As can be seen from Fig. 4, matrix cracks running in all four reinforcement directions have been induced during the machining of the hole. Similarly, fiber fractures appear as jagged short lines.

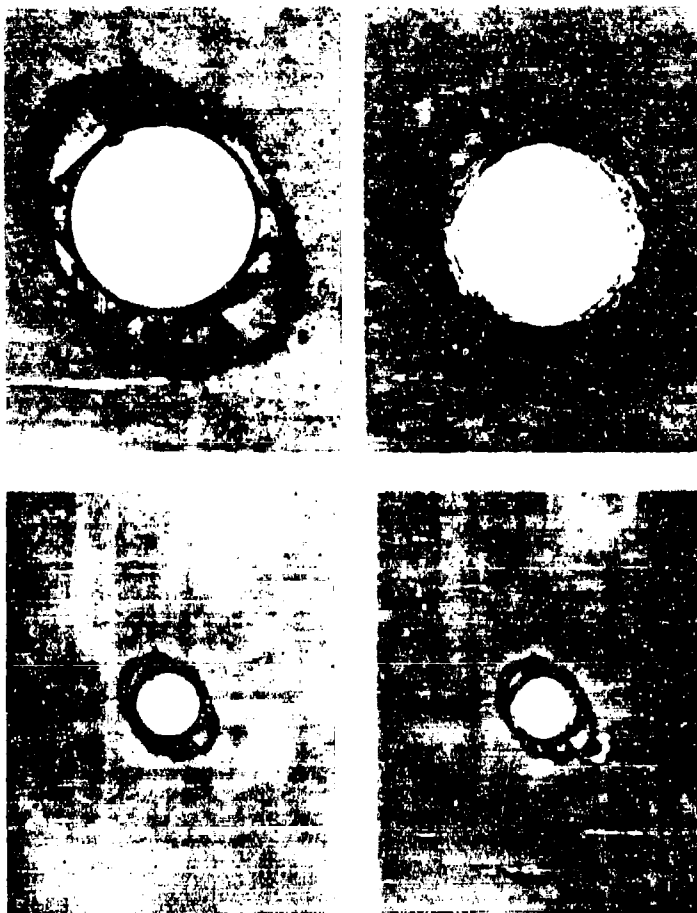


Fig. 4. Penetrant enhanced stereo x-ray radiographs of specimen, showing initial machining damage.

The interpretation of artifacts corresponding to delaminations is somewhat more difficult. The delaminations are only slightly open when the specimen is unloaded. The magnitude of the opening or thickness of the delaminations varies from almost imperceptible at the maximum extent of the delamination to relatively large inside and at the free edges. The thickness of the penetrant inside the delaminations might be expected to correspond to the thickness of the delamination. While this is true at the edges of the delamination, the situation in the interior is different. The capillary forces acting on the penetrant are not high enough to retain the penetrant inside the delamination when the delamination thickness is large. As a result, the penetrant escapes from the regions of large delamination opening. The boundary between the region in the delamination containing penetrant and no penetrant corresponds to the meniscus formed by the penetrant. Thus, delaminations appear in the photographs as broad bands of continuously varying grayness surrounding lighter gray regions. The interior regions of the delaminations may be lighter in color than the background.

As can be seen from Fig. 4, the hole drilling process has caused extensive damage consisting of matrix cracks, fiber bundle fractures, and delaminations. The matrix cracks emanate from the hole and run in the directions of the reinforcing fibers. While most of the cracks run in the 0 and -45 degree directions, some matrix cracks are present in the 45 and 90 degree lamina. In particular, the group of short 90 degree matrix cracks near the lower right edge of the hole terminate in a jagged line that

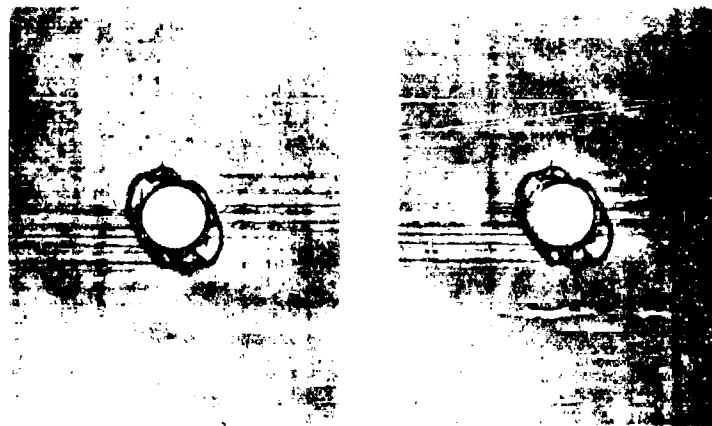


Fig. 5. Penetrant enhanced stereo x-ray radiograph of specimen after application of 13.3 kN tensile load.

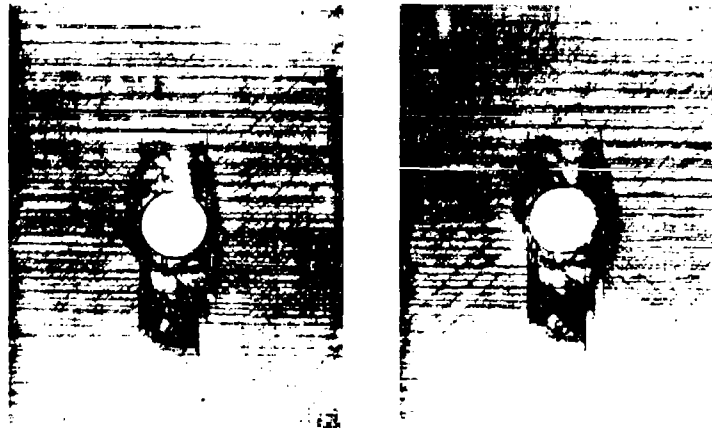


Fig. 6. Penetrant enhanced stereo x-ray radiograph of specimen after 50000 cycles of fatigue loading.

corresponds to fiber bundle fractures. The depth location of these matrix cracks can be determined from either the stereo image of the damage or the relative location of the matrix crack indications in the different views. If the stereo image is used, the depth perception of the damage details depends on how the different views are merged to form the stereo image. If the views are merged with the aid of an optical device like the stereoscope, the left eye sees the left view and the right eye sees the right one. This type of image merging is referred to as conventional stereo viewing. If the stereo pairs are viewed without optical aids, the depth perception depends on whether the stereo pairs are merged conventionally or cross-eyed. In cross-eyed viewing, the left eye sees the right image and the right eye sees the left one. As a result, the depth perception is reversed from that in conventional merging.

When the relative location of the crack indications in the different views is used to determine the depth of the cracks, the matrix cracks in the bottom surface 0 degree lamina (the lamina adjacent to the film pack during the x-raying process) have essentially zero relative displacement in the two views. The matrix cracks in the other laminas are displaced to the left in the right-hand view relative to their location in the left-hand view. The magnitude of the relative displacement indicates the depth

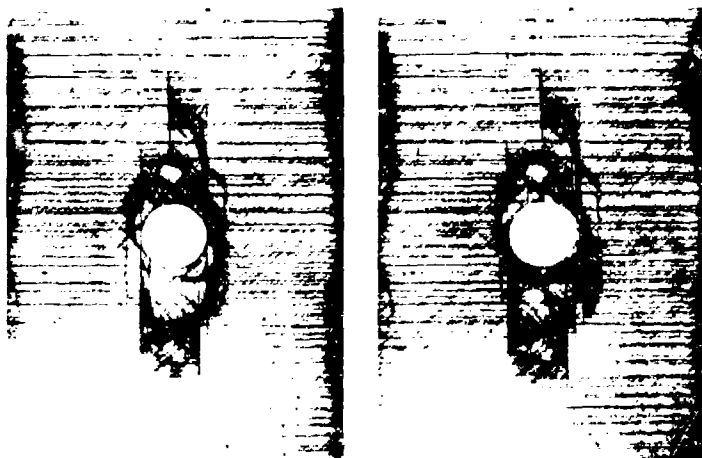


Fig. 7. Penetrant enhanced stereo x-ray radiograph of specimen after 100000 cycles of fatigue loading.

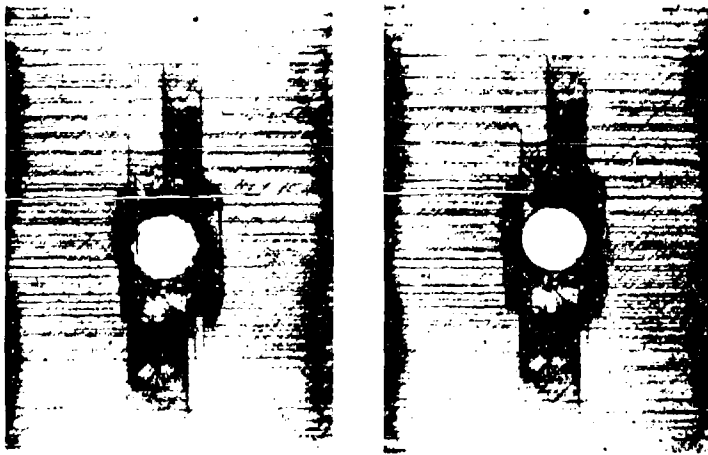


Fig. 8. Penetrant enhanced stereo x-ray radiograph of specimen after 150000 cycles of fatigue loading.

location of the matrix cracks. The matrix cracks with the largest relative displacement in the views are nearest to the top surface of the specimen, while those with an intermediate relative displacement are in the subsurface laminas.

The delaminations around the hole occur at different depths. This can be inferred from the delamination boundaries inside and crossing other delamination boundaries. Some information on the depth location of the delamination can be inferred from the matrix cracks inside and at the delamination boundaries without stereo reconstruction of the stereo pair photographs. The depth location of the delaminations can be determined positively from the stereo pairs. Thus, the delamination indicated by the letter A in Fig. 4 is between the bottom 0 degree lamina and the adjacent -45 degree lamina. Similarly, the delamination indicated by the letter B is between the -45 and 45 degree laminas closest to the bottom surface of the specimen. Based on these considerations, the initial machining damage consists of

(a) An extensive pattern of delaminations near the back surface of the specimen. The delaminations occur between various laminas. They may be due to the use of an improper feed rate during the drilling process.

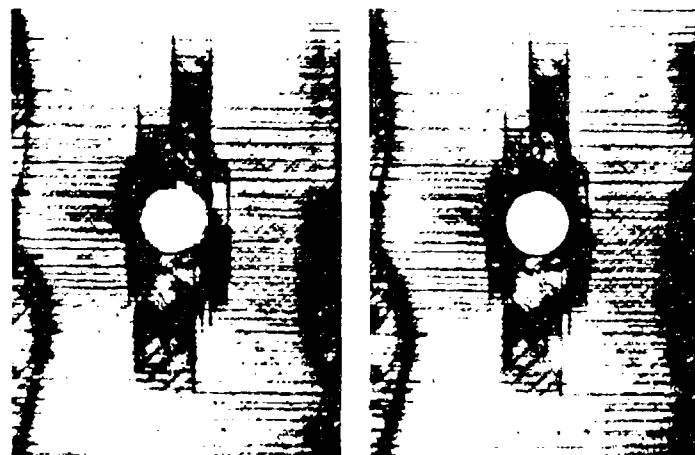


Fig. 9. Penetrant enhanced stereo x-ray radiograph of specimen after 200000 cycles of fatigue loading.

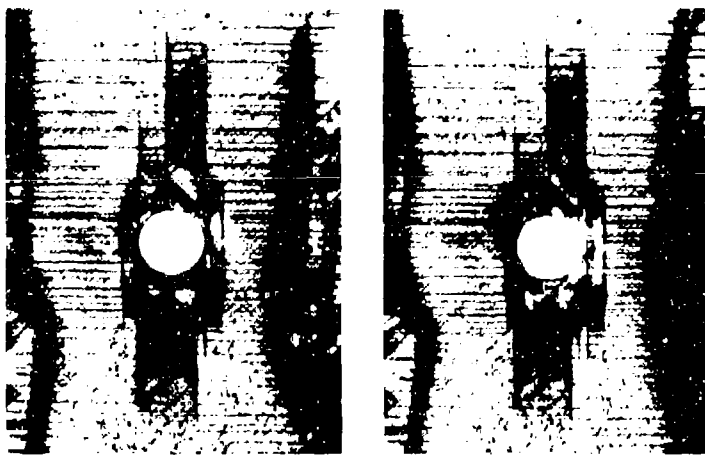


Fig. 10. Penetrant enhanced stereo x-ray radiograph of specimen after 250000 cycles of fatigue loading.

(b) Fiber bundle fractures in the 90 degree laminas nearest to the bottom surface of the specimen have been caused by the drilling process. These can be seen near the lower right edge of the hole.

(c) Extensive matrix cracking in the laminas near the bottom surface of the specimen is present. Again, this matrix cracking has been caused by the drilling process.

As can be seen from Fig. 5, the static load has caused extensive matrix cracking in the 90 and 45 degree laminas. Most of the matrix cracks in the 90 degree laminas have originated at the hole and propagated towards the edges of the specimen. This can be inferred from the horizontal dark lines emanating from the hole that do not reach the edges of the specimen. There are also some 90 degree cracks that started at the specimen edges and terminated in the interior of the specimen. A number of these cracks can be seen to the left of the hole. Finally, a 90 degree matrix crack that does not terminate at the hole or the edge of the specimen can be seen above and to the right of the hole. The matrix cracks in the 45 degree laminas are associated with those in the 90 degree laminas. Most of these matrix cracks are very short and seem to have been caused by the 90 degree matrix cracks. With the exception of a 0 degree matrix crack at the left edge of the hole, the matrix cracks in the 0 and -45 degree laminas that were originally present did not grow. The same is true for the delaminations.

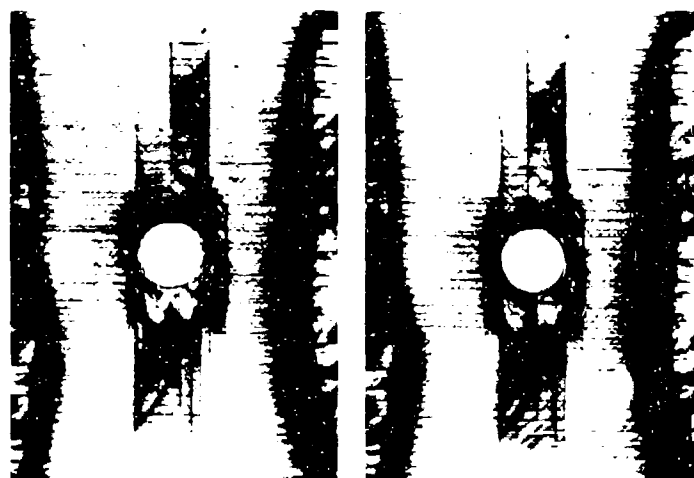


Fig. 11. Penetrant enhanced stereo x-ray radiograph of specimen after 350000 cycles of fatigue loading.



Fig. 12. Penetrant enhanced xereo x-ray radiograph of specimen after 500000 cycles of fatigue loading.

As can be seen from Fig. 6, application of 50,000 cycles of fatigue loading has caused extensive damage growth. The specimen is criss-crossed by a pattern of matrix cracks in the 90, -45, and 45 degree laminas. Matrix cracks in the 0 degree laminas and delaminations near the hole have extended. The matrix cracks occur in all of the laminas. Note that the damage artifacts are washed out in the lower portion of the figure. This is due to improper preparation of the specimen for radiography.

As can be seen from Figs. 7 through 12, the additional cyclic loading causes little change in the extent of the matrix cracking. It causes the delaminations to grow and become progressively more severe. Also, the extent of the matrix cracking in the 0 degree laminas increases. Fiber bundle fractures start occurring. Some of them can be seen in the 45 degree laminas in Fig. 12. Note that the specimen is not even close to failure at 500,00 cycles of fatigue loading.

Finally, Fig. 13 shows a conventional penetrant enhanced x-ray photograph of the specimen that was deplieed to make Figs. 2 and 3. As can be seen from this figure, the specimen contains extensive matrix cracking, delaminations, and fiber bundle fractures. By comparing Fig. 13 with Figs. 2 and 3, we can see how to interpret the damage indications in the x-ray photograph. Thus, jagged lines in x-ray photographs correspond to fiber fractures.

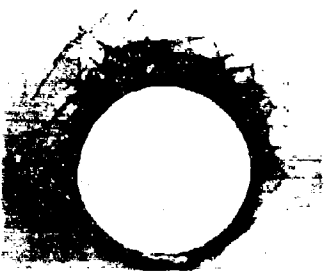


Fig. 13. Penetrant enhanced x-ray radiograph of damage in ($\pm 45/0/90/\pm 45/0/90$)_S graphite-epoxy laminate (Courtesy of S. M. Freeman).

3.2 Holographic Interferometry and Laser Speckle Photography

Holographic interferometry (Refs. 16-24) and laser speckle photography (Refs. 25-29) are two complementary techniques that can be used as NDE tools for conventional and resin-matrix composite materials. In both techniques, the object being inspected for defects or damage is illuminated with laser (coherent and monochromatic) light. When viewed under laser light, the object appears grainy or speckled. The speckle is due to random interference within the resolution limit of the eye or photographic system used to record an image of the object.

Holographic interferometry involves making a hologram (a holographic recording) of the object being inspected. Since references 16-17 contain an excellent description of how holograms are made, this topic will not be treated here. It suffices to say that holography is a technique by which the image of a three dimensional object can be stored and retrieved from a two dimensional photographic emulsion. A standard off-axis holographic setup is shown in Fig. 14. It consists of a laser, a beam splitter to split the laser light into reference and object beams, mirrors to reflect the laser beams, beam expanders to broaden the beams, object being recorder, a photographic plate to record the image of the object, and an optional optical imaging lens. The imaging lens is not used when making conventional holograms and is only required if the user wants an "image plane hologram".

The hologram is such an accurate recording that if two exposures are made on one emulsion with a slight distortion applied to the body being recorded between the exposures, the reconstructed light waves emanating from each of the recorded states interfere and produce a beat frequency pattern called interferometric fringes. These fringes are like lines of elevation on a contour map in that each fringe represents the locus of points on the surface of the object that have been displaced in the normal direction by a multiple of one-half the wavelength of the light used to record the hologram. For a Helium Neon laser, this amounts to about $0.32 \mu\text{m}$ per fringe. For NDE purposes one is interested in finding anomalies (or abrupt changes) in the fringe pattern and not in actually measuring the precise displacements everywhere on the object. If the specimen being examined is free from defects or damage, the fringe pattern will be smooth with uniform variations. This is illustrated in Fig. 15, which shows the fringe pattern caused by an axial compressive load on a fiberglass cylinder with a rectangular cutout. The fringe pattern is smooth with uniform variations everywhere, except in the region to the left of the cutout. In this region, the fringe pattern exhibits anomalies caused by surface cracks induced during fabrication. The anomalies are of two types, namely, cusps in the fringes and lack of uniformity in the variation of the spacing between the fringes. The former type of anomaly occurs just above the lower left-hand corner and approximately two-thirds of the way up the left-hand side of the cutout, while the latter type occurs near the upper left-hand corner of the cutout.

A number of methods, each of which may produce the best fringe pattern for detecting a given defect in a given material, are available for inducing a change in the surface of the specimen between exposures. Depending upon the specimen being examined, these include mechanical, thermal, and acoustic loading. It is difficult to give a specific set of guidelines as to which technique will work best for a given specimen. However, some general guidelines are possible. One must always keep in mind that the goal of the loading is to produce a localized displacement normal to the surface being inspected. Thus, the thermomechanical properties of the specimen and the type and location of the defect being sought must be considered in choosing the loading technique. For example, a small crack in a metallic sheet is very difficult to find except by stretching or bending the sheet and looking for differences in displacement across the crack faces. Thermal loading would produce practically no displacement anomaly.

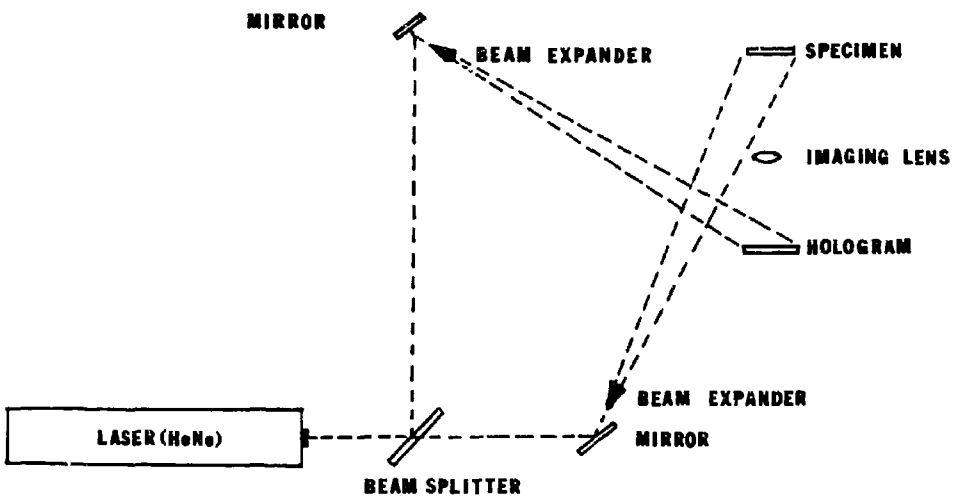


Fig. 14. Schematic diagram showing standard off-axis holographic setup.

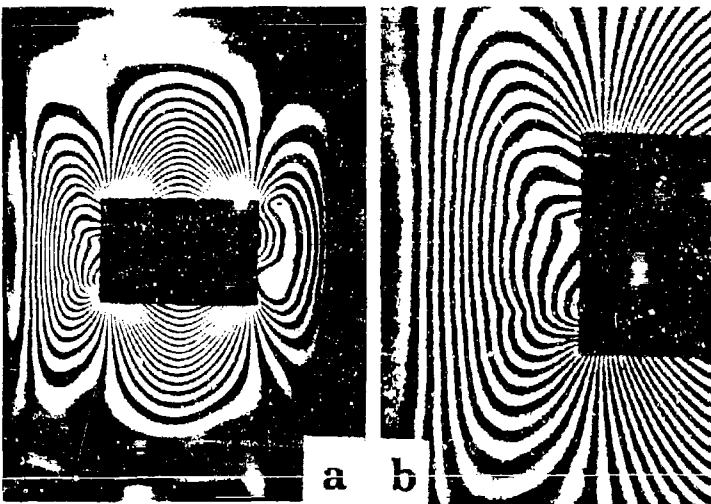


Fig. 15. Axial compressive loading induced holographic fringe pattern showing anomalies caused by manufacturing induced surface cracks in a fiberglass cylinder with a rectangular cutout.

since heat flows easily around the crack. In the case of honeycomb sandwich structures which are perhaps the easiest to inspect, thermal stressing works well since the cell walls restrain the surface except where debonds occur allowing relatively large localized displacements of the face sheet to occur.

Just as there are many possible methods for loading the specimen, the interferometric fringe patterns can be observed and recorded in a number of ways. In addition

to the double exposure technique mentioned above, real time holography can be used. In real time holography, a single exposure hologram of the specimen being examined is first made. After developing and drying the emulsion, the hologram is replaced in exactly the same position that it occupied during the exposure. If the hologram and specimen being examined are simultaneously illuminated with coherent light and viewed through the hologram, one sees the actual and reconstructed surface of the specimen exactly superimposed. If the specimen is loaded to disturb its surface, a fringe pattern is observed as in the case of the double exposure technique. This fringe pattern can be recorded by photographing the specimen through the hologram. If the loading on the specimen is changed, the fringe pattern moves and, hence, this technique can be used to examine the transient behavior of the surface of the specimen. Real time holography is often used in conjunction with thermal loading. In this case a single exposure hologram of the unheated specimen is made, developed and properly repositioned. Then, the specimen is heated and viewed through the hologram. By heating to different temperatures, any desired fringe pattern can be recorded.

As can be seen from Fig. 15, the holographic interferogram has a speckled appearance. This speckle noise can be eliminated by using image-plane holography. In image-plane holography, a standard camera lens is placed between the specimen and film plane as shown in Fig. 14 (Ref. 24). This arrangement produces a hologram from which the image of the specimen can be reconstructed using noncoherent white light. The resulting image is of higher quality than the laser reconstructed image since it does not contain the speckle noise that results from coherent light reconstruction.

A typical sequence of interferograms made from image-plane holograms of the specimen used in the stereo x-ray photographs in Figs. 4 through 12 is shown in Figs. 16 and 17. Figures 16 and 17 show front and back surface interferograms of the specimen, respectively. As can be seen from views a in Figs. 16 and 17, the specimen contains fabrication induced damage. The damage consists of a large delamination region near the back surface of the specimen (anomalous fringes in the vicinity of the hole in Fig. 16a) and a small delamination near the front surface (fringe anomalies near the hole in Fig. 17a). No evidence of matrix cracking can be seen. Thus, the interferograms do not provide the detailed information that can be obtained by using radiography (see Fig. 4).

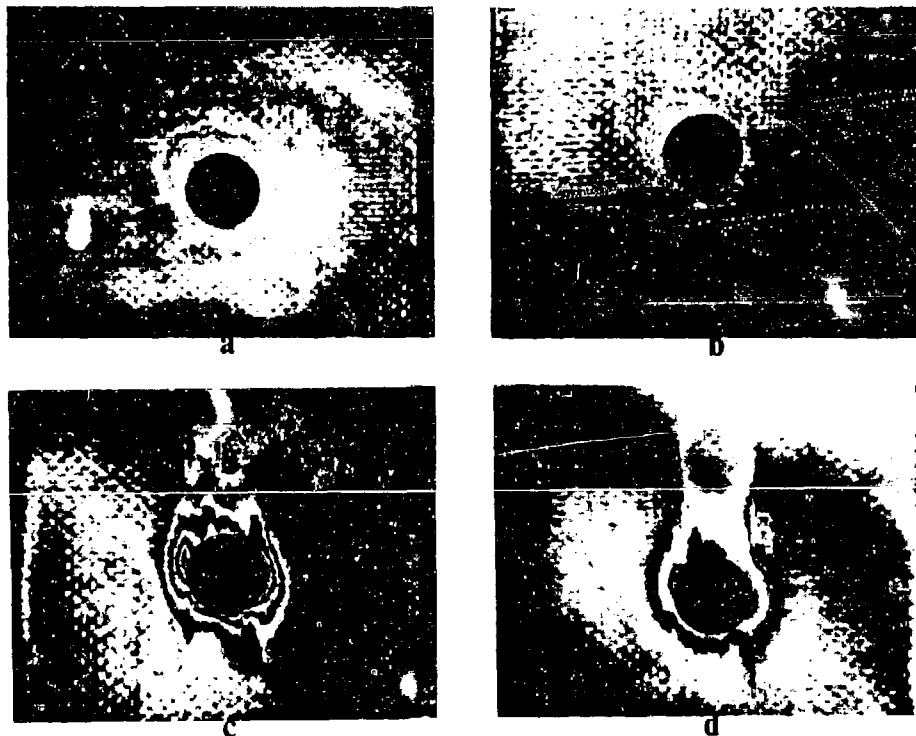


Fig. 16. Front surface interferograms for specimen showing damage present (a) initially, (b) after static load of 13.3 kN, (c) after 50000 cycles, and (d) after 100000 cycles.

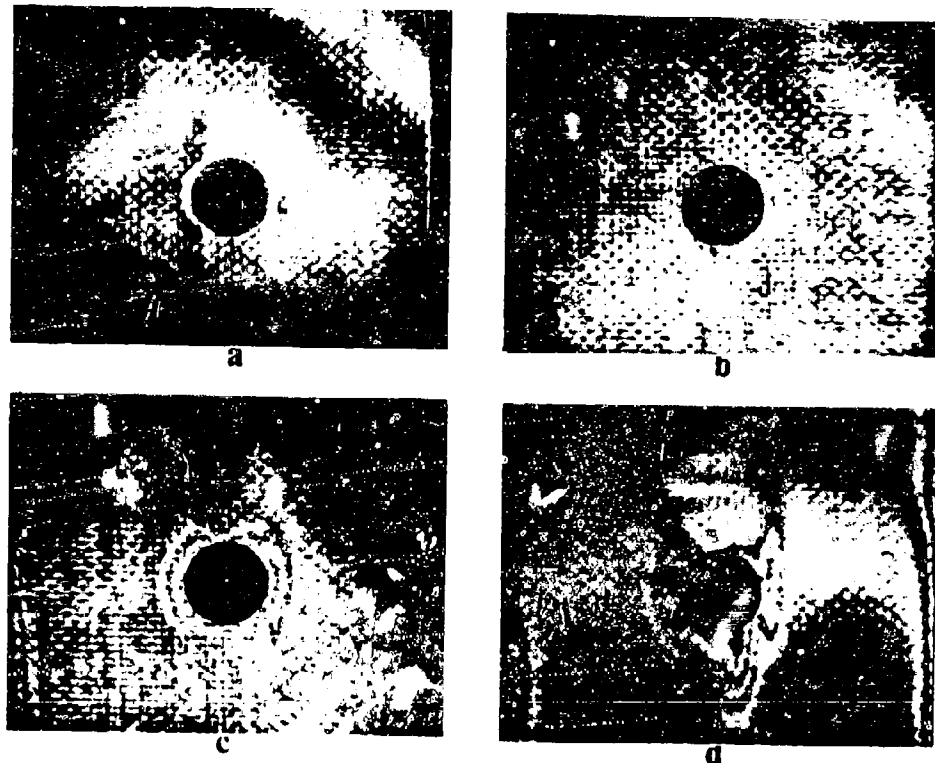


Fig. 17. Back surface interferograms for specimen showing damage present (a) initially, (b) after static load of 13.3 kN, (c) after 50000 cycles, and (d) 100000 cycles.

The damage resulting from the static tensile load is shown in views b of Figs. 16 and 17. As can be seen from a comparison of views a and b in Figs. 16 and 17, the delaminations have not grown as a result of the tensile load. The damage resulting from 50000 cycles of constant load amplitude fatigue loading is shown in views c of the figures. As can be seen from these views, the delaminations grew considerably as a result of the cyclic loading. The delamination indications in Figs. 16 and 17c are distinctly different in appearance from each other. This implies that different delaminations are actually seen in the front and back surface interferograms. The vertical cusps in the anomalous fringes near the hole suggest the presence of surface lamina matrix cracks. This is confirmed in Fig. 6, which is the corresponding penetrant enhanced stereo x-ray view of the damage. The damage resulting from 100000 cycles of constant load amplitude fatigue loading is shown in views d of Figs. 16 and 17. As can be seen by comparing views c and d in these figures, the delaminations have as a result of the additional fatigue loading. The delaminations have also caused matrix cracks in the 0 degree laminas (vertical lines in Fig. 17d) away from the hole.

Even though image-plane holography was used to eliminate the speckle noise from the interferograms shown in Figs. 16 and 17, the speckle noise contains information about the in-plane displacements of the body (Refs. 25-29). Thus, the speckle noise can be used to obtain the in-plane displacement and strain fields of the surface of the body. This is done by a process called laser speckle photography to make a specklegram. The specklegram can be made using one of the following techniques:

(a) Make a double exposure photograph of the specimen illuminated by laser light. The specimen is loaded between exposures to produce an in-plane distortion of the surface. The holography setup shown in Fig. 14 can be used to do this by eliminating the reference beam and employing the optical lens (Ref. 25).

(b) Make a double exposure image-plane hologram using a reference beam with lower intensity than the object beam. The image may be reconstructed using a laser or white light reference beam (image-plane holography) or the image can be treated as a conventional specklegram (Ref. 26-27).

(c) Make a conventional double exposure hologram of the specimen. Reconstruct the image of the specimen using laser light and photograph this image. The resulting photograph is a specklegram (Ref. 28).

The in-plane displacements are obtained from the specklegram by directing a narrow collimated laser beam (monochromatic and coherent) through the specklegram. When this is done, diffraction modifies the emerging light rays into a cone. This cone or halo is the result of diffraction from the random distribution of speckles. Since the speckles are recorded in pairs, a parallel fringe pattern (Young's fringes) also occurs in the halo. The Young's fringes are perpendicular to the displacement vector and their spacing is inversely proportional to the magnitude of the displacement. This provides the average displacement in an area the size of the beam diameter. By interrogating different portions of the specklegram, the complete in-plane displacement field can be mapped. Since this is tedious, automated methods have been developed for extracting the displacement information from specklegrams (Ref. 29). This technique can be used to non-destructively map the in-plane displacement field of a loaded specimen containing internal defects and damage, thereby providing information on the location of the defects. Moreover, it can be used to perform experimental strain analysis.

3.3 Ultrasonic Techniques

The parameters defining an ultrasonic (high frequency sound) beam are affected by the acoustic properties of the medium that the beam passes through. Any variation of the acoustic properties of the medium can produce, single or in combination, a change in the velocity, phase, attenuation (transmission amplitude), reflection amplitude, refraction angle and diffraction of the beam. These changes form the basis of various ultrasonic NDE techniques (Ref. 30). Only the ultrasonic through-transmission and pulse-echo NDE techniques are discussed herein.

The parameters that affect ultrasound propagation in composite materials include, but are not limited to, the following. First and foremost are the stiffness properties and density of the material, which determine the directions and energy partitioning of the ultrasonic beam within the material. In fact it is possible to analytically predict what fraction of the energy is partitioned into each refracted wave type by using classical equations developed for wave propagation in single crystals (Ref. 31-32). Second, the microstructure features (fiber volume fraction, porosity, matrix cracking and delaminations, ply orientation, etc.) affect the ultrasonic wave propagation characteristics. For example, the change in stiffness with ply orientation results in the reflection and refraction of ultrasound at each ply interface. Finally, such factors as the condition of the surface, the frequency and type of incident acoustic wave affect the propagation of ultrasound in the composite material.

Classical ultrasonic inspection of homogeneous isotropic materials is a process that requires care and precision if errors in the assessment of the ultrasonic data are to be avoided. The aforementioned complexities can further complicate the situation, but accurate estimates of composite microstructure can be obtained with sufficient care. In fact many of the effects that would at first seem to complicate the inspection process can be used to extract valuable information about the microstructure as will be shown later.

There are two methods, through-transmission and pulse-echo, for obtaining ultrasound propagation data from composite materials and structures. In the through-transmission method, an ultrasonic transducer on one side of the material emits an acoustic pulse which travels through the material and is received by a second transducer located on the other side of the specimen. It is common practice for the two transducers to be coaxially aligned so that their common axis is perpendicular to the surface of the specimen. With this arrangement, the amount of energy that is transmitted through the material can be easily monitored as a function of position. Regions of greater than average attenuation of the ultrasound pulse indicate the presence of microstructural features that enhance the scattering of acoustic energy. These features can be detected and mapped. It has been shown that the amount of porosity, moisture, and other distributed properties of the specimen can be easily detected. The quality of the specimen can be inferred using the through-transmission method provided the effect of all pertinent parameters can be properly taken into account (Refs.33-34). Unfortunately, this method is not sensitive to the presence of subtle flaws such as the presence of 'peel plies' and does not provide any information on the depth of the defects that are detected.

In the through-transmission ultrasonic NDE method, ultrasound is passed through the specimen and the attenuation is monitored. The attenuation results from three sources, namely, viscoelastic effects in the resin matrix, geometric dispersion due to the heterogeneity of the composite laminate, and damage dispersion due to internal damage such as delaminations and matrix cracks. By proper selection of the sound wave frequency, the attenuation due to delaminations and cracks can be maximized, while that due to material heterogeneity and viscoelastic effects minimized. The damage is recorded on a C-scan. The C-scan is a series of equally spaced traverses of the ultrasonic transducers across the specimen. With the ultrasonic instrument set to produce a dark print on the recorder paper only when sound passes freely through the specimen, attenuation due to damage causes a white region within the normally dark image of the specimen on the recording. The result is a full-scan plan-view recording of the specimen showing the planar extent of the internal damage. No information on the through-the-thickness distribution of the damage is obtained.



Fig. 18. Sequence of C-scan records showing fatigue induced delamination growth in $[(0/\pm 45/90)_{S_2}]$ graphite-epoxy specimen with circular hole.

The specimen is immersed in water to provide a uniform coupling medium to transmit the sound waves between the transducers and the specimen. If the damage regions extend to the specimen boundaries, water can easily penetrate into the damage regions. Since the attenuation of sound travelling through an interface between two materials varies as the ratio of the acoustic impedances of the materials and the water/composite impedance ratio is much smaller than the air/composite ratio, water in the damage regions is detrimental to ultrasonic detection of damage. Hence, special precautions are required. Normally, the specimen edges are sealed with adhesive tape to inhibit entry of water into the damage regions. Even with this precaution, water can penetrate into the damage if it is severe enough. If this occurs, the C-scans give distorted indications of the damage in that the C-scans show smaller damage regions than are actually present. In fact, the damage zones can be seen to decrease in size as successive C-scans are made. An example of this phenomenon is shown in Fig. 18, which shows a sequence of C-scans of a 2.54 cm wide $[(0/\pm 45/90)_{S_2}]$ graphite-epoxy specimen with a 0.475 cm diameter hole (Ref. 24). As can be seen from the figure, the C-scan after 50337 cycles shows a smaller damage region than the C-scan after 46087 cycles.

In the pulse-echo ultrasonic NDE method, a single transducer both sends and receives the acoustic pulse from one side of the specimen after being reflected from the opposite face. Since the full dynamic range of the receiver is available to amplify any back-scattered acoustic energy, this technique can be made quite sensitive to subtle defects, such as a peel ply. In addition the reflections from the front and back surfaces provide natural time markers that can be used to determine the depth location of the scatterer. The principle disadvantages of the method are that a flaw which is just below the front or just above the back surface can be easily masked by the reflections from the front and back surfaces. This means that flaws near the specimen surfaces can be easily missed. Moreover, it is necessary to record the returned echo trace and to section it at various periods of time representing various depths in the material at each point in the scan of the specimen in order to have an unambiguous presentation of the internal flaws. This is particularly important in situations where several small delaminations or voids on different levels can appear as one large one. This type of inspection is usually performed either in a water bath or by using columns of water sprayed onto the surface of the specimen. The water serves both as a couplant and delay line for the ultrasonic signals. Information is generally presented in a C-scan format in which the signal levels at each point and time or depth is printed or displayed as the transducer is traversed across the specimen. Various attempts have been made to correlate the signal levels with specific internal flaws, but unambiguous correlations have not been possible because of the large number of variables that affect the signal and over which the inspector has little or no control (Ref. 34).

When pulses of very short duration (shock waves) are used, considerably more information can be recorded. The reflected pulses can be recorded on a CRT to give an A-scan. By comparing the reflected pulses from a region containing damage to those from an undamaged region, information on the depth location of the damage can be obtained. By traversing the transducer across the specimen and proper setting of the instrument, a B-scan can be made. The B-scan is a record of the depth location of damage on a line across the specimen. By combining a series of B-scans, a complete picture of the damage can be obtained. An example of a B-scan is shown in Fig. 19, which shows the damage in a quasi-isotropic graphite-epoxy specimen after 50000 cycles of fully reversed fatigue loading. The upper view in the figure is a conventional C-scan of the damage. The lower views are B-scans showing the depth distribution of the damage indications on the three numbered cuts through the damage shown on the C-scan. As can be seen from this example, the pulse-echo ultrasonic NDE technique provides much more information than the through-transmission technique. Even so, no information on multiple delaminations and transverse matrix cracking is provided.

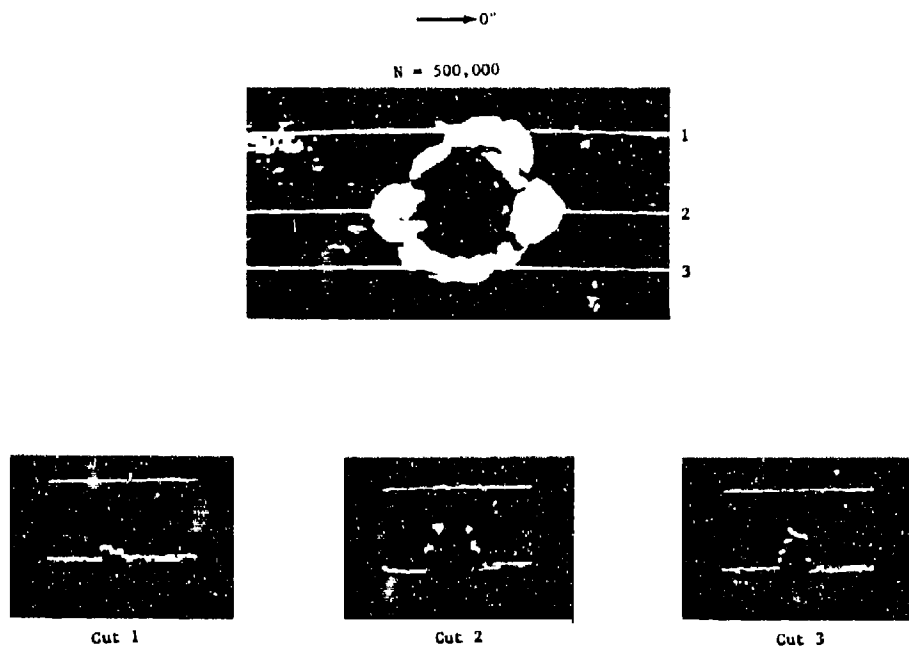


Fig. 19. C- and B-scans of 32-ply quasi-isotropic graphite-epoxy specimen with circular hole after 500000 cycles of fully reversed loading (Ref. 35).

Until recently, it was only possible to unambiguously detect and image delaminations. However, it has been demonstrated recently that it is possible to use an off-axis incidence pulse-echo technique to detect and image matrix cracks (Refs. 36-37). The technique, described in Refs. 36 and 37, can image matrix cracks in a single ply. It has the disadvantage that each ply must be scanned at a specific angle of incidence.

3.4 Thermography

Since defects and damage can perturb heat flow in a resin-matrix composite material, mapping of isotherms (contours of equal temperature) on the surface of the material can be used as a NDE method for locating flaws and damage. In conventional thermography (isotherm mapping), heat flow is set-up in the material and the isotherms are mapped. This can be done by using photochromatic coatings that change color with temperature or infrared photography. Since the defects affect the heat flow, anomalies in the isotherms occur. These anomalies can be used to locate defects.

An alternate technique that has gained acceptance is called vibrothermography (Refs. 38-39). It consists of monitoring the isotherms generated by hysteresis heating of the specimen during cyclic loading. The isotherm pattern depends on the internal damage and, hence, it provides information that can be used to infer the location of the damage. Moreover, the isotherms provide information on the temperature of the specimen, which is required for proper modeling of the fatigue failure process. Since Ref. 38 presents an excellent discussion of vibrothermography and various examples, I will not go into details herein.

3.5 Edge Replication

Edge replication has been proposed recently as an accurate technique for documenting the state of damage in narrow resin-matrix composite specimens (Refs. 40-41). It is a direct application to composite materials of the replication technique used in microscopy for duplicating small surface areas that are not suitable for direct observation.

The edge replica is made by softening one face of a strip of cellulose acetate tape with acetone and pressing the tape against the edge of the specimen. After the softened tape hardens, it is carefully removed and mounted for ease of handling. The edge replica can be examined in a microscope or used as a negative to make enlarged photographs. Normally the specimen, the edge of which is being replicated, is loaded to a low load to open up all the edge cracks.



Fig. 20. Edge replica of $(0/90)_S$ graphite-epoxy specimen after 50000 cycles at 70% of static failure load.

As an example, Fig. 20 shows an edge replica of a $(0/90/90)_S$ graphite-epoxy specimen after 50000 cycles at 70% of the static failure load (Ref. 42). As can be seen from the figure, matrix cracks in the 90 degree laminas are easily documented by this technique. Also, there is evidence of edge delamination. Note that edge replication provides no information on whether the matrix cracks run all the way across the width of the specimen. Thus, the edge replication technique is of dubious value as a research tool.

3.6 Stiffness Change Monitoring

The stiffness of a test specimen depends on its geometry and internal state of damage. As damage accumulates, the stiffness changes. Hence, stiffness change monitoring can be used as a NDE tool to monitor the development of damage (Refs. 43-44). It provides a measure and not a detailed description of the damage. Since modern fatigue test equipment has built-in displacement transducers, the stiffness change can be continuously monitored during fatigue testing. Moreover, the equipment can be set to automatically stop the test when a desired stiffness change occurs. The specimen can then be subjected to complete NDE to document the actual state of damage.

3.7 Acoustic Emission Monitoring

When a material is subjected to external loading, elastic stress waves are generated as a result of microcrack development. These stress waves (known as acoustic emission) propagate through the body and can be detected with the aid of piezoelectric transducers or similar devices. Acoustic emission (AE) in composite materials can have many causes due to the various modes of failure (fiber fracture, matrix cracking and delamination) that can occur. Various attempts have been made to use the acoustic emission as a NDE tool for documenting damage in composite materials (Refs. 42-46).

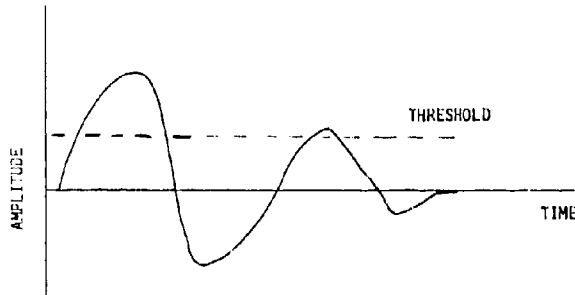


Fig. 21. Schematic representation of an AE signal.

A schematic representation of an AE signal is shown in Fig. 21. The AE signal can be characterized in many different ways. The simplest characterization scheme is to count the number of times that a threshold amplitude value, shown as a dotted line in the figure, is exceeded by the signal. Thus, this particular signal gives two AE counts (number of times the threshold is exceeded). By summing the number of AE counts as the specimen is loaded, a curve of AE counts vs. load level can be generated. By using different threshold levels, different curves can be obtained. The nature of these curves can be used to discriminate between the failure events producing the AE. This scheme is the first one applied to AE monitoring of damage accumulation in composite materials (Refs. 45-46). Since major matrix damage events can produce AE signals containing more AE counts than fiber fracture events, it is questionable whether this particular scheme is actually practical. Moreover, reflections of the stress waves from boundaries can further cloud the issue. Note that a sudden reduction in AE output has been observed to occur prior to tensile fracture (Refs. 49, 3).

The energy content of an AE burst can be easily computed by electronically squaring the AE output and summing over the duration of the burst. Equipment for doing this has been developed and used for damage monitoring (Ref. 45). This AE signal processing scheme suffers from the same drawbacks as the standard AE counting scheme.

To overcome the difficulties inherent in the two previously mentioned schemes, sophisticated frequency analysis schemes have been developed and employed. In these, a fast Fourier transform of the AE burst is performed and the frequency content of the AE signal is used to discriminate between the failure events causing the AE signal. For example, Lloyd-Graham (Ref. 45, p. 107) found that the ratio of the amplitude at 56 kHz to the amplitude at 556 kHz can be used to discriminate the causes of the AE signal. A curve of this ratio vs. time for a delamination is different from that for fiber fracture.

Since the early days, AE monitoring systems using multiple transducers have been developed that can be used to locate the AE source provided that the effect of internal damage on wave propagation in the solid is modeled properly. Since the wave propagation speed in the solid is constant, the arrival times of the AE at the transducers provide a measure of the location of the AE source. By setting the instrumentation to reject AE signals with arrival times at the transducers that are longer than the travel time between the transducers, extreme AE signals can be eliminated. Moreover, the location of the AE source can be determined.

Since AE can be monitored continuously during a fatigue test, AE monitoring can be used to determine when significant damage has occurred. Thus, AE monitoring can be used to determine when to interrupt a fatigue test for damage documentation using one of the other NDE techniques.

4. COMPARISON OF NDE TECHNIQUES

The examples presented in Section 3 were specifically selected to permit direct comparison of the various NDE techniques and to illustrate their strengths and weaknesses. By examining the different figures, it is obvious that the deplying technique provides the most detailed information on the spatial distribution of damage in resin-matrix composite materials. Since the gold chloride marker on the delaminations can obscure matrix cracks associated with the delaminations, this excellent damage documentation method must be supplemented by x-ray radiography if the damage documentation is to be complete.

Of the NDE methods, penetrant enhanced stereo x-ray radiography provides the most detailed information on the spatial distribution of damage. It can easily be used to locate matrix cracks, delaminations, and fiber bundle fractures. If stacked multiple delaminations occur, it is not possible to accurately document all of the delaminations because the penetrant in some of the delaminations may obscure other delaminations. Also, it is difficult to distinguish fiber fractures from adjacent matrix cracks. Finally, it is difficult to obtain prints of stereo radiographs that will reproduce adequately by normal report printing methods, thereby making dissemination of results difficult.

By comparison to deplying and penetrant enhanced stereo x-ray radiography, the ultrasonic NDE methods provide poor results. The conventional ultrasonic NDE methods can only find delaminations. If the delaminations are stacked, then it is questionable whether adjacent delaminations can be resolved.

Holographic interferometry and speckle photography can detect the presence of surface matrix cracks and subsurface delaminations. Only qualitative information about the delaminations can be obtained. Thus, these methods should not be used for damage documentation in damage accumulation studies.

Thermography cannot distinguish damage details unless they occur on the surface. It can be used to determine the temperature distribution on the surface of the specimen. By monitoring the temperature as a function of fatigue loading, inferences can be made about the occurrence of significant damage. Thus, it is a useful supplementary NDE technique.

Edge replication provides extremely accurate information on matrix cracking and delaminations on the surface of the specimen. For narrow specimens, it can be used as a good indicator of the matrix cracking through the width of the specimen. On wide specimens, the matrix cracking along the edges does not extend across the width and, hence, this technique can give erroneous information.

Acoustic emission and stiffness change monitoring do not provide detailed information on the nature of the damage. They indicate when significant damage occurs. Thus, one of these techniques should be used to guide the selection of NDE intervals during fatigue tests.

5. CONCLUSIONS AND RECOMMENDATIONS

The following conclusions follow from the discussion in Sections 2 through 4:

- No single technique, destructive or nondestructive, can provide complete documentation of the spatial distribution of damage in resin-matrix composite materials.

(b) Deploying, a destructive technique, provides the most detailed information on the spatial distribution of delaminations and fiber fractures. To obtain detailed information on matrix cracking, it must be supplemented with x-ray radiography of the deployed samples.

(c) Penetrant enhanced stereo x-ray radiography is the best NDE technique for studying damage accumulation in resin-matrix composite materials. It can be used to obtain an accurate spatial description of matrix cracking, delaminations (if too many are not present), and fiber bundle fractures. If multiple stacked delaminations are present, the information on location of the delaminations may be obscured. Finally, it can be used in place during testing, thereby avoiding difficulties inherent in removing the specimen from the test frame for inspection.

(d) Of the two holographic NDE techniques, holographic interferometry does not provide sufficiently detailed damage information to be useful as a research tool. While not useful as an NDE tool, laser speckle photography can be used as an experimental strain analysis tool to determine the strain distribution due to internal damage in loaded specimens.

(e) Ultrasonic NDE methods do not have the required resolution to be used as research tools for studying damage accumulation in composite materials.

(f) Thermography can provide useful information on the temperature distribution in a specimen undergoing fatigue loading. This information is necessary for rational development of life prediction methods.

(g) Edge replication is a useful damage documentation technique for narrow test specimens.

(h) Acoustic emission and stiffness change monitoring can be used to continuously monitor tests to determine when significant damage events have occurred.

Based on experience with the various NDE methods, the following recommendations are in order:

(a) A combination of NDE techniques should be used to document the damage accumulation process in resin-matrix composite materials. As a minimum, either AE or stiffness change monitoring should be used to determine when significant damage events have occurred. Penetrant enhanced x-ray radiography should be used to document the spatial distribution of the damage just before and after the occurrence of significant damage events. Deploying should be used when penetrant enhanced x-ray radiography cannot resolve the damage details.

(b) A technique should be developed to permit use of stereo x-ray photographs to convey detailed information in report and papers. One approach for doing this is to use electronic image enhancement techniques to increase the contrast between damage indications and the background. This would result in high quality photographs that could be easily printed.

6. REFERENCES

1. Mandell, J. F., Wang, S. S., and McGarry, F. J., "Fracture of Graphite Fiber Reinforced Composites," Air Force Materials Laboratory Report No. AFML-TR-73-142, June 1973.
2. Mandell, J. F., McGarry, F. J., Im, J., and Meier, U., "Fiber Orientation, Crack Velocity, and Cyclic Loading Effects on the Mode of Crack Extension in Fiber Reinforced Plastics," in *Failure Modes in Composites - II*, J. N. Fleck and R. L. Mehan, Eds., AIME, New York, 1974, pp. 33-67.
3. Freeman, S. M., "Damage Progression in Graphite-Epoxy by a Deploying Technique," Air Force Wright Aeronautical Laboratories Technical Report AFWAL-TR-81-3157, December 1981.
4. Freeman, S. M., "Characterization of Lamina and Interlaminar Damage in Graphite-Epoxy Composites by a Deploy Technique," in *Composite Materials: Testing and Design (Sixth Conference)*, ASTM STP 787, I. M. Daniel, Ed., American Society for Testing and Materials, 1982, pp. 50-62.
5. Pless, W. M., Freeman, S. M., and Bailey, C. D., "Advanced Methods for Damage Analysis in Graphite-Epoxy Composites," *SAMPE Quarterly*, Vol. 14, No. 1, October 1982, pp. 40-47. Also in *Material and Process Advances '82*, SAMPE Vol. 14, The Society for the Advancement of Material and Process Engineering, 1982, pp. 550-564.
6. Lauraitis, K. N., Ryder, J. T., and Pettit, D. E., "Advanced Residual Strength Degradation Rate Modeling for Advanced Composite Structures. Volume II - Tasks II and III," Air Force Wright Aeronautical Laboratories Report AFWAL-TR-79-3095, Vol. II, July 1981.

7. McMaster, R. C., Nondestructive Testing Handbook, The Ronald Press Co., New York, 1963, pp. 20.46-20.49.
8. Radiography in Modern Industry, Eastman Kodak Co., Rochester, New York, 1970.
9. Halbert, B., X-Ray Photogrammetry, Basic Geometry and Quality, Elsevier Publishing Co., Amsterdam, 1970.
10. Sendeckyj, G. P., Maddux, G. E., and Porter, E., "Damage Documentation in Composites by Stereo Radiography", Damage in Composite Materials, ASTM STP 775, K. L. Reifsnider, Ed., American Society for Testing and Materials, 1982, pp. 16-26.
11. Shelton, W. L., "Application of an Improved Radiographic Technique to the Evaluation of Carbitex-700 Composite Material," Technical Memorandum AFML-TM/LL-71-5, Air Force Materials Laboratory, Wright-Patterson AFB, Ohio, August 1971.
12. Shelton, W. L., "New Radiographic Inspection Technique," U.S. Patent No. 3704370, 28 November 1972.
13. Chang, F. H., Couchman, J. C., Eisenmann, J. R., and Yee, B. G. W., "Application of a Special X-ray Nondestructive Testing Technique for Monitoring Damage Zone Growth in Composite Laminates," Composite Reliability, ASTM STP 580, American Society for Testing and Materials, 1975, pp. 176-190.
14. Rummel, W. D., Tedrow, T., and Brinkerhoff, H. D., "Enhanced X-Ray Stereoscopic NDE of Composite Materials," Air Force Wright Aeronautical Laboratories Technical Report AFWAL-TR-80-3053, June 1980.
15. Rummel, W. D., Tedrow, T. L., and Brinkerhoff, H. D., "Enhanced X-Ray Stereoscopic NDE of Composite Materials," 14th Symposium on Nondestructive Evaluation, April 1983.
16. Grubinskas, R. C., "State of the Art Survey on Holography and Microwaves in Non-destructive Testing," Technical Report AMMRC MS 78-9, Army Materials and Mechanics Research Center, Watertown, Mass., September 1972.
17. Holographic Nondestructive Testing, R. K. Erf, Ed., Academic Press, New York, 1974.
18. Erf, R. K., Gagosc, R. M., Waters, J. P., Stetson, K. A., and Aas, H. G., "Non-destructive Holographic Techniques for Structural Inspection," Technical Report AFML-TR-74-130, United Aircraft Research Laboratories, East Hartford, Conn., October 1974.
19. Erf, R. K., Gagosc, R. M., and Waters, J. P., "Holography: A New NDT Tool Comes of Age," Materials on the Move, National SANPE Technical Conference Series Volume 6, Society for the Advancement of Material and Process Engineering, 1974, pp. 97-109.
20. Kurtz, R. L. and Liu, H. K., "Holographic Nondestructive Tests Performed on Composite Samples of Ceramic-Epoxy-Fiberglass Sandwich Structure," NASA Technical Report R-430, National Aeronautics and Space Administration, Washington, D.C., June 1974.
21. Kinariwala, V. R., Ranson, W. F., and Swinson, W. F., "Flaw Detection in Thin Composite Structures with Holographic Techniques," Technical Report ME-AMC-0600, Auburn University, Auburn, Alabama, February 1976.
22. Meyer, M. D. and Katayanagi, T. E., "Holographic Examination of a Composite Pressure Vessel," Journal of Testing and Evaluation, Vol. 5, January 1977, pp. 47-52.
23. Sendeckyj, G. P., Maddux, G. E., and Tracy, N. A., "Comparison of Holographic, Radiographic, and Ultrasonic Techniques for Damage Detection in Composite Materials," ICCM/2, Proceedings of the Second International Conference on Composite Materials, B. Noton, R. Signorelli, K. Street, and L. Phillips, Eds., American Institute of Mining, Metallurgical, and Petroleum Engineers, 1978, pp. 1037-1056.
24. Maddux, G. E. and Sendeckyj, G. P., "Holographic Techniques for Defect Detection in Composite Materials," Nondestructive Evaluation and Flaw Criticality for Composite Materials, ASTM STP 696, R. B. Pipes, Ed., American Society for Testing and Materials, 1979, pp. 26-44.
25. Adams, F. D. and Maddux, G. E., "On Speckle Diffraction Interferometry for Measuring Whole Field Displacements and Strains," Technical report AFFDL-TR-73-123, Air Force Flight Dynamics laboratory, Wright-Patterson AFB, Ohio, December 1973.
26. Adams, F. D. and Maddux, G. E., "Synthesis of Holographic Interferometry and Speckle Photography to Measure 3-D Displacements," Technical Memorandum 73-126-PBR, Air Force Flight Dynamics Laboratory, Wright-Patterson AFB, Ohio, September 1973.
27. Adams, F. D. and Maddux, G. E., "Synthesis of Holography and Speckle Photography to Measure 3-D Displacements," Applied Optics, Vol. 13, No. 2, February 1974, p. 219.

28. Adams, F. D., "In-Plane Displacement Measurements Using Speckle Photographs of Holographic Images," Proceedings of the 1982 Joint Conference on Experimental Mechanics, Society for Experimental Stress Analysis, May 1982, Part II, pp. 913-919.
29. Maddux, G. E., Corwin, R., and Moorman, S., "An Improved Automated Data Reduction Device for Speckle Metrology," Proceedings of the 1981 Spring Meeting, Society for Experimental Stress Analysis, May 1981, pp. 248-258.
30. Krautkramer, J. and Krautkramer, H., Ultrasonic Testing of Materials, 2nd Edition, Springer-Verlag, New York, 1977.
31. Auld, B. A., Acoustic Fields and Waves in Solids, Vol. 1, John Wiley & Sons, New York, 1973.
32. Dean, G. D. and Lockett, F. J., "Determination of the Mechanical Properties of Fiber Composite by Ultrasonic Techniques," in Analysis of the Test Methods for High Modulus Fibers and Composites, ASTM STP 521, American Society for Testing and Materials, 1973, pp. 326-346.
33. Kriz, R. D., "Monitoring of Elastic Stiffness Degradation in Graphite-Epoxy Composites," Proceedings of the American Society for Nondestructive Testing Spring Conference, Boston, MA, March 1982.
34. Teagle, P. R., "Ultrasonic Methods for Determining the Mechanical and Physical Properties of Carbon Fiber Reinforced Plastic Composites," Master of Technology Dissertation, Brunel University, 1978.
35. Pettit, D. E., Lauraitis, K. N., and Cox, J. M., "Advanced Residual Strength Degradation Rate Modeling for Advanced Composite Structures. Volume I - Task 1: Preliminary Screening," Technical Report AFWAL-TR-79-3095, Vol. I, Air Force Wright Aeronautica Laboratories, Wright-Patterson AFB, Ohio, August 1979.
36. Bar-Cohen, Y. and Crane, R. L., "Nondestructive Evaluation of Fiber-Reinforced Composites with Backscattering Measurements," 29th Defense Conference of Nondestructive Testing, McClellan AFB, Ca, 17-20 November 1980.
37. Bar-Cohen, Y. and Crane, R. L., "Nondestructive Evaluation of Fiber-Reinforce Composites with Acoustic Backscattering Measurements," Composite Materials Testing and Design (Sixth Conference), ASTM STP 787, I. M. Daniel, Ed., American Society for Testing and Materials, 1982, pp. 343-354.
38. Reifsnider, K. L., Henneke, E. G., and Stinchcomb, W. W., "The Mechanics of Vibro-thermography," Mechanics of Nondestructive Testing, W. W. Stinchcomb, Ed., Plenum Press, New York, 1980, pp. 249-276.
39. Whitcomb, J. D., "Thermographic Measurement of Fatigue Damage," Composite Materials: Tearing and Peeling (Fifth Conference), ASTM STP 674, S. W. Tsai, Ed., American Society for Testing and Materials, 1979, pp. 502-516.
40. Stalnaker, D. O. and Stinchcomb, W. W., "An Investigation of Edge damage Development in Quasi-Isotropic Graphite Epoxy Laminates," Technical Report VPI-E-77-24, Virginia Polytechnic Institute and State University, Blacksburg, Virginia, September 1977.
41. Stalnaker, D. O. and Stinchcomb, W. W., "Load History-Edge Damage Studies in Two Quasi-Isotropic Graphite Epoxy Laminates," Composite Materials: Testing and Design (Fifth Conference), ASTM STP 674, S. W. Tsai, Ed., American Society for Testing and Materials, 1979, pp. 620-641.
42. Jamison, R. D. and Reifsnider, K. L., "Advanced Fatigue Damage Development in Graphite Epoxy Laminates," Technical Report AFWAL-TR-82-3103, Air Force Wright Aeronautical Laboratories, Wright-Patterson AFB, Ohio, December 1982.
43. O'Brien, T. K., "Stiffness Change as a Nondestructive Damage Measurement," Mechanics of Nondestructive Testing, W. W. Stinchcomb, Ed., Plenum Press, New York, 1980, pp. 101-121.
44. Reifsnider, K. L., Stinchcomb, W. W., and O'Brien, T. K., "Frequency Effects on a Stiffness-Based Fatigue Failure Criterion in Flawed Composite Specimens," Fatigue of Filamentary Composite Materials, ASTM STP 636, K. L. Reifsnider and K. N. Lauraitis, Eds., American Society for Testing and Materials, 1977, pp. 171-184.
45. Williams, R. V., Acoustic Emission, Adam Hilger Ltd, Bristol, 1980.
46. Harris, D. O., Tetelman, A. S., and Darwish, F. A., "Detection of Fiber Cracking By Acoustic Emission," Acoustic Emission, ASTM STP 505, American Society for Testing and Materials, 1972, pp. 238-249.
47. Williams, R. S. and Reifsnider, K. L., "Investigation of Acoustic Emission During Fatigue Loading of Composite Specimens," Journal of Composite Materials, Vol. 8, October 1974, pp. 340-355.

48. Guild, F. J., Walton, D., Adams, R. D., and Short, D., "The Application of Acoustic Emission to Fibre-Reinforced Composite Materials," Composites, Vol. 7, July 1976, pp. 173-179.
49. Carlyle, J. M., "Imminent Fracture Detection in Graphite/Epoxy Using Acoustic Emission," Experimental Mechanics, Vol. 18, May 1978, pp. 191-195.

ACKNOWLEDGEMENTS

The paper is based on in-house work performed at the Flight Dynamics Laboratory under the Air Force Wright Aeronautical Laboratories Solid Mechanics Project funded by the Air Force Office of Scientific Research. The author is indebted to Dr. F. D. Adams for his advice during preparation of Section 3.2 and to Dr. R. L. Crane for his help in writing Section 3.3.

AD P 001912

MONITORING OF DEFECT PROGRESSION
BY ACOUSTIC EMISSION

by

Joachim Block
Institut für Strukturmechanik
DFVLR
Flughafen
D-3300 Braunschweig
Germany

SUMMARY

Acoustic Emission is a suited technique for the characterization of damage in composite materials, as also in metallic structures. A lot of tests with different CFRP specimens make sure that there are correlations between certain AE parameters, respectively their variation, and characteristics of defects, which are typical for composites. The damage history of the test specimens can be analyzed with a very good chronological resolution. This includes an exact correlation between acoustic and mechanical parameters, such as load, cycle number etc. The present results demonstrate a potential for distinguishing between some dominant failure mechanisms, as fiber failure and matrix cracking, and noise generated by internal friction. Locating existing defects and tracking spatial damage progression is another field of application. All AE data are being monitored continuously *in situ* during loading the specimen. Post-test-analysis of the stored data with suited computer programs enables a more sophisticated evaluation.

1. INTRODUCTION

Acoustic emission analysis is a NDE technique, which offers the basic test results in real time during the actual loading of the specimen. In addition, the data are being stored for a more sophisticated computer-based evaluation. The AE parameter values, composed to various graphics, may be replayed like a movie and thus give a picture of the damage history of the specimen. AE analysis is an *in-situ*-technique; one doesn't get any information, if the specimen is not being loaded. The method is basically passive, because the test equipment does not emit anything, but only receives the acoustic signals generated inside the tested object.

Release of elastic energy in solids generally leads to acoustic emission. Many phenomena in crystals, polymers, amorphous materials and composites, such as progression of cracks or dislocations, generate elastic (i.e. acoustic) waves in a measurable intensity. The frequency range of these emissions is widespread (see Fig. 1). Even a single acoustic burst generated by some microscopic failure mechanism may contain frequencies extending over several octaves. For the purpose of NDE of composites commonly frequencies of about 10⁷ Hz are being used. At lower frequencies the noise level is too high, while for very high frequencies the damping effects become too strong. Broadband measurements are in use for frequency analysis. However, all test results discussed in this presentation are founded on measurements in the 150 kHz range.

For the analyzability it is essential, that the emissions are discrete, i.e. that they occur as a sequence of separate events. Only then all measured parameters can be correlated properly, as will be discussed below. Before discussing the field of AE application or real experimental results, the signal processing technique and the necessary definitions will be introduced in the following section.

2. ACOUSTIC EVENT DATA PROCESSING

Acoustic waves generated by damage progression propagate through the specimen and hit the piezoceramic transducers (sensors), which are fixed on the specimen surface at suited positions. The transducers generate an electric voltage proportional to the normal elongation of the piezoelectric crystal, which is caused by the acoustic wave. An acoustic burst, transformed into a corresponding electric signal, is schematically shown in Fig. 2. The common expression in AE terminology appertaining to this is "event". In the following, we will use the word "event" in this and only this meaning. The event duration is defined as the time interval between the first and the last intersection of the signal voltage curve and a given threshold level. All signals below the threshold are regarded as insignificant information and being suppressed. The event is really terminated, if no renewed exceeding of the threshold occurs during a given dead-time. (Some AE systems add the event duration and the dead time, the resulting parameter is sometimes called envelope time). For information storage and evaluation the signal is being digitized. Digital pulses, so-called (ringdown-) counts, are being generated synchronously to each exceeding of the threshold level. The other digitized parameters are: the peak amplitude, the rise time (for both see Fig. 2) and the event energy

$$E = c \cdot \int_0^T U^2(t) dt$$

where T is the event duration, U(t) is the signal voltage, and c is an (unknown) constant factor. The system offers an integer number as a result of the integration.

It is proportional to the real signal energy dissipated into the transducer. Each event is given a "date" on the time axis (time from start of the test). This is a most important value, because it enables the correlation between acoustic and mechanical parameters. An arbitrarily chosen example in Fig. 3 shows the complete data set of a single event. The test has been done with 4 channels (4 transducers) used. In addition to the parameters which have been mentioned above, there is a column "timing". Differences in the acoustic waves' time of arrival at the 4 transducers, deriving from different ways from the source, are listed here. In the present example transducer C has been hit first; the last one that has been hit is transducer D, 283 microseconds later. These values contain the basic information for the location of acoustic sources and for the tracking of the spatial progression of defects.

For the analyzability it is essential, that the emissions are discrete, i.e. that they occur as a sequence of separate events. Only then all measured parameters can be correlated properly. If the signal rate becomes so high, that the events conglomerate to a quasi-continuum in an early phase of the test, during which the occurrence of serious failure processes is not yet to be expected, the gain/threshold-relation ought to be reduced. The quantity of information obtainable from AE tests depends strongly on the value of this relation. Large gain values and a low threshold level may lead to system overfeeding. Low gain and a high threshold may cause serious information loss. An optimum has to be found for each type of specimen and loading function.

All test results discussed in the present paper have been obtained with a computerized analyzer system. It is schematically shown in Fig. 4. There are 4 channels, each consisting of preamplifier, filter, main amplifier and signal processor. The digital section is Z-80-based. There are 2 floppy disk drives for data storage, a keyboard and video screen for communication between system and user. A couple of supplementary tools enable the user to get either graphic or alphanumeric type hardcopies and to use several auxiliary functions.

3. DAMAGE HISTORY RESOLUTION

The resolution of the damage progression process relating to time or to synchronously monitored parameters (as load, cycle number, stress, temperature etc.) represents the specific potential of AE analysis. The number of events per unit time and the corresponding event parameter values per unit time or per event can be combined to various distributions and histograms.

First in this section, the damage history of a ring specimen made from a laminate from M40/3000 (fibers) and Epikote 162 (resin) will be discussed as an example. Those CFRP rings have been tested with the purpose of evaluating the influence of certain fiber/resin-combinations on characteristics of the damage progression (in particular on the energy release rates). Certain problems due to the specimen clamping, which occur with other geometries, could be avoided with ring specimens. The load has been applied by a concentric oil-hydraulic tool. The process of defect progression up to failure has been monitored by various instruments; here we only ask for the contribution of AE analysis to the resolution and interpretation of the specimen's damage history. Source location has not been used in these tests because of the annular symmetry of the tested objects. For each event, the parameter values registered in the first-hit channel have been selected for analysis. We will discuss the damage progression using some selected distributions (Fig. 5a-5f).

The test took about 33 seconds. The loading curve was a ramp. The first registered events occurred 4.3 seconds after the start of the test, as to be seen in the "events vs. time"-diagram (Fig. 5a). The acoustic activity went up and down during the following 13.5 seconds, followed by a relative maximum and a sharp caesure. During 3.3 seconds the specimen was almost "silent". Subsequently, 4 phases with a very high event rate, declining towards the end, can be noticed. This diagram (Fig. 5a) shows several remarkable characteristics:

- the maximum at the beginning,
- The maximum prior to the silent phase, which is most probably due to a considerable failure phenomenon,
- the silent phase itself, and
- the slow decay towards the end. This is unusual (the normal case for virginal specimens is an increase of the event rate up to failure). The decay indicates, that critical failure has occurred earlier.

The corresponding amplitude histogram (Fig. 5b) emphasizes the maximum prior to the silent phase. Here the ratio of events per unit time to event amplitude per unit time differs from that in other parts of the distribution. The higher amplitudes are assumed to be due to "strong" failure mechanisms (fiber fracture), as will be discussed below. Fig. 5c (event duration vs. time) shows a distinct difference between the first 18 seconds and the second half of the diagram. The distribution of the "normal" event durations in the first part can not yet be resolved because of the large ordinate scale, which is caused by the enormous duration values in the second half. Since there is no significant difference between the shape of the distribution in the second half of Fig. 5c and the corresponding sections in Fig. 5a and 5b, one can assume a more or less constant ratio in event rate, event amplitude, and duration during this phase of the specimens' damage history ($t \geq 22$ sec from test start). Furthermore, the event duration values are absolutely large, while the amplitude values do not exceed the average. The latter fact becomes obvious by printing out all the event parameter values one by one alphanumerically, which cannot

COMPONENT PART NOTICE

THIS PAPER IS A COMPONENT PART OF THE FOLLOWING COMPILATION REPORT:

(TITLE): Characterization, Analysis and Significance of Defects in Composite

Materials Conference Proceedings: Meeting of the Structures and

Materials Panel (56th) Held in London on 12-14 April 1983.

(SOURCE): Advisory Group for Aerospace Research and Development, Neuilly-sur-Seine
(France).

TO ORDER THE COMPLETE COMPILATION REPORT USE AD-A134 058.

THE COMPONENT PART IS PROVIDED HERE TO ALLOW USERS ACCESS TO INDIVIDUALLY AUTHORED SECTIONS OF PROCEEDINGS, ANNALS, SYMPOSIA, ETC. HOWEVER, THE COMPONENT SHOULD BE CONSIDERED WITHIN THE CONTEXT OF THE OVERALL COMPILATION REPORT AND NOT AS A STAND-ALONE TECHNICAL REPORT.

THE FOLLOWING COMPONENT PART NUMBERS COMPRIZE THE COMPILATION REPORT:

AD#:	TITLE:
P001 910	Fractographic Analysis of Failures in CFRP.
P001 911	NDE (Destructive and Nondestructive Evaluation) Techniques for Composite Laminates.
P001 912	Monitoring of Defect Progression by Acoustic Emission.
P001 913	Growth of Delaminations under Fatigue Loading.
P001 914	Experimental Investigation of Delaminations in Carbon Fibre Composite.
P001 915	Characterization of Cumulative Damage in Composites during Service.
P001 916	An Empirical Appraisal of Defects in Composites.
P001 917	Correlation between Non Destructive Inspection Results and Performance of Graphite/Epoxy Structural Parts.
P001 918	The Effect of Damage on the Tensile and Compressive Performance of Carbon Fibre Laminates.
P001 919	Behaviour of Idealized Discontinuities and Impact Damages in CFRP under Fatigue Loading.
P001 920	Advanced N.D. Techniques for Composite Primary Structures.
P001 921	Computation of Influence of Defects on Static and Fatigue Strength of Composites.
P001 922	Fracture Mechanics of Sublamine Cracks in Composite Laminates.
P001 923	The Significance of Defects and Damage in Composite Structures.
P001 924	In-Service NDI of Composite Structures: An Assessment of Current Requirements and Capabilities.
P001 925	Effect of Defects on Aircraft Composite Structures.
P001 926	The Engineering Significance of Defects in Composite Structures.
P001 927	Defect Occurrences in the Manufacture of Large CFC Structures and Work Associated with Defects, Damage and Repair of CFC Components.

COMPONENT PART NOTICE (CON'T)

AD#: P001 928 TITLE: Delamination Growth in Composite Structures under
Inplane Compression Loading.

Accession For	
NTIS GRA&I	
DTIC TAB	
Unannounced	
Justification	
By _____	
Distribution/ _____	
Availability Codes	
Dist	Avail and/or Special
A	

DISTRIBUTION STATEMENT A	
Approved for public release; Distribution Unlimited	

be shown here. This leads to the conviction, that all emissions subsequent to the maximum 18 seconds from start have been generated by internal friction. Comparable tests show, that strong friction causes such large clusters of weak events. Here the friction noise has been generated by parts of the bursting ring specimen. The actual failure is due to fiber fracture.

To make sure that this explanation is right, we use the hydraulic oil pressure as a discrimination parameter: as schematically shown in Fig. 5d, we can set arbitrary thresholds and thus create an acceptance window for the evaluation. For Fig. 5e we have accepted all events generated at $p \geq 0,05 p_{\text{ultimate}}$; post-failure emissions are now suppressed. This diagram supports the above interpretation: Ultimate load ($p = 186$ bar) had been attained 18 seconds from test start, and the specimen failed. The corresponding energy distribution (Fig. 5f) emphasizes these facts most striking. The distribution of the "normal" AE energies cannot be resolved graphically, since the failure energy is $\approx 10^3$ times higher (the energy unit used in these diagrams is a relative one, there is no absolute calibration in Joule). The example discussed here demonstrates

- that the defect progression can be characterized by the monitored AE data
- that the accuracy of the evaluation depends on the manifoldness of analyzed diagrams and that it is important to analyze AE data in their alphanumerical form, too. (In the present example, Fig. 5a alone would easily lead to misinterpretations).

The correspondence between high AE energy release rates and progressing damage is demonstrated in Fig. 6a. A ring specimen of the same type as discussed above, but made from another laminate (Kevlar-fiber-based), failed in several steps. The lower diagram shows the load (i.e. the oil pressure) vs. time, as monitored by the AE test equipment. There are cogent correlations between the breaks in the $p(t)$ -curve and the energy distribution. For Fig. 6b, we have switched over to a smaller scale and better resolution both for the $p(t)$ -curve and for the energies. The abscissa covers (almost) the first minute from start. The energy peaks in this diagram, which disappear in Fig. 6a with its larger scale, must have been generated by the first considerable damage mechanisms. A perceptible correlation with the $p(t)$ -curve cannot be detected any more, even if the graphic resolution of $p(t)$ is improved substantially.

Numerous tests give evidence, that damage progression can be "heard" by its acoustic emissions long before mechanical parameters show any significant variation (e.g. in the stress/strain-diagram).

There is a potential to identify (or to distinguish among) certain laminates respectively their behaviour under various kinds of loading using AE test results like those discussed above. The subject of correlations between characteristics of AE results and certain failure mechanisms and material properties needs further study.

4. CLASSIFICATION OF SINGLE EVENTS

It may happen that the quantity of information obtainable merely from distributions of events or event parameters is not sufficient for a reliable characterization of defect progression. Since all distributions are composed of separate events, criteria for the classification of single AE events relating to different failure mechanisms are required additionally.

While discussing Fig. 5b in the last section we have postulated such a criterion: events generated by fiber fracture have substantially higher peak amplitudes than those generated by resin-controlled mechanisms, friction etc. Indeed numerous tests give evidence of this fact. The typical distribution of amplitudes for macroscopic damage progression in CFRP laminates is shown in Fig. 7: The above thesis means that fiber fractures contribute primarily to the tail of the histogram extending to high amplitudes. Control experiments to estimate the grave influence of damping on that distribution have been made. Preliminary results confirm, that the attenuation of the acoustic waves on their way through the material is indeed strong and depends considerably on the laminate anisotropy. But it is most unlikely, that "genuine" high-amplitude-events (e.g. in the 80 dB-range) appear in the distribution maximum (60 dB lower) because of attenuation, and vice versa. Presupposed are sufficiently limited specimen proportions.

This amplitude criterion, which is confirmed by numerous experiments, verifies results gotten by Averbuch [1].

Rotem and Altus [2] have emphasized the significance of the AE energy release rate (and its correlation with amplitude and count rate). The third parameter to be taken into account besides amplitude and energy is the frequency. Mehan and Mullin [3] have evaluated the frequency, respectively the signature of the signal voltage of single events, as to be seen on an oscilloscope.

Though the basic significance of these parameters (amplitude, energy, frequency) for a classification of signal sources (i.e. of the events) is undisputable (see Bardenheier [4], or Schwalbe [5]), many authors refer solely to the number of counts (positive threshold crossings, see Fig. 2) or count rate. This is probably due to the limitations of the respective AE test equipment. Since counts, amplitude, and the other event parameters are connected among each other, models for the characterization of certain failure modes based on counts and events alone can be developed (e.g. see Harris, Tetelman, and Darwish [6]). However, these models are again macroscopic. A reliable model for microscopic failure mode discrimination, based on the information obtainable from single events, will require all

measurable parameters. Much work on this subject is to be done.

5. AE SOURCE LOCATION

Spatial damage propagation, in particular crack tip progression, can be tracked by acoustic emission. Though the source location resolution is less exact than that of ultrasonic or X-ray techniques, the results are most useful. They enable exact chronological resolution of the spatial defect progression.

The principle of linear location is shown in Fig. 8. All acoustic signals being monitored by the two transducers with a certain transit time difference must have been generated by sources located on a well-defined curve. In the (ideal) case of isotropic velocity of sound this curve is a hyperbola; in real laminates it will look like quite different. But in any case, its intersection with the axis defined by the transducers is unequivocal. A "location value" may be given to this locus. In Fig. 8, this value is "80", i.e. 80% of the distance between the transducers. A calibration prior to the actual test is required to get the transit time of acoustic waves for the whole distance. Thus, a location method for testing laminate bars has been gotten. The condition which has to be satisfied is that the specimens are comparatively long and narrow, since only then the location values will in any case characterize the actual positions of the acoustic emission sources relating to the two transducers.

Fig. 9a-9d shows 4 consecutive location distribution histograms on the 250-, 500-, and 1000-event-level and close to failure. The specimen was unidirectional and center-notched. The notch location in the middle of the specimen can easily be determined. The abscissa corresponds to the specimen length. Progression of axial splitting emanating from the notch tip (first to the right, subsequently also to the left side) is to be seen in Fig. 9c and 9d. Some details are no more resolved graphically in Fig. 9d because of the larger ordinate scale.

The linear location technique has proved itself to be suited for composite materials testing. However, other specimen geometries require more sophisticated location techniques. Preliminary experiments on this subject establish that there are many problems to be solved:

The extension of the linear location method into two dimensions (see Fig. 10a) to planar location is difficult, since for composite materials the triangulation is being complicated by the grave influence of anisotropy. It is obvious, that planar location based on transit time measurements and triangulation is suited for metals, but problematic for laminates. Application of linear location to ring specimens (perimeter $2\pi r$ location value 100%) also creates some problems. The specimen is endless, and the annular geometry may cause equivocal solutions.

The simplest conceivable location method is the multi-channel technique with a transducer network (see Fig. 10b). It has been used for many years for applications such as hydraulic vessel or pipeline testing but is of course unsuited for laboratory investigations. The zone location method (see Fig. 11) is in principle applicable to arbitrary laminates but requires more circumstantial calibration. Here patterns of transit time differences are being stored during calibration. During the actual test they are being re-correlated to the calibration loci with more or less tolerance in the case of occurrence. For tracking of spatial defect progression in complicated specimens this technique seems promising.

6. CONCLUSIONS

Numerous specimens made from various (mainly carbon-fiber-based) laminates have been tested using Acoustic Emission. The results demonstrate a potential to characterize defect progression in such laminates by evaluation of the monitored AE data. Moreover, since AE is an in-situ-technique, the data are already available during the test, respectively during the actual employment of the structure. Thus, the loading process may be influenced or stopped or auxiliary functions may be switched on, if a crucial variation of AE parameters indicates imminent failure.

The potential of AE analysis is schematically compared to that of X-ray and ultrasonic techniques in Tab. 1. It is evident, that the combination of these NDE methods is very promising. However, the AE technique needs further development. Particularly classification criteria for single acoustic events and source location methods have to be improved.

REFERENCES

1. Awerbuch, J., "Monitoring Damage Progression in CFRP by Acoustic Emission", in: Schadensmechanik von faserverstärkten Verbundstrukturen, DFLR-Mitt. 81-25, pp. 45-83 (1981).
2. Rotem, A., and Altus, E., "Fracture Modes and Acoustic Emission of Composite Materials", Journal of Testing and Evaluation, Vol. 7, No. 1, Jan. 1979, pp. 33-40.
3. Mehan, R.L., and Mullin, J.V., "Analysis of Composite Failure Mechanisms Using Acoustic Emissions", J. Comp. Materials, Vol. 5, April 1971, pp. 266-269.
4. Bardenheier, R., "Schallemissionsuntersuchungen an polymeren Verbundwerkstoffen", Mitt. DKI, Darmstadt, in: Z. Werkstofftechnik 11(1980), pp. 101-110.
5. Schwalbe, H.J., "Risszähigkeit glasfaserverstärkter Kunststoffe", Dissertation, RWTH Aachen, W. Germany (1981).
6. Harris, D.O., Tetelman, A.S., and Darwish, F.A., "Detection of Fiber Cracking By Acoustic Emission", ASTM STP 505, American Society for Testing and Materials (1972), pp. 238-249.

	X - Ray	Ultrasonic	Acoustic Emission
Sensitivity of Discrimination (Type of Damage)	+	+	~
	(Cracks etc.)	Delaminations	
Spatial Resolution (Location of Damage)	+	+	~
	(Cracks etc.)	Delaminations	
Chronological Resolution (Generation of Damage)	-	-	+

Tab.1 : ACOUSTIC EMISSION AND COMPLEMENTARY NDE TECHNIQUES

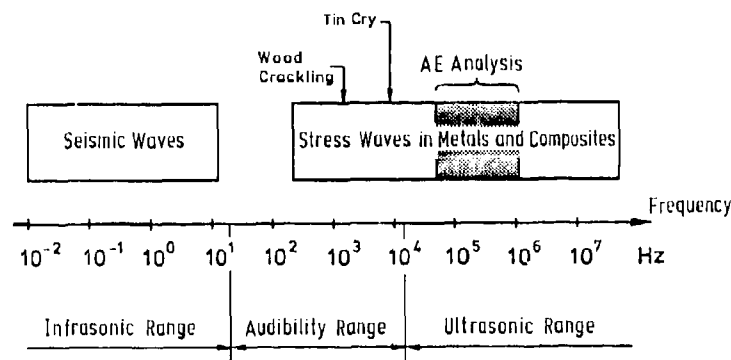


Fig.1 : FREQUENCY RANGES OF ACOUSTIC EMISSION PHENOMENA

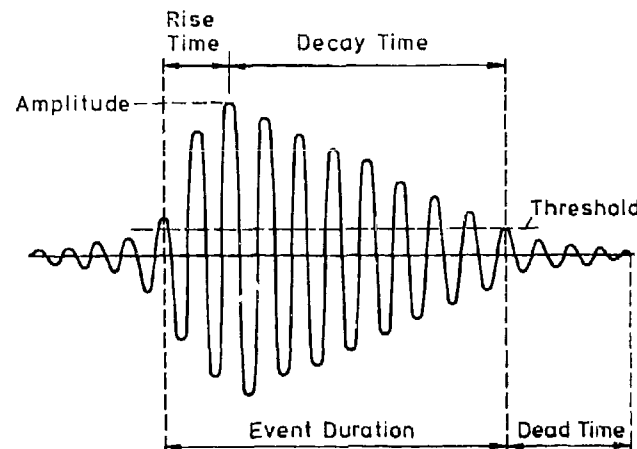


Fig.2 : AE EVENT (SCHEMATIC)

Total No. of events: 00312
 Time from start: 00:02:23.7
 Parametric input: Main Aux 1 Aux 2 Aux 3
 00.81 00.00 00.00 00.39 (Volts)
 This event numbr: 00163

	Timing us.	Duration ms.	Counts	Energy db.	Rise time us.
Channel A:	0044.6	02.099	00317	00514	0048
Channel B:	0202.4	01.330	00203	00415	0076
Channel C:	XHIT#	01.312	00169	00515	0076
Channel D:	0283.0	01.168	00148	00553	0021

Fig.3 : AVAILABLE AS EVENT DATA SET

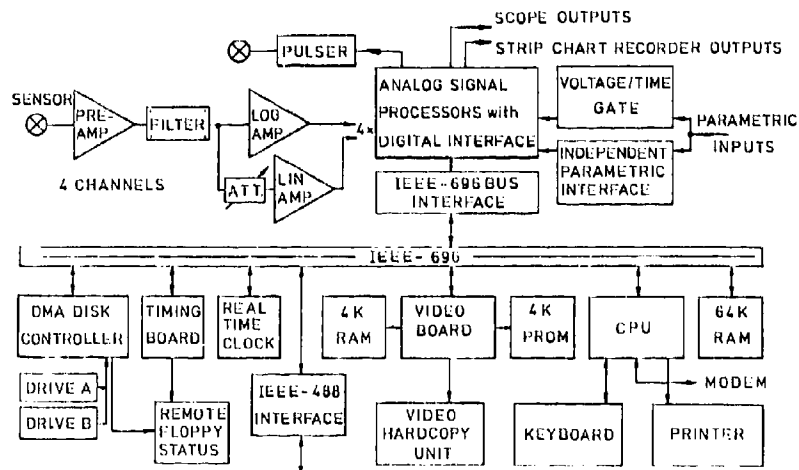


Fig.4 : ACOUSTIC EMISSION ANALYZER

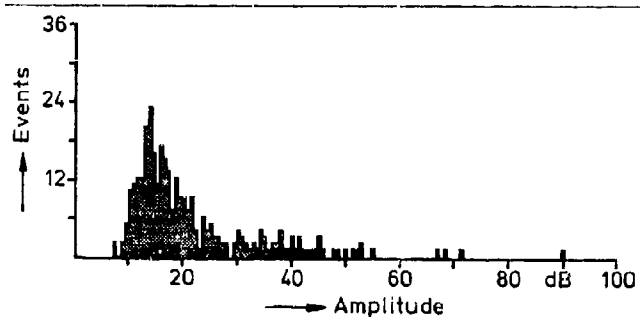
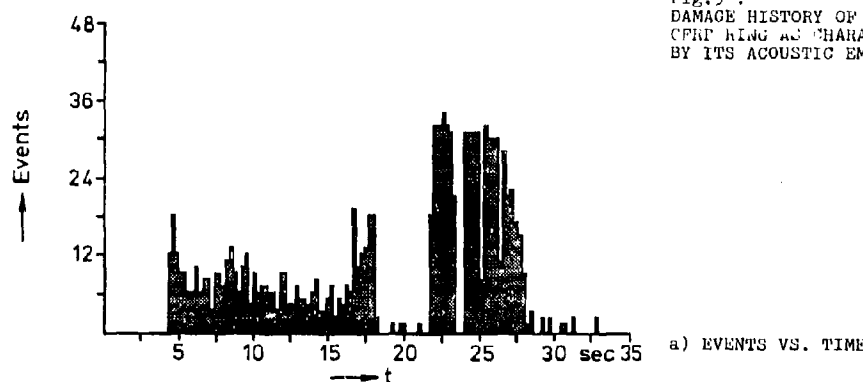
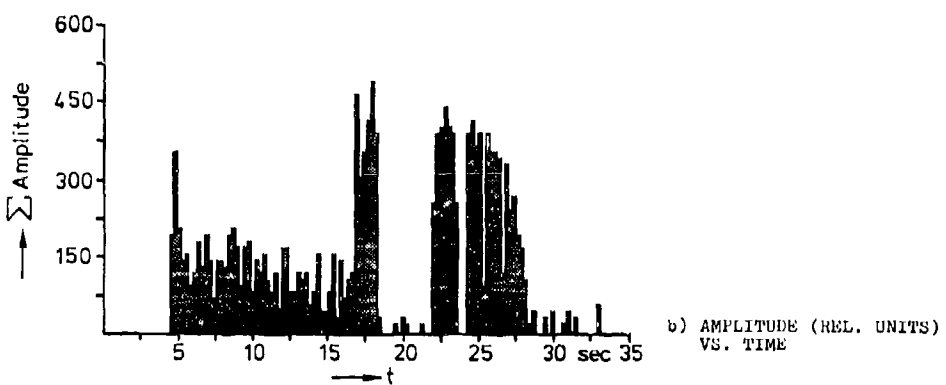
Fig.7 : DAMAGE PROGRESSION IN CFRP :
TYPICAL AMPLITUDE DISTRIBUTION

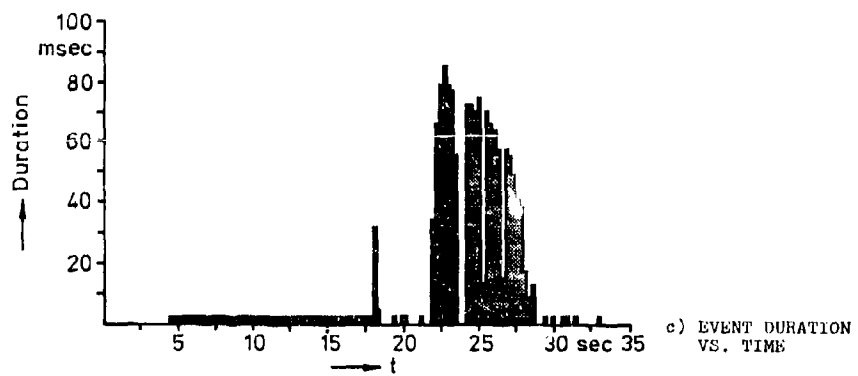
Fig.5 :
DAMAGE HISTORY OF A
CPFR WING AS CHARACTERIZED
BY ITS ACOUSTIC EMISSIONS



a) EVENTS VS. TIME



b) AMPLITUDE (REL. UNITS)
VS. TIME



c) EVENT DURATION
VS. TIME

Fig.5 : DAMAGE HISTORY OF A CFRP RING (continued)

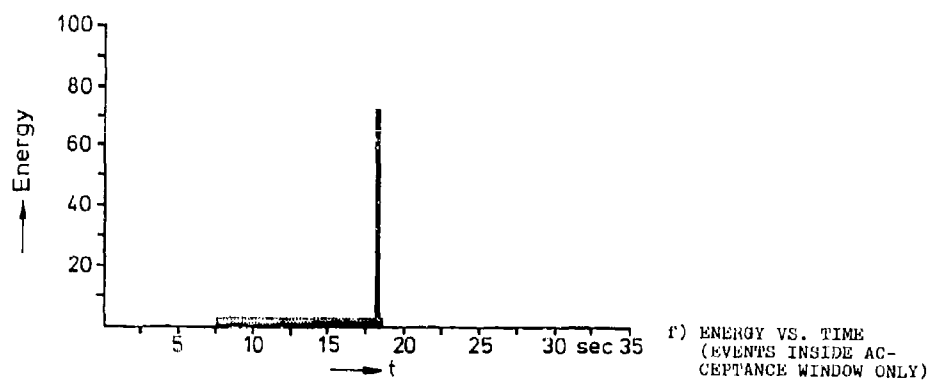
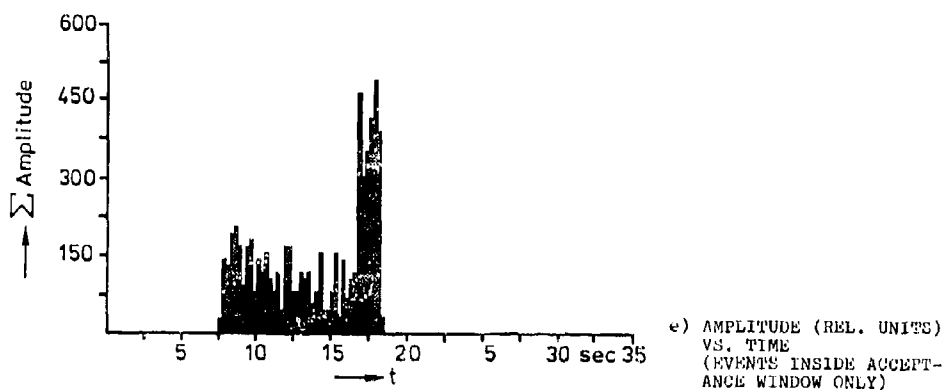
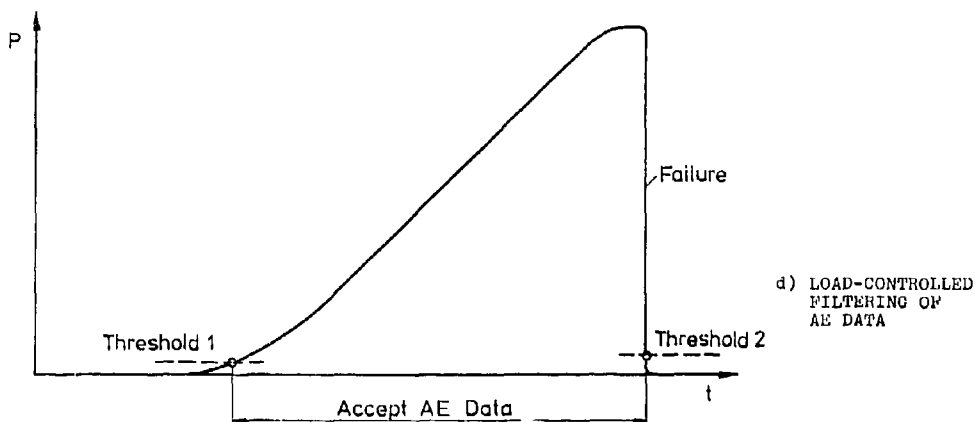
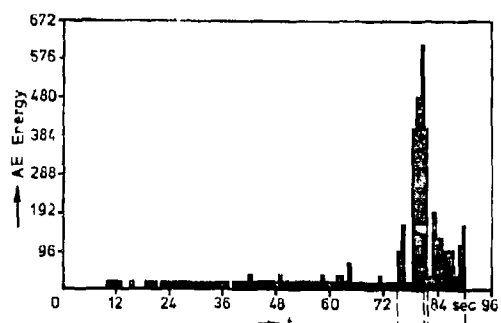
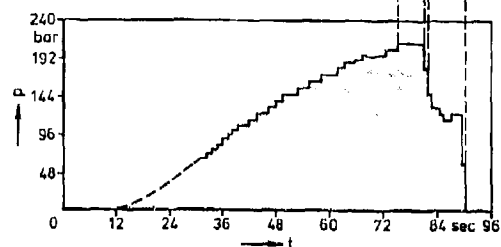


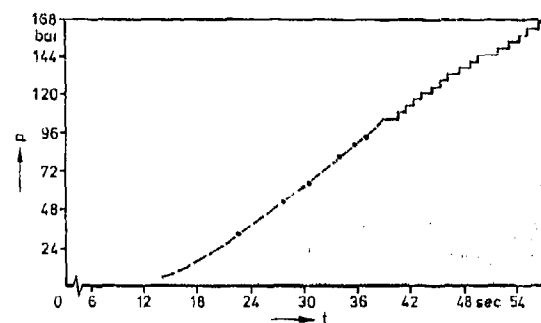
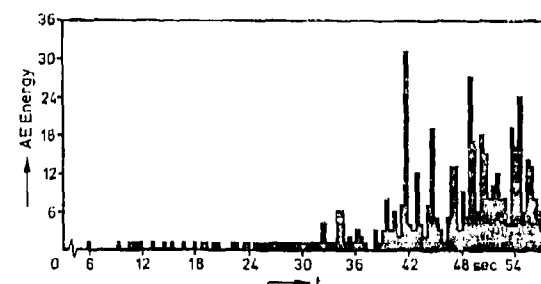
Fig.6 :
UNIDIRECTIONAL FIBER-
REINFORCED RING SPECIMEN :
AE ENERGY RELEASE VS. TIME
AND CORRESPONDING LOAD CURVE



a) UP TO FAILURE

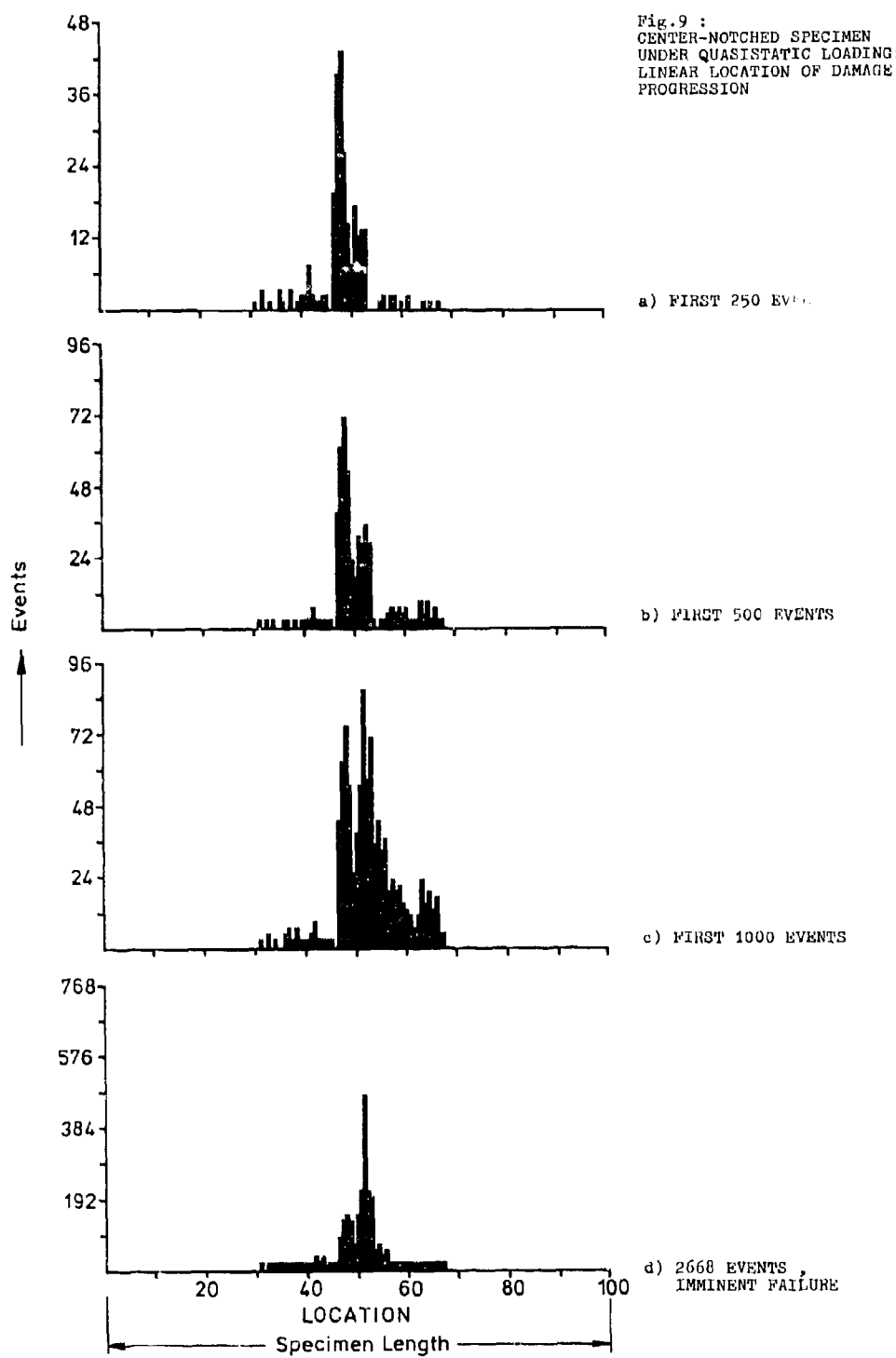


HM 50/Epikote 162 Ring AE 042

b) ENERGY PEAKS IN THE SUB-
CRITICAL LOAD RANGE
(HIGHER RESOLUTION)

HM 50/Epikote 162 Ring AE 042 (early phase of loading)

For Fig.7 please turn over



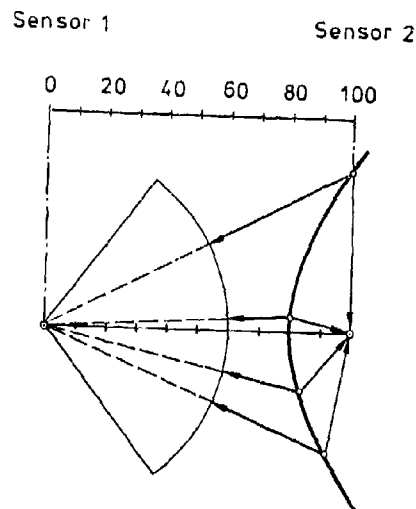


Fig.8 : LOCATION WITH 2 TRANSDUCERS

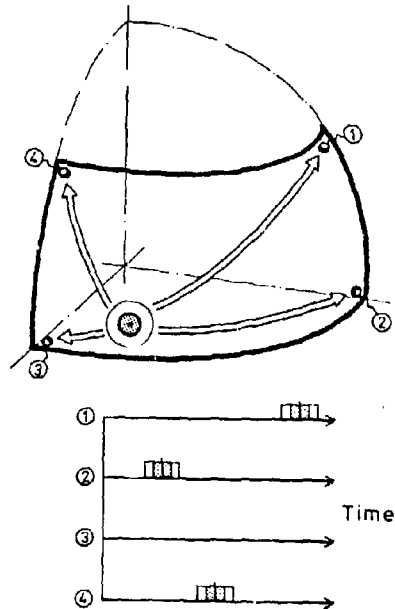
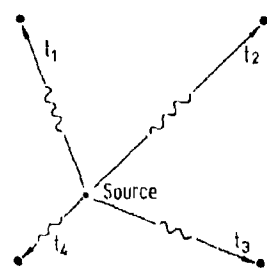


Fig.11 : ZONE LOCATION TECHNIQUE



a) Triangulation

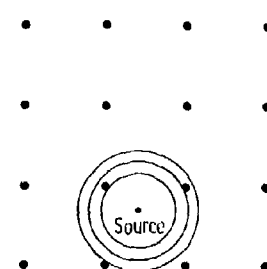
b) Approximate Location
with a Transducer Network

Fig.10 : METHODS OF AE SOURCE LOCATION IN 2 DIMENSIONS



LA DISSECTION DES PIÈCES COMPOSITES :
UNE AIDE PRÉCIEUSE À LA CONCEPTION ET AU CONTRÔLE NON DESTRUCTIF

par
M. BOURGEON

Responsable des Etudes de Méthodes de Contrôles Physico-Chimiques
 Société Européenne de Propulsion - Division Propulsion à Poudre et Composites
 LE HAILLAN
 Saint Médard en Jalles
 33160
 FRANCE

RESUME

Cet exposé montre, au travers d'exemples précis, l'importance qu'il faut attacher à la dissection des pièces en matériaux composites. Cette aide se situe à deux niveaux :
 . à la conception en apportant des informations complémentaires à celles données par les calculs (orientations privilégiées de fibres, qualité des liaisons fonctionnelles, etc...)
 . en contrôle non destructif par la signification réelle des défauts mis en évidence par les différentes techniques et l'incidence qu'il peut en résulter sur le choix des méthodes.

A SEP et plus particulièrement au département Qualité, la dissection des pièces composites est un point important dans notre système de construction de la qualité et nous avons accumulé au cours des années un grand nombre de résultats qui nous ont permis d'établir ce que nous avons appelé une "défauthèque". Cette défauthèque constitue un volumineux document de travail où sont rassemblés les résultats des examens effectués en contrôle non destructif, le rapport d'expertise et la pièce elle-même quand cela est possible.

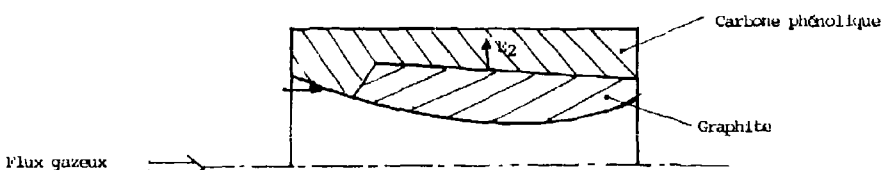
Fort de notre expérience, nous allons voir au travers d'exemples concrets tout l'intérêt que peut représenter un tel travail et ceci dans trois domaines :

- . la conception et la mise en œuvre,
- . les contrôles non-destructifs,
- . les expertises matériaux.

1 - LA DISSECTION ET LA MISE EN ŒUVRE

Dans le domaine de la propulsion, les pièces de veine sont soumises -entre autres- à des efforts thermomécaniques importants. Lorsque ces pièces sont en matériaux composites, l'orientation des strates par rapport au flux de gaz chauds est à prendre en compte. Cette orientation est maîtrisée par l'utilisation de techniques de fabrication telles que le bobinage de ruban ou le drapage de strates pré découpées. Le problème est tout autre lorsque l'on veut mettre en œuvre des matériaux moins onéreux tels que les imprégnés à fibre courte ou les chutes de tissus imprégnés découpés en petits carreaux.

Prenons l'exemple d'une pièce de tuyère d'un petit engin réalisée par une technique dite de surmoulage d'une partie composite (imprégné carbone phénolique en petits carreaux) sur une pièce graphite. La partie composite de cette pièce constitue une protection thermique qui doit également encaisser des contraintes mécaniques. Ces contraintes ont des directions parallèles à l'axe du flux dans la partie amont (E1) et perpendiculaire dans les parties centrale et aval (E2)



Le premier outillage de moulage mis en œuvre pour réaliser cette pièce conduisait à des fissurations et des éjections de la partie graphite lors des tirs au banc. Les dissections de ces pièces nous ont montré que dans la zone de contrainte E2, le flux d'écoulement de la résine conduisait à une orientation des fibres parallèles à la direction de l'effort donc tout particulièrement propice à la fissuration.
 Devant ces observations, nous nous sommes attachés à modifier l'outillage et le processus de moulage de façon à conserver une orientation des fibres perpendiculaires à l'axe du flux dans la partie amont de la pièce mais parallèles dans les parties centrale et aval permettant ainsi un fort accroissement de la résistance mécanique dans cette zone.
 Les exemples de ce type sont multiples et bien souvent la dissection des pièces permet d'apporter une réponse simple et rapide à la solution à envisager pour palier à certains

défauts.

2 - LA DISSECTION ET LES CONTROLES NON DESTRUCTIFS

Si les défauts rencontrés dans les matériaux métalliques sont aujourd'hui pour la plupart bien connus et ne posent pas de véritables problèmes d'interprétation lorsqu'on les met en évidence par des techniques CND, il n'en est pas de même avec les matériaux composites.

Nous traiterons ici l'exemple des pièces en Sepcarb (Sepcarb marque déposée des matériaux carbone carbone développés et industrialisés par SEP) nécessitant une mise en œuvre longue et délicate où le rebut coûte donc très cher. Il est impératif pour les contrôleurs CND de fournir aux ingénieurs qualité un diagnostic précis des défauts rencontrés dans de telles pièces, défauts qui selon leurs gravités sont autorisés ou non au niveau des spécifications.

Des séries de dissections effectuées sur diverses pièces défectueuses nous ont montré que les examens radiographiques habituellement pratiqués en contrôle pouvaient fournir des images identiques pour des défauts de gravité tout à fait différente et conduire par là même à des rebuts abusifs. Cette information nous a conduit à mettre en place un contrôle complémentaire dans certains cas, ici nous avons adopté les ultra-sons qui permettent d'apporter les informations complémentaires nécessaires pour la prise de décision.

3 - LA DISSECTION ET LES EXPERTISES MATERIAU

La détermination de l'origine des défauts permet bien souvent d'apporter les actions correctives nécessaires. Dans ce domaine, la dissection est également une aide précieuse.

Pour illustrer ceci nous prendrons le cas d'une pièce bobinée en carbone phénolique pour laquelle le contrôle radiographique a mis en évidence deux zones distinctes défectueuses.

Une expertise nous a été demandée en vue de déterminer l'origine de cette non-conformité tout à fait inhabituelle. A la dissection nous avons pu constater que le défaut observé correspondait à des zones de fortes porosités. L'enquête a montré que dans ces deux zones le même lot d'imprégné avait été utilisé. Un contrôle physico-chimique à postérieur a été pratiqué sur ce lot de matière et les résultats obtenus ont indiqué un état d'avancement anormal de la résine se traduisant par un manque de fluage et expliquant ainsi le défaut rencontré.

CONCLUSIONS

Nous venons de voir au travers de ces quelques exemples tirés de notre expérience que la dissection des pièces pouvait apporter une aide précieuse lors de la conception et de la mise en œuvre par son action directe sur la conduite du procédé, lors du choix des méthodes et du diagnostic en contrôle non-destructif et enfin lors des expertises matériau. Il est un quatrième volet que nous n'avons pas abordé et sur lequel nous concluerons.

La dissection est en elle-même une méthode de contrôle. En effet, au niveau de certaines spécifications il est très difficile voire impossible de s'assurer de la conformité de certains critères par des techniques de contrôle non-destructif. Dans ces cas précis et qui relèvent du domaine de la production répétitive le procédé de moulage est tout d'abord qualifié puis nous vérifions qu'il n'y a pas de dérive en prélevant une pièce de temps à autre pour dissection.

Nous avons plusieurs exemples de ce type dans nos productions, c'est le cas notamment du cône avant du moteur CRM 56, pièce composite en Kinel (fibre de verre, résine polyimide) pour lequel les spécifications prévoient un contrôle de fibrage.

La meilleure connaissance de son produit est un critère de qualité, la dissection des pièces est un des outils mis à notre disposition pour y parvenir ; il ne suffit bien souvent que d'y penser.

AD P 001913

GROWTH OF DELAMINATIONS UNDER FATIGUE LOADING.

by

R.Prinz
Deutsche Forschungs- und Versuchsanstalt
für Luft- und Raumfahrt e.V.
Institut für Strukturmechanik
D-3300 Braunschweig-Flughafen
Germany

SUMMARY

In order to determine the nature of failure mechanisms a number of fatigue tests were performed. The test specimens partly have artificial delaminations between different layers of the multidirectional laminates made from T300/914C prepgres. For better understanding of the strength degradation in fatigue a damage model, based on the delamination propagation, starting from the free edges between the plies of a multidirectional laminate, has been developed. These defects propagate due to interlaminar stresses up to an area, which is critical in the case of tension-compression fatigue against buckling or shearing of parts of the delaminated test specimen.

LIST OF SYMBOLS

(A)	Extensional stiffness matrix, KN/mm	δ	Phase lag
A_{11}	Stiffness of the laminate in x-direction, KN/mm	ϵ_x^0	Midplane strain
a	Strip delamination size, crack length, mm	v_{11}, v_{12}	Poisson's ratio
a_0	Plastic zone at the crack tip, mm	$g^{(1)} g^{(2)}$	Curvature of delaminated parts (1) and (2), 1/mm
d/dN	Delamination growth rate, mm/cycle	σ	Stress amplitude, N/mm ²
(B)	Coupling stiffness matrix, KN	σ_n	Calculated lamina normal stress, i = 1,2,3, N/mm ²
b	Width of the specimen, mm	σ_s	Calculated lamina shear stress i,j = 1,2,3, N/mm ²
c	Displacement at the edge of the specimen in z-direction, mm	σ_{xz}, σ_{yz}	Laminate normal stress in x-, y-, and z-direction
c_m	Measured value of the crack opening displacement at the edge of the specimen, mm	σ_y	Yield stress, N/mm ²
(D)	Bending stiffness matrix, KN/mm	σ_z	Axial strength, N/mm ²
d	Laminate thickness, mm	ϵ	subscript
E_f	Modulus of a lamina in fiber direction, KN/mm ²	c	Critical
E_t	Modulus of a lamina in transverse direction, KN/mm ²	d	Damaged
G_{11}	Lamina shear modulus, KN/mm ²	f	Failure by static loading
h	Lamina thickness, mm	F	Fatigue failure
k	Plate curvature, 1/mm	l	Longitudinal
M	Resultant moment, acting on the laminate Nmm/mm	T	Transverse
N	Resultant force, acting on the laminate, N/mm	R	Residual
N	Number of load cycles	u	superscript
R	Stress ratio, R = σ_u/σ_y	upper, over	
w	Displacement in z-direction, mm	y	Yield
x,y,z	Cartesian coordinates	(1)(2)	Portion, , 2

1 INTRODUCTION

In the failure analysis of composite laminates, one of the most serious problem has been the propagation of interlaminar cracking, commonly known as delamination. Delaminations may be formed during manufacture due to incomplete curing or the introduction of foreign particle; they may result from impact damage; and they may result from interlaminar stresses existing at discontinuities or at the stress-free edges of a loaded composite structure. This mode of failure is a major cause for the deterioration of laminate structural properties, including its strength, stiffness, reliability and durability. Furthermore, delaminations may grow under increasing load or cyclic loading. Delamination growth redistributes the stress in plies of a laminate, and may influence residual stiffness, residual strength and fatigue life especially under compressive fatigue loads. Hence, a fatigue analysis for composite laminates should take in to account the presence and the growth of delaminations.

The exact formation and growth mechanisms of interlaminar cracking in laminates are not well understood. The general belief is that a certain distribution of small interface flaws with a size in the order of the fiber diameter exist in laminates prior to loading. Under a critical loading condition, which include thermal (curing) stresses, swelling stresses of moist laminates and external loadings, some flaws would grow and coalesce with each other, forming a single crack of macroscopic proportion. Such an event would constitute the onset, or the initiation of the macro-crack.

In a fiber composite laminate made of $[0_2/45/90]_s$ stacking sequence the damage development under tension load usually starts with the appearance of matrix cracks in the off-axis 90° -plies transverse to the load direction. As tension load or load cycles increases, the matrix cracks in the off-axis plies grow up to the adjacent layer and a characteristic pattern of matrix cracks forms as shown in Fig. 1., see item 1. A stable pattern of regularly spaced matrix cracks develops in each off-axis ply predictable by a simple one dimensional model [1]. Riehsnider named this pattern the characteristic damage state (CDS) for matrix cracking. Where the matrix cracks terminate, local interface cracks frequently form at the ply boundaries. For the purpose of illustration a $[0,90]$ _s laminate is presented in Fig. 1. During the cyclic loading localized delaminations develops in the boundary between the 0° - and 90° -layer (see item No. 2) mainly at the edges of the specimen, but in the interior also (see for example item No. 3) [2], [3].

Early investigators focused mainly on experimental and analytical work of free edge induced delamination in laboratory test specimens. A bibliography of this work is contained in Ref. [4]. After one has an understanding of the stress distribution near a free edge by finite element calculations, the next step in treating the delamination problem is to explain the mechanism and the criterion for the edge delamination. One of the most promising techniques for characterizing delamination growth is based on the strain energy release rate G during delamination growth. Measured critical values of G have been used to predict the onset and the growth of edge delaminations in composite laminates [5], [6].

In the present study a technique was developed to characterize the onset and growth of delaminations in composite laminates. First, the damage that developed in unnotched $[0_2/+45/0_2/-45/0/90]$ _s graphite-epoxy laminates under static and cyclic tension and compression loading was determined by nondestructive test methods. During test loading crack opening displacement was monitored to relate delamination-crack opening with delamination size. Next, stress distribution generated from a finite element analysis was correlated with observed damage. The resulting test data and analysis were used to derive a closed-form equation for the edge crack opening associated with the delamination growth. Finally a correlation between delamination size and residual compression strength of fatigued specimens was established.

2. MATERIAL AND TEST EQUIPMENT

Laminates of $[0_2/+45/0_2/-45/0/90]$ _s stacking sequence were fabricated from 914C/T300B graphite/epoxy prepreg tape in a computer-controlled autoclave according to the manufacturers recommended cure procedure. Nominal fiber volume of the laminate was $60\pm 2\%$. The sixteen-ply laminate had an average ply thickness of 0.125 mm. The 380 by 380 mm panels were bonded with fiberglass tabs of 1.0 mm thickness for the clamping reinforcement. These panels were cut by a diamond saw to specimens of different size depicted in Fig. 2. Some of the type II specimens had teflon tabs or an inflation agent embeded between the boundaries of different layers. The coupons were stored and tested under laboratory conditions ($21\pm 1^\circ\text{C}$ and $50\pm 5\%$ relative humidity) 3 to 6 months after fabrication. Some specimens were stored in a climatic chamber for different times to obtain different moisture distributions and moisture contents.

All tests were conducted on a closed-loop Schenck hydraulic testing machine. For displacement measurements strain-gauge transducers (SOT) were mounted on the specimens. To prevent slippage, a fast drying glue was applied on the transducer mounts where touched the specimen.

For measurement of the transverse contraction and transverse crack opening displacement (COD) on some specimens we used the DFVLR-MDR-Transducer (magnetic field depending resistor) [7]. The mounting of the transducer on the test specimen is shown in Fig. 3.

After each step-loading or after certain load cycles, the specimen was removed from the tester and delamination size measurements (C-scan) were made by an ultrasonic testing unit with a narrow waveband emitter [8]. For an exact adjustment of the specimens in the testing machine, the end of the specimens and the clamping device contain fitting holes. Dye-penetrant-enhanced radiography was not used because of the unknown influence of the penetrant fluid on the crack propagation. A Philips SEM 505 scanning electron microscope was used to study and document the topographic features of the delaminated specimen fracture surfaces. [9] Prior SEM examination, gold was sputtered onto the fracture surface to obtain optimum resolution of the topographic features and to minimize static charging by the SEM beam.

3. OBSERVATION OF DELAMINATION GROWTH

During both quasi-static tension tests and constant amplitude tension-tension fatigue tests on $[0_2/+45/0_2/-45/0/90]$ _s laminates the same type of damage developed. First a few isolated transverse cracks formed in the 90° -plies. As these cracks grew in transverse direction the crack spacing decreased by forming new transverse cracks. These were followed almost by the onset of small delaminations along the edge at the transverse crack tip as seen in Fig. 4. The length of the small delaminations grew up to the interconnection with an other delamination during increasing static load or load cycles. Finally the delamination grew much more rapidly along the length of the specimen. In all cases delaminations on both sides of the specimen extended along the entire specimen length between the grips.

To illustrate the growth of the delamination a few ultrasonic C-scans were made on type II test specimen containing teflon circles implants between both of the 90-degree layers in the central position. Fig. 5 shows 4 C-scans of a stepwise tension loaded specimen. The right hand C-scan was made after final failure. This specimen fractured on the lower side with a V-shaped delamination inside the measurement area. Delamination started at a stress of about 750 N/mm^2 at both edges in the boundary between the 0-degree and 90-degree layer and grew slowly. Because of the clamping effect the delamination shape was twisted. There was no delamination growth during tension loading starting from the implants. In the same way a test specimen with an artificial blowing agent delamination degraded during static tension loading. Fig. 6. The internal delamination started from the sharp crack tips of the artificial blowing agent delamination and grew very slowly. The specimen failed at a ultimate strength of 1090 N/mm^2 after 30% of 90-degree layer were delaminated. There is no significant difference between the ultimate strength of artificial delaminated and no delaminated specimens. The load at edge delamination onset as well as the load at delamination the entire length and the ultimate load depend upon the moisture content and moisture profile of the specimen. Fig. 7. The tests were conducted in all cases at a temperature of 21°C .

By way of contrast during compressive loading delamination started from the implants as seen in Fig. 8. No delamination was observed up to the failure load at the edges of the specimen but a small growing of the central delamination was observed.

There are no basic differences in delamination growth between static tension test on one hand and tension-tension fatigue test on the other hand. Compared to those behavior in tension-compression fatigue test delaminations appeared between both the 90-degree and 0 degree layers as well as between the 45-degree and 0 degree layers. Fig. 9 shows the delamination opening of a specimen, which was loaded in tension-compression by a stress amplitude $\sigma_a = 500 \text{ N/mm}^2$ with a stress ratio $R = -1$. After 30.000 cycles at the upper stress state of $\sigma_u = +500 \text{ N/mm}^2$ the delaminated crack between the 0-degree and 90-degree layer was opened. The crack opening size is about 0,1 mm. Fig. 9a. The same delaminated crack is shown in Fig. 9b after unloading to a stress of 0 N/mm^2 . At this loading the size of crack opening is 0,02 mm because of the curing stress. Under compressive stress of $\sigma_c = -500 \text{ N/mm}^2$ delaminations were observed between the 45-degree and 0-degree layers. Fig. 9c.

The delamination progress in the cycling test with a stress ratio $R = \sigma_u/\sigma_c = -1$ is shown in Fig. 10 (Cyclic load, with $\sigma_u = -\sigma_c = 400 \text{ N/mm}^2$) by the aid of C-scans which were taken after various numbers of cycles until the test piece finally fractured. The initiation of the edge delaminations in the 90° layers shows up clearly after 20.000 cycles and also the increase in delamination area at both the test piece edge and at the artificial delamination as well as at the natural delaminations which happened to be present. The edge delaminations were also examined with a microscope. It was seen that delamination occurs in the interface between the 0-degree and the 45-degree layers also.

In the next illustrations is shown the planimetered area of the delamination propagation during fatigue tests. Fig. 11 and Fig. 12. Both specimen with embeded teflon tabs or inflation agent were tested with a stress ratio $R = -1$ and an upper stress of $\sigma_u = 400 \text{ N/mm}^2$. The growth of the different delamination modes were planimetered as the number of load cycles increased.

4. DELAMINATION GROWTH MODEL

The monitoring and the accurate description of the state of damage as a function of static loading and time or fatigue loading is required for successful development of procedures for predicting the residual strength and fatigue life of composite structures. Most of the available nondestructive test (NDT) methods, as for example penetrant enhanced X-ray radiography or ultrasonic C-scanning, require interruptions of testing. One have to remove the specimens out of the testing machine or at least to stop the test. The state of damage in composites can be measured indirect without interruption during testing by the measurement of the change of compliance. [5] One of the most promising techniques for characterizing delamination growth is based on the rate of strain energy released, G , with delamination growth. Measured critical G values have been used in sophisticated analyses [6] to predict the onset of edge delaminations in unnotched composite laminates.

In our present study, a technique was developed, employing the simple line-plasticity model (Dugdale-Barenblatt model).

First, during quasi-static tension loadings and during fatigue tests the transverse deformation in the thickness direction at the edge of the specimen was measured by a special home-made displacement - transducer. Next, stress distribution generated from a finite element analysis was correlated with the observed damage. Then, test data and analyses were used to derive a closed-form equation for the characterization of the delamination onset, and the delamination growth in relation to the crack opening displacement of the delamination (CDD).

4.1 MEASUREMENT OF CRACK OPENING DISPLACEMENT

For the measurement of transverse deformation in thickness direction of the specimen we used the DFVLR-MDR-Transducer (Magnetic field depending resistor). The mounting of the transducer on the test specimen is shown in Fig. 3. Three halve-circle small springs of small bonding stiffness were glued in the presented form at the specimen. The transducer was mounted by a vessel with two incorporated helical springs which supported

themselves at the opposite edge of the test specimen. The tests were conducted in quasi-static tension and constant amplitude tension-tension fatigue. Fig. 13 shows the load-time-functions. The quasi-static loading was interrupted by unloading-loading interval to measure the crack opening displacement due to curing stresses after unloading. I like to present our first test results of a very extensive test serie.

The first quasi-static tension test was run at a constant load rate of $1 \text{ KN/min} = 50 \text{ N/mm}^2/\text{min}$ up to a maximum stress of $\sigma_x = 758 \text{ N/mm}^2$. The stress-deformation recording in Fig. 14 shows at the left hand side the nonlinear lateral contraction of the specimen in thickness- or z-direction (Item 1). The maximum contraction was measured as $c_m = -4 \mu\text{m}$. Under the constant load there was a creep deformation in z-direction. After about 18 minutes the measured value of $c_m = 1 \mu\text{m}$ was positive. Then the specimen was unloaded. (Item 2). Now the specimen start to relax from $c_m = +3.7 \mu\text{m}$ to $+3.5 \mu\text{m}$. After 1 minute the specimen was loaded once more (Item 3) and after 1 minute more, at a total test time of 20 minutes, suddenly the delamination crack starts as seen in Fig. 15a. The crack opening displacement due to delamination (CODD) grew during constant loading with decreasing rate up to $c_m = 135 \mu\text{m}$ after 175 minutes. During this period the stress-deformation response $\sigma_x = f(c_m)$ by unloading-loading of the specimen was recorded at various intervals as seen in Fig. 15a. (Item 4 to 10). The test was interrupted for 18 hours. Then the test starts again with a constant stress of $\sigma_x = 758 \text{ N/mm}^2$. After 20 minutes more the stress was increased at the constant value of $\sigma_x = 826 \text{ N/mm}^2$ for 3 hours. After this time the growth rate was about zero and the crack opening displacement $c_m = 162 \mu\text{m}$. The size of the delamination was monitored by C-scan. Then the specimen was carefully cut into two parts to measure with a scanning electron microscope (SEM) the distance between the crack tip and the edge. During constant amplitude tension-tension tests the stress-deformation response of each specimen was recorded at various load cycle intervals. Fig. 16 shows a typical stress-deformation response. The first cycle starts with the increasing of the load up to an upper stress of $\sigma_x' = 650 \text{ N/mm}^2$ at a stress rate of 1 KN/min. From this stress state the sinusoidal loading starts with an upper stress of $\sigma_x'' = 650 \text{ N/mm}^2$ and the lower stress of $\sigma_x''' = 65 \text{ N/mm}^2$ (Stress ratio $R = 0.1$). The stress-deformation response during the first loading step and at various load cycle intervals seems to be equal to that which was observed in the quasi-static test. From the beginning of cycle loading the original negative deformation of the edge turn to positive values as shown in Fig. 17. The mean value of the displacement increased during the total loading time, but the amplitude decreased up to 2200 load cycles and increased for higher load cycles. After about 11000 load cycles there was a small mistake in the load control which leads to larger displacement. At 12100 load cycles the stress amplitude was raised to shorten the test time. After 13000 cycles the measured crack opening displacement remain constant. The region, in which the free edge delamination was formed, lay in between 2000 and 2200 load cycles. Fig. 18 presents the load history and the displacement history of the CODD-MDR-gage for 3 different states of the damage. The sinusoidal cycling lateral displacement response is defined by the magnitude of the amplitude $1/2 c_m$, the mean value c_m and the phase lag δ between the stress cycling and the displacement response. At the first state I the phase lag δ amounts to $\delta_1 = 180^\circ$. At the second state II the phase lag δ runs from $\delta_2 = 180^\circ$ at 2190 load cycles to $\delta_3 = 0^\circ$ at 2203 cycles. Between these cycle numbers two displacement oscillations (the lateral displacement oscillation and the delamination crack opening displacement oscillation, both of the same frequency) superimpose themselves with a phase lag of $\delta_4 = 180^\circ$. Therefore the amplitude of the measured displacement $c_m/2$ is roughly zero. This state II is the birth of the first small interlaminar cracks, which starts at the edges of the specimen from the tip of the transverse cracks in the 90°-ply (see Fig. 3 Item 4). As observed with the stereo microscope those small interlaminar cracks grew and met another during increasing load cycles. The union of the interlaminar cracks, the so-called "free edge delamination", effected the increasing of both amplitude and mean value of the displacement as seen in Fig. 18 at the state III. The transition takes place between 3000 and 3010 load cycles. The size of the delamination was monitored by Ultrasonic C-scan. The distance between the crack tip of delamination and the edge of the specimen was measured by SEM.

4.2 STRESS ANALYSIS

To obtain quantitative predictions of the onset and growth of delaminations the finite element program ASKA was used. Because delaminations form in unnotched laminates as a result of interlaminar stresses that develop at the edges, a quasi-three-dimensional finite element analysis was performed. Some details of the analysis are described in [10]. The coordinate system is shown in Figure 19. Only $1/4$ of the section needs be analysed because of its symmetry. This quarter includes 8 layers and half the width of the test piece, which was set at 5 mm under the assumption that the edge stresses would fall off very rapidly.

The results are illustrated in the following pictures. Figure 20 shows the deformation of a quarter of the test piece section under a tensile loading of $\sigma_x = 1 \text{ KN/mm}^2$. On the lower and right hand side picture edge, the displacements of the section in the direction are indicated. All originally level surfaces exhibit distortions, in the vicinity of the edge under tensile stressing; these distortions indicate the presence of secondary stresses at the edges. The distribution of tensile stress σ_{11} in the individual layers of the laminate resulting from an applied tensile stress σ_x agree with the results which would also be obtained from the layer theory. Figure 21. The stresses in the 0° layers, which carry the main portion of the load, are 40% higher than the applied mean tensile load, and do not change markedly towards the edge of the test piece. The stresses σ_{22} , arising as a result of the lateral deformation in the various layers are in equilibrium with each other and fall off to zero at the edge, as can be seen from Fig. 22. Contrary to this, the peeling stresses σ_{33} in the 90° layer,

Fig. 23 start from zero in the middle of the test piece in the compressive stress area. They then pass through zero at about 0.2 mm from the edge and display a stress peak right on the edge between the 90°-and the 0°-layer, the height of which cannot be calculated exactly by use of finite element methods. An investigation conducted in the Institut on the effect of the mesh size of the elements, [10] assuming a linear law of elasticity, indicates that the peeling stress at this point and at the edge between the 45°-layers and the 0°-layers, albeit here as compressive stress σ_{11} , under applied stress σ_x becomes infinitely high as the edge is approached. The same conclusion is also valid for the shear stresses σ_{12} and σ_{23} , which are illustrated in Fig. 24 whereas the shear stresses σ_{12} and σ_{23} within and between the individual layers on Fig. 25 and Fig. 26 fall off to zero at the edge. Of course the manufacture-induced intrinsic stresses between the individual layers are included in the investigation. With the aid of the distribution described of the secondary stresses σ_{12} and σ_{23} at the edge of a multilayer laminate, the crack initiation and the crack propagation already described which are observed in static testing or in fatigue testing on an undamaged test piece can be very well explained. As in fracture mechanics it may be assumed that no infinitely high stresses are generated in a real material (in this case the matrix resin between the fiber layers) because of plastic deformation. I will deal with the possibility of using fracture mechanics method on delamination propagation at a later point.

Calculations were also carried out on test pieces with a delamination crack on the edge between the 90°-layers. The peeling stress σ_{11} and the shear stress σ_{12} at the crack tip are of the same order compared with the corresponding edge effect stresses. These stress distributions and the deformation of the cross-section showed reasonable correlation with the observed damage that developed. Indeed, examining σ_{11} and interlaminar shear stress distributions are helpful in identifying likely delamination sites. However the calculation of interlaminar stress distributions by finite element analysis are very extensive. It is only useful for special cases of modelling damage growth qualitatively because the magnitude of calculated peak stresses at the edge varied with mesh size. Therefore, an alternative approach based upon the yield stress criterion was used to predict the delamination size.

4.3 CALCULATION OF THE DELAMINATION OPENING DISPLACEMENT

As known from the results of finite element calculations there exists a stress concentration at the edge of the considered multilayered laminate in the interface between the 90-degree and the 0-degree plies. The behavior of the matrix material in the presence of this stress concentration in interface can be estimated under the assumption, that the extend of the nonlinear stress-strain behavior is limited on a small plastic zone around the stress concentration.

In viscoelastic materials cracks can form and propagate with very low velocities and accelerate slowly [11]. Therefore, estimation of the crack tip velocity and the crack length at any time become necessary to estimate the lifetime of a structure.

A linear elastic stress analysis shows that stresses at the 90-0-degree-interface and at a crack tip become unbounded. [10]. However, materials exhibit a yield stress σ_y above which they deform plastically, and thus there must be a plastic zone around the stress concentration which limits the size of any stresses. One can model this plastic behavior in a simple linear-plasticity model (Dugdale-Barenblatt model).

To analyse the crack opening displacement c of the delamination (CODD) as a function of strip delamination size a and of the axial stress σ_x of the laminate

$$(1) \quad c = f(a, \sigma_x)$$

a simple model was used. Considering a free edge strip delamination of the size a the measured value of the crack opening displacement c_m consists of (see Fig. 27)

$$(2) \quad c_m = c_1 + c_2 + c_3 + c_4 = c + c_3.$$

c_1 is the displacement due to different transverse contractions v_{12} of the single layers in both unbalanced (unsymmetric) delaminated strip induced curvature. c_2 means the displacement due to curing stresses induced curvature; c_3 the displacement due to transverse contraction v_{12} and c_4 the displacement due to yield stress at the vicinity of the crack tip.

To calculate the displacement c_1 parts of the general constitutive equations for the laminate (see for example [12])

$$(3) \quad \begin{bmatrix} N \\ M \end{bmatrix} = \begin{bmatrix} A & B \\ B & D \end{bmatrix} \cdot \begin{bmatrix} \epsilon \\ k \end{bmatrix}$$

have been used, where N and M are the resultant forces and moments acting on the laminate. A , B and D are called the extensional stiffness matrix, coupling stiffness matrix and bending stiffness matrix, respectively. ϵ_x^0 is called the midplane strain and k the plate curvature. This curvature can be expressed for the y -direction as

$$(4) \quad k_y = -\frac{\partial^2 w}{\partial y^2}$$

The main coupling terms of the general constitutive equations (3) for this case are

$$(5) \quad M_y = B_{12} \epsilon_x^0 + D_{22} k_y$$

where the moment $M_y = 0$. Combining Eqs. (4) and (5) and integration leads to

$$(6) \quad w_1^{(1)} = \frac{B_{12}^{(1)} \epsilon_x^0}{D_{22}^{(1)}} \frac{(a+a_0)^2}{2}$$

$$(7) \quad w_1^{(2)} = -\frac{B_{12}^{(2)} \epsilon_x^0}{D_{22}^{(2)}} \frac{(a+a_0)^2}{2}$$

where the subscripts denote the coordinate axis and the superscripts (1) and (2) denote the delaminated parts of the specimen. Therefore the displacement due to different transverse contraction is:

$$(8) \quad c_1 = w_1^{(1)} + w_1^{(2)} = \frac{\epsilon_x^0}{2} (a+a_0)^2 \left(\frac{B_{12}^{(1)}}{D_{22}^{(1)}} - \frac{B_{12}^{(2)}}{D_{22}^{(2)}} \right)$$

The displacement c_1 due to curing stresses induced curvature can be expressed as

$$(9) \quad c_2 = \frac{1}{2} (g^{(1)} + g^{(2)}) (a+a_0)^2$$

where $g^{(1)}$ and $g^{(2)}$ are the individual curvatures of the delaminated parts of the specimen. The transverse contraction of the whole laminate is

$$(10) \quad c_3 = \epsilon_x^0 v_{13} (d^{(1)} + d^{(2)}) = \epsilon_x^0 v_{13} d$$

where $d = d^{(1)} + d^{(2)}$ is the thickness of the specimen. At least the displacement due to constant yield stress σ_y^0 can be estimated like a clamped beam with partly uniform load distribution of the length a_0 as

$$(11) \quad c_4 = \left(\frac{1}{D_{22}^{(1)}} + \frac{1}{D_{22}^{(2)}} \right) \sigma_y^0 \frac{a_0^4}{8} \left(1 + \frac{3a}{4a_0} \right)$$

Substituting Eqs. 8 to 11 into Eq. 2 yields

$$(12) \quad c_m = \left[\left(\frac{B_{12}^{(1)}}{D_{22}^{(1)}} - \frac{B_{12}^{(2)}}{D_{22}^{(2)}} \right) \frac{(a+a_0)^2}{2} - v_{13} d \right] \frac{\sigma_y^0}{A_{11}} + \frac{1}{2} (g^{(1)} + g^{(2)}) (a+a_0)^2 - \left(\frac{1}{D_{22}^{(1)}} + \frac{1}{D_{22}^{(2)}} \right) \left(1 + \frac{4}{3} \frac{a}{a_0} \right) \frac{a_0^4}{8} \sigma_y^0$$

where $\epsilon_x^0 = \sigma_x / A_{11}$.

In Eq. 12 all the properties are known except the length of the plastic zone a_0 . Assuming that a_0 is a material property, we can estimate the value of a_0 by the measurement of c_m on a virgin test specimen at delamination onset stress σ_x . In this case the crack length is $a = 0$ and therefore from Eq. 12

$$(13) \quad a_0 = f(c_m, \sigma_x)$$

For the tested laminates of the stacking sequence [0/+45/0/-45/0/90], fabricated from 914 C/T300B graphite epoxy prepreg tape the amount of calculated plastic zone is $a_0 = 0,5$ mm. The effective modulus properties of each unidirectional ply used for calculation are

$$\begin{aligned} E_L &= 150 \text{ kN/mm}^2, & E_T &= 10.000 \text{ kN/mm}^2 \\ G_{LT} &= 5 \text{ kN/mm}^2 \text{ and } v_{LT} = 0,30. \end{aligned}$$

With these properties the extensional stiffness A_{11} , the coupling stiffness $B_{12}^{(1)}$ and $B_{12}^{(2)}$, the bending stiffnesses $D_{22}^{(1)}$ and $D_{22}^{(2)}$ and the curvatures due to curing stresses $g^{(1)}$ and $g^{(2)}$, were calculated by using classical lamination theory for both delaminated parts.

For our example these properties are

$$\begin{aligned}
 A_{11} &= 107,261 \text{ KN/mm} \\
 B_{11} &= 3,6765 \text{ KN} \\
 D_{11}^{(1)} &= 4,5380 \text{ KN/mm} \\
 g^{(1)} &= 0,003936 1/\text{mm} \\
 G_1' &= 0,06 \text{ KN/mm}^2 \\
 B_{11}^{(2)} &= -0,1739 \text{ KN} \\
 D_{11}^{(2)} &= 0,9136 \text{ KN/mm} \\
 g^{(2)} &= 0,000956 1/\text{mm} \\
 G_x &= 0,758 \text{ KN/mm}^2
 \end{aligned}$$

The curvatures g were estimated for a difference of temperature $\Delta T = 100 \text{ K}$ between test temperature and glass transition point. The strip delamination size a was calculated by the Eq.12 as a function of the crack opening displacement c_m . The results were compared with the size of edge delamination for different delamination states on several test pieces. Therefore delamination sizes were observed by C-scans and by a scanning elektron microscope (SEM) after ending the test and cutting the specimen transverse to the load direction. A comparison made between the measured and the calculated stress-displacement curves at different delamination states is shown in Fig.28 for a quasi-static-test and in Fig. 29 for a fatigue test. The estimation was carried out under the assumption, that \bar{a}_0 (in the place of a_0 at Eq. 12) is growing linear with the increasing stress G_x up to the critical stress G_{x_c} of the delamination onset. ($\bar{a}_0 = a_0 G_x / G_{x_c}$). A good correlation was achieved for the measured and calculated stress-displacement curves.

We are still working on the formulation of delamination growth as a function of time t , $a = f(c_x, t)$ and $a = f(G_x, R, N, t)$, and on the problem of strain energie release rate associated with the delamination growth also in relation to the change of specimen axial compliance. [5].

The objective is to combine the degradation due to growing delamination size in tension-compression cycling with the residual compressive strength of fatigued and partly buckled specimens.

5. FATIGUE AND RESIDUAL STRENGTH MODEL

During quasi-static compressive testing or fatigue testing with considerable amplitudes of compressive stress, failure occurs by the buckling or kinking of individual fibers, fiber bundles or fiber layers which are more or less supported by the matrix resin. The supportive effect is reduced as the delamination progresses, under both tensile and compressive loading. Fracture occurs finally when a portion of the cross-section buckles and the remaining cross-section is no longer sufficient for the transmission of the applied loading. The effect of the antibuckling support which holds the test piece either over the entire area, or on a center line, or on the 2 edges of the gauge area, must be taken into consideration. Whilst the delamination state of a test piece in multi-layered CFRP has no material influence on the residual tensile strength or on the tensile fatigue strength, test pieces with delaminations are especially sensitive to compressive loading.

If the delamination state of a multi-layered test piece during cyclic loading is to be describe, a formulation from fracture mechanics may be used for the purpose [13, 14]. The growth of crack length (or in this case the delamination size a) with increasing number of cycles N is shown by

$$(14) \quad \frac{da}{dN} = g \cdot \bar{G}^m \cdot d^m$$

where \bar{G} is a reference stress in the vicinity of the delamination crack tip, g , m and d are constants to be determined empirically. By integration and insertion of limits for $N = 0$ with $a = a_0$, and for $N = N_d$ with $a = a_d$ the number of loading cycles N is obtained which corresponds to the delamination size a_d :

$$(15) \quad N_d = (a_d^{(1-m)} - a_0^{(1-m)}) / (1-m) g \bar{G}^m$$

Now we assume that the test piece fractures due to compressive loading when the delamination size a reaches a critical value [15]. As shown in Appendix A the critical delamination size a for a cyclic loaded specimen can be expressed as

$$(16) \quad a_d = \left(1 - \frac{G_F}{G_1}\right) \frac{A}{h} \frac{E}{E_i}$$

where G_F is the critical compressive stress, G_1 the compressive strength of the virginial specimen, A the cross section, h the thickness of delamination strips, E the modulus of the non delaminated and E_i the modulus of the delaminated cross section. In the case of fatigue failure the specimen will fracture after N load cycles at the compressive cycling stress amplitude $G_F = G_x$ when the critical delamination size $a_d = a_F$ is reached.

$$(17) \quad a_F = \left(1 - \frac{G_F}{G_1}\right) \frac{A}{h} \frac{E}{E_i}$$

In the case of residual strength test of a fatigued specimen after N_R load cycles the critical damage size $a_d = a_R$ can be expressed by

$$(18) \quad a_R = \left(1 - \frac{G_R}{G_1}\right) \frac{A}{h} \frac{E}{E_i}$$

where G_R is the residual strength. The damage state D can be formulated as a function of dimensionless number of load cycles.

$$(19) \quad D = f \left(\frac{N_R}{N_F} \right).$$

Substituting N_R and N_F by Eqs. 15, 17 and 18 yields

$$(20) \quad D = f \left(\frac{G_I - G_R}{G_I - G_F} \right)^{1-m}$$

For our further considerations we will use the simple expression for the damage state due to delamination

$$(21) \quad D = \left(\frac{G_I - G_R}{G_I - G_F} \right)^{1-m}$$

The validity of this formula was controlled by fatigue tests.

6. FATIGUE TESTS AND RESIDUAL STRENGTH.

Fatigue tests were carried out on type I specimens with a gauge length of 15 mm to determine the number of load cycles to fracture under constant stress amplitude with the stress ratios of $R = -1.0$ and $R = 0.1$. The results are illustrated in Fig. 30. The specimens were supported over their entire area against structural buckling. In order to determine the damage state of the test pieces, additional specimens were subjected to fatigue loads at $R = -1.0$. After certain number of cycles N the residual strength were checked. The results of the residual strength tests are plotted versus the number of loading cycles N_R in Fig. 31. The residual compressive strength falls off continuously with the approach to the number of cycles to fracture N_F , down to the fatigue stress σ_F . The residual tensile strength shows no significant change in comparison with the static strength.

The illustration of residual strength investigation in this form is very complex. In Fig. 32 the damage state D of the test specimens is shown with reference to the progress of delamination. Since the test results are naturally scattered, the equation (21) was expanded by a number of terms which take account of this scattering.

$$(22) \quad D = \alpha + (1-\alpha) \left(\beta \frac{G_I - G_R}{G_I - G_F} \right)^{1-m}$$

where $\alpha = \alpha_1 + \alpha_2$

and α_1 = statistical scatter for a given failure probability P based on static strength.

α_2 = average damage of a virgin test piece with a failure probability of 50%,

β = statistical scatter for a given survival probability P_d based on the load cycles to failure.

The corresponding scatter distributions and curves of equal survival probability $P_d = 90\%$, 50% and 10% are shown in Fig. 32. The damage D to be determined in the residual strength investigations is calculated from equation (20) and entered into Fig. 32. The exponents m determined from the test results as $m = 0,45$. As can be deduced from Fig. 32, the delamination progress can be described satisfactorily with the aid of equations (17), (18) and (21), taking account of the scattering of the test results.

7. SUMMARY

In the present study a technique was developed to characterize the onset and the growth of edge delaminations in multidirectional composite laminates. The delamination that formed under static and cyclic loading in the interface between the layers of the laminates was determined by ultrasonic C-scans. During test loading the transverse contraction and the transverse crack opening displacement due to peeling stresses were monitored. The observed onset of delaminations was correlated with the stress distribution generated from a finite element analysis. The test data and the analysis were used to derive a closed-form equation for the delamination size associated with the onset of cracks and the crack opening displacement. Those defects propagated slowly owing to interlaminar stresses up to an area, which is critical against buckling of parts of the delaminated test specimen in the case of tension-compression fatigue. A correlation between delamination size and residual compression strength of fatigued specimens was derived.

REFERENCES

- [1] Masters J. E. :
Reifsnider, K.L.
An Investigation of Cumulative Damage Development in Quasi-Isotropic Graphite/Epoxy Laminates.
In: Damage in Composite Materials. ASTM STP 775, (1982), pp. 40-62
- [2] Buczek, M.B. :
Berakowich, C.T.
Finite Element Models for Predicting Crack Growth Characteristics in Composite Materials.
Virginia Polytechnic Institute and State University,
Blacksburg, USA, VPI-E-29, Oct. 1982, 131 p.
- [3] Schulte, K. :
Reifsnider, K.L.
Stinchcomb, W.W.
Entstehen und Ausbreiten von Ermüdungsschädigung in CFK.
18. AVK-Jahrestagung, 5.-7. Oktober 1982 in Freudenstadt,
Seite 29-1 bis 29.8.
- [4] Rybicki, E.F. :
Schmueser, D.W.
Fox, J.
Energie Release Rate Approach for Stable Crack growth in
the Free-Edge Delamination Problem.
J. Composite Materials 11 (1977), pp. 470 - 487
- [5] O'Brien, T.K. :
Characterization of Delamination Onset and Growth in a
Composite Laminate.
In: Damage in Composite Materials, ASTM STP 775,
1982, pp. 140-167
- [6] Grossmann, F.W. :
Wang, A.S. D
The Dependence of Transverse Cracking and Delamination on
Ply Thickness in Graphite/Epoxy Laminates.
In: Damage in Composite Materials, ASTM STP 775 (1982),
pp. 118-139
- [7] Charvat, R. :
Prinz, R.
Messwertaufnehmer. German Patent No. P 32 247 57.5,
Europa-Patent Nr.
(Transducer based on magnetic field depending resistor
bridge-MDR-Transducer)
- [8] Hillger, W. :
Schütze, R.
Non-Destructive Testing of CFRP-Laminates.
In: Damage Mechanics of Fiber-Reinforced Composite Materials.
ESA-IT-758 (Dez. 1982) pp. 9-46
- [9] Prinz, R. :
Schmidt, K.
Analyse delaminiertcr Bruchflächen multidirektional aufge-
bauter Probestäbe aus CFK nach statischer oder Schwingbe-
anspruchung.
DFVLR-IB 151-83/10, 1983, 15 Seiten, 1 Tafel, 26 Bilder,
Anhang 7 Bilder
- [10] Rohwer, K. :
Stresses and Deformations in Laminated Test Specimens of
Carbon Fiber Reinforced Composites. DFVLR-FB 82-15 (1982) 82p.
- [11] Bernstorff, B.-S.v. :
Crack Growth in Viscoelastic Materials under Varying Load
Histories.
SM. Report 80-4, California Institute of Technology,
Pasadena, Cal., USA, March 1980, 50 p.
- [12] Agarwal, B.B. :
Broutman, L.J.
Analysis and Performance of Fiber Composites.
John Wiley & Sons, New York, Toronto 1980, 355 p.
- [13] Barsom, J.M. :
The Dependence of Fatigue Crack Propagation on Strain Energy
Release Rate and Crack Opening Displacement.
In: Damage Tolerance in Aircraft Structures, ASTM STP 486,
1971, pp.1-15.
- [14] Ratwani, M. M. :
Kan, H.P.
Compression Fatigue Analysis of Fiber Composites.
American Institute of Aeronautics and Astronautics,
Inc. 1980, Report 80-0707, pp.279-281
- [15] Whitcomb, J.D. :
Aproximate Analysis of Postbuckled Through-Width Delaminations.
Composites Techn. Rev. 4 (1982) 3, pp 71-77
- [16] Gerard, G. :
Becker, H.
Handbook of Structural Stability Part.I-Buckling of Flat
Plates.
NACA TN 3781, 1957, 102 p, esp. Fig. 14
- [17] Bhattacharya, A.B. :
Note on the Postbuckling Analysis of Cross-Ply Laminated Plates
with Elastically Restrained Edges and Initial Curvatures.
J. Struct. Mech. 10 (1982-83) 3 pp 359-372

APPENDIX A

A delamination propagation model under peeling stresses σ_{II} (mode I condition) may be expressed in a form similar to a crack propagation model in metals and is given by the Eq. 14. Let the initial defect characterized by a delamination size $a_0 = 0$ and the size a_d after a number of loading cycles N_d . The integration of Eq. 14 yields

$$(A1) \quad N_d = a_d^{1-m}/(1-m) g \bar{\sigma}^m$$

Assuming the edge delaminations a_i in the multilayer composite develop symmetrical from the edges to the center plane of the specimen as shown in Fig. A1. Then we may define the delaminated area $A^* = \sum_{i=1}^n a_i h_i$, and the non-delaminated area $A = A - A^*$, where $A = b d$ means the total cross section. The load distribution on both parts of the cross-section is

$$(A2) \quad P_A = \sum_{i=1}^n P_{A_i} + P_A^*$$

It was observed in tension-compression fatigue tests and residual strength tests that parts of the cross section failed by buckling. The buckling load of the delaminated section i which buckles at first can be expressed by [15], [16]

$$(A3) \quad P_i = k_i A_i^* \frac{\pi^2 E_i}{12(1-\nu_i^2)} \left(\frac{h_i}{a_i} \right)^2; \quad \sigma_i = k_i \frac{\pi^2 E_i}{12(1-\nu_i^2)} \left(\frac{h_i}{a_i} \right)^2$$

where k_i is the compressive buckling coefficient for flat plates with one single supported edge and three clamped edges as shown in Fig. A2 [16]. The value of the buckling coefficient is $2,0 > k_i > 1,2$. During fatigue loading, the delamination will grow up to the delamination size a_d . Then the strip becomes unstable. It will be assumed that the postbuckling load of the delaminated strip remains constant and equal the buckling load during increasing strain (see Fig. A3 and [17]). With increasing number of load cycles the delamination growth will continue and the buckling load will decrease after Eq. (A3). See Fig. A4. When a certain part of all delaminated strips become unstable the remaining non-delaminated cross section will fail because of exceeding its static strength (or the failure strain). Those considerations are transferable on the behavior of a delaminated laminate on residual strength test.

The residual strength at a certain number of load cycle N can be expressed from Eq. (A2)

$$(A4) \quad \sigma_N = \sum_{i=1}^n G_{A_i} \frac{a_i h_i}{A} + G_A \left(1 - \frac{\sum a_i h_i}{A} \right)$$

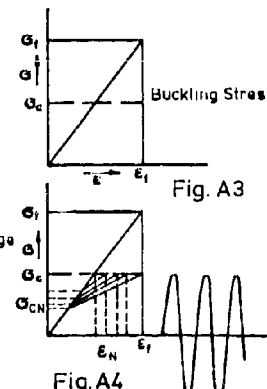
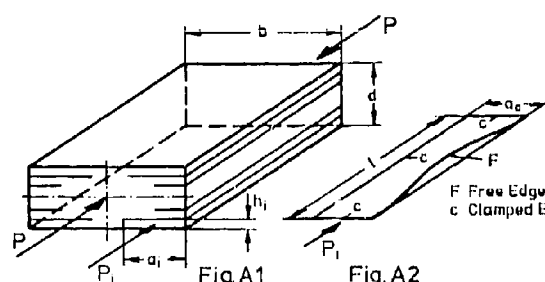
where $G_{A_i} = P_i / a_i h_i$, and P_i are the buckling loads after Eq. (A3). To form a very simple relationship between residual strength and delamination size we assume that $h_i = h = \text{const}$, $\sum_{i=1}^n a_i h_i = a_N \cdot h$ (where a_N the delamination state after N number of load cycles).

$G_{A_i} = E_i \cdot \epsilon$ and $G_A = E \cdot \epsilon$. With regard to buckling stress and the above simplifications the residual strength yields

$$(A5) \quad \sigma_N = \sigma_i \left[\frac{E_i}{E} \frac{1}{A} \left(\frac{2h^3}{\epsilon_i a_N} - a_N \cdot h \right) + 1 \right]$$

where $k_i = 2$ was used. Assuming $(G_N/\sigma_i - 1)^2 A^2 / 4h^2 > 2h^2 / \epsilon_i$, the critical delamination size can be expressed for the residual strength and for the failure load cycle as $a_R = (1 - \frac{G_N}{\sigma_i}) \frac{A}{h} \frac{E}{E_i}$ and $a_F = (1 - \frac{G_F}{\sigma_i}) \frac{A}{h} \frac{E}{E_i}$ respectively. (see Eqs. (16) to (18)).

* for $1/a > 2$



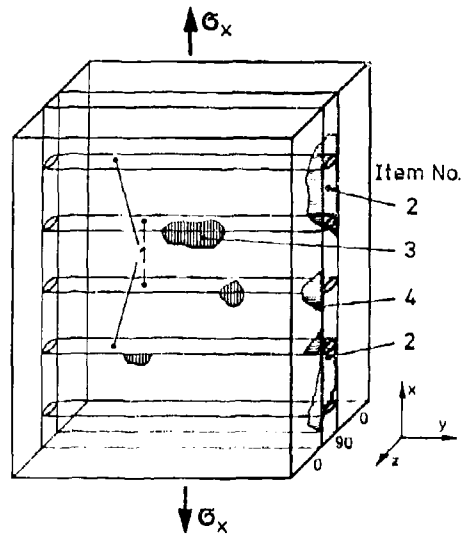


Fig. 1 Characteristic pattern of matrix cracks and delamination onset in the interlaminar plane between the 0-degree and the 90-degree-layers

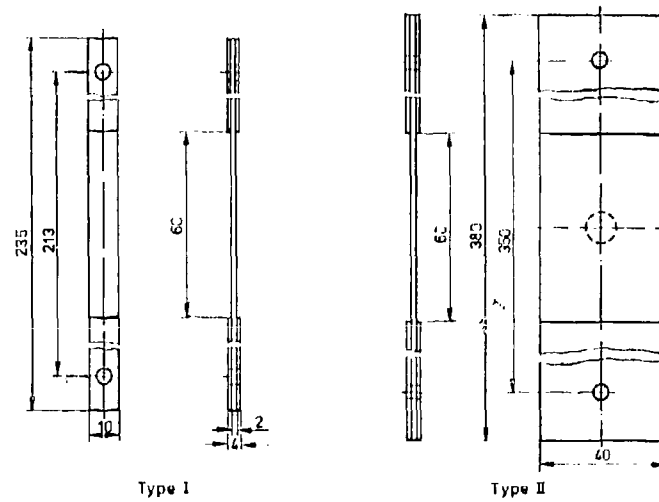


Fig. 2 Types of test specimens

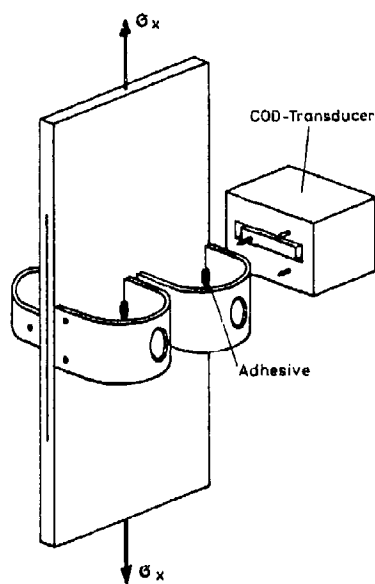


Fig. 3 Mounting of the MDR-COD transducer

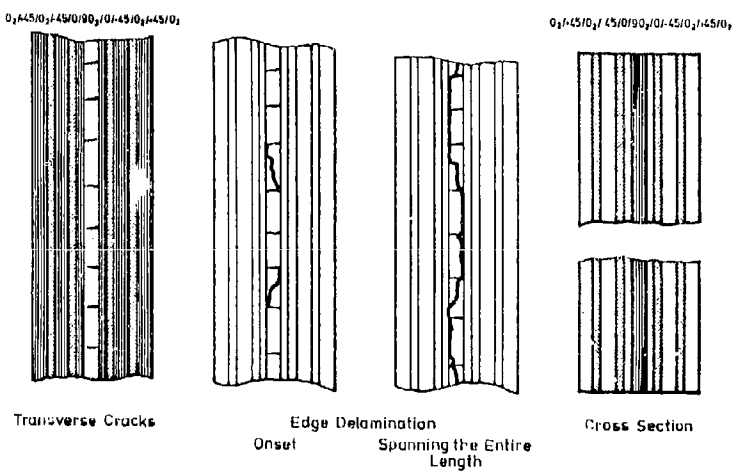


Fig. 4 Formation of edge delaminations during increasing tension load or increasing load cycles

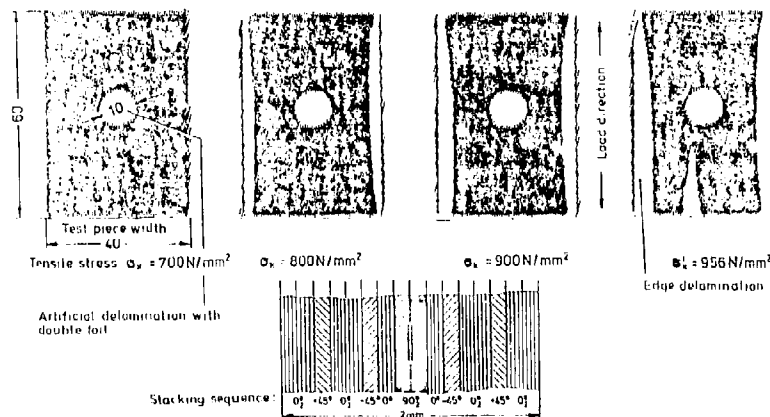


Fig. 5 State of delaminations under step-wise tensile loading to fracture.
Ultrasonic G-scans of the test specimen containing teflon circles implants

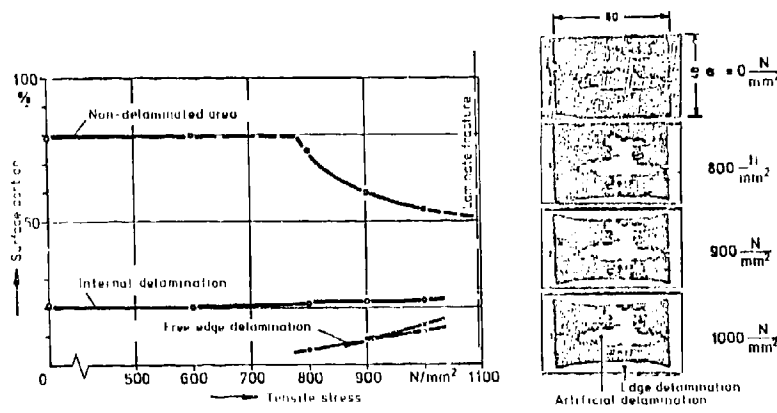


Fig. 6 Growth of the edge delaminations and of the artificial inflation agent delamination under increasing tensile loading

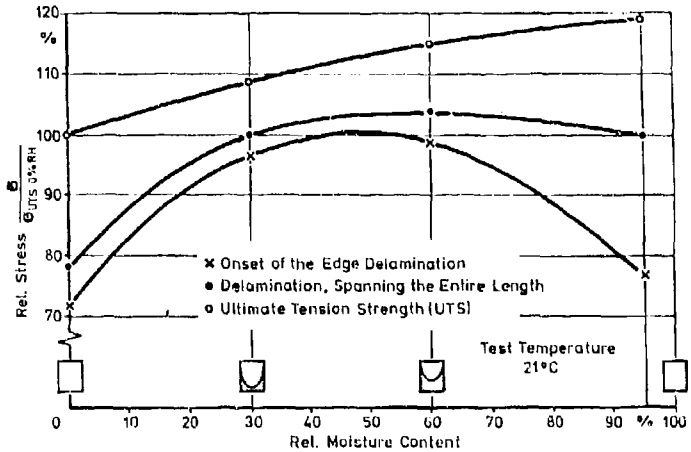


Fig. 7 The influence of moisture profile and moisture content on the formation of free edge delamination during tensile tests

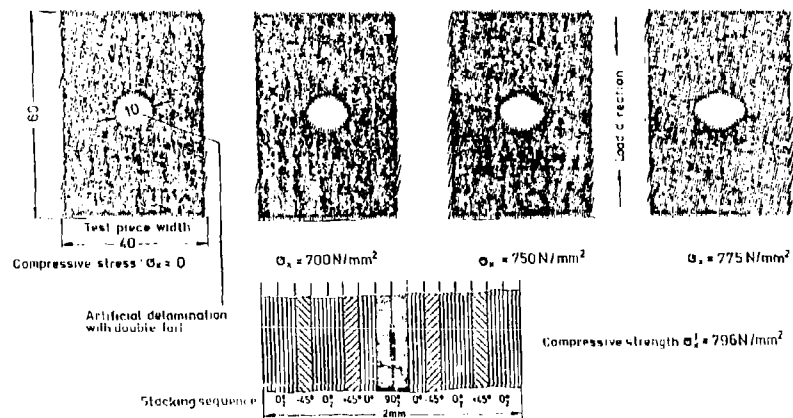
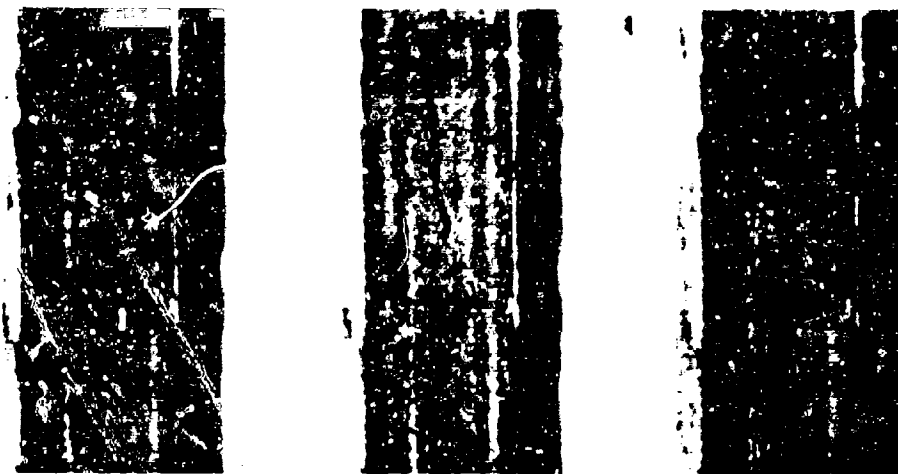


Fig. 8 Growth of artificial delamination under step-by-step compressive loading. Ultrasonic C-scans of a test specimen containing teflon circles implants



Crack opening, photographed under a stress of
 $\sigma_x^2 = -500 \text{ N/mm}^2$ $\sigma_x = 0 \text{ N/mm}^2$ $\sigma_x^1 = 500 \text{ N/mm}^2$

Fig. 9 Crack types resulting from edge effects after $5 \cdot 10^4$ load cycles.
 Stress amplitude $\sigma_a = \pm 500 \text{ N/mm}^2$, Stress ratio $R = 1$.

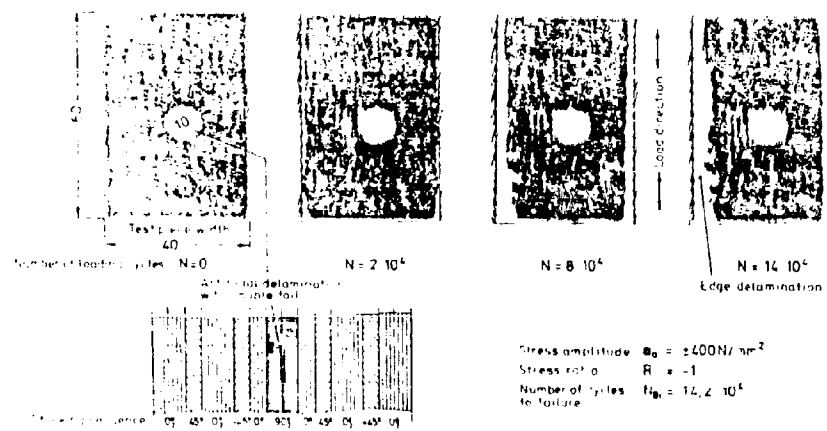


Fig. 10 Delamination states on increasing numbers of tension-compression loading cycles. Ultrasonic C-scans of a test specimen containing teflon circles implants

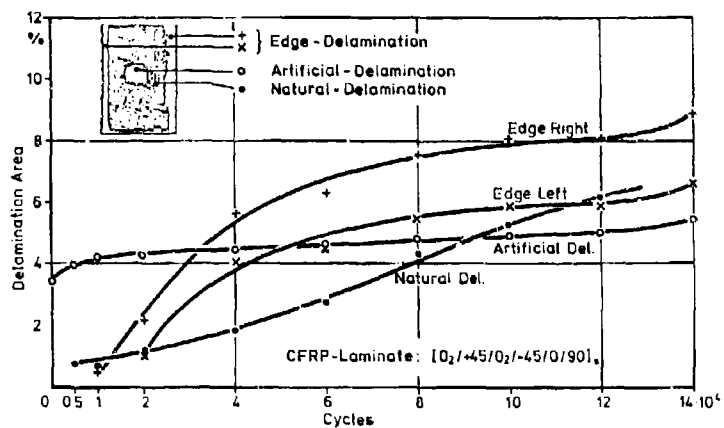


Fig. 11 Propagation of different types of delaminations during tension-compression fatigue loading. $\sigma_a = \pm 400 \text{ N/mm}^2$, $R = -1$

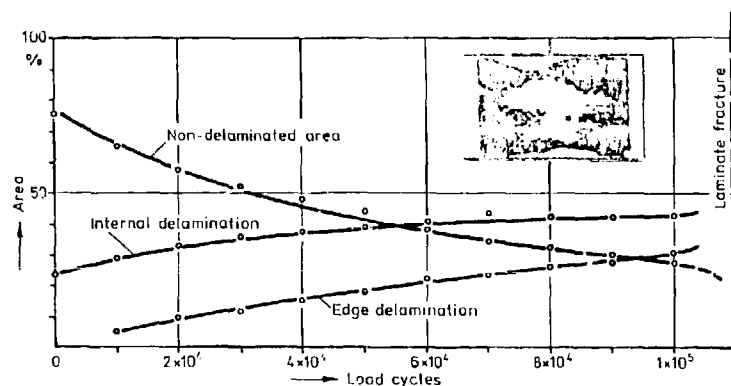


Fig. 12 Propagation of delaminations during tension-compression fatigue loading. $\sigma_a = \pm 400 \text{ N/mm}^2$, $R = -1$

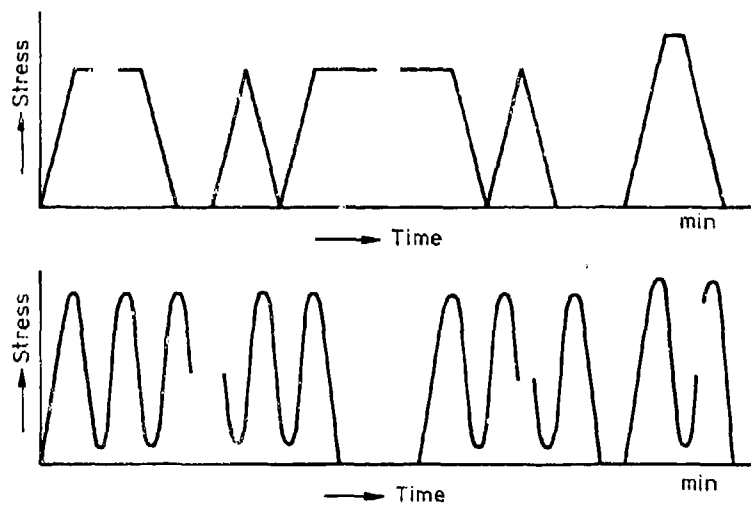


Fig. 13 Load-time-functions for the quasi-static and the cyclic loading tests

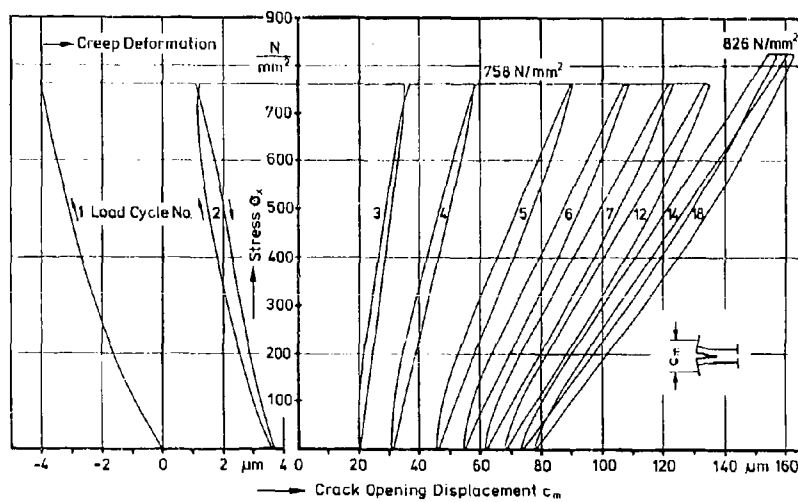


Fig. 14 Displacement c_m as a function of tensile stress for different sizes of delaminations

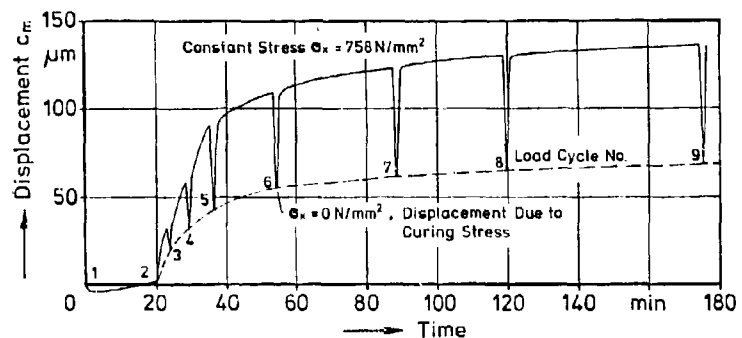


Fig. 15a

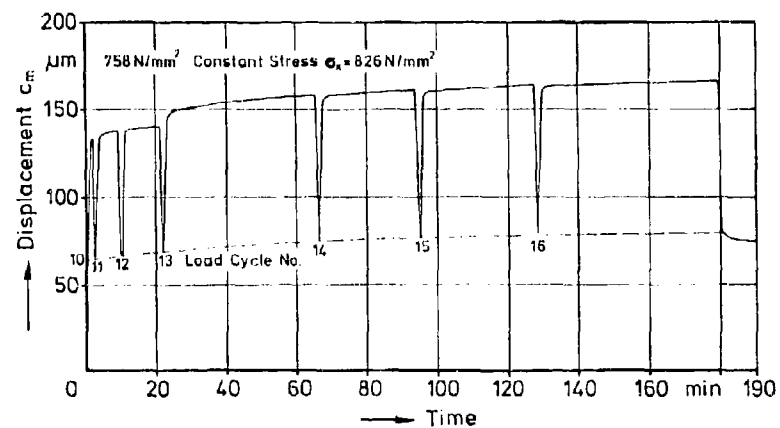


Fig. 15b

Fig. 15 Displacement c_m during constant stress as the function of time

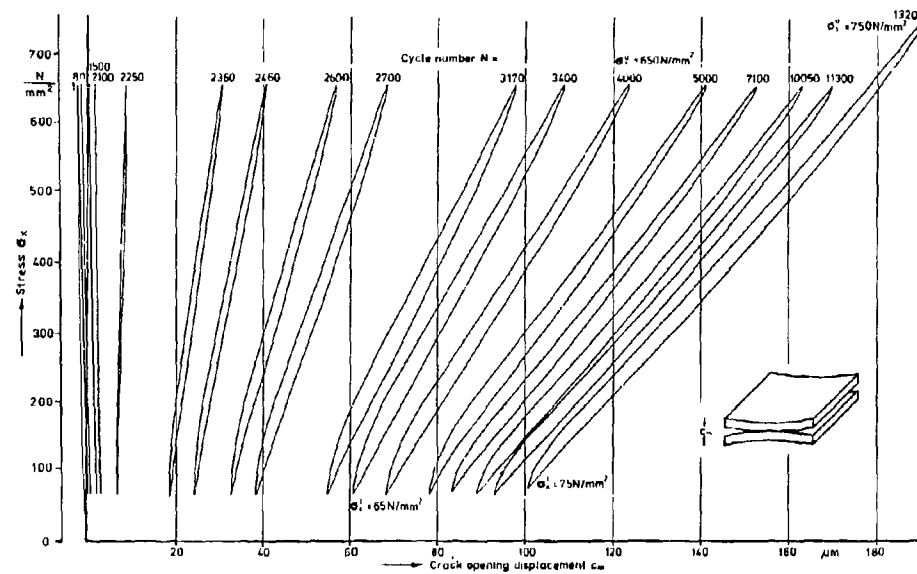


Fig. 16 Typical stress-displacement response for various numbers of load cycles in tension-tension fatigue test

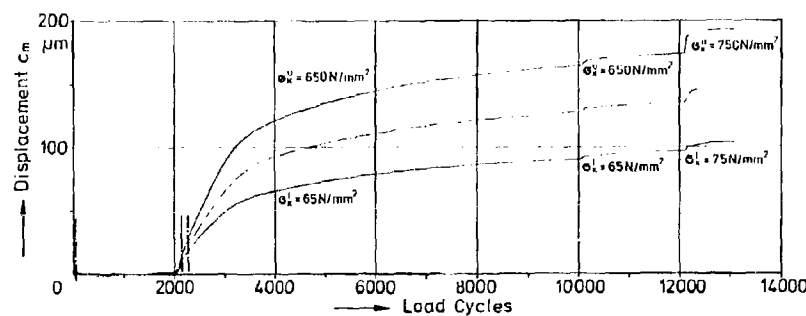


Fig. 17 Envelope of displacement c_m at the upper and the lower stress during tension-tension fatigue test

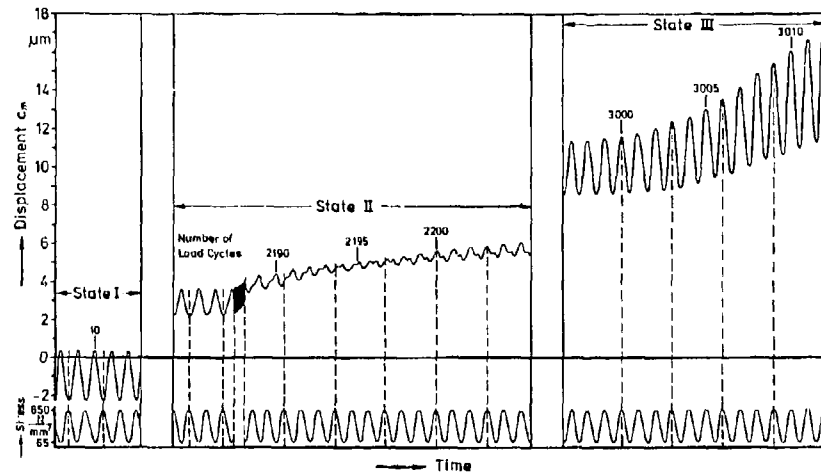


Fig. 18 Load cycling and displacement response for three various states during fatigue test
 State I : Creep phase. State II: Onset of delamination
 State III : Growth of delamination

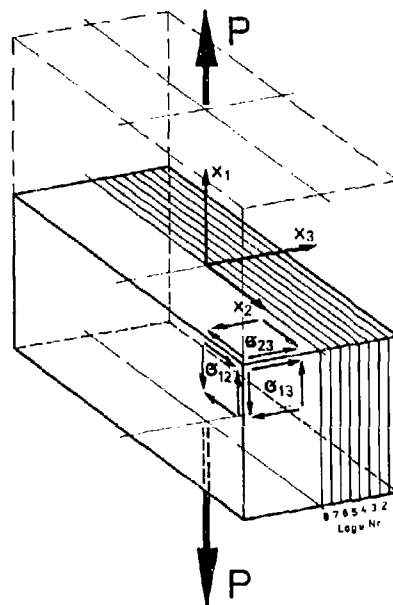


Fig. 19 Coordinate System

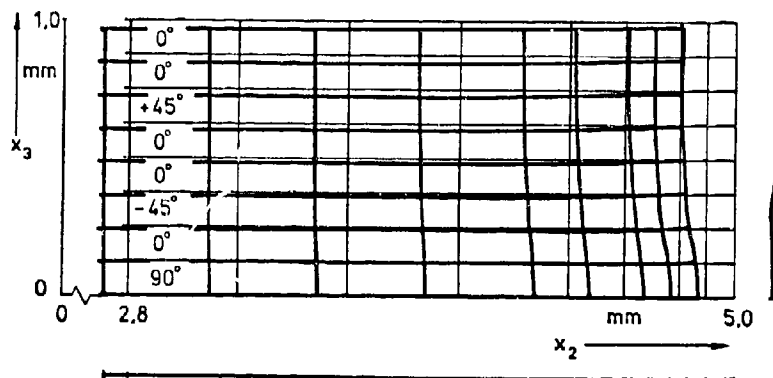


Fig. 20 Deformations of the cross-section resulting from loading of $\sigma_x = 1000 \text{ N/mm}^2$

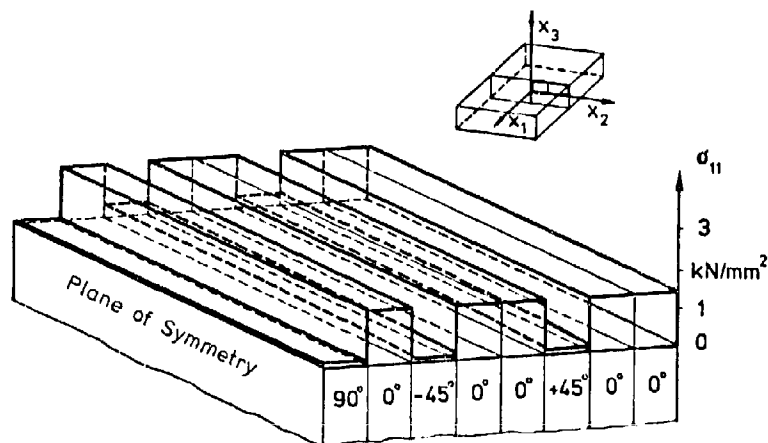


Fig. 21 Normal stresses σ_{11} in the individual layers resulting from longitudinal stress $\sigma_x = 1000 \text{ N/mm}^2$

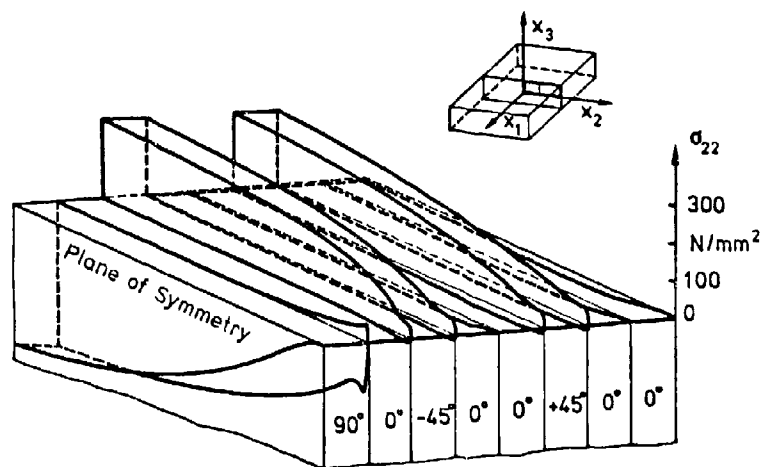


Fig. 22 Transverse stresses σ_{22} in the individual layers resulting from longitudinal stress $\sigma_x = 1000 \text{ N/mm}^2$

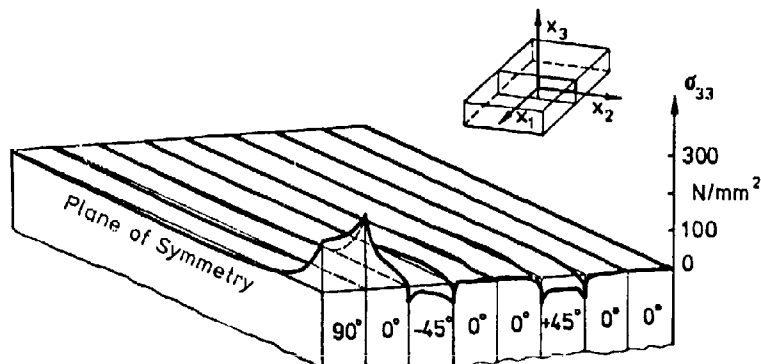


Fig. 23 Transverse stresses σ_{33} in the individual layers resulting from longitudinal stress $\sigma_x = 1000 \text{ N/mm}^2$

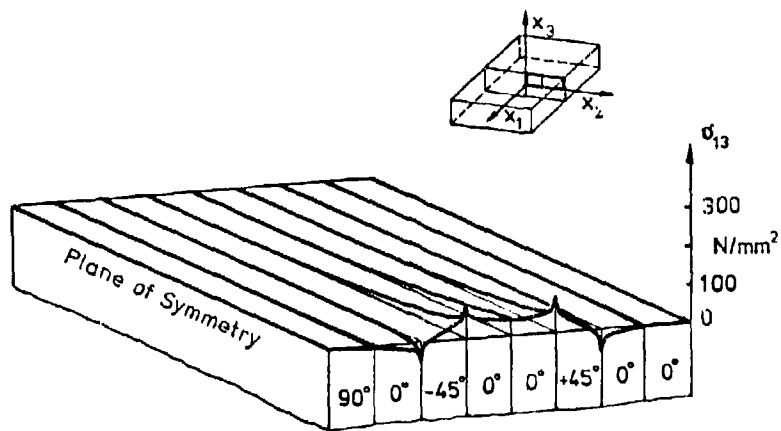


Fig. 24 Shear stresses σ_{13} in the individual layers resulting from longitudinal stress $\sigma_x = 1000 \text{ N/mm}^2$

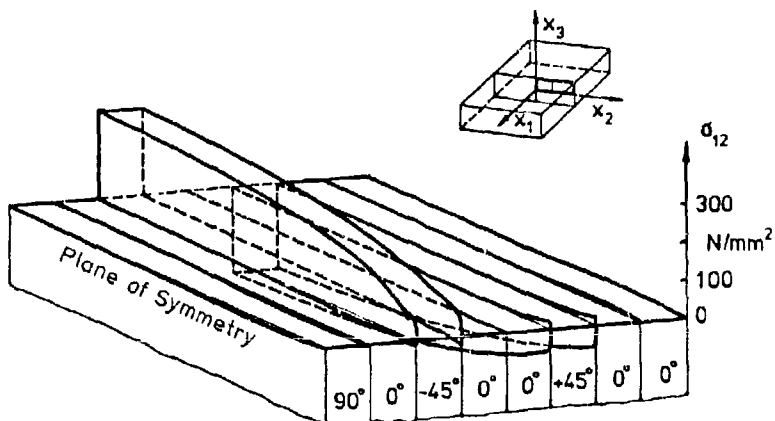


Fig. 25 Shear stress σ_{12} in the individual layers resulting from longitudinal stress $\sigma_x = 1000 \text{ N/mm}^2$

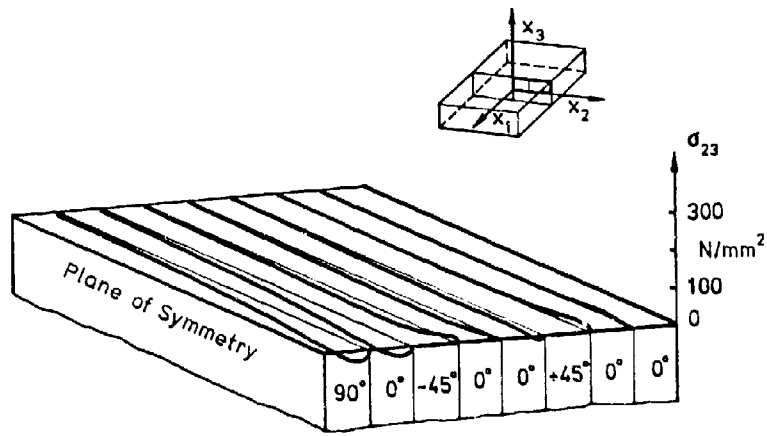


Fig. 26 Shear stresses σ_{23} in the individual layers resulting from longitudinal stress $\sigma_x = 1000 N/mm^2$

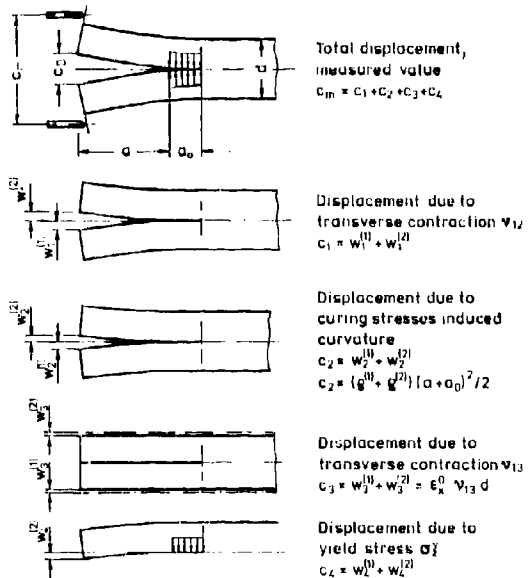


Fig. 27 Composition of the displacement c_m .

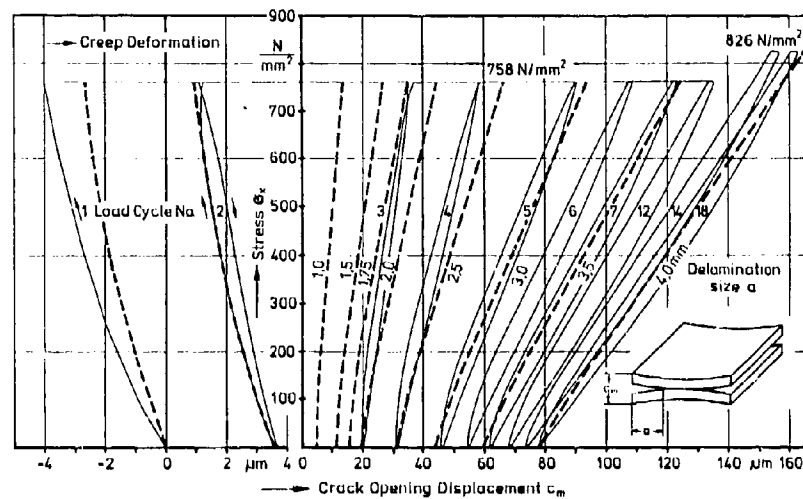


Fig. 28 Measured and calculated stress-displacement response for the quasi-static test. Calculated curves ---

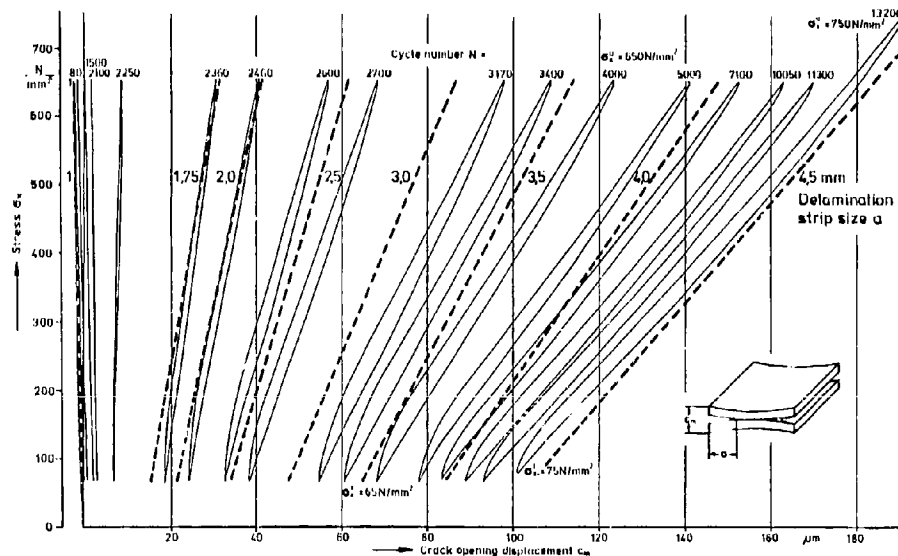


Fig. 29 Measured and calculated stress-displacement response. Calculated curves ---

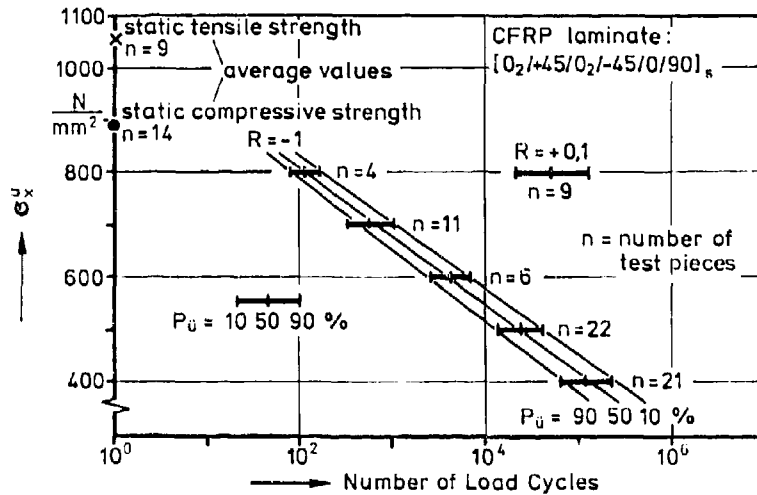


Fig. 30 Fatigue strength diagram for graphite/epoxy laminates.
Stress ratio R = -1 and R = 0.1

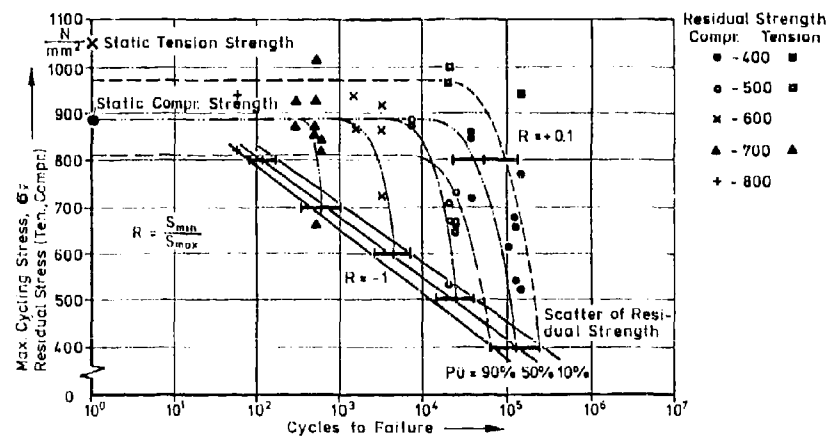


Fig. 31 S-N-curve and residual strength after cyclic loading.

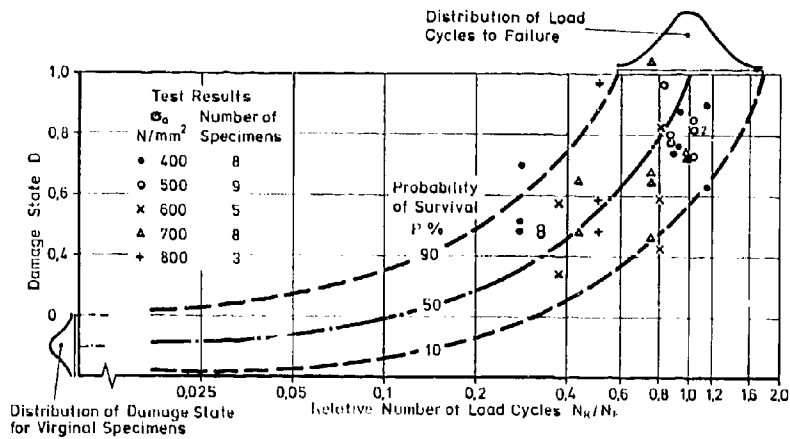


Fig. 32 Damage state D determinated from compressive residual strength after fatigue cycling.

AD P001914

EXPERIMENTAL INVESTIGATION OF DELAMINATIONS IN
CARBON FIBRE COMPOSITE

BY

W. GEIER
J. VILSMETER
D. WEISGERBER

MESSERSCHMITT-BÖLKOW-BLOHM GMBH
AIRCRAFT DIVISION
8000 MÜNCHEN 80, P.O. BOX 801160
W-GERMANY

SUMMARY

This report presents results concerning the effect of delaminations on static and fatigue strength of carbon fibre composites. The delaminations have been introduced artificially into solid laminates and sandwich structures by means of folded teflon patches. The effects of delaminations caused by low energy impact have also been investigated.

The tests have been carried out both at room temperature and at 120°C in the "as received" as well as in the wet condition.

For the sandwich structure design no loss in fracture strength could be found even in the case of fatigue and built-in delaminations.

The same results are valid for the shear angle specimens.

No significant loss in compression strength caused by 6 x 6 mm delaminations was found, although 12 x 12 and 12 x 25 mm delaminations have shown a considerable reduction in strength.

The effect of delaminations caused by low energy impact was found to be no greater than that of a 6 mm open hole which is always taken into account in the MBB design philosophy.

INTRODUCTION

Carbon fibre reinforced plastic (CFRP) materials are playing a more and more important role in advanced aircraft design due to their high specific strength and stiffness. A lot of mechanical values and characteristics are already well known, but there are still some problems to be resolved. One of this features is the behaviour of delaminations in CFRP with regard to tension and compression strength and stiffness.

Amongst other manufacturing defects (e.g. porosity, wrinkles, fiber breakout at drilled holes), delaminations are contributing to a certain amount of scrap, because of the stress engineers lack of knowledge about the influence of delaminations on static and fatigue strength.

To gain experience it would be desirable to load scrapped parts with natural defects till fracture and deduce from the test results a tolerable defect size. Unfortunately in most cases it is impossible to load a single part out of a complex structure representative. Therefore specimens with representative defects and loading are tested and the results are read across to the structure. Delaminations can result from misbonding between solid laminates or they can be caused by impact. Another type of delaminations is a misbond between solid laminates and honeycomb.

To get information about the influence of delaminations on important mechanical properties and on typical features of design the following investigations have been carried out at MBB:

Effects of delaminations:

- 1) in sandwich structure design, being representative for the interface between solid CFRP and honeycomb, where defects are likely to occur.
- 2) on shear angles, being representative of channel members
- 3) on the compressive strength of solid laminates
- 4) caused by low energy impact.

Investigations have been carried out both at room temperature (RT) on "as received" specimens and in the hot/wet condition, since some strength properties of CFRP are significantly reduced at elevated temperature by absorbed moisture.

GENERAL

The unidirectional prepreg materials used for the investigations presented in this paper were Fibredux 914C/T300-6K and Fibredux 914C/XAS-10K from Ciba Geigy with either 34% or 40% resin content. The Toray T300 fibre was used in investigations 1, 3 and 4, whereas the Courtaulds XAS fibre was used in 2. The difference in the mechanical properties due to the two types of fibre is not significant for these investigations, therefore the results are applicable to both prepreg systems.

In investigation 1, the woven fabric material Fibredux 914C/G803 (Fibre T300-3K) with 40% resin content was used, too.

The film adhesive Redux 3:9A has been used for the bonding between solid laminates and honeycombs.

All test pieces have been manufactured in accordance with the MBB manufacturing and quality assurance standards. Two methods have been used to get the zero-moisture datum for the test items to be conditioned in the climate cabinet to representative moisture levels.

These are:

- trim traveller specimen after cure and weigh immediately after post cure
- redry traveller specimen with undefined moisture level in an oven 3 days at 70°C, 3 days at 90°C and x days at 110°C till constant weight is reached.
- It was shown that these procedures are producing an equivalent zero-moisture datum.

All moisture levels which are quoted in this paper have been recalculated to a fibre volume fraction of 60 Vol.-%.

The elevated test temperatures have been applied to the specimens by means of circulated hot air or infrared heaters.

The delaminations which have been artificially incorporated into the specimens have been simulated by folded teflon patches. This method has been found to be the most satisfactory method in comparison with other trials which have been made to simulate delaminations by various methods.

TESTING AND RESULTS

ad 1) The three point bending sandwich specimen shown in Fig. 1 was designed to represent a typical section of a spine hood or access door of a fighter A/C. The outer-skin is made from 16 plies of unidirectional prepreg, the core is Nomex and the inner skin is manufactured from two plies of fabric.

Into the specimen three delaminations with a size of either 18 x 9 mm or 18 x 6.5 mm have been incorporated between the solid laminate and the honeycomb core in areas which are considered to be critical.

All specimens have been conditioned at 1% and 70% R.H. to a moisture content of 1.2% and the test temperature for the residual strength was always 120°C.

The test programme and fatigue block diagram can be seen in Fig. 2, the individual test results in Fig. 3. It can be demonstrated that neither fatigue representing 16000 flight hours nor fatigue plus built-in delaminations have shown an effect on the residual fracture load or the specimen deflection at fracture. Strain gauge measurements in the regions of delaminations have shown an increase in local strain, but this had no significant effect on the fracture load and failing mode.

ad 2) The shear angle specimen presented in Figs. 4 and 5 is considered to be representative for shear carrying channel members. Delamination like defects have been found to be more frequent in radii than in flat items. Therefore the delamination size and distance from edges has been defined according to the MBB radius defect standard. The test objective was to demonstrate that the effects of delaminations in radii as shown in Fig. 4 are covered by stressing the part to carry the bearing load in the sides of the angle. The defect size and position is shown in Fig. 4. All types of specimen have been tested in tension at room temperature and in the as received condition because the tensile load creates shear stresses in the CFRP-angles.

The specimens with built-in delaminations have been conditioned to 1% moisture at 87°C and 95% R.H. Some of the wet specimens were subjected to fatigue according to Fig. 6. Within one block of loading representing 20 simulated flights the temperature of the specimen was raised from room temperature to a maximum of 90°C and then cooled down to RT again (Fig. 6). The accumulated fatigue load is representative of 4000 flights. A load factor of 1.4 was applied to cover 16.000 flights. The moisture content of the CFRP-angles was monitored by a traveller specimen during fatigue and re-soaked to the 1% moisture level if a significant drop in moisture content occurred. The residual strength tests in test conditions B and C have been performed in tension at a test temperature of 120°C and a moisture level of 1%

At room temperature the results (Fig. 7) show a small drop in strength between the reference specimen and the specimen with built-in defects. The hot/wet tests show, of course, a loss in strength versus the room temperature values, but the results are well within the expected limits. The most surprising effect is, that the mean residual strength of the fatigue specimen is even slightly higher than the static strength. Furthermore, no significant difference in fracture load between the specimens of type 1, 2 and 3 could be found. The failure mode of some specimens was filmed by a high speed camera and it was found that the specimen failed first around the holes in the thinner part of the shear angle. An initiation of failure caused by the built-in delaminations could not be found.

- ad 3) The hot/wet compressive strength is one of the most critical properties in the proper design of CFRP structures. Therefore the effect of moisture was combined with the effect of delaminations to look for further loss of strength. After manufacture of large panels the location of the delaminations was found by ultrasonic inspection and a single specimen was machined out of the panel in a manner such that the middle of the defect coincided with the middle of the specimen.

The position of the delaminations with respect to the surface can be seen in Fig. 8. A number of the specimens was tested at room temperature in the as received condition, the rest were conditioned at 70°C and 70% R.H. to a moisture content of 1,1%. Buckling of the specimens was prevented by anti-buckling guides.

The results on Fig. 9 show that not only at room temperature, but also at 120°C in the wet condition, there is a significant drop in strength for the specimens with the 12 x 12 and 12 x 25 mm delaminations. A small loss of strength for the case of the 6 x 6 mm delamination can be seen at room temperature only.

The position of the delamination, too, is an important parameter. Equal sized defects show less influence towards the center of the specimen.

- ad 4) The test work done at MBB on low energy impact covered a large variety of parameters. In this paper only the results of impact induced delaminations are presented. The specimen geometry, the impactors and the laminates used in the investigations and the test programme can be seen in Figs. 10 and 11. An aluminium honeycomb of 30 mm height was bonded to the impact zone of the tension specimens to simulate impact on a sandwich structure. After impact the honeycomb was removed from the specimen by means of machining. The laminates used are representative of a taileron for a military A/C.

Impact was simulated by dropping tools like a screw driver and a hammer with a weight of 115 g and 300 g respectively. The impact energy was varied by different dropping heights.

Runway debris was simulated by glass bulbs of 22 mm diameter and 14 g weight. The impact velocity was recorded by light barriers. A part of the specimen was pre-loaded at impact 0.1, 0.5 and 0.1 times the fracture load to simulate the effect of impact on loaded structures.

All impact parameters have been chosen in a way that barely visible impact damage (BVID) or visible impact damage will occur. This was done to ensure that invisible damage will be covered in any case by our design concept. The specimens which were to be tested in the wet condition had been soaked to 1.0 - 1.2% moisture in a constant climate of 70° and 95% R.H. Most of the impact tests have been done in the wet condition.

The strength tests have been carried out at room temperature in the as received and wet condition and at 120°C in the wet condition.

The results of the US-inspection are tabled in Fig. 12. It can be seen that the specimen were much more insensitive to impact damage in the wet condition, e.g. the impact of a hammer with 3.0 m impact height caused on laminate B in the received condition a delamination of 38 mm diameter, in the wet condition the delamination size is 26 mm only. Preloading of the specimen does not seem to have any influence on the delamination size.

The results of room temperature testing are tabled on Fig. 13. It can be seen that results of the tension tests show a lower sensitivity to impact than the results in compression. This effect can be seen very clear on the preloaded specimens, which show a significant reduction in compression strength. On laminate A (compression) and laminate B (tension) the impact by a hammer has resulted in a considerable reduction in strength. The tests at 120°C have shown the biggest reduction in strength in compression (Fig. 14). But it is interesting that for laminate A the effect of a falling hammer (1 m height) is similar to the influence of an open hole of 6 mm diameter. In MBB philosophy invisible impact damage is designed like a 6 mm open hole. The impact damage caused by the hammer is already visible. Therefore the loss of strength in tension as well as compression is well within the design concept and must not be considered with any supplementary knock down factor.

CONCLUSIONS

The strain levels used for designing a carbon-fibre composite structure at MBB incorporate allowance for low energy impact damage and the presence of bolt holes. These strain levels very often cover a certain delamination size.

- It was shown that typical debonds at the interface of CFRP and honeycomb didn't have a significant effect on the hot/wet residual strength, even after 16000 simulated flight hours of fatigue. These results are restricted to the stress levels of secondary structures.
- In the case of pure shear - as was demonstrated by the shear angle specimen - no influence of the investigated delaminations could be established because the part is designed mainly by bearing strength and all failures occurred in the notched area. These results can be interpreted to allow greater defects or smaller edge distances for delaminations in radial but, on the other hand, pure shear is unlikely to occur in real structures, where the problem of secondary bending has always to be considered. Therefore our standard will not be released.
The effect of higher bearing strength after hot/wet fatigue was found on other bearing strength critical component testing, too.
- Delaminations in flat items are unlikely to occur frequently. The test results have shown for the static load case no significant influence of 6 x 6 mm delaminations. The 12 x 12 and 12 x 25 mm delaminations have caused a loss in strength of about 25% at room temperature and about 17% at 120°C and 1,1% moisture. For static load this reduction in strength could be tolerated because test results with the same laminate have shown about a 35% loss of strength for a 6 mm open hole. On the other hand the fatigue behaviour of delaminations is not known in detail. Therefore no allowance can be made for delaminations bigger than 6 x 6 mm for compression critical items at the moment.
- The statistical basis of the results on impact damage are still to weak to make a final decision. But, never-the-less, some important conclusions can be made:

The delamination size found by OB-inspection is significantly lower if the impacted laminate is already in a wet condition. This can be attributed to a softening effect on the matrix due to the ingress of moisture.

In our design philosophy, low energy impact is always taken into account by the allowance of a 6 mm hole in any part of the structure. The results have shown that this allowance is both, necessary and sufficient.

Some of the testwork presently going on at MBB will provide more detailed information about the behaviour of delaminations in structural components and larger structures.

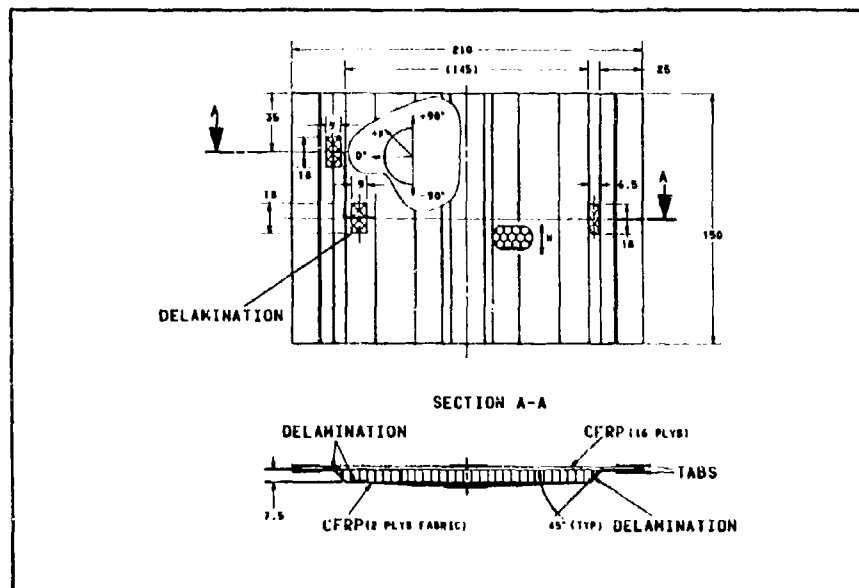


Fig. 1 Three point bending sandwich specimen with built-in delaminations

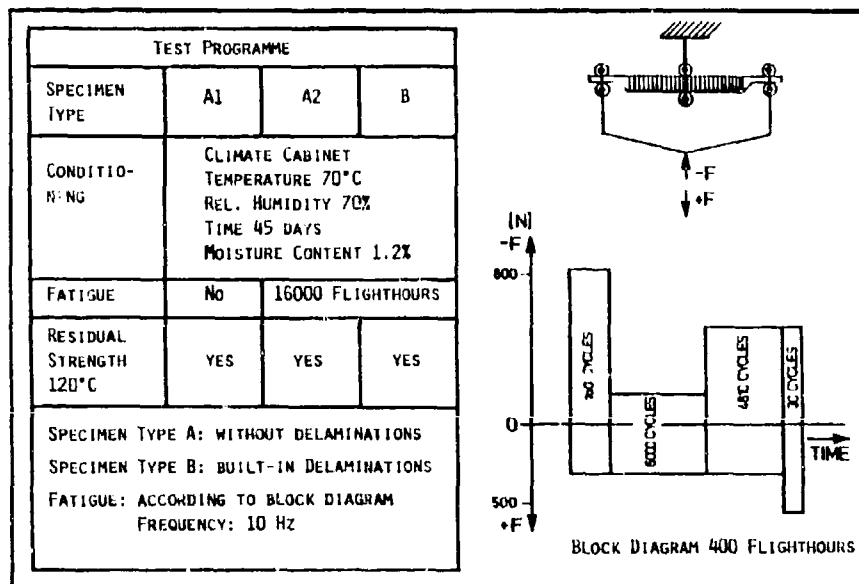


Fig. 2 Test programme and fatigue block diagram for three point bending sandwich specimen

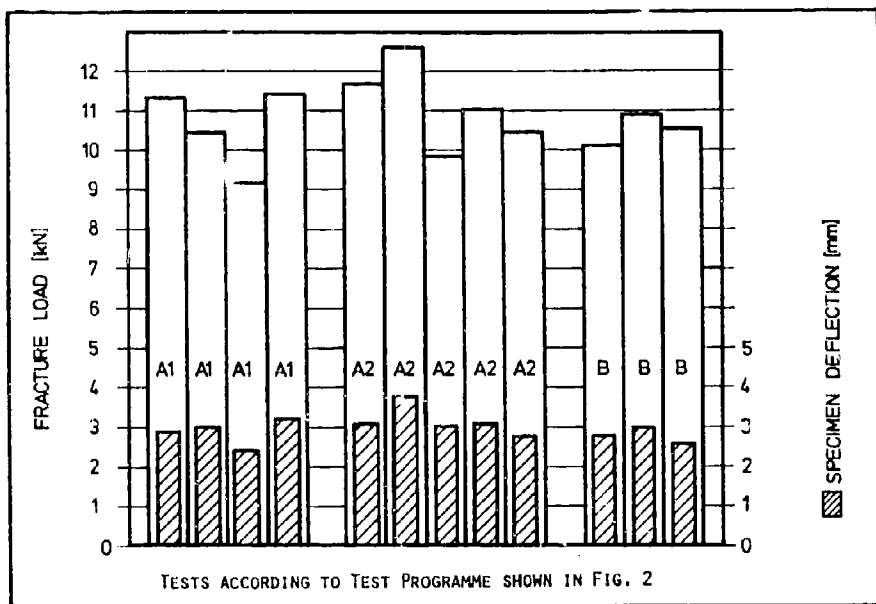


Fig. 3 Individual results of residual fracture load and specimen deflection of sandwich beam specimens

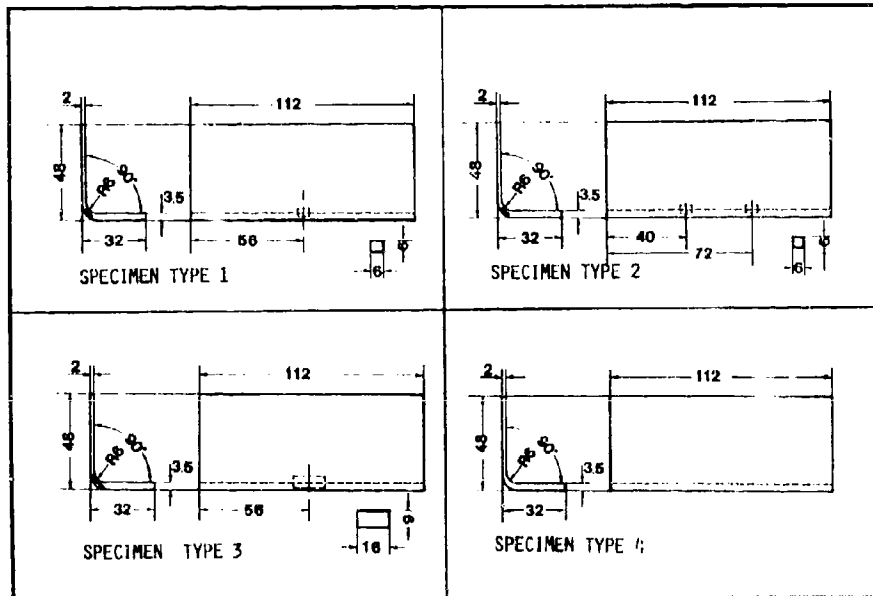


Fig. 4 Geometry, defect position and defect size of CFRP shear angles

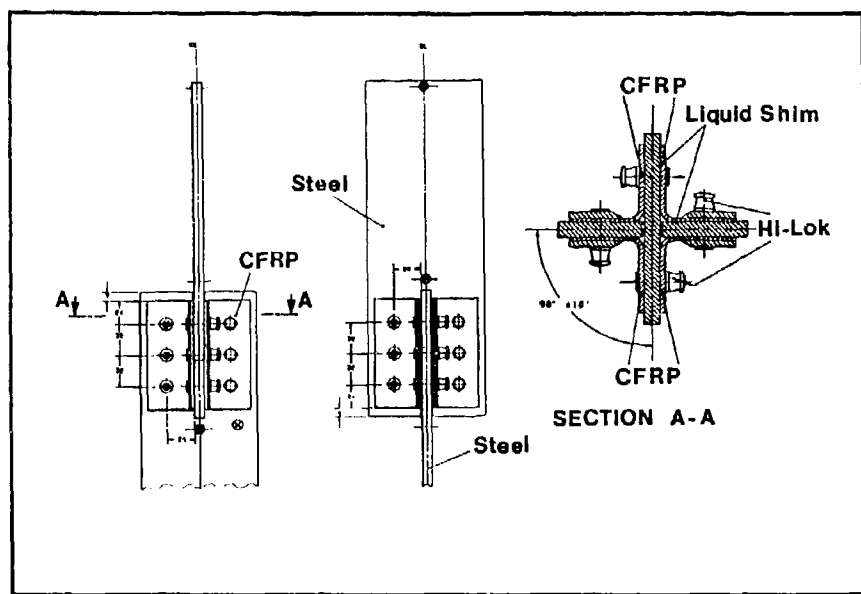


Fig. 5 Assembly drawing of shear angle specimens

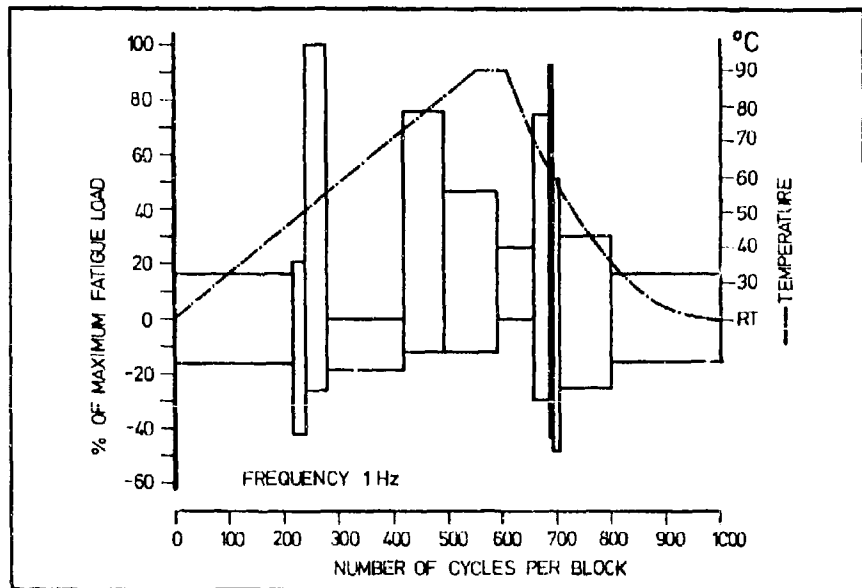


Fig. 6 Shear angle specimen - fatigue and temperature block diagram representing 20 simulated flights

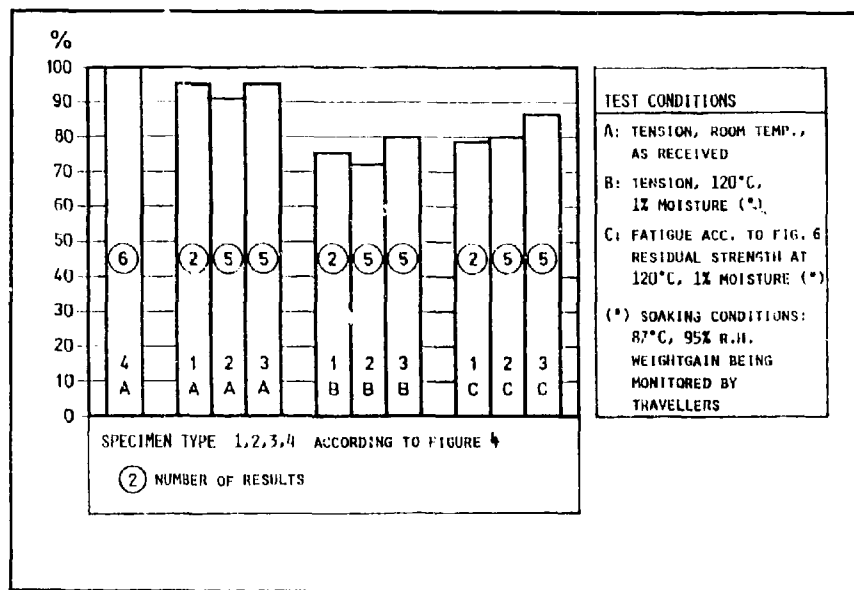


Fig. 7 Mean strength of shear angle specimen at various test conditions and three types of built-in delaminations

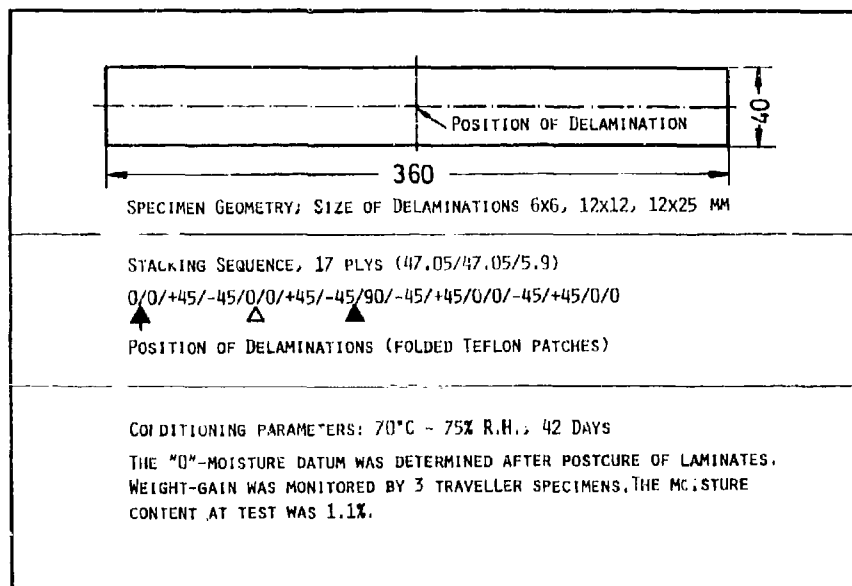


Fig. 8 Specimen geometry, lay-up, size and position of defects and conditioning of multidirectional compression specimens

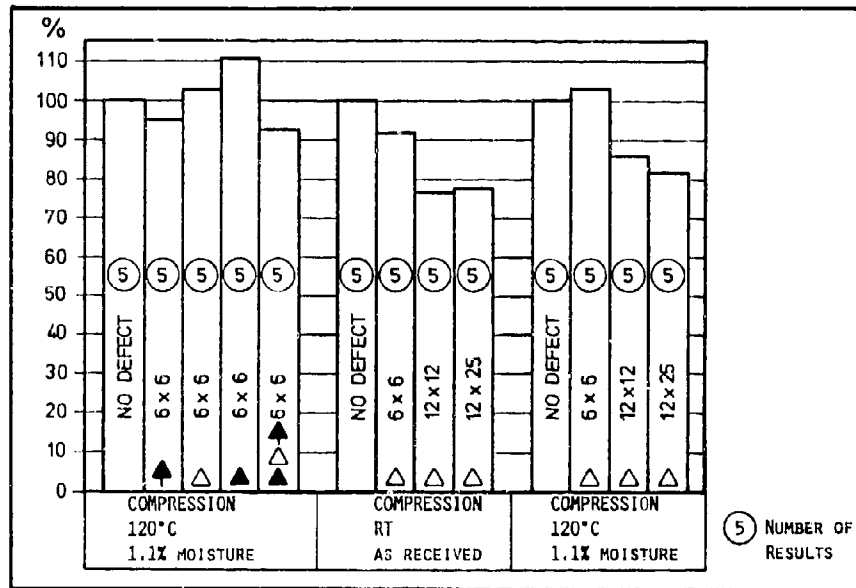


Fig. 9 Mean compression results as function of test conditions and delamination size and position

LAMINATE A, 6 PLYS (33,3/66,7/0) % STACKING SEQUENCE 0/+45/-45/-45/+45/0	LAMINATE B, 16 PLYS (37,5/50/12,5) % STACKING SEQUENCE 0/+45/-45/90/0/+45/-45/0
TEST PROGRAMME	
<p>IMPACT PARAMETERS: - DROPPING TOOLS (SCREWDRIVER, HAMMER) WITH VARYING IMPACT ENERGY</p> <ul style="list-style-type: none"> - RUNWAY DEBRIS SIMULATED BY GLASS BULBS WITH DIFFERENT IMPACT VELOCITIES AND ANGLES OF INCIDENCE - WITH AND WITHOUT PRE-LOADING OF SPECIMENS DURING IMPACT 	
<p>TEST PARAMETERS: TEMPERATURE - RT WET AND NOMINALLY DRY</p> <ul style="list-style-type: none"> - 120°C WET <p>TYPE OF LOADING- TENSION-LAMINATE A AND B</p> <ul style="list-style-type: none"> - COMPRESSION (SANDWICH BEAM) - LAMINATE A 	

Fig. 10 Lay-up of specimens and test programme for impact testing

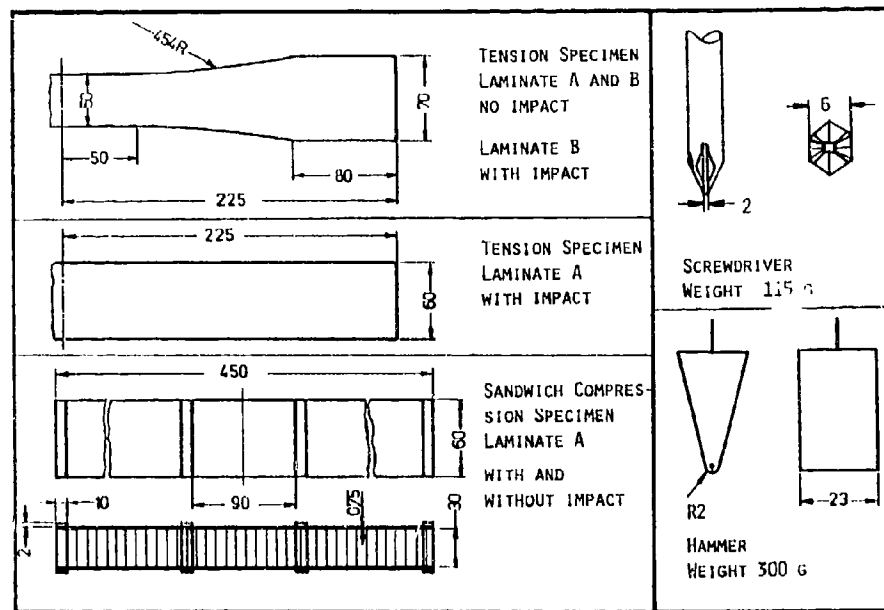


Fig. 11 Specimen geometry and impactors for impact testing

TYPE OF IMPACT	TYPE OF LAMINATE	US-INSPECTION-MAX. DELAMINATION SIZE (MM)		TYPE OF IMPACT	PRE-LOAD	US-INSPECTION MAX. DELAMINATION SIZE (MM)
		AS RECEIVED	1.0 - 1.2% MOISTURE			
SD 0.25 M	A	8	--	SR 20M/s 45°	-	15
SD 0.75 M	A	13	6	SR 20M/s 45°	0.15 R _M	17
HA 1.0 M	A	27	15	SR 20M/s 45°	0.3 R _M	16
SR 37M/s 22°	A	24	22	SP 37M/s 22°	-	22
SD 1.0 M	B	12.5	--	SR 37M/s 22°	0.15 R _M	18
HA 3.0 M	B	38	26	SR 37M/s 22°	0.3 R _M	19

NOMENCLATURE:

SD 0.25 M: IMPACT BY SCREWDRIVER; WEIGHT 115 G; DROPPED FROM 0.25 M HEIGHT.
 HA 1.0 M: IMPACT BY HAMMER; WEIGHT 300 G; DROPPED FROM 1.0 M HEIGHT.
 SR 37M/s 22°: SIMULATED RUNWAY DEBRIS; GLASS BULB; WEIGHT 14 G; DIAMETER 22 MM;
 IMPACT VELOCITY 37 M/S; ANGLE OF INCIDENCE 22°.
 0.15 R_M: SPECIMEN PRELOADED AT IMPACT WITH 0.15 OF FRACTURE LOAD R_M.

Fig. 12 Results of ultrasonic inspection of impacted specimens

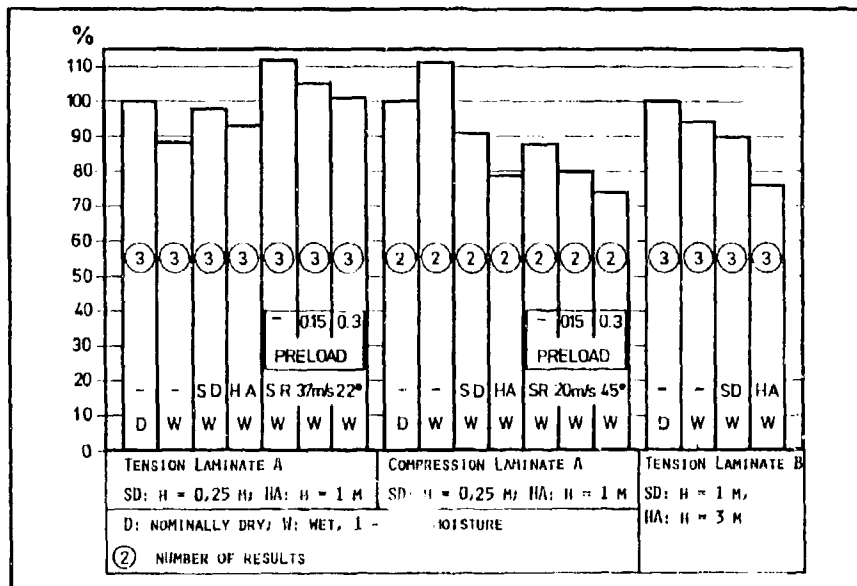


Fig. 13 Influence of low energy impact - mean test results at room temperature

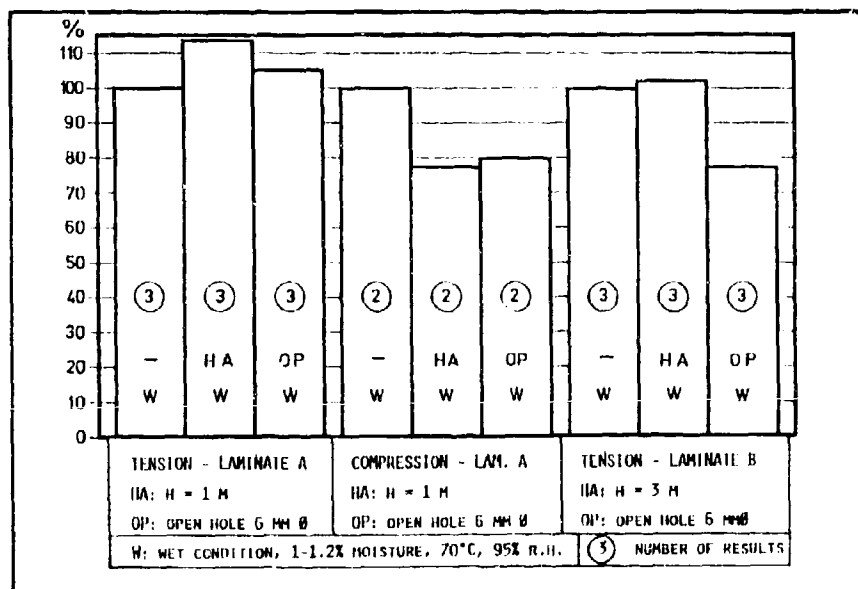


Fig. 14 Influence of low energy impact - mean test results at 120°C

AD P 0 0 1 9 1 5

CHARACTERIZATION OF CUMULATIVE DAMAGE IN COMPOSITES DURING SERVICE

by

M. E. Roylance, W. W. Houghton, G. E. Foley,
 R. J. Shuford and G. R. Thomas

Army Materials and Mechanics Research Center
 Watertown, Massachusetts 02172
 United States of America

SUMMARY

An investigation has been undertaken to study the nature of cumulative damage occurring in glass epoxy composite test coupons and sub-structures during fatigue loading, and to correlate the extent of this damage with remaining useful lifetime. Changes of stiffness in composite laminate specimens loaded in tension-tension fatigue at various load levels have been shown to reflect the extent of accumulated damage and the magnitude of the stiffness change has been used to predict the remaining life fraction of the specimens. Dynamic structural analysis techniques can be used to follow these stiffness changes in substructures, and should be useful as a field technique for following stiffness losses in composite structures. The nature of the damage which occurs during fatigue loading has been characterized by a number of nondestructive evaluation (NDE) techniques including ultrasonics and infrared thermography.

I. INTRODUCTION

Fiber reinforced materials offer significant advantages over conventional metallic materials for use in fatigue-critical structures. These advantages arise from the greater damage tolerance and resistance to high cycle (low stress) fatigue exhibited by composite materials (1). The use of these novel materials in structural applications requires the use of new nondestructive inspection techniques, since the techniques used for assessment of accumulated damage in metals are frequently not applicable to composites.

The increasing use of composite materials by the U.S. Army has prompted the development of such techniques, and also techniques for characterization of commercially supplied starting materials, including resins and prepgs. The flow chart in Figure 1 shows the standard methods used and the new techniques available for characterizing composite materials. The quality assurance and NDE techniques begin on the left with characterization of the starting materials and end on the right with in-service inspection of fielded composite structures or components.

This paper briefly reviews some of these new techniques for characterizing cumulative damage in composites subjected to fatigue loading. It also discusses the results of an experimental study in which these techniques were used. In this study, glass/epoxy composite test coupons and substructures were fatigued, the nature of the damage occurring in these materials was characterized by a number of NDE techniques, and the extent of damage was correlated with the remaining useful lifetime. Changes of stiffness in composite specimens loaded in tension-tension fatigue at various load levels have been shown to reflect the extent of accumulated damage, and the magnitude of the stiffness change has been used to predict the remaining life fraction of the specimens.

II. OVERVIEW OF NDE TECHNIQUES

A. THERMOGRAPHY

Improved thermal imaging systems manufactured within the last few years have resulted in renewed interest in the use of thermography as a quality assurance and NDE technique for characterizing composites. Real-time thermography can be used to detect damaged areas in composites by monitoring the temperature distribution when the specimen is heated either by an external heat source ("passive" thermography) or by internal thermal dissipation from applied mechanical stress ("active" thermography). The interested reader is referred to a recent state-of-the-art review of basic principles of thermography and application to composites (2).

Passive thermography involves heating the structure by conduction, convection or radiation. Differences in heat transfer characteristics due to defects yield a pattern of varying temperature on the surface. The resolution capabilities of passive thermography depend on heat transfer properties.

For composite materials, the active thermographic technique involves internal heating by means of viscoelastic dissipative hysteresis. In this case, the stress/strain level and excitation frequency used are the two most important parameters affecting heat generation in the material. In vibrothermography, a technique pioneered by investigators at Virginia Polytechnic Institute and State University, the object to be examined is coupled to an ultrasonic shaker and subjected to high-frequency,

low-amplitude vibration (3). Vibrothermography appears to be a good method for locating delaminations and other flaws in composites where the surfaces of the flaws can interact with one another during high-frequency excitation (4).

B. ULTRASONICS

Ultrasonics, which uses frequencies from 20 KHz to 24 MHz, is probably the most valuable and informative conventional NDE technique available for composite materials. This technique involves the interaction of an ultrasonic mechanical wave with a material. For example, an ultrasonic wave is passed through a material and energy is reflected off of a defect. This results in both attenuation of the wave and formation of a reflected wave which is measured at the front surface. Thus, the reflected wave and the attenuated wave both contain information about the flaw or defect. Ultrasonic testing is not a novel technique for composites, since the methods used do not differ from those used for metals.

C. DYNAMIC SIGNAL ANALYSIS

Another non-destructive evaluation technique which has been used in the current study is dynamic structural analysis. Although this technique has not been used extensively in the past to characterize the fatigue induced damage in composite structures, it has been widely used to analyze structural resonances and damping. Since changes in stiffness and hysteresis of fatigue damaged composite structures are reflected in corresponding shifts in resonant frequencies and damping, dynamic structural analysis can be used to assess the extent of fatigue damage.

Commercially available equipment for dynamic signal analysis varies in sophistication and complexity. Instruments range from simple equipment designed to pick up a single fundamental resonance excited by a mechanical disturbance such as a tap by a screwdriver to specialized mini-computers which perform Fourier transform analysis to calculate a full range of resonant frequencies and mode shapes in complex structures. Advances in instrumentation in the last five years have produced field portable systems with these sophisticated capabilities, and one such instrument, the Hewlett-Packard 5423A Dynamic Structural Analyzer, was used in this study.

D. ACOUSTIC EMISSION

When a material is significantly stressed, it emits mechanical stress waves. These stress waves are frequently known as "acoustic emissions." The observed Acoustic Emission (AE) event from a composite material is an exponentially decaying sinusoid. This signal, or "Event," is frequently characterized by its peak amplitude, or the number of times it exceeds a preset threshold, or possibly its energy. This information, when combined with the stress history, total number of events and their location can be informative.

Acoustic emission offers the unique capability of characterizing the damage occurring in composite materials undergoing stress. Investigators have used AE to characterize damage accumulation in fiber reinforced composites as a function of time under load, strain rate, stress level, and fatigue loading. An excellent state-of-the-art review has recently been written by M. Hamstad of Lawrence Livermore National Laboratory (5).

III. MATERIALS

A. CHARACTERIZATION OF STARTING MATERIALS

As Figure 1 indicates, one of the most recent techniques for characterization of epoxy resins and prepgres for incoming quality assurance is high performance liquid chromatography. With proper choice of solvent system and detector, liquid chromatography can yield a reproducible and easily recognizable "fingerprint" of a given resin system. Each important component of the resin produces a separate peak whose magnitude reflects the quantity of that specimen fraction. Hagnauer (6) and his coworkers at AMMRC have published several papers dealing with HPLC characterization of epoxy resins, including those based on diglycidyl ether of bisphenol A (DGEBA), such as used in this work. Prepreg material for the present study was screened using the experimental procedure described in reference 6. The resulting fingerprint agreed within acceptable limits with the fingerprint in Figure 2 (reprinted from reference 6) for standard prepreg.

B. FABRICATION OF TEST SPECIMENS

1. Laminate Specimens

In the present study, three types of composite laminates were evaluated. The first was a crossply laminate with a stacking sequence of (0°/90°/0°/90°). The second was an angle-ply laminate with a stacking sequence of (0°/+45°/-45°/90°). These were both fourteen-ply laminates. The third laminate studied was a sixteen-ply laminate with a stacking sequence of (45°/-45°)₄. This laminate was constructed to be as close as possible in reinforcement geometry and thickness to the +45° filament wound specimens discussed below.

The laminates were prepared by hand layup and autoclave cure of 3M SP250/E-glass unidirectional prepreg. Initial laminate size was 760mm x 1.37m. The laminates were cut into rectangular coupons 305mm long by 25.4mm wide and machined to their final configurations by means of a Pantograph-type template-controlled router. Figure 3 shows the dimensions of the AMMRC-designed streamline specimen and the standard D-638 ASTM dogbone specimen.

2. Filament-Wound Specimens

Filament-wound tubes were fabricated from E-glass roving impregnated in line with a diglycidylether of bisphenol A (DGEBA) resin (100 parts) mixed with methyltetrahydrophthalic anhydride (MTHPA) (80 parts) and benzylidimethylamine (BDMA) (1 part). The tubes were wound with +45 degree orientation on a 25.4mm mandrel. The outside diameter in the gage section was 31.8mm with a 90 degree overwrap to 38.1mm outside diameter in the grip area. After winding, the matrix was cured to gelation by rotating the tubes under infrared lamps. The tubes were then fully cured in air-circulating ovens at 93.3°C for 1 hour and 177°C for 2 hours.

C. CHARACTERIZATION OF TEST SPECIMENS

Fiber, resin and void volumes were determined on the filament wound and laminate specimens using a burn-out technique. The thickness of the laminates varies considerably from specimen to specimen, and a variation from 40-60% in the fiber volume fraction results. A nominal thickness of 0.2mm per ply was used for stress calculations, corresponding to 50% fiber volume. The fiber volume fraction of the filament wound tubes was 72.5% and varied only slightly from specimen to specimen. The void volume varied from 1.4 to 2.0%.

The extent of cure of the laminate specimens was evaluated by differential scanning calorimetry (DSC) measurements of residual curing exotherm using a Perkin-Elmer DSC-II scanning at 5°C per minute. The DSC results indicated that the extent of cure was consistent from specimen to specimen.

IV. EXPERIMENTAL PROCEDURE

A. FATIGUE TEST PROCEDURES

All laminate tests were performed on Instron model 1331 servohydraulic test systems. Static tests were done at a crosshead speed of 1.27mm/min. Fatigue tests were done at a frequency of 2 Hz and a stress ratio of 0.1. Strain measurements were obtained using dynamic strain gage extensometers with a 25.4mm gage length. Modulus measurements were made using a Nicolet digital oscilloscope and a DEC MIIC-11 computer.

The specimens were placed between the grip faces and carefully aligned to minimize any possible bending loads due to load eccentricity. They were then ramped at 1.27mm/min to the maximum stress level, unloaded to the mean level and cycled at 2 Hz until failure (see Figure 4).

In the laminates containing 0 degree plies, the initial loading stress-strain curve exhibits non-linearity due to failure of off-axis plies, but subsequent stress-strain curves appear nearly linear until the onset of final failure (Figure 5). The stress-strain behavior of the +45 degree laminates was non-linear throughout their lifetime. For all types of laminates, the initial reference modulus was taken from the first cyclic loading from minimum to maximum stress (Figure 4). In the +45 degree laminates, which exhibited non-linear behavior during this first fatigue cycle, modulus was calculated from total stress amplitude divided by the total strain amplitude, and hysteresis was calculated during this and all subsequent measurement cycles.

The +45 degree filament wound tubes were tested in tension-tension fatigue on an Instron 1323 servohydraulic tension-torsion apparatus using the same procedures employed for the +45 degree laminate specimens. Strain measurements were made using a dynamic strain gage extensometer. Modulus, as a ratio of stress amplitude to strain amplitude, and hysteresis were calculated during each measurement cycle.

B. DAMAGE CHARACTERIZATION

During the fatigue tests a thermocouple was attached to the surface of the specimen to monitor temperature. An Inframetrics model 525 infrared thermography system was also used to monitor surface temperature distribution patterns occurring as a result of fatigue. At intervals during the fatigue tests, ultrasonic C-scan, vibrothermographic, and modal analysis measurements were made on the specimens.

The streamline specimens were ultrasonically scanned using a pulsed echo technique. In this technique the specimen is immersed in water and ultrasonic pulses generated by a transducer pass through the front surface and reflect off of the back surface. Any discontinuity in the specimen reduces the amplitude of the signal received at the back surface. A conventional C-scan recording method was used to produce a permanent record of the signals from the transducer. The C-scan recording is produced by automatically scanning the transducer over the specimen in an X-Y raster pattern. The movement of the recorder pen is synchronized with the movement of the transducer. When the amplitude of the reflection falls below a preset threshold level, the recorder is set to blank or stop writing. An irregularity or defect is therefore indicated in the C-scan by the

absence of scan lines. The result is a projected true-to-scale reproduction of the length and width of discontinuities outlined against the specimen surface. The equipment used for this testing was a Sonics Mark III ultrasonic flaw detector using a Panametrics 30 MHz focused transducer.

A schematic of the vibrothermographic equipment is shown in Figure 6. The specimens were placed in a specially designed clamp and attached to an ultrasonic shaker. An excitation frequency of 10-12 KHz was used, and the resulting thermal patterns were recorded on videotape for analysis.

Dynamic structural analysis was performed on the streamline specimens using the RP 5423A. The specimens were cycled to various fractions of their fatigue lifetimes, removed from the cycler and allowed to cool to room temperature. They were then suspended from one end by a fine denier yarn to approximate a free-free condition and excited by impulse loading with an instrumented jeweler's hammer (Dytran model 5800SL).

The specimen response was measured using a Dytran model 3101A accelerometer with a nominal sensitivity of 10 mv/g and a range of ± 500 g which was placed 25.4mm above the center of the specimen. For the modal survey, seventeen impulse loading points were used evenly spaced 19mm apart along the specimen center line to pick up flexural vibration modes.

Acoustic emission measurements were attempted during fatigue loading, but noise from the servohydraulic test apparatus overwhelmed any damage related signals from the test specimen. The specimen gripping arrangement precluded gating the AE signals, and isolating the pump from the system was determined not to be feasible.

V. RESULTS AND DISCUSSION

Maximum fatigue stress versus log lifetime for all materials studied are shown in Figure 7. Only the 0,+45,90 material exhibits apparent non-linearity in its S-N curve, and then only at very low load levels—40 to 50% of ultimate tensile stress (UTS). The +45 laminates and tubes were tested in the range of 60-80% of yield stress (YS) rather than UTS, since they have a well defined yield point as shown in the stress-strain curves of Figure 8. In this range, both S-N curves appear linear, although at 55% of yield strength, the tube specimens last at least one million cycles with no detectable damage, and this suggests that the S-N curve may become nonlinear at lower stresses.

As discussed in reference 1, the 0,90 and 0,+45,90 laminates exhibit clearly defined and reproducible decreases in modulus as a function of fractional lifetime, N/N₀. Although the total change in modulus to failure is different for these two materials, the shape of the modulus decay versus life fraction is similar and essentially independent of load level.

Figure 9 shows modulus change versus life fraction curves at 60 & 65% UTS for the 0,+45,90 and 0,90 materials respectively. The initial rapid change in the modulus in the 0,90 laminates coincides with extensive damage which occurs in the 90 degree plies. The fibers in the 0 degree plies limit the strain and stabilize the modulus loss at about 5% with only about 0.2 of the specimen lifetime elapsed. In the 0,+45,90 specimens the stabilization of the modulus loss occurs after 0.4 of the specimen lifetime at a level of 30-40%.

Obviously the +45 degree plies contribute strongly to the modulus decay in the 0,+45,90 laminates, but the restraint supplied by the 0 degree plies prevents them from undergoing the extensive deformation that they exhibit in the absence of reinforcement in the direction of the applied load. This is illustrated by the stress-strain curves of the +45 degree reinforced tubes and laminates in Figure 8. As mentioned above, both specimen types exhibit yield-like behavior, followed by extensive deformation at or near constant load. The +45 laminate also exhibits apparent strain hardening and failure at 150-160% of the initial yield stress. The tubes usually fail at a stress which is about 110% of the yield stress. The strain to failure is 7-8% for the tubes (defined as the point at which the load begins to drop rapidly, since the tubes can deform more than 100% beyond this point and still carry some load) and 12-15% for the laminates. Yield strains are 0.5-1% and 2-3% respectively.

This yield like phenomenon arises from the deformation and fracture of the epoxy resin matrix. Since deformation and failure of this polymeric matrix is an activated, time and stress dependent process, the modulus change versus life fraction curves for the resin dominated +45 degree laminates varies significantly from the laminates which contain 0 degree plies and whose properties are therefore fiber dominated.

Instead of being essentially independent of load level, the curves shown in Figure 10 are shifted to the left toward shorter times at higher loads. This shift is particularly prominent in the behavior of the +45 degree laminate specimens, shown in Figure 10a, probably due to the strain hardening which occurs in this material.

At 80% of YS in these laminates the modulus decrease goes through a maximum of 50% at about 0.3 of elapsed lifetime. After this point the stiffness of the test specimen as measured by stress amplitude over strain amplitude gradually increases and levels off at about 40%. The hysteresis decreases as the modulus increases.

The surface temperature of the +45 laminate specimens reaches 60°C during cycling at 2Hz and 80% of YS. To eliminate the possibility that high temperatures in the interior of the test specimen had induced post-cure in the epoxy resin at 80% YS, DSC measurements of the extent of cure before and after cycling were performed. No increases in the extent of cure were detected, so the increased stiffness cannot be due to increases in matrix cross-link density.

This decrease in modulus followed by an increase appears to be due to yielding and subsequent strain hardening in the specimens under fatigue loading. Evidence for this is found in the stress-strain curves of the laminates at varying points in the fatigue lifetime shown in Figure 11. These curves show a decrease in initial modulus and persistence of an inflection point in the curve before the maximum ΔE , and an increase in initial modulus and disappearance of the inflection point afterwards.

The most likely cause of the observed strain hardening both in the quasi-static and high stress fatigue tests is strain induced reorientation of the fibers from the initial +45 configuration to a closer alignment with the applied load. The fatigue-induced creep strain at the point of maximum ΔE is constant from sample to sample, further suggesting that the increase in dynamic modulus is due to fiber reorientation at a critical strain level. The strain level in these specimens at maximum ΔE is on the order of the yield strain observed in a quasi-static test.

At lower fatigue stresses the yielding process apparently occurs more slowly, and fatigue failure occurs before detectable strain hardening. Significant strain hardening does not occur in the tubes, and although the ΔE vs N/N curves are shifted to shorter times with increasing fatigue stress levels, no maximum is observed, even at 80% of YS. The tubes do show a slight increase in modulus at the very early stages of the fatigue life in specimens tested at lower stress levels. A similar brief increase has been seen in some laminate geometries by other investigators (8), and has been observed in the first few cycles of loading of the 0,90 laminates in this study.

Since the +45 degree laminates cycled at higher stress levels had well defined and reproducible ΔE vs N/N curves, they were chosen for characterization by the various NDE techniques at different life fractions. Both ultrasonics and vibrothermography detected progressive damage in the gage section of fatigued specimens. Figure 12 shows the C-scan of an undamaged specimen compared with C-scans of the same specimen after 5000 and 7000 cycles at 75% of YS, or about 0.4 and 0.5 life fraction. Beyond this point the damage, especially surface damage, is so severe that no increase was detectable by further ultrasonic measurements.

Similar results are obtained with vibrothermography. The presence of damage is indicated, but the specific nature or extent of the damage is difficult to ascertain, especially during the latter part of the fatigue lifetime.

The results of the dynamic structural analysis are more sensitive to the extent of damage throughout the specimen lifetime. The deformation in the undamaged streamline specimen during first mode bending as determined by the modal survey is depicted in Figure 13. Figure 14 shows the peak in amplitude vs frequency for this resonance as a function of life fraction, and Figure 15 is a plot of percent change in frequency vs N/N for the same specimen whose ΔE vs N/N curve is shown in Figure 10a. The resonant frequency continues to decrease throughout the lifetime of the specimen reflecting a continuous accumulation of damage until failure. This accumulation of damage is also reflected in an increase in damping as shown in the table of Figure 14. This technique clearly promises to be a useful technique in detecting the occurrence of in-service damage from changes in both resonant frequency and damping. A modal survey could also indicate the location of such damage by changes in measured mode shapes.

VI. CONCLUSIONS

The major conclusions of the experimental work are as follows:

1. In none of the materials studied is the presence of an endurance limit clearly indicated, although some nonlinearity in the S-N curves is suggested, especially at low loads.
2. Fatigue-induced damage in the fiber-dominated laminates studied gives rise to a modulus decay as a function of dimensionless life fraction which is a characteristic of the laminate geometry, and essentially independent of load level. In these materials the modulus decay curve can be used as an indication of remaining life fraction during fatigue loading.
3. In the resin-dominated laminate and filament wound specimens, a time and stress dependent yielding phenomenon occurs which shifts the modulus decay curves toward shorter life fractions at higher fatigue loads. Fatigue-induced strain hardening can occur at high loads, causing the modulus to increase with increasing life fraction.
4. NDE techniques such as vibrothermography and ultrasonics can pick up the presence of damage in these fatigue specimens, but are not sensitive to the extent of damage, especially later in the fatigue life.
5. Dynamic modal analysis is a promising candidate for an in-service NDE technique which is sensitive to both the location and extent of fatigue-induced damage.

VII. REFERENCES

1. Salkind, M. J., "Fatigue of Composites," Composite Materials: Testing and Design (Second Conference), Anaheim, CA, April 20-22, 1971, ASTM STP 497, 1972.
2. Henneke, E. H. and Reifsnider, K. L., "Quality Control and Nondestructive Evaluation Techniques for Composites; Part VII: Thermography - A State-of-the-Art Review," AVRACOM TR 82-F-5, March 1982.
3. Reifsnider, K. L., E. G. Henneke and W. W. Stinchcomb, "The Mechanics of Vibro-thermography," Mechanics of Nondestructive Testing, Plenum Press, NY, 1980.
4. Chou, S., R. Brockelman, A. Broz, Y. Hinton, R. Shuford, "Analytical and NDE Techniques for Determining Crack Initiation in Graphite/Epoxy Laminates," Proceedings of ASTM Symposium: Effects of Defects in Composite Materials, December 1982.
5. Hamstad, M. A., "Quality Control of Nondestructive Evaluation Techniques for Composites, Part VI: Acoustic Emission - A State-of-the-Art Review," to be published as AVRACOM TR 83-F-7, Spring 1983.
6. Hagnauer, G. L., "Quality Assurance of Epoxy Resin Prepregs Using Liquid Chromatography," Polymer Composites. Vol. 1, No. 2, December 1980.
7. Foley, G. E., M. E. Roylance and W. W. Houghton, Life Prediction of Glass/Epoxy Composites Under Fatigue Loading, Proceedings of the ASME Conference: Advances in Life Prediction Methods, Albany, NY, April 18-20, 1983.
8. Broutman, L. J. and S. Sahu, "Progressive Damage of a Glass/Reinforced Plastic During Fatigue," Proceedings of the 24th SPI Conference, 11D, February 1969.

VIII. ACKNOWLEDGEMENTS

The authors gratefully acknowledge the following people for their contributions to this work: Elias Pattie for his help in fatigue testing and data reduction, Yolanda Hinton for the development of software for data acquisition and reduction, John DeLuca and Herb Gassett for fabrication of test specimens, Robert Brockelman for ultrasonic testing, Gary Hagnauer and Emily McHugh for chemical characterization, and Susan Mehigan for preparation of the manuscript.

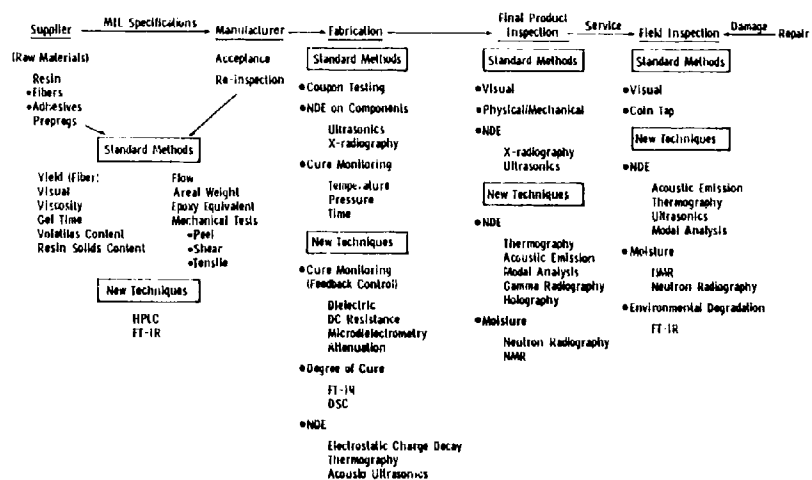


Figure 1. QUALITY CONTROL & NDE TECHNIQUES FOR COMPOSITES

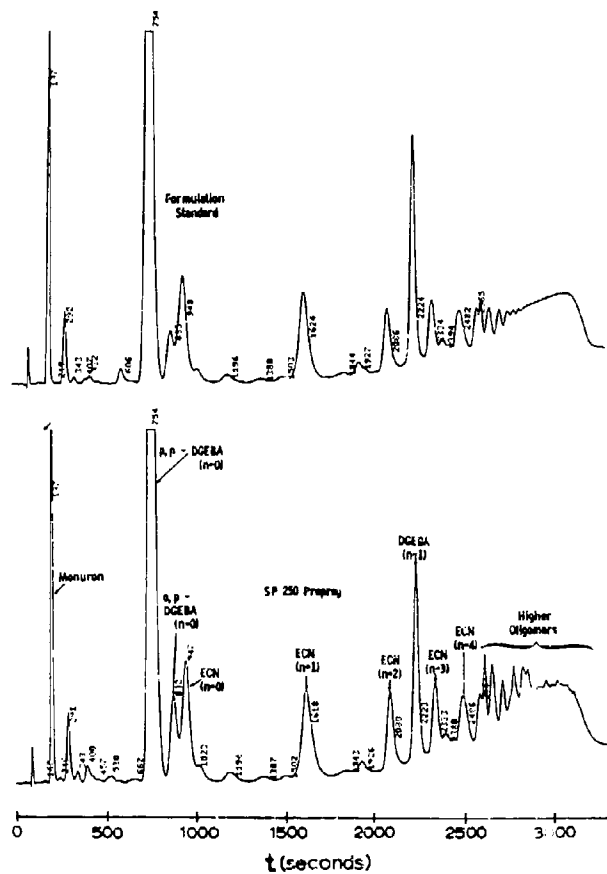


Figure 2. HPLC FINGERPRINT OF SP250 PREPREG (FROM REFERENCE 6)

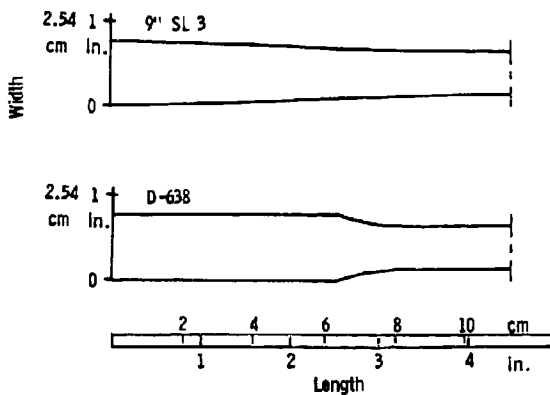


Figure 3. LAMINATE STREAMLINE SPECIMEN GEOMETRY COMPARED TO ASTM STANDARD

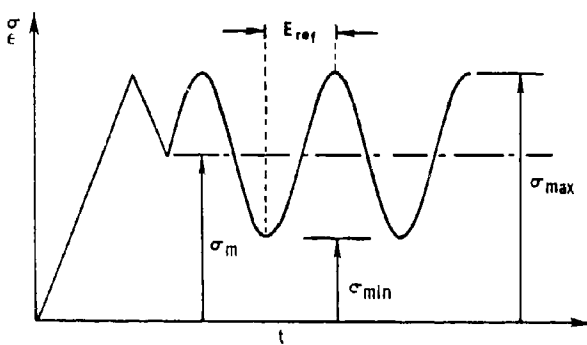


Figure 4. INITIAL LOADING HISTORY OF FATIGUE SPECIMENS

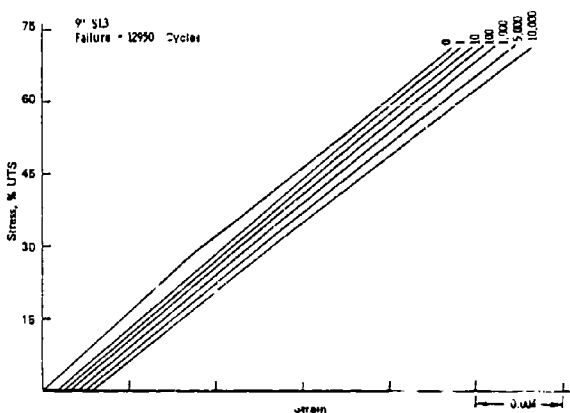


Figure 5. STRESS-STRAIN CURVES OF 0, 90° LAMINATES AS A FUNCTION OF FATIGUE LOADING

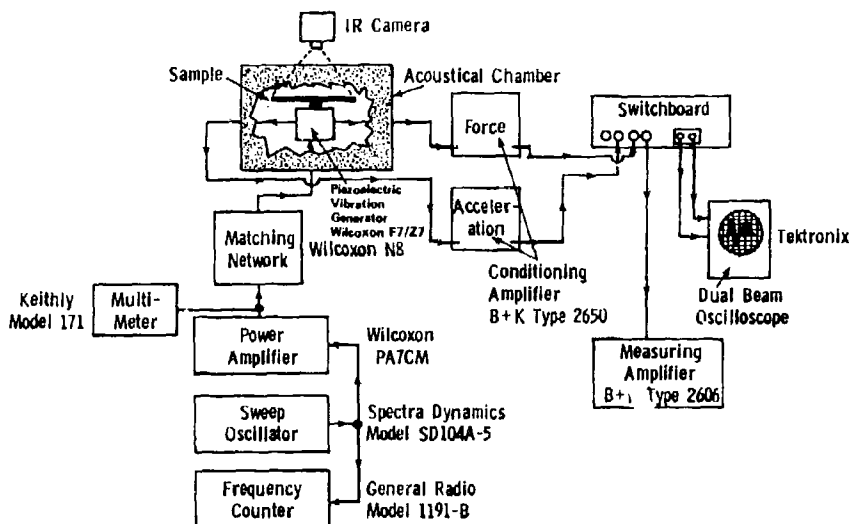
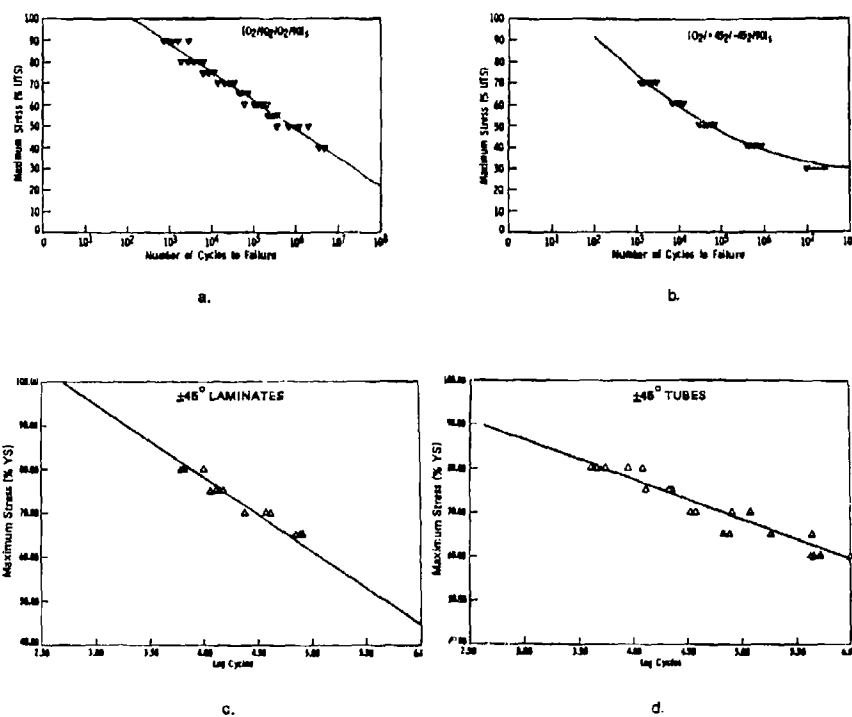
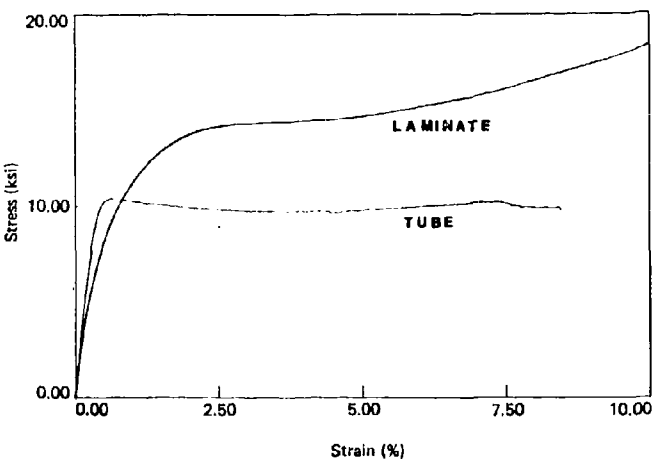
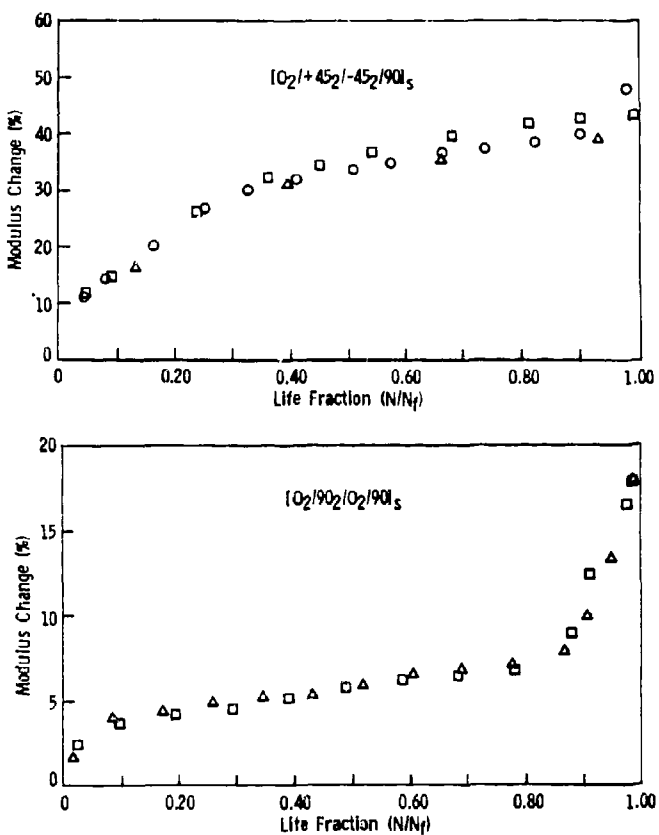
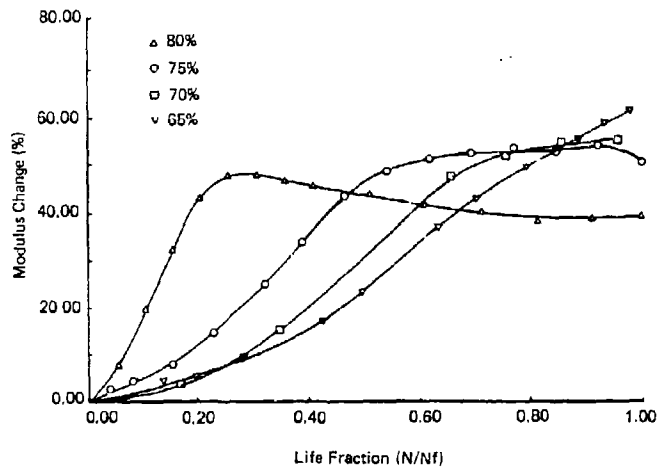


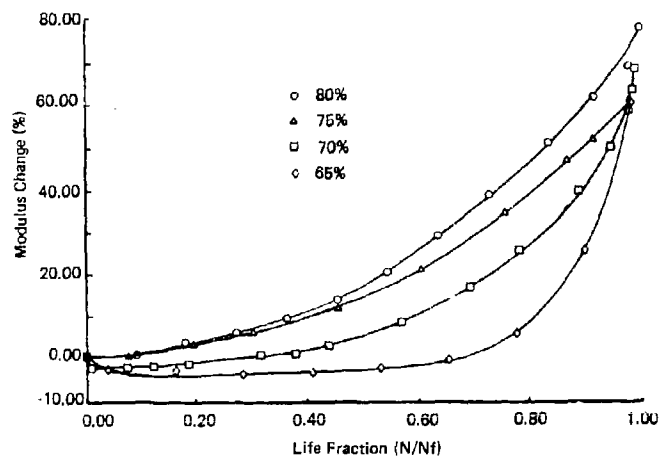
Figure 6. DIAGRAM OF VIBROTHERMOGRAPHY APPARATUS

Figure 7. MAXIMUM LOAD VERSUS LOG LIFETIME FOR THE MATERIALS STUDIED
a. 0, 90° LAMINATES, b. 0, ±45, 90°, c. ±45° LAMINATES, and d. TUBES

Figure 8. STRESS-STRAIN CURVES OF TUBES AND $\pm 45^\circ$ LAMINATESFigure 9. MODULUS CHANGE VERSUS DIMENSIONLESS LIFETIME FOR FIBER DOMINATED MATERIALS
a. $[0_2/+45_2/-45_2/90]_S$ and b. $[0_2/90_2/0_2/90]_S$



a.



b.

Figure 10. MODULUS CHANGE VERSUS DIMENSIONLESS LIFETIME AT VARYING MAXIMUM STRESS FOR RESIN-DOMINATED MATERIALS
a. 345° LAMINATES and b. TUBES

7-12

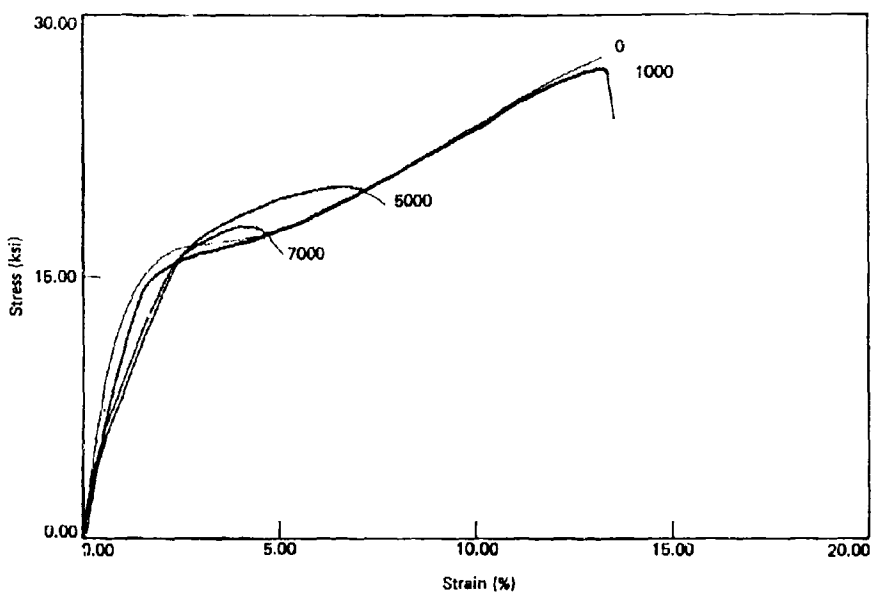


Figure 11. STRESS-STRAIN CURVES OF $\pm 45^\circ$ LAMINATES AS A FUNCTION OF FATIGUE LOADING

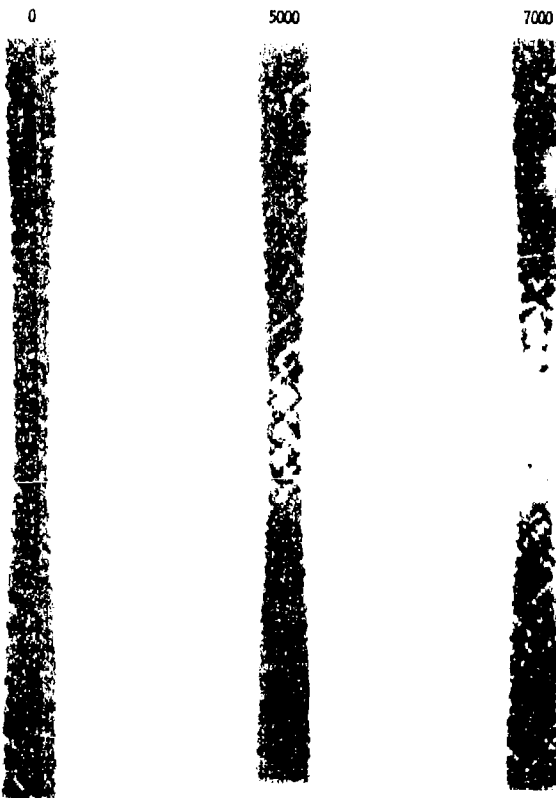


Figure 12. ULTRASONIC C-SCANS OF $\pm 45^\circ$ LAMINATES AS A FUNCTION OF FATIGUE LOADING

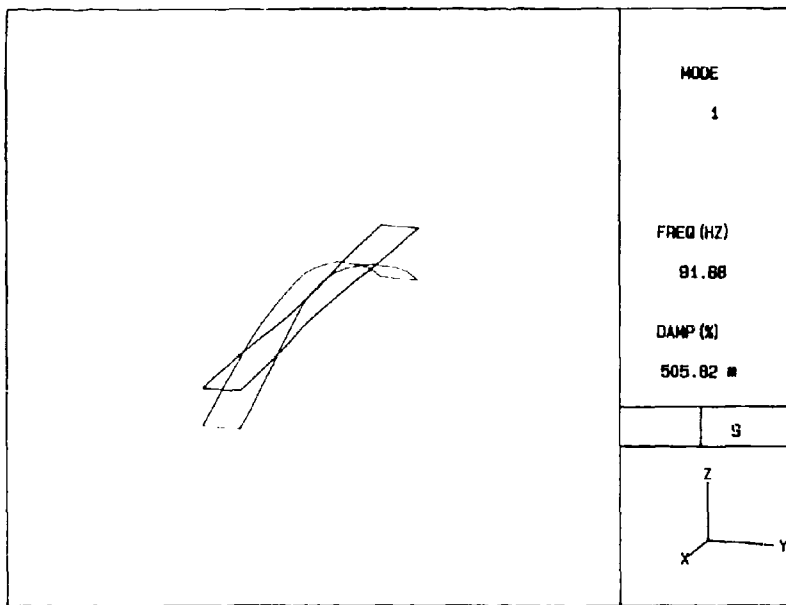
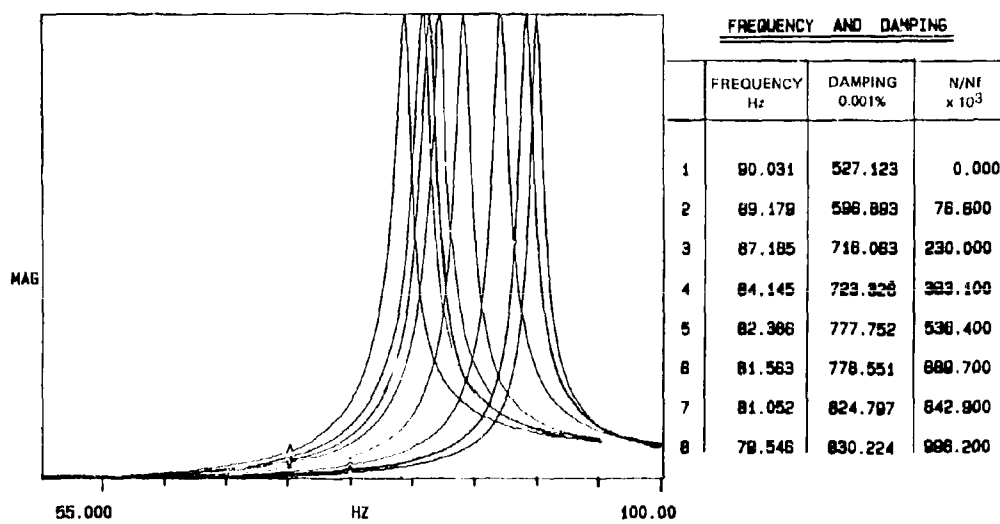


Figure 13. FIRST MODE FLEXURE IN A STREAMLINE SPECIMEN

Figure 14. FIRST MODE FLEXURAL RESONANCE PEAKS DURING FATIGUE LIFE AT 75% YS OF A $\pm 45^\circ$ LAMINATE SPECIMEN

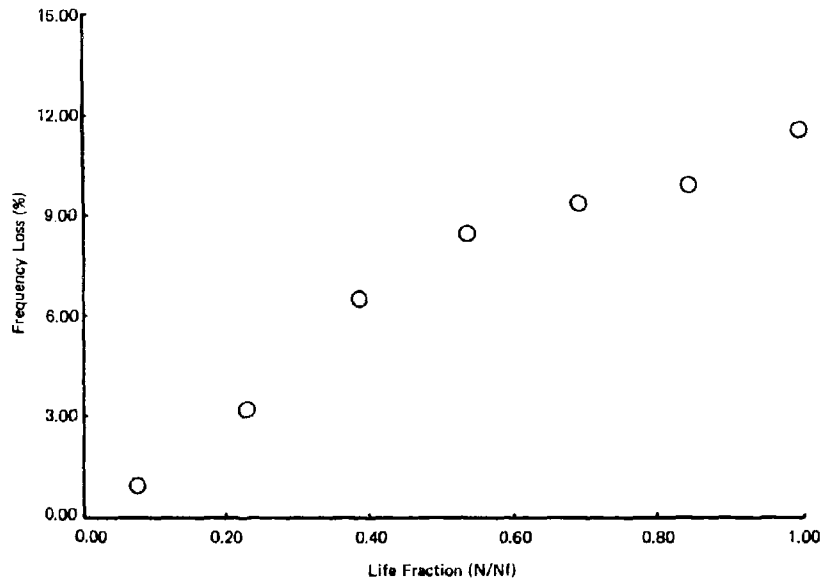


Figure 16. PERCENT CHANGE IN RESONANT FREQUENCY VERSUS DIMENSIONLESS LIFETIME
AT 75% YS FOR $\pm 45^\circ$ LAMINATE SPECIMEN

AD P 001916

AN EMPIRICAL APPRAISAL OF DEFECTS IN COMPOSITES

NIGEL PARSLAW

MATERIALS LABORATORY

WESTLAND HELICOPTERS LIMITED

YEOVIL SOMERSET

1. INTRODUCTION

The application of fibre reinforced plastic materials in aircraft structure is desirable because the material exhibits high strength to weight ratio, good fatigue properties and easy formability. Although the materials exhibit high strength along the fibre direction, the strength across fibre and interlaminar in the structure is significantly less. In addition, interference with the fibre/resin bond, interlaminar adhesion or fibre alignment would lead to a substantial reduction in the strength of the structure. Providing these deficiencies are considered in component design, the overall advantages of manufacturing aircraft structure from composite materials far outweigh the disadvantages of reduced shear properties.

A project was undertaken to develop a helicopter tail rotor blade from fibre reinforced materials. The manufacture of eighty blades was identified within the constraints of the project. The objectives of the programme were as follow:-

- a) To evaluate manufacturing techniques for composite materials.
- b) To evaluate the small testpiece properties of the constituent materials in the aged and unaged conditions.
- c) To evaluate the performance of the tail rotor blade and start a long term natural ageing programme to assess the effect on blade performance.
- d) To finalise design detail, assess non-destructive evaluation techniques and determine acceptable standards for the component.

The tail rotor blade was manufactured from pre-preg. material in the form of uni-directional glass fibre, uni-directional carbon fibre and woven glass fabric (two weave styles) all impregnated with epoxy resin. ↗

An expanding mandrel technique was used to manufacture the tail rotor blade as described below.

Plies of uni-directional and woven glass reinforced pre-preg. were wrapped around a rubber tube enveloping an aluminium mandrel. A wedge of uni-directional glass fibre reinforced pre-preg. (debulked) formed the uni-directional nose moulding and was laid along the leading edge and enclosed in the woven wraps. This tube of pre-preg. formed the blade spar. The trailing edge was made of $\pm 45^\circ$ angle plied carbon fibre skins and a foam insert, the root end was built up with two doublet stacks. Figure (i) and (ii) are schematics of the construction. The assembly was placed in a hinged aluminium tool. The tool was closed and the blade shape formed by the application of 90 psi. air pressure, in the rubber tube, which forced the pre-preg. against the inside of the aluminium tool. A two hour dwell at 90°C permitted consolidation of the pre-preg. The component was then heated to 120°C for one hour to complete the cure and harden the resin, after which the blade was cooled, demoulded and trimmed. Further operations involved bonding an erosion shield, tip caps and root end attachment bushes.

All the development blades were subjected to non-destructive evaluation to develop a technique capable of assessing the size and location of defects in the component, whilst maintaining a degree of convenience to ensure rapid inspection of the component.

During the development of the tail rotor blade, various defects and discontinuities were produced. These can be categorised into the following groups:-

- a) Raw material defects as supplied, e.g., fibre whorls, foreign bodies, non-uniform resin impregnation.
- b) Manufactured defects produced during moulding, e.g., voiding, fibre misalignment, inadvertent inclusion of extraneous material.
- c) Designed in discontinuities to allow more efficient use of the pre-preg. e.g., jointed pre-preg.

Raw material defects were removed from the material prior to lamination and the inadvertent inclusion of extraneous material can be eliminated from the component by thorough inspection methods during lamination.

2. TESTING

Coupon Evaluation

Fibre Misalignment

The spar element of the tail rotor blade was manufactured from alternate plies of woven fabric and uni-directional glass reinforcement. The uni-directional material was aligned with the centrifugal forces in the blade. A coupon test programme evaluated the effect on the static mechanical properties when two folded plies of woven fabric were included in a predominately uni-directional laminate.

Two millimetre thick GRP laminates were manufactured from 12 plies of 0.125mm. uni-directional and 2 plies of 0.25mm. woven pre-preg. Large overlapping wrinkled plies of woven material were laid into the test laminates, see figure (iii) while the control laminates were un wrinkled. The tensile and flexural strength in the 0° (along the primary fibre direction) and 90° (across the fibre direction), of both laminates were evaluated. The tensile specimen was parallel sided, end tabbed and with dimensions of 150 x 20 x 2 mm. The flexural specimen dimensions were 60 x 20 x 2 mm, loaded at a rate of 5mm./minute on a three point bend rig of span: thickness ratio of 25:1. The results appear in the table below. The value for strength is the average of six specimens.

Test	Wrinkled	Specimen	Plain	Specimen
	0°	90°	0°	90°
Flexural strength/MPa	1560	1083	1670	1233
Coefficient of Variance/%	16	12.7	2.8	7.2
Reduction in strength/%	6.6	12.2		
Tensile strength/MPa	984	40.2	1164	47.3
Coefficient of Variance/%	7	12.2	3	5.8
Reduction in strength/%	15.5	15.0		

From this evaluation, it was concluded that the inclusion of the wrinkled plies of woven fabric in a predominately uni-directional laminate affected the stability of the uni-directional materials and reduced the overall strength of the laminate. It was considered that this large reduction in static strength would produce a significant reduction in the fatigue properties and wrinkling of fibres should be strictly controlled in composite structures.

Joints in Continuous Fibre Composites

The Principle

The manufacturing technique for pre-preg. materials was to remove undesirable defects prior to lamination, and produce structure free from raw material defects. When considering the production of helicopter main rotor blades, the requirement of using only nine metre, defect free lengths in the build would lead to substantial material wastage. The effect of including a jointed ply of pre-preg. in a continuous fibre laminate was evaluated to determine whether a more efficient use of the pre-preg. material could be achieved.

Scalpel Cut Pre-preg.

The effect of including a discontinuous ply of pre-preg. in an eight ply laminate on the fatigue properties of glass reinforced epoxy was evaluated. The discontinuous ply was overlapped by 25mm. in the centre of a 150 x 10 x 2 mm. specimen, reduced to a thickness of 1mm. in the centre by means of a 125mm. radius. Figure (iv) illustrates the test specimen. Plain unjointed specimens were subjected to a P ± P loading configuration to produce a S-N curve with a range of failures between 10³ and 10⁷ cycles. The test frequency was 20 Hz.

A gap of approximately 0.5mm. was produced between the plies in the butt joint. Photograph (1) illustrates the scalpel cut butt joint. The results were presented as an S-N curve, figure (v) and the endurance limits at 10⁷ cycles for the plain and jointed specimens are presented below:-

	Endurance Limit (10^7 cycles)	MSF
Plain	250 MPa	1.214
Jointed	210 MPa	1.414

The endurance limit at 10^7 cycles was reduced by 16% and the Materials Scatter Factor (MSF) was increased by 16.5%. Therefore, the inclusion of a jointed ply in an eight ply laminate, not only gave a reduced design strength value but also lowered the confidence in achieving this strength. The plain specimens exhibited a more efficient stress system than the jointed specimens, as calculated by dividing the endurance limit by the number of continuous plies in each laminate. The plain specimens were stressed to 31.2 MPa/ply and the jointed specimens to 30.0 MPa/ply. The reduction in fatigue strength per ply was attributed to slight fibre misalignment in the continuous plies adjacent to the jointed ply.

The penalty of the reduction in fatigue strength associated with the inclusion of a jointed ply in an eight ply continuous fibre laminate was offset by the economic requirement to use material efficiently. Therefore, the design of a component would accommodate the lower fatigue strength values for a jointed ply in an eight ply laminate.

Conventional radiography was able to identify the location of joints in structure and thus post moulding control was implemented.

Automation

The inclusion of a discontinuous ply in an eight ply laminate was accepted in component design. Automatic cutting of pre-preg. was investigated to improve the time spent in cutting details for component assembly.

Laser Cutting of Glass and Carbon Pre-preg.

Ferranti CO₂ laser machine was used to cut glass and carbon pre-preg., at a power of 80 watts and a cutting speed of 15 metres/minute. The uni-directional pre-preg. was cut along and across the fibre direction. Sixteen ply laminates were manufactured with a total of sixteen butt joints, spaced 10mm. apart and staggered so that the joints were not coincident in consecutive plies. Figure (vi) illustrates the arrangement.

The following properties were evaluated:-

Longitudinal cut:	Flexural strength Tensile strength Interlaminar shear strength
Transverse cut:	Flexural strength Tensile lap shear strength

Test Methods

a) Flexural Strength (3 point bend)

GRP	Specimen = 60 x 10 x 2 mm. Support roller span = 50 mm. Cross-head speed = 5 mm./minute.
CFRP	Specimen = 100 x 10 x 2 mm. Support roller span = 80 mm. Cross-head speed = 5mm./minute.

b) Interlaminar Shear Strength (3 point bend)

Specimen = 12 x 10 x 2 mm. Support roller span = 10mm. Cross-head speed = 1mm./minute.
--

c) Tensile Strength

Specimen = 150 x 10 x 2 mm. Aluminium end tabs = 50 x 10 mm. Cross-head speed = 2mm./minute.
--

d) Tensile Lab Shear

as c), with joint at specimen centre.

Results

a) Glass Reinforced Epoxy

Property	Strength	C of V/%	Change/%
Long. Flexural Control	1.73 GPa	4.34	- 6.9
Long. Flexural laser	1.61 GPa	0.94	
Long. ILSS Control	96.8 MPa	4.77	- 0.5
Long. ILSS laser	96.3 MPa	4.02	
Long. Tensile Control	1.24 GPa	2.87	- 1.6
Long. Tensile laser	1.22 GPa	4.41	
Trans. Flexural Control	830 MPa	6.00	- 1.2
Trans. Flexural laser	820 MPa	4.56	
Trans. lap shear Control	580 MPa	2.30	- 5.2
Trans. lap shear laser	550 MPa	6.82	

b) Carbon Reinforced Epoxy

Property	Strength	C of V/%	Change/%
Long. Flexural Control	1.68 GPa	2.70	- 3.6
Long. Flexural laser	1.62 GPa	4.49	
Long. ILSS Control	94.7 MPa	2.69	- 5.8
Long. ILSS laser	88.3 MPa	1.23	
Long. Tensile Control	1.61 GPa	4.52	- 3.1
Long. Tensile laser	1.56 GPa	4.42	
Trans. Flexural Control	1.26 GPa	6.86	-26.2
	0.93 GPa	9.04	
Trans. lap shear Control	1.00 GPa	12.41	-35.0
Trans. lap shear laser	0.65 GPa	10.07	

The effect of laser cutting the pre-preg, reduced all the static strengths evaluated. The fibre/resin bond dominated properties in the carbon reinforced materials were more affected than the glass reinforced materials.

The transition in the chemical characteristics of the resin matrix was produced by the laser cutting of the pre-preg. The resin at the centre of the laser beam was charred, while away from the hot spot, the resin was only cured and 5mm. from the laser beam centre the resin appeared visually unaffected. However, long term storage of the material would tend to advance the cure of the resin in the heat affected zone and produce a wider strip of material affected by the laser beam cut than initially apparent after cutting.

The instability of the resin around the laser cut may produce a storage problem. The charred resin produced by the laser cut acted as an inclusion during moulding, restricting the resin flow around the end of the ply and resulted in voiding. The carbon fibres were swollen by the heat from the laser beam, doubling the diameter of the fibres at the cut edge, photograph (ii). This gross interference with the carbon fibres was probably the primary cause for the substantial reduction in the lap shear strength. When the glass fibre pre-preg, was cut across the fibre direction, the heat of the laser beam was sufficiently fierce to melt the ends of the fibres, forming globules of glass along

the cut edge, photograph (iii). Due to the detrimental characteristics of cutting pre-preg, the laser beam was considered unacceptable for component manufacture.

Water Jet Cutting of Pre-preg.

The pre-preg. was cut using a Flowsystems Water Knife Cutter with a 102 pump unit. The system generated 55psi. through a cutting nozzle of 0.2mm. diameter.

A similar investigation into the effect on the material properties was conducted for the water cutter as in the laser cutter, with the additional requirement to evaluate the effect of long term exposure to water and ice on the pre-preg. This requirement was identified to allow large number of details to be cut from a roll of pre-preg., which could be stored at -18°C in hermetically sealed bags, until required for assembly. A storage interval of 1000 hours was assessed.

a) Glass Reinforced Epoxy

Longitudinal Evaluation

Property	Conditioning	Strength	C of V/%	Change/%
Flexural	as cut control	1.65 GPa	2.8	
	as cut water	1.63 GPa	3.7	- 1.2%
Flexural	1000 hrs control	1.64 GPa	4.5	
	1000 hrs water	1.64 GPa	1.3	+ 0.6%
ILSS	as cut control	100.8 MPa	3.0	
	as cut water	100.8 MPa	2.0	0.0%
ILSS	1000 hrs control	97.7 MPa	2.5	- 3.1%
	1000 hrs water	96.0 MPa	1.6	- 4.8%
Tensile	as cut control	1.32 GPa	3.3	
	as cut water	1.27 GPa	2.0	- 3.8%
Tensile	1000 hrs control	1.31 GPa	3.0	- 0.8%
	1000 hrs water	1.25 GPa	6.4	- 1.6%

Transverse Evaluation

Property	Conditioning	Strength	C of V/%	Change/%
Flexural	as cut control	0.83 GPa	6.00	
	as cut water	1.07 GPa	7.22	+28.9%
	1000 hrs water	1.04 GPa	6.35	- 2.8%
Lap Shear	as cut control	0.58 GPa	2.30	
	as cut water	0.73 GPa	5.20	+25.9%
	1000 hrs water	0.67 GPa	5.5	- 8.2%

b) Carbon Reinforced Epoxy

Longitudinal Evaluation

Property	Conditioning	Strength	C of V/%	Change/%
Flexural	as cut control	1.92 GPa	7.9	
	as cut water	2.01 GPa	3.2	+ 4.7%
	1000 hrs control	1.88 GPa	4.1	- 2.1%
	1000 hrs water	1.90 GPa	3.1	- 5.5%
ILSS	as cut control	92.0 MPa	3.6	
	as cut water	95.0 MPa	2.3	- 3.1%
	1000 hrs control	97.9 MPa	2.0	+ 6.4%
	1000 hrs water	97.4 MPa	1.8	+ 2.5%
Tensile	as cut control	1.72 GPa	3.6	
	as cut water	1.74 GPa	6.2	+ 1.2%
	1000 hrs control	2.00 GPa	2.1	+14.0%
	1000 hrs water	1.93 GPa	4.0	+ 9.8%

Transverse Evaluation

Property	Conditioning	Strength	C of V/%	Change/%
Flexural	as cut control	1.26 GPa	6.9	
	as cut water	1.36 GPa	7.0	+ 7.9%
	1000 hrs water	1.22 GPa	7.6	-10.3%
Lap shear	as cut control	1.00 GPa	10.7	
	as cut water	1.02 GPa	4.6	+ 2.0%
	1000 hrs	0.76 GPa	16.8	-25.5%

Examination of the results revealed the effect of water jet cutting of the pre-preg, along the fibre direction was insignificant but when cut across the fibres, certain mechanical properties were substantially reduced and others significantly improved.

Examination of the water jet cut edge of the pre-preg, revealed a damage zone of approximately 0.5mm. into the pre-preg. The resin had been washed away from the edge of the pre-preg, and produced resin dry fibres along the pre-preg, edge. When the water jet cut edges were laminated, resin flowed from the adjacent layers into the butt joint and produced a well consolidated joint. This effect was apparent on a matrix material which included thermoplastic additives to control flow during cure, however resin matrices with different flow characteristics may not exhibit suitable flow around the water jet cut edge.

Blade Evaluation

Fibre Wrinkling in the Blade Transition Section

During the cure of some of the tail rotor blades, the plies of woven material in the spar became misaligned with the loading direction, producing folds in the plies along the length of the blade. See Photograph (iv). Conventional radiography was able to determine the length of the fold, and the degree of folding was assessed by comparing X-ray absorption contrast of known samples. Previous evidence from coupon evaluations suggested a significant reduction in strength of a woven/uni-directional glass fibre laminate was associated with wrinkling of this type. Therefore it was necessary to substantiate the performance of a blade which exhibited fibre wrinkling to evaluate the effect on blade performance.

The blade was subjected to a predetermined programme of fatigue testing, representative of a life of a blade, on a rig to simulate the lag, flap, torsional and centrifugal loads produced during flight. The blade met the minimum performance standard without failure. The blade continued testing and failed by a primary crack propagated along the edge of the erosion shield towards the tip end and also along the leading edge towards the tip. During the machine run down following the initial failure, a secondary crack through the trailing edge skins was produced. Neither of the cracks propagated through the wrinkled area of the transition section of the blade and thus the blade failure was considered to be independent of the fibre wrinkling in the spar. See figure (vii). The blade met the minimum performance design parameters, representative of a life of the blade.

Tail rotor blades free from fibre wrinkling in the spar marginally surpassed the fatigue life of the wrinkled blade, and failed by the initiation of a crack in the spar element close to the erosion shield which propagated spanwise towards the root and tip ends. To verify whether this reduction in strength associated with fibre wrinkling in the spar was significant, it would have been necessary to fatigue test at least five blades exhibiting a similar standard of wrinkling in the transition section, which would have been prohibitively expensive and outside the constraints of the development project.

Fibre Waving in Nose Moulding

A significant proportion of the centrifugal loads in the blade was carried by the uni-directional glass fibre/epoxy element located along the leading edge. It was considered essential to ensure the uni-directional glass fibres were aligned with the span of the blade to ensure the maximum strength efficiency of the element was achieved. During the development of the manufacturing procedure for the blade, it was apparent that the nose moulding exhibited local fibre waving in the plane of the blade. The glass fibres had waved between the leading and trailing edges over a distance of 2mm. The wavy fibres were confined to a local area of the nose moulding element and were apparent along 15mm. of the blade. See Figure (viii).

The blade was prepared for fatigue testing by bonding glass fibre doubler stacks onto the tip end of the blade and attaching a soft, aluminium powder filled silicone rubber prop across the chord to allow representative bending (flap) loads to be applied to the test section. Figure (ix) illustrates the arrangement.

An aerofoil section of a composite tail rotor blade was fatigue tested and completed fatigue testing representing approximately 65% of the minimum performance standard, whereupon the titanium erosion shield failed by a crack propagating through its chordwise section. The blade continued fatigue testing under fully factored flight loads and

eventually failed by a propagation of a crack through the composite uni-directional nose section. The blade met the minimum performance standard, in spite of the early erosion shield failure.

Examination of the failure showed the erosion shield crack, the composite crack and the edge of the silicone prop were coincident, see figure (ix). The silicone prop arrangement did produce a stress concentration effect where the blade failed and may have led to the early erosion shield failure and/or the composite failure. Examination of the composite leading edge section confirmed the fibre wavering in the uni-directional nose moulding produced during manufacture. The mechanical testing caused extensive delamination and broken fibres in the uni-directional nose moulding. Photographs (vi), (vii) and (viii) illustrate the damage. The cracks propagated from the origin along the nose towards the root and along the edge of the erosion shield towards the tip. The testing also caused cracking in the trailing edge section which was apparent in previous outbound fatigue test blades and was considered a usual failure mode in this test rig design.

The evaluation was inconclusive in respect of the prime contribution to the failed erosion shield and the composite nose moulding due to the inadequacies of the method of load application to the test specimen. It was not possible to eliminate non-representative stress concentration associated with the soft silicone prop.

Specimens with and without fibre wavering failed in similar modes, composite failures were always preceded by failure of the metallic erosion shield, its influence on the subsequent behaviour of the composite cannot be easily determined.

The test was primarily designed to establish the capability of the structure to satisfy minimum performance requirements for development flight clearance. This was achieved. However, the real consequence of wavy fibres in composite structures has not been ascertained. The performance requirements are not sufficiently demanding to differentiate between the two states of the material.

Notwithstanding the above, certain observations on the expected performance of the materials can be made from the test data. The magnitude and the type of damage in the wrinkled specimen was greater. The accumulated fatigue cycles for the wrinkled specimen were less than the wrinkle free specimen. This evidence can be interpreted as indicating that when component design demands optimum performance from the composite then fibre distortion cannot be tolerated and the manufacturing process must eliminate any risk of its occurrence. Where wrinkled fibre cannot be avoided due to manufacturing constraints, then satisfactory performance can be achieved from the component providing the design allowances are determined from representative specimen containing the appropriate features.

Voiding in the Leading Edge of the Nose

The development tail rotor blade exhibited voiding in the leading edge at the root end of the blade, see photograph (xi). The voiding occurred in an area where the majority of the centrifugal loads were transferred from the uni-directional nose moulding into the woven spar wraps and doublers. If the voiding was situated along the nose moulding/sparwrap interface, then the blade would be unable to transfer the centrifugal loads from the nose moulding into the doubler stack at the root end, and may lead to premature failure. However, if the voids were situated away from the critical interface, then the centrifugal loads could be transferred, and the standard of the blade would be acceptable. It was therefore necessary to non-destructively determine the precise location of the voiding.

Conventional X-ray was able to determine the presence of voiding in the composite tail rotor blade but not able to provide a complete analysis of the location. Fibre wrinkling, gross delamination and extraneous material was revealed by conventional radiography whereas the precise location of defects was evaluated by Computer Aided Tomography (CAT).

3. NON-DESTRUCTIVE EVALUATION OF THE TAIL ROTOR BLADE

The system for examining voids in the tail rotor blades was firstly to radiograph the blade and from the results, if it was impossible to determine the location of voids in contentious areas, then the blade was subjected to CAT using a Type 7020 High Resolution Body Scanner.

The CAT technique involved taking eighteen X-ray shots around a one millimetre slice of the component and transferring the data onto a computer matrix of 320 x 320 squares. The computer matrix represented a real size of 120mm. diameter, producing a resolution of 0.375mm. The scan speed was 80 seconds, the computer processing time 120 seconds, giving a component examination turn around time of approximately 5 minutes. The information taken from the scan was processed in a digital array on a chart in the form of X-ray absorption values. The absorption value range was +2000 to -1000, with glass fibre reinforced plastic and air registering 1300 and 0 respectively. The voiding in a structure was determined by selecting a threshold absorption value and joining points in the array representing air in the structure. The information was displayed initially on a VDU to reveal the size and location of the voiding. See photographs (ix and (i)). By manipulating the threshold value, it was possible to highlight different aspects of the

structure at the expense of losing the detail of other features, for example resin richness could be highlighted at the expense of losing detail on voiding. The information could also be presented in print out form in an array of absorption values as described above.

The resolution of CAT was less than that of conventional radiography and the accuracy was further reduced by the technique approximately circular details in the component into a square matrix on the computer. The current standard of CAT could not be used as a routine inspection tool because the technique only examines a one millimetre section and a tail rotor blade and would require approx. 600 shots in a full evaluation giving a total inspection time per item of 50 hours. However, in spite of the restrictions of the existing form, CAT does offer a solution for evaluating complex arrays of defects in structure.

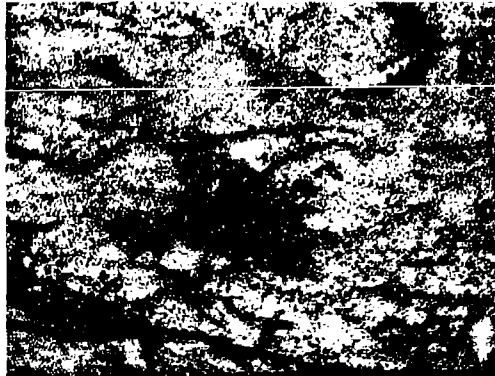
4. FINAL OUTCOME

The data generated from the joints programme indicated that joints in composite structure would be permissible provided an allowance for the loss in strength was made in the design. The size, location, quantity and method of cutting of the joint in a given structure must be controlled.

From the evidence gained from the tail rotor blade evaluations, the fatigue performance of composite structure appeared to be more tolerant of fibre wrinkling than may have been postulated at the early stages of the development project. Thus in future, designers in composite structures may adopt a less critical approach to defects in composites providing sufficient substantiation test data is accumulated on the lowest acceptable standard for the component to achieve the necessary confidence for flight clearance.



Photograph (i) Mag. X200 Scalpel Cut Butt Joint



Photograph (ii) Mag. X100 Laser Cut Carbon Prepreg, Swollen Fibres



Photograph (iii) Mag. X6 Laser Cut Glass Prepreg, Globules of Glass



Location of Wrinkling in Spar Photograph (iv)



Photograph (v) Mag. X4 Spar Wrinkling in Test Blade



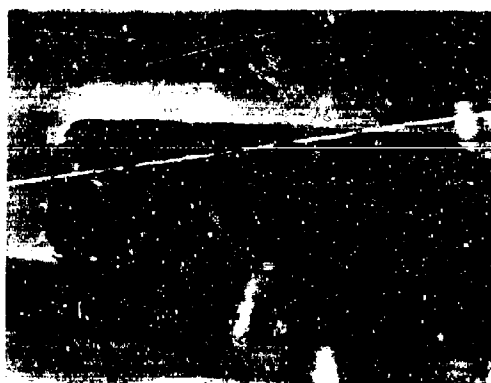
Photograph (vi) Failed Test Blade



Photograph (vii) Mag. X6 Fibre Waving and Broken Fibres



Photograph (viii) Mag. XG Delaminated Nose Moulding



Photograph (ix)



Photograph (X) Voiding At Root End Leading Edge



Photograph (xi) Mag. X4

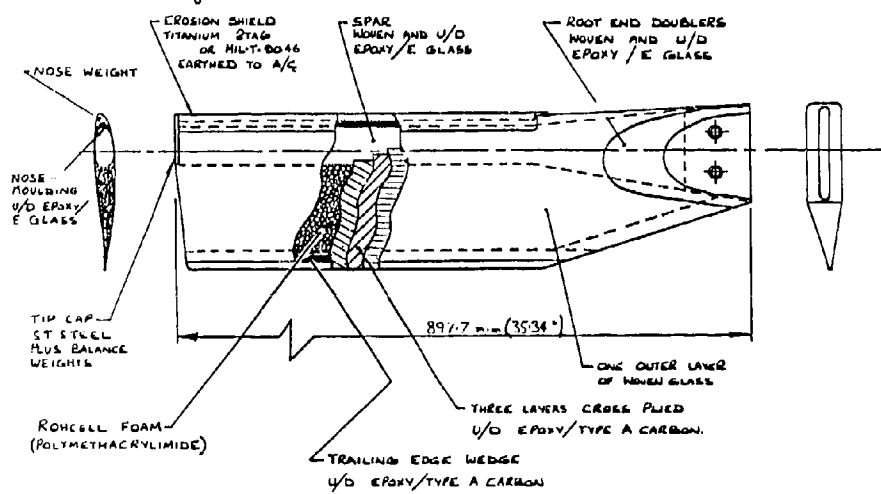
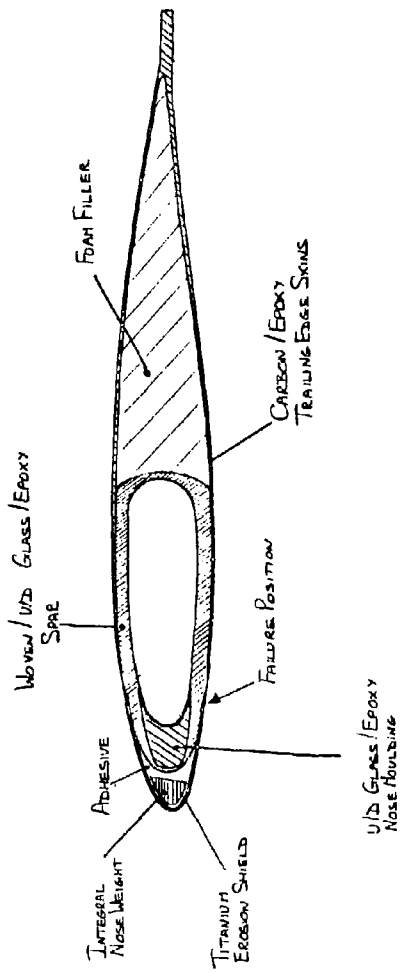


FIGURE (i)



TYPICAL BLADE SECTION : 45% - 100% ROTOR RAD. S

FIGURE (ii)

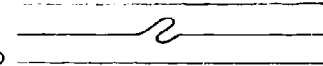
U/D GRP  2 PLIES OF WOVEN
GRP

FIGURE (iii)

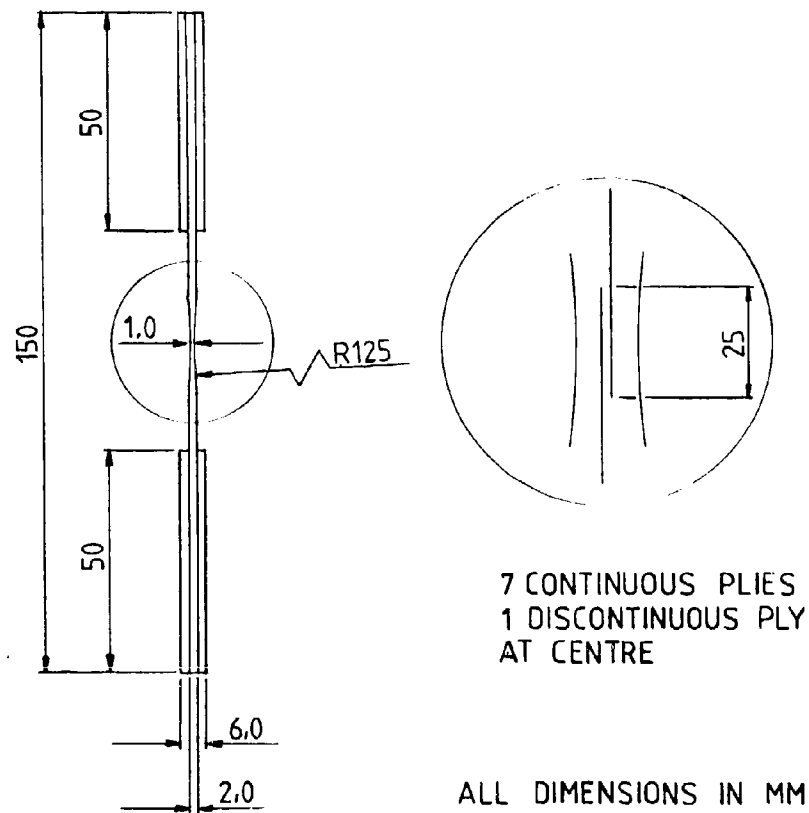


FIGURE (iv)

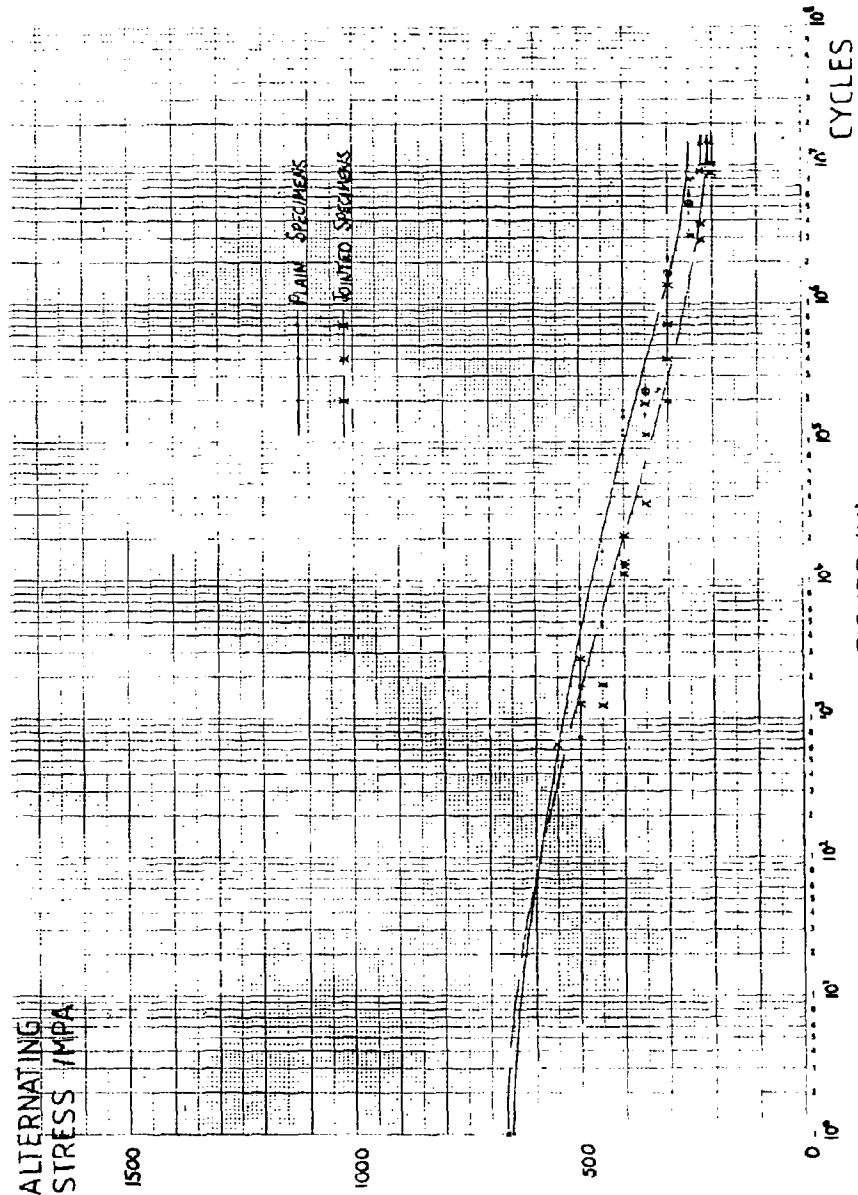


FIGURE (V)



FIGURE (Vi)

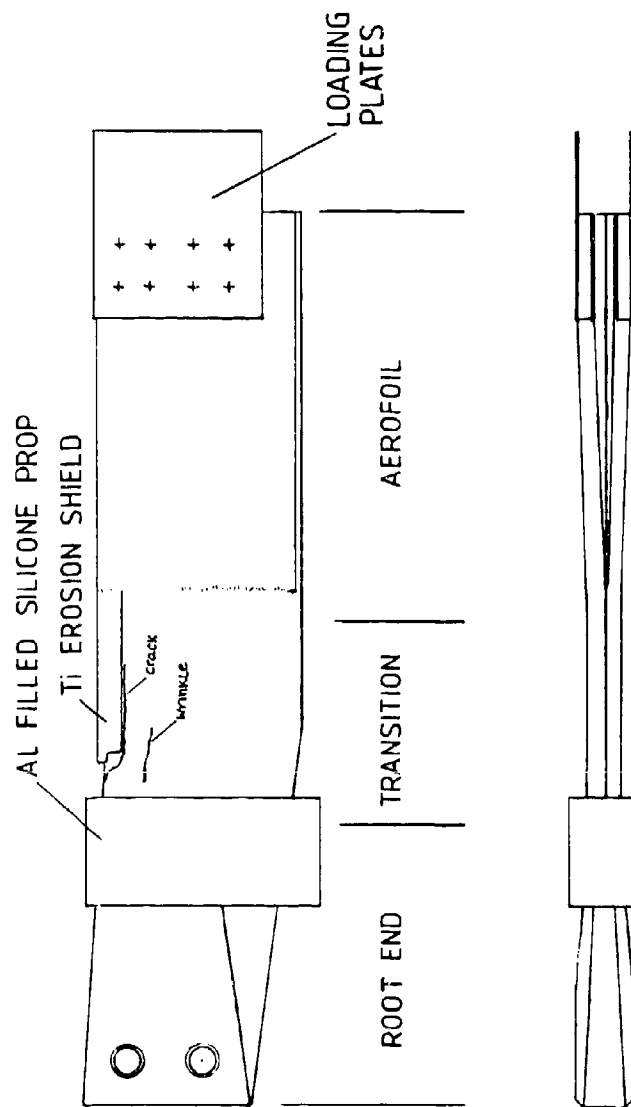
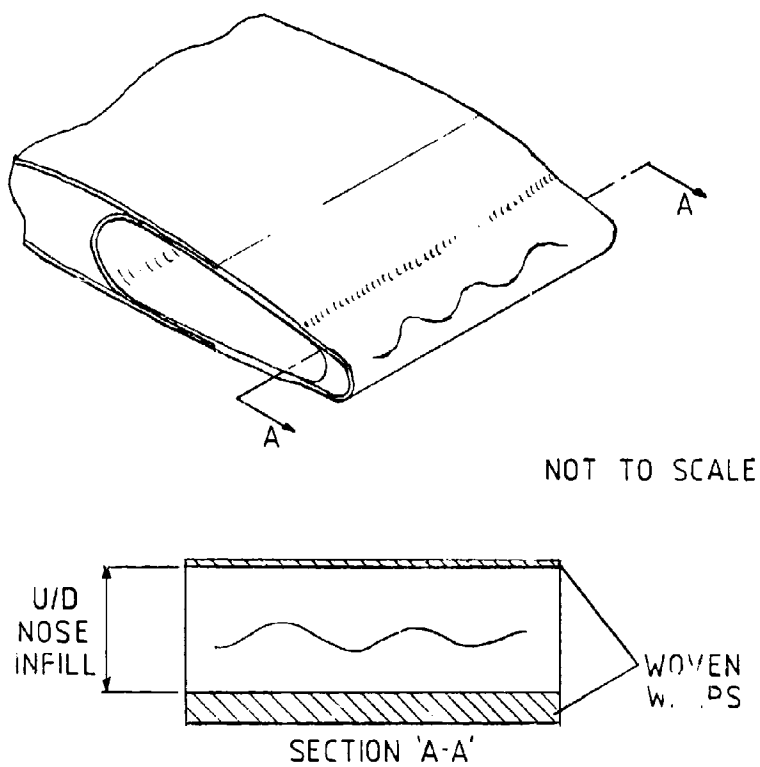
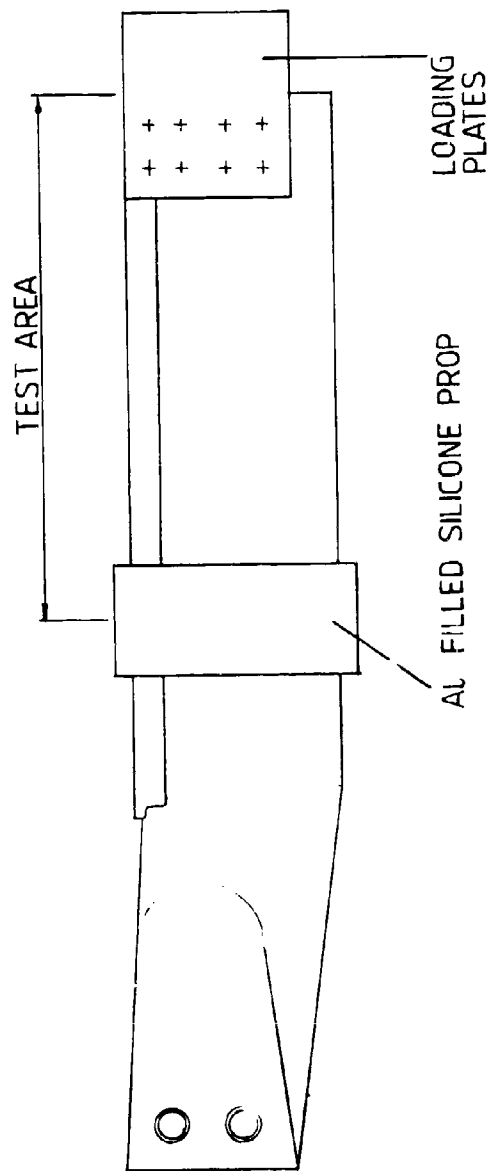


FIGURE (Vi)



FIBRE WAVING IN UNIDIRECTIONAL NOSE MOULDING

FIGURE (Viii)



OUTBOARD FATIGUE TEST

FIGURE (ix)

ADP001917

9-1

CORRELATION BETWEEN NON DESTRUCTIVE INSPECTION RESULTS AND PERFORMANCE OF GRAPHITE/EPOXY STRUCTURAL PARTS

Dr. Ing. Franco Cipri, Responsible
Materials Technology Research
AERITALIA G.V.C.
Corso Marche 41
10146 Torino, Italy

SUMMARY

During production of advanced composite structural parts, because of material or manufacturing process anomalies, some typical defects, such as porosity and/or delaminations, may become embodied into the final product. In order to improve the accept/reject criteria for typical defects, AERITALIA's G.V.C. Laboratories have carried out a static/fatigue test program on specimens in which various porosity levels were simulated. Further, an attempt has been made to correlate mechanical performances with the ultrasonic energy absorption measures.

1 INTRODUCTION

In manufacturing of composite aerospace structures the interaction among many process variables may cause the presence of typical defects in final product. Often such defects are a direct consequence of the deviation occurred on one or more process parameters and may be concentrated on small areas (delaminations, voids, inclusions, etc.) or may spread on large parts of the structure (porosity).

Once manufacturing defects have been detected, it is necessary that specialists, who are charged with the responsibility of accepting or rejecting the defective parts, may compare the actual situations with suitable reference standards, in order to foresee the decay of mechanical performances relevant to the detected defects.

Among the defects that may affect wide parts of Graphite/Epoxy (GR/EP) structures, porosity is a most typical one, particularly if fabric material is predominating in the lay-up; further the repair of porosity affected areas is difficult and expensive. When porosity is present on a coccured box shape structure, as for instance a torsion box, as it is not possible to replace defective parts (panels, ribs and spars), it may occur that the complete structure has to be rejected.

Deviations in manufacturing process that may cause porosity inside GR/EP laminates are well known and the outstanding ones are:

- inadequate pressure on the laminate, caused by bridging between ply and bag or between ply and rubber tools
- low pressure on laminate caused by a vacuum bag leakage
- phase error between temperature and pressure cycles due to autoclave malfunction
- local lack of resin overflowed out of the laminate or irregularly spread.

Porosity in laminates may be detected by means of suitable equipments for Non Destructive Testing (N.D.T.); in particular at AERITALIA Combat Aircraft Group many "Through Transmission Ultrasonic" (T.T.U.) facilities are operating for inspection of manufactured parts.

Defects are detected when some anomalous attenuation occurs on ultrasonic energy (Frequency = 1 MHz) transmitted through the material thickness when the structure is scanned. The ultrasonic energy measures are recorded on a print out paper as attenuation levels, with a resolution of 6 dB and a total dynamic range of 72 dB.

In order to evaluate the influence of porosity on mechanical performances of GR/EP composite structure, AERITALIA's G.V.C. Laboratories started a static/fatigue testing program, whose results, even though at present only on comparison basis, have to provide an experimental base for the improvement of existing accept/reject criteria.

Furthermore, an attempt has been made to correlate mechanical performances with the ultrasonic energy absorption parameters coming from N.D.T.

This paper presents the testing method adopted and the results achieved on part of GR/EP materials in the present AERITALIA composite structures. Static and cyclic fatigue tests have been carried out on lami-

nates manufactured with fabric prepreg type 3000 yarn, 7 mil. inch thickness, plain weave, 40% nominal resin content and T 300 fibers.

In addition the static behaviour of specimens laminated with unidirectional prepreg type 95 gr/m², 37% resin content, T 300 fibers, has been investigated. At present further tests on other kinds of GR/EP materials and more complete load simulation are still in progress.

2 POROSITY SIMULATION

The porosity examples in GR/EP laminates that we have most often found are those caused by lack of pressure during epoxy resin polymerization cycle. Within the aim of the present work, we have therefore selected as porosity simulation the technique of reducing the autoclave pressure below the requested values, while the temperature followed its own cycle within specification tolerances. The choice of pressure-level in the specimen fabricated for mechanical testing purposes has been guided by the results obtained during the preliminary tests; such results were compared with defective situation ascertained on actual structures.

Particularly in Fig. 1 are clearly outlined the panel sections of solid laminate obtained out of the same material but cured with 4 different pressures; the fig. number 2 shows, instead, a sandwich-panel in which strong porosity is evident with delamination trend. Each defect-degree simulated has been correlated to the ultrasonic energy attenuation levels ($f = 1$ MHz) picked up on the Non destructive Test (N.D.T.) of the type Automatic Through Transmission Ultrasonic (A.T.T.U.) operating at G.V.C. in TORINO - Factories. The simulated porosity level characterization was finally completed with the density measures and the voids percentage in each laminate. The average values of the above said measures, over the whole testing are shown at table I.

3 TEST PROGRAMME

From the panels, polymerized with four different autoclave pressures, and after the ultrasonic absorption is measured, both the specimens for fatigue and static tests were cut. For each material was in such way possible to directly relate the fatigue and the ultimate static resistance values, independently of the dispersion factor which must be recurred with whenever batches from different supply sources are used. However, limitedly to the panels obtainable from material type 3K70 PW, since the testing took place in two different stages, the results obtained at two different supply sources are available, which allows also the counterproof that between the two the behaviour is analogous, both as concerning the porosity simulation and the physical/mechanical test results.

3.1 STATIC TEST

Over a total of 249 specimens, that had not previously absorbed humidity and under ambient temperature conditions, the following tests were taken: tensile, compressive, interlaminar shear (short beam) and flexural. The shape of the specimens and test methods chosen are identical to those prescribed by the present Aeritalia Standards for incoming acceptance of the respective materials (see fig. 3).

It has thus been possible to homogeneously compare the static strength of the porous specimens with those previously obtained both from Aeritalia Laboratory and from Suppliers, totalling therefore other additional 80 specimens. The average values of the obtained results are summarized in tab. II.

As envisaged, because of the different resin viscosity and its flowing between the fibres, fabric laminates have showed a higher sensitivity to the effect of pressure variation, compared to unidirectional tape. This was evidenced before by the ultrasonic absorption and void content measures (Tab. I) and then confirmed in terms of static performances decay when decreasing the autoclave pressure (Tab. II and III). Furthermore, ever since the first tests taken on supplier A material, it appeared evident that the mechanical characteristics more greatly affected by the presence of porosity are those "resin dominated" (compression and ILSS).

From Tab. III it can be noticed that all the tested laminates have maintained nearly unchanged their mechanical performances when reducing the autoclave pressure from 600 KPa down to 300 KPa. Decreasing from 300 KPa to 150 KPa the fabric laminates have lost in average 24% in compression and 18% in interlaminar shear strength. Fabric laminates from either suppliers A and B have behaved statically in an analogous way. As already mentioned, unidirectional laminates showed a lower degree of sensitivity to the autoclave pressure variation. In fact the compression resistance of panels cured at 150 KPa has turned out to be reduced of only 6% and the interlaminar shear strength of 16%. Also panels polymerized at only 50 KPa have evidenced a remarkable residual resistance, reduced to 36% under compression and 27% under interlaminar shear.

3.2 FATIGUE TESTS

The up to now performed fatigue tests have been carried out over a total of 120 specimens, laminated in fabric material type 3K-30-PW, with lay-up 0°/90°. Besides, the same laminates from which the static test specimens were cut have also been used for the comparative evaluation of the porosity effects under fatigue loading.

In order to submit it to cyclic loads either tensile and compressive, the specimen at fig. 4 was designed; its profile is derived from that of the tensile one for fabric laminates but the width of the central section with parallel sides has been increased from 12.7 mm to 15.5 mm, in order to obtain a width/thickness proportion of about 5. Even if with such proportion the uniformity of the stresses in the usefull section of the specimen is affected by the presence of edge effects, it can be assumed that the validity of the obtained results, which are anyhow of comparative type, is reliable. Besides having the advantage of being worked out in an economical and rapid way, this specimen is easily coupled to a device that prevents its giving-in due to instability under compression loads (see fig. 5).

Furthermore this equipment, being fastened to the machine frame, assures the reproducing of the assembling conditions of the specimens between the jaws.

The performed fatigue tests have a sinusoidal wave loads, which are applied at frequencies ranging between 5 and 10 Hz, depending on load amplitude and on the loading frame used. Because the difference between ultimate tensile and compressive stresses on fabric laminate has showed to be of the same degree as the scatter between the corresponding experimental values, the fatigue stresses were calculated with a view to a single ultimate value (539 MPa), obtained averaging the results of the ultimate tensile and compressive tests on laminates cured at 600 KPa.

The section of the specimens have all been referred to the nominal thickness of 2.95 mm, neglecting thus the fact that final thickness of the polymerized laminates is affected by the autoclave cure respective pressure.

The 120 fatigue tests have all been carried out at ambient temperature and, out of these, 84 have been performed on specimens without any prior aging treatment, while 36 (18 cured at 150 KPa and 18 at 300 KPa) have undergone an aging for 21 days, immersed in water at 60°C. At the end of such period, the specimens cured at 150 KPa have absorbed the 2,1 humidity in weight, while those cured at 300 KPa have absorbed 0,9%.

The fatigue results of fabric laminates are reported in Tab. IV and in S-N curves at Tab. V. From them it seems that for lives, ranging between $5 \cdot 10^4$ and $5 \cdot 10^5$ sinusoidal cycles, the peak to peak amplitude, both with $R = 0$ and with $R = 1$, is practically the same, either for laminates cured at 600 KPa or for those at 300 KPa. In the same cycle interval, the specimens cured at 150 KPa have withstood stress levels that, referred to those of the 600 KPa specimens, at $R = 0$ are 5% lower while at $R = -1$ are only 2 + 3% lower. It is furthermore noticed that, according to S-N curves, such differences in stresses tend to further decrease when the respective lives overcome 10^5 cycles.

By comparing the results of the tests with $R = 0$ to those with $R = -1$ it is possible also to remark that between the applicable stresses, at equal lives, a constant proportion of about 2 is existing and for which the fatigue life of fabric laminates, whether in presence or absence of porosity, seems to depend more on the peak/peak range of the applied stresses than on their sign.

The behaviour of the specimens, aged in a humid environment, under fatigue loads $R = -1$, has appeared consistent with that of dry specimens. In particular specimens cured at 150 KPa have withstood stress levels about 2% below those cured at 300 KPa, which have in turn, exhibited 3% slump in respect of the non aged specimens 600 KPa at $5 \cdot 10^5$ cycles life.

5 CONCLUSIONS

Comparing the results of static tests with those of fatigue tests it is possible to assume that the presence of porosity in GR/EP laminates causes a decay in mechanical performances which is more sizable in static conditions than under fatigue loads. The above occurrence makes the results of static tests appear more conservative compared to the fatigue ones, conferring them sufficient validity in the characterization of the porosity effects, especially when suitable fatigue test results are not available yet.

Even if by means of the N.D.T. system A.T.T.U. type was possible to evidence the presence of porosity in laminates, it appears premature to correlate at this stage such indications directly with the structural performances. In fact the effect of porosity on mechanical performances has also showed up on laminates that had not previously yielded appreciable variation on N.D.T. results.

Studies are therefore being conducted at Aeritalia in order to improve the sensibility and resolutions of the existing ultrasonic methods, as well as set up new instrumentation endowed with more advanced performance capabilities.

TABLE I - PHYSICAL CHARACTERISTICS OF TESTED LAMINATES

	LAMINATE TYPES	NOMINAL VALUES AT 600 KPA	AUTOCLAVE CURE PRESSURE (KPA)				
			50	150	300	600	
THROUGH TRANSMISSION ULTRASONIC AVERAGE ABSORPTION (DB/MM)	3K-70-PW FABRIC 3 MM THICKNESS	SUPPLIER "A" SUPPLIER "B"	2	10	4	2	2
	GR. 95 U.D. TAPE (1.2 MM) (SUPPLIER "A")			-	6	2	2
VOID CONTENT %	3K70 PW FABRIC	SUPPLIER "A" SUPPLIER "B"	2 Max	10,7	1,7	0,81	0,2
		SUPPLIER "A" SUPPLIER "B"		-	1,33	0,22	0
DENSITY (GR/CM ³) (ASTM D 792)	3 MM THICKNESS		1,53	1,36	1,49	1,52	1,52
				-	1,45	1,50	1,53

TABLE II - ULTIMATE STATIC STRENGTH OF LAMINATES CURED AT DIFFERENT AUTOCLAVE PRESSURES

LAMINATE MATERIAL	ULTIMATE TESTS	50 KPA			150 KPA			300 KPA			600 KPA			INCOMING SUPPLIER TESTS (MPa)	
		STRENG. (MPa)	S.DEV. (MPa)	C.V. %											
3K-70-PW FABRIC	SUPPLIER A	TENSILE	-	-	532	26,1	4,9	547	19,8	3,6	-	-	-	570 565	
		COMPRESSIVE	335	26,2	7,6	450	20,9	4,6	549	20,8	3,8	-	-	-	605 604
		IL SHEAR	38	2,5	4,9	60	1,7	2,9	72	3,7	5,1	-	-	-	69 75
		FLEXURAL	374	20,5	5,5	610	21,7	3,6	618	27,7	4,5	-	-	-	-
	SUPPLIER B	TENSILE	-	-	556	47,3	8,5	580	20,9	3,6	580	23,1	3,9	563 585	
		COMPRESSIVE	-	-	495	46,6	9,4	600	25,4	4,2	627	76,5	12,2	593 603	
		IL SHEAR	-	-	54	1,3	2,4	62	4,2	6,8	66	4,4	6,7	69 74	
		U.D. TAPE	COMPRESSIVE	767	51,8	6,8	1118	75,3	6,7	1160	39,5	3,4	-	-	1160 1220
	GR. 95	IL SHEAR	78	3,7	4,7	90	3,5	3,9	96	4,9	5,1	-	-	-	108 105

TABLE III - VARIATION OF LAMINATES ULTIMATE STATIC STRENGTH DUE TO POROSITY

LAMINATE MATERIAL	ULTIMATE TESTS	REF.ULTIMATE STRENGTH AT 600 KPA (MPa)	50 KPA		150 KPA		300 KPA	
			(MPa)	%	(MPa)	%	(MPa)	%
3K-70-PW FABRIC	SUPPLIER A	TENSILE	566	-	-	34	- 6	- 19 - 3
		COMPRESSIVE	605	- 270	- 45	- 165	- 26	- 56 - 9
	SUPPLIER B	IL SHEAR	72	- 34	- 47	- 12	- 17	0 0
		FLEXURAL	618	- 244	- 39	- 8	- 1	0 0
U.D. TAPE GR. 95	SUPPLIER A	TENSILE	586	-	-	- 30	- 5	- 6 - 1
		COMPRESSIVE	627	-	-	- 132	- 21	- 27 - 4
	SUPPLIER B	IL. SHEAR	66	-	-	- 12	- 18	- 4 - 6
		COMPRESSIVE	1190	- 423	- 36	- 72	- 6	- 30 - 3
	IL. SHEAR	107	- 29	- 27	- 17	- 16	- 11	- 10

TABLE IV - AXIAL LOADING FATIGUE TEST RESULTS - FABRIC LAMINATES

SPECIMEN AGEING	LOADING RATIO MIN/MAX	FATIGUE LIVES (CYCLES)	FATIGUE STRESS LEVELS					
			150 KPA		300 KPA		600 KPA	
			STRESS AMPLITUDE (MPa)	% ULTIMATE STRESS	STRESS AMPLITUDE (MPa)	% ULTIMATE STRESS	STRESS AMPLITUDE (MPa)	% ULTIMATE STRESS
UNAGED	R = 0	$5 \cdot 10^4$	463	78	492	83	492	83
		10^5	445	75	468	79	474	80
		$5 \cdot 10^5$	397	67	415	71	423	72
	R = -1	$5 \cdot 10^4$	225	38	243	41	243	41
		10^5	213	36	225	38	225	38
		$5 \cdot 10^5$	190	32	202	34	202	34
AGED	R = -1	$5 \cdot 10^4$	196	33	208	35	-	-
		10^5	190	32	196	33	-	-
		$5 \cdot 10^5$	172	29	184	31	-	-

TABLE V - S-N CURVES

AUTOCLAVE
CURE PRESSURE150 KPa300 KPa600 KPa

% ULT STRESS

90

80

70

60

R = 0

A) UNAGED

40

35

30

R = -1

B) UNAGED

40

35

30

R = -1

C) AGED

25

 $10^4 \quad 2 \quad 3 \quad 4 \quad 5 \quad 6 \quad 8 \quad 10^5 \quad 2 \quad 3 \quad 4 \quad 5 \quad 6 \quad 8 \quad 10^6 \quad 2$

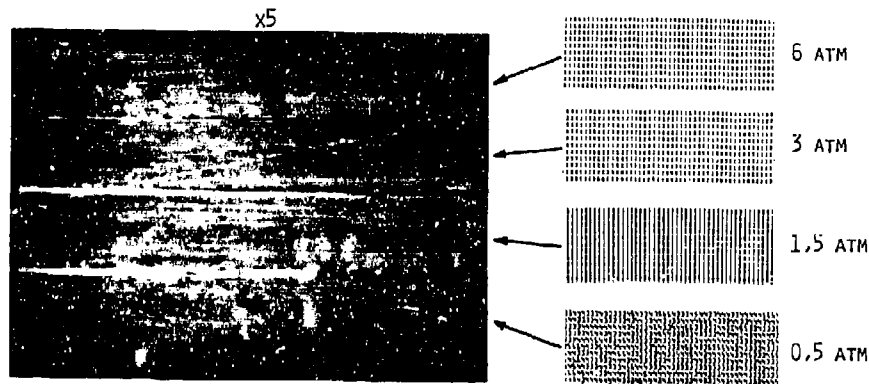


FIG. 1 - MACROGRAPH OF SAMPLES CURED AT 0.5; 1.5; 3; 6 ATM
AND RELEVANT A.T.T.U. PRINT OUT.

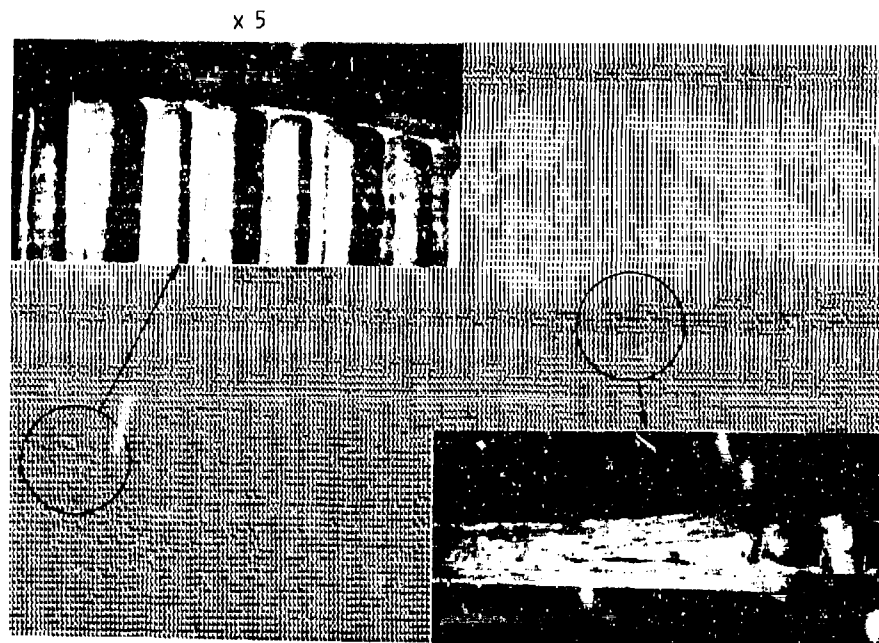
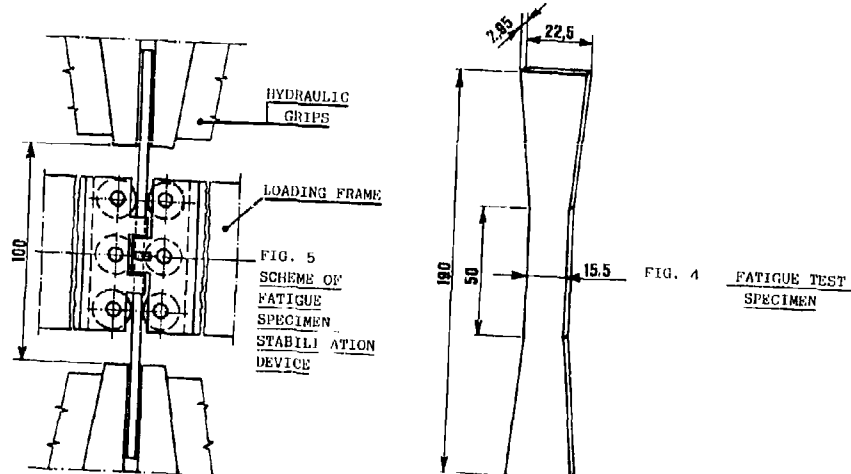
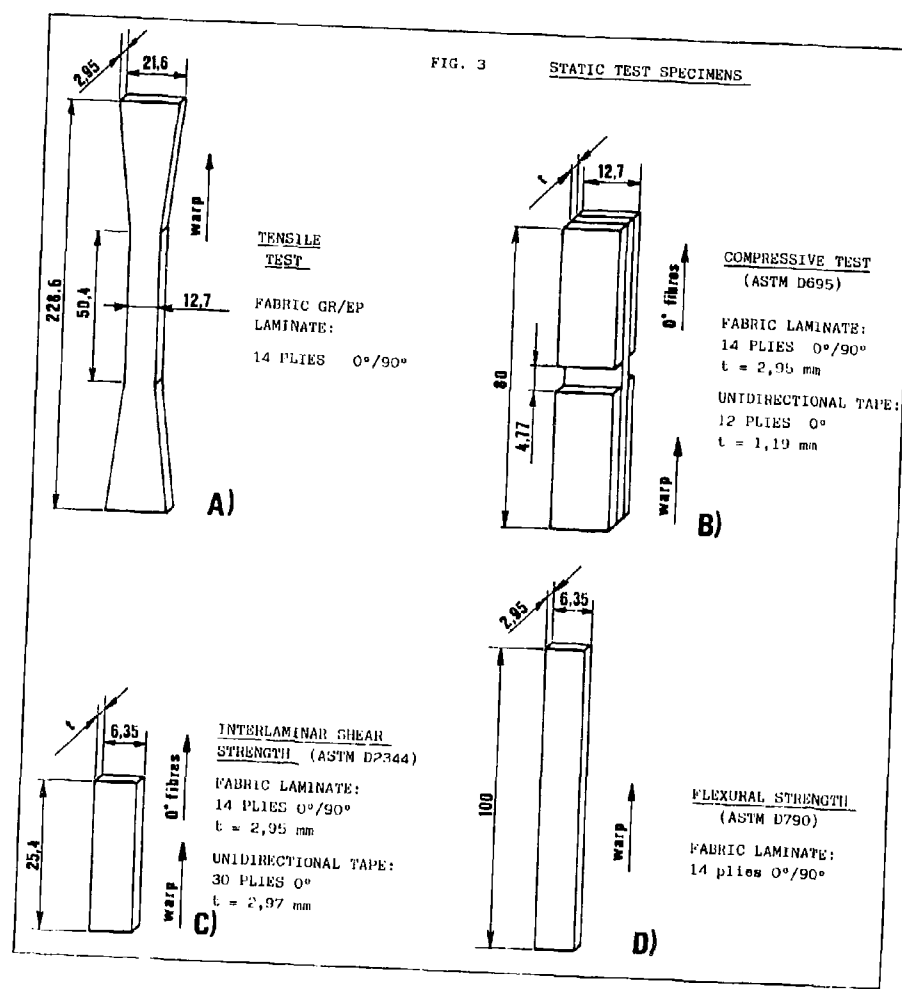


FIG. 2 - MACROGRAPHS OF HONEYCOMB PANEL SECTIONS INCLUDING
POROSITY AND RELEVANT A.T.T.U. PRINT OUT.

FIG. 3 STATIC TEST SPECIMENS



AD P001918

10-1

THE EFFECT OF DAMAGE ON THE TENSILE AND COMPRESSIVE PERFORMANCE OF CARBON FIBRE LAMINATES

by

Sarah M Bishop
Graham Dorey

Materials & Structures Department
Royal Aircraft Establishment
FARNBOROUGH
Hampshire

SUMMARY

The type of defect or flaw produced when CFRP is damaged in service depends on the structural design and the conditions of damage such as the energy and momentum of an impact. These defects are stress risers which may reduce the strength of the structure. There is a need, following non-destructive inspection, to be able to predict the residual performance so that decisions can be made on whether to monitor, repair or replace the component.

Various types of damage produced by typical impact situations have been assessed non-destructively and the effect on strength determined in tension and compression under both static and fatigue loading. For example areas of delamination, shown by sectioning, to be multiple delamination between the plies, reduce the compressive strength by local buckling processes. Detailed examination of the fracture mechanisms at machined notches emphasizes the importance of effects in neighbouring plies influencing the stress concentrations in the load carrying 0° fibres. These studies have given a better insight into the factors which affect the toughness and strengths of CFRP with stress raisers, and have helped explain the residual strengths of damaged carbon fibre laminates.

INTRODUCTION

Carbon fibres are strong, stiff and light making them attractive for aerospace load bearing structures. The high strength and stiffness is only exhibited in the fibre direction and for most practical applications laminates are made from layers of fibres laid at angles to each other so that loads can be carried in several different directions in the plane of the laminate. Because there is a marked reduction in modulus for off-axis fibres, when a laminate is stressed most of the load is carried by the fibres in the loading direction (0° fibres).

Damage and defects act as stress raisers which can cause premature fracture. In homogeneous materials the behaviour may be predicted by calculations of stress concentration or for sharp cracks by fracture mechanics; the main effect is the propagation of cracks perpendicular to the main tensile stress. Composite materials however contain weak fracture paths parallel to the fibres, and cracks can propagate in any direction and any plane relative to the main applied load, depending on the local stresses and local material properties. Some of these cracks may be detrimental and reduce the material strength but some may be beneficial in blunting notches and increasing the material toughness. Of major concern is the effect on the load-carrying 0° fibres.

When carbon fibre reinforced plastics (CFRP) are subjected to impact, the type of damage which occurs depends on the incident energy and momentum, material properties and the geometry¹. No damage occurs if the energy of the projectile is accommodated by the elastic strain energy in the material. Simple calculations have been made of the energies necessary to cause:

- a. delamination $(2/9)(\tau^2/E)(w^3/t)$
- b. flexural fracture $(1/18)(\tau^2/E)(wt)$
- c. penetration $w\sqrt{td}$

where τ is the interlaminar shear strength, σ the flexural strength, E the Young's modulus, w the through-thickness fracture energy, d the diameter of the projectile, and w , t the width, length and thickness of the flexed part of the test specimen. Whether delamination or flexural fracture occurs depends on the relative values of τ and σ and the span-to-depth ratio w/t ; impact damage is less likely when there are low modulus layers on the outside such as 45° layers or Kevlar or glass fibres. Whether penetration occurs depends not only on the incident energy but on the size of the projectile; penetration is more likely for small masses travelling at high velocities.

Dropweight impact, generally results in either delamination or flexural fracture (tensile or compressive) where fibres are broken. In the work now reported, damage was produced by a weighted projectile with a 10mm diameter nose dropped through 1 metre onto the laminate supported on a 100mm ring. The effect that such damage has on the tensile and compressive strengths of current high strength carbon fibre/epoxy composites is illustrated in Figure 1 for a 2mm thick (0° , $\pm 45^\circ$) laminate with the 0° fibres on the outside². (In this paper, strengths are always expressed in terms of the applied stress remote from the damage or notch.) Delamination produced by 1-2 Joule impact energies resulted in a 60% decrease in compressive strength whereas the tensile strength was unchanged. Broken 0° fibres, in addition to delamination, produced at higher impact energies resulted in a 25% reduction in tensile strength but no

further reduction in compressive strength was measured. In this case the impact damage reduced the compressive performance more than the tensile performance. However in a more brittle composite (see Figure 2) the reduction in strength was slightly more in tension than compression. In this 1.5mm thick multidirectional laminate the fibre-matrix bond strength was greater and less delamination occurred such that broken fibres had the bigger effect and greater reductions in tensile strength occurred.

Thus broken fibres have more effect on the tensile properties and delamination has more effect on the compressive properties.

2 NOTCH SENSITIVITY OF CARBON FIBRE REINFORCED PLASTICS UNDER TENSION

An understanding of the factors affecting the tensile behaviour of damaged CFRP where fibres are broken can be obtained from studies of the failure mechanisms at machined notches and holes.

When a tensile load is applied to a notched laminate, zones of damage form at the notch tips as a result of the high stresses in these regions. These damage zones consist of shear cracks parallel to the fibres, delamination between the layers and occasionally broken fibres. Generally the effect of a damage zone is similar to that of a plastic zone in metals; released energy is absorbed by the formation of the zone and the peak stress at the notch tip is reduced. Effectively the damage zone blunts the notch.

In Figure 3, a laser moiré technique^{3,4} has been used to show the damage zones produced at the tips of a sharp transverse notch in a (0°, ±45°) laminate. The moiré fringes are contours of constant in-plane deformation with deformation of 2.5μm occurring between fringes. Shear cracks in the surface layer are indicated by discontinuities in the fringes and cracks in the layer below the surface are indicated by closely spaced fringes associated with high surface strains.

In Figure 4, surface deformations due to damage zones obtained at sharp notches and circular holes just before failure are shown for two (0°, ±45°) laminates with the layers stacked in different sequences. Damage zones at sharp notches were larger than at circular holes and surface observations consisted of shear cracks parallel to the fibres in the surface layer, deformations due to cracks in the layers below, and delamination; at circular holes only shear cracks in the surface layer were observed. The blunting effect of the damage zones at sharp notches was such that the failure stresses were very similar to those for circular holes.

In Figure 5, the variation of tensile failure stress with notch size and shape is shown for another (0°, ±45°) carbon fibre/epoxy laminate. In this case the failure stresses for sharp notches (length 2a) were only 10-20% lower than those for circular holes of diameter 2a. In the range considered, all specimens with a notch tip radius of 2.5mm and length 2a failed at stresses within a few percent of those for circular holes of diameter 2a. It can be seen that, because of the presence of a damage zone, the stress concentration effect when a sharp notch is present is significantly less than might be expected from homogeneous anisotropic plate theory. This reduction in stress concentration will also occur for damage involving broken fibres in CFRP.

All cracking mechanisms in the damage zone absorb energy. However 0° shear cracks parallel to the load bearing 0° fibres are the most beneficial in that they blunt the notch in the 0° layer and reduce the stress concentration at the notch tip. Such 0° shear cracking is constrained by the neighbouring layers. Local delamination in the damage zone between 0° layers and adjacent layers is beneficial in tension in that it removes these constraints and allows more notch tip blunting to occur.

The significance of delamination in reducing notch sensitivity can be illustrated by looking at the effect of layer thickness⁵ in Figure 6. It can be seen that increasing the specimen thickness by keeping the layers thin and repeating the basic stacking sequence had little effect on the notched tensile failure stress. However increasing the layer thickness by four times resulted in almost a 50% increase in failure stress. This is because the interlaminar shear stress increases with increased layer thickness, more delamination occurs and thus there is less constraint on 0° shear cracking.

When delamination does not occur, interactions take place between the load-bearing 0° layer and the adjacent layers⁶. In Figure 7 is shown the effect on the 0° layer at the notch tip of 45° shear cracking in a neighbouring 45° layer. Crack opening and shear along the 45° crack results in a high stress band in the 0° layer. With increased applied stress the 45° crack grows, the stress in the 0° layer increases due to increased crack opening and shear and eventually 0° fibres break along the 45° line. The formation of 0° shear cracks at the tip of this crack in the 0° layer may stabilize crack growth. Thus 45° cracking in 45° layers has a detrimental effect on adjacent 0° layers. This effect is removed if local delamination occurs between the 0° and 45° layer.

Thus, to summarize, at a notch in a (0°, ±45°) laminate under tension

- 1 0° shear cracking is beneficial because it reduces the stress concentration on the loadbearing 0° layers;
- 2 45° shear cracking is detrimental because it increases the stress on the 0° layers;
- 3 delamination between the 0° and 45° layers is beneficial in that it increases the amount of 0° shear cracking and reduces effects due to 45° shear cracking.

The actual failure mechanisms which occur at the notch tip depend on the stacking sequence of the layers.

In Figure 8, failed specimens with (0°, ±45°) lay-ups are shown. In both cases the proportions of 0° layers and ±45° layers are the same but the stacking sequences are different. In Figure 8a, the outer 0° layers have failed along a 45° line from the notch tip; no delamination has occurred between the 0° layer and the adjacent +45° layer (the delamination seen in Figure 8a is between the +45° layers and the

-45° layers). In Figure 8b, the inner 0° layers have delaminated from the 45° layers and, although there is 0° shear cracking, the main failure direction is along a 90° line from the notch tip.

In Table 1, details of the failures at 10mm notches are related to the stacking sequence for four different lay-ups with the same proportions of 0° layers and $\pm 45^\circ$ layers. The direction of the line of failure in 0° layers, the delaminations (shown by arrows) and the effect these had on the failure stress are shown. In all cases delamination occurred between the $+45^\circ$ layers and the -45° layers. In the first lay-up the 0° layers failed along a 45° line with no delamination between the 0° and 45° layers. In this case it should be noted that the two 45° layers on either side of each 0° layer were orientated in the same direction. In the second lay-up delamination occurred between the outer 0° layers and the 45° layers and these 0° layers failed at 90° . Note the 45° layers either side of these outer 0° layers were orientated in different directions; the inner 0° layers bounded by $+45^\circ$ layers failed in the $+45^\circ$ direction. The failure stress was greater for the second lay-up where there were more delamination planes, delamination occurred between the 0° and 45° layers and 0° fibres had failed at 90° . The types of failures for the third and fourth lay-ups were mixed within the same specimen. In both lay-ups, 45° layers either side of 0° layers were orientated in the same direction but because the 0° layers were thick delamination, sometimes occurred between 0° layers and 45° layers. The mean failure stresses were higher than for the other two lay-ups but there was more scatter in the results probably because of the mixed types of failure mechanisms.

In Table 2, failure mechanisms at notch tips are summarized for this and other work⁶. Delamination usually takes place between $+45^\circ$ and -45° layers thus separating the laminate locally into smaller layered units. Where one or two 0° layers lie between a $+45^\circ$ layer and a -45° layer, or sometimes when 0° layers are thick, delamination occurs at the $0^\circ/45^\circ$ interface, 0° shear cracking takes place and the detrimental effects of 45° cracking are reduced, and the 0° layers fail along a 90° line. In laminates where the 45° layers adjacent to 0° layers are orientated in the same direction and the 0° layers are thin, cracking of the 0° layers along 45° lines occurs. Sometimes this effect is seen for thicker 0° layers where delamination does not take place. The 45° cracking results in a lower failure stress.

One way of possibly reducing the extent of 45° cracking is to use fibres in the form of woven cloth. Woven material is an attractive material for use in aircraft structures because of its handleability. However, it is not desirable to use woven material to carry the primary loads because the fibres will be distorted, but woven cloth can be used in the $\pm 45^\circ$ layers.

Some work has been carried out⁷ on the effect of substituting woven $\pm 45^\circ$ layers for non-woven $\pm 45^\circ$ layers in $(0^\circ, \pm 45^\circ)$ laminates. Cloth with a five shaft satin weave was used in the $\pm 45^\circ$ layers. In Table 3, mean failure stresses for specimens with 10mm sharp notches are compared for laminates with woven $\pm 45^\circ$ layers and those of non-woven material for three lay-ups. For the first and second lay-ups, the failure stresses were similar for woven and non-woven $\pm 45^\circ$ layers despite the lower volume fraction of fibres in the woven material. Comparing lay-ups 1 and 2 it can be seen that the greater failure stress due to thicker 0° layers was still obtained for the laminate containing woven $\pm 45^\circ$ layers. The first and third lay-ups with non-woven $\pm 45^\circ$ layers failed by 45° cracking of the 0° layers as a result of detrimental 45° shear cracking as described earlier. With woven $\pm 45^\circ$ layers it would be expected that such 45° shear cracking might be limited by the weave. Indeed for the third lay-up a greater mean failure stress was obtained with woven $\pm 45^\circ$ layers indicating that this can occur.

3 THE EFFECT OF DELAMINATION IN COMPRESSION AND FATIGUE LOADING

In Figure 9, areas of delamination produced by dropweight impact and detected by ultrasonic C-scanning techniques are shown for a $(0^\circ, \pm 45^\circ, 90^\circ)$ lay-up for a range of incident impact energies. Elongated strips of delamination of the outer 0° layers on the back surface are evident for the greater energy levels.

In Figure 10, a scaled diagram is shown of the damage obtained from a microscopic examination of a polished cross-section of a $(0^\circ, \pm 45^\circ)$ laminate after impact with an incident energy of 2 Joules. Delamination occurred throughout the laminate thickness between $+45^\circ$ and -45° layers and between 0° and 45° layers but was more extensive between layers towards the back surface. Shear cracks in the 45° layers were evident but no broken 0° fibres were seen.

Delaminated areas in impacted $(0^\circ, \pm 45^\circ)$ specimens were assessed before and after testing in compression. Some of these results are shown in Figure 11. During the compression test, an antibuckling device was used which constrained the specimen along its edges and at its ends leaving a central rectangular area (see dashed lines in Figure 11) free to deform out of plane. Small impact areas ($\sim 10\text{mm}$) such as that shown for 1 Joule impact failed in a compressive mode with the area of delamination seen after test resulting from the energy released during failure. However larger delaminated areas such as those shown due to 2 and 4 Joule impacts produced buckling instabilities under compression loading and the delaminations grew transversely in the specimen without extending along the length. Such behaviour has been predicted theoretically⁸.

In Figure 12, delaminated areas due to dropweight impact are compared for $(0^\circ, \pm 45^\circ)$ laminates with non-woven and woven $\pm 45^\circ$ layers (45° layers were on the laminate surfaces). The laminates with non-woven 45° layers showed extensive delamination in the 45° direction but this was not seen with woven $\pm 45^\circ$ layers because delamination between $+45^\circ$ and -45° layers and 45° shear cracking was limited by the weave. Thus the transverse dimension of the delaminated area was much narrower with woven $\pm 45^\circ$ layers. However for this lay-up with thick 0° layers, delamination between 0° and 45° layers appeared to be greater for woven $\pm 45^\circ$ layers. It can be seen that the substitution of woven cloth for non-woven material can have a significant effect on the extent and shape of impact damage.

In Figure 13, the properties of plain, notched and damaged specimens are compared in tension and compression for these $(0^\circ, \pm 45^\circ)$ laminates with woven and non-woven $\pm 45^\circ$ layers. Generally the compressive strengths were lower than the tensile strengths. There was little difference between the properties

obtained for woven and non-woven $\pm 45^\circ$ layers. The laminate with woven $\pm 45^\circ$ layers had a slightly lower plain tensile strength, as expected from the lower fibre volume fraction, but had a slightly greater notched tensile strength indicating that the woven material may have modified the failure mechanisms at the notch tip advantageously. The most significant difference was obtained for specimens containing damage due to 3 Joule impact. The residual compressive strength was 40% greater for woven $\pm 45^\circ$ layers than for non-woven $\pm 45^\circ$ layers almost certainly due to containment of shear cracking and delamination in the woven layers. However no significant difference was found in the residual compressive strengths of specimens containing damage due to 5 Joule impact. Also the compressive strengths of damaged and notched specimens with non-woven $\pm 45^\circ$ layers were similar in all cases showing that broken fibres can also contribute quite significantly to a reduction in compressive strength.

A programme of work has been carried out to investigate the effect of impact damage on the tension-compression fatigue performance of a (0° , $\pm 45^\circ$, 90°) CFRP laminate. The results for specimens containing damage due to 3 Joule impact were compared with those for undamaged specimens. In Figure 14, the static strengths of the laminate are shown for a range of incident impact energies. The residual tensile strength of a specimen with 3 Joule impact damage was similar to that for undamaged specimens indicating that no fibres had been broken, but the residual compressive strength was reduced by almost 50% due to delamination. In Figure 15, the effect of this delamination is shown in specimens subjected to fully reversed cyclic loading (CP); since all failures occurred in compression the values of static strength plotted were only of compressive strength. For undamaged specimens the difference between the static strength and the stress amplitude for fatigue lives of 10^5 cycles was 200 MPa whereas for the impact damaged specimens fatigue lives of 10^2 - 10^3 cycles to failure were achieved at stress amplitudes only 80 MPa less than the static strength. Thus, although the static compressive strength was substantially greater for undamaged specimens, the stress amplitude at which long fatigue lives could be achieved appeared to be converging for undamaged and damaged specimens. The results indicate that in the damaged specimens delamination did not grow substantially during fatigue and that any failure processes occurring in the surrounding undamaged material did not significantly interact with the impact damage.

4 SUMMARY OF RESULTS AND CONCLUSIONS

When damage occurs in multidirectional carbon fibre/epoxy laminates, broken fibres reduce the tensile strength whereas delaminations between layers reduce the compressive strength. Studies carried out on specimens with machined notches show that notch sensitivity in tension depends on the detailed failure mechanisms occurring at the notch. Shear cracking parallel to 0° fibres and local delamination is beneficial whereas shear cracking parallel to 45° fibres can have detrimental effects. Whether these failure mechanisms occur and to what extent depends on the material properties and the layer stacking sequence. In (0° , $\pm 45^\circ$) laminates, woven $\pm 45^\circ$ layers can be substituted for non-woven $\pm 45^\circ$ layers with little difference in notch sensitivity but some modification of failure mechanisms and a reduction in detrimental 45° shear cracking.

The effect of impact damage consisting of multiple delaminations has been assessed in compression. Large delaminated areas produce buckling instabilities and grow transversely during compression testing. A significant effect on the extent and shape of impact damage can be achieved by using woven cloth instead of non-woven material in the $\pm 45^\circ$ layers of (0° , $\pm 45^\circ$) laminates. Delamination and 45° shear cracking are limited by the weave and some improvement in compressive performance can be obtained. During tension-compression fatigue loading, delamination caused by impact does not appear to grow significantly, such that long lives can be obtained with little further reduction in stress amplitude.

Acknowledgments

The authors gratefully acknowledge the help in the experimental work of J Hutchings and R F Mousley of the Royal Aircraft Establishment, and D J Portsmouth and C J Wood, sandwich students from the University of Surrey and North Staffordshire Polytechnic respectively.

REFERENCES

- 1 Graham Dorey, "Relationships between impact resistance and fracture toughness in advanced composite materials". AGARD-CP-288, Effect of Service Environment on composite materials (1980)
- 2 Graham Dorey, "Fracture of composites and damage tolerance". AGARD-IS-124, Practical considerations of design, fabrication and tests for composite materials (1982).
- 3 M Marchant, S M Bishop, "An interference technique for the measurement of in-plane displacement of opaque surfaces". Journal of Strain Analysis, 2, (1), 36-43 (1974).
- 4 Sarah M Bishop, "Deformation near notches in angleplied carbon-fibre composites". RAE Technical Report 77093 (1977)
- 5 Sarah M Bishop, K S McLaughlin, "Thickness effects and fracture mechanisms in notched carbon-fibre composites". RAE Technical Report 79051 (1979)
- 6 Sarah M Bishop, "Effect of moisture on the notch sensitivity of carbon fibre composites". Composites, July 1983
- 7 Sarah M Bishop, P T Curtis, "An assessment of the potential of woven carbon-fibre reinforced plastics for aerospace use". RAE Technical Report 83010 (1983)
- 8 Byron Pipes, Private communication.

Table 1

STACKING SEQUENCE EFFECTS ON
TENSILE FAILURE OF NOTCHED CFRP

1	LAY-UP	$0^\circ -45^\circ +45^\circ 0^\circ 0^\circ +45^\circ -45^\circ 0^\circ$				
	FAILURE	-45°	↑	$+45^\circ$	↑	-45° 294 ± 9 MPa
2	LAY-UP	$-45^\circ 0^\circ +45^\circ 0^\circ 0^\circ +45^\circ 0^\circ -45^\circ$				
	FAILURE	90°	↑	$+45^\circ$	↑	90° 333 ± 20 MPa
3	LAY-UP	$-45^\circ +45^\circ 0^\circ 0^\circ 0^\circ +45^\circ -45^\circ$				
	FAILURE	90°	↑	90°	↑	370 ± 37 MPa
	AND		45°			
4	LAY-UP	$0^\circ 0^\circ -45^\circ +45^\circ +45^\circ -45^\circ 0^\circ 0^\circ$				
	FAILURE	-45°	↑	$+45^\circ$	↑	-45°
	AND	90°	↑	90°	↑	309 ± 19 MPa
					↑	DELAMINATION

Table 2

SUMMARY OF FAILURE MECHANISMS AT NOTCH TIPS IN
($0^\circ, \pm 45^\circ$) CFRP LAMINATES

STACKING SEQUENCE	FAILURE LINE OF 0° LAYERS	DELAMINATION BETWEEN 0° AND 45° LAYERS
$\dots +45^\circ 0^\circ 0^\circ +45^\circ \dots$	$+45^\circ$	NO
$\dots -45^\circ 0^\circ 0^\circ +45^\circ \dots$ and $\dots -45^\circ 0^\circ +45^\circ \dots$	90°	YES
$\dots \dots +45^\circ 0^\circ 0^\circ \dots$ and $\dots \dots +45^\circ 0^\circ 0^\circ \dots$	$+45^\circ$ or 90°	NO (45°) YES (90°)

Table 3

TENSILE FAILURE OF NOTCHED 0° , $\pm 45^\circ$ CFRP*
WITH NON-WOVEN OR WOVEN $\pm 45^\circ$ LAYERS

LAY-UP	FAILURE STRESS MPa	
	NON-WOVEN $\pm 45^\circ$	WOVEN $\pm 45^\circ$
1 $[0^\circ, \pm 45^\circ, 0^\circ]_s$	334	325
2 $[(\pm 45^\circ, (0^\circ)_2]_s$	392	390
3 $[(\pm 45^\circ, 0^\circ]_s$	267	288

*ALL 0° LAYERS NON-WOVEN

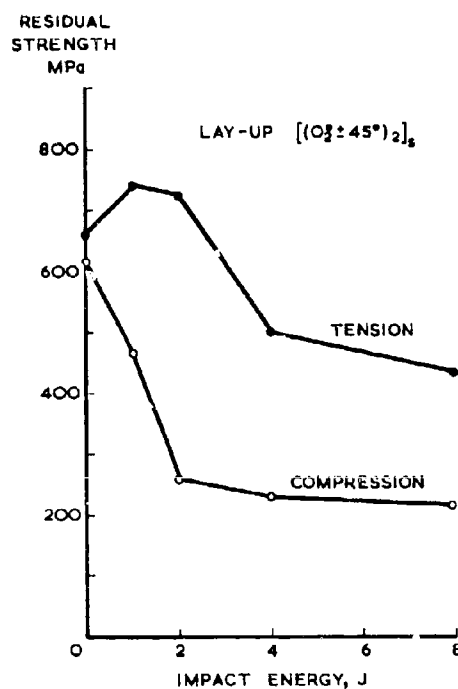


Fig 1 The residual tensile and compressive strengths of a ($0^\circ, \pm 45^\circ$) CFRP laminate following impact

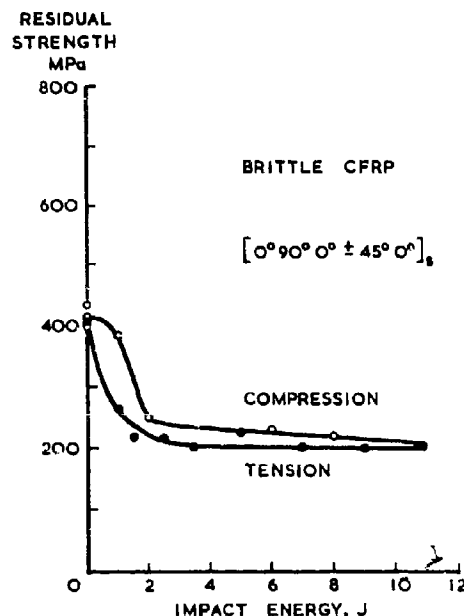


Fig 2 The residual tensile and compressive strengths of a brittle CFRP laminate following impact

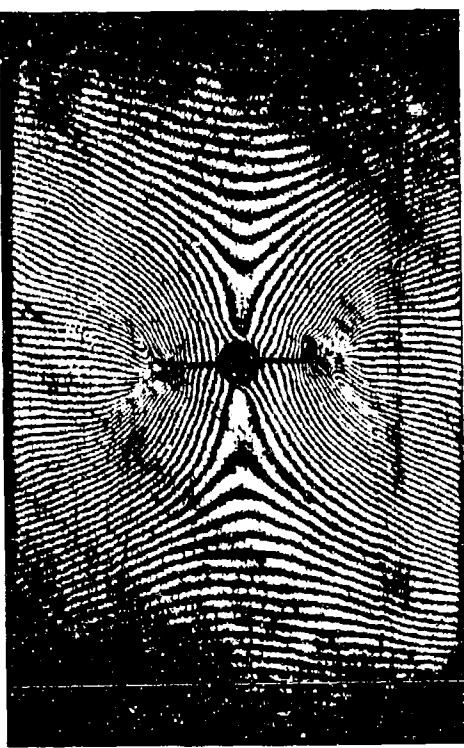


Fig 3 Laser moiré fringe pattern on a notched ($0^\circ, \pm 45^\circ$) CFRP specimen under tension showing damage zones formed at the notch tips

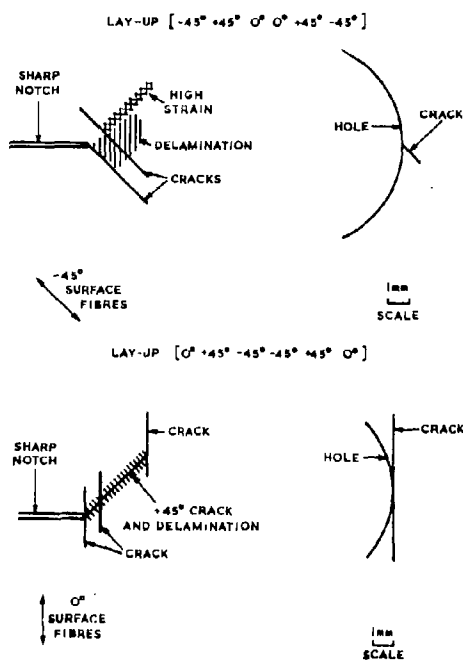


Fig 4 Surface delaminations due to damage zones at sharp notches and circular holes in ($0^\circ, \pm 45^\circ$) CFRP laminates under tension

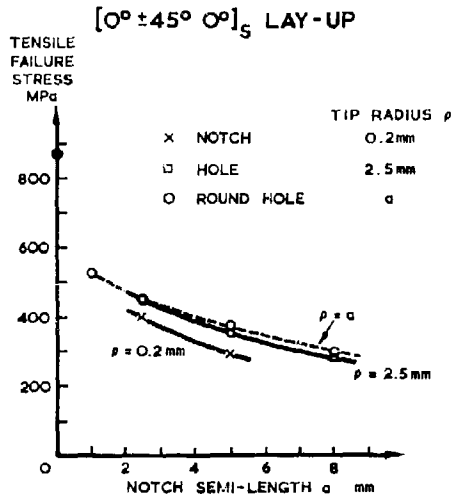


Fig 5 Variation of tensile failure stress with notch size and shape for a ($0^\circ, \pm 45^\circ$) CFRP laminate

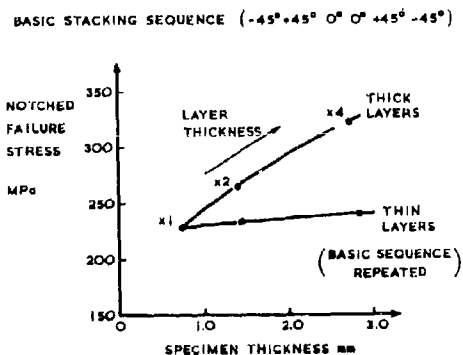


Fig 6 The effect of layer thickness on the failure stress of notched ($0^\circ, \pm 45^\circ$) CFRP under tension

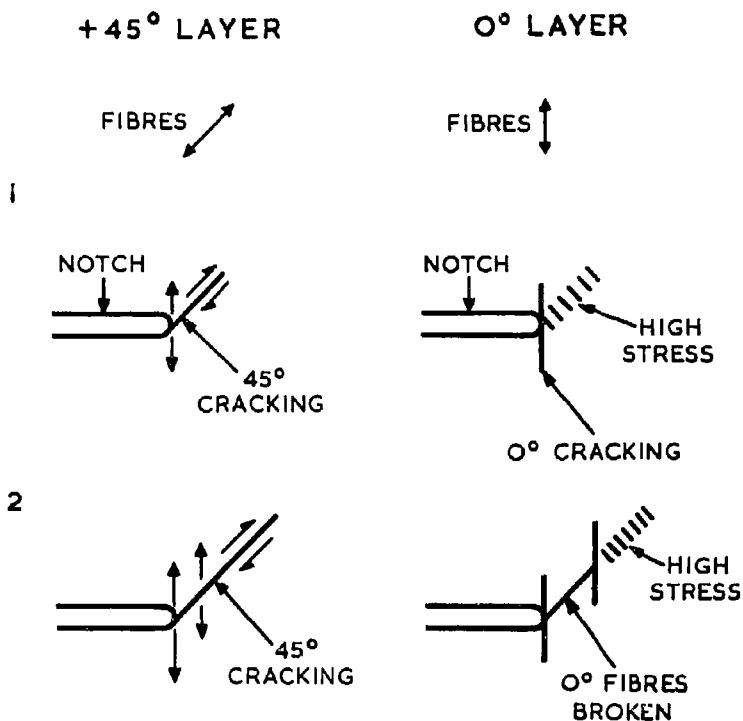


Fig 7 Layer interactions at notch tips in CFRP under tension showing the effect on the load-bearing 0° layers of 45° shear cracking

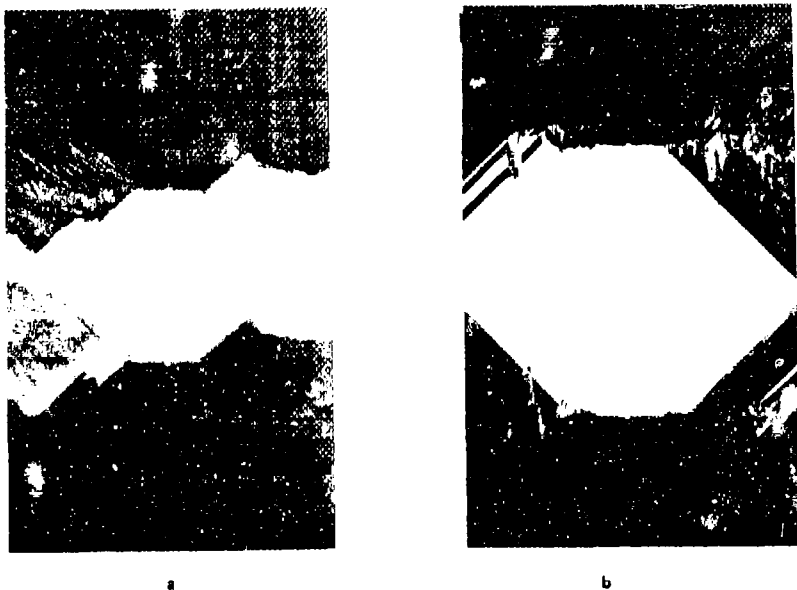


Fig 8 Notched CFRP specimens failed in tension showing line of failure of 0° layers
 (a) at 45° for $[0^\circ, \pm 45^\circ, 0^\circ]_s$ lay-up; (b) at 90° for $[+45^\circ, 0^\circ, -45^\circ]_s$ lay-up

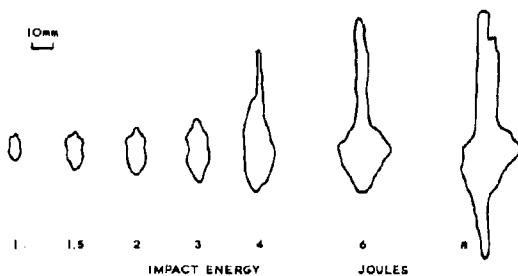


Fig 9 Delaminated areas due to dropweight impact detected by ultrasonic C-scanning techniques in $[0^\circ, 90^\circ, 0^\circ, \pm 45^\circ, 0^\circ]_5$ CFRP

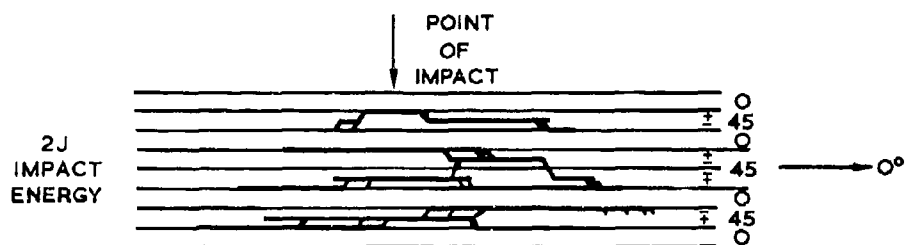


Fig 10 Scaled diagram showing delaminations observed microscopically in a polished cross-section of impacted $[(0^\circ, \pm 45^\circ)_2]_5$ CFRP

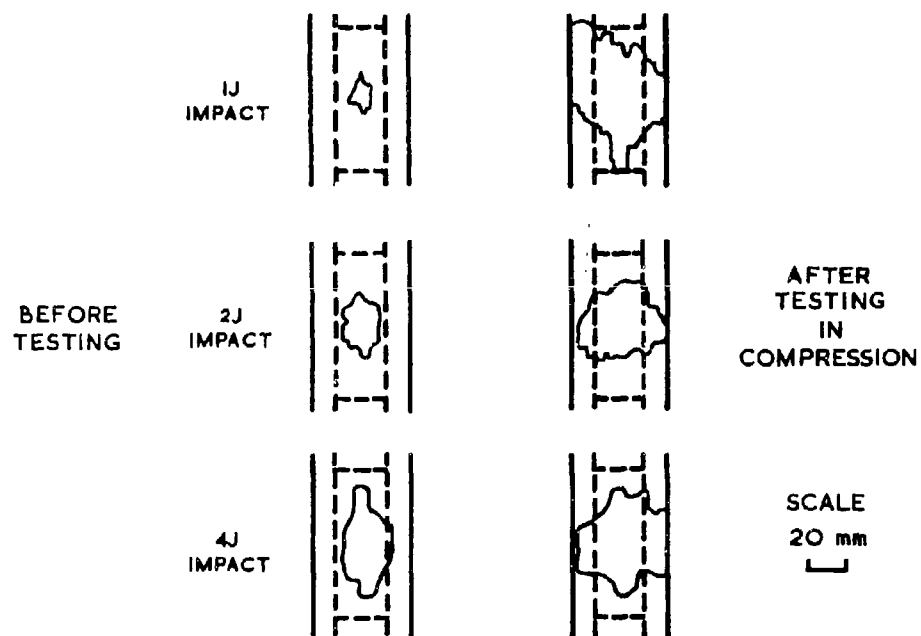


Fig 11 Delaminated areas in impacted specimens of $[(0^\circ, \pm 45^\circ)_2]_5$ CFRP before and after testing in compression (dashed lines indicate position of antibuckling guides along specimen edges)

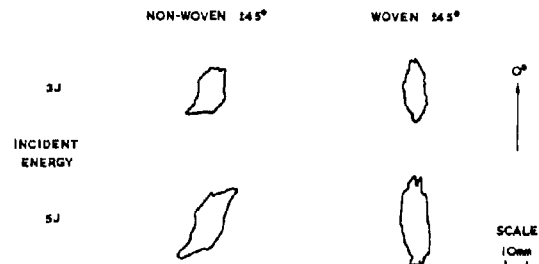


Fig 12 Comparison of areas of impact damage for woven and non-woven $\pm 45^\circ$ layers in $[\pm 45^\circ, 0^\circ]_3, [\pm 45^\circ, 0^\circ]_2, 5$ CFRP (all 0° layers were non-woven)

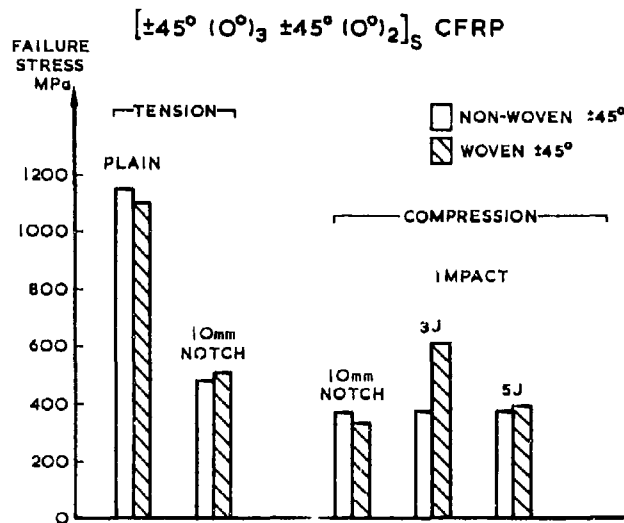


Fig 13 Comparison of the strengths for woven and non-woven $\pm 45^\circ$ layers, of plain, notched and damaged CFRP with $[\pm 45^\circ, 0^\circ]_3, [\pm 45^\circ, 0^\circ]_2, 5$ lay-up (all 0° layers were non-woven)

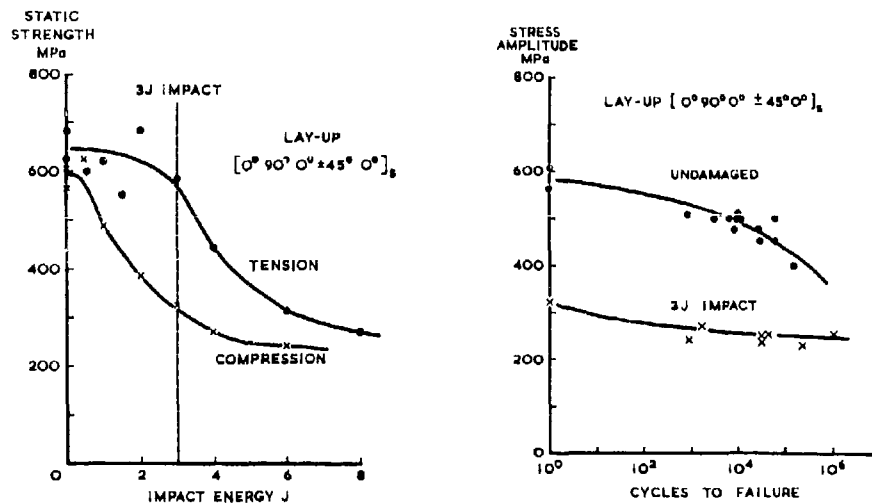


Fig 14 The static tensile and compressive strengths of undamaged and impacted CFRP specimens with a $[0^\circ, 90^\circ, 0^\circ, \pm 45^\circ, 0^\circ]_5$ lay-up

Fig 15 The fatigue performance of undamaged and impacted CFRP specimens in fully reversed cyclic loading

AD P001919

11-1

BEHAVIOUR OF IDEALIZED DISCONTINUITIES AND
IMPACT DAMAGES IN CFRP UNDER FATIGUE LOADING

by

R.M. AOKI

Institut für Bauwesen- und Konstruktionsforschung
Deutsche Forschungs- und Versuchsanstalt
für Luft- und Raumfahrt E.V.
7 Stuttgart 80, Pfaffenwaldring 38-40, Germany

ABSTRACT

Current results of an ongoing experimental program concerning the behaviour of impact damaged CFRP specimens are presented. The purpose of this ongoing research program is to determine the characteristics resulting from localized low-energy impact damage and also the behaviour of the damaged specimens under harmonic fatigue loading. Damage simulating a dropped medium weight (300 g) tool was introduced by drop weights with various geometry impactors. Also circular defects were built into specimens as idealized discontinuities. The damage propagation under static and fatigue loading ($R = 0.1$, $R = -1$) was monitored using NDI methods consisting of US-C-scan, temperature measurements and acoustic emission. The basic parameters of this investigation included the influence of stacking sequence and impactor tip radius, as well as the degree of local discontinuity in the outer layers of the specimens. The straight sided specimens with quasi-isotropic lay-up ($0/\pm 45/90$) are manufactured from T300/Code 69. The feasibility of simulating impact damages with this form of built-in idealized discontinuities is shown.

INTRODUCTION

The key to the reliable and optimum use of composites is to understand their stress and strength characteristics under static and fatigue loading. These characteristics are highly sensitive to ply orientation and stacking sequence, as well as the presence of holes and impact damage. Low velocity impact damage may occur during manufacture, maintenance, or in service by accidentally dropped tools, runway debris or hailstones.

The purpose of this ongoing research program is to determine the characteristics resulting from localized low-energy impact damage and also the behaviour of the damaged specimens under harmonic fatigue loading. To obtain a better understanding of the damage mechanism, the impact damage was simplified as an ideal discontinuity and the stacking sequence of a quasi-isotropic laminate varied.

The effect of nearly invisible impact damages and idealized discontinuities were studied by measuring strength and damage propagation of various specimens with different stacking sequences.

EXPERIMENTAL PROCEDURE

All specimens were fabricated from T300/Code 69 graphite/epoxy unidirectional tape preprints from Fotherhill and Harvey. The flat plates (300 x 300 mm) were cured in an autoclave, according to the manufacturers recommended cure cycle.

The stacking sequence changes of quasi-isotropic ($0/\pm 45/90$)_n laminates investigated are shown in Table I. Other variations have been investigated in West-Germany by 1, 2, 3/.

To introduce the idealized discontinuities, the laminates were fabricated in the same manner as described above with the exception that, depending on the laminate, the two or three outmost sheets were perforated (4mm diameter) before fabrication, see Table II.

All specimens were straight-sided coupons 25mm or wider and 90mm in gage section. Specimens were endtabbed with crossply glass/epoxy tabs.

To determine the effects of impact, idealized discontinuities, and holes on the CFRP specimens, static and fatigue tests were performed.

Static tensile tests were performed in a stroke controlled machine.

Fatigue tests were performed on a servo-controlled hydraulic test machine at constant amplitude and load-controlled sinusoidal axial loading at a frequency of 5 Hz. Several specimens were tested under zero tension ($K = 0.1$) for each stacking sequence and damage type. Non-damaged specimens and those with idealized discontinuities were also tested under one of the most severe loading conditions, i.e. tension-compression loading ($R = -1$). All tests were performed at room temperature.

On account of the multiplicity of failure mechanisms and the corresponding complexity of damage progression in composite materials a variety of analytical tools and experimental procedures is required for characterizing material mechanical properties and failure mechanisms. Different NDI techniques are needed for evaluating the degree and the type of damage imparted to composite materials by impact and static loading as well as for evaluating the damage propagation under fatigue loading.

Here ultrasonic (US), acoustic emission (AE), temperature measurement, and microscopic investigations were used to monitor damage progression.

Our US-equipment consists of a Brandson 330B and a selfmade scanning mechanism. One of the characteristics of the device, which applies the echo method, is that the specimen doesn't need to be immersed in a water bath. A thin water film is used as coupling medium between probe and specimen [4]. Thus it is possible to choose the "better" surface as scanning surface and avoid water infiltration in the broken parts of the specimen. Water infiltration would change the registered delaminated area, depending on immersion time. Some specimens were sectioned at selected locations with a low-speed diamond circular saw. The sections were then polished for examination by light microscopy. These section studies were useful, both for locating the particular ply or ply interface at which delamination occurred, and to locate damages such as ply cracking not detected by US inspection.

In some cases a scanning electron microscope (SEM) was used to examine the fracture surface of the specimens.

Monitoring acoustic emission appears to offer a practical procedure for detecting damage and damage growth because it is as easily used in actual service as in the laboratory. For some specimens tested here, acoustic emission were monitored using a Physical Acoustic Corporation PAC-3400 system. The most pertinent operating parameters were: preamplifier fixed gain of 40dB; postamplifier gain control 35dB; transducer type R15; system threshold level of 1 to 3V, depending on test.

Heat generation due to fatigue damage of composites is a phenomenon which has been observed by other investigators [5,6]. The temperature on the specimens surface was measured with thermocouples (Cu-Kon). Strain gage rosettes were placed on several of the static tensile specimens.

Damage Introduction

Impact Damage. Parameters were chosen with the aim of generating defects invisible at the front surface of the impacted specimen. The plane plates were cut into two pieces, so that they could match in the impact test fixture shown in Fig.1. The specimen plates were circularly clamped ($R=19\text{mm}$) between steel plates. A cylindrical weight ($m=298\text{g}$) with exchangeable steel tip, hemispherical with 5mm diameter, and blunt with $D=5\text{mm}$ diameter, was dropped from specified heights to achieve the desired damage. An accelerometer on top of the impactor enabled the determination of force, displacement, and energy consumption, see Table III. More details pertaining to impact procedure and impact test evaluation are given in [1,3].

Idealized Discontinuities. Earlier experiments on low velocity, low energy impacts exhibited the presence of fiber breakage and delamination at the opposite surface of the impacted region. To simulate this, the damage was idealized by perforating the 2 or 3 outer layers of the specimens before curing, as shown in Fig.2. The hole diameter of the perforation was 4mm . This diameter was chosen as a representative fiber damaged region in an impact damaged specimen under the specified conditions. Due to this choice, the specimens width did not need to be very large. After the curing process the periphery of the idealized discontinuity could be distinguished as a shadow. For comparison purpose some specimens had a central 4mm diameter hole through the thickness.

EXPERIMENTAL RESULTS

Impact Damages. Micrographs and SEM pictures made from damaged specimens show interply crack, interlaminar delamination and fiber breakage near the impact focus and beneath the rear surface relative to impact [7, 8], Fig. 3.

The influence of the contacting tip shape of the impactor on the damage is demonstrate in Fig.4. The US-C-scan pictures show that the hemispherical tip generally causes a larger damage than the blunt tip. Damage extension and orientation are influenced by the outmost layers at the rear surface of the impacted specimens. Flaws in direction of the outmost fiber orientation could be observed under the impact conditions stated before. The damage caused by the blunt impactor under the same conditions ($m=298\text{g}$, $v=2.21\text{m/s}$) has a more circumferential delamination shape and there is no flaw visible along the outmost fiber orientation. In both cases there is no visible damage at the front surface of the specimen. Other experimental investigations [1,3,10] showed an increase of absorbing energy with increasing momentum of impactor until penetration. Internal delamination reaches a maximum and then drops again to a limit which is determined by the impactor shape: the sharper the impactor tip, the more localized the damage and the more the specimen behaves as a specimen containing a hole.

Idealized Discontinuities. Micrographs from idealized discontinuities show a perturbed region where the outmost layers were perforated, see Fig.5. In this region some of the inner layers are no longer flat, but have a curved shape. As shown in [11] the waviness of plies can reduce strength and stiffness of laminates up to 60%.

Static Tests.

Static tensile test results of undamaged, impact damaged, and specimens with idealized discontinuities show similar behaviour. The influence of stacking sequence is noticeable in the static tensile strength values. Specimens from laminate B, see Table I, reach the highest values, specimens from laminates A and C have almost the same static strength values. Both stacking sequences show delamination at the free edges prior to catastrophic failure. Similar results were also found by [13,14,15]. This phenomenon can be attributed to the interlaminar tensile stress σ_z . This interlaminar peeling stress is present when the specimens with stacking sequence A or C are subjected to axial tensile loading, and can be calculated using the simplified model of Pagano and Pipes [12,13].

The strain state of the undisturbed region of the specimen is compared with the strain state in the layer opposite the idealized discontinuity in Fig. 6. This behaviour is also representative for other specimens with this same kind of discontinuity but different stacking sequence. The measured longitudinal strain (EPSL) and the transversal strain (EPSQ) at the rear part of the discontinuity are larger than in the undisturbed region. Similar behaviour was observed in the impact damaged specimens with the hemispherical tip impactor. Stiffness degradation under static tensile loading of damaged and undamaged specimens with different stacking sequences are given in Tables I, II and III. The highest stiffness degradation occurs for specimens with a hole, followed by those with idealized discontinuities (3A, 3B, 3C). The influence of the impact damage on the static tensile strength of specimens with different stacking sequences is also

given in Table III. Generally specimens damaged with a blunt impactor reach almost the same strength values as the undamaged. All other specimens show a static strength decrease, depending on damage. Specimens with shallower discontinuities (2A,2B,2C) were stronger than those with deeper discontinuities (3A,3B,3C), indicating that laminate strength is sensitive to minor variations in the depth of the discontinuity as it relates to specific orientations. The highest decrease in strength could be observed in specimens with a hole, as anticipated.

Monitoring of acoustic emission signals during the static tensile loading showed that, after an initial period of small AE-activity, there is an onset of a large increase in the count rate, coinciding with the occurrence of longitudinal edge cracking in laminate A and C. In laminate B in which longitudinal edge cracks were not observed, the acoustic emission were much smaller. This is similar to that observed by /9,14/.

Fatigue Tests

Fatigue test results of specimens with impact damages and idealized discontinuities are presented in Figs. 7 through 10. All stacking sequences show a similar behaviour, i.e. a decrease in fatigue strength with increasing number of cycles. This decrease being larger under tension-compression loading than in the case of zero tensile loading.

A comparison of the non-damaged specimens under zero tension show that the laminate B has the highest fatigue strength. This can be attributed to the fact that specimens with lay-ups A and C show an edge delamination, because the loading stress level is high enough to induce this kind of failure. With growing edge delamination the debonded area will increase towards the middle of the specimen and the test is reduced to a tensile test of 2 nonsymmetric specimens clamped together at the grips. Due to the resulting non-symmetric built-up of the specimen, twisting and bending could occur as stated in /17/ and leads to a lower tensile fatigue strength.

Specimens with stacking sequence B also show a free edge delamination after tensile fatigue loading, although G_2 is a compressive stress. The delamination enlargement is much smaller than in the case of the A and C laminates. The US-C-scan pictures in Fig.11 show the difference in the damage development between laminate A and B. Although the stress level and the number of cycles are smaller in case of laminate A, the delaminated area at the edges is larger than in the case of laminate B. The development of the delamination in the impact damaged region is almost the same in both cases and is a very small enlargement compared to the initial delamination area before loading. This behaviour could be observed in specimens with idealized discontinuities, too, as long as their fatigue loading condition was zero tension. Depending on the stacking sequence of the laminates, the delamination in the damaged region can take place at different locations: between the 90 layers in case of laminate A, or in the interface between the 90 and -45 layers in laminate B, or between 0 and -45 layers in laminate C, as shown in Fig.5 (right hand side).

In some experimental works /3,5/ interrelation of temperature rise and stiffness degradation could be observed. Heat generation is the consequence and contributing factor to fatigue damage. Delamination and cracking results in a significant local internal friction which generates heat. The heat in turn rises the temperature of the structure and reduces its resistance to fatigue. Because of this, the temperature was continuously monitored on the surface of different zero tension fatigue loaded specimens. For damaged specimens a pronounced temperature rise in the first 10³ cycles was observed as shown in Fig.12. After this period the temperature either stabilized until the onset of failure or continued to climb until catastrophic failure occurred. If the test was stopped the specimen cooled to ambient temperature. Upon restart the temperature rised quickly to the high temperature attained before, indicating the irreversibility of the damage. For reversible damage temperature after test restart would rise more slowly, similar to the untested specimen. Many fatigue specimens exhibited a temperature rise just prior to fracture, even though the temperature had previously leveled off. This observation is consistent with a more rapid accumulation of damage in the last stages of fatigue. This behaviour can be explained with the sudden death model /16/. Some other specimens showed a continuous increase in temperature until catastrophic failure, fitting better to the degradation model. The small temperature difference observed between the undamaged specimens with stacking sequences A and B is due to the pronounced free edge delamination in laminate A. Similar behaviour was observed with specimens of laminate C. Rise in temperature prior to catastrophic failure was not so pronounced in laminate B as in the case of the other two laminates.

As anticipated, AE monitoring during tensile fatigue loading showed a different behaviour depending more on stacking sequence, than on damage type. Laminate A and C showed very high AE activity due to edge delamination development. A comparison of AE activity with corresponding load showed that the activity was not always at the highest fatigue load, periodical emissions were found at intermediate loads. From this behaviour it can be assumed, that the damage propagation is probably the result of the agglomeration of many small sites to form a dominant damage which propagates more rapidly. The same phenomenon as with the temperature was observed: there were cases in which the AE activity increased sharply before catastrophic failure and other cases where there was no pronounced increase in emission rate before failure. Specimens with stacking sequence B showed less activity at the beginning of fatigue life but increased with higher load cycles. With the AE-equipment used, planar location of the damage was not possible.

The residual strength data although scant, allows it to be noted that residual strength mostly exceeds the fatigue curve ($R=0.1$), often reaches the static strength values, and sometimes goes beyond it, as published elsewhere /3/.

Specimens with idealized discontinuities under tension-compression loading showed a different damage development than those tested under zero tensile loading. Due to the compression loading and the stability conditions associated with this phenomenon the damage progression in the region of the idealized discontinuity was much more accentuated /18,19/. Fig.13 shows the delamination development observed in the US-C-scan pictures. The influence of the stacking sequence on the delamination development is noticeable. In laminate A the damage increases in the direction of the 0 deg layer, a phenomenon which is currently observed in specimens with a hole through the thickness and 0 deg outer layer. Specimens with stacking sequence B do not show large increase of delaminated area. In case of laminate C, the edge delamination is linked with the delamination departing from the idealized discontinuity.

A comparison of the delaminated area development under tension-compression and zero tensile fatigue loading for laminate A with idealized discontinuity as well as in specimens damaged with a spherical impactor is presented in Fig.14. Here, only the delaminated area in the damaged region and not that at the free edges was taken into account. Delamination development in specimens with deeper idealized discontinuities (3A) show the same behaviour as specimens damaged with a spherical impactor. Specimens with shallower idealized discontinuities (2A) show a smaller increase in delamination area at the same load level.

As matter of fact, the delamination growth of impact damaged specimens under tensile fatigue loading appears to be reproducible with idealized discontinuities, opening the possibility to treat the influence of impact damages analytically.

The steep increase of delaminated area under tension-compression loading for the idealized damage is also characteristic for impact damaged specimens [3]. Under compression loading, delamination growth and concurrent bulging of the thinner delaminated region occurs as hypothesized by the model of Konishi and Johnston [2a].

Although no effort was put into relating residual strength to delamination extent during this study, the process appears feasible.

CONCLUSIONS

CFRP composites are susceptible to low energy, low velocity impact. The damage introduced in the laminates is dependent on the contacting shape of the impactor. Blunt impactors caused less damage than hemispherical tip impactors under the investigated conditions.

The predominant method in which damage grew in two of the investigated laminates ($0/\pm 45/90$)_s and ($\pm 45/0/90$)_s, was the propagation of the delamination from the specimen free edges toward the impact damaged area. The ($0/90/\pm 45$)_s laminate did not exhibit this extensive free edge delamination and therefore had the highest strength values under the specified loading conditions.

Delamination growth from the impact damaged area was small under tensile fatigue loading. Due to the stability conditions associated with tension-compression fatigue loading, the damage development is the most severe in this case.

The delamination development in the impact damaged specimens was reproducible with idealized discontinuities.

Continuous temperature measurement was seen to be an adequate method for detecting damage progression. The interrelation of temperature rise and stiffness degradation will be pursued in the near future.

Acoustic emission techniques need further development. Classification criteria for acoustic events along with source location methods will be necessary.

Further research work is foreseen taking into account the details of the local damage propagation.

References

1. Stellbrink,K.K., "Schlagfestigkeit von ebenen CFK-Laminaten" Vortrag Nr. 82-005, DGLR-Symposium." Entwicklung und Anwendung von CFK-Strukturen, 26. u. 27.Mai 1982, DFVLR-Stuttgart, W-Germany
2. Gerharz,J.J., Rott,D. and Schuetz, D., Schwingfestigkeitsuntersuchungen an ungekerbten und gekerbten Faserverbundwerkstoffen aus multidirektionalem Laminat. BMVg - FBW 79-25, 1979.
3. Stellbrink, K.K., R.M.Aoki, "Effect of Defect on the Behaviour of Composites", ICCC IV, October 25-28, Tokyo/Japan, 1982.
4. Heyduck, J., "Ultraschall-Prüfung an Faserverbundwerkstoffen", Internal Report IB 454-79/16, DFVLR-Stuttgart, 1979.
5. Nevadunsky, J.J., Lucas, J.J., Salkind, M.J., Journal of Composite Materials, Vol.9, October 1975.
6. Hahn, H.T. in Composite Materials: Testing and Design (Fifth Conference), ASTM STP 674, S.W.Tsai Ed., American Society for Testing and Materials, 1979.
7. Rhodes, M.D., Williams, J.G., Starnes, J.H., "Low-velocity Impact Damage in Graphite-Fiber Reinforced Epoxy Laminates", 34th SPI, 1979.
8. Aoki, R.M., Stellbrink, K.K., "The Influence of Defects on the Behaviour of Composites", AGARD-CP-208, Athen, Greece, April 14-17, 1980.
9. Awerbuch, J., in Workshop on Failure Mechanics in Composites DFVLR-Braunschweig, W-Germany, 1982.
10. Dorey, G., Fracture Behaviour and Residual Strength Of Carbon Fibre Composites subjected to Impact Loads. AGARD-CP-163, Munich, W-Germany, October 13-19, 1974.
11. Schelling,H., Aoki,R.M., "Einfluß der Laminatwelligkeit auf die physikalischen Kennwerte einer Bauteilprobe", Internal Report IB 454-77/9, DFVLR-Stuttgart, 1977.
12. Pagano,N.J., Pipe,R.B., Some Observations on the Interlaminar Strength of Composite Laminates, Int.J.Mech.Sci. 15, 1973.
13. Kim,R.Y., Aoki,R.M., Transverse Crack Formation in Composite Laminates, IV Nat. and I International Meeting on Composite Materials, Milano, Italy, November 19-20, 1980.
14. Curtis,P.T., The Effect of Edge Stresses on the Failure of (0,45,90) CFRP Laminates, RAE, Technical Report 80054, 1980.

15. Soni,S.R., "Stress and Strength Analysis of Composite Laminates at Delamination", ICCM IV, October 25-28, Tokyo/Japan, 1982.
16. Chou,P.C.,Cromam,R. in Composite Materials:Testing and Design (Fifth Conference), ASTM STP 674, S.W.Tsai Ed., American Society for Testing and Materials, 1979.
17. Tsai,S.W.,Hahn,H.T., Introduction to Composite Materials, Technomic Publishing Co., 1980.
18. Prinz,R., Schadensfortschritt in CFK bei Schwingbelastungen, Strukturmechanik Kolloquium 1981, DFVLR-Braunschweig, June 1981.
19. Ratwani,M.M.,Kan,H.P. in AIAA/ASME/ASCE/AHS 21st Structures,Structural Dynamics, and Materials Conference,Seattle,USA,May 12-14,1980.
20. Konishi,D.Y.,Johnston,W.R. in Composite Materials:Testing and Design (Fifth Conference), ASTM STP 674, S.W.Tsai,Ed.,Am.Soc.for Testing and Materials,1979.

TABLE I

laminate	stacking seq.	tensile strength N/mm ²	stiffness ratio [§]	net strength 4 mm hole	stiffness ratio ^{§§}
A	(0/±45/90) _s	472	0.98	360	0.58
B	(0/90/±45) _s	560	0.99	370	0.59
C	(±45/0/90) _s	460	0.92	360	0.57

§ stiffness before catastrophic failure to stiffness at the beginning of loading
 §§ measured at the hole boundary

TABLE II

laminate	stacking seq.	perforated layers	tensile strength N/mm ²	stiffness ratio
2A	(0/±45/90) _s	0, +45	390	0.89
3A	(0/±45/90) _s	0, ±45	360	0.80
2B	(0/90/±45) _s	0, 90	450	0.88
3B	(0/90/±45) _s	0, 90, +45	440	0.87
2C	(±45/0/90) _s	+45	450	0.86
3C	(±45/0/90) _s	+45, 0	360	0.77

TABLE III

laminate	tip geom. 5mm diam.	mass g	abs.energy J	int.delamination mm ²	tensile strength N/mm ²	stiffness ratio
A	hemisp.	298	0.428	184	410	
A	blunt	298	0.15	123	450	0.95
B	hemisp.	298	0.378	210	410	
B	blunt	298	0.127	173	530	
C	hemisp.	298	0.37	196	420	
C	blunt	298	0.087	157	450	0.92

impact velocity v=2.21 m/s

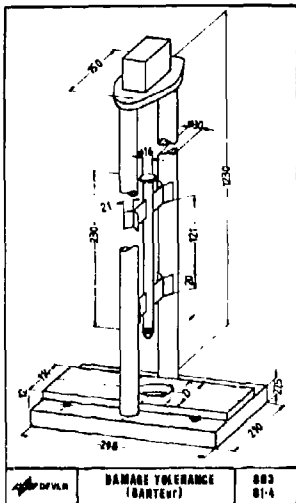


Fig. 1-Drop weight apparatus

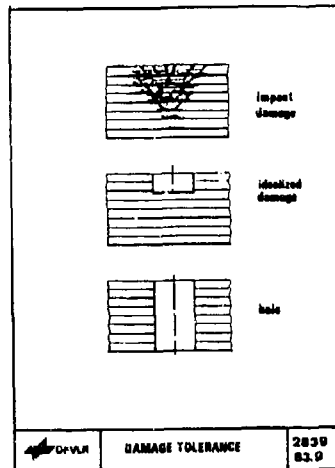
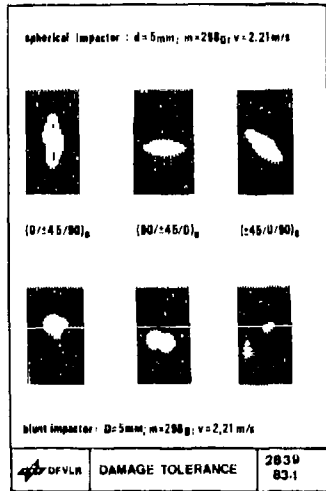


Fig.2-Sketch showing idealized discontinuities

Fig.3-Microscope (2x) and SEM-photograph (700x)
of an impact damaged specimen.Fig.4-C-scan pictures from da-
maged specimens with different
impactor-tips.

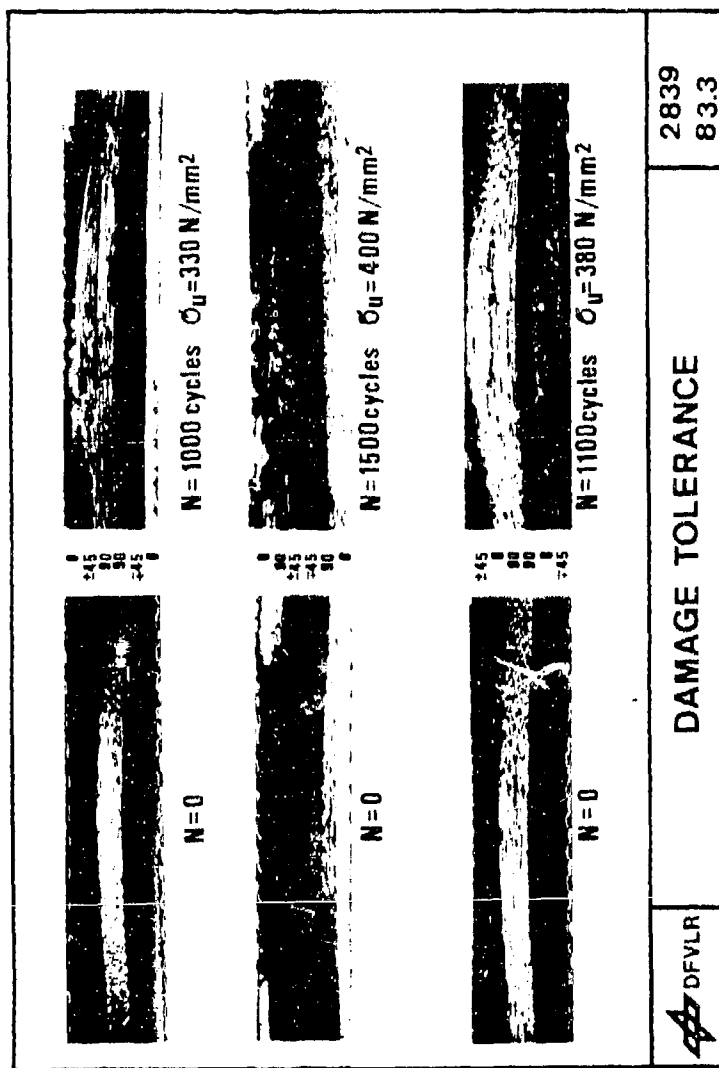


Fig.5-Micrographs of specimens with idealized discontinuity before and after tensile fatigue loading

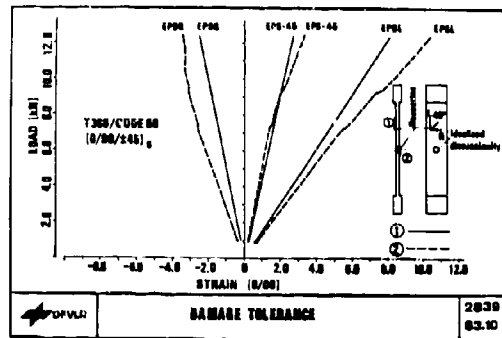


Fig.6-Tensile load-strain behaviour for specimen with idealized discontinuity.

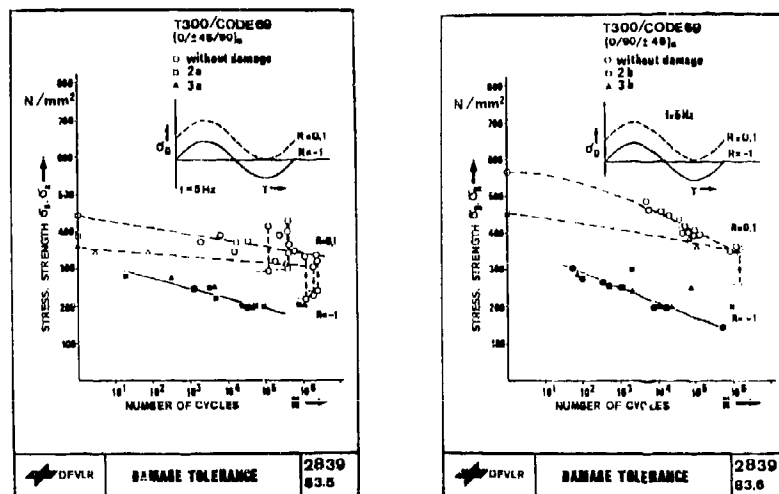


Fig.7-Fatigue test results
(0/245/90)_s id.discontinuity.

Fig.8-Fatigue test results
(0/90/±45)_s id.discontinuity.

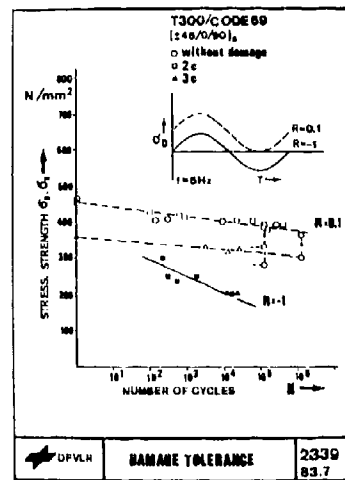


Fig.9-Fatigue test results
 $(\pm 45/0/90)_s$ id. discontinuity.

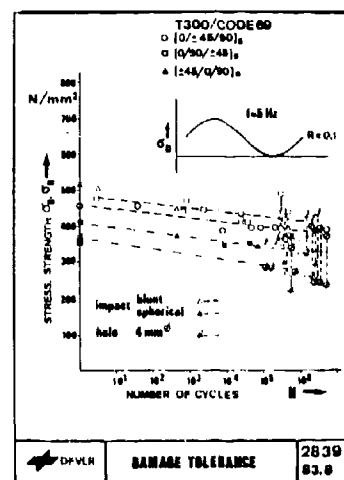


Fig.10-Fatigue test results
impact damaged and
hole.

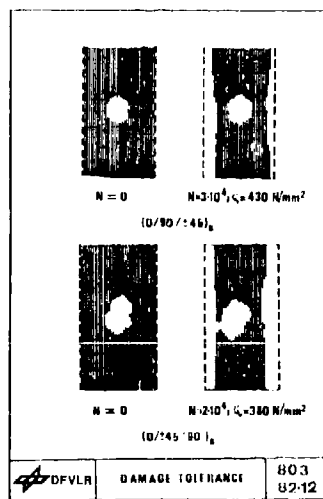


Fig.11-Delamination development
in impact damaged specimens
with different stacking se-
quence.

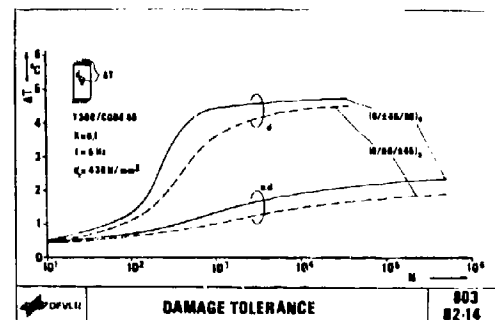


Fig.12-Temperature development at the
surface of the specimens under
zero tension fatigue loading.

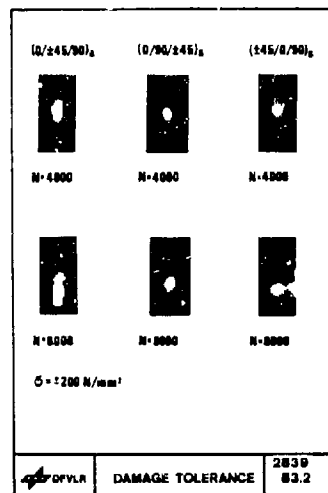


Fig.13-Delamination development in specimens with idealized discontinuity under tension-compression fatigue loading.

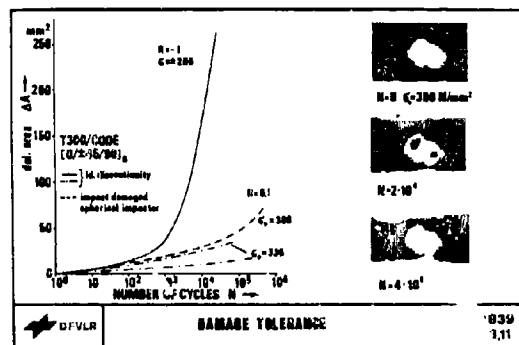


Fig.14-Delamination area development for damaged specimens with stacking sequence (0/±45/90)₃ under fatigue loading.

**INFLUENCE DE DÉFAUTS DE FABRICATION SUR LE
COMPORTEMENT STATIQUE ET DYNAMIQUE
DES STRUCTURES EN COMPOSITE CARBONE-RESINE**

J. Cuny et G. Briens
AEROSPATIALE
Laboratoire Central
12, rue Pasteur - 92152 Suresnes

Après avoir examiné les types de défauts apparaissant en fabrication, ainsi que les moyens adaptés à leur détection, nous étudierons l'influence des défectuosités affectant uniquement la résine ou l'interface fibre-résine.

Les matériaux à couches unidirectionnelles ou croisées seront sollicités à l'état initial ou après vieillissements divers, lors d'essais statiques ou dynamiques conduits à différentes températures.

1 - INTRODUCTION

Dans l'industrie aéronautique, les structures métalliques secondaires, voire primaires, sont remplacées de plus en plus par des structures en matériaux composites carbone-résine multicouches qui, outre le gain de masse appréciable (10 % à 40 % selon les cas), un prix de revient parfois attractif, peuvent entraîner un meilleur comportement en fatigue, et des frais de maintenance réduits en exploitation.

Les pièces en composites sont obtenues à la forme définitive par moulage d'un empilement de couches croisées de préimprégné fibre-résine, dont les directions sont orientées en fonction de la résistance et de la rigidité à obtenir. Cette élaboration pose un certain nombre de problèmes car, à la différence des pièces métalliques, la conformité de la structure avec le plan ne constitue plus la préoccupation majeure du contrôleur. Le matériau composite s'élaborant en même temps que la pièce, il faut en plus s'assurer de la santé du produit.

La fabrication de pièces en matériaux composites exige le respect de règles strictes telles que :

- utilisation de matériau, le plus souvent nappes ou tissus à l'état préimprégné, ayant satisfait les critères de réception matière contractuels entre fabricant et utilisateur,
- respect des gammes de fabrication :
 - . conditions de stockage, destockage des produits souvent entreposés à - 18°C et qu'il faut réchauffer à température ambiante avant utilisation en évitant la prise d'humidité,
 - . découpe méthodique des couches,
 - . orientation précise des couches en fonction des plans de drapage et compactage des plis,
 - . cycle de polymérisation (pression, vitesse de montée en température en veillant au niveau et à l'homogénéité de celle-ci sur l'ensemble de la pièce).

Malgré les précautions prises, les structures peuvent présenter des défauts bien souvent aléatoires d'une pièce à l'autre, ce dont il faut tenir compte avant d'accepter le montage sur appareil.

Après avoir abordé rapidement les principaux défauts rencontrés en fabrication, ainsi que les moyens de contrôle non destructif appropriés à leur détection, nous nous pencherons plus particulièrement sur l'influence de ces défauts envers les caractéristiques mécaniques statiques et dynamiques du matériau.

L'exposé sera limité aux structures fabriquées à partir de nappes carbone haute résistance imprégnées de résine époxydique (type TGMDA + DDS) polymérisées dans les tolérances admissibles de la gamme de fabrication. Les défauts étudiés seront particulièrement ceux affectant la résine du composite.

2 - PRINCIPAUX TYPES DE DÉFAUTS RENCONTRES EN FABRICATION

2.1 - Porosités

On entend par "porosités", des cavités généralement de faibles dimensions, réparties d'une façon uniforme ou presque dans toute l'épaisseur du stratifié, entraînant une hétérogénéité de la matrice (figures 1 et 2).

Ce type de défaut peut avoir des origines diverses que l'on peut regrouper selon trois causes principales :

- technique d'imprégnation des fibres,
- humidité excessive lors des opérations de drapage,
- propriétés rhéologiques de certaines résines lors du cycle de polymérisation.

L'imprégnation des fibres en phase solvant (résine rendue fluide par dissolution dans un solvant) entraîne plus de porosités que celle en phase hot melt (imprégnation à chaud par transfert de résine).

En effet, les produits volatils résiduels emprisonnés dans les couches compactées de pré-imprégné se transforment en gaz lors de la montée en température pendant la polymérisation, ce qui crée plus ou moins de porosités en fonction de la maîtrise du cycle de cuisson.

Le même phénomène se produit si le préimprégné a absorbé de l'humidité lors des opérations de drapage :

- condensation d'eau si le matériau, sorti froid du congélateur, n'a pas été maintenu dans son emballage étanche pour revenir à température ambiante avant utilisation,
- absorption d'eau si le préimprégné a été laissé trop longtemps en ambiance humide dans l'atelier de fabrication avant et pendant les opérations de drapage.



FIGURE 1 - Répartition des porosites entre couches - Vue en bout -



FIGURE 2 - Forme de porosites sur une couche après délamination du matériau - Vue de dessus -

En dehors du cas de certaines résines visqueuses admettant une pression dès le début du cycle de polymérisation les formulations passant par une phase liquide lors de la montée en température exigent l'application de la pression pendant la phase de gélification. Or le principal problème avec ces derniers systèmes est que la moindre fuite de bordurage, ou un pompage excessif de la résine, peut provoquer une migration importante de celle-ci à l'extérieur du matériau. La pression n'est plus alors efficace sur la résine, car les fibres se trouvent au contact entre les plis successifs.

Les porosités observées avec les formulations à application de pression retardée sont donc :

- soit à un flot trop important de résine,
- soit à une application de pression trop tardive qui ne peut plus assurer le compactage correct des plis trop gélifiés (cas d'outillages à fort gradient thermique, dans les zones chaudes)

2.2 - Manque de cohésion intercouches



Par opposition aux porosités qui donnent une idée de répartition homogène de défauts de très petites dimensions, le manque de cohésion intercouches que l'on désigne bien souvent par le terme "délamination" donne plutôt une idée de défauts plus importants localisés à quelques endroits bien précis.

Ces défauts, souvent situés dans une ou deux intercouches, peuvent atteindre plusieurs centimètres carrés (échelle macroscopique). Ils sont généralement dus à la complexité des pièces réalisées (structures autoraidées, profils tournants) associées à leur technologie de fabrication (figure 3).

FIGURE 3 - Délamination dans un rayon

Les difficultés proviennent de trois facteurs, essentiellement :

- utilisation de préimprégné à faible taux d'imprégnation (proche du taux final à obtenir dans le composite) n'exigeant plus la technique d'évacuation de résine excédentaire imposée par les préimprégnés à taux d'imprégnation plus élevé,
- utilisation des propriétés thermo-expansibles des silicones pour la mise en pression des plis, en remplacement de la technique autoclave qui assure une pression pneumatique plus homogène,
- suppression dans certains cas de phase "mise sous vide" au cours du cycle de polymérisation.

On peut attribuer l'origine des manques de cohésion intercouches à deux causes principales :

- étanchéité trop importante des préimprégnés, due à une pégosité excessive. Si des poches d'air sont emmagasinées entre couches, le déballage peut devenir impossible malgré une phase importante de mise sous vide,
- manque de pression locale le plus souvent dans des zones difficiles d'accès (rayons de profilés). La dilatation thermique des outillages silicone peut créer des arc-boutements avant mise en pression théorique, ou le temps de gel de la résine peut être dépassé avant application de la pression effective ne permettant plus l'accostage des plis.

2.3 - Inclusions de corps étrangers

La réalisation de pièces en matériaux composites qui, en dehors de l'enroulement filaire, est essentiellement manuelle encore aujourd'hui, demande une main-d'œuvre très qualifiée. Les risques d'inclusion de corps étrangers sont minimisés en prenant un maximum de précautions dans les salles de drapage ; le principal problème reste celui des séparateurs protégeant le préimprégné avant emploi.

Avec les préimprégnés les plus usuels, on trouve deux types de séparateurs : soit du papier enduit d'un agent démolant (silicone, ...) soit du film plastique (polyéthylène, terphane, ...).

Mis à part l'oubli de retrait d'un séparateur lors des opérations de drapage (cas rarement rencontré), un problème sournois se pose avec les films plastiques. En effet, des morceaux généralement de petite taille laissés par inadvertance sur le lieu de drapage peuvent venir, par électricité statique, se coller sur la face cachée de la découpe que l'on tranfère sur l'outilage.

Actuellement, aucun contrôle des oubliés de séparateurs n'est possible avant polymérisation si ce n'est la reconstitution méthodique des différentes couches drapées.

2.4 - Défauts de collage

Suivant les types de structures, plusieurs cas de collage sont à envisager :

- composite-composite,
- composite-métal (titane-alliage léger),
- composite-nid-d'abeille.

D'autre part, l'assemblage peut se faire soit sur matériaux déjà polymérisés, soit sur produits à l'état préimprégné. Dans ce dernier cas, le collage et la cuisson du composite se fait au cours du même cycle de polymérisation.

On entend par défaut de collage, les anomalies pouvant se situer au niveau de l'adhésif et qui se traduisent le plus souvent par un manque de cohésion ou d'adhésion de la colle sur les surfaces à assembler.

Les collages des matériaux composites à l'état préimprégné sont souvent réalisés avec des cycles de polymérisation constituant des compromis entre l'"optimal adhésif" et l'"optimal composite".

Les manques d'adhérence rencontrés ont bien souvent les mêmes origines que les manques de cohésion intercouches des composites :

- étanchéité des préimprégnés ne permettant pas l'évacuation de l'air emmagasiné au niveau du film de colle,
- manque de pression locale provoqué par un outillage mal adapté ou un préimprégné travaillant en membrane et ne transmettant pas la pression sur le film de colle,
- oubli de séparateurs.

3 - GENERALITES SUR LES CONTROLES NON DESTRUCTIFS

Les méthodes utilisables venant en premier lieu à l'esprit sont des méthodes globales permettant en une seule opération d'obtenir une vue d'ensemble de tout ou partie de la santé de la pièce.

Ces méthodes telles que holographie, thermographie, rayons X deviennent toutefois assez rapidement limitées sur structures composites-résine surtout au point de vue type et taille des dommages recherchés.

Le maximum d'informations sur la qualité de la pièce est obtenu par les méthodes ultra-soudure, qui en contre partie sont lentes de mise en œuvre car basées sur l'analyse ponctuelle du matériau.

Si les ultrasons, dans les fréquences envisagées (1 à 15 MHz) se transmettent très bien dans les liquides ou les solides, ils ne se transmettent que difficilement dans les milieux gazeux ; d'autre part, le changement de milieu crée des réflexions partielles ou totales aux interfaces. Ce sont ces propriétés que l'on utilise dans les méthodes de contrôle non destructif par ultrasons, ces dernières exigeant un milieu transmetteur, le plus souvent l'eau, entre l'émetteur et la pièce. On distingue alors :

- la méthode par immersion : la pièce est entièrement immergée dans un milieu aqueux,
- la méthode par semi-immersion : les ultrasons sont transmis de l'émetteur à la pièce par un jet d'eau,
- la méthode par contact : réservée aux opérations de contrôle manuel, l'émetteur est mis en contact avec la pièce par l'intermédiaire d'un liquide de couplage.

La détection d'un défaut peut se faire par "transmission" (analyse de la diminution d'amplitude du faisceau transmis à travers le matériau) ou par "réflexion" (analyse des échos réfléchis par les hétérogénéités du matériau).

Lié au déplacement des capteurs de mesure, un système d'enregistrement par brûlage de papier plus ou moins important (du blanc ou noir) obtenu en fonction de l'amplitude du signal recueilli, donne une cartographie de l'ensemble de l'élément contrôlé.

- Méthode_par_transmission

La transmission peut être simple dans le cas de la méthode en semi-immersion avec un émetteur ultrasonore d'un côté de la pièce, un récepteur de l'autre côté.

La transmission peut être double dans le cas de la méthode par immersion où l'on dispose d'un appareil unique émetteur-récepteur. Le faisceau d'ultrasons émis traverse le matériau puis se réfléchit sur un réflecteur (plaqué de verre) afin d'effectuer un deuxième passage dans la zone à contrôler, avant d'être capté par le récepteur :

On mesure ainsi :

- l'atténuation due aux réflexions sur les interfaces,
- l'absorption intrinsèque du composite,
- l'absorption due aux défauts éventuels.

Les contrôles par transmission ne sont possibles que si l'élément à contrôler est accessible des deux côtés.

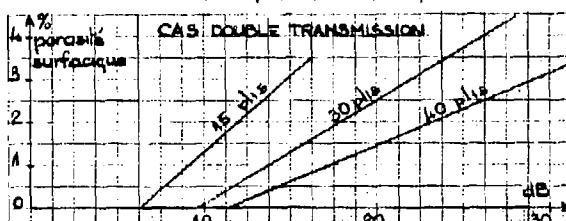
- Méthode_par_réflexion

Cette méthode permet d'analyser la position des défauts situés dans l'épaisseur du matériau. Elle est surtout employée comme complément de la méthode par "transmission". N'exigeant l'accèsibilité de la pièce que d'un seul côté, c'est un moyen de contrôle adapté au suivi de la qualité du matériau monté sur appareil.

4 - INFLUENCE DU TAUX DE POROSITES

En partant de l'hypothèse que les porosités se trouvent uniformément réparties sur tous les interplis du matériau, un calcul statistique permet de traduire ces absorptions ultrasonores en pourcentage de porosité surfacique par pli par rapport à la surface totale du faisceau ultrasonore.

La courbe suivante donne à titre d'exemple, pour un matériau carbone-résine constitué de nappes unidirectionnelles, la corrélation absorption-taux de porosités surfaciques en fonction des différentes épaisseurs du composite.



Afin de se rapprocher de la conception réelle des structures, les essais mécaniques cités dans ce rapport porteront le plus souvent sur des éprouvettes à couches croisées, fabriquées à partir de nappes T300, NARMCO 5208.

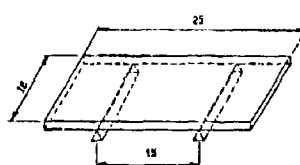
4.1 - Influence sur le cisaillement interlaminaire

Deux taux de fibres 51 % et 62 % en volume, ont été étudiés avec ou sans porosités.

Les essais conduits à trois températures

- 55°C, 20°C, 120°C sur matériau à l'état initial ou après vieillissement humide 750 h à 70°C, 100 % HR font ressortir les conclusions suivantes : (Figure 4)

- . l'influence des porosités est plus importante sur matériau possédant un taux volumique de fibre élevé (7 % de porosité pour Vf = 62 % donnent autant de chute en cisaillement interlaminaire que 10 % pour Vf = 51 %)
- . l'influence des porosités n'est pas plus marquée à - 55°C, qu'à 20°C ou 120°C (on obtient une chute d'environ 50 % de performances aux 3 températures lorsque l'on atteint 7 à 10 % de porosité selon le taux volumique de fibre).
- . la présence de porosités n'amplifie pas la dégradation du matériau en vieillissement humide ; on constate d'ailleurs que l'effet "plastifiant" de l'eau sur la résine est plus important sur matériau sain que sur matériau de mauvaise qualité lors des essais de cisaillement interlaminaire à 120°C.

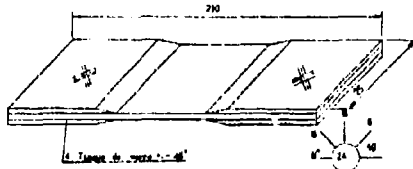


4.2 - Influence sur le comportement en traction

Les éprouvettes ont été fabriquées avec deux taux volumiques de fibres, 51 % et 62 %, et ce avec ou sans porosités.

Afin de nous dégager du paramètre épaisseur des éprouvettes constituées d'un nombre identique de plis, nous avons exprimé les résultats mécaniques en flux (charge supportée par unité de largeur).

Un taux de porosité compris entre 7 et 10 % fait chuter le comportement en traction à 20°C sur matériau à couches croisées de l'ordre de 15 %.



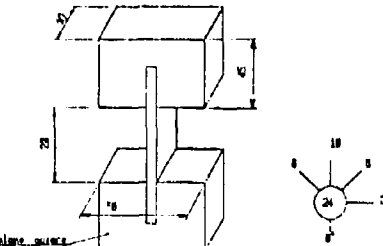
4.3 - Influence sur le comportement en compression

Avec les mêmes matériaux que ceux utilisés pour la traction, on constate que les essais de compression conduits à 120°C, entraînent une chute d'environ :

- 15 % pour 7 % de porosité,
- 20 % pour 10 % de porosité.

On observe qu'après vieillissement humide 750 h à 70°C, 100 % HR :

- la porosité ne modifie pas le comportement du matériau par rapport à ses performances à l'état initial,
- sur faible taux volumique de fibre (51%) l'humidité fait légèrement chuter les performances à 120°C alors que son effet est plutôt bénéfique sur taux de fibre plus élevé (62%) et ce, sans ou avec porosités.

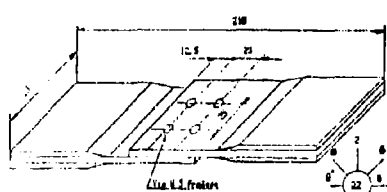


4.4 - Influence sur le comportement des fixations mécaniques

Les éprouvettes ont été sollicitées à 80°C :

- à l'état initial,
 - après vieillissement humide et sollicitations de fatigue,
- 250 h à 70°C, 100 % HR
+ 33 000 cycles de fatigue traction 0,3 FR/compression 0,1 FR

Ce cycle est répété trois fois avant d'effectuer l'essai statique résiduel à 80°C. FR correspond à la charge de rupture en traction de l'éprouvette neuve non poreuse.



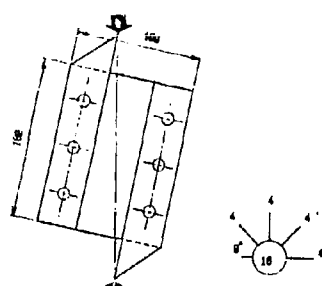
Dans tous les cas, la rupture a lieu par déboutonnage et délamination dès au moment secondaire engendré par le type d'éprouvette.

On constate une chute de résistance statique par rapport aux témoins non poreux d'environ :

- 20 % pour 5 % de porosité,
- 40 % pour 8 % de porosité.

La fatigue et le vieillissement humide, tels que définis, n'ont pas plus d'influence sur matériau de mauvaise qualité que sur matériau sain.

4.5 - Influence sur le cisaillement plan

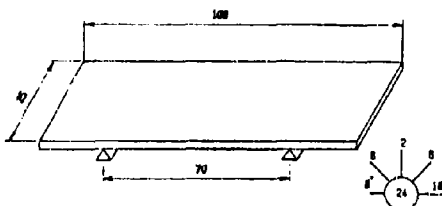


Pour un taux volumique de fibre de l'ordre de 63 % :

- un taux de porosité surfacique de 12 % fait chuter la contrainte de cisaillement d'environ 15 % lors des essais à température ambiante, et de 10 % lors des essais à 120°C,
- les porosités n'accélèrent pas la dégradation du matériau exposé en ambiance humide 1000 h à 70°C, 100 % HR.

4.6 - Influence sur le comportement en flexion

Sur deux taux volumiques de fibre, 51 % et 62 %, des essais à 20°C et 120°C ont été conduits sur matériaux sain et de mauvaise qualité (7 % et 10 % de porosités surfaciques).



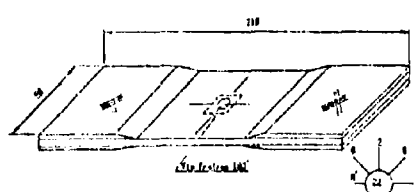
On constate que :

- à l'état initial, des chutes de l'ordre de 20 % peuvent être atteintes avec les matériaux à 10 % de porosités surfaciques.
- le vieillissement humide 750 h à 70°C, 100 % HR a un effet analogue sur matériau de bonne ou de mauvaise qualité (la porosité n'amplifie pas la dégradation du produit).

5 - INFLUENCE DES DELAMINAGES

Les décohésions intercouche ont été obtenues artificiellement dans la phase drapage du stratifié par interposition entre 2 plis d'un morceau de VAC-PAK ou de TEFILON détectable en contrôle ultrasonore.

5.1 - Sur le comportement en traction avec trou habité



Le défaut de dimensions 14 x 14 mm est situé à mi-épaisseur du matériau entre deux plis disposés à $\pm 45^\circ$.

La présence de la décohésion au niveau d'un trou diamètre 5 mm habité ne modifie pas la résistance à la traction à 80°C ni à l'état initial, ni après vieillissement plus fatigued.

Cycle de sollicitation répété 3 fois :

- 250 h de vieillissement humide 70°C, 95% HR
- 33 000 cycles de fatigue
0,3 Fr traction/-0,1 Fr compression.

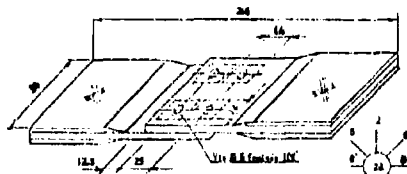
Fr = charge de rupture de l'éprouvette neuve sans délaminaison.

Aucune propagation du défaut n'a été détectée en contrôle ultra-sonore après les cyclages vieillissement + fatigue.

5.2 - Sur le comportement des jonctions mécaniques

Les 4 défauts de dimensions 14 x 14 mm sont situés à mi-épaisseur du matériau entre deux plis disposés à $\pm 45^\circ$, à l'emplacement des 4 vis de fixation diamètre 5 mm.

Les décohésions ne modifient pas le comportement de la jonction mécanique à 80°C, aussi bien à l'état initial, que sur matériau ayant subi un cyclage vieillissement plus fatigue, comme défini au paragraphe 5.1.



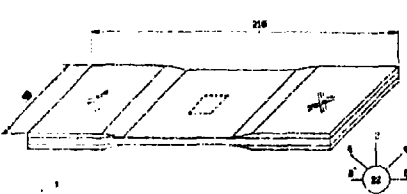
5.3 - Sur le comportement en compression

Que le défaut 14 x 14 mm soit situé à mi-épaisseur (entre deux plis à $\pm 45^\circ$) ou après la sixième couche en partant de la surface (entre deux plis à $0^\circ - 45^\circ$), on constate la même chute de performance en compression à 80°C.

Les bords de l'éprouvette sont maintenus latéralement pour éviter le flambage généralisé de l'éprouvette.

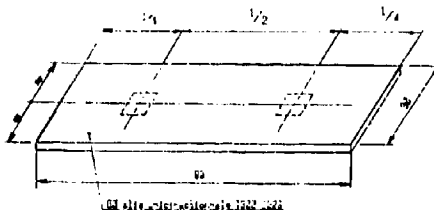
On constate ainsi que la décohésion étudiée entraîne à 80°C :

- une chute de 10 % de la contrainte à l'état initial,
- une chute de 20 % après conditionnement vieillissement humide + fatigue, tel que défini au paragraphe 5.1.



5.4 - Sur le cisaillement interlaminaires

Seul un matériau à 60 plis ($e = 0,13 \text{ mm}$) unidirectionnels a été sollicité en présence de défauts de dimensions 7,1 x 7,1 mm = 50 mm² positionnés sur la fibre neutre.



Que ce soit à l'état initial, ou après cyclage, cycle répété 3 fois :

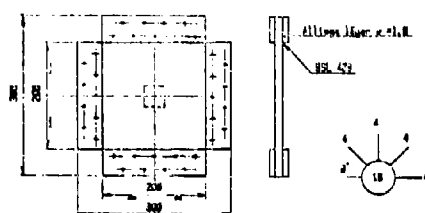
- 330 h de vieillissement humide 70°C, 100% HR sous charge constante 0,3 charge de rupture
- 33 000 cycles de fatigue à 0,3 charge de rupture.

Le délamination étudié fait chuter la tenue résiduelle en cisaillement interlaminaire de 30 % à température ambiante.

5.5 - Sur le cisaillement plan

Sur drapage isotrope 16 plis, deux dimensions de défauts positionnés entre les 8ème et 9ème plis, ont été sélectionnées :

- 17,3 x 17,3 mm soit 300 mm² ou 0,8 % de la surface
- 64,8 x 64,8 mm soit 3000 mm² ou 8 % de la surface.



Que ce soit à l'état initial, ou après sollicitation en fatigue 100 000 cycles à 0,5 FR/0,05 FR (FR = charge de rupture statique du matériau neuf sans défaut), la présence d'une décohésion intercouches, représentant jusqu'à 8 % de la surface travaillante, n'a aucune répercussion sur la résistance en cisaillement plan d'un matériau à couches croisées.

Bien que la charge de fatigue appliquée était supérieure à la charge de plissement, le défaut n'a pas progressé.

6 - INFLUENCE DES DEFAUTS DE COLLAGE

L'étude porte sur matériau constitué de couches unidirectionnelles (T300, NARMCO 5208) à l'état préimprégné associées par co-cuisson à l'adhésif REDUX 319 A.

Les défauts sont obtenus par découpe du film de colle avec remplacement de ce dernier par un film séparateur évitant l'adhérence des parties à assembler.

6.1 - Comportement des jonctions collées soumises à un flux de cisaillement constant.

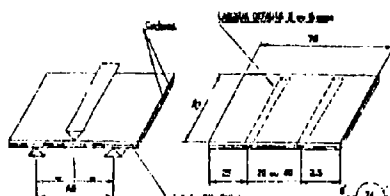
C'est le cas, par exemple, d'un collage longeron-revêtements.

6.1.1 - Assemblage carbone-carbone

Deux largeurs de défauts ont été sélectionnées : 2 et 6 mm.

Les essais conduits à -55°C, 20°C, 120°C font apparaître que :

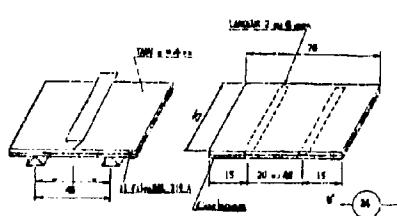
- à 20°C et 120°C, la rupture n'a pas lieu au niveau des défauts de collage, mais entre les couches de carbone (respectivement ≈ 80 MPa et ≈ 55 MPa quelles que soient les configurations essayées),
- à -55°C, on obtient une rupture au niveau du joint collé. Les défauts de largeur 2 et 6 mm entraînent respectivement une chute en cisaillement de 10% et 30% par rapport à l'épreuve sans défaut de collage tenant 60 MPa.



6.1.2 - Assemblage carbone-titane

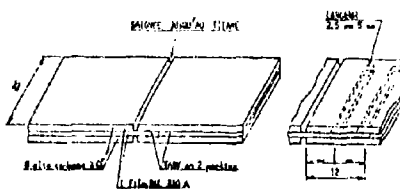
Les mêmes largeurs de défauts 2 et 6 mm sont étudiées. Toutes les ruptures ont eu lieu par cisaillement de l'adhésif (ruptures cohésives dans le film).

On constate que les défauts étudiés n'ont aucune influence sur le comportement du joint aux trois températures -55°C, 20°C et 120°C. On obtient respectivement ≈ 115 MPa, ≈ 100 MPa et ≈ 65 MPa, quelles que soient les configurations.



6.2 - Comportement des jonctions collées soumises à un flux de cisaillement variable.

C'est le cas, notamment, des introductions d'effort dans un composite par l'intermédiaire d'un insert titane.



Dans la zone de cisaillement 12 mm, deux tailles de défauts sont retenues : 2,5 et 5 mm, associées à deux positions : milieu et extrémité de la zone collée.

Les défauts intéressent toute la largeur des éprouvettes. Les contraintes moyennes sont calculées en prenant toujours pour section apparente 12 x 25 mm (figure 6).

Vu la rigidité des substrats et la faible longueur de recouvrement, l'emplacement du défaut (milieu ou extrémité du joint collé) n'a que peu d'influence sur le comportement de la liaison aux trois températures -55°C, 20°C, 120°C.

Si l'on calcule les contraintes de cisaillement (figure 6) avec les surfaces collées vraies (déduction des défauts), on constate qu'il y a proportionnalité entre charge et section collée lors des essais à 120°C (pas de phénomènes de surcontrainte) alors qu'une altération de la tenue du joint est constatée aux plus basses températures : jusqu'à 15% à -55°C et 30% à 20°C.

7 - CONCLUSIONS

La maîtrise de la qualité des pièces fabriquées en matériaux composites doit être un objectif prioritaire, car des chutes très importantes peuvent être constatées sur les performances mécaniques.

On peut souligner que les résultats présentés lors de cet exposé font ressortir que le rôle néfaste des défauts de fabrication apparaît essentiellement à l'état neuf du matériau, et que ces défauts n'amplifient pas la dégradation du matériau lors d'exposition en ambiance humide, ou de sollicitation sous charge cyclique.

On veillera donc particulièrement à optimiser la conception des structures (bureaux d'études), à appréhender les paramètres sensibles des matériaux (laboratoires), à concevoir des outillages adaptés (services méthodes), à maîtriser les gammes de fabrication (services production).

Sur pièces finies, des moyens adaptés de contrôle automatisé devront permettre à coût réduit d'obtenir une appréciation réaliste de la qualité du matériau, afin de pouvoir apprécier les marges de sécurité sur les pièces destinées à être montées sur appareils.

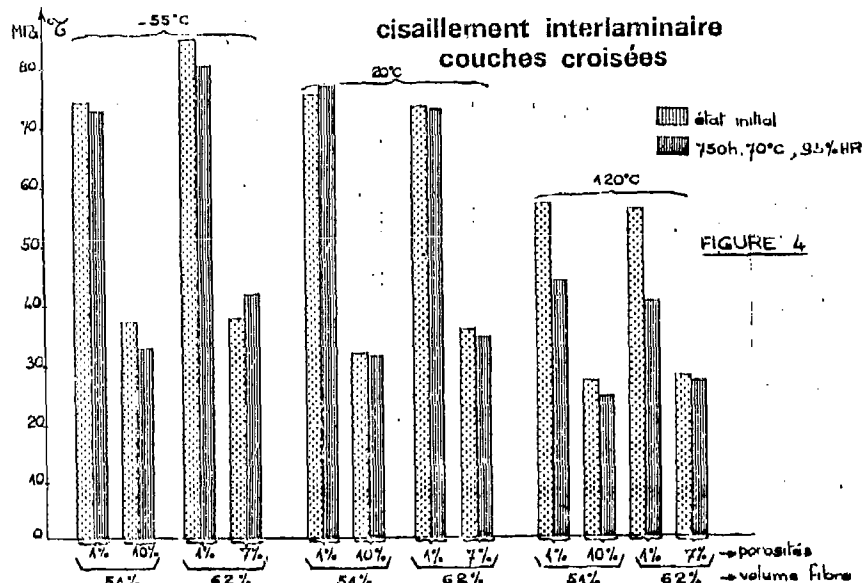
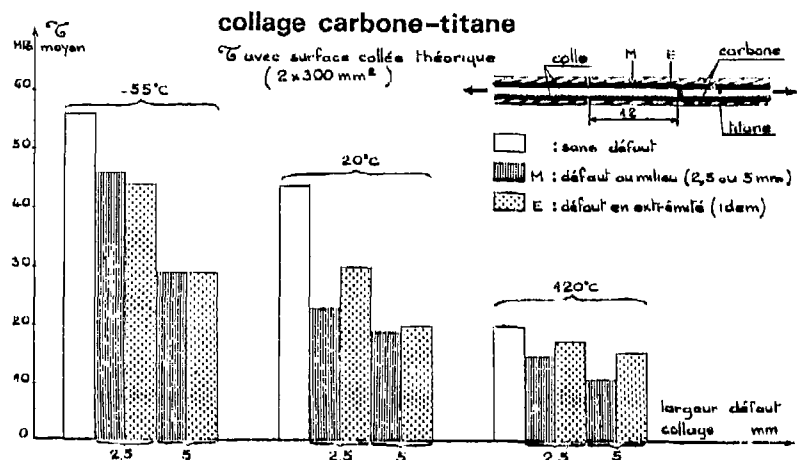
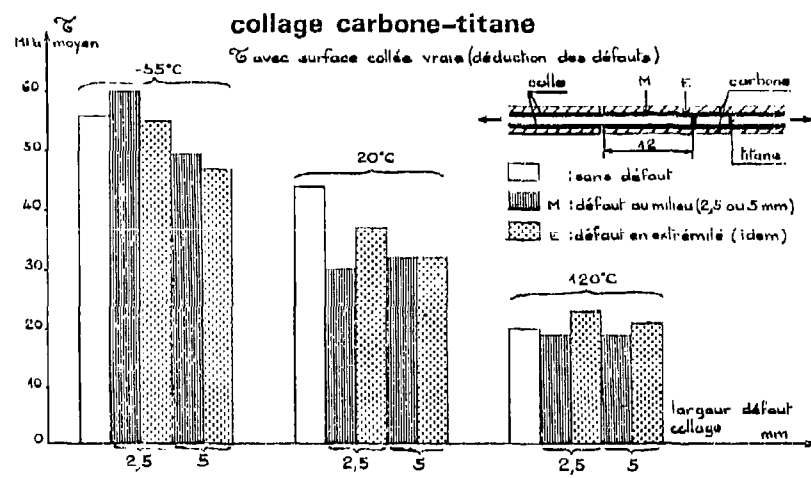


FIGURE 5FIGURE 6

AD P001920

13-1

ADVANCED N.D.TECHNIQUES FOR COMPOSITE PRIMARY STRUCTURES

M.FARIOLI-F.PORRO-G.SAMANNI-V.WAGNER

TECHNOLOGICAL DEVELOPMENT DEPARTMENT -L.T.S.-
COSTRUZIONI AERONAUTICHE G.AGUSTA - Gallarate - Italy

(Note to readers: When presented, this paper was illustrated with coloured photographs which are here reproduced in black and white only.
As a result, certain references in the text to coloured features of the photos are no longer meaningful - Editor.)

ABSTRACT

The applications of composite materials in primary aircraft structures need deep investigations on the materials themselves and reliable techniques of control of the products. The last topic represents one of the most weak points in the composites and adhesives technology because there is no one N.D. method useful and valid for all kinds of defects but a variety of N.D. methods in order to achieve good results in the inspectability of the configurations are necessary. This paper contains, in its first part, an overview of some most popular techniques for maximum sensitivity, determination on standard defects using a proof specimens, that is :

- X-ray radiography and in-line radioscopy electronically supported
- X-ray xeroradiography
- Neutron radiography
- U.S.Investigation

The second part presents some examples of application of the above mentioned techniques on significant aircraft components i.e.:

- main rotor spar and blade
- main rotor blade grip

and the results are discussed.

INTRODUCTION

This work was carried out without the aim of introducing new N.D. control techniques for composite materials but the philosophy was to show the possibilities of conventional N.D. techniques supported by some expedient to emphasize the resolution and the quality of controls. To make this we used the facilities already present in our factory as well as equipments coming from other laboratories in the field of Penetrant radiations, U.S. inspections and dye penetrant systems.

In this work we are going to show the improvements of the results obtained with these very common systems optimizing control parameters and procedures and, for radiation inspection, choosing the best system, to print the X-image, both in the field of standard industrial materials, and out of this.

The goal was to reach the maximum results, minimizing typical shortcomings of each technique.

We consider only radiation and U.S. inspections because from our experience we noted that dye penetrant systems for finite components were practically useless because of the adsorption of the resin (especially for intermediate components of a structure), and because of rough surfaces.

GENERAL CONSIDERATIONS

We compare the above mentioned techniques and several sensitive materials, in order to gain the conditions of maximum sensitivity and resolution on each of them, as well as the best working conditions of the equipment, for these purposes we prepared a special sample panel.

This sample panel, made with fiberglass-epoxy composite material, was obtained from a continuous prepreg tape; all kinds of standard defects typical of composite structures were put into the laminate.

The defects were chosen on the basis of our experience of destructive analysis of several samples and from literature examples.

In other words we put into the panel the following flaws :

- 1) foreign material inserts among plies like support silicon paper (a) protective teflon cover (c) and peel ply (b);
- 2) fiber gaps, between two adjacent tapes in the same ply (g);
- 3) cutted fibers (f);
- 4) twisted (e) and knots (a) of fibers;
- 5) delaminations (debonded areas among plies).

The above mentioned panel is shown in picture 1.



Pjcture N°1: The sample panel

We are quite sure that combining opportunately the techniques of X-ray and U.S.investigation sufficient information about the flaw conditions of the material under test are normally warranted.

In this paper we did not discuss the physical rules governing the techniques themselves as well as all the procedures followed in finding the best parameters and working conditions because they have been explained by several authors (1.2.3) but only the results obtained analysing composite structures.

To analyze the test panel with X-ray we needed to use k-voltage as low as possible(normally arranged between 20+30 KV depending on the X-ray sensitive material).

For the best results we needed also to use a microfocus X-ray tube with Berillyum window. For U.S. inspection we used a transmission immersed C-scan equipment with a characteristic frequency of 5 MHz.

We would like to emphasize that this frequency comes from the industrial system used for aluminium sandwich panels.

RADIOGRAPHIC INSPECTIONS OF THE TEST PANEL

We carried out the following tests :

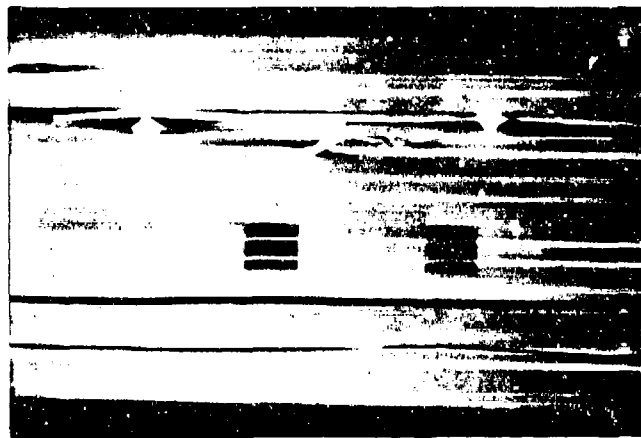
- a) conventional X-ray radiography with standard ASTM class 1 (DIN II°) films, extra-fine grain, low speed : DUPONT NDT 45 and 55, AGFA-GEVAERT D4, KODAK M, example reported in picture 2;
- b) conventional X-ray radiography with standard ASTM special class (DIN I°) films, ultra fine grain, very low speed: DUPONT NDT 35, AGFA-GEVAERT D2 double coated, KODAK R; an example is given in picture 3;
- c) conventional X-ray radiography high definition copline films AGFA-GEVAERT HD-3p with a grain dimension of about 1 μm ultra slow films (in the following we will name simply HD films), an example is shown on picture 4;
- d) radiographic re-impression techniques for the use of industrial D4 and D2 films example is given in figure 5;
- e) X-ray very low K-voltage radiography in vacuum with conventional D2 film; the example is at picture 6;
- f) X-ray electro-radiography (xeroradiography)by medical equipment Xerox system 125;positive and negative impression; the example of the positive image is at picture 7;
- g) Neutron radiography by means of a N- Gd converter (direct impression) with Kodak R films,example in picture 8 ;
- h) industrial X-ray radioscopy investigation with eletronic support and treatment of the signal: image intensifier, TV camera and monitor (image example in picture 9),grey densitometric analysis and eight colour syntetizer associated video monitor (picture 10) and deflection mode video signal presentation, virtual 3D image (picture 11).

From the above listed and following pictures it appears that all the mentioned techniques are useful ; the following consideration must be taken as a guide in the choice of the most suitable technique.

a) Test: D4 film radiography.

Because of the large use of this film in standard industrial high-quality inspections we consider the quality of these image as a reference to quote the quality of the others.

Remark: we cannot see the foreign insert.



Picture N°2: Test a

b) Test: D2 film radiography.

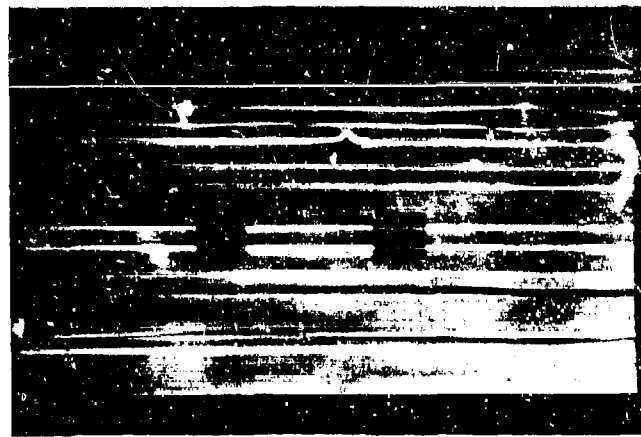
We have an improvement in definition and resolution of the same family of defects detected in a) using a larger exposure time.

This film can be used in challenge with D4 when an higher precision and quality of the control is required.

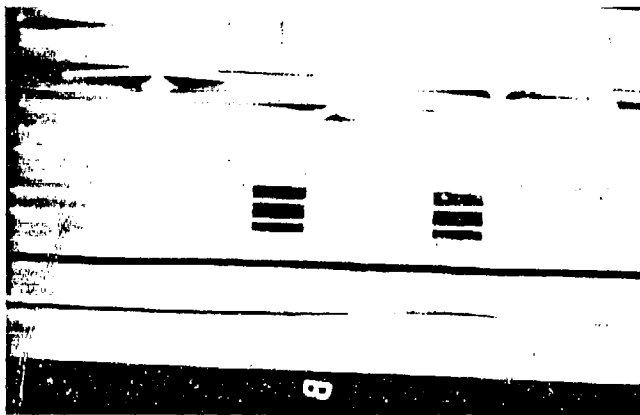
c) Test: HD film radiography.

The image is more detailed than in a).
The very fine grain structure allows a precise densitometric analysis (i.e. by grey analysis of the transmitted image with an image analyzer) or for a projection magnified analysis. Nevertheless the exposure time becomes too long to be used for routine quality control.

We remark that the use of this particular film involves only a longer exposure time but does not need particular devices and materials for development; this film can be very interesting for particular laboratory use.



Picture N°3: Test b

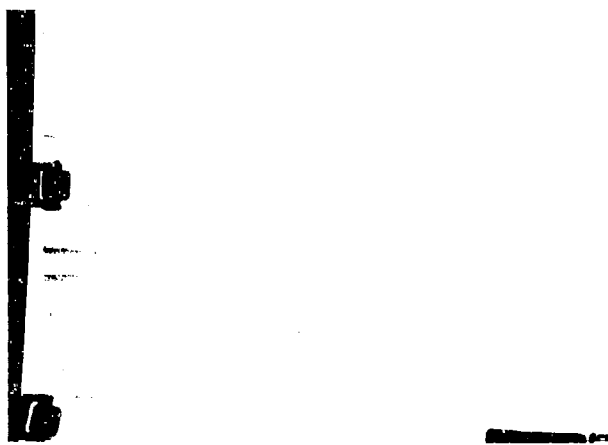


Picture N°4 : Test c

d) Test: D2 film (from D4 overexposed radiography).

This technique is useful to improve the "exposure latitude" without utilizing higher K voltages and can be used for components having different thickness or "blackboxes" when it is impossible to have a precise idea of correct exposure parameters as well as to recover some information by an overexposed film (or zone of a film) when the sample is no more available.

The resolution of this techniques is lower than a), any way it is lower than the correspondent well done single impression radiography (4).



Picture N°5:Test d

e) Test: HD film vacuum radiography.

The "vacuum radiography" allows the reduction of an absorbed and diffused radiation by air so that we can reduce the K-voltage of irradiation with an increase of the resolution of the image.

The necessity of a vacuum light-proof chamber introduces some limitation in the use of this system, not always payed by the improved resolution.

f) Test: Xeroradiographic positive image.

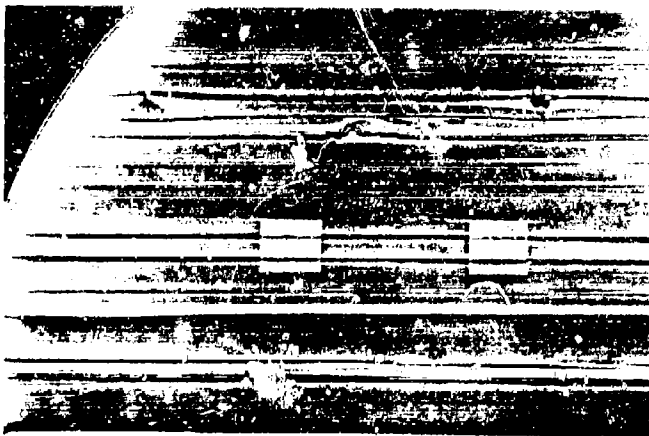
From our point of view this is the best technique in the field of X-ray inspection, because the highest quality in resolution is reached (5).

The advantages (6-11) of this technique can be listed as follows:

- no time loss for development
- high-life time sensitive materials
- high sensitivity to fast density variation (edge effect)
- possibility to choose positive or negative final image
- low sensitivity to gradual variation of X-ray density or material thickness.



Picture N°6: Test e



Picture N°7: Test f

The cost of the system is very high but each image is cheaper than a pure X sensitive film and the interpretation is not affected by the real quality of the transilluminator. All the above arguments give an interesting pay off of the system.

We point out that the device till now was developed only for medical use. We are quite sure that if this system will be redesigned for industrial purposes it will be possibile to improve the results again.

g) "Test: neutron radiography on film by Gd n - converter.

This technique gives interesting results through different information coming from the characteristic of the neutrons. In this case differently from X-ray inspection the N-opaque material is the resin and fibers are quite not visible (the sign of fiber directions is due to the "holes" in the resin): by means of this feature it is possible to see very well flaws in the resin like bubbles and anomalous distributions of the resin itself. Through this system is possible to detect the foreign materials inserts, too. Nevertheless this technique is quite expansive because it needs a nuclear facility with obvious problem of carriage and handling of samples.



Picture N°8: Test g

h) Test: radioscopy.

This is the fastest technique because of the direct image of the samples. The radioscopic image produced on fluorescent screen, is intensified by a fluorescent magnifier and collected by a normal TV-camera which sends the image on a TV-monitor, at this point the resolution is worse than the standard radiographic D4 result. In order to improve the quality of the image the video signal is electronically processed by :

- densitometric grey analysis.

Through an eight-colour synthesizer which converts a certain range of grey levels into a colour in order to improve the contrast between acceptable areas and defects. Of course a precise knowledge of the equipment and a good quality of signal is needed to have a warranty of good control.

Moreover the quality of the image is still worse than radiographic one.

- deflection mode analysis.

This system inserts the video signal into the y - amplifier of the CRT: the deflection of any line given by the different grey level of any point on the line, allows to create a virtual 3D image. This quite interesting image is not always useful because its quality is too strongly dependent from the original TV-image from the intensifier and the camera.

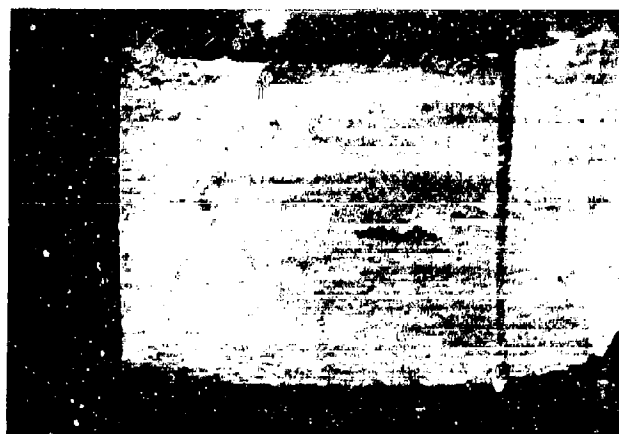
Anyway all the information are coming from the original black and white radioscopic image: these two systems cannot increase the quality.



Picture N°9: Radioscopic TV image: section of the panel.



Picture N° 10 :
The same panel section that in fig.9 converted in eight-colour image in order to improve the contrast between "adjacent" grey-levels.



Picture N° 11 :
The virtual 3D image of the same panel area.

U.S. INSPECTION ON TEST PANEL

For the detection of delaminations and debonding an useful technique is the U.S.inspection. In analogy with U.S. inspection of metallic structures,we think that the best system to monitor composite components is the immersion transmission U.S. analysis (in this field we include the use of "squirters" governed by the same principles of U.S.transmission in the water without a real immersion of the structures) supported by an automatic C-scan equipment. We employed a facility designed for helicopter aluminium rotor blades, a fixed frequency of 5 MHz was used.

We could not verify the best frequency to be used for this material and thickness. Using the immersion system we found some problems in the set up of the equipment,moreover we found also that the moisture absorption of the material affects the repetitivity of results. Any way the technique is to be improved because we found some delaminations not detectable by other N.D.test. The C-scan is shown in picture N°12.

To be sure of the delaminations detected a direct contact reflected U.S. inspection by focused probes with characteristic frequencies of ,75 and 3 MHz,from Gilardoni RG 20 was used.

The results confirmed the previous analysis, but using this technique it is very difficult to assure the repetitivity of the measurements because they are too dependent on the operator. We have not found till now a good procedure to be followed.



Picture N° 12

PROTOTYPICAL SAMPLES

After the experience on the test panel we could start the investigations on more complicated structures in order to verify the various techniques and sensitive materials on thick samples complicated as the real helicopter components.

We have to remark that the geometry of the samples could be a very difficult parameter to process especially for X-ray investigation, and thickness can affect U.S. inspection; in other words we have to consider very well the lay-up characteristics of any structures in order to define the control procedure.

In order to perform the above mentioned investigations some different tests were performed on a thick sample similar to an helicopter component part but full of defects; than we check some prototypical components.

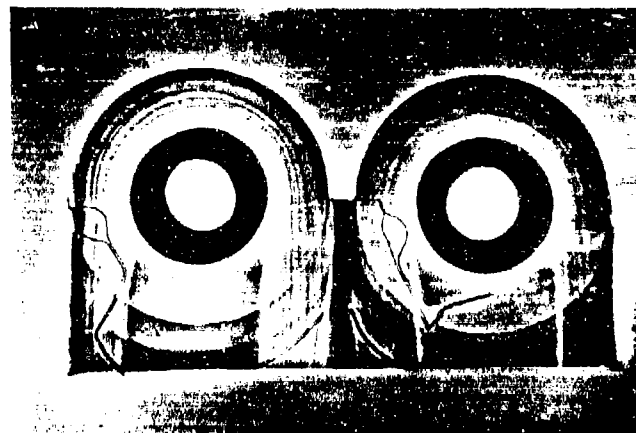


Picture N° 13: Top view of the "eyes".

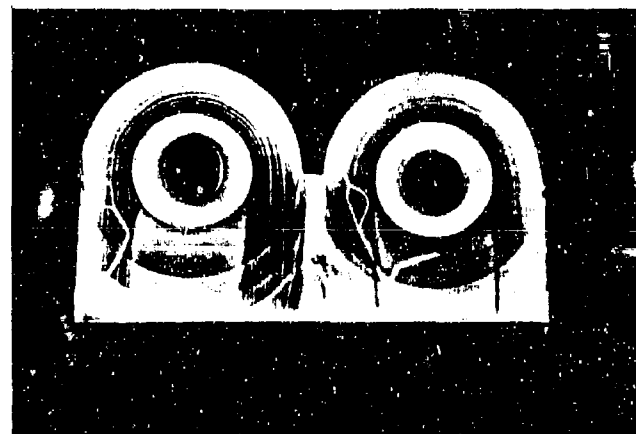
In picture N°13 we show the thick sample N° 2 similar to the "eyes" of the spare root. This sample is made by fiberglass-epoxy prepreg tapes, the difference between two "eyes" is due to the resin system and its content.

a) Positive (fig.14) and negative (fig.15) xeroradiography.

In both images it is possible to see very well the delaminations among the plies; we remark that this is possible only by the particular angle of irradiation. The images are well exposed for both the eyes.



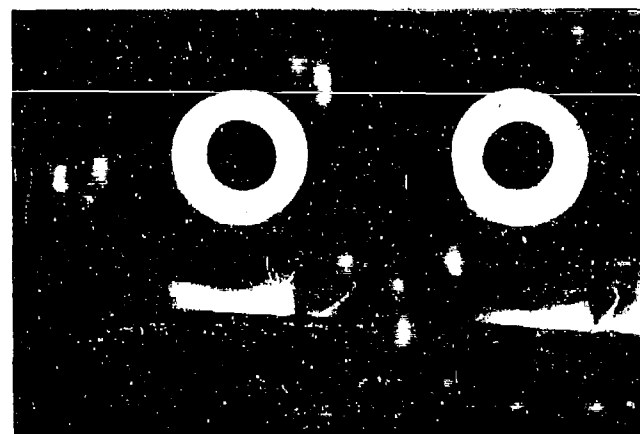
Picture N°14 : Top view positive



Picture N°15 : Top view negative

b) D2 conventional radiography.

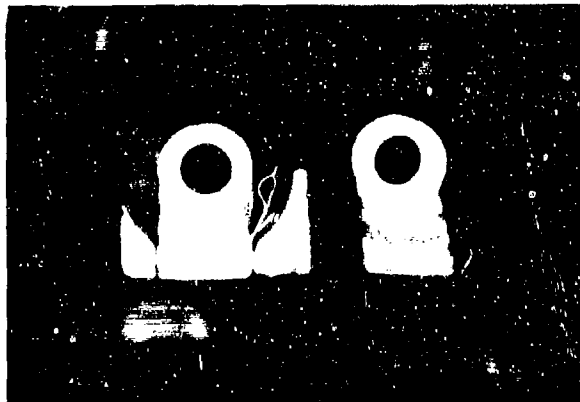
By the film is not possible to have the right exposure for both the eyes; the resolution is lower than xeroradiography.



Picture N°16 : Bottom view

c) Re-impression radiography (D4 and 22 films).

In picture N° 17 we can see that the starting image is completely ununderstandable in some areas, by this technique we can recover the information from these areas directly by the film, without repeating the examination on the real sample (picture N°18). The exposure latitude is increased but the resolution is worse than a) and b).



Picture N°17: Overexposed D4
film (RI) top view.



Picture N°18 : R2 on D2 film
Inverted view.

d) U.S. inspection.

This is a very critical situation because of material thickness and shapes: practically we have no results.



Picture N°19: The C-scan plot:
quite ununderstanding image.

ANALYSIS ON REAL COMPONENTS

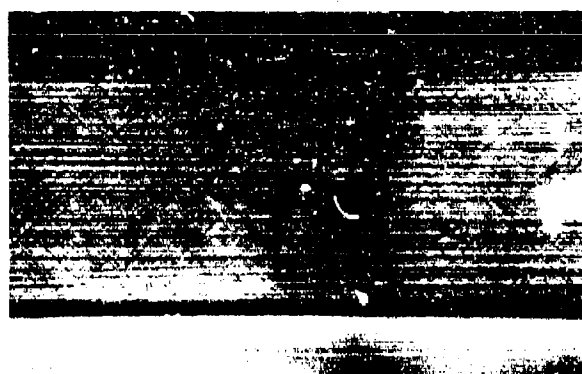
Helicopter main rotor blade spare

In the picture two spares are shown.
The spare under test presents some defects i.e. twisted fibers and delamination due to
the crash of the pressure mandrel in the curing cycle. The defect is good resolved by
xeroradiography.

In picture N° 21 and 22 we show the two views of defect.



Picture N°20 : Two spars.



Picture N°21 : Plane view of
spar.



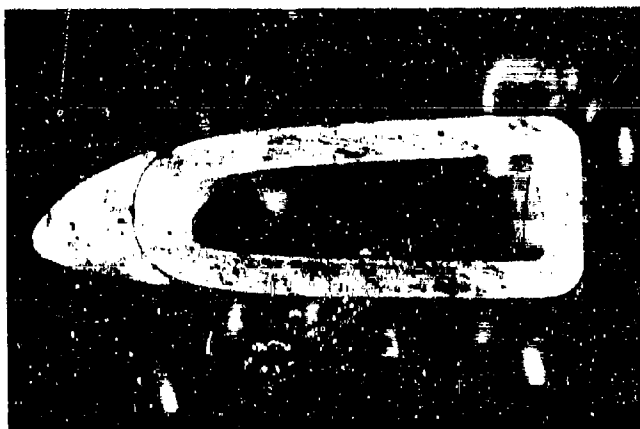
Picture N°22 : Side view.

MAIN ROTOR BLADE SPAR WITH TITANIUM ABRASION STRIP.

In the picture 23 and 24 the spar section is shown.



Picture N° 23 : Plane view of the spar with a bonded titanium foil.

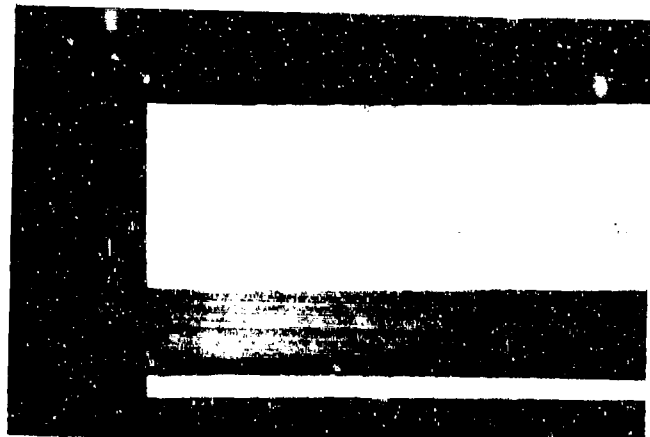


Picture N° 24 : The side view of the spar section.

The radiographic inspection need two different exposures for the complete control of the sample.

- 1) A low K-voltage irradiation to examine the "free" area, that is the surface not covered by the Ti sheet.
We can see the fiber orientations and the "tracers" (coloured lines in the 23 and 24 pictures).
- 2) A second exposure at an higher K-voltage to examine the area covered by Ti, we have a good resolution in this image, too, we see the fiber orientation and tracers.

Through xeroradiography inspection we obtain the same results (or better), with a single shoot, as it is shown in picture N° 27.



Picture N° 25: Low K-voltage
irradiation (D2 film).



Picture N° 26: High K-voltage
exposure (D2 film).

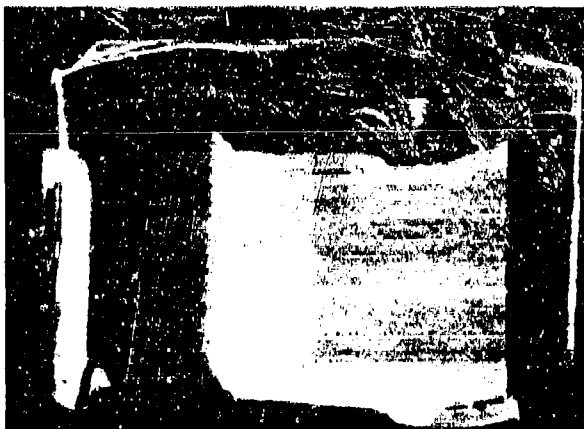


Picture N° 27: Xeroradiography
of the spar .

Also radioscopy can help the control but only when the deflection mode is employed.
Picture N° 28 and N° 29.



Picture N° 28 : Radioscopy:
TV Image does not resolve
fibers orientation and tracers
are quite invisible.



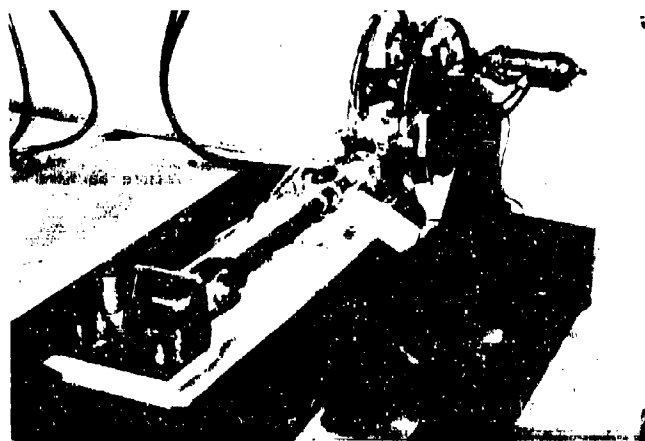
Picture N° 29 : Radioscopy :
deflection mode increases the
resolution emphasizing tracers
and fibers orientation.

MAIN ROTOR BLADE (SECTION)

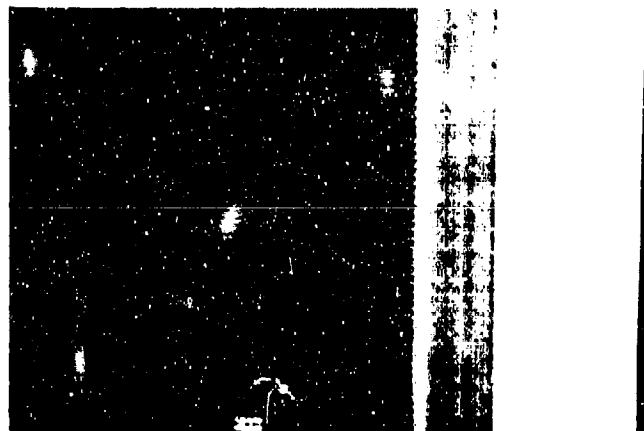
We performed some investigation on blade sections after mechanical test, one of these samples and the testing machine are shown in picture N°30.

In the following picture(N°31 and 32) two images of this samples are presented. A radiography (performed before the test) and a xeroradiography (after the test; it shows very well crashes in Ti sheet) are shown:the pictures emphasize the great advantage of xeroradiography that allows some good resolution all over the blade.

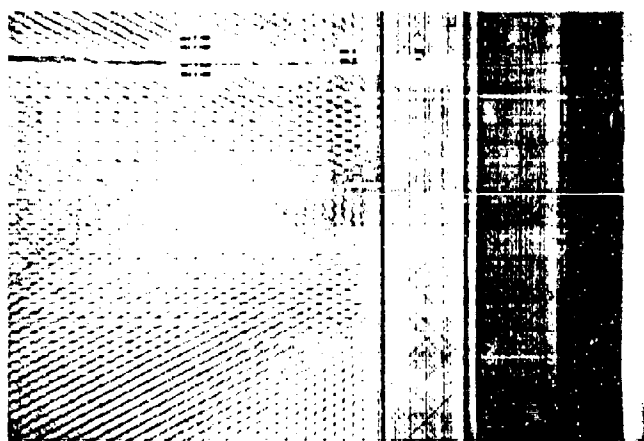
The radiography is overexposed for the honeycomb zone and completely unexposed everywhere: we can see either the tracers or skins over honeycomb,either fibers orientation under the titanium foil.



Picture N° 30: A blade section
in the testing machine.



Picture N° 31: D2 film radio-
graphy of the blade before test.



Picture N° 32: Xeroradiography
of a blade section; we can see
cracks in Ti abrasion strip.

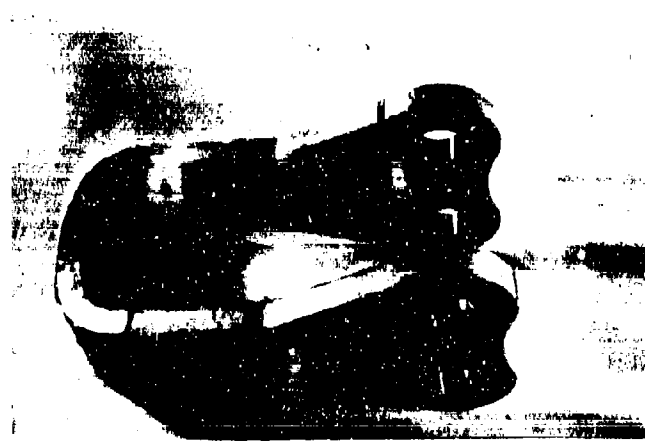
BLADE GRIP

Probably this may be one of the simplest specimen to be controlled because of its geometry (no thickness variations); it is shown in picture N°33.

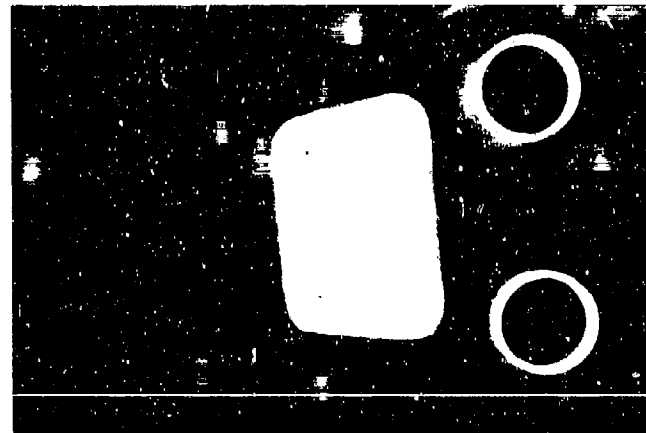
The radiography allows to control very well the eyes lamination and because of the constant thickness,gives a good image all over the piece.

Also U.S.inspections was employed and the results are shown in picture 35.

By this techniques it is possible to detect some debonded areas between the surfaces cover and internal filler materials (with areas in the picture)but it is impossible to find delaminations around "eyes".



Picture N° 33: Blade grip.



Picture N° 34: Radiography of blade grip; we can see delaminations in the eyes zone.



Picture N° 35:U.S.inspection
C.Scan.

CONCLUSIONS

The defects in composite components built by stack up of prepreg tape plies, is, from our experience, typically flat.

This kind of defects is detectable by X-rays inspection only when its direction is quite parallel to the radiations, normally this is a shortcoming of the technique.

In our case, we know the "surface" of lay up and we can determinate the correct direction of inspection, in this way it is possible to find easily all lamination defects (like debonded areas, marcel, etc.) better than by U.S. investigation.

Moreover, the geometry of many components don't allow the inspection in the correct direction (high surface/thickness ratio, where thickness is perpendicular to the lay-up plane) and in this situation U.S. technique became very useful.

From this considerations it appears that in order to control composite helicopter components we need at least two techniques: the best results are obtained combining xeroradiography and C-scan immersion U.S. inspection when possible.

BIBLIOGRAPHY

- 1) J.L.CAMAHORT,D.CARVER,R.PFEIL and B.J.MULROY Jr.: Process Control N.D.E. Procedures for Advanced Composite Structures S.A.M.P.E. 1978 pages 337-389.
- 2) D.HAGEMAIER and R.FASSBENDER: Non Destructive Testing of Adhesive Bonded Structure. S.A.M.P.E. Quarterly, July 1978 pages 36-58.
- 3) D.HAGEMAIER, H.J.MC FAUL and D.MOON : Non Destructive Testing of Graphite Fiber Composite Structures. National Aeronautic and Space Engineering and Manufacturing Meeting, Los Angeles 5-9 October 1970.
- 4) P.JEHLINSON,F.LUCHTMANS: "Recupero di informazioni contenute nelle zone sovraesposte di una radiografia classica "La rivista italiana della saldatura N°3 1978 pagg.153-166.
- 5) V.WAGNER,G.SAMANNI,F.PORRO,L.ROTA,C.PELUFFO: Xeroradiography: High Quality Radiography for Glass Reinforced Composites. S.A.M.P.E. European Chapter 1, Cannes, Intercontinental Conference, 12-14 January 1981.
- 6) G.LUZZATTI and MORASI: La xeroradiografia - Presentazione del metodo e basi fisiche; La Radiologia Medica Vol. 60 N° 9 pag. 721-736 Sett. 1974.
- 7) G.BORASI and G.TOSI: Le caratteristiche dell'immagine xeroradiografica : La Radiologia Medica Vol.N° 60 N°9 pag.737-749 Sett.1974.
- 8) Rank Xerox Corp. data sheet on 125 Model.
- 9) Rank Xerox Corp. Technical application, Bulleting N°1.
- 10) K.C.Mc MASTER and H.L.HOYT: Xeroradiography in the 1970's:Material Evaluation vol.XXIX N°12 Pages 265-274 (By courtesy of Rank Xerox Corp.).
- 11) A.BURGER, C.VIEWEG and L.BAUER
Rontgenprufung von Gusstücken mittels Xeroradiographie.
Rank Xerox GmbH Munchen
(By courtesy of Rank Xerox Corp.).

AD P001921

COMPUTATION OF INFLUENCE OF DEFECTS
ON STATIC AND FATIGUE STRENGTH OF COMPOSITES

by
R. C. Tennyson, J. S. Hansen, G. R. Heppler
University of Toronto
Institute for Aerospace Studies
Toronto, Ontario, Canada
and
G. Mabson, G. Wharam
Engineering Research Associates
Toronto, Ontario, Canada
and
K. N. Street
Defence Research Establishment Pacific
Department of National Defence
Victoria, British Columbia, Canada

SUMMARY

A combined analytical and experimental investigation has been undertaken to determine the effects of flaws on the static strength and fatigue life of graphite/epoxy (AS1/3501-6) laminates. Both bond-line defects in sandwich beam construction and inter-laminar disbond flaws were studied. Up to present, compressive strength test data have been obtained for ambient and elevated temperature, moisture-saturated conditions, including results from thermal-spike cycling simulating supersonic flight. In addition, baseline data have been obtained to define the strength parameters associated with the tensor polynomial lamina failure criterion. Although this model was originally derived for static 'unflawed' strength predictions, it is being extended to include the effect of holes and flaws. In the latter case, a finite element approach is described to illustrate the methodology for computing the influence of flaws. Finally, a formulation for predicting the fatigue life of laminates is presented based on the experimental evaluation of fatigue functions which are utilized in a form of the tensor polynomial failure criterion.

NOMENCLATURE

d	hole diameter or flaw size parameter
E_{xc}	modulus of elasticity of composite measured in x-direction
E_{11}, E_{22}	orthotropic moduli of elasticity measured in 1 and 2 directions, respectively
G_{12}	shear modulus of elasticity measured in 1-2 plane
$\lambda_{T,C,S,B}$	characteristic distances for tension, compression, shear and biaxial loading, respectively
n	frequency
N	fatigue life, cycles
N_x, N_y	normal stress resultants
N_c	shear stress resultant
r	ratio of algebraic minimum/maximum cyclic stresses
S	static lamina shear strength measured in 1-2 plane
S_D	fatigue shear strength of lamina measured in the 1-2 plane for given N and R value
W	sample width
X, X'	tensile and compressive static lamina strengths measured in the 1-direction
X_D, X'_D	tensile and compressive lamina fatigue strengths measured in the 1-direction for given N and R values
Y, Y'	tensile and compressive static lamina strengths measured in the 2-direction
Y_L, Y'_D	tensile and compressive lamina fatigue strengths measured in the 2-direction for given N and R values
Subscript:	
b, u	buckling, ultimate
x, y	orthogonal in-plane structural axes
1, 2, 3	lamina material axes parallel and orthogonal to the fiber reinforcement, respectively
4, 5, 6	indicates shear properties relative to the 2-3, 3-1 and 1-2 planes, respectively

Greek Symbols

α_T	coefficient of thermal expansion
θ	fiber orientation relative to the x-axis
ν	Poisson's ratio
σ	stress
σ^*	ultimate static, ambient dry, unflawed, specimen strength for a given batch and manufacturing process
σ_{ults}	ultimate static specimen strength
σ_{xc}	composite failure stress in x-direction

1. INTRODUCTION

With the advent of graphite-epoxy primary structural components in advanced high performance aircraft, the need for proven predictive formulations to quantify the effects of defects in composite materials becomes of paramount importance. The determination of critical crack dimensions in complex heterogeneous composite structural components which are subjected to multimode stress fields is receiving priority treatment in a number of countries, including Canada. Efficient systems management programs require the ability to define accept/repair criteria and non-destructive inspection intervals both of which necessitate the development of a methodology for assessing the effect of defects.

In the design of laminates, one of the major difficulties still confronting the analyst is that of selecting a suitable strength criterion. This problem is of course further compounded by the presence of holes, interlaminar flaws and boundary conditions which give rise to local stress concentrations and three-dimensional stress fields. Suffice it to say that an accurate static strength prediction for a laminate subject to these conditions represents a considerable analytical task. To extend this predictive capability to include fatigue loading represents an even more difficult problem. One can illustrate the various aspects involved by examining the flow chart of Fig. 1. For a given external load system (i.e., including temperature), one first needs to calculate the stress state in each lamina. If the effects of flaws and boundary conditions are not considered, then classical laminate theory can be used. Otherwise, recourse to complex analytical models and fracture mechanics considerations are necessary.

Classically, high strength, low strain-to-failure isotropic metals have been successfully characterized by linear elastic fracture mechanics techniques. Since composites also display brittle-like behaviour, considerable attention has been devoted to extending the existing fracture mechanics methodology to include anisotropic homogeneous/heterogeneous materials.

An analytical foundation for such an extension was established by Sih et al [1] who showed that the crack tip stress fields in anisotropic, homogeneous, infinite plates exhibit a singularity of the form $r^{-\frac{1}{2}}$ and that a stress intensity factor K can be defined in a manner analogous to that for isotropic materials. Due to anisotropy, complex mixed-mode displacement-loading interactions can occur but were shown to disappear when the crack was confined to a principal direction of the composite. Furthermore, K values can be related to the Griffith strain energy release rate ' G ' in a manner similar to that found for isotropic materials.

Most work to date has concentrated on tensile failure mode examinations of through-thickness crack propagation. Wu [2] carried out an extensive experimental study on unidirectional Scotchply and found that fracture mechanics techniques were applicable to splitting fracture parallel to the fibers in both pure mode I tensile opening and pure mode II forward shear loadings. Konishi [3] and Slepetz and Carlson [4] have added further experimental evidence to the general usefulness of a fracture mechanics approach to composite failure.

A number of researchers have also deviated from the classical theory of fracture mechanics in order to better explain evidence of non-self-similar crack growth and mixed mode failure. Sih's [5] theoretical work established critical crack growth conditions based on the strain energy density of a small volume of material in the vicinity of, but not at, the crack tip. Wu [6] proposed a somewhat similar model which predicted both the critical load and the direction of crack propagation when a stress vector surface intersected a generalized material failure surface. The latter was determined at some distance away from the crack tip utilizing the censor polynomial failure criterion and biaxial test data for the unnotched material. Of significance is the fact that both these treatments are limited to crack propagation in the matrix, parallel to the fibers in unidirectional material.

The application of any failure criterion for composite components first requires a relatively accurate evaluation of the stress field. This is not at all a trivial task as in general composite failures result from complex three-dimensional stress states and the materials are anisotropic. Thus, from an applications point of view it seems that the assumption of laminate homogeneity must be made and this assumption has been determined to be reasonable for cracked structures provided that the elastic crack tip singularity contains a sufficient number of fibers [7]. In addition there are several other aspects of the problem which must be considered. First, is the failure dominated

by planar or three-dimensional phenomena? For example, if delamination is a predominant mode of failure then a three-dimensional analysis is a necessity. On the other hand, if the failure is planar, then it is reasonable to approach the problem from a conventional lamina-laminate approach.

The second aspect relates to the absence or presence of flaws. In this regard there are basically three cases; nominally flaw free, sharp flaws (cracks, delaminations) and smooth flaws (circular holes, cutouts). The failure criterion adopted and the corresponding stress analysis should probably address each of the above situations individually as it seems, at least at the present, that it is not possible to encompass all failure possibilities using a single failure criterion.

The application of linear elastic fracture mechanics concepts for cracked composite materials was discussed previously. In order to provide a stress analysis capability for this situation, a sequence of singular finite elements have been developed for both planar and bending situations while work is presently progressing on a three-dimensional singular element. In Refs. 8, 9 a singular finite element was derived for the direct calculation of combined modes I and II stress intensity factors for planar rectilinear anisotropic structures subject to arbitrary planar loading. The element was developed based on a twelve-node conventional element which incorporated the appropriate $r^{-1/2}$ singularity as dictated by linear elastic fracture mechanics to form an "enriched" element. These enriched elements are located about the crack tip as shown in Fig. 2 to form a macro-element which will typically be contained within a net of conventional elements. This formulation has been tested extensively on a range of composite material properties and specimen geometries. Some typical test geometries are shown in Fig. 3 while typical results for the evaluation of the mode I stress intensity factor for an orthotropic centre-cracked rectangular specimen subjected to an axial load are shown in Fig. 4. It is noted that the results due to Bowie and Freese [10] to which the present formulation was compared are taken to be exact.

A second development of interest relates to a singular element with the capability of providing modes I, II and III stress intensity factors for composite plates. This work [11] makes use of Mindlin plate theory and quarter-point isoparametric mapping techniques to provide the appropriate $r^{-1/2}$ crack tip singularity. This element has also been extensively tested and Ref. 11 should be consulted for details.

Finally, for three-dimensional situations work is progressing using quarter-point elements. Two formulations are being adopted. One is based on a fully three-dimensional finite element while the second involves a pseudo three-dimensional approach based on Ref. 12 which allows the displacements up to a cubic dependence on the thickness coordinates.

Once the three-dimensional stress field is known, it would appear that the application of a lamina failure criterion would be appropriate, at each 'point' or 'element' throughout the laminate. Because of local stress concentrations, one would presume that failure initiates in the highest stressed region and progresses through the laminate. However, previous analytical and experimental studies on holes and cracks [Refs. 13, 14] have shown poor correlation using this approach and recourse to 'characteristic distances', which define either 'evaluation points' or 'integration intervals' was necessary. These 'characteristic distances' were obtained from test data on laminates in combination with the calculated stress fields.

It should also be noted that environmental effects can readily be taken into account by measuring the change in the constitutive properties (such as E_{11} , E_{22} , G_{12} , ν_{12} , aT_{11} , aT_{22}) and strength parameters. In the latter case, however, one requires a strength criterion before evaluating the appropriate coefficients. Such a criterion should also include three-dimensional stress effects consistent with the stress analysis.

An alternative method to that involving detailed stress calculations coupled with selected laminate strength measurements is a phenomenological approach. Assuming a given lamina failure criterion, one can proceed to evaluate the strength parameters as a function of flaw size/plate width, flaw location and environment. Thus, a laminate is treated as though it had no flaw but consisted of individual lamina having strength properties suitably reduced according to the above parameters.

Up to present, the discussion has focussed on static strength predictions. It is of interest to examine if these methods can be extended to predict fatigue failure of laminates. Previous work by other authors [15-17] has shown that the use of 'fatigue functions', based on simple static, quadratic failure relations, can yield reasonable correlation with test data in many instances. In these cases, only the fatigue strengths under tension-tension and shear loading were required (X , Y , S) although a delamination effect was included. Similar work based on a quadratic Tsai-Hill failure criterion has also been completed [18, 19], again using only the X , Y and S strength parameters. Although reasonable comparisons with test data were reported in Ref. 18 for S-glass/epoxy (SP-250-SF1), such was not the case for graphite/epoxy (E 788/T300) based on limited results to date [19]. However, despite the disagreement, it is felt that this approach should be pursued utilizing an improved strength criterion in combination with fatigue functions derived from tension, compression, torsion and biaxial load tests.

At this point, it is worthwhile providing some background on the applications relevant to this program. It is well known that the combined effects of moisture and elevated temperature can seriously degrade the strength of polymer matrix composite materials.

This is particularly true for epoxy resin systems where it has been found that the glass transition temperature is significantly affected due to absorption of moisture. When one considers the composite laminates used on modern fighters, such as the graphite/epoxy wing skin panels on the CF-18 (F-18 Hornet) for example, questions arise concerning their strength under elevated temperature-high moisture (i.e., hot-wet) conditions. This problem is compounded by the thermal spikes that arise in the structure during supersonic flight. One parameter that has aroused serious concern is the compressive strength of such laminates. For example, from a design viewpoint, upper wing skin panels are subject to compressive bending loads during flight. Thus it is of prime importance to understand the extent to which the compressive strength (and stiffness) of such materials is affected during exposure to specified environments such as the 'hot-wet' case and by the presence of interlaminar flaws. However, the significance of defects on these compressive properties has received little attention to date. Unlike isotropic materials, composites do possess unique failure modes in compression which are sensitive to certain types of defects. One of these judged to be particularly important is the interlaminar crack or delamination which has been shown to occur readily under low energy or subcritical impact. Russell and Street [20] consider that delaminations will be amongst the most frequently encountered defects due to the relatively low fracture energies found in their experimental program investigating 'opening' and 'shear mode' failure. Furthermore, this is likely to be found in applications such as the CF-18 aircraft where approximately forty percent of the exposed surface area is graphite-epoxy material. A similar defect, the skin-core disbond, is also expected to occur due to impact damage on honeycomb sandwich components.

Because of the major interest of the Canadian DND in the fighter program, it was decided to use AS1/3501-6 graphite/epoxy, similar to the skin material of the CF-18 aircraft, as the basis for this investigation. Furthermore, the quasi-isotropic lamination consisting of $(0, 45^\circ, 90^\circ)_s$ plies was employed throughout the study. The major objective of the program is to develop a methodology for predicting the static and fatigue strengths of laminates with and without defects, including the effects of moisture and elevated temperature. Both experimental and analytical methods are being examined with particular attention to a finite element based fracture mechanics approach and a modified phenomenological three-dimensional tensor polynomial failure criterion.

2. LAMINA STRENGTH CRITERION

The most general failure criterion available for unflawed composite materials is the tensor polynomial which was advocated as early as 1966 by Malmeyer [21] and developed extensively by Tsai and Wu [22] in quadratic and higher order forms [23]. The failure surface in stress space is then described by the equation,

$$F_1^{\sigma_1} + F_{ij}^{\sigma_i \sigma_j} + F_{ijk}^{\sigma_i \sigma_j \sigma_k} + \dots = f(\sigma) = \begin{cases} < 1 & \text{no failure} \\ 1 & \text{failure} \\ > 1 & \text{exceeded failure} \end{cases} \quad (1)$$

for $i, j, k = 1 \dots 6$. F_1 , F_{ij} and F_{ijk} are strength tensors of the 2nd, 4th and 6th rank, respectively.

Plane Stress State

If one restricts the analysis to a plane stress state and considers only a cubic formulation as being a reasonable representation of the failure surface, then Eq. (1) can be reduced to [17],

$$\begin{aligned} F_1^{\sigma_1} + F_2^{\sigma_2} + F_{11}^{\sigma_1^2} + F_{22}^{\sigma_2^2} + F_{66}^{\sigma_6^2} + 2F_{12}^{\sigma_1 \sigma_2} + 3F_{112}^{\sigma_1^2 \sigma_2} \\ + 3F_{221}^{\sigma_2^2 \sigma_1} + 3F_{166}^{\sigma_1 \sigma_6^2} + 3F_{266}^{\sigma_2 \sigma_6^2} = 1 \end{aligned} \quad (2)$$

Simple tension, compression and shear tests will yield the principal strength components which are defined by

$$F_1 = \frac{1}{X} - \frac{1}{X'} \quad F_2 = \frac{1}{Y} - \frac{1}{Y'} \quad F_{11} = \frac{1}{XX'} \quad F_{22} = \frac{1}{YY'} \quad F_{66} = \frac{1}{S^2} \quad (3)$$

The remaining interaction strength parameters can be determined from biaxial stress tests and constraint equations, details of which are given in Ref. 23.

At this point it is reasonable to question the need for retaining the cubic interaction terms. It has been found that in certain biaxial load cases, these terms contribute substantially to the ultimate strength prediction. For example, Fig. 5 illustrates the calculated failure strength for $(\pm 0^\circ)$ symmetric laminates subject to varying biaxial loads ($\alpha = N_x/N_y$, $N_{xy} = 0$) and the corresponding optimum fiber angles. Included in this graph is the 'quadratic' prediction, based on setting the cubic terms to zero in Eq. (2). It can readily be seen that large differences in failure loads are predicted.

Limited experimental confirmation of the cubic strength criterion was obtained from internal pressure tests conducted on $(\pm 0^\circ)$ graphite/epoxy tubes [23]. A comparison of the test data with both quadratic and cubic predictions is shown in Fig. 6. It is clear that agreement with the cubic model is quite good while the quadratic formulation substantially underestimates the strength, particularly in the optimum fiber angle range.

However, it should be emphasized that for many load cases, particularly simple tension and compression, little difference in failure loads is predicted between the quadratic and cubic models. This feature will be implemented later when the quadratic form is employed to analyse samples containing circular holes as well as predicting the fatigue strength of samples subjected to uniaxial cyclic loads.

Three-Dimensional Failure Criterion

The cubic form of Eq. (1) for a three-dimensional stress state presents one with a virtually intractable problem of determining the multitude of interaction coefficients. However, for laminate stress analysis purposes, the simpler quadratic form could be readily incorporated to predict 'element' failure. This is given by,

$$\begin{aligned} F_1 \sigma_1 + F_2 \sigma_2 + F_3 \sigma_3 + F_{11} \sigma_1^2 + F_{22} \sigma_2^2 + F_{33} \sigma_3^2 + F_{44} (\sigma_4^2 + \sigma_5^2) + F_{66} \sigma_6^2 \\ + 2F_{12} \sigma_1 \sigma_2 + 2F_{13} \sigma_1 \sigma_3 + 2F_{23} \sigma_2 \sigma_3 = 1 \end{aligned} \quad (4)$$

where odd order terms in shear stress have been set to zero [22].

3. APPLICATION OF STRENGTH CRITERION TO LAMINATES WITH HOLES

Prior to undertaking extensive tests on laminates with interlaminar flaws in order to obtain principal strength parameter data, it was decided to apply this methodology to plates with holes under simple loading conditions. This stems from the fact that previous investigators [such as Refs. 13, 14] have shown that reasonably good correlations with such test data can be achieved using a combined fracture mechanics approach and the notion of 'characteristic distances', as described earlier. Note that this latter method also relies on test data to solve for the 'characteristic distances'. To illustrate the difference between this technique and the 'all experimental' method, a flow chart comparison is given in Fig. 7.

This phase of the program involved a series of tension tests on off-axis (0°) and angle-ply (45°) glass/epoxy laminates (3M, 1003) containing circular holes with $d/W = 0.15, 0.25$ and 0.40 . Two or three replicates were tested for varying values of θ for both laminate configurations, the results of which are presented in Figs. 8 and 9. Note that 'first failure' was taken as the laminate 'strength' value. This is consistent with the tests conducted on 0° and 90° laminates to determine both the tensor polynomial parameters and the 'characteristic distances' used in the 'point stress' calculations. As noted in Figs. 8 and 9, the predicted curves are based on 'point stress' calculations of the strength parameters for varying d/W . In Fig. 10, the curves were obtained from the experimentally determined strength coefficients for $d/W = 0.25$ (given in Table I). One can readily see that both methods are in good agreement with test data.

4. APPLICATION OF STRENGTH CRITERION TO FATIGUE LIFE PREDICTION

Let us assume that the fatigue life equation can be expressed in the same form as the tensor polynomial failure criterion [Eq. (1)]. However, in this case, the fatigue strength parameters are not constants, but rather are functions of the frequency of loading (n), the number of cycles (N) and the stress ratio $R = \sigma_{min}/\sigma_{ax}$, i.e., $F = F(n, N, R)$. The stresses in Eq. (1) shall be regarded as the maximum cyclic principal lamina stresses.

Under simple loading conditions when n and R are constants, then the fatigue strength parameters are only a function of the number of cycles, N . As stated earlier, the quadratic formulation provides good strength predictions for such load cases as uniaxial tension and compression. Consequently, for this limited set of conditions, which are typical in fatigue tests, then the fatigue strength functions necessary to characterize a lamina, are given by,

$$\begin{aligned} F_1 &= \frac{1}{X_D(N)} - \frac{1}{X'_D(N)} & F_2 &= \frac{1}{Y_D(N)} - \frac{1}{Y'_D(N)} & F_{11} &= \frac{1}{X_D(N) \cdot X'_D(N)} \\ F_{22} &= \frac{1}{Y_D(N) \cdot Y'_D(N)} & F_{66} &= \frac{1}{S_D(N)^2} \end{aligned} \quad (5)$$

To determine the remaining quadratic interaction term would require a biaxial fatigue test. However, for non-biaxial loading, it has been found that F_{12} contributes little to the static strength prediction. In any case, fatigue tests must be conducted on 0° and 90° samples for given R values to determine the fatigue functions contained in Eqs. (5). This involves tension and compression fatigue tests in both the fiber (1) and transverse (2) directions, as well as pure shear in the 1-2 plane.

5. DESCRIPTION OF TEST PROGRAM

5.1 Ambient Fatigue Tests - 'Unflawed' Specimens

At the outset, it was decided that to minimize bending stress effects, a sandwich beam sample would be employed to determine static and fatigue tensile and compressive

strength properties in the fiber (1) and transverse (2) directions. Using a four-point load system and thin laminates, a relatively uniform in-plane stress field can be achieved in a central test section. Shear fatigue data are currently being generated using circular tubes mounted in a torsion fixture.

As noted earlier, the primary material under consideration is graphite/epoxy prepreg tape (Hercules, AS1/3501-6) requiring a 350°F cure temperature at ~ 85 psig. Flat sheets of 11" x 24" were initially laid up and then cut into samples 1" wide x 22" long. These strips were then bonded to aluminum honeycomb core of 1/8" cell size (Hexcell, 1/8 - 5052 - 0.003) using FM 300 adhesive with BR 127 primer (American Cyanimid Co.). Details on the fabrication and testing procedures can be found in Refs. 24 and 25.

To accommodate fatigue tests using a four-point beam bending set-up, a special load fixture was designed and fitted to a Sonntag SF-IU fatigue machine (see Fig. 11) which provided 30 Hz sinusoidal excitation. It was observed from bonded thermocouples that the specimen surface temperature reached an equilibrium value about 10°F above ambient at this frequency.

A 'pure' compression fixture similar to that of the IITRI design was also constructed to provide both static and fatigue data comparisons. Figure 12 illustrates the set-up for a short coupon with aluminum end tabs.

5.2 Flaws and Environmental Testing

Flaws

To provide specified delaminations, Teflon discs were inserted either into the laminate or, for the case of sandwich beams, at the laminate-core interface. The purpose was to obtain static and fatigue strength data as a function of flaw size and location.

Two environmental parameters were investigated — temperature and moisture absorption.

Moisture Control Specimens

Two sets of control specimens corresponding to different test sample thicknesses were used to provide a measure of the moisture content in both the sandwich beams and pure compression coupons. In addition, to study the effect of the bonded composite face sheet, each beam specimen had two controls; one being a 'plain' unprotected composite coupon, the other having thin aluminum foil bonded to one side with the honeycomb/facing adhesive.

The control samples were subjected to the same environmental conditions as the specimens for which the moisture content was evaluated.

Environmental Chamber

An environmental chamber was designed to provide controlled elevated temperature and humidity levels for in-situ compression testing (Fig. 13). This chamber was constructed from aluminum sheets which were welded to form the box structure. A pair of heating coils were attached to the lower surface of the chamber to provide the appropriate test temperatures. Saturated moisture conditions were obtained by boiling distilled water in the chamber during testing. Instrumentation leads (strain gauges and thermocouples) were passed through the chamber lid opening and connected to a Vishay automatic strain recording system and an X-Y plotter.

A support fixture was constructed within the chamber to test standard, 22 inch long, four-point beam bending specimens. Each of the load application points on the beams consisted of one inch square pads which were designed to provide simple support boundary conditions (Fig. 14).

Environmental Conditioning

Specimen Dry-Out

To eliminate any initial moisture content, all specimens were subjected to a drying-out period of six days at 200°F and a pressure of about 10⁻⁶ torr.

During the dry-out, the temperature, total pressure and partial pressures of the various constituents in the vacuum chamber were monitored. Based on mass spectrometer data it was determined that water vapour was the dominant species of the outgassing products. Thus, when the outgassing conditions in the vacuum chamber stabilized after about three days, it was concluded that the test specimens were essentially devoid of water moisture.

The percent moisture loss was found by weighing the control specimens before and after being subjected to the dry-out. The average mass loss for 8-ply specimens without backing, 8-ply specimens with aluminum backing and 16-ply specimens without backing was 0.13%, 0.10% and 0.008%, respectively.

Water Bath Soak

A subset of specimens to be tested with high moisture contents were subjected to a long term water bath soak in an attempt to reach saturation levels. Several control

specimens were weighed periodically during the : to obtain the rate of mass gain. Of all the specimens, the control samples with a backing absorbed more moisture than the other specimens. This can be explained by noting that the adhesive also absorbs moisture.

Thermal Spikes

Each specimen selected for thermal spike testing was first exposed to the long term soak and then subjected to ten spikes over a period of five days. The 'spikes' were obtained by placing each specimen in the environmental testing chamber along with a small amount of water. The chamber was then heated at which point the temperature rose to the boiling point where it stabilized until the water was completely vapourized. The temperature then rose to about 300°F, after which the heat was turned off and the chamber allowed to cool. This procedure ensured a very humid atmosphere and thus the moisture loss from the specimen was minimized. A typical temperature-time profile is shown in Fig. 15.

6. SUMMARY OF RESULTS

6.1 Ambient Fatigue Tests - 'Unflawed' Specimens

Up to present, fatigue functions have been obtained only for 0° tension and compression, the results of which are presented in Figs. 16, 17 for R = 0.05 and 20, respectively. Note that after $\sim 10^6$ cycles, the fatigue test was terminated and the specimen statically tested to failure. It was observed that only about a 10% reduction in strength occurred (relative to the N = 1/2 value).

Based on least squares fit to these data, the following fatigue functions were derived:

$$x_D = 0.918 \times N^{-0.0462} \quad x'_D = 0.972 \times N^{-0.0348} \quad (6)$$

Although it is premature at this stage of the program to apply the strength criterion for fatigue predictions, one can illustrate the methodology. For example, assume the remaining fatigue curves associated with shear and transverse tension and compression loading have the same general form as Eq. (6). Based on the manufacturer's specified static strength values of Y = 9.5 KSI, Y' = 38.9 KSI, S = 17.3 KSI, one can then obtain the following fatigue functions:

$$\begin{aligned} x_D &= 33.36 \times 10^4 N^{-0.0462} & x'_D &= 23.18 \times 10^4 N^{-0.0348} \\ y_D &= 8.72 \times 10^3 N^{-0.0462} & y'_D &= 37.81 \times 10^3 N^{-0.0348} \\ s_D &= 16.35 \times 10^3 N^{-0.0405} \end{aligned} \quad (7)$$

These values are then substituted into the quadratic form of Eq. (2) and the fatigue life equation plotted for any laminate configuration. Note however that this analysis must be applied to each lamina to determine which ply (or plies) fail first in fatigue. Assumptions must then be made regarding the residual laminate stiffness, and Eq. (2) is subsequently applied to the remaining plies until overall laminate failure occurs. One conservative approach that can be employed is to remove the failed plies entirely when re-calculating the modified laminate stiffness and corresponding lamina stresses.

To demonstrate this method, the compressive fatigue curve for a (0, ±45, 90)_s laminate was calculated with the predicted S-N curve being shown in Fig. 18 together with test data obtained from the sandwich beam samples. As noted earlier, it is premature to make such comparisons with confidence, however, the favourable agreement provides sufficient impetus to warrant continued study.

6.2 Effect of Flaws and Environment on the Compressive Static Strength

It was observed over the course of this investigation that the static strength values varied not only with material batch ($\sim 15t$), but with manufacturing method as well. Although the cure procedure was maintained constant, expediency led to fabrication of prepreg laminate sheets from which the samples were cut. Earlier work involved the individual preparation of the strip samples. Interestingly enough, the former method yielded specimens having substantially higher strengths, although the stiffness remained the same. Thus, the test data described in the following sections have been normalized by the average static, 'unflawed', ambient strength values (S^*) which are listed in the appropriate tables and graphs. Again, it should be noted that both sandwich beam and coupon samples were studied, the results of which are summarized in Tables 2 and 3, respectively.

The effect of mid-laminate flaw size is shown in Figs. 19-21 for ambient, hot-wet and thermal spike conditions, respectively. In some cases, local delamination produced buckling failures prior to ultimate fracture of the laminate (see Fig. 22, for example).

*Based on average numerical coefficients.

6.3 Effect of Flaw Size on Ambient Compressive Fatigue Strength

Table 4 presents a summary of the compression sandwich beam fatigue tests, the results of which are shown in Fig. 23. Note that the stress levels have also been normalized by σ^* . One interesting observation was that the fatigue failure modes corresponded to the equivalent static failure modes for a given flaw size.

7. CONCLUSIONS

- (a) There is reasonable cause to conjecture at this time that the tensor polynomial failure criterion can be modified to incorporate 'fatigue functions' which will permit preliminary estimates of fatigue life to be made for a given material laminate under uniaxial load conditions.
- (b) The application of the tensor polynomial failure criterion to the strength analysis of laminates with holes has been shown to provide the same degree of correlation with test data as the method of 'characteristic distances'. Both approaches work well for uniaxial loading but insufficient evidence exists for biaxial load cases.
- (c) It is proposed at this point in time to incorporate the quadratic form of the tensor polynomial failure criterion, including three-dimensional stress components, into a finite element-fracture mechanics analysis to treat the problem of laminates with flaws.
- (d) Elevated temperature ($\sim 212^\circ\text{F}$) combined with the 'dry' state produces no significant change in compressive stiffness or strength relative to the ambient values.
- (e) Elevated temperature ($\sim 210^\circ\text{F}$) combined with high moisture content ($\sim 1.7\% \text{ H}_2\text{O}$) results in no significant change in compressive stiffness but a large reduction in compression strength ($21\% \sim 43\%$), relative to ambient state values.
- (f) The superposition of ten thermal spikes (up to 300°F) in combination with high moisture content ($\sim 1.6\% \text{ H}_2\text{O}$) produces a small increase in compressive stiffness and strength relative to the elevated temperature values obtained without thermal spikes. However, the strength is still substantially below the ambient state value.
- (g) The sandwich beam test method yields compressive stiffness values consistently higher than the 'pure' compression data for all environmental conditions studied.
- (h) High moisture content (estimated at $> 1.7\%$) affects the failure mode under static compressive loading. Both test methods showed delamination as being the primary mode for high moisture content.
- (i) Buckling occurs for large delamination flaws, relative to the specimen dimensions. This phenomenon can be predicted reasonably well [Ref. 25].
- (j) Small interlaminar flaws caused a reduction in compression strength, probably due to interlaminar stresses near the flaw.
- (k) The endurance strength in fatigue was relatively unaffected by the presence of delamination flaws.

REFERENCES

1. Sih, G. C., Paris, P. C., Irwin, G. R., "On Cracks in Rectilinearly Anisotropic Bodies", *Int. J. Fract. Mech.* 1, N3, 1965, pp. 189-203.
2. Wu, E. M., "Application of Fracture Mechanics to Anisotropic Plates", *J. Appl. Mech.*, 34, 1967, pp. 967-975.
3. Konishi, H. J., "Mode I Stress Intensity Factors for Symmetrically-Cracked Orthotropic Strips", *Fracture Mechanics of Composites*, ASTM STP 593, 1975, pp. 99-116.
4. Slepetz, J. M., Carlson, L., "Fracture of Composite Compact Tension Specimens", *Fracture Mechanics of Composites*, ASTM STP 593, 1975, pp. 143-162.
5. Sih, G. C., "A Special Theory of Crack Propagation", *Mechanics of Fracture*, Vol. 1, *Methods of Analysis and Solutions of Crack Problems*, G. C. Sih, Editor, Noordhoff, 1972.
6. Wu, E. M., "Strength and Fracture of Composites", *Composite Materials*, Vol. 5, *Fracture and Fatigue*, L. Broutman and R. Krock, Eds., Acad. Press, London, 1974, pp. 191-247.
7. Snyder, M. D., Cruse, T. A., "Crack Tip Stress Intensity Factors in Finite Anisotropic Plates", *Air Force Materials Laboratory*, AFML-TR-73-209, Aug. 1973.
8. Heppner, G. R., Hansen, J. S., "Mixed Mode Fracture Analysis of Rectilinear Anisotropic Plates by High Order Finite Elements", *Int. J. Num. Meth. Engng.*, 17, 1981, pp. 445-464.

9. Heppeler, G. R., Hansen, J. S., "The Influence of Forcing Conforming Boundaries on a High Precision Enriched Fracture Element", Comp. Meth. in App. Mech. Engng., 36, 1983, pp. 155-166.
10. Bowie, O. L., Freese, C. E., "Central Crack in Plane Orthotropic Rectangular Sheet", Int. J. Frac. Mech. 8(1), 1972, pp. 49-58.
11. McNeil, N. J., "An Improved Mindlin Plate Bending Element and the Compatible Quarter Point Crack Tip Derivative", M.A.Sc. Thesis, University of Toronto, Dept. of Aerospace Science and Engineering, 1982.
12. Lo, K. H., Christensen, R. M., Wu, E. M., "A High-Order Theory of Plate Deformation, Part 2: Laminated Plates", J. Appl. Mech. 44, Dec. 1977, pp. 669-676.
13. Nuismer, R. J., Whitney, J. M., "Uniaxial Failure of Composite Laminates Containing Stress Concentrations", Fracture Mechanics of Composites, ASTM STP 593, 1975.
14. Garbo, S. P., Ogonowski, J. M., "Strength Predictions of Composite Laminates with Unloaded Fastener Holes", AIAA J., Vol. 18, No. 5, May 1980.
15. Hashin, Z., Rotem, A., "A Fatigue Failure Criterion for Fiber Reinforced Materials", J. Composite Materials, Vol. 7, Oct. 1973.
16. Rotem, A., Hashin, Z., "Fatigue Failure of Angle Ply Laminates", AIAA J., Vol. 14, July 1976.
17. Rotem, A., "Fatigue Failure of Multidirectional Laminate", AIAA J., Vol. 17, March 1979.
18. Sims, D. F., Brogdon, V. H., "A Comparison of the Fatigue Behavior of Composites Under Different Loading Modes", Proc. ASTM Symp. on "Fatigue of Filamentary Composite Materials", Denver, Colorado, Nov. 1976.
19. Private Communication, Bell Helicopter, Sept. 1980.
20. Russell, A. J., Street, K. N., "Factors Affecting the Interlaminar Fracture Energy of Graphite/Epoxy Laminates", Proc. ICCM-IV, Progress in Science and Engineering of Composites, Eds. Hayashi et al, JSCM, Tokyo, Japan, 1982, pp. 279-286.
21. Malmeister, A. K., "Geometry of Theories of Strength", Mekhanika Polimerov, Vol. 2, No. 4, 1966.
22. Tsai, S. W., Wu, E. M., "A General Theory of Strength for Anisotropic Materials", J. Composite Materials, Vol. 5, 1971.
23. Tennyson, R. C., MacDonald, D., Nanyaro, A. F., "Evaluation of the Tensor Polynomial Failure Criterion for Composite Materials", J. Composite Materials, Vol. 12, 1978.
24. Mabson, G. E., Tennyson, R. C., "Environmental Effects on the Compression Strength of Graphite/Epoxy Laminates", Canadian DND/DSS Contract No. 08SB-3290021, Final Report, April 1981.
25. Mabson, G. E., Hansen, J. S., Tennyson, R. C., Wharam, G. E., "Investigation of the Strength and Fatigue Properties of Graphite/Epoxy Laminates", Canadian DND/DSS Contract No. 05SB-97708-1-0043, Final Report, June 1982.

ACKNOWLEDGEMENT

Funding for this program was provided by the Canadian Department of National Defence under Contract No. 05SB-97708-1-0043.

Table 1. Comparison of Principal Tensor Polynomial Strength Parameters
for Glass/Epoxy Material (3M, 1003)

Case	Strength Parameters				
	F_1 (ksi) $^{-1}$	F_{11} (ksi) $^{-2}$	F_2 (ksi) $^{-1}$	F_{22} (ksi) $^{-2}$	F_{66} (ksi) $^{-2}$
No hole (d/W = 0)	-3.076×10^{-3}	9.398×10^{-5}	2.344×10^{-1}	2.270×10^{-2}	2.142×10^{-2}
d/W = 0.25 Experiment only	-8.013×10^{-3}	4.045×10^{-4}	0.382	6.090×10^{-2}	8.000×10^{-2}
d/W = 0.25 Point stress -characteristic distance* from tests	-6.520×10^{-3}	3.397×10^{-4}	0.386	7.500×10^{-2}	8.300×10^{-2}

* $\ell_T = 0.07"$, $\ell_C = 0.09"$, $\ell_S = 0.10"$.

Table 2. Static Sandwich Beam Tests ~ Summary of Averaged Results

Condition	Flaw Diameter (in)	ℓ ($\times 10^6$ psi)	$ \sigma_{x_c}^b $ (ksi) Buckling	$ \sigma_{x_c}^u $ (ksi) Ultimate	$\sigma_{x_c}^b/\sigma^*$	$\sigma_{x_c}^u/\sigma^*$
75°F, 1981 0% H ₂ O-Strip		7.34		66.2	1.00	
75°F, 1982 0% H ₂ O-Strip		7.59		76.4	1.00	
75°F, 1982 0% H ₂ O-Sheet		7.41		111.9	1.00	
75°F, 1982 0% H ₂ O-Sheet	5/32 Mid	6.78		102.9	0.92	
75°F, 1982 0% H ₂ O-Sheet	1/4 Mid	6.84		96.4	0.86	
75°F, 1982 0% H ₂ O-Sheet	3/8 Mid	6.78	65.8	70.6	0.59	0.63
75°F, 1982 0% H ₂ O-Sheet	1/2 Mid	7.19	55.3	58.5	0.49	0.52
75°F, 1982 0% H ₂ O-Sheet	3/4 Mid	7.45	20.9	49.6	0.19	0.44
75°F, 1982 0% H ₂ O-Sheet	1/2 Bond	7.39		105.5	0.94	
75°F, 1982 0% H ₂ O-Sheet	3/4 Bond	7.20		109.5	0.98	
75°F, 1982 0% H ₂ O-Sheet	1/2 Outer		0.70	88.0	0.006	0.79
212°F, 1981 -0.05% H ₂ O-Strip		6.98		73.7	1.11	
209°F, 1981 1.69% H ₂ O-Strip		6.91		52.8	0.80	
212°F, 1982 1.67% H ₂ O-Sheet	1/4 Mid	7.25		70.0	0.63	
212°F, 1982 1.63% H ₂ O-Sheet	1/2 Mid	6.87	36.4	46.4	0.33	0.41
212°F, 1982 1.62% H ₂ O-Sheet	1/2 Outer		0.8	58.7	0.007	0.52
210°F, 1981 1.39% H ₂ O-Strip Thermal Spikes		7.14		55.5	0.84	
212°F, 1982 1.09% H ₂ O-Sheet Thermal Spikes	1/4 Mid	7.79	71.8	77.5	0.64	0.69
212°F, 1982 1.12% H ₂ O-Sheet Thermal Spikes	1/2 Mid	6.14	Not Measured	40.5	Not Measured	0.36

Table 3. Static Coupon Tests - Summary of Averaged Results

Condition		Flaw Diameter (in)	E_{xc} ($\times 10^6$ psi)	$ \sigma_{xc}^b $ (ksi)	$ \sigma_{ult}^u $ (ksi)	$ \sigma_{ult}^c $ (ksi)	$\frac{\sigma_{xc}}{\sigma^*}$	$\frac{\sigma_c}{\sigma^*}$
75°F 1981	.022% H ₂ O Strip		7.00		69.0	74.7	1.00	
75°F 1982	0% H ₂ O Sheet		7.18		88.3	92.5	1.00	
75°F 1982	0% H ₂ O Sheet	1/4	6.14		68.6	73.5	0.79	
211°F 1981	.001% H ₂ O Strip		6.72		66.1	72.2	0.97	
210°F 1981	1.75% H ₂ O Sheet		6.93		41.3	42.8	0.57	
212°F 1982	1.61% H ₂ O Sheet		7.25		42.8	46.0	0.50	
212°F 1982	1.59% H ₂ O Sheet	1/4	7.30	25.4	42.6		0.27	0.46
210°F 1981	1.81% H ₂ O Thermal Spikes Strip		7.28		49.8	53.3	0.71	
212°F 1982	1.59% H ₂ O Thermal Spikes Sheet	1/4	6.58	30.9	59.9		0.33	0.65

^tCorrected for bending stresses.

Table 4. Beam Fatigue Tests - Experimental Results

Spec. No.	$\frac{\sigma_{min}}{\sigma_{ult}}$	$\frac{\sigma_{min}}{\sigma^*}$	Number of Cycles to Failure	$\frac{\sigma_{min}}{\sigma^*}$	$\frac{\sigma_{ult}}{\sigma_{ult}}$	$\frac{\sigma_{ult}}{\sigma^*}$	$\frac{\sigma_{ult}}{\sigma^*}$
24	52.6	0.69	43	727	0.69		
25	45.5	0.60	59	7,879	0.60		
28	39.0	0.51	71	7,165,000 ¹	0.51	44.1	0.58
29	46.6	0.61	20	46,250	0.61		
30	42.7	0.56	20	15,315	0.56		
31	38.4	0.50	20	1,705,000	0.50		
47	56.0	0.50	20	100,000	0.50		
57	58.6	0.52	20	105,000	0.52		
EE	53.3	0.55 ^a 0.68 ^b	20	262,000	0.48		
FF	53.3	0.55 ^a 0.68 ^b	20	144,000	0.48		
GG	61.5	0.64 ^a 0.75 ^b	20	44,636	0.55		
HH	57.0	0.59 ^a 0.73 ^b	20	477,000	0.51		
II	68.9	0.72 ^a 0.88 ^b	20	2,197	0.62		
VV	56.0	0.58	20	88,000	0.50		
YY	51.1	0.53	20	121,360	0.46		
ZZ	60.0	0.62	20	28,180	0.54		
AA2	55.0	0.57	20	188,000	0.49		
I	53.4	0.91	20	16,633	0.48		
J	33.4	0.57	20	9,880,000 ¹	0.30	63.2	1.08
K	45.1	0.77	20	2,447,000 ¹	0.40	61.3	1.05
L	53.5	0.92	20	288,000	0.48		
M	52.7	0.90	20	851,000	0.47		
N	49.3	0.84	20	575	0.44		
45	68.3	0.65	20	14,212	0.61		
46	68.3	0.65	20	10,633	0.61		
49	58.6	0.56	20	371,482	0.52		
50	58.6	0.56	20	816,820	0.52		
58	63.5	0.60	20	96,000	0.57		
62	58.6	0.54	20	52,757	0.52		
63	53.7	0.49	20	437,240	0.48		

¹Specimen did not fail under fatigue loading, test termination cycles shown.^a σ_{ult} used was that for centred flaw.^b σ_{ult} used was that for flaw near edge.^{*} σ_{ult} ambient unflawed average for the batch and manufacturing method used.^{ult} σ_{ult} static average for environment and flaw condition, batch and manufacturing method used.

1/2" bond line

1/4" mid-lam flaw

1/2" mid-lam

3/4" bond line

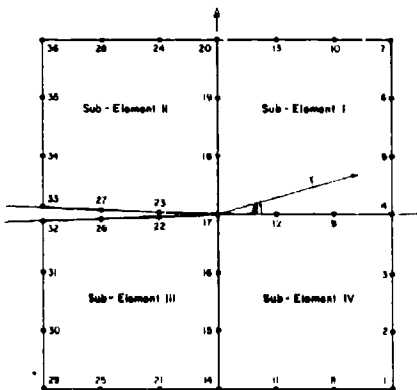
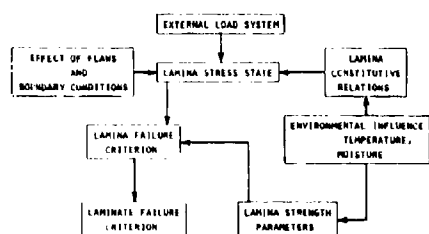


FIG. 2 - MACRO-ELEMENT MODELLING OF THE CRACK TIP.

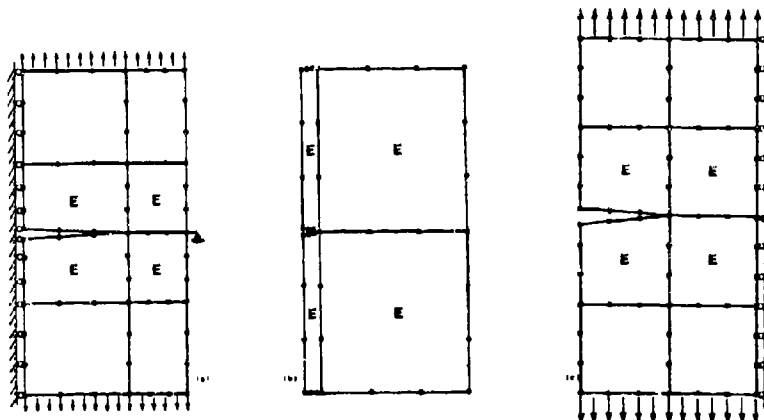
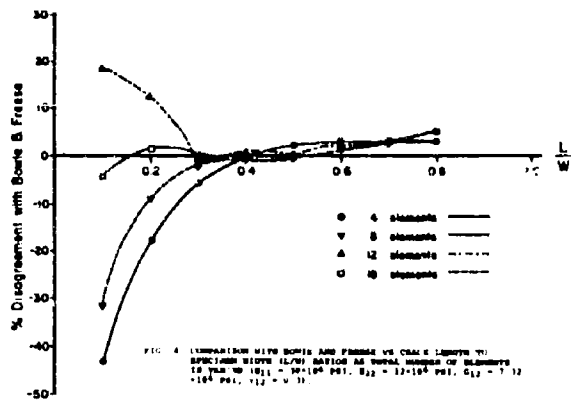
FIG. 3 - (a)-(c) Mesh refinement near a crack tip checked against
finite difference analysis and (b)-(c) the 8-element
model for a 1/4 of a cylinder with a central crack
model of a double edge cracked specimen.FIG. 4 - COMPARISON WITH BEMEL & FRESE VS CRACK LENGTH TO
SPECIMEN WIDTH (L/W) RATIO AS TOTAL NUMBER OF ELEMENTS
IS 4 (1/4 ELEMENT), 8, 12 AND 16 ELEMENTS. $E_1 = 12 \times 10^9$ PSI, $E_{12} = 7.12$
 $\times 10^9$ PSI, $G_{12} = 11$.

Fig. 5 LOCUS OF MAXIMUM STRENGTH and OPTIMUM FIBER ANGLE
FOR VARYING BIAXIAL STRESS RATIO
(Symmetric Balanced (S0) Compl. - α_0)
 $\sigma_x > 0, \sigma_y > 0$

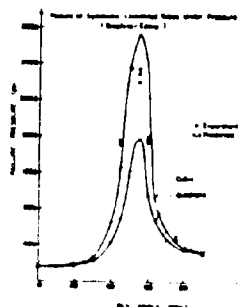
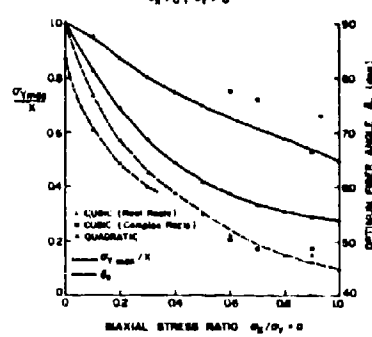


FIG. 6

Fig. 7 Methods of Failure Analysis for Laminates with Holes

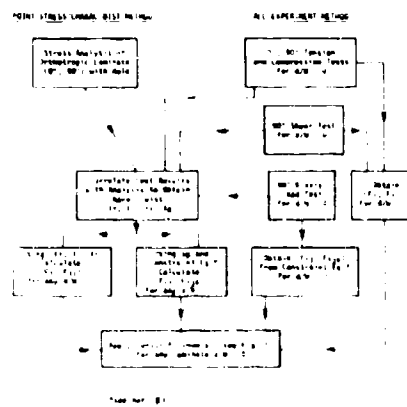
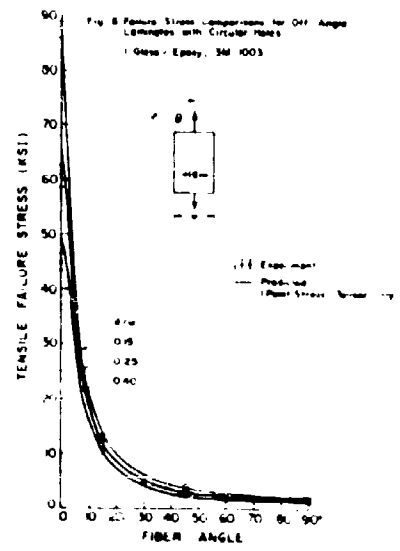


Fig. 8 Failure Stress Comparison for Off-Angle Laminates with Circular Holes
1 Glass + Epoxy, 3M 1003



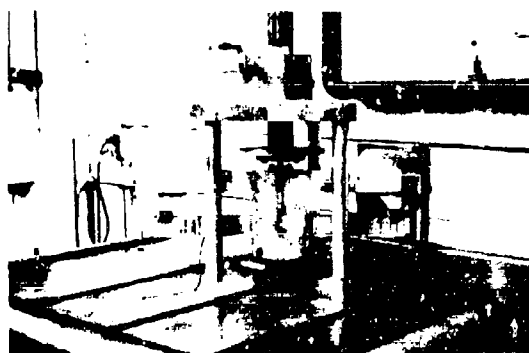
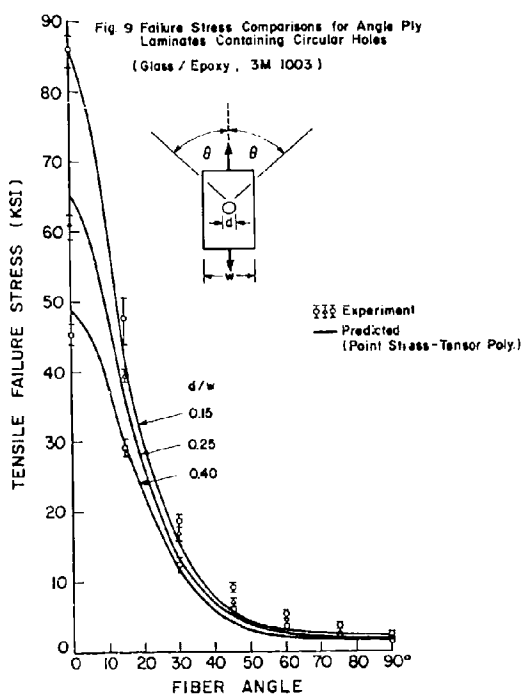


FIG. 11 FATIGUE TEST SET-UP USING SANDWICH BEAM UNDER FOUR-POINT LOADING.

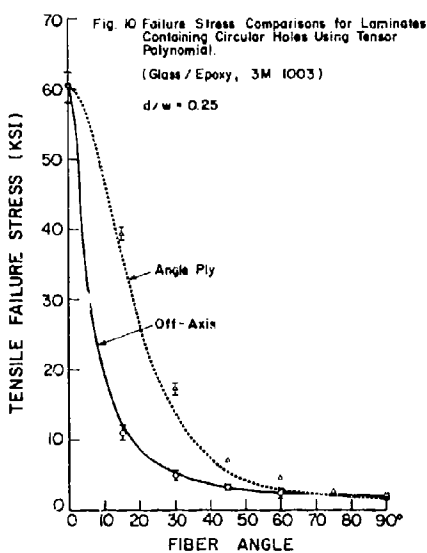


FIG. 12 IITRI COMPRESSION FIXTURE FOR COUPON TESTS (STATIC AND FATIGUE LOADING).



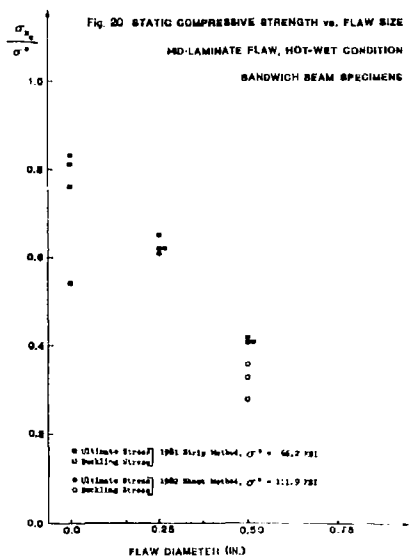
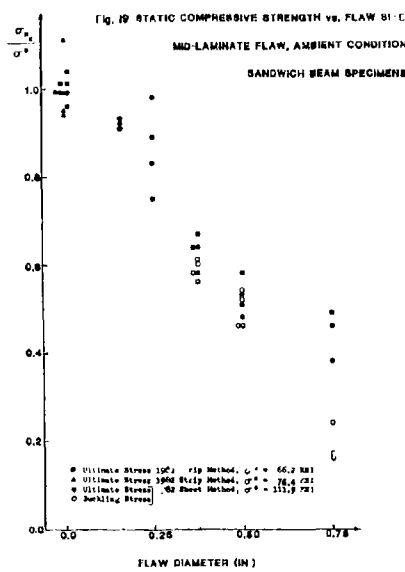
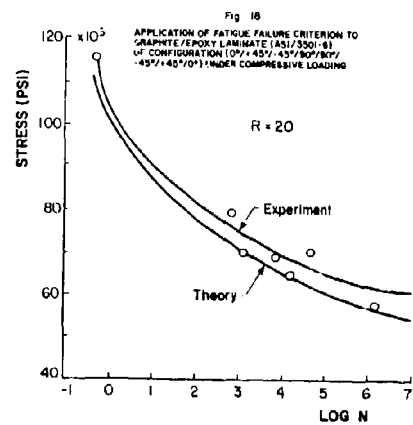
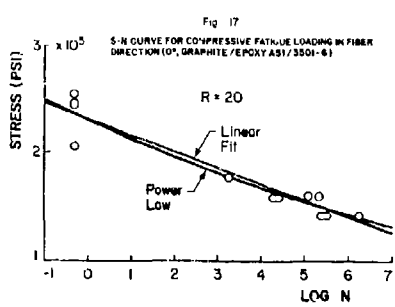
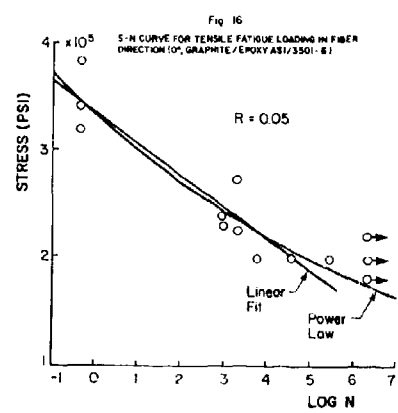
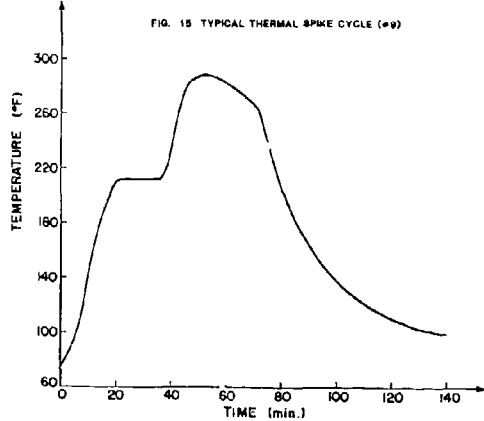
FIG. 13

ENVIRONMENTAL CHAMBER FOR STATIC TESTING.



FIG. 14

VIEW OF SANDWICH BEAM MOUNTED ON SUPPORT FIXTURE IN ENVIRONMENTAL CHAMBER.



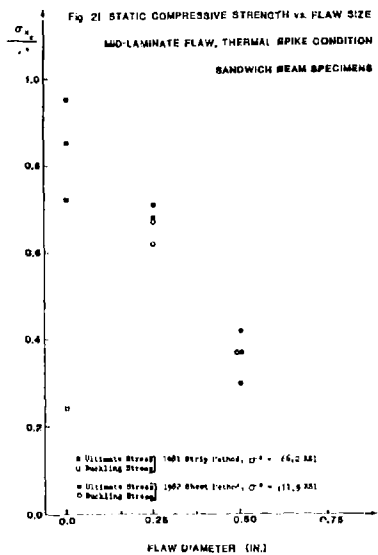
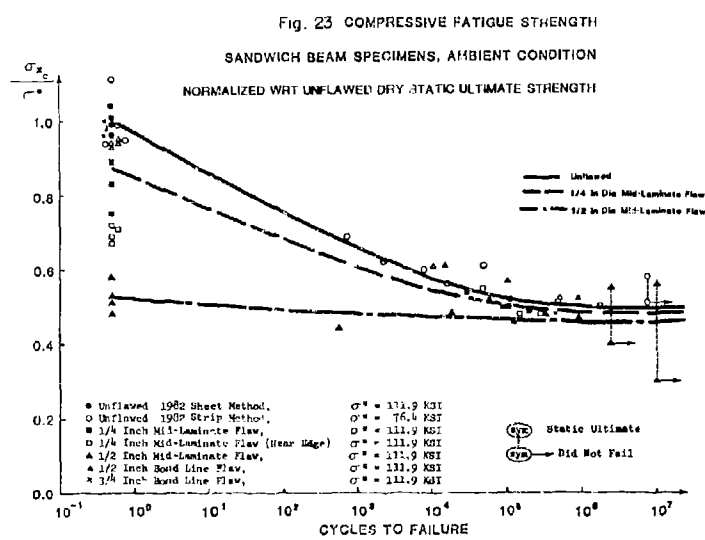


FIG. 22 COMPRESSIVE FAILURE OF GRAPHITE/EPOXY LAMINATE UNDER HOT-WET CONDITIONS.



ADP001922

FRACTURE MECHANICS OF SUBLAMINATE CRACKS IN COMPOSITE LAMINATES

A. S. D. Wang
 Drexel University
 Department of Mechanical Engineering
 Philadelphia, PA 19104

SUMMARY. This paper presents an overview of a fracture mechanics approach to some of the most frequently encountered matrix-dominated, sub-laminate cracks in epoxy-based composite laminates. By "sub-laminate", it is meant that the cracks are internal to the laminate, generally invisible macroscopically; but are much larger in size than those microcracks considered in the realm of micromechanics. The origin of sub-laminate cracks is assumed to stem from the coalescence of natural material flaws (also microcracks) which occur under a certain favorable laminate stress condition. Thus, the modelling of the mechanisms of sub-laminate crack initiation and propagation is essentially mechanistic and probabilistic in nature. Some specific results from several analytical/experimental investigations using graphite-epoxy laminates are presented and discussed in this paper. ←

INTRODUCTION

Failure mechanisms in structural composite laminates have been viewed at several dimensional levels. Consider, for instance, the curved laminated panel shown in Figure 1(a). Failure of this structural component may be caused by a loss of the global stiffness when the applied load reaches a certain critical value. To describe analytically the associated failure mechanisms and hence to determine the critical load, structural mechanics methods such as buckling and post-buckling theories are employed, which relate the change of the structural geometry to the applied load. In this type of analysis, the stiffness of the laminated panel and the kinematics of its displacements are among the most predominant factors.

On the other hand, the same panel may fail due to a loss of strength at a local defect; for example, at a bolt-hole, Figure 1(b). In this case, rupture of material will begin at the hole and may propagate into a large crack whenever a certain load condition is reached. But in order to define the conditions for rupture initiation and propagation, a knowledge of the actual stress field around the hole, and the physical mechanisms of the material rupture process is essential. To this end, it will be necessary to focus further on the local defect area at a much smaller dimensional level. As illustrated in Figure 1(c), for instance, the lamination details of the panel, such as layer interfaces and the stacking sequence are now identifiable. Consequently, quantities of size comparable to the layer thickness become important; the influence of an interface defect (i.e. delamination), a translaminate crack, a fiber split, etc. are new factors to be considered. For it is believed that the development of rupture around the hole is precipitated by these sub-laminate cracking activities, any failure analysis performed at this dimensional level must first address the individual mechanisms of the various sub-laminate cracks, and, then their interaction and coalescence mechanisms when they occur simultaneously and/or sequentially.

It is well known that the formation and propagation mechanisms of a crack are governed by the conditions that exist in the close vicinity of the crack front. In the case of the sub-laminate cracks mentioned above, further focusing of the crack front region will reveal the microstructure of the composite system, Figure 1(d). Here, a clear distinction can be made between the fiber and the matrix phases of the material. At this dimensional scale, one also finds a random distribution of material microflaws, be it voids, broken fibers, matrix crack, debonded fiber-matrix interfaces, just to mention a few, see Figure 1(e).

Although the inherent microflaws are small in size, usually on the order of the fiber diameter, they may behave as local stress risers under the applied load. When a certain local condition is reached, the microflaws interact and coalesce to form an actual crack, much larger in size, and identifiable at the sub-laminate level. Hence, a proper analysis of the mechanisms must be capable of delineating the individual behavior of the various types of stress risers, and their interactions when one is located close to another. All these depend profoundly on the probabilistic nature of the microflaws in terms of their size, location and density distributions.

The physical process of material failure as portrayed in the proceeding discussions is seen to span a wide range of dimensions. Though the entire process is essentially one continuous event, failure analysis could be conducted only within isolated dimensional regimes. As illustrated in Figure 1, the entire dimensional spectrum is separated roughly into three analysis regimes; namely the structural mechanics, the macromechanics and the micromechanics regimes. Within each analysis regime, the material failure process involves a distinct set of material and geometrical parameters.

Analytical and experimental treatments on laminate failure at the structural mechanics level have generally been approached, using the classical lamination theory (see [1]). Stiffness-predominant structural responses such as panel

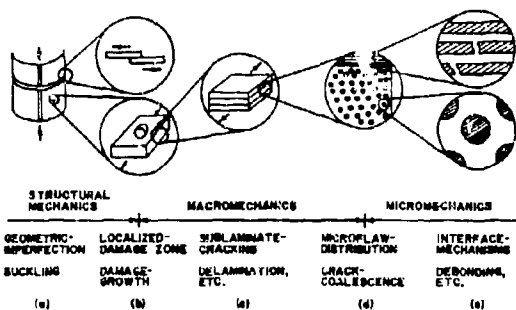


Figure 1 Dimensional Regimes of Failure Analysis in Composite Materials

buckling and post-buckling have been successfully analyzed [2]. The effect of local material damage (e.g. from a bolt-hole, a delamination caused by impact, etc.) upon the global response can also be evaluated [3]. But, a more detailed description about the damage formation and propagation mechanisms always required separate treatment.

For a class of epoxy-based composite laminates, e.g. graphite-epoxy systems, material damage mechanisms around a bolt-hole or near the tip of a line-notch have been modeled by an empirical formulae which is derived from the classical fracture mechanics for structural metals [4 - 6]. Essentially, the notched laminate is regarded as a 2-dimensional body, and the crack growth from the notch is assumed self-similar and catastrophic. In order for the fracture formula to correlate with a body of experimental data, the notch size parameter must be adjusted to include an empirically defined "intense energy region" at the crack tip. Thus, together with the laminate's fracture toughness (K_c or G_c), yet to be determined experimentally, the model consists of two disposable parameters which must be adjusted to fit a given set of test data.

Clearly, the empiricism in this approach is less than desirable. As was discussed earlier, the development of material damage, say around a small bolt-hole, is precipitated by a multitude of sub-laminate cracking activities in that region. The term "intense energy region" is in fact a gross representation of these activities at a larger dimensional scale. It would be ideal, therefore, to carry the analysis across the dimensional boundary into the macromechanics regime (see Figure 1), so as to understand how sub-laminate crackings lead to the damage development around the hole.

Early studies on fibrous composites dealt mostly failure mechanisms in the micromechanics regime. For instance, a considerable amount of theoretical and experimental treatments was given on the subject of the fiber-matrix interface mechanics [7 - 10]. Fracture models for various microcracks such as depicted in Figure 1(e) are characterized in terms of energy absorption processes, including interface debonding, fiber pull-out, matrix crack bridging [11], etc. Although the modeling of these various microflaws is basic to the strengthening mechanisms of the composite system at the fiber-matrix level, it remains to incorporate these "micro" models into some analysis which includes the mutual interaction and the coalescence mechanisms of the microflaws. Indeed, it would be ideal, again, to have a fracture model which accounts for both the mechanistic failure behavior of the microflaws and the probabilistic nature of their existence; the analysis can then be carried into the regime of macromechanics.

Several mechanistic/probabilistic failure models have been attempted in the past. Zweben and Rosen [12] studied, for example, the tensile strength characteristics of unidirectional composites, assuming the microflaws a distribution of local broken fibers. The basic concept can be extended to multi-directional laminated systems, but the complexity in geometry as well as the multiplicity of failure modes make this type of effort so far unproductive.

In recent years, increased attention has been given to fracture modeling within the general confines of macromechanics, as illustrated in Figure 1(c). At this analysis level, the individual material layers in the laminate are approximated as being homogeneous and anisotropic, where no distinction of the fiber and the matrix phases need be made. Essentially, the stiffness properties of the material layer are represented by some "effective" values characterized experimentally as basic material constants, but failure in the material layer is not governed by a set of strength constants. Rather, it is determined by a certain fracture event which occurs at the "sub-laminate" level. Since by a homogeneous approximation the identity of the inherent material microflaws also becomes lost, only their gross effects upon the formation and propagation of sub-laminate cracks can be retained. Thus, an empirically defined "effective" crack size is introduced.

As it will be discussed in detail later in this paper, the macroscopic view point allows a rational formulation for a general fracture model for a class of sub-laminate cracking in epoxy-based composite laminates. Early studies, notably by Carter [13], Wu [14], Kanninen, et. al. [15], have articulated the viability of such an approach. Major advances have since been made, due mainly to the ever-expanding computational capabilities and ever-revealing NDT methods. These modern facilities have provided a means for a more rational correlation between experiments and analysis.

In a series of papers [16 - 22], Wang, Crossman, et. al. developed a unified energy model within the context of macromechanics. It describes the growth mechanisms in a class of matrix-predominant sub-laminate cracks. The specific cracks considered included interlaminar (delamination) and translaminar (fiber-split) crackings, found most prevalent in graphite-epoxy laminates.

This paper is a summary of their major findings obtained during the course of several analytical and experimental investigations.

FRACTURE CONSIDERATIONS IN MACROMECHANICS

The energy model developed by Wang and Crossman is formulated on the energy release rate concept of the linear elastic fracture mechanics (LEFM). All variables in the model are defined within the context of the macromechanics. Since fibrous composites possess some unique characteristics, special considerations had to be given to defining some of the variables.

Application of the Griffith Criterion

The essence of the LEFM is that material failure is not defined from the stand-point of strength as a constant material property. Rather, it is determined by an analysis of the kinetics of the actual process of fracture propagation. The classical result of Griffith [23] pertained to an elastic plate which is uniformly stretched in one direction by σ . The plate has a through crack of size $2a$, orientated normal to the direction of σ . The length of the crack is assumed small but finite; and, the material is homogeneous and isotropic. Griffith postulated that at the instance of crack extension, a loss of the stored elastic strain energy near the crack-tip region is resulted; this energy is converted into the surface energy of

the crack. A balance of energy during a virtual crack extension leads to the criterion

$$\frac{\partial U}{\partial a} = \frac{\partial S}{\partial a} \quad (1)$$

Equation (1) defines the general condition under which the existing crack begins to propagate in self-similar mode.

For the plate problem, the critical stress at the instance of crack extension can be derived from (1), giving

$$\sigma_c = \left(\frac{2EY}{\gamma a} \right)^{1/2} \quad (2)$$

where γ is the free surface energy density of the material.

When applied to engineering problems, the Griffith theory is often modified for practical considerations. For instance, Equation (2) becomes unbounded as $a \rightarrow 0$. Certainly, no real material can sustain an infinite stress. This limitation, however, can be circumvented by invoking the existence of material flaws. That is to assume for the material some characteristic distribution of flaws; the worst of which, having a size of $2a_0$, acts like a real crack. It then determines a finite critical stress according to Equation (2).

Of course, flaws do exist in real materials, especially in fibrous composite systems. But the physical identity is lost at the dimensional level where the analysis is performed. The quantity a_0 can be defined only empirically as an intrinsic material property. As it will be discussed later, the value of a_0 can be orders of magnitude larger than the fiber diameter in, say, graphite-epoxy systems.

Another practical consideration is related to the definition of γ , the free surface energy density of the material. For crack in brittle material such as glass, then γ is as defined. For most other engineering materials, crack extension is found to associate a certain degree of inelastic deformation near the crack-tip region. Furthermore, the crack extension path, or the crack surface, shows a certain degree of ruggedness, depending on the heterogeneity of the material viewed at a microscale. Early studies by Irwin [24], Orowan [25] and others on structural metals considered the right-hand side of Equation (1) the irreversible work required to create a unit crack surface area. Hence, the quantity γ can be interpreted as the energy dissipated in the crack-tip region during crack extension. Clearly, γ will then depend on the inelasticity as well as the microscopic heterogeneity of the material locally (near the crack-tip). It, therefore, must also be regarded as an intrinsic property of the material to be defined at the macromechanics level. Conceivably γ has to be an averaged value over a relatively large crack surface area for fibrous composites in order for it to be a material constant.

These considerations are of fundamental importance when a crack-like failure is modeled at the macroscopic dimensional level. For only in this context can a macroscopic fracture model be developed along the rational arguments of the classical fracture mechanics.

In common practice, the right-hand side of Equation (1) is replaced by G_c ($= 2\gamma$), known as the critical energy release rate of the material. The left-hand side is a function of the applied load, the geometry of the body and the size of the crack. Thus, for a crack undergoing self-similar extension, the Griffith criterion is expressed as

$$G(\sigma, a) = G_c \quad (3)$$

Accordingly, the development of the fracture model for sub-laminate cracks rests upon the calculation of $G(\sigma, a)$ and the physical measurement of G_c . The latter is regarded as a material property.

The Calculation of $G(\sigma, a)$

In the theory of the LEFM, the singular stress field near a crack tip in a homogeneous, isotropic elastic body is represented by analytical functions in the theory of complex variables [26]. The near-field stresses are obtained for three particular modes of the crack opening. These are known as the opening mode (I), the sliding mode (II) and the anti-plane shearing mode (III). For each mode, the stresses are expressed in terms of the associated stress intensity factor K [27]; and consequently, the associated $G(\sigma, a)$ is computed in terms of K . Since the relation between K and G is one-to-one, Equation (3) reduces to the form

$$K(\sigma, a) = K_c \quad (4)$$

Similar relations between K and G for orthotropic media having a crack orientated along one of the major axes can also be obtained [28]. But the analytical solutions for the singular stress field often require tedious mathematical derivations.

Direct solution methods for $G(\sigma, a)$ have been available; among them are the well-known J-integral method [29, 30] and the method of virtual crack closure technique by Irwin [31].

Irwin [31] observed that the elastic strain energy released during a virtual crack extension Δa is equal to the work done in closing it again. The inverse problem provides the solution for the surface tractions σ over Δa . The crack-tip energy release rate is then represented by

$$G = \lim_{\Delta a \rightarrow 0} \frac{1}{2\Delta a} \int_0^{\Delta a} (\bar{\sigma} \cdot \Delta \bar{u}) da \quad (5)$$

where $\Delta \bar{u}$ is the crack opening displacement vector over Δa .

If the crack extension involves all three modes (I, II, III), the vector product in Equation (5) will give a sum of three scalars, associated respectively with G_I , G_{II} , and G_{III} .

The virtual crack-closure representation is particularly adaptive to machine computations. Rybicki and Kanninen [32] suggested a 2-dimensional finite element technique to evaluate G for a line crack in a plane. The crack-tip stress vector $\bar{\sigma}$ and the displacement vector $\Delta \bar{u}$ in Equation (5) are approximated by the nodal forces and displacements respectively, in a finite element representation (for detail, see [18]).

Wang and Crossman applied this technique in a generalized plane strain finite element routine [33], which can simulate a line crack propagation in the 2-dimensional cross-section of a laminate. Since a general laminate under load may suffer cross-sectional warping, the routine actually computes 3-dimensional stresses and displacements [33].

If a laminate is subjected to the far-field stress σ_o and a sublaminate crack is to be simulated, the crack-tip energy release rate can be expressed in the general form

$$G_e = C_e (a/t) \cdot t \cdot (\sigma_o/E_o)^2 \quad (6)$$

where E_o is laminate stiffness in σ_o direction, and t is the linear scale between the actual model and the finite element model. C_e is a function dependent only on the crack size a , which is routinely generated for a given type of crack in a given laminate.

Similarly, if the laminate is subjected to a uniform temperature load ΔT , and if a thermally induced crack opening is resulted, then the associated energy release rate at the crack tip is expressed by

$$G_T = C_T (a/t) \cdot t \cdot (\Delta T)^2 \quad (7)$$

Generally, the laminate is prestressed by a $-\Delta T$ due to curing, so a combined effect is resulted when σ_o is applied;

$$G = [(C_e)^{1/2} \cdot e_o + (C_T)^{1/2} \cdot \Delta T]^2 \cdot t \quad (8)$$

where e_o is the far-field strain ($= \sigma_o/E_o$).

It is seen that the finite element technique is extremely versatile, and can be efficiently executed for simulating complicated sub-laminate crackings such as delamination.

Nonetheless, the accuracy of the technique has been a subject of concern of many analysts, because of its approximate nature in representing a mathematically singular stress field. As has been demonstrated by Raju and Craw [34], Spilker and Chou [35], and Wang and Choi [36], the finite element stress solutions could lose significant accuracy in the small vicinity of the singular point; the region in which the stress becomes inaccurate is generally much smaller than, say, a fiber diameter, due to the very nature of the singularity [36]. However, it can also be demonstrated that the stresses in that small region do not contribute significantly to the crack opening energy release rate, especially for a crack size much larger in proportion.

Figure 2 shows a close comparison between the finite element computed G and the elasticity solution counter-part, for a transverse crack located in the mid-layer of a 3-layer laminate (see inset of Figure 2). The extreme layers are designated as material 1 and the mid-layer as material 2. Both had to be assumed elastic isotropic materials. The exact solution for G as a function of the crack size a is given by Isida [37], using complex stress potentials; while the finite element solution is computed using a rather coarse constant-strain, triangular element mesh. It is seen that the finite element solution for $G(a)$ compares well with the exact solution. To obtain accurate stress closest to the crack tip, one can still resort to the finite element method using either a finer mesh or a higher-order element formulation [38]. But, such extreme measures are often unnecessary for the computation of G .

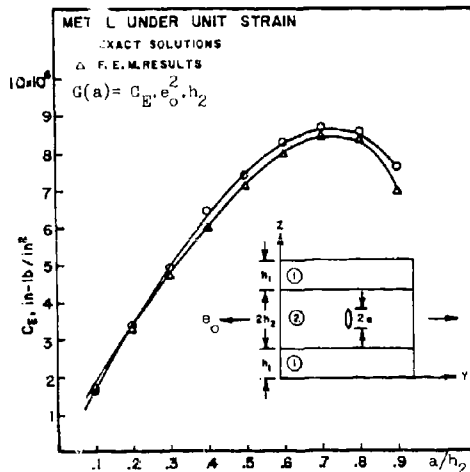


Figure 2 Comparison of the Exact and Finite Element Solutions for $G(a)$. $E_1/E_2 = 5$; $h_1 = h_2$; $v_1 = v_2 = 1/3$.

The Evaluation of G_c

When fracture occurs in the material, the energy released in the process is expected to depend on the morphology of the fracture surface, which must be examined at the microscale. Fibrous composites are known to possess complex fracture surface details, even in matrix-predominant cracks. The observed delamination surfaces in graphite-epoxy composites show, for instance, a considerable ruggedness because the crack must pass around the reinforcing fibers. But, at the macroscopic level, the crack surface details are "smoothed out"; and their effects are reflected in the measured quantity of the fracture resistance G_c .

For this reason, G_c measured for some matrix-predominant fractures in epoxy-based composites has been found to depend on the direction of fracture propagation. Cullen [39] and Williams [40] considered two different cases of delamination as illustrated in Figure 3. The first case is $0^\circ/0^\circ$ delamination in which the crack path is in the fiber direction, while the second is $90^\circ/90^\circ$ delamination where the crack path is transverse to the fiber direction. The experiments were performed using a graphite-epoxy unidirectional laminate, subjected to mode-I cracking condition. They found that the microscopic morphology of the $90^\circ/90^\circ$ delamination surface exhibited considerably more ruggedness than the $0^\circ/0^\circ$ delamination surface. This resulted in marked differences for the measured G_c . Note that these two fracture events occur essentially in the same interface when viewed macroscopically. Yet, the respective G_c values can differ greatly depending on the direction of the crack propagation.

Hence, when the Griffith formula (3) is applied for cracks in composites, the term G_c requires a precise qualification. Similarly, when a test method is devised to measure G_c , it is also necessary to consider the dimensional and directional characteristics of the measured data.

Mode-I interlaminar G_{Ic} . A commonly used test method to determine interlaminar G_{Ic} is the splitting cantilever beam. Cullen [39] and Wilkins [41] have used this method to determine the interlaminar G_{Ic} when the crack is propagating in the direction of the fibers ($0^\circ/0^\circ$ delamination). For some graphite-epoxy systems, they found that G_{Ic} at room temperature is about 0.85 lb/in, or 130 J/m^2 . This value is about twice the G_{Ic} measured for pure epoxy resin. Williams [40] used a compact specimen which simulates roughly a $90^\circ/90^\circ$ delamination. He found, for the same material system, a G_{Ic} value of 1.3 lb/in, about three times that of the pure resin. Williams explained that the fracture surface in his specimens showed fiber breakage as well as fractured epoxy debris; this had resulted in a higher value for G_{Ic} than that found for $0^\circ/0^\circ$ delamination by Cullen [39].

In another paper by Wilkins, et. al. [42], it is reported that G_{Ic} in delamination of $0^\circ/90^\circ$ interface is also higher than that of $0^\circ/0^\circ$ delamination. These findings reaffirm the directional dependent nature of G_{Ic} .

Mixed-mode interlaminar $G_{(I, II, III)c}$. The splitting cantilever beam method has also been used in mixed-mode cracking experiment. In this case, it is necessary to apply different loads at the top and the bottom parts of the split so as to create both an opening (I) and a sliding (II) action. Vandercley [43] and Wilkins [41] conducted tests on the same graphite-epoxy system (used for their mode-I tests), and found the total energy release rate $G_{(I, II)c} = G_{Ic} + G_{IIc}$ which exhibited a strong dependence on the G_{II}/G_I ratio.

This phenomenon is not uncommon in mixed-mode fracture. Similar observations were reported for brittle metals as well as pure epoxy resins [44]. It is, perhaps, more pronounced in fibrous composites. Generally, it is thought that the increased fracture resistance is the result of excessive matrix yielding under shear, as well as crack-closure friction due to the sliding action.

In an experiment on double-notched off-axis unidirectional graphite-epoxy laminates, Wang, et. al. [45] measured the mixed-mode $G_{(I, II)c}$ as a continuous function of G_{II}/G_I , see Figure 4. It is seen that $G_{(I, II)c}$ is monotonically increasing with G_{II}/G_I .

But in the same experiment, it shows also that the opening part G_{Ic} remains roughly independent of G_{II}/G_I . This suggests that mixed-mode crack is essentially controlled by mode-I. Of course, such a suggestion is only temporary; more study is needed to fully understand the true nature of the mixed-mode crack mechanisms.

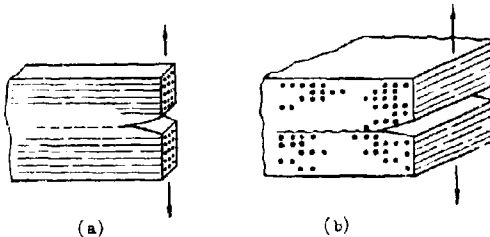


Figure 3 Mode-I $0^\circ/0^\circ$ Delamination (a); and Mode-I $90^\circ/90^\circ$ Delamination

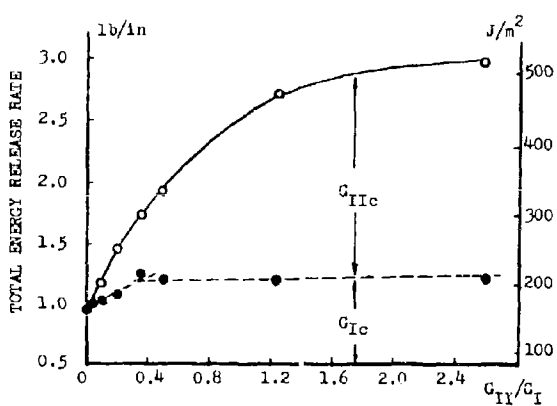


Figure 4 Mixed-Mode $G_c (=G_{Ic} + G_{IIc})$ As a Function of G_{II}/G_I Ratio.

MECHANICS OF TRANSVERSE CRACKS

Physical Mechanisms at the Macroscale

Transverse cracks are found in epoxy-based laminates, even at a low loading level. When viewed at the macroscopic scale, the cracking action is simply a sudden separation of fibers by breaking the epoxy bond. To illustrate, consider as an example a [0/90]_n type laminate such as shown by the inset in Figure 2. There, material 1 is the 0°-layer and material 2 is the 90°-layer. Under the far-field tensile load, material 2 could suffer multiple transverse cracks. Generally, the sequence of events is as follows: A single crack forms first when the applied load reaches a certain critical value, which defines the "onset" of the events; as the applied load increases, more similar cracks are formed. If there is no other failure mode setting in at high load (e.g. 0°-rupture, delamination, etc.), the number of transverse cracks will continue increasing, until it reaches a saturation density.

Figure 5 shows a load-sequence x-radiographs taken for a [0/90]_n graphite-epoxy laminate under ascending tensile load. Transverse cracks in the 90°-layer are seen to form in increasing numbers. From these photographs, a plot of crack density (e.g. cracks per inch of specimen length) versus the applied load can be obtained. Figure 6 shows a family of such experimental plots for a series of [0/90]_{n/0} laminates, n = 1, 2, 3, 4.

Examination of the plots in Figure 6 reveals several interesting features. First, the onset load for the first transverse crack seems to be influenced profoundly by the 90°-layer thickness, especially when it is very thin. Take, for example, the case of n = 1 in Figure 6, the onset load is almost twice that of n = 2.

Secondly, the crack density also shows dependence on the same thickness factor. Generally, the laminate with thinner 90°-layer is capable of yielding a higher crack density. (But, for the case of n = 1, failure of 0°-layer at high load interrupted the development of more transverse cracks).

The 90°-layer thickness effect on transverse cracking was first documented experimentally by Bader, et. al. [46]. They attributed the effect to the constraining actions of the adjacent 0°-layers. Observing that a transverse crack can be no larger than the 90°-layer thickness, the energy release rate which drives the crack is thus limited by the same factor. It is the total strain energy trapped in the 90°-layer which determines the onset of the cracking, not the in-situ tensile stress.

As for the effect on crack density, it has been explained by the existence of a "shear lag" zone at the transverse crack root [46 - 48]. That is an interlaminar shear stress is developed on the 0/90 interface where a transverse crack terminates. This shear stress is singular at the crack root, but decays exponentially a distance away [20]. Similarly, the in-situ tensile stress in the 90°-layer is nil at the transverse crack, but it regains its far-field value outside the shear-lag zone. Thus, ideally, any two adjacent cracks should be spaced by the shear-lag distance. Since this distance is proportional to the 90°-layer thickness [20], hence the observed thickness effect on crack density [46].

Although the shear-lag concept is ideally correct, the so-called "characteristic" spacing of transverse cracks does not occur exactly in practice, due to reasons to be discussed later in this section. Often, transverse cracking leads to other failure modes, and/or vice versa [21].

At the microscopic level, the mechanisms of a transverse crack are much more perplexed. For example, the exact kinematics of crack formation is not fully known. Post-test SEM examination of the crack surfaces generally gives a very ragged appearance; tiny epoxy debris and sometimes broken fibers are also seen [40]. Figure 7 shows an x-ray plane view of a [+25/90₂]_n laminate after transverse cracking, left, and an edge-view micrograph on the right. It is seen that the transverse crack is practically a plane crack of a rectangular dimension, which is bounded by the width of the specimen and the 90°-layer thickness. There is no evidence to indicate that the crack formation is progressive in nature. In fact, all experiments tend to suggest a sudden dynamical formation.

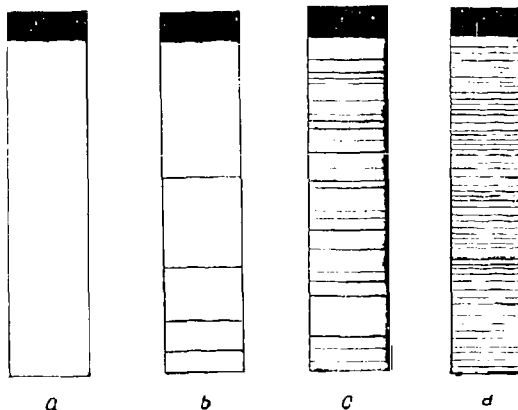


Figure 5 X-Radiographs of Transverse Crack Formation Under Increasing Loading. T300/934 [0/90]_n Laminate.

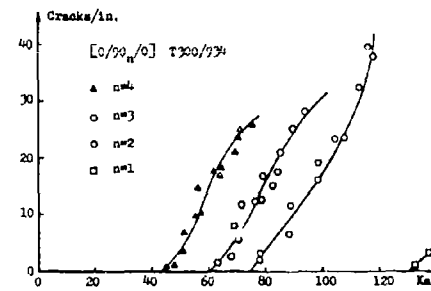


Figure 6 Transverse Crack Density Vs. Applied Load. [0/90]_{n/0}.

This dynamical nature, though still conjectured, has been qualified by many who monitored the acoustics emitted during the crack formation (see, e.g. [49]).

While it is difficult to reduce these physically observed facts into a general law, they nevertheless provide the necessary rationale for the formation of an analytical model. In what follows, an energy formulation is presented, which describes the most essential observed characteristics of the transverse crack-ing phenomenon.

The Energy Formulation

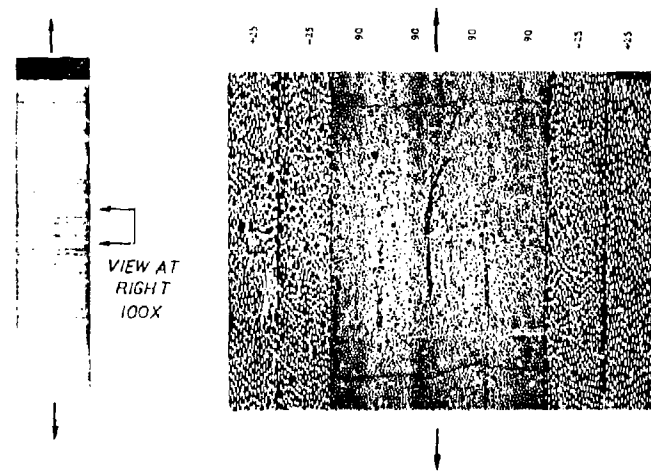
For purpose of clarity, consider a $[0/90]_s$ type laminate, as shown in Figure 8. It will be assumed that, in the 90° -layer, the material has a random distribution of microflaws. The gross effects of the microflaws at the macroscopic scale are represented by a characteristic distribution of "effective" flaws which cannot be physically seen. But, under stress, these effective flaws are capable of propagating suddenly into transverse cracks, which are physically real. The individual size of the effective flaws is denoted by $2a$; and any two adjacent flaws are spaced by a distance S , see Figure 8.

Given a unit length of the specimen, there is a probability density function $f(a)$, and a probability density function $f(S)$. For sake of no evidence to suggest otherwise, the two functions are assumed to take a form for normal distributions [50];

$$f(a) = \frac{1}{a\sqrt{2\pi}} \exp \left[-\frac{(a - \mu_a)^2}{2\sigma_a^2} \right] \quad (9)$$

$$f(S) = \frac{1}{S\sqrt{2\pi}} \exp \left[-\frac{(S - \mu_S)^2}{2\sigma_S^2} \right] \quad (10)$$

Figure 7 Micrograph (right) Showing Two Transverse Cracks In a $[\pm 23/90]_s$ Laminate.



where μ and σ are the mean and the standard deviation of the respective distribution functions.

Among the effective flaws, the size of the "worst" one is denoted by $2a_0$. For definiteness, assume a_0 the 99 percentile of $f(a)$. That is 99% of the flaws are smaller than $2a_0$.

Then, under the far-field load, say e_0 , the "worst" flaw $2a_0$ will become the first transverse crack. The critical value for e_0 at the onset is calculated by substituting Equation (8) into the Griffith criterion (3):

$$[(C_e)^{1/2} \cdot e_0 + (C_T)^{1/2} \cdot \Delta T]^2 \cdot t = G_c \quad (11)$$

where G_c and C_T are evaluated at $a = a_0$.

As has been detailed earlier, the energy release rate coefficients C_e and C_T are generated numerically by the finite element crack-closure routine, given the geometry and material moduli of the laminas. Thus, in Equation (11), all quantities except e_0 will be given: ΔT is the temperature load due to cooling; t is the linear scale between the finite element

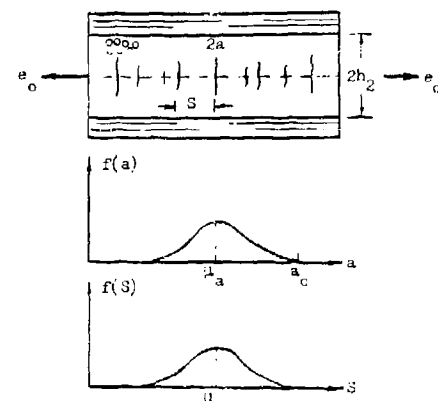


Figure 8 Effective Flaws; Size and Spacing Distributions.

model and the actual model; and G_c takes the value of G_{Ic} which is measured for mode-I 90°/90° delamination.

Now, the difficulty rests upon the choice of a_0 ; or for the same matter, the choice of μ_a and σ_a in the distribution function (9).

Clearly, $2a_0$ must be smaller than the 90°-layer thickness. But the latter can be made arbitrarily large. Hence, a finite bound on a_0 exists even if the 90°-layer thickness is unbounded.

As an example, consider the experimental results reported in [21]. The tensile strength of T300/934 [90g] laminates averaged $\sigma_u = 7000$ psi. If the same "effective" flaw concept is assumed, then the "worst" flaw in the laminate (parallel to fibers) determines the strength according to the Griffith formula (2), yielding

$$a_0 = G_c E / \pi \sigma_u^2 \quad (12)$$

with $E = 1.7 \times 10^6$ psi and $G_c = 0.9$ lb/in for 0°/0° mode-I delamination. Equation (12) determines $a_0 \sim 0.01"$, or about 2 times the ply thickness of the T300/934 system.

It may be assumed that for the 90°/90° mode-I delamination in an unbounded 90°-layer, the "worst" effective flaw size should be no greater than $a_0 = 0.01"$. Indeed, in several experimental correlations conducted by Wang and Crossman [19, 20, 21], using the same material system, a_0 is found in the order of 0.0075", or 1.5 times the ply thickness.

Numerical Examples by Monte-Carlo Simulation

In what follows, the transverse cracking phenomenon will be simulated numerically by the so-called Monte-Carlo random search technique. The considered laminates are in the form {0₂/90_n}, $n = 1, 2$ and 3. The material system is the AS-3501-06 graphite-epoxy system (for the material moduli, see [51]). The nominal ply thickness of this system is 0.0052".

In order to define the parameters μ and σ in the $f(a)$ and $f(S)$ distribution functions, the following values are chosen for the laminate $n = 2$ and 3:

$$\mu_a = 0.0036", \sigma_a = 0.0013" \quad (13)$$

$$\mu_s = 0.0125", \sigma_s = 0.0046" \quad (14)$$

These are chosen to reflect the fact that a_0 , being over 99% of $f(a)$, may take a value (see [50]),

$$a_0 = \mu_a + 3\sigma_a \sim 0.0075" \quad (15)$$

and that for $\mu_s = 0.0125"$ it implies 80 effective flaws to the inch. The choice of the standard deviations is a matter of adjusting to the actual data scatter [51].

As for the laminates of $n = 1$, the thickness of the 90°-layer is only 0.0104" or $a_0 < 0.0052"$. For this case, the choice of μ_a and σ_a are as follows:

$$\mu_a = 0.0021", \sigma_a = 0.00075" \quad (16)$$

so that

$$a_0 = \mu_a + 3\sigma_a \sim 0.0044" \quad (17)$$

The choice of the spacing parameters remains the same for $n = 1$.

The Monte-Carlo simulation procedures start with the generation of a set of $N (= 80)$ flaws whose random sizes and spacings are represented by the respective density functions (9) and (10). This is done by generating first a set of N random values in the interval (0, 1). Then, by equating the cumulative function of $f(a)$ to each of the random values, a random set $\{a_i\}$, $i = 1, N$ is computed. Among the values in $\{a_i\}$, the probability of the largest to be equal or greater than a_0 as defined in (15) or (17) is about 99%.

Similarly, a random set $\{S_i\}$, $i = 1, (N - 1)$, is also generated by the random number scheme. S_i is then assigned to be the spacing between the i th and the $(i + 1)$ th flaws.

Thus, a computer research follows, which determines the flaw most likely to become a transverse crack. The first to occur, clearly, is the worst flaw in the $\{a_i\}$ set, and the corresponding applied load for the onset of the first crack is then determined using Equation (11).

After the first crack is formed, another flaw in the $\{a_i\}$ set will become a crack at a slightly higher load. But this flaw is located at a random distance from the first crack. And the presence of the physical (real) crack has a stress reducing effect on the rest of the flaws. Thus, if the second flaw to become a crack is located outside the shear-lag zone, it will not feel the presence of the first crack; and hence, its available energy release rate at the instant of cracking is given by $G_o(o, a)$, the same as in Equation (8).

On the other hand, if the second flaw is located inside the shear-lag zone, then the available energy release rate is reduced by a factor depending on its distance from the first crack.

Generally, for the flaw to become the k th crack, one must search to the left and to the right for the nearest cracks. If so, the energy release rate at the instance of the k th crack is given by

$$G_k(\sigma, a) = R(S_l) G_0(\sigma, a) R(S_r) \quad (18)$$

where S_l is the distance to the left crack, S_r the distance to the right crack.

In Equation (18), $R(S)$ is the energy rate retention factor which is generated by the finite element routine for a flaw of $2a$ ($< 2a_0$) and is placed at varying distance S from a transverse crack, see Figure 9.

For the laminate family $[0/90]_S$, a single $R(S)$ curve can be generated if expressed in terms of S/t , t being the thickness of one 90°-ply, see Figure 9. Note that 100% energy rate retention is expected beyond $S = 9nt$; the latter is actually the size of the shear-lag zone [19].

The applied load, corresponding to the k th crack is determined from

$$G_k(\sigma, a) = G_c \quad (19)$$

The search essentially simulates the cracking process as it would occur naturally. Each random simulation represents an actual test case; and repeated simulations represent actual tests on replicas. Table A illustrates the flow-chart for the Monte-Carlo simulation.

Figures 10, 11, and 12 show the simulated crack-density versus load plots for respectively, $[0_2/90]_S$, $[0_2/90_2]$ and $[0_2/90_3]$ laminates. In the simulations, the quantities appearing in Equation (11) are assigned as follows:

$$\Delta T = 225^\circ\text{F}, t = 0.0052", G_c = 1.3 \text{ kip/in} \quad (20)$$

The shaded band in each of these plots is the corresponding experimental data band from 4 test specimens. These test data were reported earlier in Reference [52]; and the details for the simulation computer routine are reported in Reference [51].

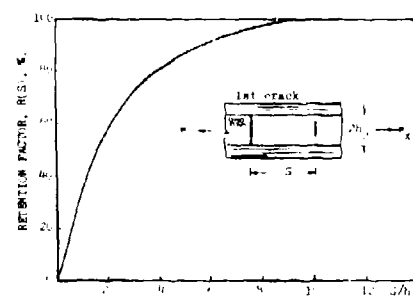


Figure 9. Retention Factor of Energy Release Rate For A Flaw Located at S From A Transverse Crack.

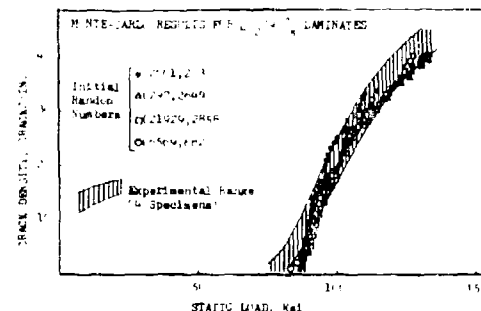


Figure 10. Monte-Carlo Simulations of Transverse Cracks. $[0_2/90]_S$.

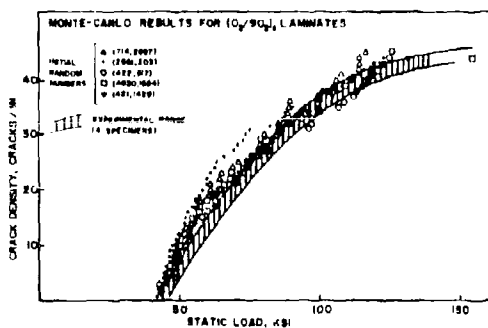


Figure 11. Monte-Carlo Simulations of Transverse Cracks. $[0_2/90_2]_S$.

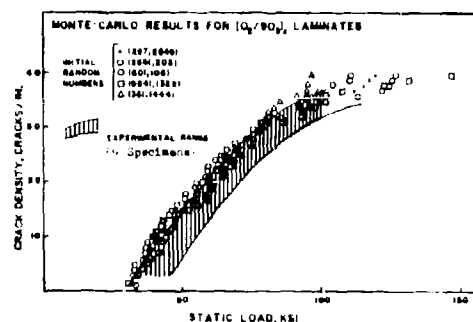
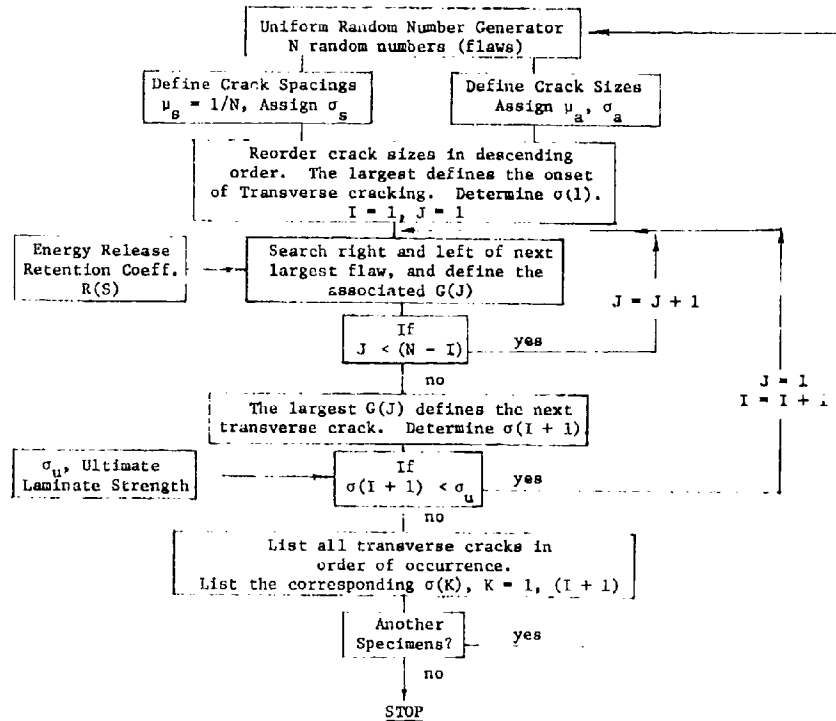


Figure 12. Monte-Carlo Simulations of Transverse Cracks. $[0_2/90_3]_S$.

TABLE A FLOW-CHART FOR MONTE-CARLO SIMULATION



MECHANICS OF FREE EDGE DELAMINATION

The Classical Free-Edge Problem

The free edge delamination problem has attracted increased research interests ever since the advent of composite laminates. The phenomena are frequently observed as the most damaging sub-laminate failure mode. Generally, it is a plane crack which forms along the laminate free edge and propagates inward along an interface of two adjacent layers.

Figure 13 shows an x-ray plane view of a $[+45/0/90]_s$ graphite-epoxy laminate under uniaxial tension (left). Delamination is seen to occur along both edges of the laminate, with essentially uniform growth toward the center. An edge view of this crack is shown on the right, which indicated that the crack is basically contained inside the 90° -layer, not necessarily in any one given layer interface. Moreover, the cracked plane is quite zig-zagged along the length of the free edge.

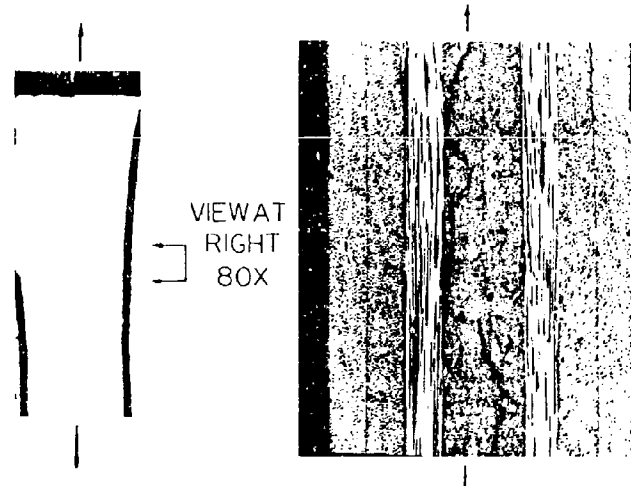


Figure 13 Micrograph (right)
Showing Free Edge Delamination In
A $[+45/0/90]_s$ Laminate.

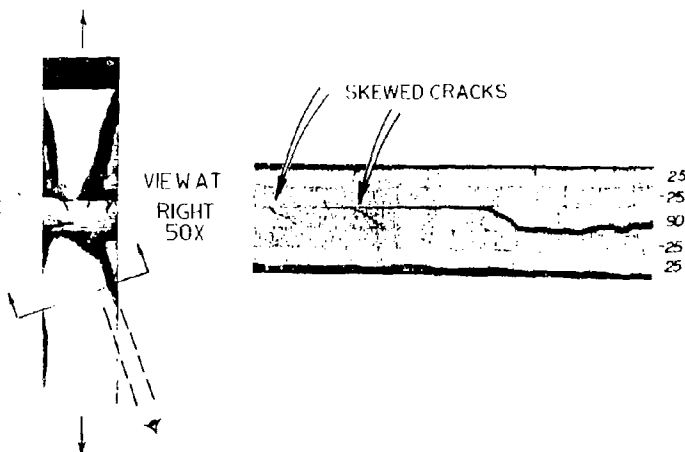


Figure 14 Micrograph (right) Showing Free Edge Delamination of a $[+25/90]_{1/2}s$ Laminate After Failure.

Similar photographs, taken for a $[+25/90]_{1/2}$, laminate after failure, are shown in Figure 14. Here, the edge crack is seen to have formed inside the 90° -layer, but branched to the $25/90$ interface as it propagated. The branch-out is due to the skewed cracks which occur in the 90° -layer ahead of the edge delamination front.

Note that both laminates have a 90° -layer; and they could suffer transverse cracking under the tensile load. But, because the thickness of the 90° -layer is thin, a high load is required for transverse cracking according to the energy theory earlier. Instead, in this case, edge delamination is induced as the first event of sub-laminate failure.

Analytical studies of the free edge delamination problem have originated from the much celebrated work of Pipes and Pagano [53], who formulated and computed the boundary-layer interlaminar stress solutions for a long symmetric laminate under tension. The formulation is based on the macroscopic ply-elasticity theory, which regards the material layers as individually homogeneous media; material and geometrical discontinuities exist only across the layer interfaces.

Generally, the free edge stress field is three-dimensional, and is singular at the intersect of the free-edge with the layer interface [36]. Hence, interface delamination is caused by the highly concentrated edge stresses, especially the interlaminar normal stress σ_z .

In a series of tensile strength tests, Bjeletich, et. al. [54] examined the failure modes of six families of quasi-isotropic laminates by alternating the stacking sequence of the 0° , 90° and $\pm 45^\circ$ layers. Edge stress analysis indicated a compressive σ_z along the free edge of the $[0/90/\pm 45]_s$ laminate, while a

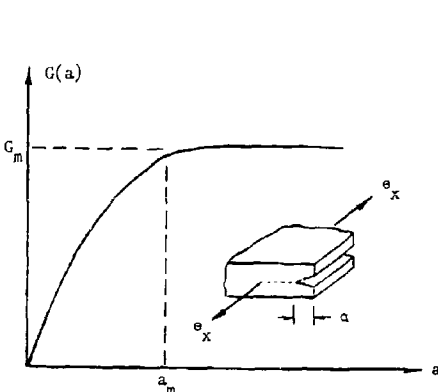


Figure 15 Typical Shape of Energy Release Rate for Delamination



Figure 16 Delamination Under Compression.
 $[90/0/±45]_s$

tensile σ_z for the $[+45/0/90]_s$ laminate. The latter developed premature delamination; and the growth of it had led to a much lowered tensile strength. Clearly, knowledge of the free-edge stresses can provide an explanation why delamination occur; but a quantitative prediction for its occurrence requires a more precisely defined criterion.

In a study on delamination for similar graphite-epoxy laminates, Rodini, et. al. [55] determined experimentally the critical tensile loads at the onset of free edge delamination in a $[+45_n/0_n/90_n]_s$, $n = 1, 2, 3$ family. They found that the critical laminate tensile stress $\bar{\sigma}_x$ varied greatly with the value of n . Specifically, the critical $\bar{\sigma}_x$ decreases at the rate of about \sqrt{n} , even though an edge stress analysis yields identical σ_x for the same $\bar{\sigma}_x$ for all values of n .

Such a 90°-layer thickness dependent behavior is similar to that found in the transverse cracking problems, suggesting the observed phenomenon is again fracture in nature.

The Energy Criterion

In the work of Wang and Crossman [18], it is assumed that material flaws exist randomly on any one of the interfaces between the material layers. Those flaws which are located within the free-edge stress zone form an "effective" flaw having a size a_0 at the instance of onset of delamination, see inset in Figure 15. Following the finite element crack-closure procedure by allowing virtual extension of a_0 along the layer interface, an energy release rate curve is generated, such as shown in Figure 15.

It is seen that the energy release rate G increases sharply with a , but reaches an asymptote at $a = a_m$. Generally, the value of a_m is about one-half the layer-thickness which contains the delamination [18]. Thus, the layer thickness affect the value of a_m , and also the value of G .

Expressing the computed energy release rate, Equation (6),

$$G(a_0, a) = C_E(a) \cdot t \cdot e_0^2 \quad (21)$$

and applying the Griffith criterion (3) for the onset of delamination, one obtains the critical far-field strain.

$$(e_0)_{cr} = [G_c/C_E(a) \cdot t]^{1/2}, a = a_0 \quad (22)$$

Note that in (22), the thermal residual effect is not included. In most laminates, thermal effect on delamination is minimal [56].

The problem comes down to two important questions; namely, what value is a_0 , and which interface is likely to delaminate?

To answer the first question, recall the earlier discussions about a_0 in unbounded 90° laminates. As inferred from the Griffith's criterion, a_0 is in the order of 0.01", or 2 times the ply thickness for commercial graphite-epoxy systems. It is believed that a_0 for delamination is at least of this magnitude if not larger, because of possible additional cutting flaws along the free edge. In any event, if a_m in Figure 15 is less than 3 times of the ply thickness, one simply uses $a = a_m$ and predicts from Equation (22) the minimum possible load for the onset of delamination. Thus,

$$(e_0)_{cr} = [G_c/C_E(a_m) \cdot t]^{1/2} \quad (23)$$

The answer to the second question, however, is complicated, if not inconcise. Consider as an example a $[90_2/0_2/+45_2]_s$ under uniform compression. Interlaminar tensile σ_z is developed in this laminate and edge delamination is induced before global buckling, see Figure 16. A 3-dimensional through-thickness display of σ_z is shown in Figure 17(a). It is seen that the largest σ_z is located on the 45/-45 interface (in fact, this σ_z is singular at the free edge). On the other hand, σ_z along the mid-plane ($z = 0$) is finite at the free edge. In addition, there is also a singular interlaminar shear stress τ_{xz} along the 45/-45 interface. Thus, the stress analysis suggests the 45/-45 interface as the most probable delamination site.

However, according to the energy release rate argument as well as the "effective" flaw hypothesis, one must calculate the energy release rate curves along all possible interfaces in order to determine the interface most energetically favorable for delamination.

The finite element crack-closure results of the $G(a)$ curves for this example problem is shown in Figure 17(b). Indeed, the interface that yields the highest energy release rate is the mid-plane ($z = 0$), not the 45/-45 interface. Furthermore, a delamination in the mid-plane is in mode-I, while it is mixed-mode (I, III) in the 45/-45 interface. As has been discussed earlier, mixed-mode G_c is usually higher than G_{Ic} . Thus, the mid-plane is the predicted delamination site, not the 45/-45 interface.

This conclusion is confirmed by experiments conducted by Wang and Sliomana [57], who also investigated compression-induced delamination in $[0_2/90_2/+45_2]_s$ and $[0/90/0/90/+45/+45]_s$ laminates. In all cases, mid-plane and mode-I delamination was predicted and observed. Using the energy criterion of Equation (23), and setting $G_c = 1.3$ lb/in, their predicted minimum onset loads ($\bar{\sigma}_x$) compared well with the experimental findings (average of 3 specimens). The following table illustrates the closeness between the prediction and the experiment:

Laminates	Predicted onset of σ_x	Experimental Finding
$[90_2/0_2/\pm 45_2]_S$	43.9 ksi	45.7 ksi
$[0_2/90_2/\pm 45_2]_S$	50.9	52.0
$[0/90/0/90/\pm 45/\pm 45]_S$	59.1	62.0

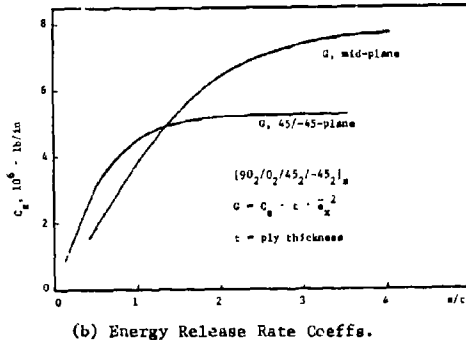
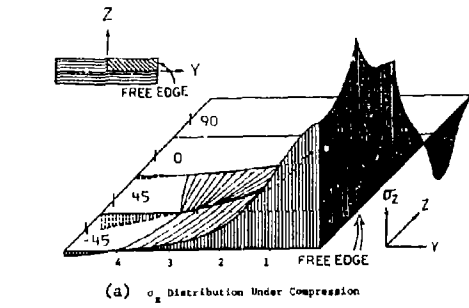


Figure 17 σ_x Distribution and Energy Release Rate Coefficients for $[90_2/0_2/\pm 45_2/\pm 45_2]_S$ Under Compression.



Figure 18 Delamination Induced Transverse Cracks (a). $[+25/90_2]_S$. Transverse Cracks Induced Delamination (b). $[+25/90_4]_S$.

Edge Delamination and Transverse Cracking: Their Interactions

In the previous examples, edge delamination is the first and only sublaminate failure mode before laminate buckling. The onset load for delamination is synonymous to the final laminate failure load. In most other cases, edge delamination and transverse cracking are often two competing failure modes, which interact each other through a complicated mechanisms.

Examine again the photomicrographs shown in Figure 13 and 14, where a $[+45/0/90]_S$ and a $[+25/90_1/2]_S$ laminates were loaded by axial tension. The thickness of the 90°-layer in both laminates is so small that transverse cracking is possible only at a high load. Instead, an edge delamination is induced as the first sub-laminate failure mode. Nonetheless, the stress field in the 90°-layer, which contains the delamination, appears to be extremely complex. The skewed cracks shown in Figure 14 are indicative of the complex stress field ahead of the delamination front. But, just how profoundly these secondary cracking events influence the delamination growth is far from known.

On the other hand, Figure 18(a) shows an x-ray plane view of a $[+25/90_2]_S$ laminate after delamination. Actually, this laminate suffered first transverse cracks in the 90°-layer; subsequent edge delamination in the 25/90 interface developed at a higher load. It is seen from the picture that delamination actually caused many more transverse cracks because of stress concentration along the curved delamination front. In the area where delamination had not occurred, only a few transverse cracks are visible. This phenomenon has repeatedly been observed in experiments [21]; but no serious account has been attempted to analytically modelling it.

Law [56] assumed that when transverse cracks occur in the 90°-layer, the tensile modulus E_T and the Poisson ratio ν_{TL} of the 90°-layer both reduce to nearly zero. With reduced moduli in the 90°-layer, the overall laminate becomes energetically delamination prone in the 25/90 interface, resulting in a mixed-mode cracking (I, II). Law was able to predict the onset loads for this and other similar cases in an approximate manner. Some details of his work will be discussed later in a case study.

Figure 18(b) shows an x-ray plane view for a $[+25/90]_8$ laminate soon after transverse cracking took place. In this case, scattered transverse cracks appeared first, which immediately caused delamination on both 25/90 interfaces in the area where they occurred. The delamination is, in fact, a combined effect stemming from the transverse crack-tip and free edge stress concentrations. Figure 19 illustrates this combined effect in an isometric view. The interface shear stress τ_{xz} , which is developed at the transverse crack root, tends to delaminate the 25/90 interface in the x-direction; and the interlaminar normal stress, σ_z , which is a free edge effect, tends to open up the same interface in the y-direction. The combined action gives rise to a mixed-mode, delta-shaped delamination. Evidence of this type of delamination can be found by examining Figure 18(b).

Law [56] approximated the combined effect by first computing G_x for the x-direction delamination by a 2-dimensional analysis; and then by computing G_y for the y-direction as in the case of free edge delamination. Since both G_x and G_y are considered crack-driving forces, their vector sum is used to predict the onset of the delta-shaped delamination. Obviously, such an approximate approach is only tentative; the problem remains to be treated more rigorously by a 3-dimensional analysis which can simulate a contoured plane delamination. But, as it will be shown in the next section, Law's approach was at least qualitatively correct.

It is now apparent that sub-laminate crackings, especially delamination, are physically complicated even under simple tension. The energy model presented earlier may be applied only in cases where a single failure mode is present. Interactions amongst multiple failure modes are yet to be investigated more extensively.

An Experimental Case Study

An experimental case study on transverse cracking, free edge delamination and their mutual interaction was conducted by Crossman and Wang [21]. They chose a family of graphite-epoxy laminates (T300/934) in the form of $[+25/90_n]_8$. By varying the single parameter $n = 1/2, 1, 2, 3, 4, 6$ and 8, they were able to control the occurrence of the various competing failure modes in

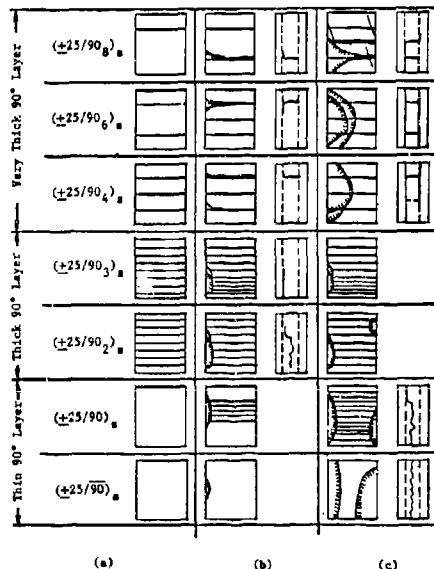


Figure 20 Schematic of the Fracture Sequence in the $[+25/90]_8$ Laminates (a) Just Prior to Edge Delamination, (b) Subsequent to Edge Delamination, (c) Just Prior to Final Failure.

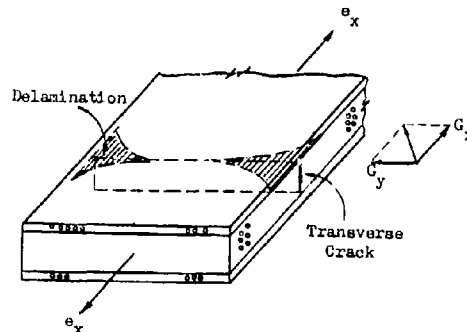
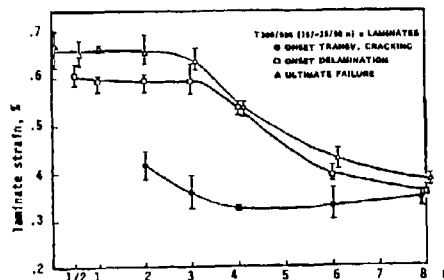
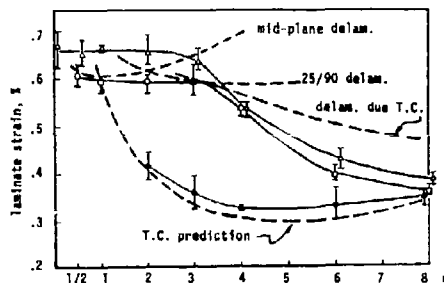


Figure 19 Transverse Crack/Edge Delamination Interaction.



(a) Experimental Results



(b) Experiment/Prediction Comparison

Figure 21 Onset Loads for Transverse Crack, Delamination and Final Failure. $[+25/90_n]_8$ Series.

the laminates when loaded in tension. Both x-radiography and microphotography were used to monitor the sub-laminate cracking development as a function of the applied load. For clarity, a graphical summary of their experimental findings is shown in Figure 20. For $n = 1/2$ and 1, the laminates are classified as having a "thin" 90°-layer. Transverse cracking is suppressed due to the lack of sufficient strain energy stored in the 90°-layer. Hence, free edge delamination occurs as the first sub-laminate failure mode. For $n = 1/2$, a stable mode-I delamination is produced during the loading until final failure. For $n = 1$, however, transverse cracks are induced in the area of delamination. Because of these cracks, the delamination plane is often branched to the 25/90 interface. This latter appearance is indication of an interaction taking place between the two failure modes.

When $n = 2$ and 3, the laminates are denoted as having "thick" 90°-layer. In both, transverse cracks occur first long before delamination. It may be thought that the onset of transverse cracking is an independent event, while delamination is caused, at least partially, by the presence of the multiple transverse cracks. Indeed, the delamination plane in the case of $n = 2$ resembles that for $n = 1$; and the delamination plane in the $n = 3$ laminate is entirely in the 25/90 interface. Also, for $n = 3$, the growth of delamination becomes more rapid.

The laminates with "very thick" 90°-layer are those for $n = 4, 6$ and 8. In all cases transverse cracks occur first followed immediately by delta-shaped delaminations emanating from the transverse crack roots. These soon coalesce to form large scale 25/90 delamination, resulting in premature laminate failure.

Figure 21(a) summarizes the various onset loads for each of the laminates (signified by the value of n). Since the laminate stress-strain response for all cases is essentially linear until final failure, it is convenient to use the laminate tensile strain, ϵ_x as a measure of the applied load. Note that except for $n = 1/2$ and 1, transverse cracking is the first sub-laminate failure event. Generally, growth of multiple cracks is fully developed, followed by interlayer delamination. However, as $n > 3$, the load-gap between the transverse cracking and delamination events grows closer. In fact, for $n = 8$, these two events are closely linked to final laminate failure.

Note also that except for $n = 1/2, 1$, and 2, onset of delamination and final failure are separated only by less than 5% of loading.

By means of the energy model presented earlier, Law [56] conducted a computer simulation of the transverse cracking and delamination processes in the $[+25/90_n]_S$ family. The numerical results are shown in Figure 21(b), which is superscribed on the experimental results shown in Figure 21(a).

Law has conducted four different types of crack simulations: (a) onset of transverse cracking in the 90°-layers for all values of n ; (b) mid-plane ($z = 0$), mode-I delamination for $n = 1/2, 1, 2$ and 3; (c) 25/90 interface delamination for $n = 2, 3$ and 4 (the 90°-layer is saturated with transverse cracks; and is represented by reduced moduli); and (d) transverse crack root/free edge delamination of the 25/90 interface for $n = 3, 4, 6$ and 8 (as illustrated in Figure 19).

It is seen from Figure 21(b) that the predicted onset loads for transverse cracking agree well with the experiment, while the predicted delamination loads (represented by 3 curves) form an envelope to which the experimental points fall below. Although the predicted delamination loads for $n = 6$ and 8 are off considerably from the experimental points, the energy analysis seems to capture the physical mechanisms of these various failure modes; the analysis gives correctly the trend of the failure loads.

Final Failure Mechanisms

In the case study discussed above, the sub-laminate failure sequence is seen to lead to the final rupture of the laminate. It is generally thought that final failure is determined essentially by the strength of the load-carrying plies; i.e. in the case of the $[+25/90_n]_S$ family, the +25-plies should carry practically all the load. But, what determines the strength of the +25-plies? And, is it adversely influenced by the sub-laminate cracking events that proceeded the final laminate rupture? These questions relate to the final failure modes and their associated fracture mechanisms.

Crossman [58] conducted recently an extensive experimental investigation into the failure sequence of several families of laminates under uniaxial tension. Some of his results may help to answer the above questions.

Consider first the effect of thickness of the load-carrying plies by examining the results in Table B.

It is noted that the final failure mode of $[+25/-25]_n$ is due simply to fiber breaking across the laminate, while the final failure mode of $[25_2/-25_2]_n$ involves a major transverse crack in the center core (-25°-layer) followed by multiple fiber-splitting in the 25₂-layer. In particular, there is no fiber breakage involved in the latter case, see Figure 22.

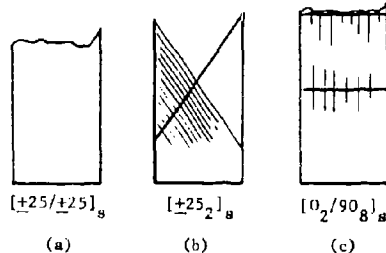


Figure 22 Final Failure Modes: (a) Cross-sectional Fiber Break; (b) 25-layer Transverse Cracks; (c) 0-layer Fiber Splits over 90-layer Transverse Cracks.

TABLE B

<u>Laminate</u>	<u>Sequence of Failure Modes</u>	<u>Total Load in lbs.</u>
$[+25/-25]_s$	no transverse cracking no edge delamination cross-section fiber break	<u>3103(2895-3245)</u>
$[25_2/-25_2]_s$	single transverse crack in -25-layer, followed by multiple transverse cracks in the +25-layer final failure involved no fiber break	occur at 98% P_u <u>2272(2001-2480)</u>
$[+25/+25/90_2]_s$	transverse cracks in 90-layer stable edge delamination cross-section fiber break in the 25-layers	occur at 80% P_u occur at 90% P_u <u>3040(3001-3250)</u>
$[25_2/-25_2/90_2]_s$	transverse cracks in 90-layer rapid edge delamination fiber-split in 25-layer	occur at 90% P_u occur at 98% P_u <u>2648(2500-2830)</u>

TABLE C

<u>Laminate</u>	<u>Sequence of Failure Modes</u>	<u>Total Load in lbs.</u>
$[+25/90_2]_s$	transverse cracks in 90-layer stable edge delamination cross-section fiber break in 25-layers	occur at 85% P_u occur at 95% P_u <u>1802(1747-1893)</u>
$[+25/90_8]_s$	scattered transverse cracks local delamination from T.C. tip; combined with edge delam. fiber split in 25-layer few fiber break in 25-layer	occur at 95% P_u <u>1606(1500-1660)</u>
$[0_2/90_2]_s$	transverse cracks in 90-layer no edge delamination cross-section fiber break of 0-layer	occur at 80% P_u <u>5163(4600-5730)</u>
$[0_2/90_8]_s$	scattered transverse cracks local delamination from T.C. tip; local fiber-split in 0-layer above transverse crack coalescence of fiber-splits in 0-layer final 0-layer failure	occur at 75% P_u occur at 85% P_u <u>4220(4120-4320)</u>
$[+30/90_2]_s$	transverse crack in 90°-layer stable edge delamination cross-section fiber break in 30-layer	occur at 80% P_u occur at 95% P_u <u>1650(1625-1670)</u>
$[+30/90_8]_s$	transverse crack in 90°-layer local edge delamination from T.C. tip; fiber break in 30-layer	occur at 80% P_u occur at 85% P_u <u>1622(1620-1625)</u>

An energy analysis of the respective failure modes indicated that the transverse cracking mode in the $[+25/+25]_s$ is suppressed by the actual thickness of the 25° -layer; there is not enough strain energy to cause this failure mode at a lower load level. Hence, it forces a fiber breakage instead. However, by doubling the layer thickness, in the case of $[25_2/-25_2]_s$, the transverse cracking mode emerges at a much lower load. The difference in the failure modes results in the difference in the applied ultimate loads.

Clearly, the strength of the so-called "load-carrying" plies in a laminate depends also on the particular fracture modes that cause failure. In the examples above, the ply-thickness factor is seen again to play a profound role in the final failure mechanisms.

When the respective load-carrying plies are laminated with a 90° -layer, such as in $[+25/+25/90_2]_s$ and $[25_2/-25_2/90_2]_s$, transverse cracks in the 90° -layer and edge delamination are found to proceed any failure in the 25° -plies. From the results displayed in Table B, it is seen that the sub-laminate cracking events neither changed the failure mode of the 25° -plies, nor decreased the final ultimate loading, although the presence of the 90° -layer in $[25_2/-25_2/90_2]_s$ slightly increased the laminate load-carrying capacity. The reason is that $[25_2/-25_2]_s$ has four (4) 25° -plies in the core, while $[25_2/-25_2/90_2]_s$ has only two (2) 25° -plies scattered by the presence of the 90° -layer in the core.

However, adverse effects of sub-laminate cracking on laminate final failure modes are seen from the test results displayed in Table C. Here, the failure modes in $[0/90_2]_s$ and $[+0/90_2]_s$ are compared. Note that the 90° -layer thickness in the latter is exaggerated in order to separate widely the respective sub-laminate crack modes.

In the cases of $[0_2/90_2]_s$ and $[+25/90_2]_s$, the final failure mode in the load-carrying plies involves multiple fiber-splitting, which occur along the root of a 90° -layer transverse crack; see Figure 22. On the other hand, there is no fiber-splitting in the $[0_2/90_2]_s$ or the $[+25/90_2]_s$ laminates.

A three dimensional stress analysis will show that there is a stress concentration at the 90° -layer transverse crack root; both the applied tension and thermal cooling contribute to the stress concentration. In particular, the size of the stress concentration zone is proportional to the 90° -layer thickness; which explains why the considerable difference in the final loads between $[0_2/90_2]_s$ and $[0_2/90_2]_s$; and between $[+25/90_2]_s$ and $[+25/90_2]_s$, see Table C.

Fiber-splitting seems to be the triggering failure mode in the $[0_2/90_2]_s$ and $[+25/90_2]_s$ laminates. The splitting mechanism is due to the existence of the tensile stress normal to the fibers, which is magnified in amplitude by the 90° -layer transverse crack root.

Similar stress condition also exists in the $[+30/90_2]_s$ laminates. But in this case, the tensile stress (normal to $+30^\circ$ -fibers) is not large enough to cause fiber splitting; see also Table C. As a result, the final failure modes for $[+30/90_2]_s$ and $[+30/90_2]_s$ all involve fiber breaking; and their final failure load are essentially the same. Thus, a mere increase in the angle from 25° to 30° changes the failure mode.

Clearly, the final failure modes in the "load-carrying" plies can be influenced by nature from the sub-laminate crackings. Moreover, there are probably a host of other possible modes that are competing for dominance. The specific failure occurrence in a given laminate is generally determined by the laminate geometry as well as the intrinsic material properties. And, of course, there are always the statistical uncertainties in the "intrinsic" material properties.

CONCLUSIONS

This paper has attempted to give an overview of a fracture mechanics approach to some of the frequently observed sub-laminate cracks in epoxy-based composite laminates. The laminates discussed in the paper served mainly to illustrate how a certain failure sequence is developed and how the predictive model is constructed. They are certainly not the ones which may be used in practical design applications. The major objective here is to enable to see through the various fracture mechanisms and try to understand them; to this end, one often had to exaggerate the geometric parameters (e. g. the thickness of 90° -layer) in order to ascertain their full range of influence.

Indeed, the field of fracture in composites seems infinitely complex. Yet, numerous past and present investigators have toiled the field with many successes. And, new discoveries are being continuously made to further its advancement. The results reported in this paper represent but one effort to fill the dimensional span from micromechanics to structural mechanics in composite failure analysis.

REFERENCES

- [1] Tsai, S. W. and Hahn, H. T., "Introduction to Composite Materials," Technomic, 1980.
- [2] Starnes, J. H. and Rouse, M., "Post-Buckling and Failure Characteristics of Selected Flat Rectangular Graphite-Epoxy Plates Loaded in Compression," Proc. AIAA/ASME/ASCE/AHS, 22nd Structures, Structural Dynamics and Materials Conference, 1981.
- [3] Starnes, J. H. and Williams, J. G., "Failure Characteristics of Graphite-Epoxy Structural Components Loaded in Compression," NASA-TR-84552, 1982.
- [4] Waddoups, M. E., Eisenmann, J. R. and Kaminski, B. E., "Macroscopic Fracture Mechanics of Advanced Composite Materials," J. Comp. Mat., Vol. 5, 1971, p. 466.
- [5] Cruse, T. A., "Tensile Strength of Notched Composites," J. Comp. Mat., Vol. 7, 1973, p. 218.
- [6] Whitney, J. M. and Nuismer, R. J., "Stress Fracture Criteria for Laminated Composites Containing

- Stress Concentrations," J. Comp. Matls., Vol. 8, 1974, p. 253.
- [7] Cooper, G. A. and Kelly, A., "Role of the Interface in the Fracture of Fiber-Composite Materials," ASTM STP 452, 1969, p. 90.
- [8] Greszczuk, L. B., "Theoretical Studies of the Mechanisms of the Fiber-Matrix Interface in Composites," ASTM STP 452, 1969, p. 42.
- [9] Kelly, A., "Interface Effects and the Work of Fracture of a Fibrous Composites," Proc. Roy. Soc., A319, 1970, p. 95.
- [10] Phillips, D. C. and Tetelman, A. S., "The Fracture Toughness of Fiber Composites," Composites, Vol. 3, 1972, p. 216.
- [11] Piggott, M. R., "Theoretical Estimation of Fracture Toughness of Fibrous Composites," J. Matl. Sci., Vol. 5, 1970, p. 669.
- [12] Zweben, C. and Rosen, B. W., "A Statistical Theory of Material Strength with Application to Composite Materials," J. Mech Phys. Solids, Vol. 18, 1970, p. 189.
- [13] Corten, H. T., "Fracture Mechanics of Composites," Fracture, Vol. 7, Ed. H. Liebowitz, Academic Press, N.Y., 1972, p. 676.
- [14] Wu, E. M., "Application of Fracture Mechanics to Anisotropic Plates," J. Appl. Mech., Vol. 34, 1967, p. 967.
- [15] Kanninen, M. F., Rybicki, E. F. and Brinson, H. F., "A Critical Look at Current Applications of Fracture Mechanics to the Failure of Fiber-Reinforced Composites," Composites, Vol. 8, 1977, p. 17.
- [16] Wang, A. S. E., Crossman, F. W. and Law, G. E., "Interlaminar Failure in Epoxy-Based Composite Laminates," Proc. 29th MFG Symp. Advance Composites-Design and Applications, NBS, 1979, p. 255.
- [17] Wang, A. S. D. and Law, G. E., "An Energy Method for Multiple Transverse Cracks in Graphite-Epoxy Laminates," in Modern Dev. in Composite Materials and Structures, Ed. J. Vinson, ASME, 1979, p. 17.
- [18] Wang, A. S. D. and Crossman, F. W., "Initiation and Growth of Transverse Cracks and Edge Delamination in Composite Laminates: Part 1. An Energy Method," J. Comp. Matls., Suppl. Vol., 1980, p. 71.
- [19] Crossman, F. W., Warren, W. T., Wang, A. S. D. and Law, G. E., "Initiation and Growth of Transverse Cracks and Edge Delamination in Composite Laminates: Part 2. Experimental Correlation," J. Comp. Matls., Suppl. Vol., 1980, p. 88.
- [20] Wang, A. S. D., "Growth Mechanisms of Transverse Cracks and Ply-Delamination in Composite Laminates," Proc. ICCM-III, Vol. 1, Paris, 1980, p. 171.
- [21] Crossman, F. W. and Wang, A. S. D., "The Dependence of Transverse Cracks and Delamination on Ply Thickness in Graphite-Epoxy Laminates," ASTM STP 725, 1982, p. 170.
- [22] Wang, A. S. D., Miller, H. R. and Chou, P. C., "A Theory for Multiple Transverse Cracks in Composite Laminates," in Advances in Aerospace Structures and Materials, Ed. J. Vinson, ASME, 1982, p. 51.
- [23] Griffith, A. S., "The Phenomena of Rupture and Flow in Solids," Phil. Trans. Roy. Soc., Vol. A231, 1920, p. 163.
- [24] Irwin, G. R., "Fracture Dynamics," in Fracture of Metals, ASM, Cleveland, 1948, p. 147.
- [25] Orowan, E. O., "Fundamentals of Brittle Behavior of Metals," in Fatigue and Fracture of Metals, W. M. Murray, Ed. Wiley & Sons, N.Y., 1950, p. 139.
- [26] Muskhelishvili, N. I., "Some Basic Problems From the Mathematical Theory of Elasticity," Noordhoff, Holland, 1953.
- [27] Sneddon, I. N., "Integral Transform Methods," in Methods of Analysis and Solutions of Crack Problems, Noordhoff, Holland, 1973, p. 315.
- [28] Lekhnitsky, S. G., "Theory of Elasticity of an Anisotropic Elastic Body," Holden-Day, San Francisco, 1963.
- [29] Rice, J. R., "A Path Independent Integral and Approximate Analysis of Strain Concentration by Notches and Cracks," J. Appl. Mech. Trans. ASME, 1968, p. 379.
- [30] Bucci, R. J., Paris, P. C., Landis, J. D. and Rice, J. R., "J-integral Estimation Procedures," in Fracture Toughness, ASTM STP 514, 1972, p. 40.
- [31] Irwin, G. R., "Fracture," Handbuch der Physik, Vol. 5, Springer-Verlag, 1958, p. 551.
- [32] Rybicki, E. F. and Kanninen, M. F., "A Finite Element Calculation of Stress Intensity Factors by a Modified Crack-Closure Integral," Eng. Fract. Mech., Vol. 9, 1977, p. 931.
- [33] Wang, A. S. D. and Crossman, F. W., "Some New Results on Edge Effects in Symmetric Composite Laminates," J. Comp. Matls., Vol. 11, 1977, p. 92.

- [34] Raju, I. S. and Crews, J. H., "Three Dimensional Analysis of [0/90]_s and [90/0]_s Laminates with a Central Circular Hole," Composites Tech. Rev., Vol. 4, 1982, p. 116.
- [35] Spilker, R. L. and Chou, S. C., "Edge Effects in Symmetric Composite Laminates: Importance of Satisfying the Traction Free Edge Condition," J. Comp. Matls., Vol. 14, 1980, p. 2.
- [36] Wang, S. S. and Choi, I., "Boundary Layer Effects in Composite Laminates," Part 1 and Part 2, J. Appl. Mech., Vol. 49, 1982, p. 541, p. 549.
- [37] Isida, M., "Method of Laurant Series Expansion for Internal Crack Problems," in Methods of Analysis and Solutions of Crack Problems, Ed. G. C. Sih, Noordhoff, 1973, p. 56.
- [38] Whitcomb, J. D., Raju, I. S. and Goree, J. G., "Reliability of the Finite Element Method for Calculating Free Edge Stresses in Composite Laminates," Computers & Structures, Vol. 15, p. 23.
- [39] Cullen, J. S., "Mode-I Delamination of Unidirectional Graphite Epoxy Composite Under Complex Load Histories," M. S. Thesis, Texas A & M University, 1981.
- [40] Williams, D., "Mode-I Transverse Cracking in an Epoxy and a Graphite Fiber Reinforced Epoxy," M. S. Thesis, Texas A & M University, 1981.
- [41] Wilkins, D. J., "A Comparison of the Delamination and Environmental Resistance of a Graphite-Epoxy and a Graphite-Bismaleimide," NAV-GB-0037, Naval Air System Comme., 1981.
- [42] Wilkins, D. J., Eisenmann, J. R., Camin, R. A., Margolis, W. S. and Benson, R. A., "Characterizing Delamination Growth in Graphite-Epoxy," ASTM STP 775, 1982, p. 168.
- [43] Vanderkley, P. S., "Mode-I and Mode-II Delamination Fracture Toughness of an Unidirectional Graphite-Epoxy Composite," M. S. Thesis, Texas A & M University, 1981.
- [44] Bascom, W. D., Cottingham, R. L. and Timmons, G. O., "Fracture Design Criteria for Structural Adhesive Bonding - Promise and Problems," Naval Eng. Jour., Aug. 1976, p. 73.
- [45] Wang, A. S. D., Kishore, N. N. and Feng, W. W., "On Mixed-Mode Fracture in Off-Axis Unidirectional Graphite-Epoxy Composites," Proc. ICCM-IV, Vol. 1, Tokyo, 1982, p. 599.
- [46] Bader, M. G., Bailey, J. E., Curtis, P. T. and Parvizi, A., "The Mechanisms of Initiation of Development of Damage in Multi-Axial Fiber-Reinforced Plastics Laminates," in Mechanical Behavior of Materials, ICM-3, Vol. 3, 1979, p. 227.
- [47] Aveston, J. and Kelly, A., "Theory of Multiple Fracture of Fibrous Composites," J. Matls. Sciences, Vol. 8, 1973, p. 352.
- [48] Reifsnider, K. L. and Masters, J. L., "Investigation of Characteristic Damage States in Composites Laminates," ASME Paper No. 78-WA-AERO-4, 1978.
- [49] Chou, S. C., Brockelman, R., Broz, A., Hinton, Y. and Shuford, R., "Analytical and NDE Techniques for Determining Crack Initiation in Graphite-Epoxy Laminates," ASTM Symp. Effects of Defects in Composite Materials, San Francisco, 1982.
- [50] Juvinall, R. C., Stress, Strain and Strength, McGraw-Hill, N.Y., 1967, p. 346.
- [51] Wang, A. S. D. and Lei, C. S., "Multiple Transverse Cracks by a Monte-Carlo Simulation," (in press).
- [52] Chou, P. C., Wang, A. S. D., and Miller, H. R., "Cumulative Damage Model for Advanced Composite Materials," AIAW-TR-82-4083, U. S. Air Force Wright Aeronautical Lab., 1982.
- [53] Pipes, R. B. and Pagano, N. J., "Interlaminar Stresses in Composite Laminates Under Uniform Axial Tension," J. Comp. Matls., Vol. 4, 1970, p. 538.
- [54] Bjeletich, J. G., Crossman, F. W. and Warren, W. J., "The Influence of Stacking Sequence on Failure Modes in Quasi-Isotropic Graphite-Epoxy Laminates," Failure Modes in Composites - IV, AIME, 1979.
- [55] Rodini, B. T. and Eisenmann, J. R., "An Analytical and Experimental Investigation of Edge Delamination in Composite Laminates," in Fibrous Composites in Structural Design, Ed. E. M. Leno, et. al., Plenum Press, N.Y., 1978, p. 441.
- [56] Law, G. E., "Fracture Analysis of [+25/90]₁₀ Graphite-Epoxy Composite Laminates," Ph.D. Thesis, Drexel University, 1981.
- [57] Wang, A. S. D. and Slomianka, M., "Fracture Mechanics of Delamination - Initiation and Growth," NADC-TR-79056-60, 1982.
- [58] Crossman, F. W., "Experimental Documentation of the Sequential Failure Modes in Graphite-Epoxy Laminates," (in press).

Acknowledgments. Many results reported in this paper were obtained in collaboration with Drs. F. W. Crossman, G. E. Law, H. Miller and N. N. Kishore. Financial supports have been provided by the U. S. Air Force Office of Scientific Research, Wright Aeronautical Laboratory and the Naval Air Development Center.

THE SIGNIFICANCE OF DEFECTS AND DAMAGE IN COMPOSITE STRUCTURES

by

R T POTTER
Materials and Structures Department
Royal Aircraft Establishment
Farnborough
Hampshire GU14 6TD - UK

SUMMARY

The significance of defects and damage in fibre composite structures depends upon a wide range of decisions taken at every stage of the life of each particular structure, from the initial design conception, through detailed design and manufacture, to inspection, maintenance and repair procedures. Since many of these decisions interact, there is need for a coherent overall philosophy for the management of defects and damage if fibre composite structures are to be efficient and cost-effective. In the present Paper the general requirements of such a philosophy are considered and it is seen that further research is required particularly on the interaction of defects and damage with structural features. Some initial results and observations from the RAE programme devised to study such interactions are presented.

1 INTRODUCTION

No matter how carefully designed, manufactured and maintained, fibre composite aerospace structures will always be subject to both manufacturing and service-induced damage. As in metallic structures, the more severe defects may reduce the strength or endurance of the structure and the efficient exploitation of fibre composite materials will require a rational approach to the management of defects and damage. Although defects of any magnitude are undesirable, many of the microstructural defects such as the occasional broken or misaligned fibre, will be of little significance. Clearly, attention must be focussed on those defects which may affect the performance of practical structures, and to this end it is necessary to define the structural significance of the various types of defects and damage that are considered likely to occur.

For the purposes of this Paper, a defect will be defined as any unintentional local variation in physical or mechanical properties. Thus, the general term defect will relate to all forms of local manufacturing defects and service-induced damage. A structurally significant defect can be defined arbitrarily at this stage as that which, within the expected lifetime of the structure, will reduce the load carrying capacity of the structure to a level less than or equal to the design ultimate load (DUL). Such a definition does not directly include loss of stiffness as a criterion of failure but, in relation to the defects considered here, loss of stiffness will not normally be significant.

In the present Paper, the method by which the effects of defects are accommodated in current carbon fibre reinforced plastic (CFRP) designs is briefly described and the limitations of this approach are discussed. By consideration of the requirements of a more coherent approach to the management of defects and damage, it is seen that further work is required particularly on the interaction of defects with structural features. Some initial results and observations from an RAE programme devised to study such interactions are described.

2 CURRENT DESIGNS AND THE EFFECTS OF DEFECTS

To illustrate the current design approach, consider the design of wing skin panels. Such panels are the primary load carrying members of a wing and usually contribute more than half of the total wing structure mass. They must react direct loads due to wing bending and shear loads due to wing torsion and, in addition, they must react the out-of-plane loads due to aerodynamic effects, internal pressure and the inertia of the fuel.

Consider the design requirements for direct loading due to wing bending. Figure 1 shows a typical element of a wing skin panel which contains a row of bolt holes used to attach the skin to the substructure. The primary function of the attachments is to provide panel stability in compression and to react the aforementioned out-of-plane loads. The in-plane bearing loads on these bolts is generally small and, to first approximation, we may consider the element to contain a series of filled but unloaded holes. Tests on composite specimens containing holes show that, in tension, room temperature static strength will be critical, whilst in compression, elevated temperature fatigue loading in the presence of moisture will limit performance. Quasi-static tensile tests on carbon fibre-epoxy resin composites tend to show that the overall tensile strain along the row of bolts must be limited to about 4000 microstrain. Similarly, elevated temperature compressive fatigue tests on environmentally conditioned specimens indicate an overall compressive strain limitation of about -4000 microstrain along the row of bolts. Strain compatibility requirements of the complete element impose the same tensile and compressive strain limits on the material remote from the row of bolts even though the unperforated material could generally sustain strains of more than twice that magnitude.

Designs incorporating features such as softening strips along the line of bolts have been proposed to overcome this limitation but it is recognised that some allowance must be made for the effects of defects and damage and, in the absence of sufficient data to justify the use of higher strain levels in the unperforated material, such techniques have not been vigorously pursued.

The design allowable strain limit of about ± 4000 microstrain has been widely adopted as the primary method of accommodating defects and damage in those areas of CFRP structures subject to near uniform in-plane stress. However, whilst recent experiments on the effects of typical defects on material properties suggested this limit to be of the right order, it should be noted that it was not derived from consideration of the effects of defects and damage and is not therefore directly related to the probability of occurrence of defects or damage of any particular severity.

In areas of non-uniform stress induced by structural features, the situation is more complex since the significance of a given type of defect is likely to vary according to its location with respect to the perturbed stress field. Currently, quantitative prediction of the interaction of defects with structural features can not be achieved by analytical methods and such interactions must be evaluated by experiment. For the more common structural features such as bolted and bonded joints, angled sections etc., data on the effects of commonly occurring defects is gradually being accumulated. However, the interaction of defects with features whose geometry tends to be specific to a particular design, or features which give rise to only limited stress concentrations have received little attention. In consequence, there is no well-established design procedure and each design authority tends to apply different rules derived from the locally available data.

3 REQUIREMENTS OF A GENERAL DESIGN PHILOSOPHY

3.1 General Requirements

From the above description of the current design approach, which has of necessity been of a brief and generalised nature, it is evident that there is currently no coherent overall design philosophy for accommodating the effects of defects and damage in composite structures. Apart from the general use of a design allowable strain limit in areas of uniform stress, the approach has generally been of an ad-hoc nature. Indeed even the design allowable strain limit has not been derived specifically from the consideration of defects and damage. Thus for current designs, the types and severity of defects and damage which are structurally significant are not directly related to their probability of occurrence. Furthermore, many of the experimental programmes aimed at evaluating the effects of defects have been concerned merely with demonstrating the adequacy of existing designs to tolerate the types of defects and damage which might be expected to occur. This approach is unlikely to lead to the most efficient use of fibre composite materials in aerospace structures. In some areas, current designs may be too conservative and hence inefficient, whilst in other areas they may be unconservative and necessitate frequent inspection and repair.

The primary aim of future work on the effects of defects should be to generate the data and understanding that will allow the formulation of a coherent overall design philosophy. Such a philosophy would incorporate the following elements:-

- a. Assessment of the probability of occurrence, the probable severity and locations of the various types of defects and damage.
- b. Prediction, or if necessary experimental measurement, of the effects on the performance of materials and structures of those defects considered likely to occur, including consideration of damage growth.
- c. Assessment of inspection and repair capabilities in relation to these defects.
- d. Derivation of design allowable stresses or strains in materials and structural elements to achieve a balance between maximum structural efficiency and minimum inspection, maintenance and repair requirements.

Clearly, some of the information required to develop and implement such a design philosophy is not currently available. Moreover, it might be argued that, at certain structural locations, the stresses may be ultimately limited by factors other than the effects of defects. Nevertheless, the performance of structural features generally will be limited by defects and the approach advocated above should be considered in the formulation of future research programmes. Detailed discussion of the various elements of this approach is beyond the scope of this Paper, but the extent of available data related to this philosophy is considered briefly in the following sections.

3.2 Common Defect Types and Locations

Reliable data concerning the probability of occurrence of particular types of defects and damage, including information on the likely severity and location, will be accumulated only through an in-depth evaluation of manufacturing and service experience. Initial experience of carbon fibre/epoxy resin composites suggests that there is a limited range of commonly occurring defects and these are often associated with particular structural features. For example, voids often occur at angled sections due to inadequate consolidation in the concave corners of moulds. Fibre kinks also occur at these locations due to the folding of the preimpregnate. Machining and assembly damage most frequently occur at features such as cut-outs and bolted joints whilst rough handling usually results in damage to the free edges. Service-induced damage such as that due to local impacts may occur at many points on the structure, but the regions around access panels and attachment points are particularly prone to low velocity impacts whilst external lower surfaces and leading edges are prone to higher velocity impacts from objects such as runway stones. Local heating damage is clearly most likely in regions of the structure surrounding engines or in areas affected by off-flux from engines or weapons.

The above list of defects and their likely locations is not exhaustive but it does contain many of those that are currently considered most likely to occur and whose significance should be considered.

3.3 The Effects of Defects on Structural Performance.

In flat structural panels under uniform in-plane loading the structural significance of defects may be determined without reference to the particular structural form simply in terms of the known effects on material properties. Thus, a method similar to the current strain limit approach will almost certainly continue to be used for the accommodation of defects in these areas. As indicated above, the significance of defects adjacent to particular structural features is more difficult to assess, their effects being dependent upon a number of factors such as the location and relative size of the defect with respect to the feature. There is a wide range of potential defect/feature interactions and those that are likely to be structurally significant may generally be deduced from consideration of the stresses induced in any given feature and the known effects of defects on the material properties. Some of the more common interactions, such as those of defects associated with mechanical joints, have been investigated in particular research programmes, see for example References 1 and 2. However, defects associated with structural features that tend to be specific to particular designs or with minor features that give rise to interlaminar stresses or to out-of-plane bending moments have received little attention. Clearly, these latter features could be particularly sensitive to defects affecting interlaminar integrity and further work is required in this area.

3.4 Inspection and Repair Considerations

Inspection of composite structures during manufacture is likely to be more thorough than that which may be achieved in service, and it seems likely that the routine use of techniques such as ultrasonic scanning, perhaps backed up by other techniques which will yield information on complex shaped components, will allow the identification of most structurally significant manufacturing defects. Experimental evidence derived from essentially flat coupon specimens suggests that current manufacturing acceptance criteria, which were largely determined on the basis of the manufacturing quality that could readily be achieved and the defects which could be reliably detected, appear to be sufficiently conservative to virtually eliminate the majority of structurally significant manufacturing defects in most surface structure. There is less data applicable to substructure, but it is possible that, at current design levels, any requirement to accommodate manufacturing defects in design could be based on the cost effectiveness associated with the accept/reject/recover by repair criteria applied to the manufacturing processes.

Clearly, service-induced damage cannot be eliminated in the same manner and the minimum design requirement must be that the damage should not become structurally significant before it can be detected by routine inspection. Thus, in-service inspection methods will form an integral feature of any coherent philosophy for the management of defects and damage. Of course, there will be several levels of inspection, from the frequent visual check of the external surfaces, through the more thorough inspection during routine maintenance, to the detailed inspection possible during a major overhaul. It follows that for a given type of defect, the designer must allow for a maximum acceptable size which is defined by the damage growth rate, the frequency, sensitivity and reliability of inspection at the various levels. Some areas of the structure may be more highly stressed or more critical than others so that defect acceptance criteria and inspection requirements may vary from one region to another. In-service inspection methods are discussed in detail by Stone and Clarke⁷ but, in general, inspection will be a two stage process. The primary inspection will enable the rapid scanning of the structure to locate defects above a certain predetermined size. The secondary inspection will employ techniques capable of more detailed analysis to characterize and measure both the area and through-thickness location of the defects and damage identified by the primary inspection. This data may then be compared with the defect acceptance criteria for the particular area of the structure.

A design philosophy based upon the ability to reliably detect defects and damage before they become structurally significant implies the ready availability of suitable repair techniques. Some techniques, such as adhesive injection to repair delaminations, may prove to be sufficiently simple and reliable to be used relatively frequently. But in general frequent repair is unlikely to prove a cost effective way of controlling the effects of defects and damage and the design aim should be to keep the frequency and complexity of repairs to a minimum.

4 RAE EXPERIMENTAL PROGRAMME

4.1 General Objectives.

As indicated in Sections 2 and 3, it is observed that there is little data concerning the interaction of defects with certain structural features and that design for these effects tends to be of an ad-hoc nature. One of the major problems is that many structural features tend to be specific to particular designs so that the applicability of the available data is often difficult to assess. The objective of the RAE programme is therefore to investigate a limited range of defect/feature interactions and to assess the extent to which such interactions may be related to the effects of similar defects in plane panels subject to uniform stress.

Two types of structural feature which commonly occur in skin structure were selected for evaluation and these were tapered-thickness elements and cut-outs. The first of these features gives rise to interlaminar stresses and the second generates substantial in-plane stress concentrations. These features were subjected to impact damage since this is a primary concern for skin structure. Composite substructure was represented by an I-beam element loaded in 3-point bending. For this type of element, damage growth from manufacturing defects will probably be more significant since, being internal, it is both less prone to impact and more difficult to inspect.

4.2 Tapered Thickness Elements

The tapered-thickness specimens were manufactured from Fibrodex 914/XAS preimpregnate with a basic ply stacking sequence [(0,+45,-45, 90)_n]. This lay-up was selected since it contained the four

commonly used ply orientations in proportions which were not untypical of structures such as wing skins. The basic laminate contained 32 plies, plies 5 to 8 and plies 25 to 28 being discontinuous and therefore piviting rise to the taper. The laminates were cured on a flat plate so that, as will generally occur in practice, one face remained plane. Two plies were dropped every 5 mm to give a taper which was considered to represent about the most severe taper likely to be used in practice and which is considerably more severe than that used in wing skin designs such as that of the AV-8B.

Specimens were subjected to 5 Joule impacts from a 6 mm steel ball projected from a compressed air gun, the energy level being appropriate to a typical runway stone impact. The ball was fired perpendicular to the flat face producing damage which was barely visible from the impacting surface. The internal damage was roughly conical in shape as illustrated in Figure 2. The maximum area of delamination occurred near the rear face of the laminate and was about 30 mm diameter. Fractographic analysis of the damaged region showed that the shape of the delamination at each ply interface was a function of the fibre orientation in the adjacent plies. Delamination tended to spread along the axes of maximum stiffness so that the greatest area of damage tended to occur between orthogonal plies. The impacting sphere produced a small indentation on the surface which was visible to the naked eye but fibre fractures were not obvious. Microscopic examination revealed however, that there were a significant number of broken fibres, say a total of a few hundred, in the first two or three plies.

The initial results, presented in Table 1, show that under quasi-static tensile loading the undamaged taper has little effect on the strength of the specimen; the stress achieved in the material at the thinner end of each specimen reached about 75% of the material strength. The impact-damaged specimens achieved only about 85% of the material strength but it was observed that, in the absence of the taper, impact damage alone produced a similar drop in strength.

To ensure damage growth in the tensile fatigue tests, a high peak load was chosen, the aim being simply to compare damage growth from the impact at the tapered section with that from the impact in the thinner, plane section. A peak load equal to 80% of the static strength of the undamaged specimens was therefore chosen. Only two specimens have so far been tested, one of which contained impact damage. After 10,000 cycles the unimpacted specimen exhibited damage in the region of the taper across the full width of the specimen. Ultrasonic B-scans showed that most of the damage occurred at the ends of the discontinuous plies. After 100,000 cycles the damage had extended considerably towards the thicker end of the specimen as shown in Figure 3. Similar fatigue damage was observed at the taper of the impact-damaged specimen, as may be seen from Figure 4. However, there was no evidence of damage growth from either impact. Indeed a three-dimensional image of the damage at the taper after 10,000 cycles, which is illustrated in Figure 5 and was generated from about 50 separate B-scans, indicates that the presence of the impact damage may even have tended to inhibit the formation of fatigue damage at the ply discontinuities since the two forms of damage do not merge into each other. The most likely explanation for this effect is that the impact damage caused a local decrease in axial stiffness and that the axial stress at the centre of the specimen was therefore reduced. Penetrant-enhanced X-ray images tend to confirm this hypothesis since the cracking of the 90 degree plies, which is known to be a good indicator of local strain level, was considerably more severe at the free edges of the impacted specimen than at those of the unimpacted specimen whilst the cracking at the centre was much less.

The peak loads used in the above tests were sufficient to induce a strain of about 7900 micro-strain in the thinner end of each specimen, a level which corresponds to about twice the currently accepted DUL. A further impacted specimen was therefore subjected to 100,000 cycles at 4000 micro-strain after which no damage could be detected by ultrasonic C-scan. On the basis of the present evidence, it would therefore appear that under purely tensile loading to current design levels there is unlikely to be any structurally significant interaction between barely visible impact damage and tapered thickness sections. The static performance was limited by the impact damage but was not made worse by the presence of the taper, whereas the fatigue performance was limited by the taper and this was not made worse by the presence of impact damage.

In compression, it was necessary to stabilise the panels and so they were bonded to an aluminium honeycomb core to form column specimens as shown in Figure 6. The panels were oriented so as to keep the flat faces on the outside as would generally occur in practice. In order to maintain a constant core thickness, and hence simplify specimen manufacture, the face panels were rotated so that the thicker section on one face was opposite the thinner section on the other. Measurements of the lateral displacement under load demonstrated that the specimen remained stable up to failure and that the reversed orientation of the face panels did not give rise to any undesirable bending effects. Impact damage was produced in the same way as for the tensile specimens and, although the support conditions for the composite were slightly modified by the presence of the honeycomb, the damage was observed to be very similar. It was noted that the impact caused some local disbonding of the honeycomb core over an area of about 25 mm diameter.

At the time of writing there are few results available but it has been observed that impact damage reduced the compressive strength of the tapered specimen to about 66% of the strength of the undamaged specimen. This reduction in strength is consistent with the known effects of impacts on untapered panels² and resulted in a strain at failure of about 4900 microstrain in the thinner end of the specimen. Fatigue loading was again carried out at a peak stress of 80% of the strength of the impacted specimen so as to enable the comparison of damage growth in the plane and tapered sections. This load level gave rise to a strain of about 3900 microstrain in the thinner section which corresponded approximately to values currently associated with DUL. Figure 7, which has been prepared from a series of ultrasonic C-scans, shows the extent of damage both in the tapered and plane sections at various numbers of cycles. Perhaps surprisingly it may be seen that the damage at the taper appears to have grown less than that at the thinner section. During loading, out-of-plane deflection of the surface plies was monitored using a shadow moire technique and this proved to be a very effective indicator of the area of damage. This technique will therefore be used more extensively during the remainder of the programme to reduce the amount of effort deployed on ultrasonic scanning. After 5000

cycles the loading was terminated to allow detailed fractographic analysis. The damaged areas were studied by removing individual plies and recording the damage at each interface. An example of the damage observed by this method is presented in Figure 8, from which the area of delamination may be clearly seen. It was deduced that the damage growth occurred primarily between the +45 and -45 degree plies nearest the outer surface. Farther from the surface there was very little evidence of damage growth due to fatigue; the damage at each interface was observed to be remarkably similar to that of a specimen which had not been loaded. It would seem therefore that the damage grew only where significant out-of-plane deflection was possible and that the stabilising effect of the adjacent plies or the honeycomb was sufficient to prevent damage growth in the body of the laminate even though the original delaminated area may have been considerably greater than that near the outer surface. A second specimen also exhibited damage growth at both the tapered and the plane sections but failed at the taper after only 622 cycles.

To assess the extent to which the honeycomb may have inhibited damage growth in the above specimens it is proposed to test tapered-thickness panels using a panel buckling rig. Initial trials have been carried out on panels measuring 350 mm by 110 mm in which the ends were fully clamped and the sides were simply supported, giving a free area of 300 mm by 100 mm. The out-of-plane bending moment due to the presence of the taper caused significant lateral deflections as soon as load was applied and, whilst it is believed that the panels did not suffer conventional instability, there is little doubt that the deflections were sufficient to significantly affect local strains and panel strength. Quasi-static loading resulted in failure at an effective mid-plane strain in the thinner section of about 3700 microstrain. The significance of this single result is difficult to assess at this stage of the programme particularly since the lateral deflections were larger than expected and could be untypical of practical structures, but it is evident that further work is required.

4.3 Cut-outs

The panels used in this part of the programme were again manufactured from Fibredex 914/XAS preimpregnate and had a fibre lay-up [(0, +45, -45, 90)₅]s. The panels were tested in the buckling rig briefly described above. Measurements of lateral deflections showed that the panels did not buckle but the limited free area between the supports prevented the evaluation of cut-outs greater than about 25 mm diameter.

Panels with 25 mm circular cut-outs were subjected to 5 Joule impacts from a drop-weight having a 6 mm tip radius. This energy corresponds approximately to that of a heavy spanner (500 g) dropped through about a metre, the type of impact considered quite likely in the region of an access hole. It was found that if the specimen were supported on a solid block of CFRP the damage was concentrated within an area of about 10 mm diameter. Although such a test may not be regarded as fully representative, indeed the damage only spread half-way through the laminate thickness, it was thought that the small area of damage relative to the cut-out would allow a better evaluation of the significance of damage location.

Under quasi-static loading the undamaged panels failed at a field strain of about 5800 microstrain. Impact at the point marked A in Figure 9 resulted in no reduction in panel strength. At this impact location the primary stress is a tensile stress tangential to the edge of the hole and, in view of the limited effect of impact damage on tensile strength this result is perhaps not surprising. Impact damage at the point marked B in Figure 9 reduced the strength to about 90% of that of the undamaged panel. The limited magnitude of the effect is probably due to the aforementioned fact that the damage affected only half of the laminate thickness.

Compressive fatigue loading of damaged panels was carried out at a peak stress equal to 80% of the static strength. For the specimen impacted at point A (see Figure 9) the peak load gave rise to an overall strain of about 4600 microstrain but there was no damage growth from the impact. Instead, fatigue damage spread from the sides of the notch until after about 4000 cycles a relatively large delamination occurred near one face of the panel over the area indicated in Figure 10. A penetrant enhanced X-ray image confirmed that the impact damage and the fatigue damage were physically unconnected.

Impact damage at the point marked B in Figure 9 initiated fatigue damage growth (at an overall strain of about 4200 microstrain) as indicated in Figure 11 and after 1000 cycles there were also the first signs of fatigue damage on the opposite (unimpacted) side of the cut-out. It is of interest to note that, whereas in the tapered specimens the damage grew laterally under fatigue, damage growth from the impact damage at the compressive stress concentration due to the cut-out tended to grow along the specimen axis. This effect is almost certainly due to the localised nature of the compressive stress concentration.

The few results generated so far confirm that the significance of defects and damage associated with cut-outs is strongly dependent upon defect location. Due to test limitations the data are not quantitatively relevant to structural design and it is likely that the effects could be more pronounced in thinner panels, or with larger cut-outs, or with more severe damage.

4.4 I-beams

The I-beam specimen, which is illustrated in Figure 12, was manufactured from two Fibredex 914/XAS channel sections having a +45 degree fibre lay-up. The reinforcements at the loading points were co-cured with the channel sections and the channels were subsequently bonded back-to-back before finally bonding the tapered caps.

Under quasi-static loading failure occurred in the defect-free I-beam when the shear strain at the centre of the web was about 7500 microstrain. The measured strains indicated a small stress concentration at the point marked A in Figure 12 such that the shear strain reached about 8000 microstrain. These strain levels are considered reasonable since, in attempts to measure the shear properties of +45 degree CFRP, strains significantly greater than this are difficult to achieve due to the stress

concentrations associated with the method of load introduction. The failed beam is illustrated in Figure 13 from which it may be seen that damage occurred both in the shear web and in the cap which was subjected to compressive stress. Fractographic analysis revealed that failure was initiated by a bonding defect between the channel sections and the tapered cap. This defect was located at the mid-length of the beam at a point where the tensile stress across the bond would be high. In view of the relatively high shear strains measured in the web the reduction in failing load due to this defect may not be large. Nevertheless, the result emphasises the significance of defect location.

The defective beam contained artificial delaminations at the mid-plane of one of the two 8-ply channels used to form the I section. The defect locations are shown in Figure 12. This beam was subjected to fatigue at a load which generated a shear strain of about 4000 microstrain at the centre of the web and after 10,000 cycles ultrasonic scanning indicated no damage growth either from the artificial delaminations or in the region of the shear stress concentration. The load level was therefore increased so as to produce a shear strain of about 5000 microstrain in the web. After 10,000 cycles at this level there was still no evidence of fatigue damage either from the delaminations or from the shear stress concentrations. Clearly the defects considered here were not sufficiently severe to produce a significant effect suggesting that, where the composite element gives rise to a complex three-dimensional stress distribution, only a small proportion of the material may be critically stressed and therefore defect significance will be highly dependent upon location.

5 CONCLUDING REMARKS

The accommodation of the effects of defects and damage in current designs has not been achieved as a result of a coherent overall philosophy but through an ad-hoc approach necessitated by the lack of adequate data and understanding on the effects of defects on structural performance. The requirements for a more coherent approach have been briefly considered and some experimental observations related to the interaction of defects with structural features have been presented. In general, it is observed that the significance of defect location increases with the complexity of the stress field, and that the most significant interactions are likely to occur due to impact damage or delaminations in regions in which interlaminar integrity is important. Typically, these regions are likely to be in areas subject to high in-plane compressive or shear stress, or in areas subject to interlaminar stress or out-of-plane bending moments.

For experimental purposes, composite specimens and structural elements are usually subjected to carefully aligned uniaxial loads, but in actual structures pure uniaxial loading is relatively rare. In practice, most structural elements are subject to a variety of secondary loads and those will often give rise to interlaminar shears and out-of-plane bending moments. Even in defect-free structures it is possible that these secondary loads may cause discrepancies between the structural performance achieved and that predicted on the basis of data from accurately loaded test pieces. From the limited experimental evidence presented here it seems possible that in the presence of defects the significance of these secondary loads could be considerably increased.

In conclusion, it is evident that considerable research remains to be done before sufficient data, analytical techniques and general understanding have been generated to facilitate a fully coherent policy for the management of defects and damage in composite structures.

REFERENCES

- 1 J J Pengra Study of the influence of hole quality on composite materials. NASA CR 159257 (1980)
- 2 R M Verrette E Demutts Effects of manufacturing defects and in-service defects on composite materials. Presented at the Army symposium on solid mechanics 1976 - Composite materials; the influence of mechanics of failure on design. AMMRC MS 76-2
- 3 D E W Stone B Clarke In service NDI: an assessment of current requirements and capabilities. AGARD specialists meeting on Characterisation, analysis and significance of defects in composite materials. 12-14 April 1983.
- 4 D Puslow Some fundamental aspects of composites fractography. Composites 12, 241-247 (1981)

Specimen type	Stress in thin end at failure (MN.m)	Coefficient of variation (%)
Control (no taper)	555*	5.0*
Undamaged taper	532†	5.5†
Damaged taper	475†	6.8†
Damaged control (no taper)	463†	7.7†

* Based on 6 specimens

† Based on 3 specimens

Table 1 Tensile Test Results

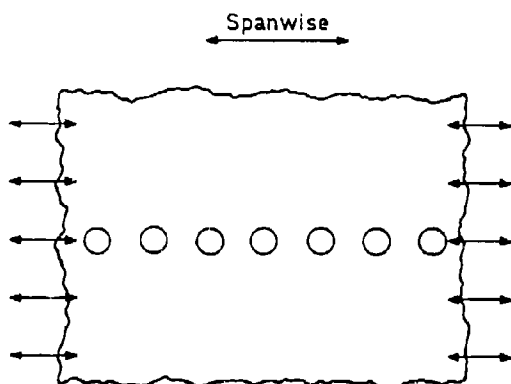


Fig 1 Typical wing skin element

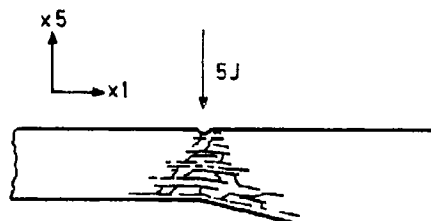


Fig 2 Impact damage

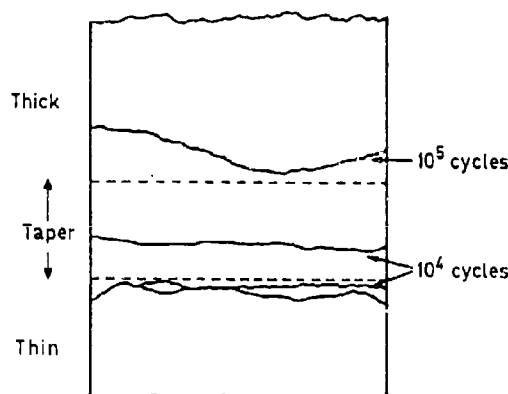


Fig 3 Tensile fatigue damage - unimpacted specimen

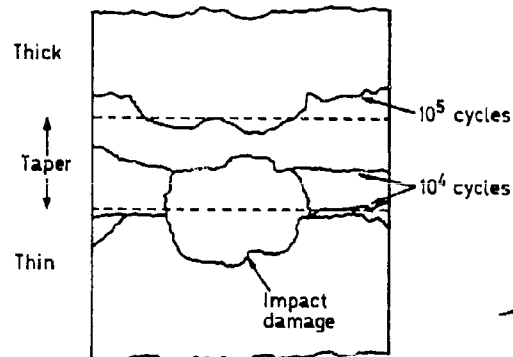


Fig 4 Tensile fatigue damage - impacted specimen

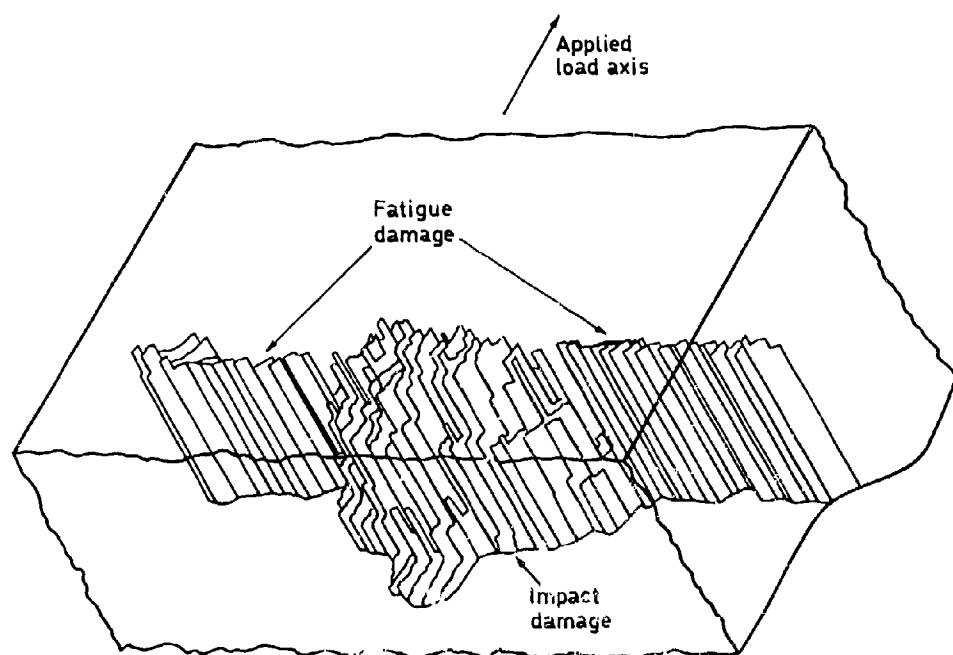


Fig. 5 Fatigue and impact damage

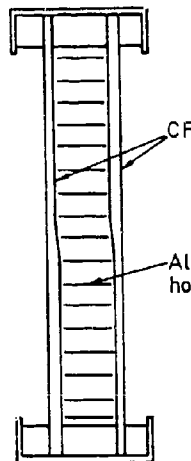
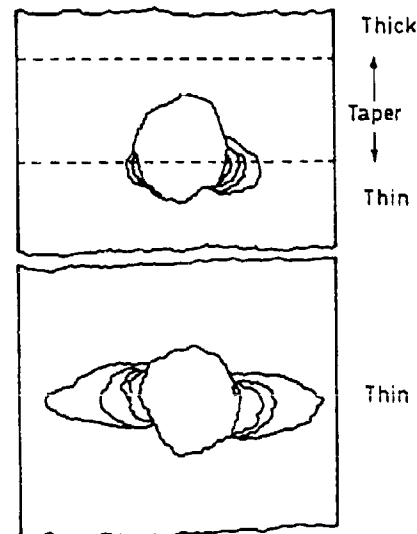


Fig. 6 Compression column specimen



Damage contours at 0, 500,
1000, 2500 and 5000 cycles

Fig. 7 Compressive fatigue damage - column specimen

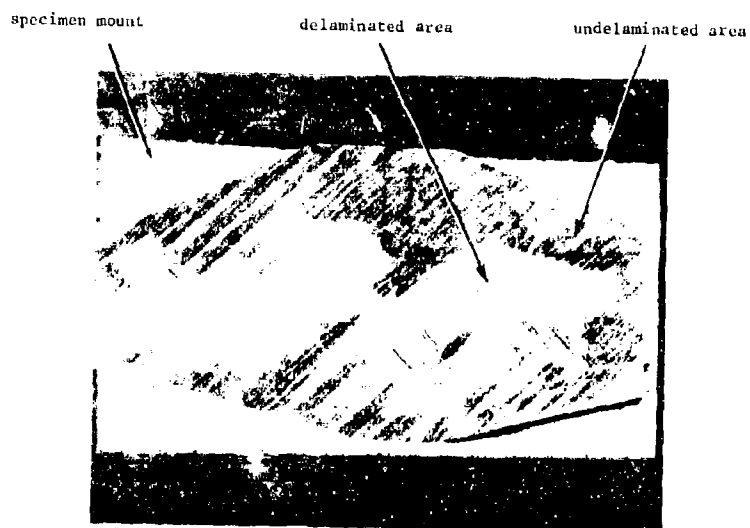


Fig 8 Delamination due to compressive fatigue

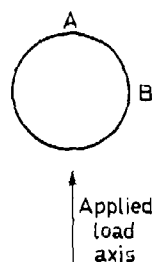
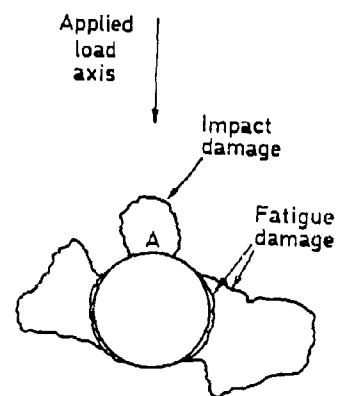
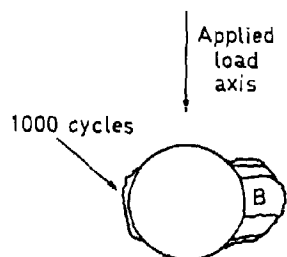


Fig 9 Impact locations



Damage contours at 0, 1000
and 4478 cycles

Fig 10 Fatigue damage at cut-out



Damage contours at 0, 100
and 1000 cycles

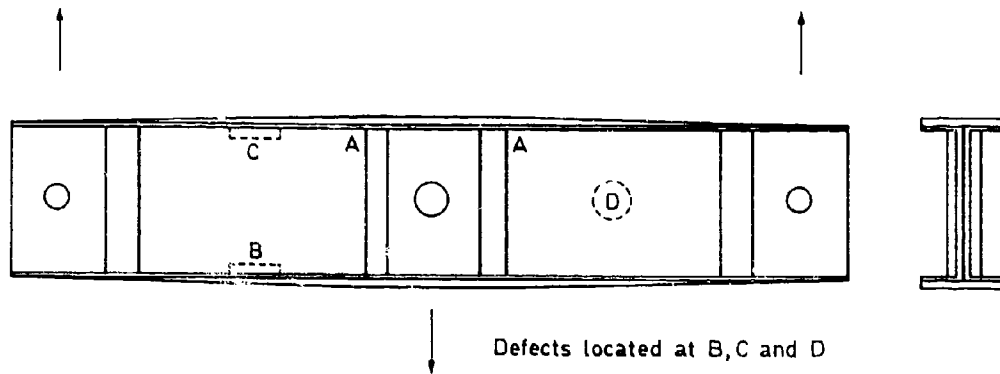


Fig 12 I-beam specimen

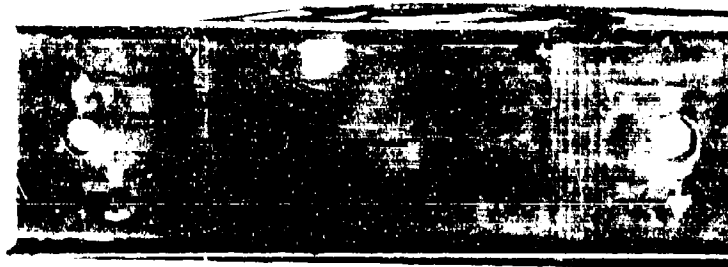


Fig 13 Failed I-beam



AD P 001924

IN-SERVICE NDI OF COMPOSITE STRUCTURES:
AN ASSESSMENT OF CURRENT REQUIREMENTS AND CAPABILITIES

by

D.E.W.Stone and B.Clarke
Royal Aircraft Establishment
Materials and Structures Dept.
Farnborough
Hants GU14 6TD

SUMMARY

Practical design criteria and the structural significance of defects and damage in carbon fibre composite components are briefly reviewed. Consideration is given to the principal sources of in-service damage and the possibility of the interaction of damage mechanisms. The concept of providing a map of damage acceptability for a given structure is then discussed.

An assessment is made of the probable current requirements for in-service NDI, the capabilities and limitations of currently available NDI techniques are reviewed and some recent developments described.

1 INTRODUCTION

Although the great majority of aircraft in service today were designed on a safe-life principle the ability to inspect for defects that have arisen in service is still a vital part of the airworthiness clearance procedure. This is because many components have been shown, by service experience or by structural fatigue testing, to be suspect and have to be treated on a damage tolerant (slow crack growth) basis. Furthermore, modern damage tolerant design philosophy requires a known inspection capability, since this forms an integral part of the clearance procedure, and considerable efforts are currently being expended on trying to quantify the probability of various defects being missed by inspection. All of this has, however, been developed for structures fabricated from metallic materials in which the failure processes are generally well understood. In addition there is a vast fund of service experience with metallic structures which can be drawn upon to assist in assessing the integrity of a given component. Furthermore, although defects caused by mechanisms such as corrosion or stress corrosion are of course important, in the majority of cases it is a fatigue crack that is sought. Indeed it has been suggested¹ that those fatigue cracks that initiate around highly stressed fastener holes are alone responsible for more than 50% of all aircraft structural failures (ie damage involving significant maintenance and repair penalties). Thus in broad terms the inspector knows what he is looking for and, at least for military aircraft, he is told where to look.

With structures fabricated from composite materials the situation differs in a number of important ways:

- i Essentially the material and the component are fabricated in the same operation so that not only is there often a greater probability that inherent flaws of a significant size will be present, but also any inspection will have to be performed on the finished component which may be of complex geometry.
- ii The types of defect induced both at the fabrication stage and in service have no direct counterpart in the metallic component.
- iii The significance of these defects in terms of their effect on the performance of various structural features is only now starting to be quantified.²
- iv There is only a very limited amount of service experience on advanced composites in primary structure.
- v Arising from (iii) and (iv) there could be a requirement for general survey techniques (in contrast to the past practice of only inspecting specified areas).
- vi Airworthiness certification procedures are still being developed^{3,4}.

In the light of the above it might be supposed that the introduction of composites into primary aircraft structure had resulted in some rather daunting NDI problems. It is of course difficult to generalise, and this paper will only address the problems of organic matrix composites, but it will be shown that the problems of inspecting these materials do appear at present to be much less serious than had been feared. Nonetheless considerable areas of uncertainty remain, and it is the object of this paper briefly to examine practical design criteria and current knowledge on the structural significance of defects, and in the light of these to consider both the possible, demand, for in-service NDI and the ways in which these demands might be met.

2 TYPES OF DEFECT ENCOUNTERED

2.1 Manufacturing Defects

It is possible at the manufacturing stage to introduce a number of anomalies which may or may not be regarded as defects. Several of these may be shown to affect the basic mechanical properties of the material, but despite this they often have little effect on the structural performance because the effect of the various structural features tends to dominate. For practical purposes, only the void content and degree of delamination need to be quantified. It has been suggested that fibre kinking may also need to

be detected, particularly where kinks in a number of plies are coincident (as may occur in the fabrication of angled sections), but the usual random distribution of fibre kinks would not appear to be of concern.

There is, however, one other important feature for which inspection procedures are required at this stage, and that is the integrity of adhesive bond-lines. First consider the adhesive bond between laminates; small delaminations are covered by the existing inspection procedures, but there is also the possibility that a complete release film could be left in place. The thick treated paper is readily detectable but the thin film (usually a polyester such as 'Melinex') is much harder to find, especially in thick sections. When considering bonds between sub-components there are really two situations. For co-cured components bond failures are of course effectively the same as delaminations, but when components are initially cured and subsequently bonded together the bond-line inevitably varies somewhat in thickness and usually some form of filled adhesive is employed. There is also the possibility of surface contamination or the use of different surface preparation procedures. Thus inspection procedures are required to detect bond failures and if possible to check that the bond strength is adequate.

2.2 In-Service Damage

In-service damage may result from static overload, fatigue, environmental effects, overheating (transient or continuous), impact or simple surface scratching; these effects may act singly or, as is more likely, in some complex combination. The resultant defects are, however, considered to be essentially straightforward and may be listed as follows:

a. Surface Scratches

These can of course have a variety of forms but the essential feature is that they break the fibres in the outer laminae.

b. Delaminations

These may occur under normal service loading at features where large stresses are generated normal to the plane of the laminate, but the usual cause of in-service delaminations is impact damage; this may or may not be accompanied by surface damage. If there is little or no surface damage then the term BVID (barely visible impact damage) is often employed; typical BVID is shown in Fig 1. It is also possible for overheating to cause delamination; thermal spiking of a laminate that has previously absorbed moisture is one example of this.

c. A High Density of Translaminar Cracking

A translaminar crack will be considered to be any crack running in the matrix, or fibre-to-matrix interface, parallel to the fibres. It will usually be confined to one ply (or block of plies having a similar orientation) and will be aligned approximately normally to the plane of the laminate. It is not considered that isolated translaminar cracks are structurally significant; here we are concerned with a high density of cracks.

d. Bearing Damage

This is local damage at fasteners which is of a complex nature but includes, fibre fracture. It will result in a reduction in stiffness of the joint.

e. Matrix crazing

This is possible with some organic matrices but is not usually encountered with epoxy resins.

f. Bond Failure

Weak bonds may not be detected at the manufacturing stage but fail under service loading. Such bonds could be composite/composite, composite/metal or composite/sandwich core.

It should be noted, however, that when damage of types (c) and (d) is severe enough to be structural significant it will probably be accompanied by some degree of delamination. This is important because it makes the detection of such damage a great deal easier.

The above comments are intended to relate to localised areas of damage that could occur during normal service and might need to be detected. There is, however, the possibility that a military aircraft could suffer much more serious damage, primarily from battle damage or from a severe lightning strike; such damage would of course be clearly apparent and the role of NDI would then be to delineate the area of non-visible damage in order that a repair scheme could be devised. It is not, however, envisaged that the NDI methods required would be significantly different from those considered for localised areas in Section 5, so that aspect of in-service damage will not be pursued further here.

3 PRACTICAL DESIGN CRITERIA AND THE STRUCTURAL SIGNIFICANCE OF DEFECTS.

As noted by Potter² much of the design to date has been somewhat ad hoc in nature and a considerable amount of coupon and structural element testing has been necessary in order to substantiate the design procedures. It is helpful to examine the basic design criteria for a component such as a wing box, in order to demonstrate the role of defects and to consider those that may need to be detected; these criteria are:

i Room temperature static notch tensile strength.

ii Elevated temperature notch compressive fatigue strength.

iii Local buckling.

iv Overall buckling.

In order to select the potentially most adverse condition criteria (ii)-(iv) are usually applied to material in an environmentally degraded condition.

Criteria (i) and (ii) are dealt with by defining an allowable overall strain of, say, 4000 micro-strain. It is anticipated that limiting the overall strain in this way to accommodate notch effects will also enable quite large defects to be tolerated. There is only limited data available to support this but at present such evidence as is available indicates that areas of essentially uniform overall stress can indeed tolerate defects of a type and size that would present no difficulty to NDI. Take for example surface scratches. It has been demonstrated³ that the major effect of a scratch on the static strength properties is simply to reduce the tensile strength approximately in proportion to the number of 0° plies that have been cut; a scratch 3 plies deep cutting two of the eight 0° plies in a 0 + 45° laminate still exhibited a failure strain of nearly 9000 $\mu\epsilon$. What has yet to be demonstrated, however, is whether such a scratch could, under fatigue loading, generate delamination damage which could result in an unacceptably low compressive strength. If this were the case then scratched areas would require more detailed monitoring in service.

The effect of impact induced delaminations on the strengths of uniformly stressed panels has been quite widely investigated but, because of the range of types of damage induced, and test specimens and materials employed, it is difficult to make a general statement on the size of delamination that can be tolerated in this situation. However, as a guide, one may use the results of Lebar⁶, who investigated the effects of impact damage on specimens subjected to fatigue spectral loading. For sandwich specimens both fatigued and residually strength tested in compression he found that severe (clearly visible) damage grew under fatigue loading, and some specimens failed within the two lifetimes of the test. Damage stated to be marginally visible, however, did not grow under fatigue loading, and specimens containing such damage exhibited residual strains of about 5000 microstrain. Ultrasonic inspection showed the damaged area to be about 15 mm diameter. He also tested some box beam specimens, however, and showed that even severe damage did not grow significantly under a load spectrum having maxima close to the theoretical buckling load. These specimens again exhibited residual strains of about 5000 microstrain, even though the damage zones were about 25 mm diameter.

In their considerations of static strength requirements for airworthiness Guyett and Cardwick⁴ suggest that for uniformly stressed areas of carbon fibre composite it may generally be assumed that:

i the effect of BVID is comparable to that produced by a notch;

ii the insertion of such a notch or damage produces proportionally no greater reduction in fatigue strength than in static strength (in the interaction between accidental damage and fatigue damage is not significant).

Probably more important, however, than the effect of defects in uniformly stressed areas is their effect when located at various structural features. It seems likely that they would be less tolerable at such locations and RAE has recently begun a programme to investigate this. Some data has already been produced² on the effect of impact induced delaminations on two structural features, one (a taper) giving rise to interlaminar stresses, and the other (a hole) generating in-plane stress concentrations. With some reservations it was demonstrated that the defects were tolerable, but it was emphasized how the presence of out-of-plane bending moments could drastically alter this. This has been confirmed by some recent tests elsewhere⁷ which showed how impact damage on a tapered section of a wing box skin reduced the static compressive strength by some 20%.

In the latter case the failure mechanism may in fact have been by local buckling. If so, then it might be an indication that the significant amount of post-buckled strength that is exhibited by composites, and which introduces a degree of conservatism into the overall buckling criterion, may not extend the same degree of protection to the local buckling case.

Clearly a great deal more needs to be done before it is possible to specify with confidence exactly what effect defects can have on the various structural features. At this stage therefore it can only be said that there may well be a need to monitor certain features with particular care, and this should be borne in mind when assessing the probable requirements for NDI.

The role of translaminal cracks is again not entirely clear. Isolated cracks may appear from time to time, but they have little structural significance. The case of possible concern is when concentrations of such cracks appear, usually at a stress concentration such as a notch or hole^{8,9}. In such a situation there are only part of a complex damage zone also involving delaminations and it is likely that only a general delineation of the extent of this damage zone will be required. However, examination of a radiograph enhanced by the use of a radio-opaque penetrant (Fig 2) shows that extensive translaminal cracking may extend beyond this zone or even appear independently. Such cracking may not be very significant structurally at this stage but its detection may nonetheless be desirable, since translaminal cracks are often the precursor to more serious delamination damage.

A somewhat similar situation occurs at fastener holes except that, additionally, bearing damage is possible. There does not appear as yet to be any evidence that such damage needs to be quantified separately, from the point of view of maintaining adequate structural strength; just as for the case of a simple hole, it is only the overall area of damage that will probably require to be known. It is, however, important to note that bearing damage will significantly reduce the stiffness of the joint and, should bearing damage occur at a number of fastener holes in one area, then the overall stiffness of the structure could be affected. This could result in an unacceptable change in the dynamic or aeroelastic

properties of the structure. The possibility of a requirement to provide a means of detecting such changes in service does not appear to have received much attention as yet, but it should not be ignored - particularly in view of the increasing importance of aeroelastic tailoring techniques.

4 REQUIREMENTS FOR IN-SERVICE NDI

The major function of all structural inspection procedures for aircraft is, of course, to assist in ensuring airworthiness, but it has to be recognised that the process of airworthiness certification is not fully established at present. It is therefore not wise simply to assess NDI requirements in the light of the clearance procedures currently being applied. It is quite possible that an increased understanding of the significance of defects, especially at structural features, may require these procedures to be modified quite significantly.

Now to apply strict damage-tolerant design procedures to composite structures would require considerably greater knowledge than exists at present of the degree of damage that can be detected, of the rate of growth of damage, and of residual strength in the presence of damage. Thus, at least for military aircraft in the UK, certification is done on a safe-life basis, but incorporating as many features as possible of the damage-tolerance concept³. In practice this means that the following sources of degradation have to be taken into account:⁴

- i Barely-visible impact damage (BVID);
- ii The possibility that repair patches may have to be bolted on;
- iii The reduction in residual strength due to fatigue.

These effects are combined in setting the design allowable strain and each structural member must be designed to this level, and thus be capable of sustaining BVID, loss of strength due to fatigue and the addition of fastener holes, occurring together in a realistic way. Some relaxation is possible if one or more of these effects could not occur in practice.

The acceptance standards applied for inspection at the manufacturing stage should therefore be designed to ensure that no defect is initially present that will prove more structurally detrimental than the standard notch (usually taken as about 6 mm diameter), or than BVID. It was, however, necessary in the past to set acceptance standards in the absence of much information on the significance of defects, and the standards which emerged were based largely on those defects that could be found with a reasonable (albeit unquantified) level of confidence by the available NDI techniques.

These standards vary from organisation to organisation but they concentrate almost entirely upon an assessment of the local void content and degree of delamination, together with an allowable spacing between defective areas, or between such areas and structural features or free edges. Present evidence would suggest that, for areas of reasonably uniform stress, these standards are proving more than adequate. As noted in Section 3, however, the situation with regard to the acceptability of defects as structural features is much less clear; in particular the role of fibre kinking requires further investigation.

Thus if clearance is obtained on a safe-life basis there is, strictly speaking, no requirement for further monitoring of these initial defects. What needs to be found are those defects that are created in service and which have a detrimental effect equal to or greater than the existing notches or BVID. The nature of these defects was considered in Section 2.2 and it was suggested that from the point of view of defect detectability (as opposed to defect characterisation) only surface scratches and delaminations need be sought. Furthermore Section 3 has shown that it is probable that, if impact-induced delamination is severe enough to be structurally significant, then it will also be accompanied by surface-visible damage. Thus it is clear that a great deal can be achieved by straightforward visual examination of accessible surfaces; once the presence of a defect has been detected other means may be employed to characterise it further. It has in fact been suggested that, for accessible components, visual examination alone may be sufficient to ensure the detection of all structurally significant defects that arise in service. It must, however, be recognised that delaminations can be generated by mechanisms which are not accompanied by surface damage; thermal spiking of environmentally degraded material has already been mentioned and fatigue loading could well cause delaminations to be initiated at other defects such as translaminar cracks. Indeed it has already been stated that translaminar cracks are most readily detected by means of the delaminations that they generate.

The extent to which these other mechanisms will occur in practice on a particular component is hard to quantify. Clearly there are many components to which thermal damage is most unlikely and it could well be that the other mechanisms will occur only rarely. At present it can only be stated that such situations could arise and that, even for uniformly stressed areas, the development of appropriate NDI techniques would be prudent. Such techniques would be complementary to visual inspection and would be designed to provide a means of rapidly scanning large areas of accessible structure with the primary aim of detecting quite large areas of delamination damage (say > 20 mm diameter).

Areas containing structural features, however, cannot be regarded in the same light. There is still considerable uncertainty as to the role of defects at many features and these should therefore be inspected much more carefully. In particular there is a need to know whether such defects are stable or whether there is a tendency for their severity to increase during service. Not only is such information required in order to ensure the safety of the particular component involved, but it can also provide an invaluable complement to the various programmes aimed at understanding the role of such defects. It is possible that the results of these programmes may indicate that more precise characterisation of the defects is required, such as the through-thickness position of a delamination, but at present some indication of defect magnitude should be sufficient. It should be a task of the design authority to identify areas or features that are regarded as being of primary structural significance.

Equally, until more confidence has been generated by testing and by service experience, there may be a case for designating certain areas as being of secondary structural significance. In this category would come, for example, areas containing known defects which had met the initial acceptance standards (or been granted concessions), or known areas of BVID. This damage would not be expected to grow, but it would be valuable to have confirmation of this. It is envisaged that the best way of documenting this for the inspector would be to prepare a defect map at the manufacturing stage, which could be modified as required in service. The relevant NDI techniques would, of course, be accordingly either less stringent than those for the primary areas or would be applied at less frequent intervals.

Thus on the evidence available it would appear that the NDI requirements will vary quite widely from area to area and a brief summary of these requirements is presented in Table 1.

5 GENERAL INSPECTION TECHNIQUES FOR COMPOSITE MATERIALS

Before considering techniques specific to in-service requirements it may be useful to review those that have been, and are currently being, used to inspect composites. Initially two conventional techniques, ultrasonic inspection and x-radiography, were applied with differing degrees of success. Although radiographic inspection is the preferred technique for GRP, its use on GFG fabricated from pre-preg material is usually limited to those geometries where the defect orientation can be presented parallel to the X-ray beam. Insufficient changes in density result from defects presented normal to the beam and therefore in many cases the interlaminar defects (delaminations and interply porosity) of GFG are not detected by conventional X-radiography.

Ultrasonic techniques, however, are particularly sensitive to defects aligned normal to the interrogating beam and as a result are the most widely used inspection methods for production inspection of GFG components. Of the many options for presenting the ultrasonic response to anomalies at interfaces the most common method is the now familiar C-Scan. This method presents a plan-view display of defect area obtained by selectively gating the time domain signal of a conventional ultrasonic flaw detector and monitoring the amplitude of a specific echo. If the back-wall echo is monitored then delamination produces a marked reduction in signal amplitude as shown by the light area in Fig 3(a). If however, the gate is positioned between the front and back-echoes then there is only a signal within the gate when delamination is present. Higher frequency interrogation is usually necessary in order to obtain the required resolution; the delamination is now revealed as a dark area and Fig 3(b) shows the increase in discrimination. The total attenuation through the thickness of the component may be displayed in this way, or selected depths may be gated to inspect a particular bond line for example. However, to evaluate through thickness defect position for the multi-layer defects such as those associated with BVID would be extremely tedious and difficult to interpret by this method; for this reason a complementary presentation of data is preferred. The B-Scan (Fig 4) presents through-thickness defect position in the form of a cross-sectional slice through the composite. A combination of both B & C-Scan information can be particularly advantageous as has been shown by Potter² for a specimen subjected to fatigue loading following impact damage. Other ultrasonic techniques in both the time and the frequency domain are currently in use and there are various possibilities of combining complementary data to provide far more information than is obtainable from any single technique.

These then, briefly, are the two principal inspection techniques for composite quality control and production component monitoring. Other techniques considered and applied with varying degrees of success have included:

- 1 Optical holography
- 2 Resonance/Impedance plane bond testers
- 3 Vibration and/or mechanical damping methods
- 4 Acoustic emission
- 5 Thermography
- 6 Body currents
- 7 Neutron radiography
- 8 Positron annihilation

Clearly there would be practical difficulties in applying some of these methods in service, but it will be shown in the next section that others do show promise.

6 IN-SERVICE INSPECTION METHODS

It has been suggested in Table 1 that the in-service NDI requirements may conveniently be divided into three tasks. These tasks will however, probably only require two different standards of NDI equipment because the difference between tasks 2 and 3 lies not in the sensitivity or discrimination capabilities of the technique, but the structural significance of the feature and hence in the required frequency of inspection. In-service NDI methods may therefore be considered under two broad headings:

- i Rapid survey methods;
- ii Localised inspection methods.

It must however be recognised that the second heading potentially covers a wide range of methods varying from simple defect detection to sophisticated characterisation. It is to be hoped that the former

will be sufficient for airworthiness purposes but the latter may nonetheless be desirable from time to time since it can provide very valuable information on the true behaviour of defects in service. In this way information gained from the first generation of composite military aircraft structures may be used to optimise designs for second generation aircraft.

Some of the most promising methods will shortly be discussed in more detail, but Table 2 is an attempt to summarise the capabilities of all those methods that are at present considered capable of in-service application. The defects considered are those listed in section 2.2 and it is important to note that the detection of defects (c) and (d) (high density transplaminar cracks and bearing damage) is taken to be required at a stage when they are not yet structurally significant, and hence not accompanied by delamination damage.

6.1 Rapid Survey Methods

Here we are primarily looking for quite large areas of delamination; this will include BVID but damage may also be induced by other means. The most likely current options are the following:

6.1.1 Roller Probes

The use of ultrasonic techniques employing roller-probes has the great attraction that no couplant is required. One such technique which appears promising is the Balteau-Sonotest "shadow technique" in which two ultrasonic roller-probe transducers are mechanically linked, one a broad-band transmitter, the other a selectively filtered narrow-band receiver. The use of adjustable filtering allows various defect types to be detected (and possibly identified) over a range of component thicknesses. The system is capable of detecting what is currently regarded as significant BVID at a reasonable scanning speed but the technique is unlikely to detect single delamination or skin-to-substructure disbonds.

6.1.2 Multi-element Transducers

A unit derived from the medical ultrasonics field has been developed by Diagnostic Sonar Ltd at the request of BAE (Warton); it is comprised of a hand-held transducer containing 84 crystals which are sequentially pulsed, the response being displayed in the B-scan format on a storage oscilloscope (Fig 5). This unit is currently undergoing evaluation at Warton where it has demonstrated a capability to detect the minimum defect size (3 mm) simulated in samples of CFC used as C-scan production inspection standards. Because of its higher operating frequency (5 MHz) this technique offers improved resolution compared to roller-probes and is capable of resolving and positioning a single delamination or disbond. It does however, have the disadvantage of requiring some form of couplant.

6.1.3 Thermal Pulse Video Thermography

This technique which is still in the research stage at AWE Harwell, offers the possibility of providing a rapid, contact free, couplant free method. Essentially it displays the rate of thermal diffusion in the composite when subjected to a fast high intensity thermal pulse. An image of the thermal pattern at the surface of the component is displayed on a monitor and stored on video tape. The latter is a very important feature because the response is transient and a slow replay facility allows the technique to be used more effectively. In addition image processing procedures may be used to enhance the method. Defects in the form of interlaminar BVID have already been shown to be detectable but the resolution capability of the technique at various depths remains to be evaluated. Preliminary results on representative CFC specimen seem to indicate a sensitivity to near surface (ie < 2 m) defects equivalent to production ultrasonic C-scan capability (Fig 6).

6.1.4 Impact-Sensitive Coatings

As was discussed in section 3, sub-surface damage produced by accidental impacts is often accompanied by a degree of surface damage. This is of course extremely helpful because it gives a readily detectable indication of those areas requiring closer inspection. It is, however, not yet possible to be certain that impact damage that is severe enough to be structurally significant will always be accompanied by such a surface indication. It is therefore very attractive to consider the possibility of providing some form of impact-sensitive "witness coating" which would clearly indicate that an impact had occurred. It might even be possible to relate the indication to the degree of BVID, but this is less likely because the damage resulting from a given impact is strongly dependent on factors such as skin thickness and the nature of support provided by the sub-structure.

Some preliminary work has been done in the UK using a coating containing a micro-encapsulated dye, but the results so far are rather inconclusive.

6.2 Localised Inspection Methods

6.2.1 Meccanronics In-situ Ultrasonic Scanner

For known defective areas, or when an area of possible BVID or delamination has been detected by one of the rapid scan techniques, a small portable C-scan frame as shown in (Fig 7) may be used. This can be fixed to the structure in any plane by means of suction pads and using a gimballed contact transducer is capable of following aerofoil curvatures and producing a hard copy C-scan. The unit which is light, portable and compatible with existing RAF ultrasonic equipment is capable of producing a scan approximately 20 cm x 30 cm and, using a 5 MHz transducer has a resolution equivalent to that of production inspection ultrasonics. One drawback is the requirement for a thin gel couplant but, since this would only be necessary over relatively small areas at defined locations, it is not expected to cause any difficulty. Data could be stored on a small computer if desired, this could then be accessed during subsequent inspections so that any defect growth would readily be apparent. Such a unit could also be used to record repair integrity.

6.2.2 Penetrant Enhanced X-Radiography (PEXR)

As previously stated the use of conventional radiography is limited to gross areas of damage or defects in preferred orientations. By using some form of radio-opaque penetrant, however, radiography can be made to be probably the single most sensitive inspection technique for composites. Fig 8, shows the detail of damage in composites obtained by this technique using zinc iodide as the heavy metal in an iso-propanol solvent carrier. A range of possible organic and inorganic penetrants is also currently being assessed for RAE to find the best compromise of sensitivity, ease of handling and chemical inertness in the presence of matrix resins. Of the techniques evaluated so far PEXR offers the most promise for the detection of matrix cracking, high density translaminar cracking and bearing damage that precedes delamination. Detectability of course depends on access for the penetrant through a free edge. The requirement to detect these minor forms of damage is, as stated, perhaps debatable. However, if the objective of assessing the significance of defects is to be realised, then it is through techniques such as PEXR that most information will be obtained.

6.2.3 Eddy Currents

Some previous work has indicated that the use of high frequency (12 MHz) Eddy currents could be informative on CMC components. Mead and Dingwall¹³ found that material up to 8 mm thick could be inspected and they demonstrated an ability to detect through thickness cracks which had previously been monitored by Acoustic Emission and which were subsequently confirmed using high frequency ultrasonics. The attraction of the eddy current method is that, like PEXR, it gives information on defects aligned in the through-thickness direction (translaminar cracks) but does not require access from a free edge. It is hoped that further work in the near future will establish the viability of this technique.

6.2.4 Bond Testers

Commercially available bond testers such as the Inspection Instruments Acoustic Flaw Detector are currently used on CMC production components. In this technique the amplitude and phase response of a resonant transducer are monitored and it has proved particularly useful for checking the integrity of the bond between composite skins and honeycomb sub-structure. The main attraction of this form of bond tester is that there is no requirement for couplant and there is also the possibility of producing a 0-scan presentation in a scanner perhaps similar to that mentioned in section 6.2.1. Disadvantages seem to be the limitations as to thickness that can be inspected in CMC and the inability to detect delamination of the BVID type.

7 EFFECT OF PAINT SCHEMES

The possible effects of paint schemes on the ability to detect BVID is currently being evaluated. Care must be taken not to allow conventional paint strippers to degrade the composite matrix therefore it will probably be necessary to inspect without removing the paint layer. Tests so far have involved the ultrasonic inspection of composite samples with BVID; some untreated, some painted and some weathered. No significant difference in response was found, the BVID was readily detected in all three cases. However, yet to be established are the effects of impact on the painted surface. Certain questions remain to be answered:

- a. Does the painted surface degrade or enhance the ability to visually inspect for impact damage?
- b. If a paint delbond is caused during impact will this or subsequent degradation of the bond create significant difficulties in interpretation?

8 CONCLUSIONS

8.1 For Uniformly Stressed Areas

- a. If impact-induced damage is severe enough to be structurally significant then it will usually be accompanied by visible surface damage, but NDI may still be required to assist or confirm visible indications.
- b. Other sources of damage are possible; these will, in general, not be accompanied by visible surface damage and NDI would be required if these mechanisms are considered likely.

8.2 For Structural Features

- a. The role of defects at such locations is less well understood and they should therefore be inspected more carefully.
- b. The design authority should be called upon to identify areas or features that are regarded as being of primary structural significance.

8.3 For All Areas

Until more confidence has been generated by testing and by service experience:

- a. Areas of secondary structural significance should be designated. These would largely consist of areas containing known defects that are considered acceptable, but occasional NDI would be advisable to confirm this.
- b. A defect map should be provided and updated.

c. Every opportunity should be taken to use NDI to monitor potential damage growth, even when this is not a safety requirement.

8.4 There is a need for two main types of NDI:

- a. Rapid survey methods primarily to detect large delaminations (20 mm diameter).
- b. Localised inspection methods to provide more detailed characterisation.

8.5 Equipment is already available that can largely satisfy the above requirements although for the former an increase in both the speed and convenience of operation would be an advantage.

8.6 The possibility of a future requirement for NDI equipment that is capable of more detailed characterisation than is currently demanded should be borne in mind.

REFERENCES

- 1 P J Klaus Non-destructive Evaluation Effort Grows. Aviation Week and Space Technology 59-65, February 1976
- 2 R T Potter The Significance of Defects and Damage in Composite Structures. AGARD Specialists' meeting on characterisation, analysis and significance of defects in composite materials 12-14 April 1983.
- 3 P R Guyett A W Cardwick The Certification of Composite Airframe Structures. The Aeronautical Journal of the Royal Aeronautical Society 188-203 July 1980
- 4 P R Guyett A W Cardwick Design Philosophies with Non-metallics - The Airworthiness Viewpoint RAE TM Structures 1017 (1982)
- 5 C S Frame The Effects of Surface Scratches in CFC Laminates. British Aerospace (Warton) Report SOM(P) 131 November 1982
- 6 J D Labor Impact Damage Effects on the Strength of Advanced Composites Non-destructive Evaluation and Flaw Criticality for Composite Materials. ASTM STP 696 Ed R B Pipes, 172-184 (1979)
- 7 British Aerospace (Kingston) Private communication
- 8 R T Potter On the Mechanism of Tensile Fracture in Notched Fibre Reinforced Plastics. RAE Technical Report 77023 (1977)
- 9 Sarah M Bishop Deformation near Notches in Angleplied Carbon Fibre Composites. RAE Technical Report 77093 (1977)
- 10 J Dickson General Description of the Sonatest Shadow Technique NTIAC Newsletter Vol 7 No 9 March 1980
- 11 W N Reynolds G Wells Video Camera Thermography AERE Harwell Technical Report to be published.
- 12 A T Johnstone I F Paterson N Evans A witness coating for carbon fibre reinforced plastic tubes Tech Report No BM JV-TR-927-1981 BAEVickern Ltd
- 13 P F Dingwall D L Mead Non Destructive Inspection and Volume Fraction Determination of CFRP using an Eddy Current Method RAE Technical Report No 76078

ACKNOWLEDGEMENTS

The Authors wish to express thanks to those concerns supplying material for the following figures: BAE Warton (Fig 5), AERE Harwell (Fig 6) and Meccanomics Ltd (Fig 7).

SUMMARY OF CURRENTLY ENVISAGED NDI REQUIREMENTS

AREA	REQUIREMENT
All accessible areas	Rapid survey methods, primarily to detect delaminations < 20 mm diameter
Areas of secondary structural significance	Intermittent monitoring of either i defined features to detect defects and/or ii known defects to detect growth.
Areas of primary structural significance	Regular inspection of defined features i to detect defects ii to assess defect magnitude and/or to monitor growth (The possibility of a future requirement for more detailed characterisation should be borne in mind.)

Table 1

A SUBJECTIVE ASSESSMENT OF TECHNIQUES FOR THE IN-SERVICE INSPECTION OF CARBON FIBRE COMPOSITE

In-Service Defect	Ultrasonics								Thermography	Penetrant enhanced X-radiography	Bond testers Resonance/Impedance	Eddy currents	Visual inspection	Impact sensitive coatings	Dye/W penetraants	
	A-Scan	B-Scan	C-Scan (in-situ scanner)	Spectroscopy	Roller-probes	Shear wave	Surface wave									
a. Surface scratches and cracks	-	-	-	-	-	-	✓	-	✓	-	✓	✓	-	-	✓	
b. Delaminations BVID	✓	✓	✓	✓	✓	✓	-	✓	✓*	?	?	-	?	-	-	
c. High density trans-lamellar cracking	-	-	-	-	-	?	-	-	✓*	-	?	-	-	-	-	
d. Bonding damage	-	-	-	-	-	?	-	-	✓*	-	?	-	-	-	-	
e. Matrix crazing	-	-	-	-	-	-	-	-	✓*	-	-	-	-	-	-	
f. Adhesive bond defects																
i. Failures	✓	✓	✓	✓	?	-	-	✓	✓*	✓	-	-	-	-	-	-
ii. Quality	-	-	-	✓	-	-	-	-	-	-	-	-	-	-	-	-

* Dependent on access to free edge.

? Possible but unproven.

Table 2

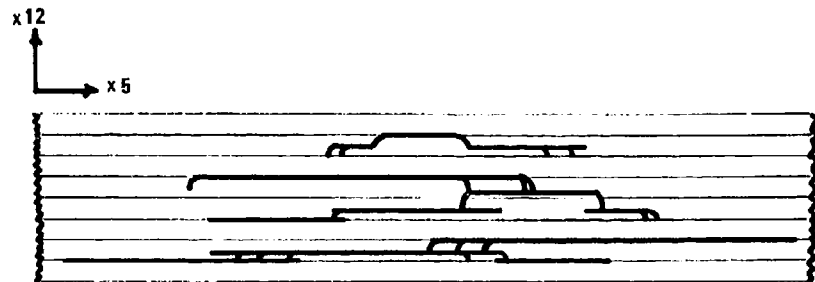
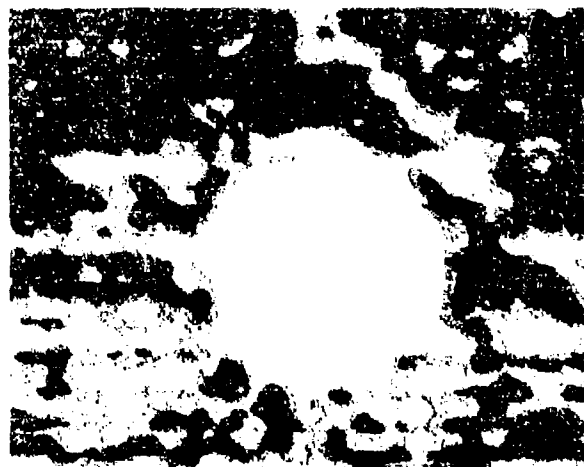


FIG 1 SCHEMATIC OF BVID SHOWING MULTIPLE DELAMINATIONS



FIG 2 TRANSLAMINAR CRACKS REVEALED BY PENETRANT ENHANCED RADIOGRAPHY



a. GATE POSITIONED ON BACK WALL ECHO



b. GATE POSITIONED BETWEEN FRONT AND BACK ECHOES

FIG 3 G-SCANS OF BVID SHOWING DIFFERENT METHODS OF DATA PRESENTATION

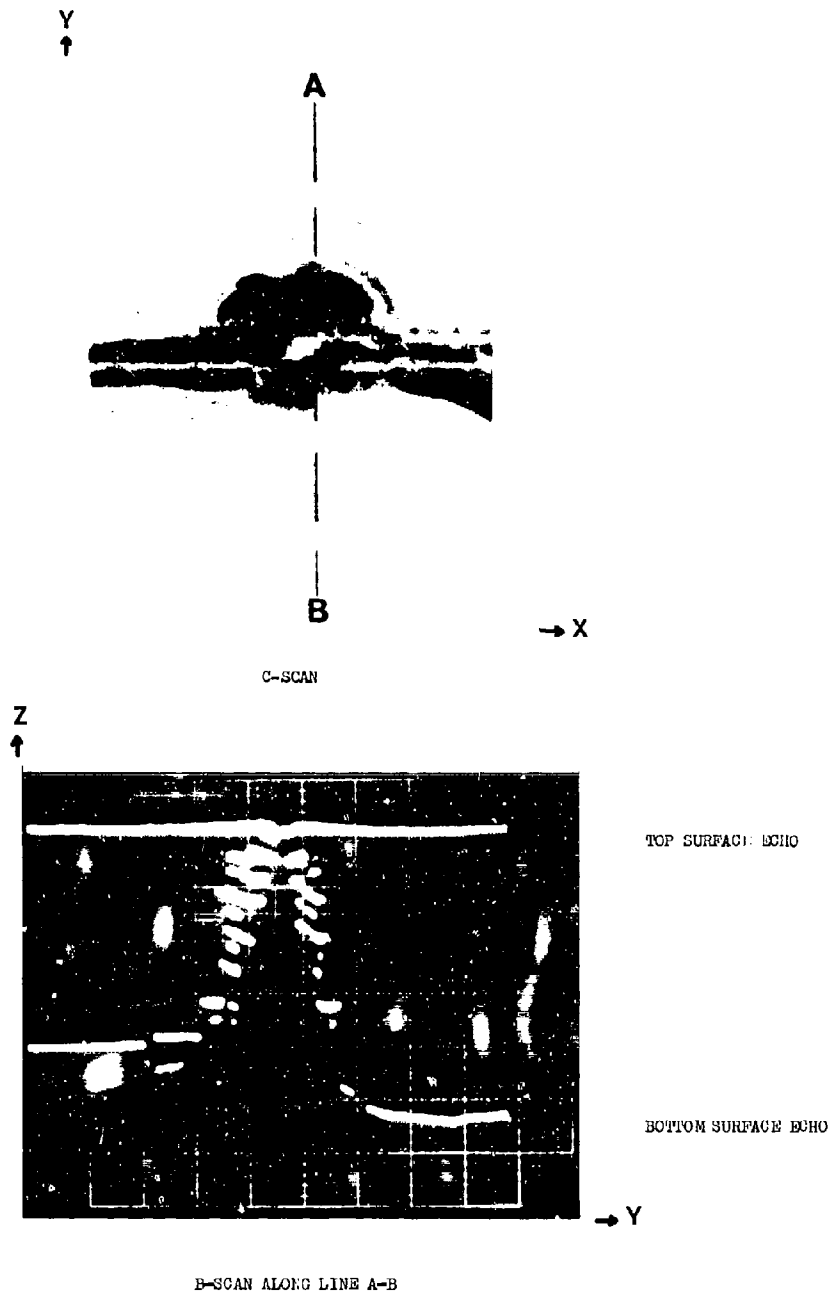


FIG 4 COMPLEMENTARY PRESENTATION OF ULTRASONIC DATA FROM IMPACT DAMAGE AT A TAPERED SECTION

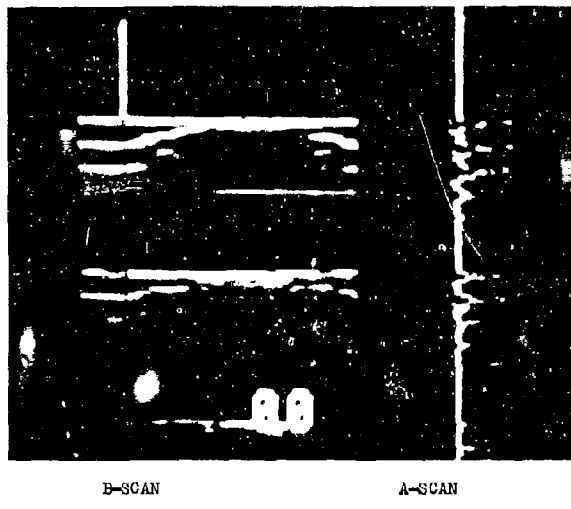


FIG 5 DISPLAY OF EVID BY DIAGNOSTIC SONAR EQUIPMENT



FIG 6 THE USE OF THERMOGRAPHY TO REVEAL EVID IN A
3 mm THICK LAMINATE

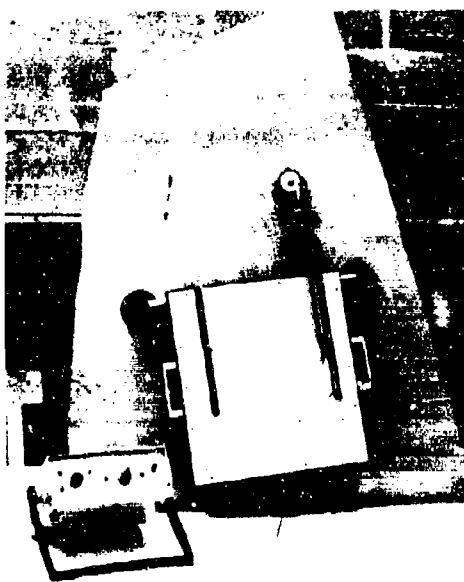


FIG 7 MECCASONICS IN-SITU ULTRASONIC SCANNER



FIG 8 THE USE OF PEAK TO REVEAL DAMAGE IN A SPECIMEN IMPACTED AND THEN FATIGUE LOADED

AD P 001925

19-1

EFFECT OF DEFECTS ON AIRCRAFT COMPOSITE STRUCTURES

by

R. A. Garrett
Branch Chief, Technology
McDonnell Aircraft Company
P. O. Box 516, St. Louis, Missouri 63166
USA

SUMMARY

This paper describes the effects of manufacturing and service-induced damage on the static and fatigue strength of aircraft composite structures.

Seven manufacturing defects associated with mechanical fasteners were investigated; out-of-round holes, broken fibers on the exit side of drilled holes, porosity, improper fastener seating depth, tilted countersinks, interference fit, and multiple fastener installation and removal cycles. Both static and fatigue test results are described, along with correlation with analysis techniques. The interaction of the effects of these defects on hole wear, measured in fatigue tests of structural joints, is described.

The effects of two types of service-induced damage are also described; low energy impact damage and 23mm HEI ballistic damage. The relative sizes of visible and non-visible damage as determined by visual and non-destructive inspection techniques are compared. An evaluation of stitching and the inclusion of glass or Kevlar fiber buffer strips to improve the damage tolerance of carbon/epoxy structures is included. Results of tests of carbon/epoxy panel structures are discussed. Correlation of experimental results with predicted residual static strength is good.

LIST OF SYMBOLS

C	- compression
d	- diameter
e	- edge distance
E_a^b	- extensional modulus measured in the "a" direction due to "b" loading
ETW	- elevated temperature test with prior specimen moisture conditioning
pbru	- ultimate failing bearing stress
G	- shear modulus
LEID	- low energy impact damage
N	- number of fatigue cycles
NDI	- nondestructive inspection
Nxy	- shear load intensity
N_{xy}^{cr}	- shear load intensity at initial buckling
R	- fatigue load ratio; minimum load divided by maximum load
RT	- room temperature
RTD	- room temperature test with no specimen moisture conditioning
RTW	- room temperature test with specimen moisture conditioning
T	- tension
w	- specimen width
ϵ_a^b	- strain measured in the "a" direction due to "b" loading
ϵ^u	- ultimate failing strain
AS/3501-6 (typ.)	- material system nomenclature for type AS carbon fibers in a 3501-6 epoxy resin matrix
50/40/10	- laminate nomenclature in which the three numbers describe the percent of plies oriented in the 0°, +45° and 90° directions, respectively; i.e., 50% of total number of plies are oriented in the 0° direction, 40% of the plies are oriented in the +45° directions and 10% of the plies are oriented in the 90° direction.

1. INTRODUCTION AND BACKGROUND

Future aircraft will require airframes that are lighter weight, easier to maintain and more durable than current construction approaches and materials. The use of composite materials in primary structures offers promise of significant weight savings, due to their greater specific static strength and even larger improvement in fatigue strength. However, proof of the ability of composite structures to be tolerant of both initial manufacturing defects and damage induced by service usage was necessary before their application to aircraft primary structures.

Programs to evaluate the damage tolerance of composite structures have been initiated by several different agencies under the Department of Defense. Each of these programs have been directed towards a different aspect of the subject area; this paper summarizes some of the work performed by the McDonnell Aircraft Company in each area.

The effect of manufacturing defects on the static and fatigue strength of laminates with loaded and unloaded fastener holes was conducted in Reference (1) program and is described in Section 2. The effect of low energy impact damage on composite structures was included in several programs with the United States Navy (References 2, 3, and 4); the results are described in Section 3. Finally, the effect of ballistic damage caused by 23 mm high-explosive projectiles conducted in conjunction with Reference (2) program is described in Section 4.

2. MANUFACTURING DEFECTS AT FASTENER HOLES

The effects of several types of manufacturing defects commonly found in aircraft structures were investigated under Reference (1) program. This investigation was performed using laminates with loaded fastener holes, a common critical structural design feature in aircraft composite structures. In many cases, tests were conducted with specimens in which the defect or anomaly was more severe than expected from current manufacturing processes. In all cases, defects which resulted in strength reductions greater than 15% would have been detected using current industry inspection techniques and would have been rejected or repaired to meet current acceptance criteria.

Tests were performed to determine the effects on static strength, compared to baseline specimens, and the effects on fatigue strength and hole wear.

(a) Static Strength - The effect of seven manufacturing defects on static strength was evaluated by comparing static strength of joints with a particular defect with the static strength of baseline joint specimens with no defect. The test matrix is presented in Figure 1.

Anomaly		Number of Tests Per Environment			Total Specimen Tests
		RT (Dry) Tension	RT (Wet) Compression	ET (Wet) Compression	
1. Out-of-Round Holes "1" Laminate (50/40/10) "2" Laminate (30/60/10)		4 4	- -	- -	4 4
2. Broken Fibers on Exit Side of Hole Severe Delamination Moderate Delamination		4 4	4 4	4 4	12 12
3. Porosity around hole Severe Porosity Moderate Porosity		4 -	2,2  2,2 	4 4	12 8
4. Improper Fastener Seating Depth 80% of Thickness 100% of Thickness		4 4	-- --	-- --	4 4
5. Tilted Countersinks Away from Bearing Surface Toward Bearing Surface		4 4	- -	4 4	8 8
6. Interference Fit	Layup				
	0.003 in. 1 2	4 4	- -	4  4	8 8
0.008 in. 1 2	4 4	- -	- -	4 4	8 8
7. Fastener Removal and Reinstallation 100 Cycles		4	-	4	8
				Total	116

 After freeze-thaw cycling

 Tension tests

QPA-80117-3

Figure 1. Evaluation of Manufacturing Anomalies - Test Matrix

Specimens were tested to failure in tension and compression at three environmental conditions: room temperature dry (RTD), room temperature wet (RTW), and elevated temperature wet (ETW). ETW tests were conducted at 250°F with specimen moisture contents of approximately .80 percent by weight. Hercules AS/3501-6 carbon/epoxy was used for fabrication of test specimens.

Results from tests are summarized in Figure 2. Indicated percentages of increased or decreased strength are based on a comparison with baseline specimens. Detailed results are discussed below.

	RTD TENSION	COMPRESSION	
		RT Δ	250°F Δ
OUT-OF-ROUND HOLES			
• 50/40/10 LAMINATE	+	—	—
• 30/60/10 LAMINATE	-4.8	—	—
BROKEN FIBERS EXIT SIDE OF HOLE			
• SEVERE	-7.3	-8.4	-9.2
• MODERATE	-1.4	-3.2	-4.2
POROSITY AROUND HOLE			
• SEVERE	+	-10.3	-30.6
• SEVERE WITH FREEZE-THAW	—	-11.6	—
• MODERATE	—	-7.1	-13.3
• MODERATE WITH FREEZE-THAW	—	-6.4	—
IMPROPER FASTENER SEATING DEPTH			
• 80% THICKNESS	-16.4	—	—
• 100% THICKNESS	-34.3	—	—
TILTED COUNTERSINKS			
• AWAY FROM BEARING SURFACE	+	—	-16.7
• TOWARD BEARING SURFACE	-21.4	—	-16.7
INTERFERENCE FIT TOLERANCES (INCH)			
• 50/40/10 ± 0.003	+	—	+9.1 Δ
± 0.008	+	—	+9.1 Δ
• 30/60/10 ± 0.003	+	—	• Δ
± 0.008	+	—	• Δ
FASTENER REMOVAL AND REINSTALLATION			
• 100 CYCLES	+	—	-8.3

Δ 0.86% moisture content Δ Tensile loading *Less than 2% change - No test GP13-011B-10

Figure 2. Strength Reduction Summary

Out of Round Holes - Effects of out-of-round holes on joint strength were evaluated by drilling offset (.004 inch) holes as shown in Figure 3. Test results of specimens from two laminates (50/40/10 and 30/60/10, where #0*plies/#45°plies/#90°plies are denoted in that order) indicated little sensitivity to out-of-round holes.

Broken Fibers on Exit Side of Hole - Specimens were tested for two conditions; "moderate" delaminations and "severe" delaminations. In order to obtain the various degrees of delamination, drill procedures included use of dull bits without backup material, and improper drill and feed speeds.

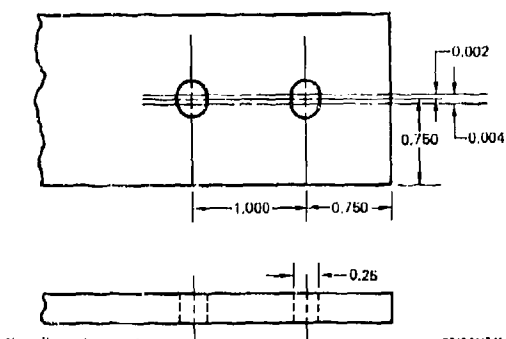


Figure 3. Out-of-Round Holes - Specimen

Delaminations were detected visually and with ultrasonic C-scan. Delaminations were defined as "moderate" when they extended 10-20 percent (2-4 plies deep) into the laminate thickness on the exit side. Delaminations were defined as "severe" when they extended 20-30 percent (4-6 plies) of the laminate thickness on the exit side. Non-destructive C-scans in the area of the fastener holes with moderate and with severe delaminations are illustrated in Figure 4 and compared with a nominal condition.

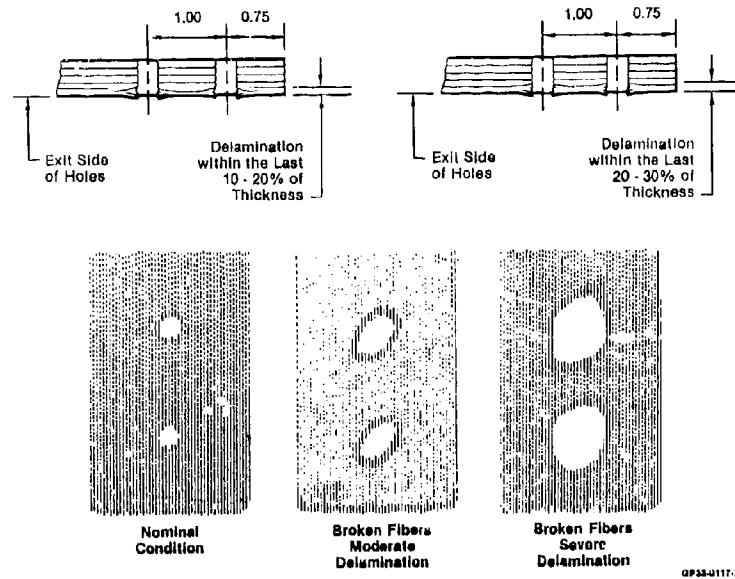
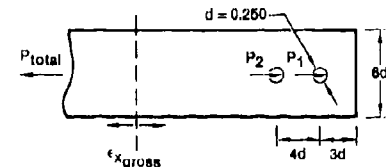


Figure 4. C-Scans of Laminates with Delaminations at Fastener Holes

Joint tension strength was evaluated by tests of dry laminates at room temperature. Because of its sensitivity to environment, joint compression strengths were evaluated at RTW and ETW test conditions.

Test results are summarized in Figure 5 along with baseline strength data. Strength reductions of 1.4 percent and 7.3 percent occurred in RTD tension tests for specimens with moderate and severe delaminations, respectively. Severe delaminations caused a 9.2% reduction of compression strength at 250°F.



Test Condition (50/40/10 Layup)	Baseline Data		Specimens with Delaminations		% Change		Loading
	F _{bru} E _{x2} (ksi)	ε _x _{gross} (μin./in.)	F _{bru} E _{x2} (ksi)	ε _x _{gross} (μin./in.)	F _{bru}	ε _x _{gross}	
RTD	+140	+3,990	+138	+3,790	-1.4	-4.9	Ten Comp Comp
	-155	-4,740	-150	-4,450	-3.2	-6.2	
	-120	-3,790	-115	-3,810	-4.2	+0.6	
Moderate							
RTW	+140	+3,990	+130	+3,790	-7.3	-9.5	Ten Comp Comp
	-155	-4,740	-142	-4,680	-8.4	-3.5	
	-120	-3,790	-109	-3,330	-9.2	-12.2	
Severe							
ETW	+140	+3,990	+130	+3,610	-	-	Ten Comp Comp
	-155	-4,740	-142	-4,680	-	-	
	-120	-3,790	-109	-3,330	-	-	

Figure 5. Effect of Delaminations on Joint Strength

Porosity - Two levels of porosity were evaluated; "moderate" and "severe". Desired levels of porosity in the 50/40/10 laminate were obtained by using the altered collation and curing procedures summarized in Figure 6. Specimens were located within panels such that fastener holes occurred in areas of desired porosity levels as indicated by photomicrograph and nondestructive inspections (Figure 7).

Curing Procedure	Process Used for Good Panels	Process Used to Produce	
		Moderate Porosity	Severe Porosity
Vacuum Debulk	Yes	None	None
Intermediate Temperature Hold	1 hr @ 275°F	None	None
Bag Vacuum	0.05 in. Hg	0.8 in. Hg	1.5 in. Hg
Autoclave Pressure	100 psig	50 psig	50 psig
Added Moisture Δ	None	Every 7th Ply	Every Ply

Δ Fine mist sprayed between plies

GP33-0117-27

Figure 6. Panel Fabrication Procedures Used to Produce Panel Porosity

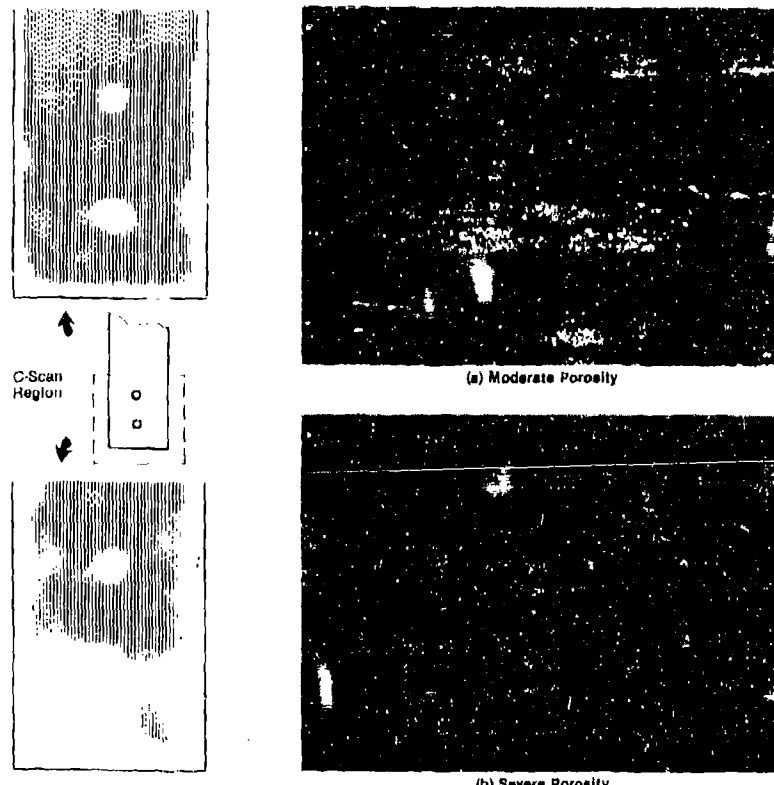
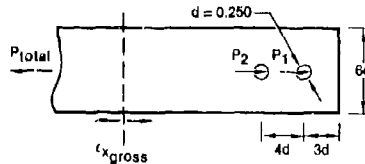


Figure 7. Examples of Panel Porosity

Strengths of baseline specimens and specimens with porosity are compared in Figure 8. Little sensitivity to severe porosity was indicated under tensile loading. Under compressive loadings, strength reductions ranged from 7-13.3 percent for specimens with moderate porosity and 10-30.8 percent for specimens with severe porosity. The greatest reductions occurred at 250°F test condition.

Improper Fastener Seating Depth - Effects of excessive countersink depth on joint strength were evaluated by testing composite joint members having fasteners seated too deeply in a typical laminate (50/40/10). Two conditions of countersink depth were evaluated at room temperature in tension.

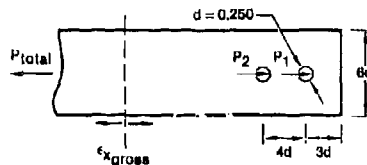
Strengths are compared with baseline strengths in Figure 9. Strengths for joints with excessive countersink depths (80% and 100%) are compared with strength of specimens with nominal countersunk depths (52% of laminate thickness). Joint strengths for countersink versus noncountersink laminates indicated no significant reductions occurred when fastener seating depth was nominal. The relative amount of cylindrical bearing area as compared to countersink bearing area may account for the demonstrated loss in strength. Earlier tests have indicated that the maximum cylindrical bearing capacity is nearly 160 ksi for large edge distances. An analysis of the forces in the region of the countersink indicates an effective bearing capacity of 110 ksi, when friction is accounted for and when sufficient head bearing area still remains. Using these capacities results in predicted reductions of 14% and 30%, to be compared with the demonstrated reductions of 16.4% and 34.3%, respectively.



Test Condition (50/40/10 Layup)	Baseline Data		Specimens with Porosity		% Change		Loading
	F_{bru}^u x_2 (ksi)	$\epsilon_{x,gross}^u$ ($\mu\text{in./in.}$)	F_{bru}^u x_2 (ksi)	$\epsilon_{x,gross}^u$ ($\mu\text{in./in.}$)	F_{bru}	ϵ_{gross}	
			Moderate Porosity				
RTD	+ 140	+ 3,990	—	—	—	—	Ten
RTW	- 155	- 4,740	- 144	- 4,480	- 7.1	- 5.4	Comp
RTW (F-T) Δ	- 155	- 4,740	- 142	- 4,370	- 8.4	- 7.9	Comp
ETW	- 120	- 3,790	- 104	- 3,110	- 13.3	- 17.9	Comp
		Severe Porosity					
RTD	+ 140	+ 3,990	+ 140	+ 3,940	0	- 1.2	Ten
RTW	- 155	- 4,740	- 139	- 4,170	- 10.3	- 12.1	Comp
RTW (F-T) Δ	- 155	- 4,740	- 137	- 4,110	- 11.6	- 13.3	Comp
ETW	- 120	- 3,790	- 83	- 2,550	- 30.8	- 32.8	Comp

Δ (F-T) - exposed to freeze-thaw cycles

Figure 8. Effect of Porosity on Joint Strength



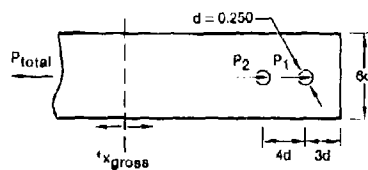
Countersink Depth (50/40/10 Layup) RTD, Tension	F_{bru}^u x (ksi)	$\epsilon_{x,gross}^u$ ($\mu\text{in./in.}$)	% Change	
			F_{bru}	ϵ_{gross}
Nominal	140	3,990	—	—
80%	117	3,240	- 18.4	- 18.8
100% (Knife Edge)	92	2,540	- 34.3	- 38.3

Figure 9. Effect of Countersink Depth on Joint Strength

Tilted Countersinks - Countersink perpendicularity was investigated for two conditions of misalignment. The misaligned countersink was tilted 10° away from the bearing surface for one condition and tilted 10° toward it for the other. Tests were conducted in tension at RTD and in compression at 250°F after specimen moisture conditioning. Experimental results are summarized in Figure 10.

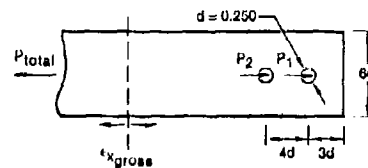
Interference Fit - The effects of fastener interference fits on joint strength were investigated in two different laminates (50/40/10 and 30/60/10). Two-fastener-in-tandem specimens were tested to failure in tension at RTD and ETW conditions. Specimens with both .003 and .008 inch levels of interference fit were tested.

Results (Figure 11) for both layups indicate an insensitivity to interference at room temperature. Joint strength of the more fiber-dominant 50/40/10 layup improved under ETW conditions for both levels of interference. However, joint strengths of the matrix-dominant 30/60/10 layup showed no change at the ETW test condition.



Test Condition (50/40/10 Layup)	Baseline Data		Tilted Countersink		% Change		Loading
	F _{bru} X ₂ (ksi)	x _{Gross} (in./in.)	F _{bru} X ₂ (ksi)	x _{Gross} (in./in.)	F _{bru}	x _{Gross}	
RTD ETW	+140	+3,990	Away From Bearing		0	-2.0 -20.2	Tens Comp
	-120	-3,750	+140	+3,910			
RTD ETW	+140	+3,990	Toward Bearing		-21.4 -16.7	-24 -22.7	Tens Comp
	120	3,750	+110	+3,030			
GPM-0117-10							

Figure 10. Effect of Tilted Countersink on Joint Strength



Test Condition	Baseline Data		Interference Fit		% Change		Loading
	F _{bru} X ₂ (ksi)	x _{Gross} (in./in.)	F _{bru} X ₂ (ksi)	x _{Gross} (in./in.)	F _{bru}	x _{Gross}	
50/40/10 Layup:			0.003 Interference		0	+0.4 +14.7	Tens Tens
	140 110	3,990 3,080	140 120	4,000 3,530			
RTD ETW	140 110	3,990 3,080	0.008 Interference		0 +0.1	+0.9 +11.2	Tens Tens
	140 120	3,990 3,420					
30/60/10 Layup:			0.003 Interference		0	-0.2 +2.4	Tens Tens
	140 120	6,470 4,710	140 120	5,460 4,820			
RTD ETW	140 120	6,470 4,710	0.008 Interference		0	+0.3 -1.8	Tens Tens
	140 120	6,490 4,620					
GPM-0117-11							

Figure 11. Effect of Fastener Interference Fit on Joint Strength

Laminate damage due to fastener installation at interference fits ranging from .002 to .008 inch were further evaluated for fasteners requiring pull-through installation techniques. Representative photomicrographs are shown in Figure 12. Little or no damage resulted from a fastener interference of .0035 inch or less; however, damage is indicated at the fastener exit side as well as along the entire fastener length for interference fits from .004 through .008 inch.

Fastener Removal and Reinstallation - These tests were used to evaluate whether repeated installation and reinstallation would locally damage the laminate hole area, and/or affect joint strength. Fasteners were installed, torqued to 50 inch-pounds, and completely removed. This procedure was repeated 100 times prior to strength testing. Specimens were tested to failure in tension at RTD and in compression at ETW.

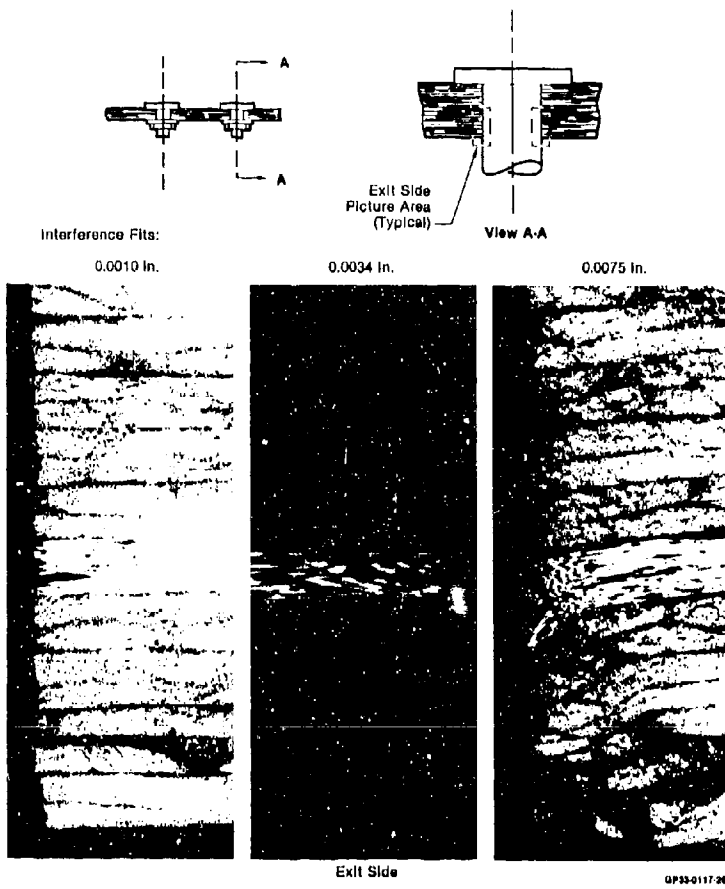


Figure 12. Photomicrograph Examination of Laminates with
Interference Fit Holes

Visual appearance of all fastener holes after installation and re-installation cycling was unchanged. Strength data listed in Figure 13 indicates little sensitivity to RTD tensile test conditions. Compressive strength values indicated an increased sensitivity (8.3% reduction); however, test scatter for the compression tests was large.

(b) Fatigue Strength and Hole Wear - Tests were conducted with specimens with and without internal porosity to determine the effects on joint fatigue life, hole wear, and failure modes. Emphasis was placed on generation of hole wear data and its relation to joint fatigue life.

Test Condition (50/40/10 Layup)	Baseline Data		After 100 Cycles Fastener Installation		% Change		Loading
	$F_{\text{bhu}}^{x_2}$ (ksi)	$\epsilon_{\text{gross}}^u$ ($\mu\text{in./in.}$)	$F_{\text{bhu}}^{x_2}$ (ksi)	$\epsilon_{\text{gross}}^u$ ($\mu\text{in./in.}$)	F_{bhu}	ϵ_{gross}	
RTD ETW	+140 -120	+3,990 -3,790	+140 -110	+3,900 -3,510	0 -8.3	-2.2 7.4	Ten Comp

GPSS-0117-26

Figure 13. Effect of Fastener Removal and Re-installation on Joint Strength

A pure bearing test specimen was used (Figure 14). Tension-tension ($R = +0.1$) and tension-compression ($R = -1.0$) constant amplitude testing was performed at room temperature with specimens in the as-manufactured condition. Hercules AS/3501-6 carbon/epoxy was also used for fabrication of all fatigue and hole wear test specimens.

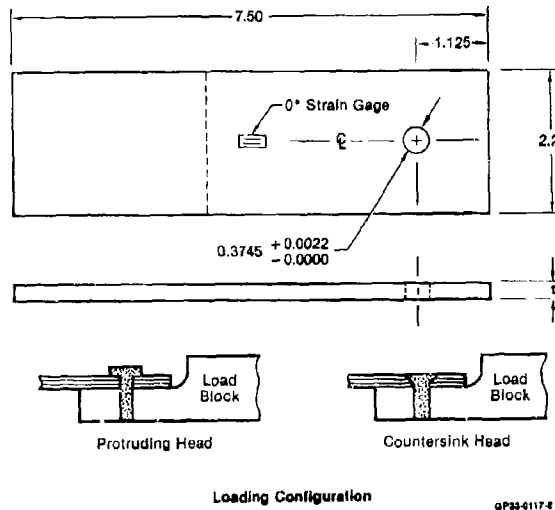


Figure 14. Fatigue Specimen Configuration

GP344117-4

All constant-amplitude fatigue specimens were cycled to failure, or 10^6 cycles, whichever occurred first. Specimens which did not fail in 10^6 cycles were tested to determine residual strength. Constant amplitude fatigue testing was performed at three stress levels for each specimen type. Selection of the stress levels for fatigue testing was based on load-deflection data obtained from static tests. During fatigue testing, load-deflection data were also obtained each time a specified hole wear level was reached.

The evaluation included three layups; the fiber-dominated layup 50/40/10, and two matrix-dominated layups: 19/76/5 and 30/60/10.

Residual strengths were, in general, equal to or greater than nonfatigued specimen static strengths; however, in most cases, these specimens had acquired hole wear of .02 inch or greater during fatigue testing. For structural applications, hole elongations of .02 inch exceed the usual yield criteria for metallic joints which may also represent a tentative criteria for composite joints.

Results of tension-tension ($R = +0.1$) and tension-compression ($R = -1.0$) cyclic loading on each laminate at room temperature, dry (RTD) test conditions are summarized in Figures 15, 16, and 17, in terms of fatigue cycles required to produce an .02 inch hole wear in the fastener hole. The results indicate similar static and fatigue strength for all layups for tension-tension ($R = +0.1$) cycling, as summarized in Figure 18. For tension-compression ($R = -1.0$), the 19/76/5 and 30/60/10 matrix-dominant layups sustained fewer load cycles prior to developing an .02 inch hole wear, as compared to the 50/40/10 layup (Figure 19).

Tests of specimens with moderate porosity were conducted to evaluate the effects of this anomaly on joint durability. Earlier static tests indicated that moderate levels of porosity had a minor effect on static joint strength at room temperature. Specimens with moderate porosity in regions of fastener holes were tested under $R = +0.1$ and $R = -1.0$ fatigue loadings at room temperature dry conditions. Life data is compared in Figure 20 with baseline data. No reduction of static strength or joint fatigue life was indicated.

The rate of hole wear in other tests of composite joints without porosity at $R = +0.1$ is summarized in Figures 21, 22, and 23 for three levels of wear (.005, .010, and .020 inch). These data indicate that the matrix-dominant 19/76/5 layup exhibited earliest initiation of hole wear, but had the most gradual rate of accumulation. Conversely, the fiber-dominant (50/40/10) layup exhibited the most-delayed initiation of hole wear, but had the most rapid accumulation. The 30/60/10 layup exhibited an intermediate performance.

The spring rates of the test specimens for the 50/40/10 layup were also determined at various times in the constant amplitude fatigue testing to determine correlation with hole wear data. Hole wear data for this layup at RTD, shown in Figure 24 are similar in threshold points and trends to joint spring rate data summarized in Figure 25.

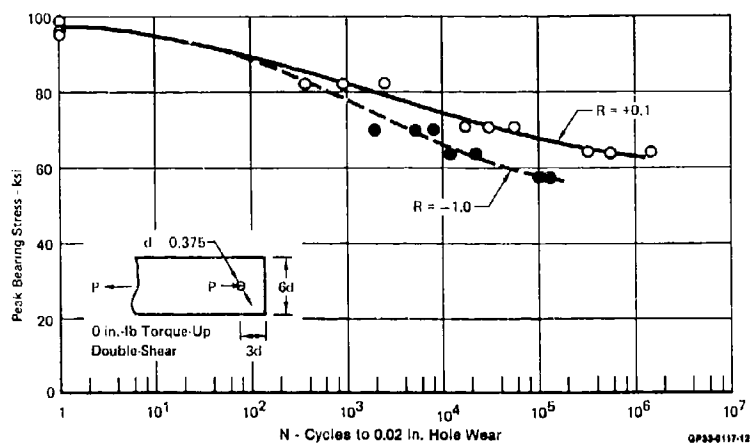


Figure 15. RTD Baseline Joint Fatigue Life
50/40/10 Layup

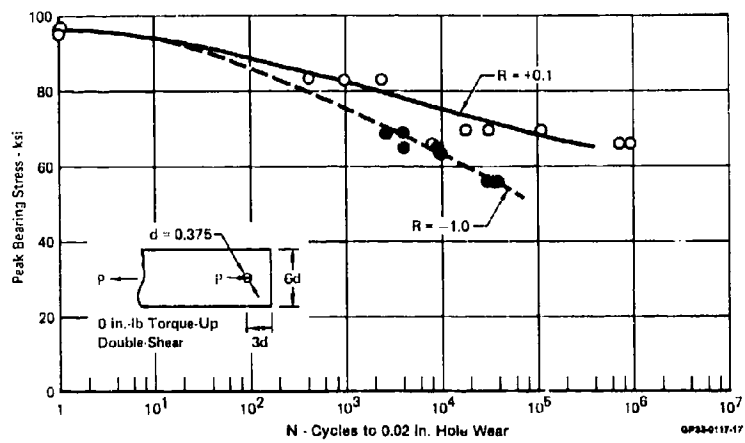


Figure 16. RTD Baseline Joint Fatigue Life
30/60/10 Layup

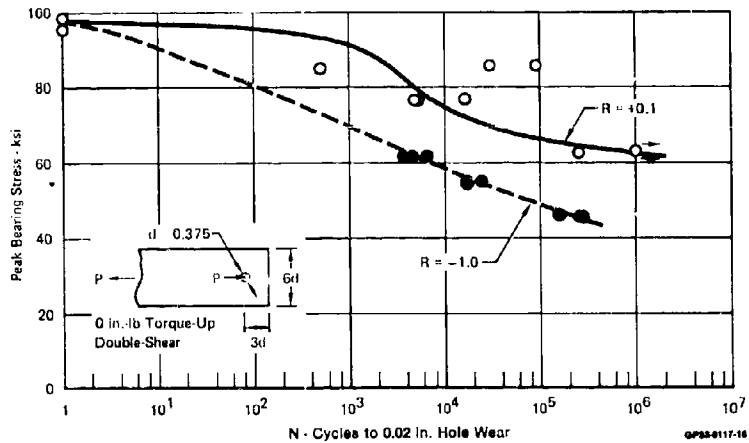
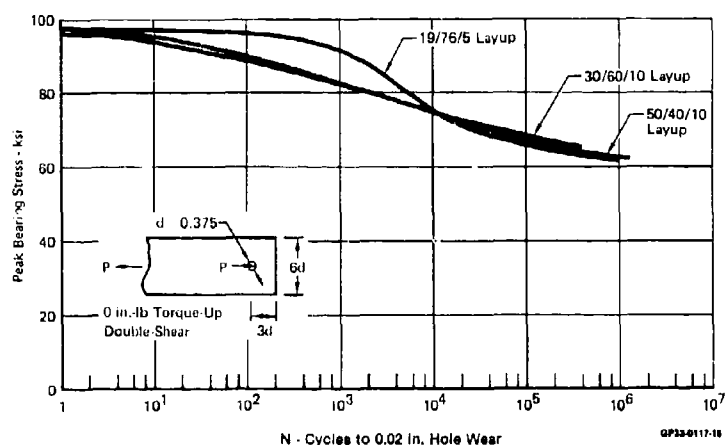
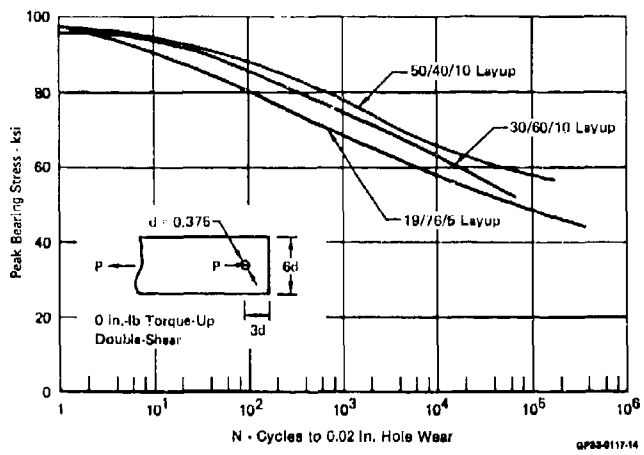
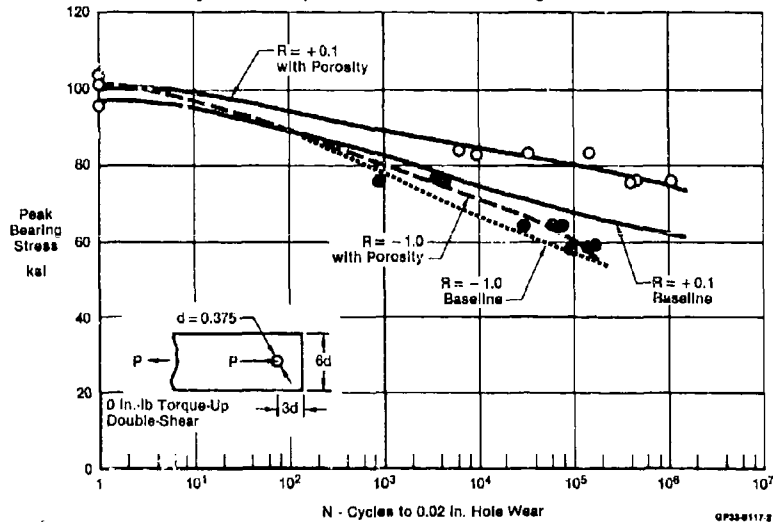


Figure 17. RTD Baseline Joint Fatigue Life
19/76/5 Layup

Figure 18. Comparison of $R = +0.1$ Joint Fatigue LifeFigure 19. Comparison of $R = -1.0$ Joint Fatigue LifeFigure 20. Effect of Porosity on Joint Fatigue Life
50/40/10 Layup

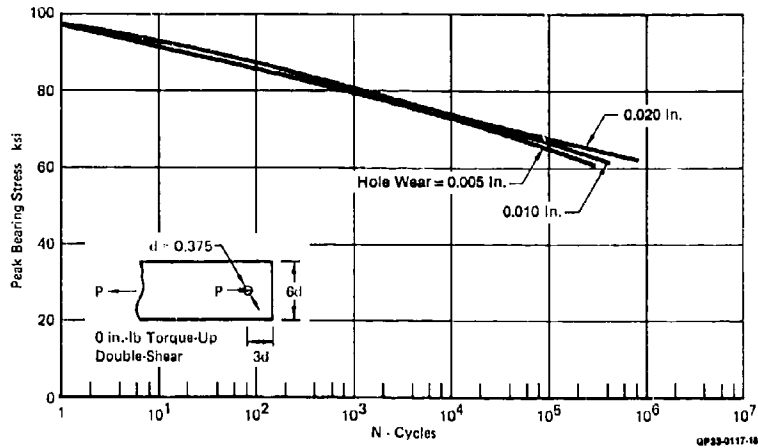


Figure 21. Hole Wear Under Fatigue Loading
50/40/10 Layup

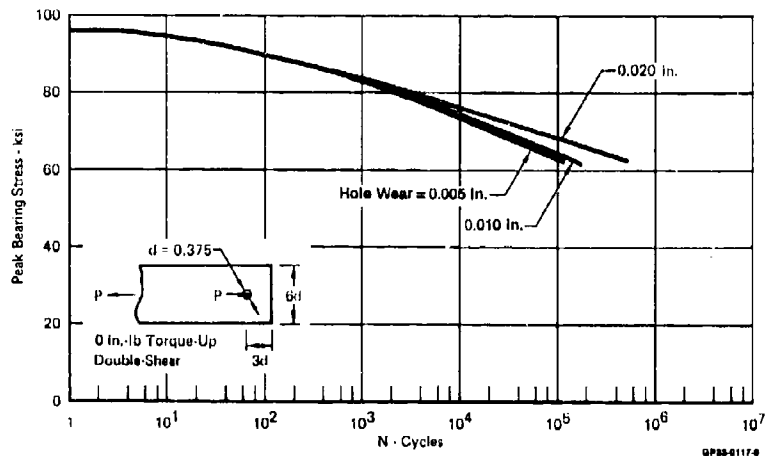


Figure 22. Hole Wear Under Fatigue Loading
30/60/10 Layup

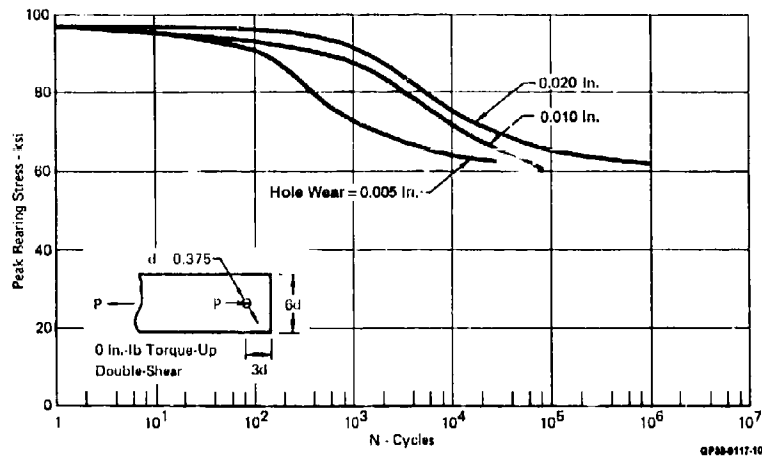


Figure 23. Hole Wear Under Fatigue Loading
19/76/5 Layup

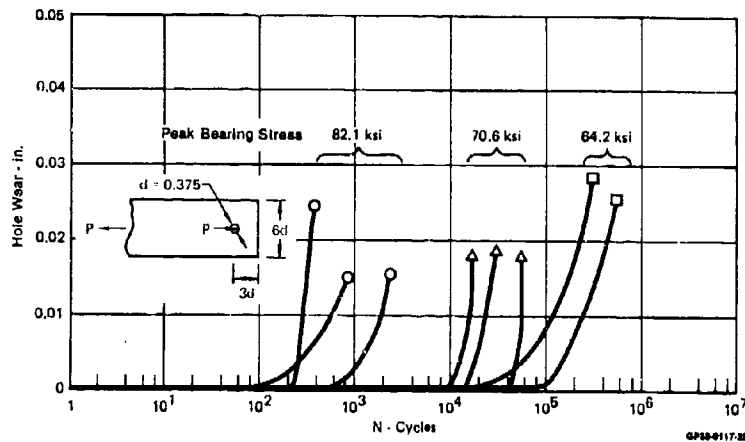


Figure 24. Effect of $R = +0.1$ Loading on Hole Wear
50/40/10 Layup

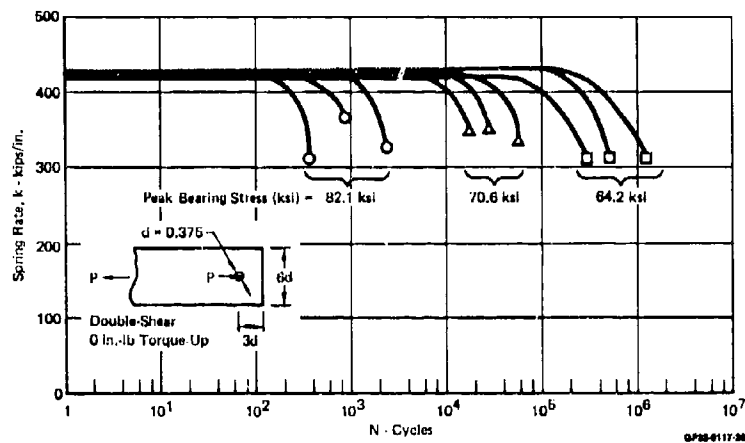


Figure 25. Effect of Fatigue Loading on Joint Spring Rate
50/40/10 Layup $R = +0.1$

3. LOW ENERGY IMPACT DAMAGE

The effect of low energy impact damage on the static and fatigue strength of carbon/epoxy wing cover skin structures and of integrally stiffened panels typical of postbuckling fuselage structures was evaluated.

(a) Wing Cover Skin Structural Panels - Effects of low-energy impact to an upper wing-skin were evaluated in static compression and fatigue tests (Reference 2). Specimens incorporated spanwise rows of Kevlar stitches simulating the patterns proposed for reinforcing cocured skin-to-stiffener joints.

The specimen configuration is presented in Figure 26. Various impact energies were evaluated to determine the energy level representing the threshold between visible and nonvisible impact damage. A .50-inch diameter indenter was used while specimens were supported over a 3-by-3-inch opening. An 8-ft-lb energy level was determined to be the minimum level to produce visible surface damage. The 8 ft-lb energy level was also considered to be representative of expected damage from dropped tools and damage from runway stones. Resulting internal damage detected in ultrasonic inspection of the four specimens ranged from 1.2-inch to 1.5-inch diameter.

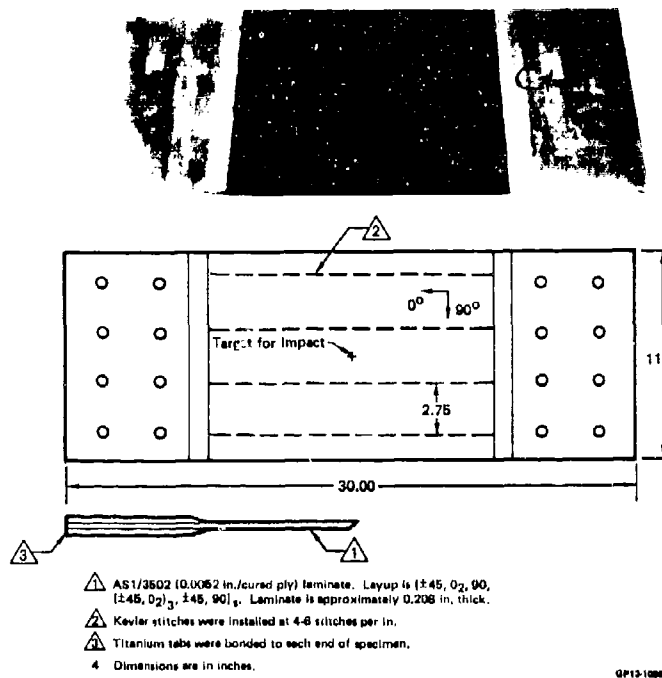


Figure 26. Specimen Configuration - Skins with Nonvisible Impact Damage

The setup for these compression tests is shown in Figure 27. Each end of the specimen was bolted to a loading adapter which fit within hydraulic grips in the upper and lower platens of the test machine. Back-to-back channels having access holes for instrumentation were clamped onto the specimen for skin stabilization. The area between the two central rows of stitches in the specimen contained the damage and was not stabilized by the channels. The column composed of the specimen with loading adapters on each end was supported at two locations by additional fixturing which was attached to the test machine. Strain data from back-to-back gages on the specimen indicated little bending. Measured strains in the stabilizing channels were negligible.

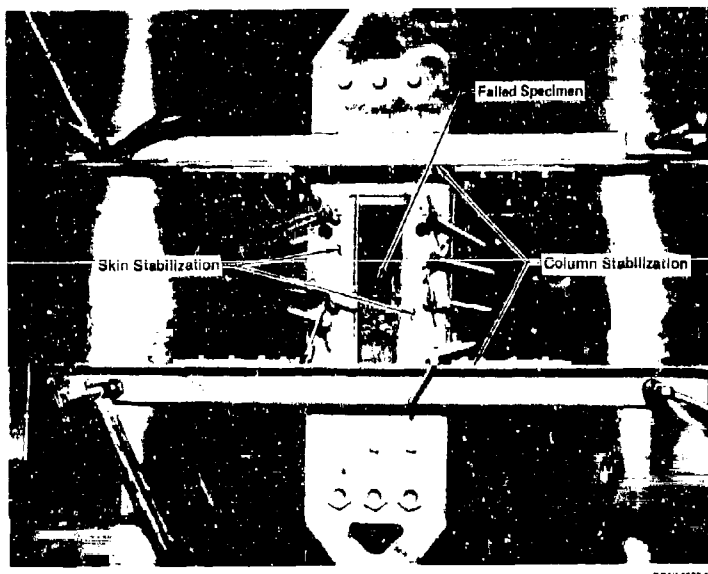


Figure 27. Structural Test Setup - Compressive Strength of Damaged Specimens

Results of static compression tests indicated that stitches were not sufficient to prevent damage propagation and overall failure at strain levels above $-4500 \mu\text{in/in}$. Strain data indicate local bending in the damaged area at low loads, possibly contributing to the failures.

A fatigue test of the remaining specimen was conducted to assess damage containment features of the stitch pattern. A compression-dominated spectrum was used. Damage detected in ultrasonic inspection was initially 1.6-inch long and 1.4-inch wide but grew to 1.7-inch long and 2.7-inch wide after 24,000 equivalent flight hours of spectrum loading. For the one specimen tested at the reduced strain level, damage was contained by parallel rows of stitches which were spaced at 2.75 in. In residual strength tests of this specimen, the far-field strain at failure was $-4200 \mu\text{in/in}$.

These test results are summarized in Figure 28 in terms of far-field failure strains as a function of damage sizes detected in ultrasonic inspections. Test results for coupons with a .25-inch diameter hole are also shown in Figure 28. The predicted strengths, presented as a solid line, were determined using the methodology of Reference 1 and the material properties shown in Figure 29. These predictions correlate well with test results for specimens having a .25-inch diameter hole. Predictions for specimens containing impact damage were made for damage modeled as open round holes.

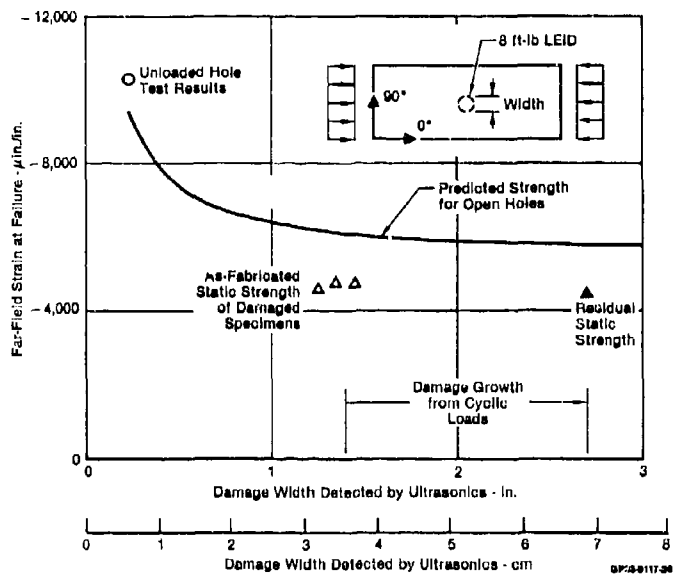


Figure 28. Residual Strength of Specimens with Nonvisible Impact Damage

Ply Property	Average Test (RTD)	
	AS1/3502	S-Glass/Epoxy*
$E_1^T \cdot \text{psi (GPa)}$	18.3×10^6 (126.2)	8.0×10^6 (55.2)
$E_1^C \cdot \text{psi (GPa)}$	17.3×10^6 (119.3)	7.5×10^6 (51.7)
$E_2^T \cdot \text{psi (GPa)}$	1.4×10^6 (9.7)	2.7×10^6 (18.6)
$E_2^C \cdot \text{psi (GPa)}$	1.8×10^6 (12.4)	2.7×10^6 (18.6)
$G_{12} \cdot \text{psi (GPa)}$	0.9×10^6 (6.2)	0.8×10^6 (5.6)
V_{12}	0.3	0.25
$\epsilon_1^T \cdot \mu\text{in./in.}$	12,900	35,700
$\epsilon_1^C \cdot \mu\text{in./in.}$	-18,200	-13,600
$\epsilon_2^T \cdot \mu\text{in./in.}$	5,000	3,500
$\epsilon_2^C \cdot \mu\text{in./in.}$	-28,500	-20,000
$\epsilon_{12} \cdot \mu\text{in./in.}$	60,000	60,000

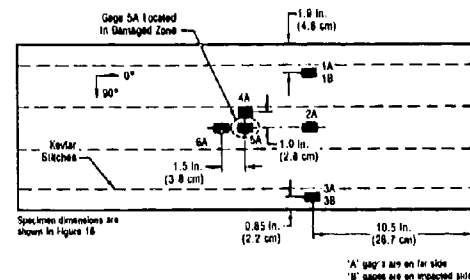
*Plastics for Aerospace Vehicles:
Part 1 - Reinforced Plastics, MIL-HDBK-17A, January 1971

DP24117-1

Figure 29. Composite Material Properties

Test results indicate that impact damage produced an effective strain concentration greater in magnitude than a round hole of equivalent size. Strengths predicted for an equivalent hole size were unconservative by approximately 30%, possibly due to local structural instability of delaminated plies within the damaged zone.

Test results are summarized in Figure 30, where strain data are shown for a nominal applied load of -20,000 lbs, the limit load level used for the fatigue test, and the failure load levels. Sizes of nonvisible impact damage were determined by ultrasonics and are also shown in this figure. A typical strength failure is shown in Figure 31. No fatigue failure occurred in four design lifetimes of spectrum fatigue loads.



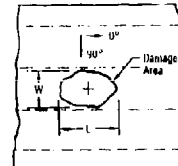
Event	Load, kips (kN)	Specimen Number	Typical Strain Data							
			1A	1B	2A	3A	3B	4A	5A	5B
Low Load Strain Survey	-20 (-89)	C1-2	-809	-809	-902	-930	-970	-	-	-
		C1-3 (0 SFH)	-684	-670	-914	-1,044	-1,027	-876	1,125	-971
		C1-3 (24k SFH)	-794	-785	-878	-930	-818	-866	F	-910
		C1-4	-713	-906	-838	-782	-775	-818	-1,119	-842
		C1-5	-936	-858	-860	-780	-771	-	-	-
Strains at Maximum Fatigue Load	-64.5 (-287)	C1-2	-2,916	-2,922	-3,063	-2,924	-3,010	-	-	-
		C1-3 (0 SFH)	-2,607	-2,532	-2,931	-3,282	-3,206	-3,092	-5,310	-3,096
		C1-3 (24k SFH)	-2,914	-2,874	-2,912	-2,957	-2,923	-2,856	F	-3,182
		C1-4	-2,340	-3,472	-2,571	-2,793	-2,688	-3,333	-5,544	-3,015
		C1-5	-3,248	-3,182	-2,200	-2,551	-2,471	-	-	-
Ultimate Strength	-100 (-446)	C1-2	-4,735	-4,728	-4,763	-4,851	-4,820	-	-	-
	-94 (-416)	C1-3 (24k SFH)	-	-	-	-	-	-	-	-
	-100 (-460)	C1-4	-3,817	-5,276	-3,656	-4,493	-4,034	F	F	-4,524
	-96 (-420)	C1-5	-4,691	-4,500	I	-3,854	7,746	-	-	-

Notes:
 Strains are in units of microstrain.
 All tests conducted at room temperature.
 Specimen C1-3 tested in spectrum fatigue to an equivalent of 24,000 Spectrum Flight Hours (SFH).
 Specimens C1-2 and C1-5 did not have strain gages 4A, 5A, and 5B.
 No ultimate strains recorded for specimen C1-3 because of instrumentation malfunction.

F = Fracture Failure

Specimen	Size of Internal Damage	
	L, in. (cm)	W, in. (cm)
C1-2	1.57 (3.99)	1.55 (3.43)
C1-3 (0 SFH)	1.57 (3.99)	1.36 (3.45)
C1-3 (24k SFH)	1.70 (4.32)	2.70 (6.86)
C1-4	1.70 (4.55)	1.43 (3.63)
C1-5	1.78 (4.52)	1.25 (3.18)

Dimensions given are projected damage size except where noted.



GP1210647

Figure 30. Residual Strength of Specimens with Nonvisible Impact Damage

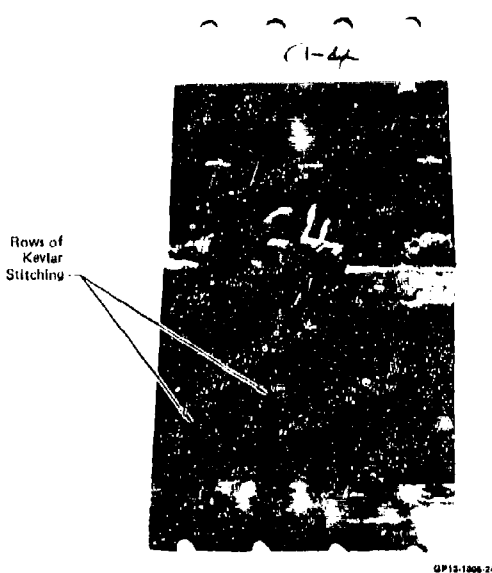


Figure 31. Typical Failed Skin Specimen

(b) Integrally Stiffened Postbuckling Fuselage Panels - The effects of low energy impact on the structural integrity of two types of fuselage panels were evaluated: fuselage compression panels and fuselage shear panels.

Fuselage Compression Panels - Tests were performed to evaluate the effectiveness of Kevlar stitches for containing nonvisible low-energy impact damage in cocured skin-stiffener joints of buckled composite panels loaded in compression. Such damage nucleates disbonds which grow under cyclic loads and lead to panel failure. One method for containing disbonds and improving the durability of skin stiffener joints is to reinforce such joints with Kevlar stitches.

The baseline behavior of curved stiffened panels under compression postbuckling loads was determined in a previous test program (Reference 3). Fatigue failures were precipitated by local disbonds occurring in undamaged skin-stiffener joints.

Cyclic load tests were conducted on a curved stiffened panel identical to those previously tested except that each cocured joint was reinforced with two rows of Kevlar stitches. Low energy impacts were made to produce internal damage in two areas of high peel stress areas (Figure 32) where disbonds had occurred in the earlier cyclic load panel tests (Reference 3). The damage shown in Figure 32 (white areas of C-scan) was produced by a spherical indenter with 10 ft lb impact energy.

Disbonds were detected and growth was monitored by periodic ultrasonic inspections. C-scan inspection records for the center stiffener of a baseline panel (3F) are shown in Figure 33, where sound attenuation occurring from disbonds and from air trapped within hat stiffeners is indicated by a black area. Disbonds in baseline panels initiated and grew from the base of the flange with increasing load cycles. An identical panel with stitching survived 1,000,000 cycles and showed only minor evidence of disbonding.

The damage containment capability of Kevlar stitches was significant. An unstitched, undamaged baseline panel suffered failure after 3,500 load cycles where the peak load was -55 kips. A stitched, undamaged panel was cyclically loaded without failure for 280,000 cycles to -50 kips followed by an additional 280,000 cycles to -55 kips. This test sequence using a stitched, damaged panel was repeated; again the reinforced panel survived both groups of 280,000 load cycles. In addition, ultrasonic inspections conducted after each block of 140,000 cycles indicated good containment of the impact damage with no disbond growth. Reinforcement with Kevlar stitches was, in this case, an effective means of assuring durability of cocured joints having nonvisible impact damage.

Fuselage Shear Panels - Tests were also performed to determine the effect of low energy impact damage on the static and fatigue strength of integrally stiffened shear-loaded panels operating in the postbuckling regime (Reference 4). The as-manufactured ultimate strength of the baseline test panel was 829 lb/in. A typical panel under postbuckling loads is shown in Figure 34. Maximum mid-panel lateral deflection for the static panels was in order of 0.2 inches.

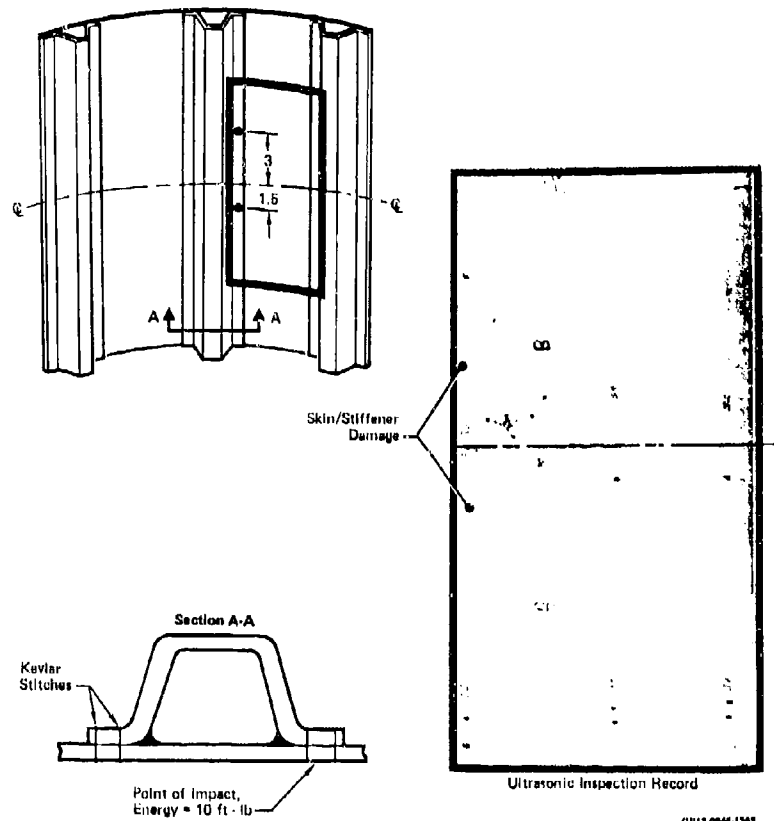
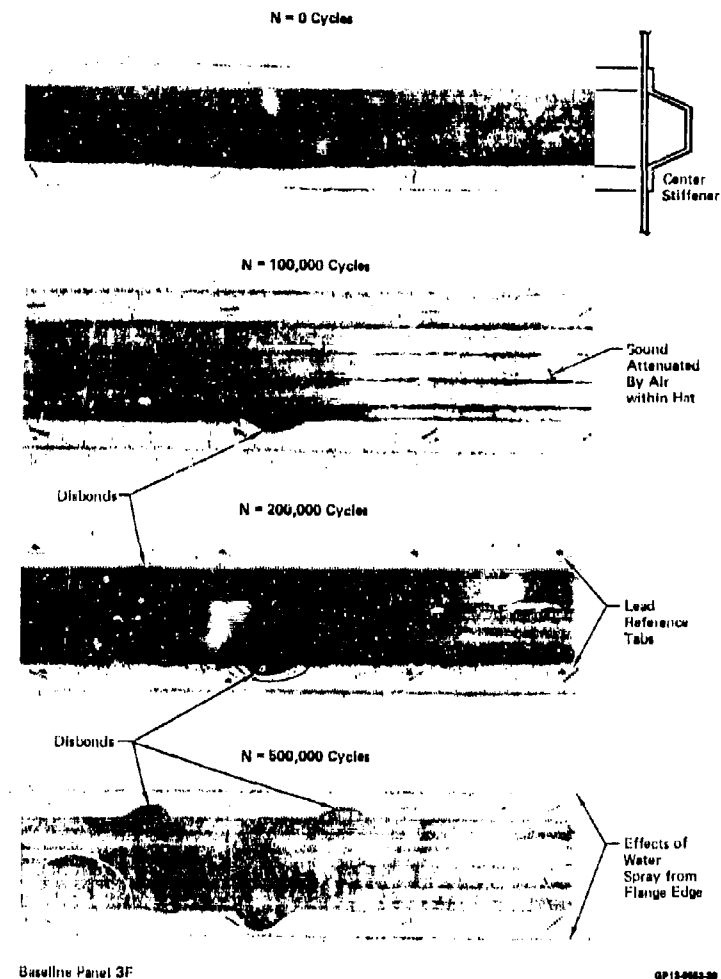


Figure 32. Damage Containment in Stitched Skin-to-Stiffener Joints

GP13-0044-1048



Baseline Panel 3F

GP19-0003-50

Figure 33. Growth of Disbonds in Flange-to-Skin Joint

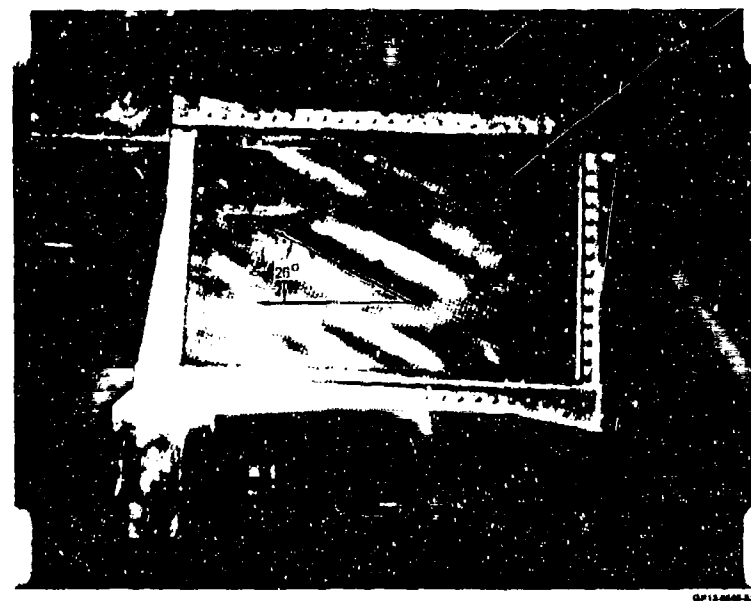


Figure 34. Buckled Shear Panel

The panel configuration and the locations of low energy impact damage is shown in Figure 35. An impact apparatus was designed with the capability of impacting the panels from either side. A slotted metal impact tube was used to direct the impact weight to the desired impact point. The 1/2 inch diameter round ball impact tool, Figure 36, rests against the panel and is centered inside the impact tube by a tool guide. All damaged panels were impacted on the skin side.

Panels were first impacted in the center bay using decreasing energy levels starting at 10 ft-lbs. The threshold level at which full penetration was achieved was in the range of 4.0 to 4.5 ft-lbs. Impact energy levels up to 4.0 ft-lbs have been estimated for fuselage lower surface for foreign object damage such as ice and gravel impacts during landing and take-off situations and for fuselage vertical sides and corners for ground handling impacts from hard objects such as tools (Reference 5).

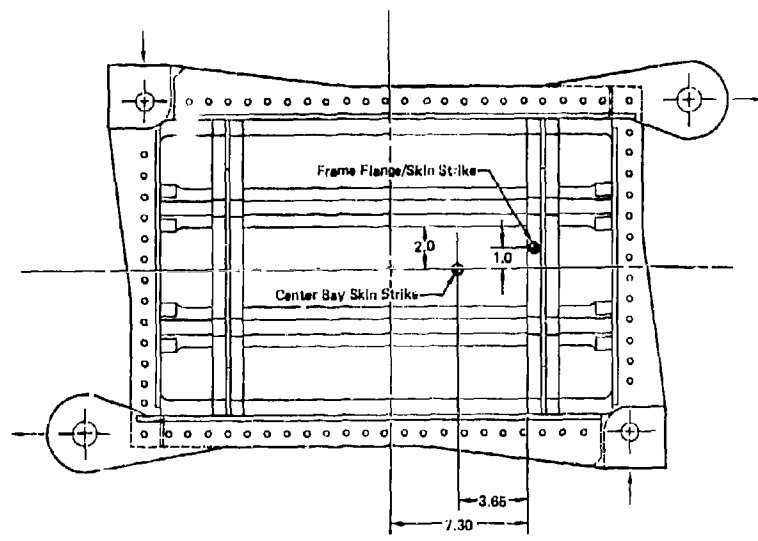


Figure 35. Shear Panel Configuration and Impact Damage Locations

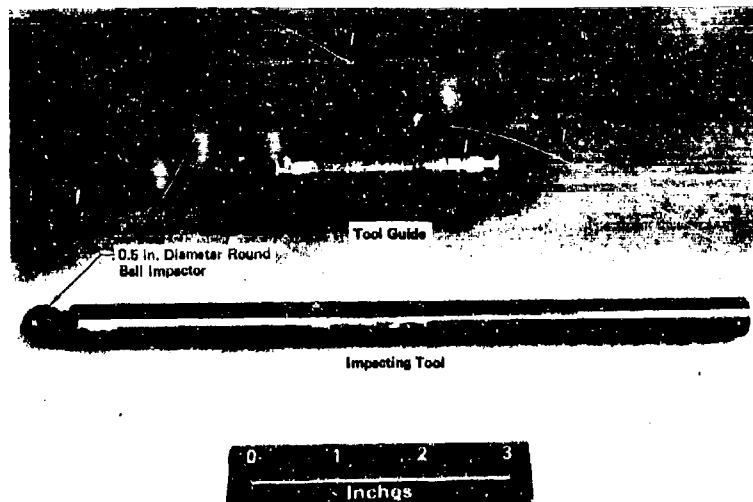


Figure 36. Impacting Tool and Guide

GPO:1978-20

A test panel after being subjected to multiple strikes in the range of 4.0 to 4.5 ft-lbs is shown in Figure 37. It was observed that while damage on the skin outer surface appeared different at different energy levels, the damage on the inner surface, in the form of delamination of the outer +45° ply, was similar for all strikes. A second impacted panel showed similar behavior.

Enhanced radiographic inspections of the strikes at 4.25 and 4.3 ft-lbs are shown in Figure 38. An energy level of 4.30 ft-lbs was adequate to achieve broken fibers across full 1/2 inch diameter. Internal damage was diamond shaped, probably due to 0, +45, 90 ply orientations. Through-the-thickness damage as indicated by radiographic inspection was similar for both energy levels, although visual appearances were different. Delamination on the inner surface of the skin (stiffener side) in the outer +45° ply extended to the adjacent hat flange (both sides).

Five additional panels were damaged using an energy level of 4.30 ft-lbs. Three panels were impacted at a buckle crest location in the center bay of the panel. The remaining two panels were impacted at a location where failures occurred during fatigue loading of the baseline panels. These impact locations are shown in Figure 35. All panels were impacted on the skin side.

Of the three panels impacted in the center bay, one panel was statically tested to failure; the remaining two panels were fatigue tested at a load level to preclude stiffener disbonding. The two panels impacted at the critical stiffener/skin interface region were fatigue tested to a load which produced stiffener disbonding in the baseline panels.

The damage sustained by the panel for static testing which was subjected to a center bay impact of 4.30 ft-lb is shown in Figure 39. The radiograph of this area is shown in Figure 40. The degree and type of damage was similar to that obtained in the exploratory tests.

Initial buckling for the impacted panel occurred at 104 lb/in and panel static failure occurred at 771 lb/in, compared to an average of 829 lb/in for the undamaged static test panels. Strain data was similar to data obtained in tests of undamaged panels; however, the maximum strain magnitudes achieved were less due to the lower failing load. This panel failed across the tension diagonal through the impacted region, preceded by stiffener separation similar to baseline static test panels.

The two fatigue test panels which were subjected to center bay impact damage were tested to a maximum fatigue load of 50% of ultimate strength ($N_{xymax} = 415$ lb/in). Previous tests showed this level to be the endurance limit of the as-manufactured panels.

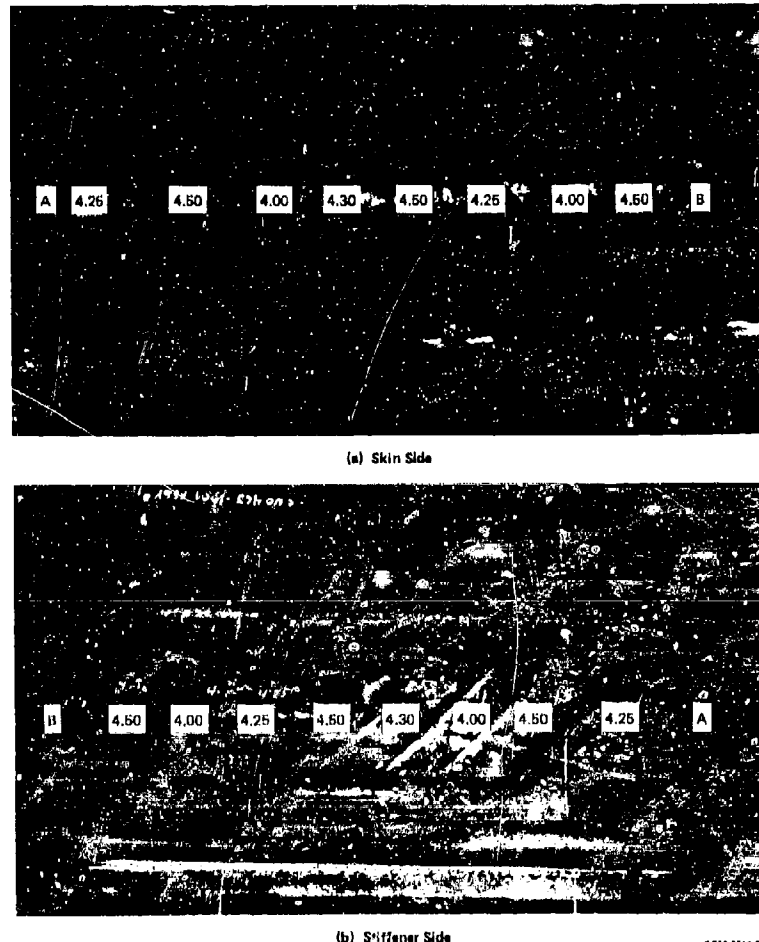


Figure 37. Impact Damage Investigation

GP63-0738-21

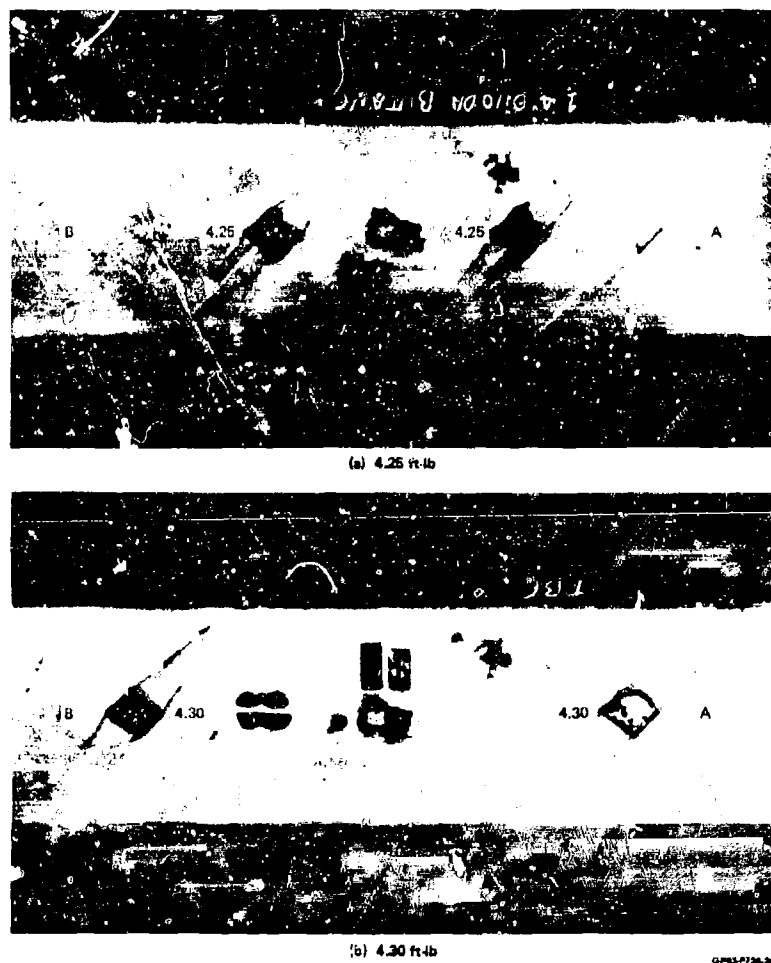


Figure 38. Radiographic Inspection



(a) Skin Side



(b) Stiffener Side QP03-070-23

Figure 39. Impact Damage

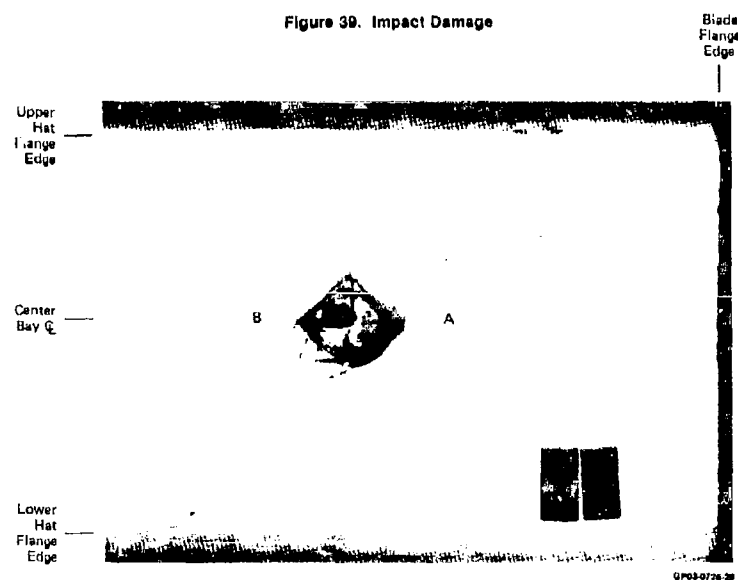


Figure 40. Radiographic Inspection of Impact Damage

All panels were subjected to constant amplitude fatigue loading at a stress ratio $R = 0.1$ for two blocks of 50,000 cycles each for a total of 100,000 cycles or failure, whichever occurred first. Strain surveys were taken prior to testing, and after each block of cycling to determine the effect of fatigue on panel performance. Panels surviving 100,000 cycles were subjected to a residual strength test. A summary of all fatigue results is presented in Figure 41 and in Figure 42.

Panel	N_{xy}^{cr} 1 Cycle (lb/in.)	Static Strength (lb/in.)	N_{xy}^{max} Fatigue (lb/in.)	$\eta \approx N_{xy}^{max}$ N_{xy}^{cr} avg	Cycles to Visible Disbonding	Cycles Completed	N_{xy}^{cr} 50,000 Cycles (lb/in.)	N_{xy}^{cr} 100,000 Cycles (lb/in.)	Residual Static Strength (lb/in.)	Comments
1	88	851	—	—	1	1	—	—	—	As-Manufactured Static Test Panels
2	80	797	—	—	1	1	—	—	—	
3	93	838	—	—	1	1	—	—	—	
4	97	—	580	5.69	2,100	94,700	—	—	—	
5	102	—	580	5.69	1,000	50,000	—	—	—	
6	96	—	580	5.69	1,200	50,000	—	—	849	
7	88	—	407	4.87	7,500	50,000	38	—	—	
8	108	—	497	4.87	3,000	50,000	48	—	—	
9	112	—	415	4.07	100,000+	100,000	112	112	947	As-Manufactured Fatigue Test Panels
10	77	—	415	4.07	100,000+	100,000	30	30	973	
11	135	—	456	4.47	33,000	100,000	114	90	860	
12	78	—	456	4.47	4,500	100,000	48	48	890	
13	104	754	—	—	1	1	—	—	—	Impact Damage - Center Bay Skin
14	102	—	415	4.07	100,000+	100,000	102	98	858	1 Static Panel
15	124	—	415	4.07	300 [▲]	100,000	73	66	778	2 Fatigue Panels
16	115	—	456	4.47	950	100,000	63	54	918	Impact Damage - Blade Flange/Skin
17	120	—	456	4.47	2,300	100,000	77	77	861	2 Fatigue Panels

+Visual disbonding not observed after 100,000 cycles

[▲] Porosity noted prior to test

QPO3-0726-78

Figure 41. Summary of Test Results

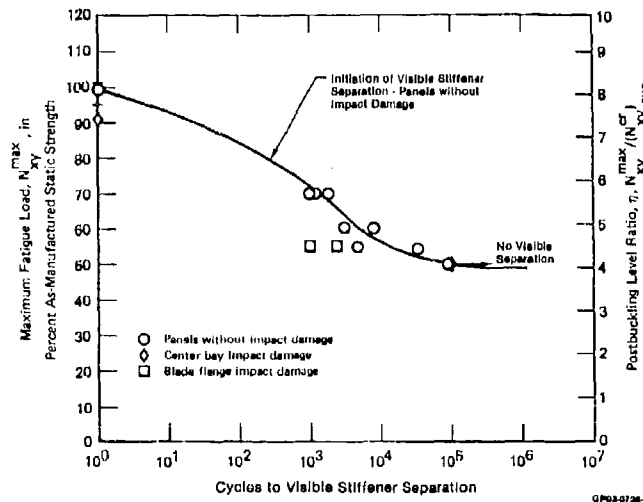


Figure 42. Panel Fatigue Performance

The impact damage sustained by the first fatigue test panel was similar to that observed both in the exploratory tests and in the static test panel. This panel survived 100,000 cycles with no visible stiffener separation or significant decrease in initial buckling strength observed. Radiographic inspections of the impact region prior to fatigue testing, after 50,000 cycles, and after 100,000 cycles are shown in Figures 43, 44, and 45 respectively. The damaged region did not grow during fatigue loading. Residual strength for the panel was 778 lb/in with sheet rupture occurring across the tension diagonal through the impacted region similar to that observed for the static test panel.

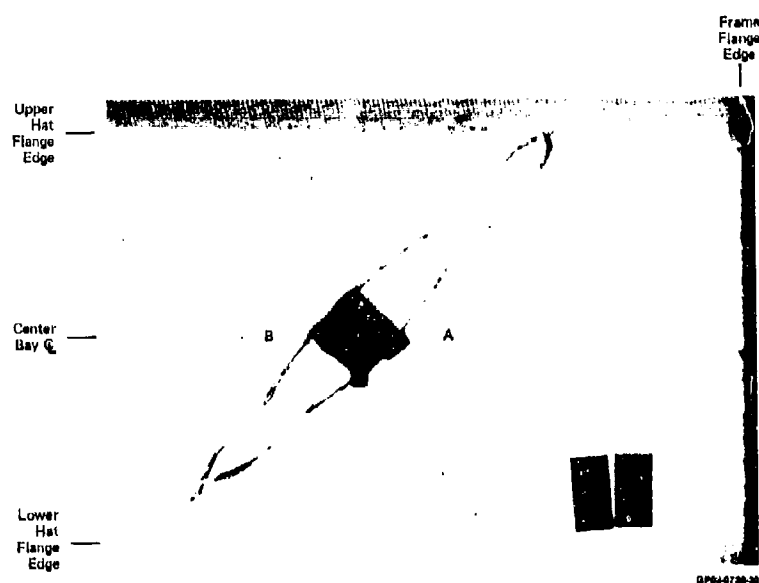


Figure 43. Radiographic Inspection of Initial Impact Damage

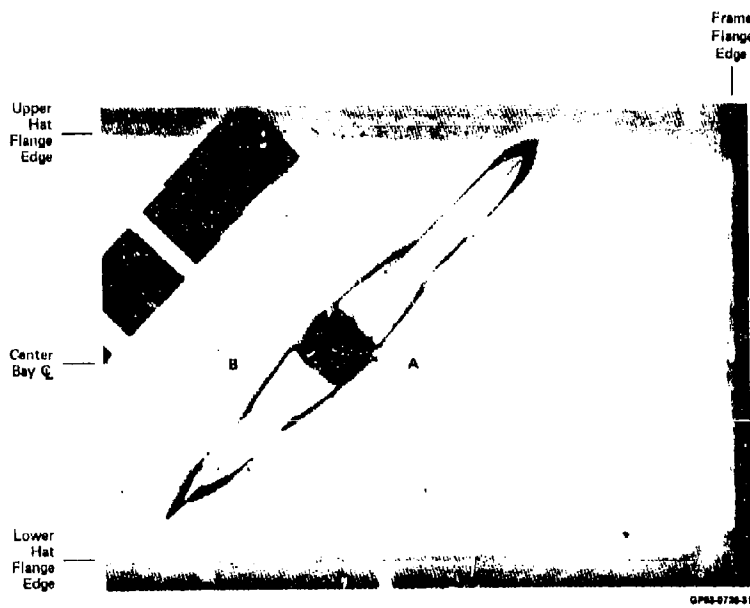


Figure 44. Radiographic Inspection of Impact Damage After 50,000 Cycles

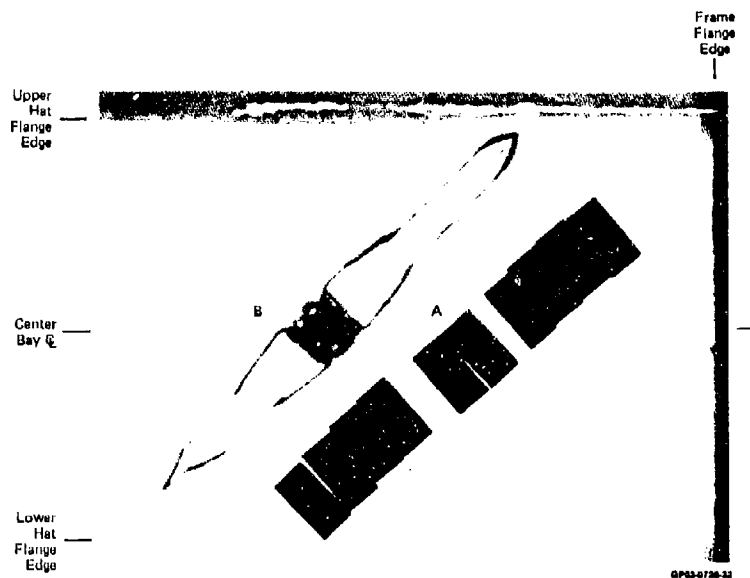


Figure 46. Radiographic Inspection of Impact Damage After 100,000 Cycles

Two other panels were impacted at the critical frame flange/skin location and subsequently fatigue tested. These panels were tested to a maximum fatigue load of 55% of ultimate strength to assure frame flange/skin separation. Both panels survived 100,000 cycles with visible stiffener separation occurring at the impact location at 950 and 2300 cycles respectively. Baseline panels tested to this level separated at 4500 and 33,000 cycles, respectively.

The frame flange/skin separation in the impacted region became extensive for both panels during the first 50,000 cycles. The frame flange along the impacted side of the center bay became nearly totally separated from the skin, causing a shift in the center bay buckling mode. Mid-panel strain response, Figure 46, indicated that the majority of separation occurred during the first 50,000 cycles causing a shift in buckling mode as indicated by the change in strain data for cycles 50,000 and 100,000. Buckling strengths of 115, 63, and 53 lb/in prior to fatigue testing and after 50,000 and 100,000 cycles, respectively, also indicate that the majority of damage occurred during the first 50,000 cycles. Residual strengths for both impacted panels was greater than the baseline panels, with sheet rupture across the tension diagonal.

4. BALLISTIC DAMAGE

Tests and analyses were performed to evaluate the effects of damage from impact of 23 mm high-explosive ballistic projectiles on the residual strength of composite structure incorporating various damage containment features. Various test setups were used to simulate air-to-air and ground-to-air ballistic threats to upper and lower wing skins. Good correlation was obtained between measured residual strengths and predictions made using the maximum strain failure criterion in conjunction with peak strains calculated about a hole in an orthotropic plate.

Carbon/epoxy specimens representative of monolithic wing skins and, for comparison, an aluminum specimen were damaged using 23 mm HEI projectiles. All specimens were flat, unstiffened plates.

Three damage containment features were incorporated in some composite specimens and evaluated relative to the performance of baseline composite specimens. These features, Figure 47, included parallel rows of Kevlar stitches, closely-spaced parallel rows of imbedded glass/epoxy buffer strips, and wider-spaced parallel rows of wide glass/epoxy buffer strips.

The stitched specimens utilized Kevlar thread having a breaking strength of 120 lbs and installed at four to six stitches per inch. Improved durability and damage containment were previously demonstrated in structures where cocured skin-to-substructure joints were reinforced with Kevlar stitches. In the specimens which incorporated glass/epoxy buffer strips, the 0° plies of graphite/epoxy were locally replaced, through the thickness, with 0° plies of glass/epoxy on either 3.5 inch centers or 13.5 inch centers.

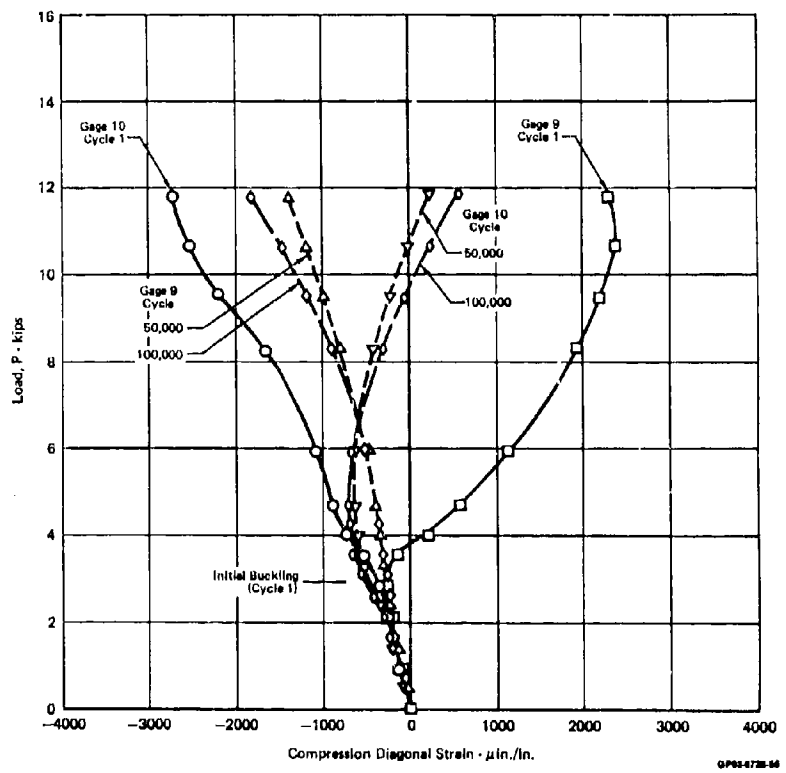


Figure 46. Mid-Panel Compression Diagonal Strains

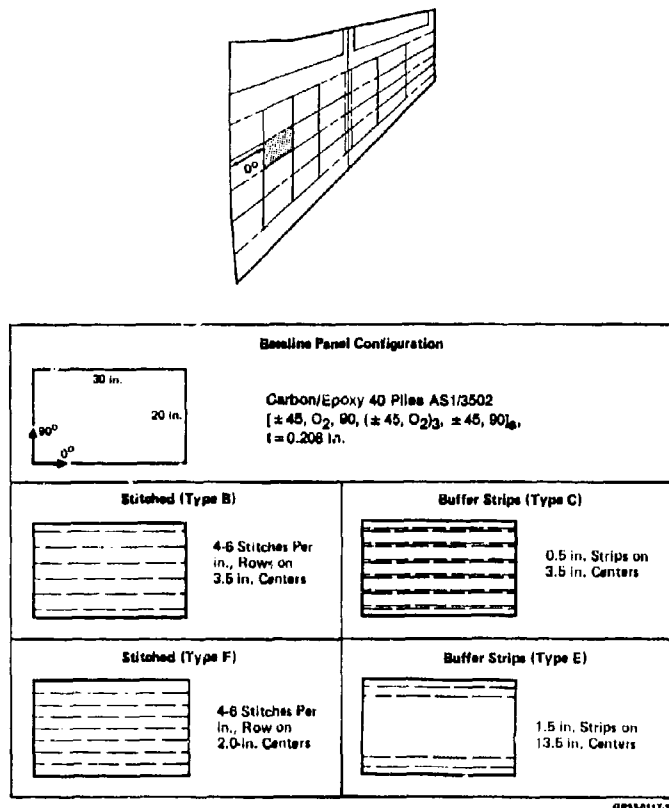


Figure 47. Ballistic Test Specimens

The test setup is shown in Figure 48. Projectile velocities, measured with photoelectric screens, ranged from 1773 fps to 1891 fps. The 23 mm projectile available for use in this program incorporated a "quick fuze" which was armed by inertial forces and, although triggered upon initial impact, featured a delay to allow 2-3 inch penetration prior to detonation. In this setup, the performance with a "superquick" fuze (instantaneous detonation) was simulated by positioning a striker plate in front of the specimen. Specimens were positioned normal to the trajectory. A water tank with deflector plate was used to capture fragments.

Damage from ballistic impact, Figure 49, ranged from a small, relatively clean, hole to a large diameter hole surrounded by delaminated plies, to a large multiple-penetration zone. Delay-fuze projectiles penetrated the entrance-side skin, leaving the small hole shown in Figure 49(a), detonated in the wingbox, and sprayed fragments over a wide area of the exit-side skin, (Figure 49 (b)). Other projectiles, when a striker plate was positioned to simulate effects of superquick fuzes, led to the damage shown in Figure 50. Delaminated areas of test panels, detected in ultrasonic inspections, are identified by the dotted lines in Figures 49 and 50.

Ultrasonic inspection records presented in Figure 51 illustrate the extent of delamination in specimens incorporating the various containment features. Relative to baseline composite specimens, delaminations in stitched specimens were limited in width to the rows of stitches adjacent to the fragment-penetration hole. Ability of stitches to contain delaminations has been noted in other investigations. Damage in specimens incorporating buffer strips was also limited in width by the imbedded strips; however, some additional laminate damage was noted along the strips.

The relative behavior of carbon/epoxy and aluminum skins having the same flexural stiffness was also evaluated. The test setup was for simulating damage to the exit-side from a projectile with a delayed fuze. Test results are shown in Figure 52. The plasticity of the aluminum permitted to the blast/impact energy to be absorbed by permanent deformation of the metal. The composite specimen remained flat; however, it exhibited numerous penetrations and delaminations throughout the damage zone.

The residual tensile strength of damaged specimens was determined in room-temperature static tests and correlated with analytic predictions. Specimens with buffer strips, particularly the wider strips at spar locations, exhibited significant improvement in strength relative to baseline specimens. Stitching had no effect on residual strength.

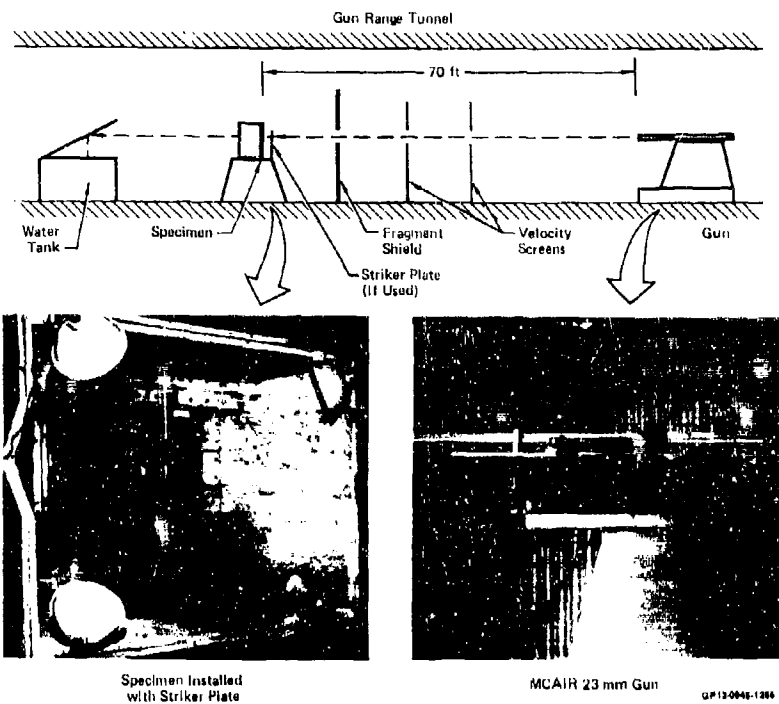


Figure 48. Ballistic Test Setup

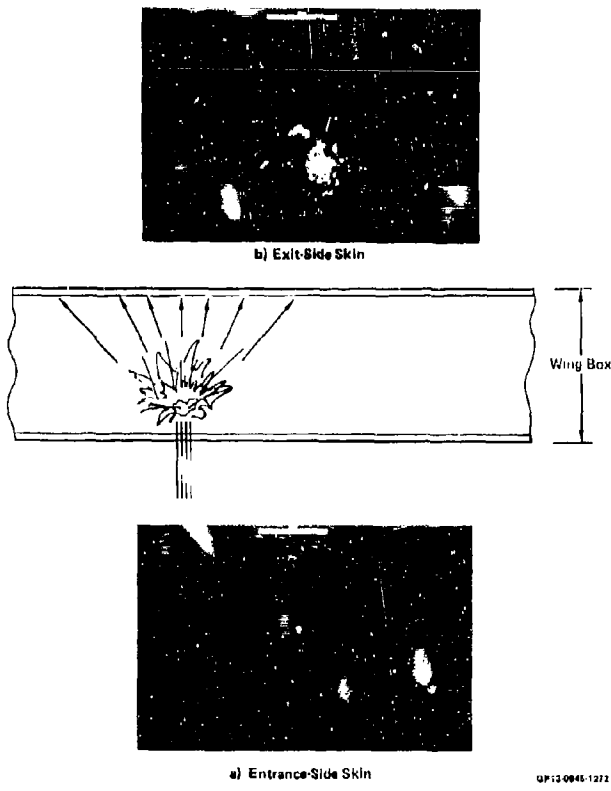


Figure 49. Typical Ballistic Damage - Delayed Fuze Projectile

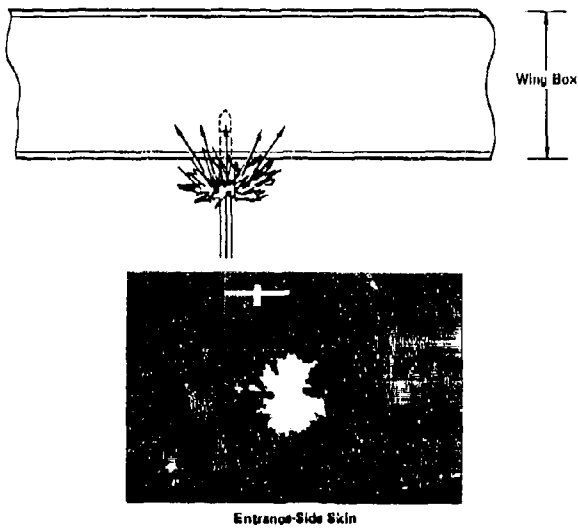


Figure 50. Typical Ballistic Damage - Superquick Fuze Projectile

GP13-0648-1272

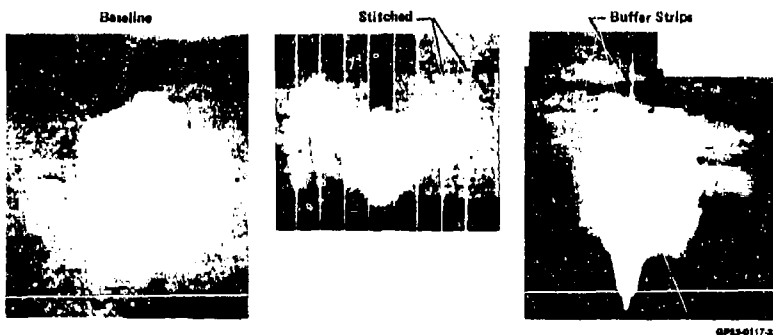


Figure 51. Delamination Damage Detected in Ultrasonic Inspections

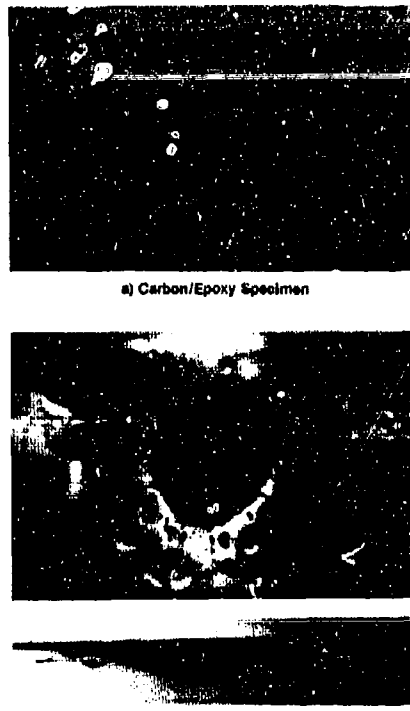


Figure 52. Typical Damage of Composite Specimen Compared to Metal Specimen

GPI10048-1244

Residual strengths are tabulated in Figure 53, along with the maximum visible damage and the maximum delamination damage detected by ultrasonics. Static failures were sudden with little time after failure initiation, except for those panels with buffer strips. Wide buffer strips stopped cracks from propagating across the width and turned the cracks lengthwise to propagate along the imbedded strips. Narrow, closely spaced buffer strips generally slowed to the propagation across the width. In general, use of buffer strips increased residual panel strength, except for specimens with a multi-penetration "shotgun blast" type of damage (Figure 49 (b)).

Residual tensile strengths are presented in Figure 54 as strain-to-failure for corresponding damage sizes. Strain-to-failure was calculated on the basis of the applied load at failure and gross-section properties. The range of damage presented for each specimen covers sizes from the maximum visible damage to the internal damage detected with ultrasonics. Specimens with buffer strips (shaded) exhibited significant improvement in residual strength relative to strength of baseline specimens (unshaded) having similar damage.

Specimen		Striker Plate Located to Simulate Damage for -	Measured Projectile Velocity (ips)	Visible Damage, Diameter (in.)	Internal Damage Length (0.01") x Width (0.01") (in.)	Residual Tensile Strength (lb)
Type	ID					
Baseline Carbon/Epoxy	A1	Delayed Fuze, Entrance-Side Skin	1,881	1	2 x 2	180,250
	A2	Delayed Fuze, Exit-Side Skin	1,784	2	△	66,250
	A3△	Superquick Fuze, Entrance-Side Skin	1,883	5	8 x 8	△
	A4△	Superquick Fuze, Entrance-Side Skin	1,883	9	14 x 10	84,000
	A5△	Superquick Fuze, Entrance-Side Skin	1,870	9	14 x 14	50,600
	B1△	Superquick Fuze, Entrance-Side Skin	1,848	6	8 x 6	△
Carbon/Epoxy with Rows of Stitches on 3.5-in. Centers	B2△	Superquick Fuze, Entrance-Side Skin	1,879	10	12 x 12	68,950
	B3	Delayed Fuze, Exit-Side Skin	1,829	4	△	△
	B4	Superquick Fuze, Entrance-Side Skin	1,826	6	8 x 8	△
	C1△	Superquick Fuze, Entrance-Side Skin	1,790	7	12 x 8	105,000
Carbon/Epoxy with 0.5-in. Buffer Strips on 3.5-in. Centers	C2	Delayed Fuze, Exit-Side Skin	1,880	2	△	74,200
	C3△	Superquick Fuze, Entrance-Side Skin	1,787	8	16 x 9	107,500
	C4△	Superquick Fuze, Entrance-Side Skin	1,862	3	16 x 8	143,250
	D1	Delayed Fuze, Exit-Side Skin	1,859	4△	-	△
Carbon/Epoxy with 1.5-in. Buffer Strips on 19.5-in. Centers	E1	Superquick Fuze, Entrance-Side Skin	1,865	6	10 x 10	115,000
	E2	Superquick Fuze, Entrance-Side Skin	1,864	10	16 x 13	88,500
Carbon/Epoxy with Rows of Stitches on 2.0-in. Centers	F1	Superquick Fuze, Entrance-Side Skin	1,871	8	8 x 8	△
	F2	Superquick Fuze, Entrance-Side Skin	1,854	7	8 x 11	△

Notes:

- △ Tests conducted as part of NAUC contract N02269-80-C-0130
 ▲ Multiple penetrations over 20 in. x 20 in. area
 □ Structural tests not planned
 ▨ Permanent deformation over 16-in. diameter with multiple penetrations
 △ Structural tests not complete

OP13-0946-1275

Figure 53. Test Results - Ballistically Damaged Specimens

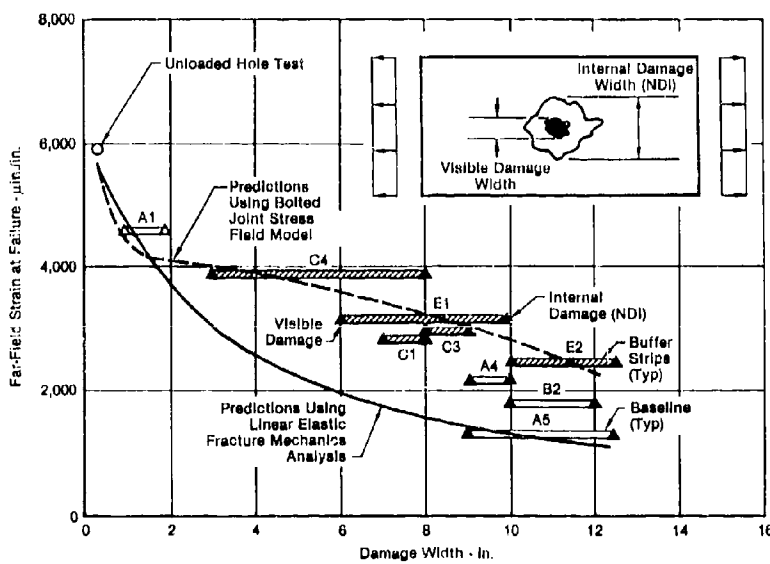


Figure 54. Residual Strength of Ballistically-Damaged Specimens

Two analytical procedures for predicting residual strength were evaluated. All predicted strengths were corrected for a finite specimen width (20 in.). Linear elastic fracture mechanics analysis techniques (Reference 6) were used to predict a lower bound. Projectile damage was assumed to consist of through-the-thickness defects equal in width to the maximum visible and maximum internal damage.

In the second approach, the damage was assumed to be a circular hole in an orthotropic plate, and the methodology of Reference 7 was used to predict strain distributions about the hole. These strains were used in conjunction with the Maximum Strain Failure Criterion to predict far-field strain to failure as a function of damage (hole) size. Good correlation was first obtained between predictions and test results for a 0.25-inch-diameter fastener hole followed by extension of predictions to larger damage sizes. The residual strength of specimens with buffer strips compare well with these predictions.

5. CONCLUSIONS

Several conclusions were drawn from results of the programs described above.

First, it was concluded that manufacturing defects which produced the more significant strength reductions were easily found by current NDE techniques and would have been rejected or repaired by current acceptance criteria. Tolerances and controls being used in fabrication and assembly of composite aircraft structures are adequate to assure uniform strength and structural performance.

Second, the propagation of damage from low energy impact is dependent on type of loading and strain levels. The strength loss of the damaged laminate can be approximated on the basis of an "equivalent" round hole. The propagation under repeated loads is relatively slow and can be confined by relative simple reinforcement techniques such as stitching.

Third, the damage caused by 23mm HEI ballistic impact is more significant than LEID. The loss of laminates strength due to ballistic damage of a given size is greater than from LEID of the same apparent size. To reduce the strength loss, more significant reinforcement techniques such as buffer strips are required; stitching is not adequate.

REFERENCES

1. S. P. Garbo and J. M. Ogonowski, "Effect of Variances and Manufacturing Tolerances on the Design Strength and Life of Mechanically Fastened Composite Joints", Contract F33615-77-C-3140, USAF RPT AFWAL-TR-81-3041, April 1981.
2. T. V. Hinkle and R. A. Garrett, "High Strain Composite Wing for Fighter/Attack Type Aircraft - Concept Validation", NADC-80146-60, September 1982.
3. T. V. Hinkle and R. A. Garrett, "Examination of Postbuckled Compression Behavior of Curved Panels", MCAIR/NASC Contract NU0019-79-C-0204, MDC RPT A7264, August 1982.
4. M. P. Renieri and R. A. Garrett, "Postbuckling Fatigue Behavior of Flat Stiffened Graphite/Epoxy Panels Under Shear Loading" NADC Contract NO2269-79-C-0463, RPT NADC-78137-60, July 82.
5. Butler, B.M., "Wing/Fuselage Critical Component Preliminary Design (Northrop)", AFDDL-TR-78-174, March 1979.
6. Avery, J.G. and Bradley, S.J., "Design Manual for Battle Damage Tolerant Fiber Composite Structures", NASC Contract NU0019-80-C-0048. Boeing Report D180-26092-1, June 1980.
7. Ogonowski, J.M., "Effect of Variances and Manufacturing Tolerances on the Design Strength and Life of Mechanically Fastened Composite Joints: Volume 3-Bolted Joint Stress Field Model (BJSFM) Computer Program User's Manual", AFWAL-TR-81-3041, Volume 3, April 1981.



20-1

AD P001926

THE ENGINEERING SIGNIFICANCE OF DEFECTS IN COMPOSITE STRUCTURES

by
D. J. Wilkins
Engineering Staff Specialist
GENERAL DYNAMICS
P.O. Box 748
Fort Worth, TX
76101

SUMMARY

The significance of defects in composite aircraft structures is described from a broad, practical viewpoint. The description is organized by concentrating on three generic defect types (cut fibers, matrix cracks, and delaminations) and on simple load components that can be generalized to the most complex loading cases. Methods for evaluating manufacturing and in-service damage in terms of the resulting local damage are reviewed. In addition, the possible benefits of more damage tolerant forms of composite materials are explored.

INTRODUCTION

Recent work in the area of damage tolerance of composites has stimulated a new level of understanding of the effects of defects in composites. The subject is developed here by first discussing the loading conditions. The classification of damage into three generic types then sets the stage for descriptions of how the damage types can be treated. Finally, the implications of different forms of composite materials are explored.

LOADING

This discussion is intended to encompass all types of loading conditions to which composite aircraft structures may be subjected. Both static and cyclic loadings are specifically addressed. To simplify the discussion, loads caused by thermal and/or moisture sources are assumed to be included as equivalent mechanical loadings. In addition, the discussion is restricted to environmental combinations of temperature and moisture at which the matrix behaves as a brittle, glassy solid. In other words, viscoelastic effects are assumed to be negligible.

Because of the overwhelming dominance of the fibers in the structural behavior, fibrous composite laminates are most useful in membrane applications. Consequently, they are most often intended to carry in-plane tension, compression, or shear loads. In-plane shear will be assumed to always be resolvable into tension and compression components, so will not be specifically addressed.

Loadings that put the fibers in tension bring out the best features of fibrous composites. The fibers tend to straighten and approach their theoretical stiffness and strength potential. In fatigue, tension-loaded composites are superior to virtually any material of equal weight. On the other hand, the notch sensitivity of the best structural fibers is a driving concern for engineering applications, and merits considerable attention from designers and analysts, as described later.

In-plane compression of laminates is greatly complicated by the tendency for the fibers to bend and buckle. Because the fibers within a ply are not really straight, axial compression produces shear components of load between the fiber and matrix. These out-of-plane components can lead to tension loads in the matrix that may cause premature structural failure. Cyclic compression load applications are especially likely to trigger unwanted matrix effects. In compression, notches also aggravate the sensitivity by producing areas of concentrated load.

Engineering applications of fibrous composites on aircraft have almost always had to consider the most general possible loading conditions. Some combination of cyclic tension and compression, in the presence of structural penetrations, is the typical case.

LOCAL FAILURE MODES

Because of the distinct nature of defects and damage in composite laminates constructed from uni-directional tape, three definitions are established to describe these damage states. Figure 1 illustrates the cut fiber, matrix crack, and delamination damage types that may occur in composite laminates. Cut fibers occur at every hole, cutout, and through-crack in a laminate. Matrix cracks are characterized as partial through-cracks that are constrained to arrest inside the laminate and do not break fibers. A delamination is a crack that occurs between the plies of a laminate.

The relationship between various threats of structural damage and the resulting local damage in a composite laminate is illustrated qualitatively in Figure 2. The threats are listed in increasing order based on the extent of damage to the laminate. It is seen that minor threats cut or break few fibers and cause only minimal delamination.

Conversely, severe threats cut many fibers and may cause extensive delaminations. Since matrix cracks generally occur under fatigue load conditions, it is appropriate to assume that a characteristic spacing (References 1-2) of these cracks exists in the laminate. Cut fibers represent an important damage mode because the fibers clearly control the stiffness and strength of the laminate. When cut-fiber damage occurs as a hole or through-notch, it is generally detectable by visual means. This damage does not grow under fatigue loading, but rather causes a one-time reduction in the static strength. Although delaminations cause reduced stiffness and tensile strength, their major effect is to significantly lower the compressive buckling load of a composite laminate. Delaminations are generally not detectable by visual means. They often grow as stable cracks under continued cyclic loading.

Expanding on these ideas with the aid of Figure 3, we ask the question of how each of the three types of damage is affected by fatigue loading. For example, consider the cut-fiber form of damage. This is superficially the same as a flaw or crack in a metal structure. But unlike the flawed metallic structure, the cut-fiber damage does not grow under fatigue loading. Furthermore, the residual tensile strength of the composite laminate has been observed in many experiments to increase when a small notch is present (Reference 3).

Matrix cracks generally form under fatigue load conditions. Although they are not identified directly as a structural failure mode, the matrix cracks may provide initiation sites for delaminations as shown by Jamison, et al, in Reference 4. This interaction between matrix cracking and delamination deserves careful scrutiny during the design and qualification test phases to ensure that a delamination-prone laminate is not put into service.

When subjected to fatigue loading, delaminations tend to follow growth laws that are similar to those observed for metals. However, two unique features of delaminations are that they can exhibit slow, stable, subcritical flaw growth in structural applications (Wilkins, Reference 5), and that buckling failure under compressive loading is quite sensitive to the size of the delamination (Whitcomb, Reference 6). A frustrating feature of delaminations is that they are not usually detectable by visual means, and generally require sonic methods of inspection.

For the simple case of a single-load-path structure, the effect of the local damage modes on the residual strength is outlined in Figure 4. Although the cut-fiber/through-crack damage does not grow under fatigue loading, the static residual strength may be reduced by the number of fibers cut (the size of the through-crack). The damaged laminate must therefore be checked against the in-service residual strength requirement, which is generally some percentage above design limit load.

The matrix-cracking form of local damage has no real effect on the residual strength of the component. Matrix cracking is only relevant as it relates to initiation sites for delamination.

Delamination is the flaw type to which damage growth provisions will typically apply. The compression residual strength of the composite structure may be controlled by the size and location of the delamination. Thus, it is imperative that the design of the composite structure not only be resistant to the formation of delaminations, but also control the growth of delaminations. Since it is virtually impossible to control the low-energy impacts that can initiate delaminations, the designer must assume that such delaminations exist in the laminate a priori and control their growth by design.

CUT-FIBER DAMAGE

As discussed above, cut-fiber damage is insensitive to fatigue and is one of the strongest reasons for applying composite structures to aircraft. An analysis benefit is also realized because only the residual static strength of the cut-fiber-damaged laminate needs to be predicted.

An approach advanced by Waddoups, Eisenmann, and Kaminski (Reference 3) is based on the postulation that linear elastic fracture mechanics describes the notch size effect on static strength. Further, the fracture toughness of the laminate is based on the fracture toughness of the individual plies. For example, in the case of a circular hole in a laminate, a fracture analysis can be performed on the element of the laminate containing the hole, as illustrated in Figure 5. In all but the simplest cases, this element is loaded by a general set of in-plane stresses consisting of tensile (or compressive) normal stresses and a shear stress. The magnitudes of these stresses can be obtained either from a finite-element analysis of the structure or from a hand calculation for simple configurations. The element loads can be broken down into a set of simple loads, as shown in Figure 6. Anisotropic solutions, developed by Lekhnitskii (Reference 7), provide the stresses acting along the hole boundary for these load cases. The solutions may be superposed to determine the stresses acting in the composite laminate along the hole boundary for the general loading case.

Because in-plane fracture is controlled by the fibers, attention may be restricted to those locations where the fibers become tangent to the boundary of the hole. As a result, fracture analysis solutions are only required for three cases, as shown in Figure 7. Stress-intensity-factor solutions have been numerically determined by Eisenmann (Reference 8) for these three load cases in orthotropic laminates.

The value of the unidirectional fracture toughness can also be calculated following the work of Konishi and Cruse (Reference 9). This calculation requires only that critical strain-energy-release rates for the constituent plies of the laminate are known.

While considerable controversy still surrounds the application of linear elastic fracture mechanics to composite laminates, this method has proved its worth for engineering predictions of structural behavior for over 10 years at General Dynamics (See Figure 8). Although the colinear crack assumption of classical fracture mechanics is clearly violated by cracks that cut fibers, the strength of notched composites appears to be adequately described by such a fracture approach when the notch dominates the response.

DELAMINATION

Some insight into the nature of delamination in graphite-epoxy can be obtained by exploring the toughness of some typical laminates in all three directions. Figure 9, adapted from the results of Konishi and Cruse (Reference 9), plots fracture toughness as a function of the percentage of 0-degree plies in a laminate containing only 0-degree and ±45-degree plies. The data were obtained with edge-notched beams and center-notched coupons. The trends are typical of the Thornewood/Narmco 5208 class of graphite-epoxy, but the absolute numbers are not strictly valid because no ASTM standards have been developed for fracture toughness of composites. Nevertheless, we would agree that an all ±45-degree laminate has a reasonable toughness slightly less than aluminum. As ±45-degree plies are replaced by 0-degree plies, the toughness in the x-direction would be expected to increase until it was about doubled. On the other hand, as ±45-degree plies are replaced by 90-degree plies, the toughness in the x-direction is expected to decrease until it reaches a minimum represented by a crack running completely in the resin between the fibers. The real point is that in the interlaminar mode, the toughness in the z-direction is always at the minimum, regardless of the laminate orientations.

These low values of interlaminar toughness are only significant as they relate to the magnitude of typical out-of-plane load sources, as shown in Figure 10. Five of the most common design details from which real hardware is constructed are shown schematically. Each of these details, even under in-plane loading, gives rise to interlaminar normal and shear stresses. Direct out-of-plane loads come from fuel pressures, air pressures, and from structural mismatches associated with assembly of detail parts. These direct loads combine with those already present from lamination effects. The interlaminar forces act directly on the plane of minimum toughness. As a result, delaminations may form, and if the in-plane forces are compressive, buckling becomes a pertinent issue.

The traditional solution to this interaction of defects and compressive buckling would be an extensive test program. However, creation of a compression coupon data base is impractical because interlaminar tension and shear interact with local and overall buckling. Consequently, questions of specimen size, end conditions, and lateral support make scaleup to real hardware almost impossible.

A simpler, more direct approach, as depicted in Figure 11, is to use an analysis to define the transfer function between applied loads and local rupture forces that tend to concentrate at laminate defects. Then the experimental effort can focus on tension and shear failure mechanisms in the matrix.

The capability is available from adhesive fracture technology, as described by Anderson, Bennett, and DeVries (Reference 10), for computing the profiles of strain-energy release rate around a delamination in a laminated plate under general loading. Applications of the technology to composite laminates have been reported in References 11-14. As schematically depicted in Figure 12, the profiles can be broken into components for use in a fracture-mechanics-based failure theory such as proposed by Wu (Reference 15). The strain-energy-release-rate calculations can be performed with finite-element methods coupled with the virtual-crack-closure technique as described by Rybicki and Kanninen (Reference 16).

These techniques were successfully used by General Dynamics to predict the effects of defects in the F-16 horizontal tail for the U. S. Air Force fleet management program. Various aspects of the program have been reported in References 5, 17-18. Wilkins, Eisenmann, Camin, Margolis, and Benson (Reference 17) discussed the development of methods to characterize delamination growth by creating a coupon data base. Wilkins (Reference 5) presented the full scale verification of the methodology as outlined in Figure 13 to evaluate damage tolerance of composite hardware. In Reference 18, Wilkins discussed the net analysis approach in terms of its implications for design, analysis, and testing of composite structures.

In contrast to the comments previously made about the controversy surrounding the application of fracture mechanics to the cut-fiber problem, fracture mechanics should be much more appropriate for describing not only the strength but also the growth behavior of delaminations. Because no fibers are cut during the delamination process, the colinear crack growth assumption is not violated.

IMPLICATIONS OF DIFFERENT COMPOSITE FORMS

Up to now, only composites constructed with unidirectional tapes have been discussed. Laminates made from tape have been preferred at General Dynamics because of

their structural efficiency and the economy with which they can be laid up with tape-laying machines.

In view of the preceding discussion of the effects of defects and damage, it is appropriate to generalize the treatment to include other common forms like fabrics, and even uncommon forms like braided or 3-dimensionally reinforced composites. Such forms can provide damage tolerance benefits beyond their proven manufacturing utility for parts with complicated shapes.

Referring back to Figures 1 and 2, it is clear that woven fabrics remove the matrix cracking damage from consideration. Because matrix crack damage is relatively benign, and was only of concern as it provided initiation sites for delamination, the benefit of removing the matrix crack damage mode is relatively small. At some expense of in-plane stiffness and strength, only cut fibers and delamination remain to be interrogated with regard to the effects of defects in fabric laminates. According to Bascom, et al, (Reference 19) the interlaminar toughness for fabrics has been shown to be higher than that for tape of the same constituents because of the component of fibers in the thickness direction and the larger resin pockets between the plies. However, fabric laminates still exhibited only a fraction of the toughness of the bulk resin.

The removal of delamination as a failure mechanism by selective placement of fibers through the thickness of a laminate could drastically simplify the structural integrity evaluation of laminated composite structures. At least two techniques for achieving 3-dimensional composites are possible. From the world of textiles, procedures for braiding are rather well-advanced. The successful braiding of detail parts seems only a question of how large a part can be economically manufactured.

From the world of shoemakers, the technology of stitching is readily available. One impediment to successful stitching of composites seems to be modifying existing equipment to handle stiff threads such as graphite, which would be preferred for most efficiently transferring interlaminar stresses.

Whichever method is eventually perfected, a properly designed 3-dimensional composite should be completely insensitive to all forms of matrix damage. Thus, referring back to Figure 4, the only remaining damage type would be the cut fiber. As mentioned previously, the cut fiber damage requires only a static strength analysis, and visual inspection methods can usually discover the damage. The overall payoff is a level of structural efficiency, damage tolerance, inspectability, and reliability that should easily offset the increase in design and manufacturing complexity.

CLOSURE

The aim of this discussion has been to review an approach for evaluating the significance of defects and damage in structural composites. The approach is based on segregating the possibilities into a practical, workable set of problems whose solutions can be worked out by structural engineers. Adoption of such procedures can lead to more efficient and useful applications of composite materials to engineering structures.

REFERENCES

- 1 Reitsnider, K. L., and Masters, J. L., "Investigation of Characteristic Damage States in Composite Materials," ASME Paper No. 78-WA/AFRO-4, 1978.
- 2 Grossman, J. W., Warren, J., Wong, A. S. D., and Law, G. L., "Initiation and Growth of Transverse Cracks and Edge Delamination in Composite Laminates: Part 2. Experimental Correlation," Journal of Composite Materials, Supplemental Vol., 1980.
- 3 Waddoups, M. L., Eisenmann, J. R., and Kaminski, B. E., "Macroscopic Fracture Mechanics of Advanced Composite Materials," Journal of Composite Materials, Vol. 5, 1971.
- 4 Lamison, R. D., Schulte, K., Reitsnider, K. L., and Stinchcomb, W. W., "Characterization and Analysis of Damage Mechanisms in Fatigue of Graphite/Epoxy Laminates," Effects of Defects in Composite Materials, ASTM, to be published.
- 5 Wilkins, D. J., "A Preliminary Damage Tolerance Methodology For Composite Structures," Workshop on Failure Analysis and Mechanisms of Failure of Fibrous Composites, NASA/Langley Research Center, 1982.
- 6 Whitcomb, J. D., "Finite Element Analysis of Instability-Related Delamination Growth," Journal of Composite Materials, Vol. 15, 1981, pp. 403-426.
- 7 Lekhnitskii, S. G., Anisotropic Plates, translated by S. W. Tsai and T. Cheron, Gordon and Breach Science Publishers, Inc., New York, NY, 1968.
- 8 Eisenmann, J. R., "Bolted Joint Static Strength Model for Composite Materials," Third Conference on Fibrous Composites in Flight Vehicle Design, NASA TMX-337, Williamsburg, VA, 1975.
- 9 Konishi, H. J., Jr., and Cruse, T. A., "Determination of Fracture Strength in Orthotropic Graphite-Epoxy Laminates," Composite Reliability, ASTM STP 580, 1974, pp. 490-503.

- 10 Anderson, G. P., Bennett, S. J., and DeVries, K. L., Analysis and Testing of Adhesive Bonds, Academic Press, New York, 1977.
- 11 Roderick, G. L., Everett, R. A., and Crews, J. H., Jr., in Fatigue of Composite Materials, ASTM STP 569, 1975, pp.295-306.
- 12 Rybicki, E. F., Schmueser, D. W., and Fox, J., Journal of Composite Materials, Vol. 11, 1977, p. 470.
- 13 Wang, S. S., "Edge Delamination in Angle-Ply Composite Laminates," Proceedings of the 22nd AIAA, ASME, ASCE, AHS Structures, Structural Dynamics, and Materials Conference, Part 1, Atlanta, GA, April, 1981, pp. 473-484.
- 14 Chatterjee, S. N., Pipes, R. B., and Blake, R. A., Jr., "Criticality of Disbonds in Laminated Composites," Effects of Defects in Composite Materials, ASTM, to be published.
- 15 Wu, E. M., "Applications of Fracture Mechanics to Anisotropic Plates," Journal of Applied Mechanics, Vol. 34, 1967, pp.967-975.
- 16 Rybicki, E. F., and Kanninen, M. F., "A Finite Element Calculation of Stress Intensity Factors by a Modified Crack-Closure Integral," Engineering Fracture Mechanics, Vol. 9, No. 4, 1977, pp. 931-938.
- 17 Wilkins, D. J., Eisenmann, J. R., Camin, R. A., Margolis, W. S., and Brannon, R. A., "Characterizing Delamination Growth in Graphite-Epoxy," Damage in Composite Materials, ASTM STP 775, 1982, pp. 168-183.
- 18 Wilkins, D. J., "Damage Tolerance of Composites: Changing Emphasis in Design, Analysis, and Testing," Sixth Conference on Fibrous Composites in Structural Design, New Orleans, LA, 1983.
- 19 Bascom, W. D., Bitner, J. L., Moulton, R. J., and Siebert, A. R., "The Interlaminar Fracture Toughness of Organic-Matrix, Woven Reinforcement Composites," Composites Journal, Vol. 11, 1980, pp. 9-18.

ACKNOWLEDGEMENTS

This work was supported by the F-16 Airplane System Program Office, Aeronautical Systems Division, United States Air Force, as part of the F-16 Production Fleet Management Program. Air Force engineers contributing to its results were N. P. McManus, B. K. Archer, D. O. Tipps, and J. C. Halpin. The important contributions of my colleagues at General Dynamics are gratefully acknowledged.

LIST OF FIGURES

- 1 Local damage can be effectively described by 3 fundamental mechanisms
- 2 Various structural threats cause different amounts of local damage
- 3 Fatigue loading stimulates delamination growth
- 4 Residual strength depends on cut fibers and delamination size
- 5 Fracture analysis is performed on an elemental basis
- 6 Simple loads superpose for general loads
- 7 Basic stress intensity solutions superpose for general load case
- 8 Procedure predicts notched strength
- 9 Interlaminar toughness is low compared to in-plane values
- 10 Interlaminar stresses arise from typical details
- 11 Transform the compression problem
- 12 Delamination analysis uses fracture mechanics approach
- 13 Combine into damage tolerance evaluation

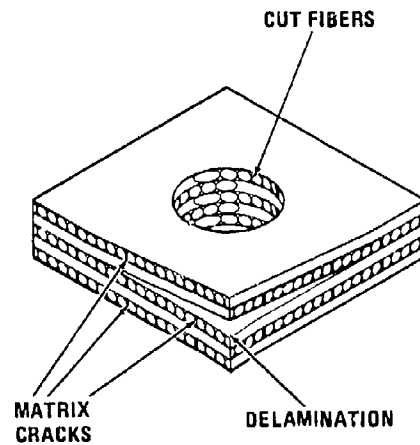


Figure 1 Local Damage Can Be Effectively Described by 3 Fundamental Mechanisms

NATURE OF THREAT	RESULTING LOCAL DAMAGE		
	CUT FIBERS	MATRIX CRACKS	DELAMINATION
MATERIAL FLAW	FEW		
MFG ERROR			MINIMAL
IMPACT	MANY		
PUNCTURE		CHARACTERISTIC SPACING ASSUMED	MODERATE
HYDRODYNAMIC HAM	VERY LARGE NUMBER		
23mm Hg E			EXTENSIVE

Figure 2 Various Structural Threats Cause Different Amounts of Local Damage

NATURE OF THREAT	RESULTING LOCAL DAMAGE		
	CUT FIBERS	MATRIX CRACKS	DELAMINATION
MATERIAL FLAW	FEW		
MFG ERROR			
IMPACT	MANY		
PUNCTURE		CHARACTERISTIC SPACING ASSUMED	
HYDRODYNAMIC RAM	VERY LARGE NUMBER		
23mm HE			
EFFECT OF SUBSEQUENT FATIGUE LOADING	NONE	MAY PROVIDE SITES FOR DELAMINATION INITIATION	MAY GROW IN $\frac{d\delta}{dn}$ vs G SENSE

Figure 3 Fatigue Loading Stimulates Delamination Growth

NATURE OF THREAT	RESULTING LOCAL DAMAGE		
	CUT FIBERS	MATRIX CRACKS	DELAMINATION
MATERIAL FLAW	FEW		
MFG ERROR			
IMPACT	MANY		
PUNCTURE		CHARACTERISTIC SPACING ASSUMED	
HYDRODYNAMIC RAM	VERY LARGE NUMBER		
23mm HE			
EFFECT OF SUBSEQUENT FATIGUE LOADING	NONE	MAY PROVIDE SITES FOR DELAMINATION INITIATION	MAY GROW IN $\frac{d\delta}{dn}$ vs G SENSE
RESIDUAL STRENGTH	ABOVE OR BELOW P_{xx} DEPENDING ON NO. OF CUT FIBERS	NO EFFECT ON RESIDUAL STRENGTH	ABOVE OR BELOW P_{xx} DEPENDING ON DELAMINATION SIZE

Figure 4 Residual Strength Depends on Cut Fibers and Delamination Size

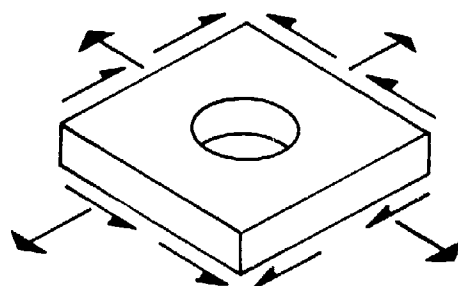


Figure 5 Fracture Analysis Is Performed on an Elemental Basis

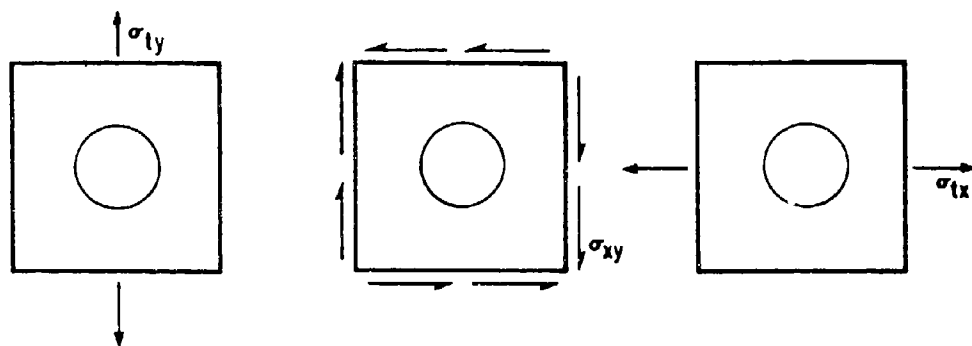


Figure 6 Simple Loads Superpose for General Loads

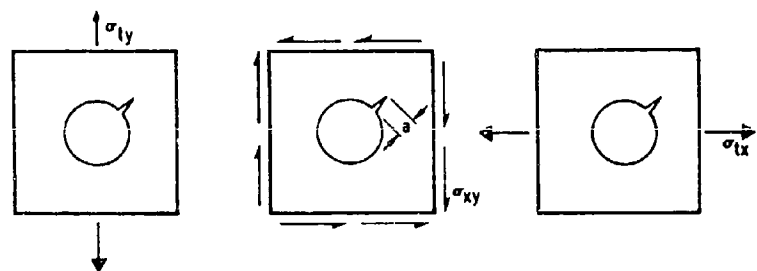


Figure 7 Basic Stress Intensity Solutions Superpose for General Load Case

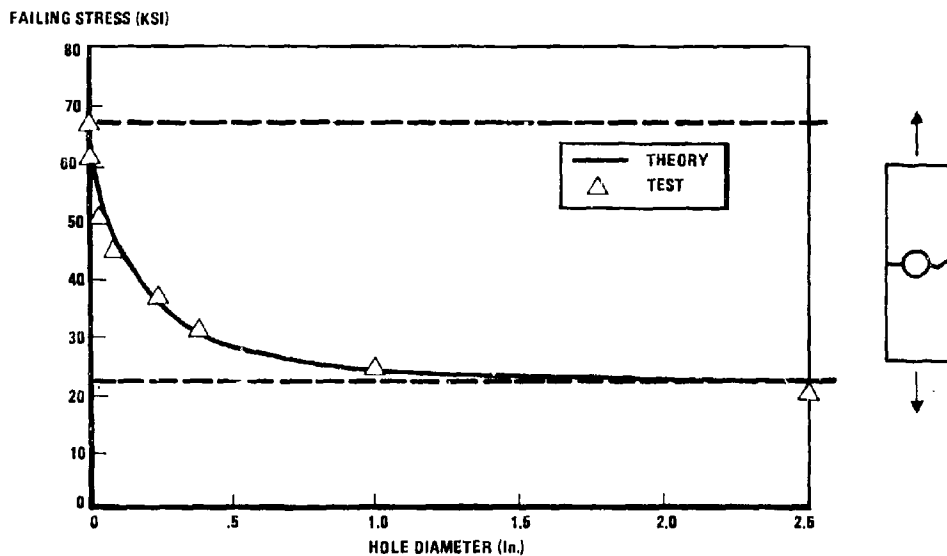


Figure 8 Procedure Predicts Notched Strength

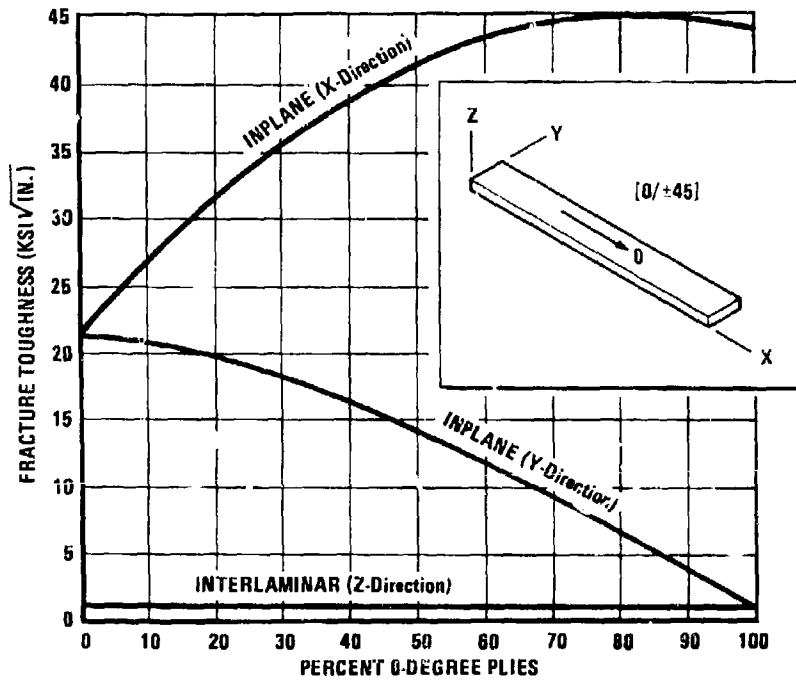


Figure 9 Interlaminar Toughness Is Low Compared to In-Plane Values

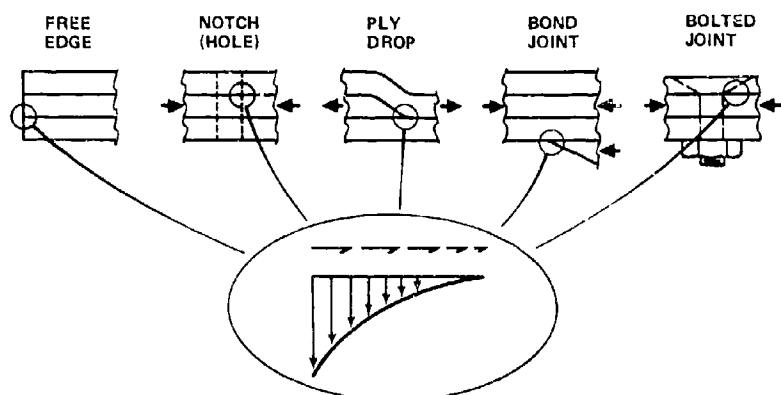


Figure 10 Interlaminar Stresses Arise from Typical Details

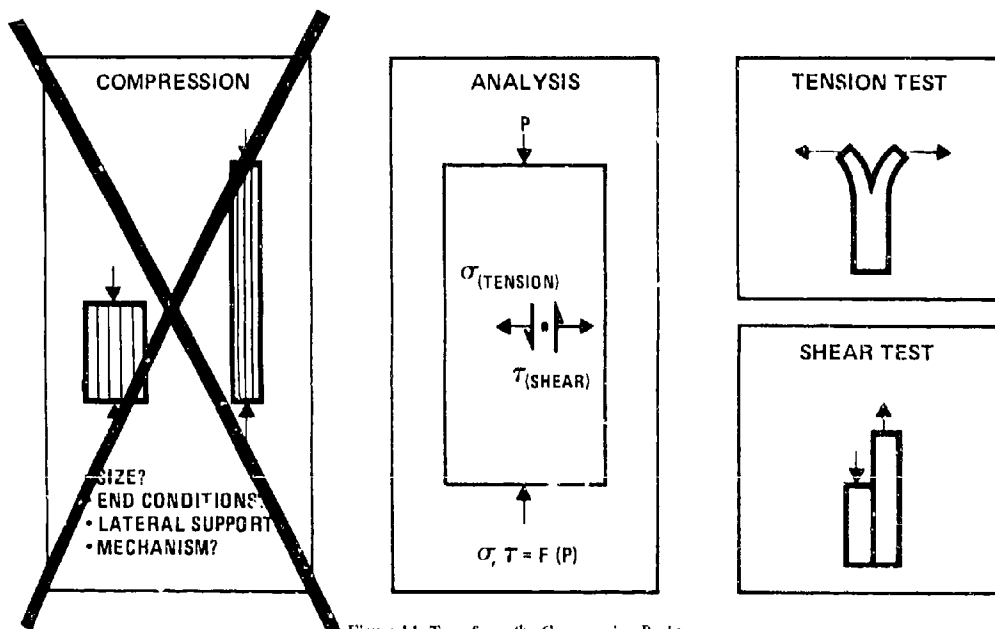


Figure 11 Transform the Compression Problem

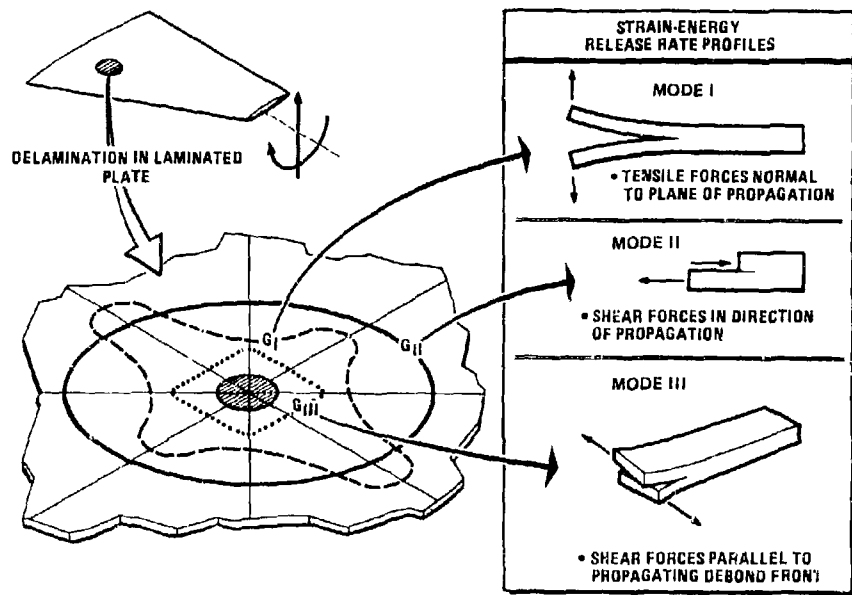


Figure 12 Delamination Analysis Uses Fracture Mechanics Approach

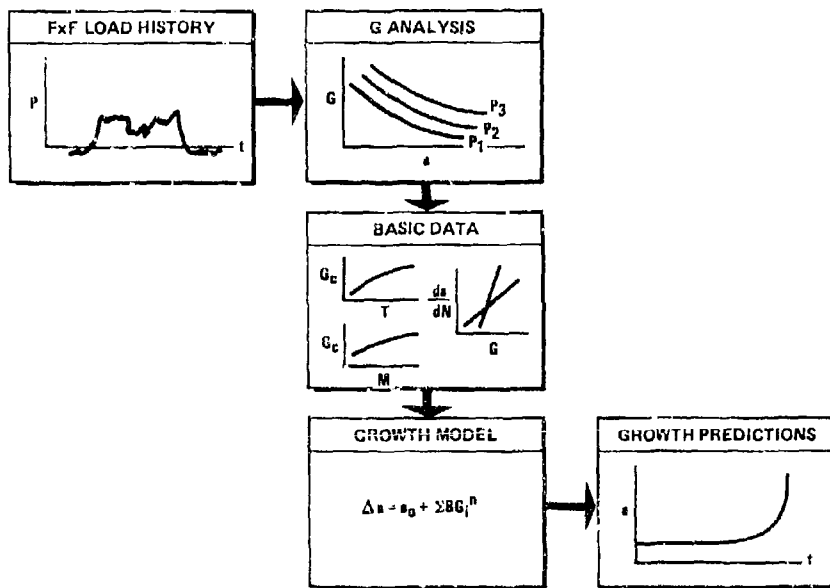


Figure 13 Combine into Damage Tolerance Evaluation

AD P001927

DEFECT OCCURRENCES IN THE MANUFACTURE OF
LARGE CFC STRUCTURES AND WORK ASSOCIATED
WITH DEFECTS, DAMAGE AND REPAIR OF CFC COMPONENTS

BY

C S FRAME & G JACKSON
British Aerospace PLC
Aircraft Group
Warton Division
Preston PR4 1AX
U.K.

SUMMARY

→ Current activities in a Ministry of Defence funded research investigation into the effects of defects and damage, and their repair, are reviewed. Future work in this field is also discussed.

The occurrences of defects and damage in large CFC structures (eg. Tornado taileron, Jaguar wing etc) are then presented and comments made on experience gained from flight and ground testing.

Current NDT detection and characterisation methods are presented together with an outline of the work proposed to overcome existing problem areas and limitations. ←

INTRODUCTION

Since the early 1960s CFC has increasingly been considered for use in aerospace structures. As usage and confidence has increased over the years, the trend has been from lightly loaded secondary structures, through stiffness designed items, towards more highly loaded strength designed primary structures. As the performance requirements of CFC have increased, so too has the demand for improved quality assurance and more detailed knowledge of the effects of defects and damage. The increase in utilisation is dramatically illustrated in Figure 1.

Ideally the effects of both manufacturing and in-service defects and damage should be established by manufacturing CFC items, putting them into service and examining the effects of any naturally occurring instances of defects and/or damage. This, however, can only give an insight into one defect in one specific item and is totally impractical.

BAe Warton is gaining valuable, practically derived information via 3 separate routes. The primary source of information is a Ministry of Defence funded "Defect, Damage and Repair Programme" which is a multiphase investigative project which simulates natural defects and damage by artificial means and is also being used to assess efficient, viable in-service repair techniques. Secondly, several CFC items have been manufactured and put into service enabling any naturally occurring defects/damage to be monitored and, where necessary, repaired. Finally, several demonstrator programmes have been embarked upon, some of which will be flight tested. This again allows examination of naturally occurring defects/damage.

In parallel with these activities, the specialist N.D.T. group are ensuring that defects can be successfully located and defined, damage areas accurately mapped and that repairs are of high integrity; again the prime aim is that all equipment and techniques are eventually suitable for in-service use.

DEFECT, DAMAGE & REPAIR

This multiphase Ministry of Defence funded programme is being used to gain essential information on the effects of typical defects and damage and also to examine repairs.

Phase 1, which is currently in progress, takes a spectrum of typical defects and damage and will give an initial insight into the effects of these on parent "undamaged" strengths. At the same time, repairs are being investigated to establish efficient viable repairs which can be carried out in an in-service environment. Lessons learned, or questions raised, by this phase will be addressed in Phase 2.

Since many of the test results presented here have only recently become available, full analyses and definitive conclusions cannot always be presented.

DEFECTS AND DAMAGE

Surface Scratches

The effects of surface scratches are shown in Figure 2 as they apply to one basic layup, ambient conditions and static test. A prediction method based on scratch

depth and remaining net layup was used; these predicted values are shown and compare reasonably well, if a little pessimistically, with the test mean results.

Bolted Joint Defects

The effects of several different defects in bolted joints are shown in Figure 3. The defects had little, if any, effect when tested under ambient conditions and even the effects of temperature and moisture reduced the bolted joint strength by only 15%. The fatigue specimens were subjected to the equivalent of 30,000 hours by spectrum loading and showed a slight increase in strength when residually tested.

Bonded Joint Defects

The effects of a disbond type defect in bonded joints is shown in Figure 4. At room temperature the disbond specimens showed a 22% reduction in strength for an 8% reduction in bond area but no difference in strength was evident under hot/wet conditions.

An increase in strength was observed in both no defect and disbond specimens when residually strength tested after 10^6 cycles of fatigue loading.

Corner Radii Delaminations - Tension Cleats

The effects of delaminations in corner radii when tested as tension cleats are shown in Figure 5.

A large amount of scatter in results was evident in the static tests where neither the delamination location (between plies 4 and 5 or on layup centre line) nor the variation in percentage length delaminated showed any clear trend. The effect of fatigue loading for 10^6 cycles did show some reductions in residual strength for delaminated specimens.

Skin Delaminations

These tests were conducted using honeycomb sandwich beams which were initially curved and designed to be essentially flat at failure under 4-point bending.

The results of the $0^\circ/\pm 45^\circ$ skinned specimens are shown in Figure 6 and the $0^\circ/\pm 45^\circ/90^\circ$ skinned specimens in Figure 7.

The delaminations on skin centre line of the $0^\circ/\pm 45^\circ$ skins show a maximum effect of reducing the failure strain level by 50% whereas the delamination 2 plies below the outer surface of the $0^\circ/\pm 45^\circ/90^\circ$ skins reduced the failure strain level by only 30%.

Although the results and failure modes have not yet been fully analysed it is interesting to note that the greatest reduction in failure strain usually occurred in the 150mm wide specimens.

Impact Damage and Skin/Core Disbonds

Will be carried out on curved honeycomb beams following completion of skin delaminations.

REPAIR COUPONS

The aim of these tests is to determine the most effective bonded repair configurations. The testing is initially being carried out at room temperature in the "as received" condition under tensile loading. Any joints performing well under these conditions will then be considered for testing hot and wet.

The configurations evaluated combine 3 different resin systems and cure temperatures, pre-preg tape and woven fabrics, varying scarf angles and step geometry, pre-cured and co-cured inserts and different ways of applying the repair insert material. Figure 8 shows the various configurations and associated test number, the room temperature results for these being shown in Figure 9.

Initial conclusions are that a scraped joint is more efficient than a stepped one and that hot curing adhesives are better than those which cure at room temperature.

Since all the repair configurations were a simulation of a heater mat and vacuum bag technique, a varying amount of bond line porosity was experienced. This meant that several specimens were shown to be very poor by ultrasonic NDT although they performed well under test which highlights the need for an NDT technique to cope with this problem.

MAJOR BOX REPAIR

A major test box with CFC skin and metallic sub-structure from the Jaguar CFC Wing Programme was made available following its test to failure. The box had been tested in 3-point bending at $87^\circ\text{C}/1\%$ moisture with the CFC skin in compression. Failure occurred at 113% Design Ultimate Loading. The dimensions of the box and location of the failure site is shown in Figure 10.

The CFC skin was repaired in-situ on the test box in a typical service hangar environment using hand held tools, electric heater mats and vacuum bags only. The damage was removed by hand scarfing, new CFC skin insert material was cured and bonded, followed by an external reinforcing strap. The total repair was based on the configuration and materials of Test 9A (see Figures 8 and 9) which had the highest test mean strength and least amount of variability.

The repair was ultrasonically inspected by both hand-held probe and through transmission C-scan which correlated extremely well; again a large degree of bond-line porosity was present.

The repaired box was re-tested in the original rig, but, to reduce costs/timescale, at room temperature in the as received condition. Compression skin failure occurred in the repaired section as shown in Figure 11 at 145% Design Ultimate Loading. From an examination of a variety of data, the compression strength at 87°C and 1% moisture content would be some 20% below that in the room temperature, "as received" condition. This would indicate a failure at $145 \times 0.8 = 116\%$ compared with the original 113% D.U.L.

The next step is to carry out in-situ repairs to both CFC sub-structure and CFC skins and test these under hot/wet conditions.

FURTHER WORK IN PHASE 2

The content of Phase 2 of the Defect, Damage and Repair programme is at present under discussion but, besides considering any further work requirement arising from Phase 1, will probably include evaluation of bolted and metallic repairs to CFC; EMC and lightning strike requirements and performance for repairs; delamination growth; effects of contamination on bonded repairs and alleviation of moisture pull-through from adherends; the problems associated with damage size and laminate thickness; and multiple damage sites in close proximity.

Throughout this work, NDT techniques will need to be developed to cope with any encountered problems. All NDT methods and equipment must ultimately be quick and easy to use in a service environment.

STRUCTURAL ITEMS

SERVICE EXPERIENCE

JET PROVOST RUDDER TRIM TAB (Fig. 1A)

These items first entered service in early 1970 and of 4 aircraft still fitted with these items the leading aircraft has flown in excess of 4500 hours without occurrence of either defect or damage.

JAGUAR ACCESS PANELS (Fig. 1B)

The underwing flap shroud and the spine access panels were first flown in early 1978 and 30 aircraft sets were delivered to the services in 1979 of which the leading items have flown some 300 hours. Some panels have suffered bolt hole elongation due to repeated removal and refitting and are repaired by filling and re-drilling. If these items were to be productionised, the core insert material at the bolt positions would be changed to a more durable material or have metallic ferrules fitted. Flap shroud panels which have suffered leading edge delamination have been repaired by adhesively bonding a wrap-around of GRP cloth. One panel has suffered skin fracture and honeycomb core damage whilst removed from the aircraft and was repaired as shown in Figure 12.

The spine cover panels occasionally receive impact damage to the inner skin when being refitted. When necessary this is repaired as shown in Figure 13.

30 aircraft sets of the rear tank access panels have recently entered service and to date no reports of defects or damage have been received. 50 aircraft sets of a further 7 Jaguar panels are currently being manufactured prior to delivery to the RAF.

DEMONSTRATORS

TORNADO TAILERONS (Fig. 1C)

The taileron programme has demonstrated the capability to manufacture large Class 1 or Primary CFC structures to flying standards. One pair (left and right hand) have been manufactured for static and fatigue purposes respectively and another pair for flight trials. Very few manufacturing defects of any significance have arisen and also very little damage. A typical repair to one of the few occurrences of damage is shown in Figure 14.

The static and fatigue tests are currently proceeding and the flight test tailerons were successfully flown in late 1982. The few defects and instances of repaired damage have shown no detrimental effect on the testing achieved to date.

A further five pairs of production standard taileron are scheduled for the near future.

JAGUAR WING (Fig. 15B)

The Jaguar wing programme, which includes the largest single item so far manufactured at Warton with each wing skin being approximately 5.4 meters long, was originally planned to be for static and flight test. The programme has since been reduced to static testing only.

Again very few instances of significant defects or damage have occurred; the two main instances are shown in Figure 16 which have been repaired as shown in Figures 17 & 18.

Due to the location and nature of these repaired areas, no detrimental effect is anticipated. The areas will, however, be monitored during testing.

JAGUAR ENGINE BAY DOOR (Fig. 15A)

BAe Warton has collaborated with Grumman Aerospace in the design and manufacture of a pair of CFC engine bay doors for the Jaguar. The manufacture is virtually complete at the time of writing and the possibility of a test programme is being considered.

DEMONSTRATOR FRONT FUSELAGES

Two complete front fuselages have been built to gain manufacturing experience, improve expertise and demonstrate specific design and tooling concepts. One right hand half fuselage has also been built to evaluate the all co-cured/co-bonded concept. There were very few manufacturing defects but this was the biggest test for the NDT team, where some difficulty was experienced with the in-situ scanning of some of the bond lines.

One of the complete front fuselages has recently been subjected to bird strike testing and performed very well, the worst damage being a permanent "dent" in the honeycomb sandwich construction side skin. This is now being considered for an in-situ repair, to be followed by further bird strike tests.

NON-DESTRUCTIVE TESTING

The production NDT inspection of components manufactured from Carbon Fibre Composites, is performed at BAe, Warton Division using automated ultrasonic scanning. Facilities include both immersion tanks and water jet probe (squirter) systems. In both cases a raster motion is generated, and linked by variable ratio devices to a platten recorder, in order to produce a hard copy 'C' scan, on electro-sensitive paper. The normal techniques of through-transmission, reflector plate and pulse echo, are used as appropriate. Naturally, through transmission is preferred, since many of the problems associated with probe characteristics, near and far zones, and signal gating problems are avoided. More recent developments have led to the introduction of computer controlled data acquisition and processing systems.

Radiography is also an important NDT technique for composite components. However, until recently, there have been limitations with regard to equipment capability. The present generation of Be window, low KeV, X-Ray Units, do not perform reliably below about 25 KeV, i.e. Indicated Kv can vary greatly from actual emission. Also with some units it is not possible to attain any useful emission below an indicated 20 KeV. Fortunately X-Ray equipment manufacturers have now recognised the special requirements for composites radiography, and are producing systems capable of operating down to 10 KeV with very high Ma outputs.

With regard to defect characterisation, it was recognised at the outset in the 1960's that some form of Reference Standard would be needed, thereby introducing the Carbon Fibre equivalent of the Flat Bottom Hole. Some areas of the European Aerospace Industry did, in fact, use Flat Bottom Holes. Others, including BAe Warton, elected for the system favoured in the U.S.A. wherein laminar defects are modelled by P.T.F.E. patches, inserted into "Stepwedge" specimens during the lay-up process. Yet another model defect which proved very realistic, took the form of a deer hair inserted in the lay-up to simulate long tubular voids. The hair of the deer being similar in diameter to the actual defects, and being hollow, produced an effective ultrasonic attenuator/reflector.

The approach on defect acceptance levels started in a somewhat arbitrary manner, as in fact, was the case in the 1950's, when standards for aluminium alloy plate were being sought. The criteria then as now, being based on the best that the current state of Ultrasonic technology could realistically achieve. The BAe Warton system is based on the use of graded acceptance scales, with P.T.F.E. patch reference standards of 3mm, 6mm and 12mm square. Other criteria of defect to defect proximity, and defect to hole or edge proximity, are also applied. Fortunately, as with the Flat Bottom Hole standards applied to aluminium plate, the 6mm square standard for Carbon Composite, proved realistic from both Design and Manufacturing points of view. Some may wonder why a 'square' was chosen rather than a 'round', defect model. The reason is very simple, it is much easier to cut a square patch of 6mm x 6mm, than one 6mm diameter, using a pair of scissors!

It is interesting and very significant to note that the introduction of fairly exhaustive NDT processes, produced dramatic changes in the material lay-up and curing technologies. In fact, over recent years, defect occurrence is very low. The trend now is toward, normally, virtually defect free parts. Exceptions are when problems have occurred during processing; backing materials from the pre-preg can still get left in the lay-up, in spite of good housekeeping and quality control, and vacuum bags are still prone to the occasional burst. One fairly consistent area of concern is the corner radii of channel section spars, where defects can occur in laminar form around the radius.

The requirements of in-situ NDT on aircraft structures in service presents some very different problems to those of Manufacturing. These problems are currently being addressed in depth at Warton, with regard to the aspects of Survey, Monitoring and Repair Assessment. The single most problematical factor is the inherent inability to apply through-transmission techniques in-situ. Thus from the ultra-sonic approach, the fundamental problems of the basic physics of pulse echo methods are encountered. However, some relief is likely, in terms of the sizes and locations of defects to be found. Attention has been mainly concentrated on impact damage and post repair requirements, and to meet these requirements we have developed, in conjunction with two very co-operative equipment manufacturers, two items of specialised N.D.T. tools which have proved very effective.

The first of these is a highly portable, battery powered, ultrasonic 'C' scan package. The ultrasonic probe is a contact type with a plastic stand-off column. It is mounted in a low friction material disc which is fully gimballed to give freedom of normalisation in all axes, and is held in contact by a spring system. The probe is carried on an arm, which is integral with a box housing the drive motors and an A4 size recorder for electro-sensitive paper. The whole unit weighs less than 7 kg, and is attached to the aircraft structure by manually latchable suction cups. It is capable of operating in any attitude including, for example, the underside of a wing. An A4 size 'C' scan is performed in under 2 minutes. This unit is shown in Figure 19.

Where a smaller area of search is dictated and/or information on defect depth location is required, then hand held contact 'A' scan, with a stand-off probe, provides a very adequate technique.

A further development very recently occurred when we recognised the potential usefulness of the Medical 'B' Scan approach. The advantages of interrogating quite wide areas at one sweep of the probe are self evident, typically some 75mm. Also the presentation of 'B' Scan, shows defect width and depth simultaneously, in the form of a cross-sectional image which is readily intelligible to the non-NDT man. This system being primarily designed for medical use, needed appreciable modification and probe development for industrial use on Carbon Fibre Composites. It is felt that we are only at the beginning, and considerable scope for the development of this system exists, in order to meet the needs of post repair NDT inspections with regard to bond-line porosity problems etc. This unit is shown in Figure 20.

Finally, another NDT method which may prove beneficial in making qualitative assessments of porous bond lines is Ultrasonic Spectroscopy. This method analyses the frequency spectrum of the reflected ultrasonic signal, but at present it is still in the early stages of experimentation.

CONCLUSIONS.

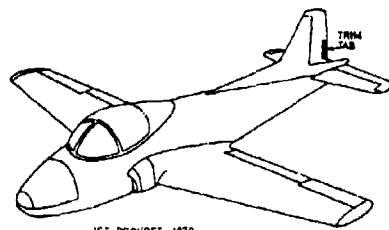
The large number of items made either for demonstrator or flight have been subject to stringent quality control and acceptance standards. Current production NDT techniques are confident of finding defects down to the maximum acceptable size and smaller, which has led to very few occurrences of "significant" defects or damage failing their way to being tested or flown. On large structures, defects and damage which could be categorised as significant have been locally repaired and to date have shown no adverse or detrimental effect on either performance or test results.

Defects as, or more severe than, the requirements of the acceptance standards have been used in the Defect, Damage and Repair programme where, in general, the effects have been somewhat less severe than was originally anticipated. However, this must be qualified by the fact that for this Phase of the programme only a limited number of results exist for each test condition (defect type, test type, test conditions, and variety of layups examined). It is envisaged that a greater variety of test conditions and more specimens at each condition, will be used to check further the worst defects/damage in Phase 2 of the programme.

The repair work has so far been encouraging. The repair joint coupons have demonstrated the ability to restore un-notched parent laminate strength and the major test box with damage much larger than would normally be anticipated in service has been repaired in-situ to original box strength.

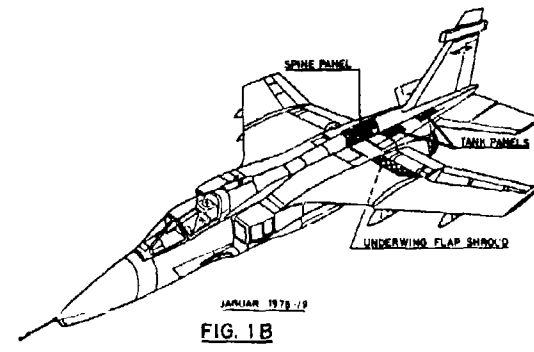
In-situ bonded repairs using heater mats and vacuum bags have been shown to have porosity in the adhesive bond line. Current NDT methods will register this porosity but cannot, generally, differentiate between porosity and a no-bond situation. Hence the repair would, from NDT results alone, be categorised as unacceptable. Subsequent structural tests have shown that, even with bondline porosity, full strength repairs can be achieved.

It is expected in the near future that advances in NDT equipment and techniques will enable the degree of porosity to be categorised and also give an indication of the attainable structural strength.



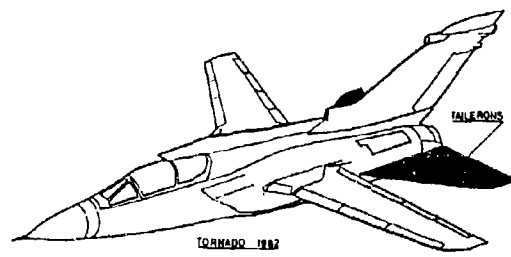
JET PROVOST 1970

FIG. 1A



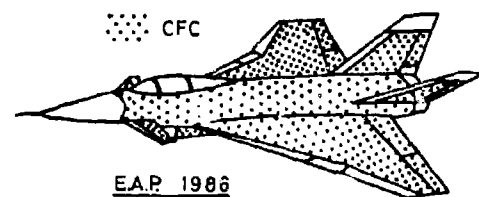
JANUARY 1978-19

FIG. 1B



TORNADO 1982

FIG. 1C



E.A.P. 1986

FIG. 1D

FIG. 1 INCREASING UTILISATION OF C.F.C.

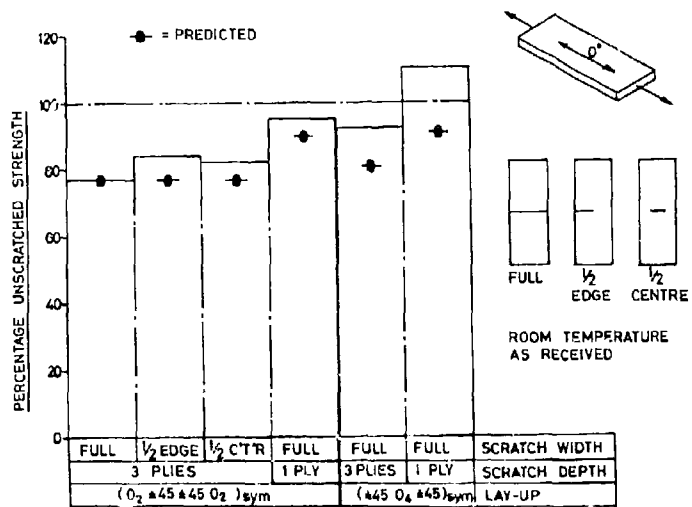


FIG. 2 SURFACE SCRATCHES

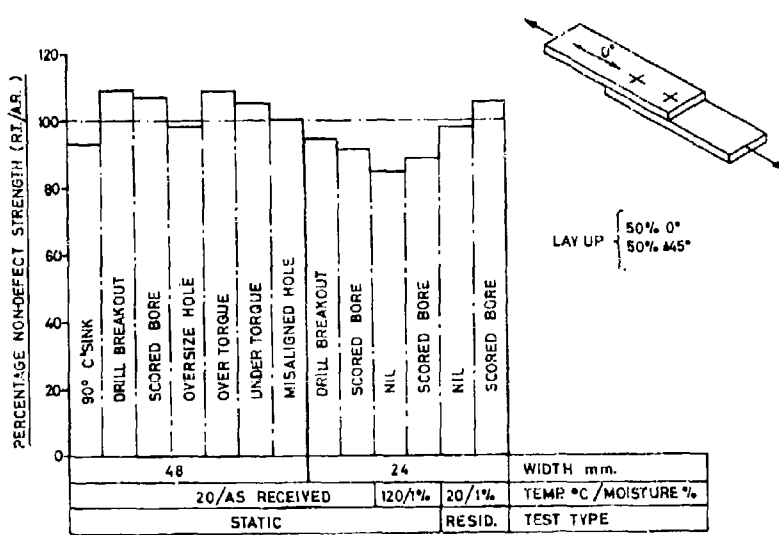


FIG. 3 BOLTED JOINT DEFECTS

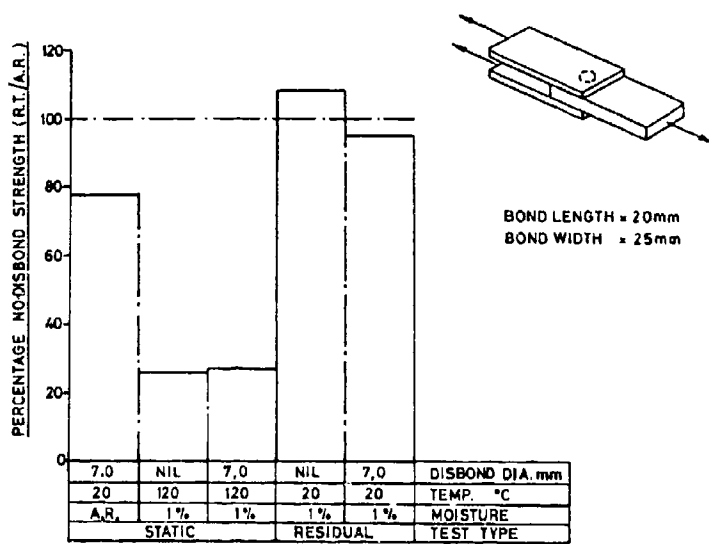


FIG. 4 BONDED JOINT DEFECTS

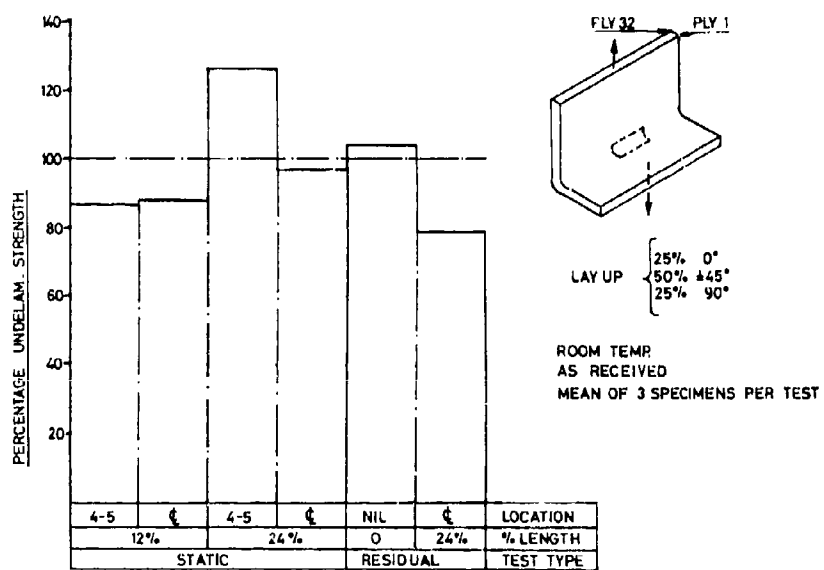
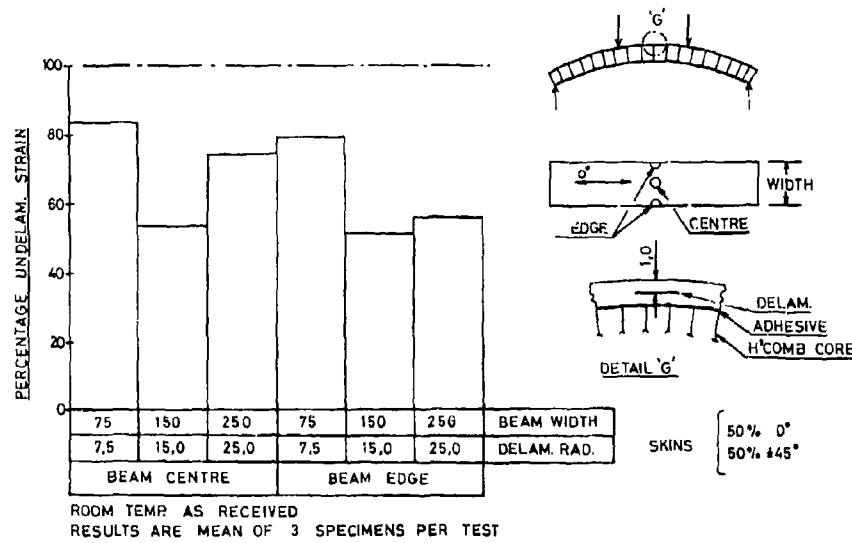
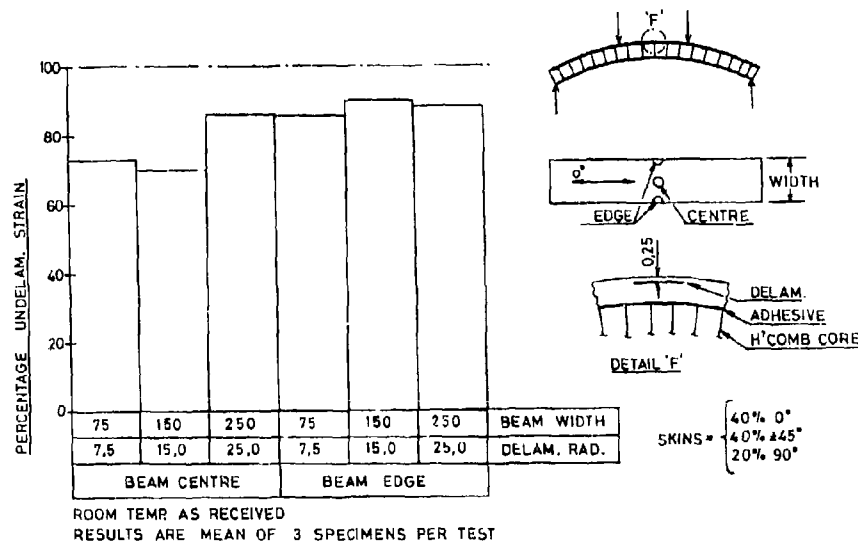
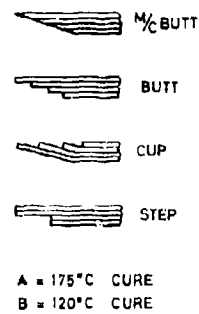


FIG. 5 TENSION CLEAT DELAMINATIONS

FIG. 6 SKIN DELAMS $0^\circ/\pm 45^\circ$ FIG. 7 SKIN DELAMS $0^\circ/\pm 45^\circ/90^\circ$

TEST N°	GEOMETRY	INSERT MAT ⁺ PRE/CO-CURED	CUP or BUTT	ADHESIVE
2	SCARF 40mm	A PRE	M/C BUTT	B
3	SCARF 40 mm	B CO	BUTT	B
4	SCARF 40 mm	B CO	CUP	B
5	SCARF 30 mm	A CO	CUP	A
6	SCARF 20 mm	A CO	CUP	A
7A	SCARF 40 mm	A PRE	M/C BUTT	A
7B	STEP 15 mm	A PRE	BUTT	B
7C	1/2 SCARF 40mm	B CO	BUTT	B
8A	SCARF 40mm	A CO	BUTT	A
8B	STEP 15 mm	B CO	BUTT	B
9A	SCARF 40 mm	A CO	CUP	A
9B	STEPS 4x15mm	B CO	BUTT	B
10	SCARF 40 mm	A PRE	BUTT	C
11	SCARF 40 mm	C CO	BUTT	C
12	SCARF 40 mm	C CO	CUP	C
13	1/2 SCARF 40mm	C CO	CUP	C



A = 175°C CURE
B = 120°C CURE
C = 20°C CURE

FIG. 8 JOINT CONFIGURATIONS

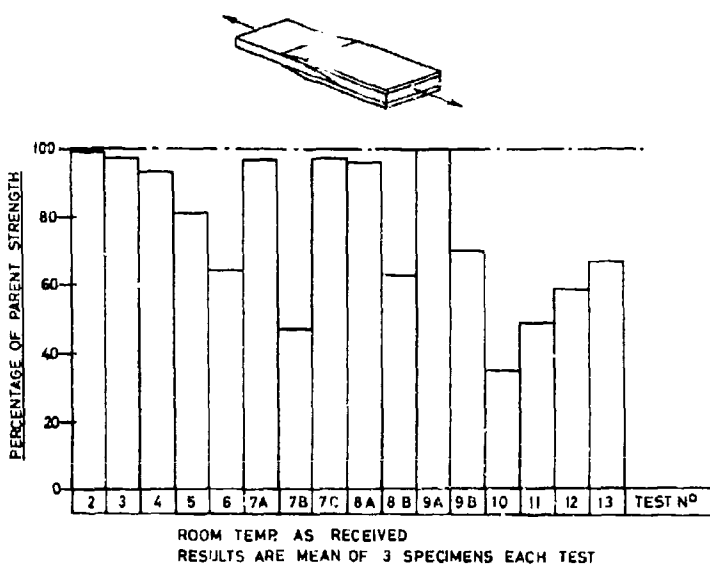


FIG. 9 JOINT COUPON RESULTS

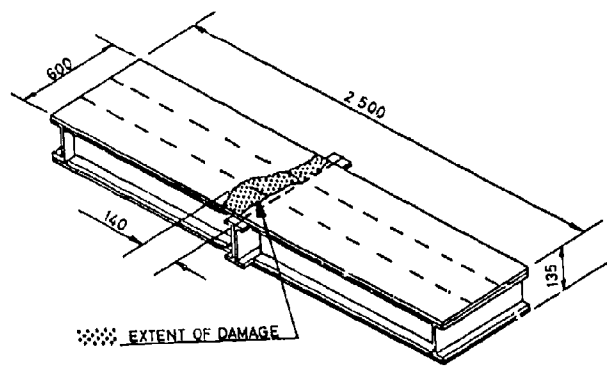


FIG. 10 BOX AFTER ORIGINAL TEST

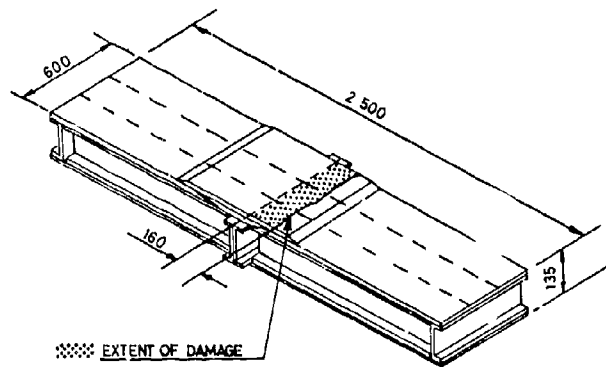


FIG. 11 REPAIRED BOX AFTER TEST

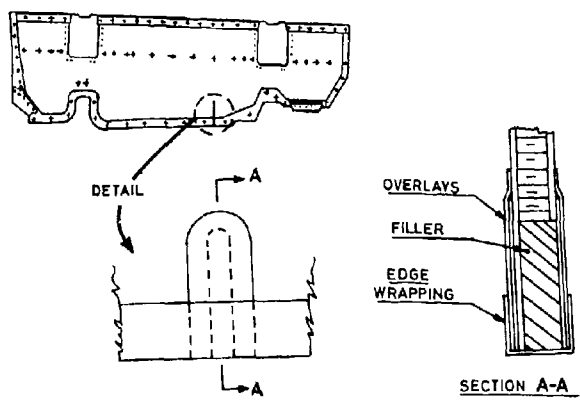


FIG. 12 SHROUD PANEL REPAIR

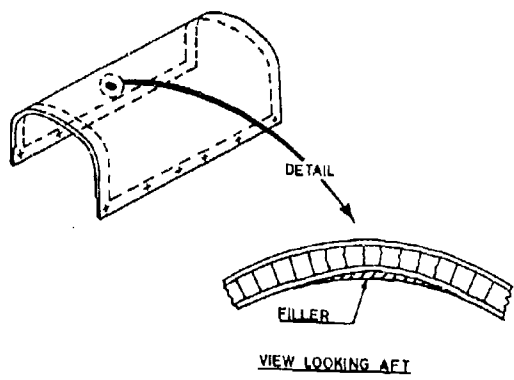


FIG. 13 SPINE PANEL REPAIR

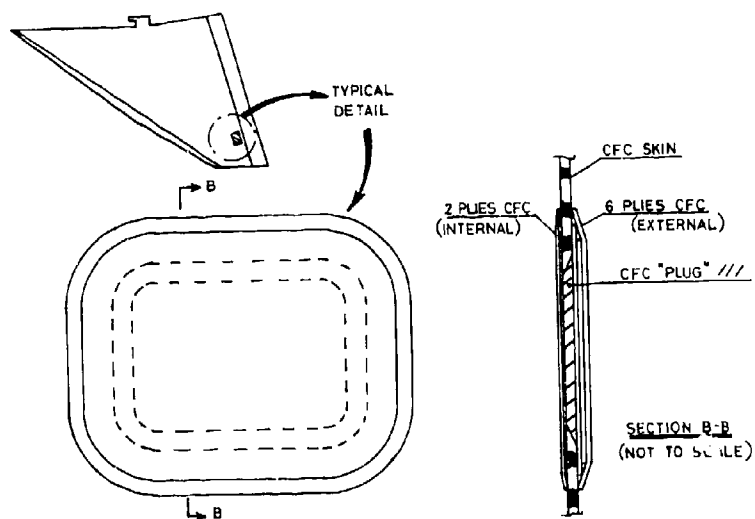


FIG.14 TAILERON REPAIR



FIG.15A ENGINE BAY DOORS

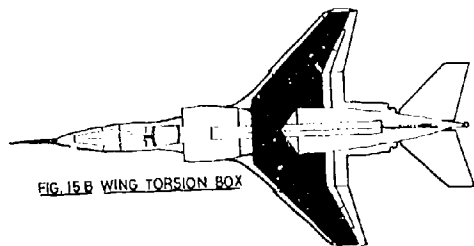


FIG.15B WING TORSION BOX

FIG.15 JAGUAR DEMONSTRATORS

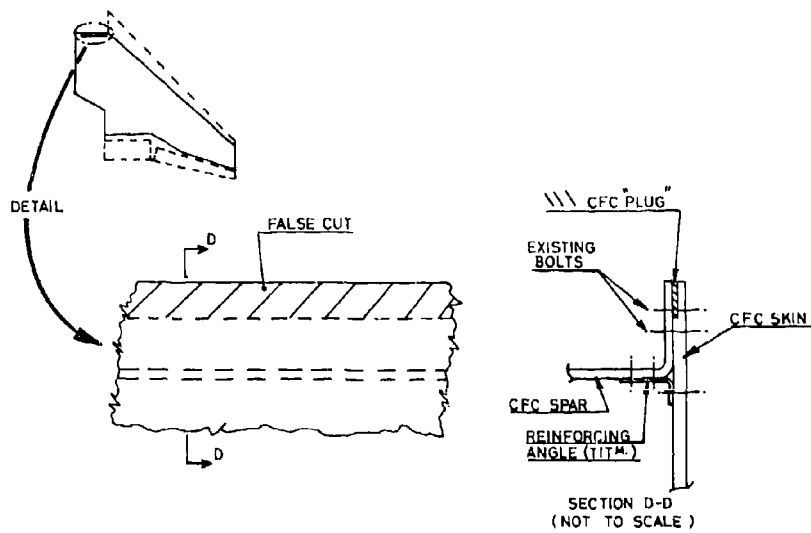
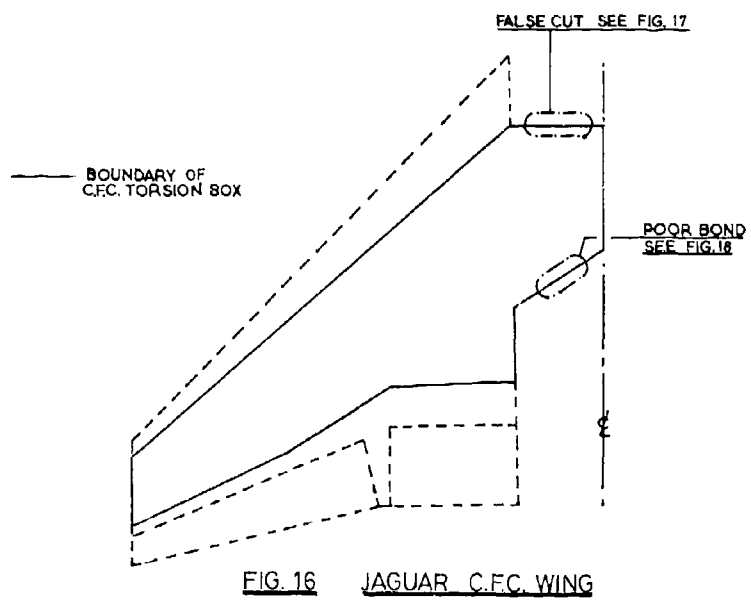


FIG. 17 FALSE CUT REPAIR

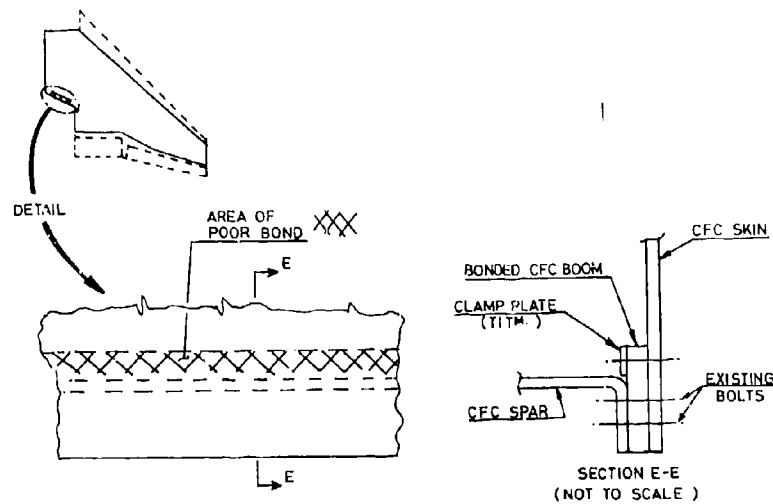


FIG. 18. POOR BOND REPAIR

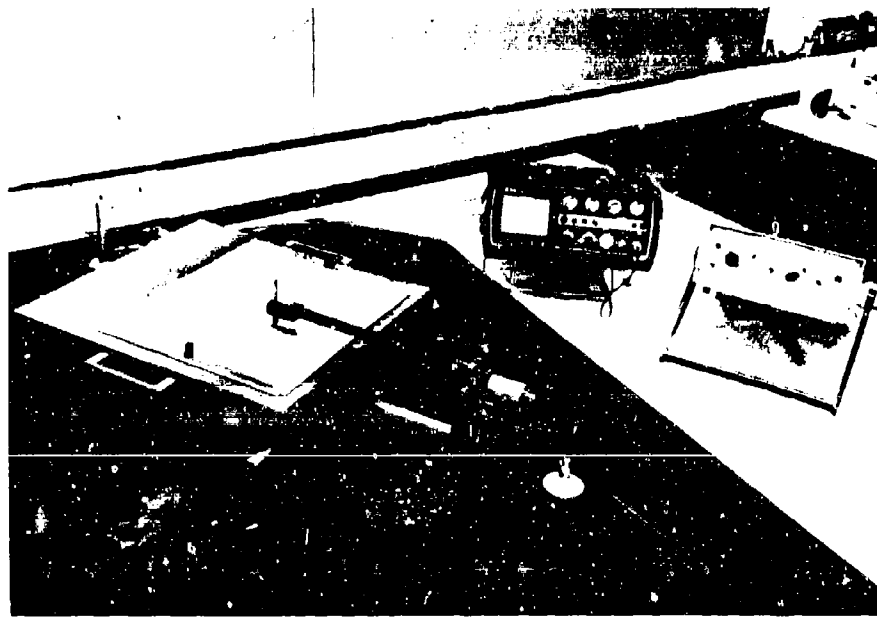


FIG. 19 PORTABLE C-SCAN UNIT

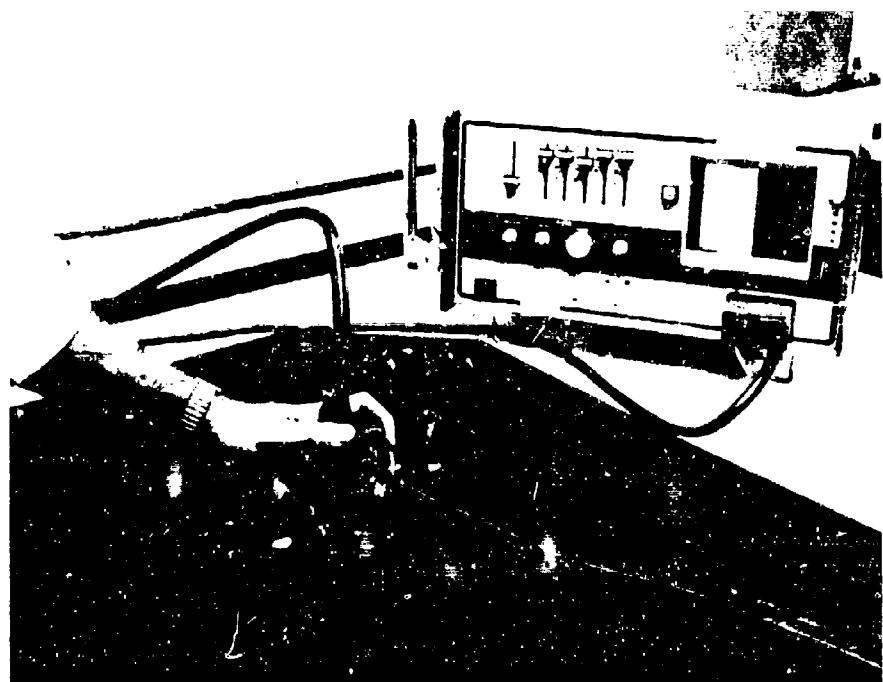


FIG. 20 ULTRASONIC IMAGING B-SCAN UNIT

AD P 001928

DELAMINATION GROWTH IN COMPOSITE STRUCTURES UNDER INPLANE COMPRESSION LOADING

by

Don Y. Konishi
Member Technical Staff
Rockwell International
N.A. Operations
P.O. Box 92098
Los Angeles, CA 90009
USA

ABSTRACT

An approximate solution to the stress field causing delamination under biaxial loading, where the principal load is compressive, has been developed. It utilizes a Raleigh-Ritz approach for the finite amplitude deflection analysis of a rectangular or elliptical plate which has bending/membrane coupling terms and clamped boundary conditions. The solution as developed determines the complete stress field on the boundary, including the short transverse stress field. This leads to delamination growth trajectories which can be analyzed to determine constant gradient dw/dt growth configurations. These results can be analyzed to establish design criteria to be used to minimize the impact of delamination growth considerations by stacking sequence selection, etc., as well as to maximize the residual strength capabilities of the structure.

1. INTRODUCTION

In order to enable certification of an aircraft comprising advanced composite panels in primary structure, its durability and damage tolerance must be assessed when it contains a delamination. Since delamination growth is due to the short transverse stress field within or in the region of the delamination, existing techniques for the stress field determination involves elaborate three-dimensional finite element models. "Exact" solutions for the buckling load have also been heretofore limited to orthotropic or specially anisotropic plates under specialized loading conditions such as compression or shear in the material coordinate system.

In order to enable an engineering approach to the problem, the "thinner" (region with lowest buckling strain) region is treated as a postbuckled plate clamped on four sides. This study will focus on this region.

A model is presented to represent the behavior of a delaminated region in an advanced composite plate under membrane compressive loading. The rectangular plate model was initially presented as an "initially deformed" plate under compressive loading in 1979 (1) and has been extended here into the postbuckled region. In addition, an elliptic plate is considered. The model utilizes a one-term Rayleigh-Ritz energy formulation with the initial estimates of the deflected shapes being symmetric about both the x and y axes. Finite amplitude kinematic relationships are utilized. Anisotropic and flexural membrane coupling terms as well as combined loading are included. This method was previously presented for simply supported boundary conditions (2) in order to ascertain the behavior of postbuckled compression and shear webs.

2. APPROXIMATE SOLUTIONS

In order to obtain an approximate solution to the problem, models for rectangular and elliptical clamped plates in the postbuckling range have been developed. Figure 1 shows the geometry.

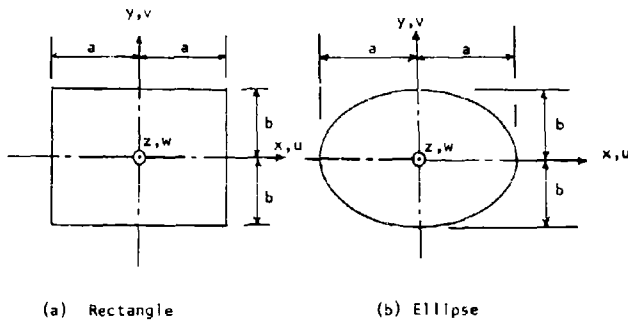


Figure 1. Geometry

3. DISPLACEMENTS

For the rectangle, the displacement functions chosen are:

$$\begin{aligned} W &= \frac{f}{4} (1 + \cos 2\bar{x}) (1 + \cos 2\bar{y}) \\ U &= -c_1 \sin 2\bar{x} \cos \bar{y} - e_x x - \frac{\gamma_y}{2} \\ V &= c_2 \cos \bar{x} \sin 2\bar{y} - e_y y - \frac{\gamma_x}{2} \end{aligned} \quad (1)$$

where:

$$\bar{x}, \bar{y} = \frac{\pi x}{2a}, \frac{\pi y}{2b}$$

For the ellipse, the displacement functions chosen are: (3)

$$W = \frac{F}{2} (1 - \bar{x}^2 - \bar{y}^2)^2$$

$$U = C_1 (1 - \bar{x}^2 - \bar{y}^2) \bar{x} - a e_x \bar{x} + b \bar{y} y/2 \quad (2)$$

$$V = C_2 (1 - \bar{x}^2 - \bar{y}^2) \bar{y} - b e_y \bar{y} + a \bar{y} \bar{x}/2$$

where: $\bar{x}, \bar{y} = \frac{x}{a}, \frac{y}{b}$

and, e_x, e_y, γ = far field strain field

These displacement functions satisfy the geometric boundary conditions for clamped support.

$U = V = W = W_{,x} = W_{,y} = 0$ on the boundary,
where the comma followed by a subscript implies partial differentiation with respect to the subscript.

4. STRAINS

Finite amplitude kinematic relationships are used:

$$\begin{aligned} \epsilon_x &= U_{,x} + \frac{1}{2} W_{,x}^2 \\ \epsilon_y &= V_{,y} + \frac{1}{2} W_{,y}^2 \\ \gamma_{xy} &= U_{,y} + V_{,x} + W_{,x} W_{,y} \end{aligned} \quad (3)$$

$$x_x = -W_{,xx}$$

$$x_y = -W_{,yy}$$

$$x_{xy} = -2 W_{,xy}$$

5. CONSTITUTIVE RELATIONSHIPS

The constitutive relationships for an advanced composite laminate are:

$$N_i = A_{ij} \epsilon_j + B_{ij} x_j \quad i, j = x, y, xy \text{ df } 1, 2, 3 \quad (4)$$

$$M_i = B_{ij} \epsilon_j + D_{ij} x_j$$

where repeated subscripts imply summation over the range of the subscript.

6. ENERGY

The total energy in the considered panel is:

$$U = \frac{1}{2} \int_a^b \int_{-b'}^{b'} \delta_{ij} (N_i \epsilon_j + M_i x_j) dy dx \quad (5)$$

where for a rectangle and ellipse

$$b' = b, b \sqrt{1 - \bar{x}^2}$$

and δ_{ij} is the Kronecker delta

$$\delta_{ij} = 0 \quad i \neq j$$

$$\delta_{ij} = 1 \quad i = j$$

Carrying out the indicated operations yield:

$$\begin{aligned} \frac{2U}{ab} = & \frac{1}{2} F_{11} C_1^2 + F_{12} C_1 C_2 + F_{13} C_1 f^2 + F_{14} C_1 f + \frac{1}{2} F_{22} C_2^2 \\ & + F_{23} C_2 f^2 + F_{24} C_2 f + \frac{1}{4} F_{33} f^4 + F_{34} f^3 + G_{13} f^2 e_x + G_{23} f^2 e_y + \\ & G_{33} f^2 e_z + H_3 f^2 + I_{11} e_x^2 + I_{12} e_x e_y + I_{13} e_x e_z + I_{22} e_y^2 + I_{23} e_y e_z + I_{33} e_z^2 \end{aligned} \quad (6)$$

where for the rectangle:

$$F_{11} = \pi(2A_{11} + \frac{1}{2}\bar{\alpha}^2 A_{33})$$

$$F_{12} = \frac{32}{9} \left(\frac{\pi}{\bar{\alpha}}\right)^2 (A_{12} + \bar{\alpha} A_{33})$$

$$F_{13} = \frac{2\pi^2}{15b} (2A_{12} - A_{33})$$

$$F_{14} = -\frac{2\pi^2}{3a} (4B_{11} + \bar{\alpha}^2 B_{12} + 2\bar{\alpha}^2 B_{33})$$

$$F_{22} = \pi^2 (2\bar{\alpha}^2 A_{22} + \frac{1}{2} A_{33})$$

$$F_{23} = -\frac{2\pi^2}{15b} (2A_{12} - A_{33})$$

$$F_{24} = \frac{2\pi^2}{3b} (B_{12} + 4\bar{\alpha}^2 B_{22} + 2B_{33})$$

$$F_{33} = \frac{2\pi^4}{128^2} (105 A_{11} + 50\bar{\alpha}^2 A_{12} + 105 \bar{\alpha}^4 A_{22} + 100 \bar{\alpha}^2 A_{33})$$

$$F_{34} = \frac{\pi^4 \bar{\alpha}^2}{16} (B_{12} - B_{33})$$

$$G_{13} = -\frac{3\pi^2}{16} (A_{11} + \bar{\alpha}^2 A_{22})$$

$$H_3 = -\frac{\pi^4}{16} (3D_{11} + 2\bar{\alpha}^2 D_{12} + 3\bar{\alpha}^4 D_{22} + 4\bar{\alpha}^2 D_{33})$$

$$I_{11}, I_{22}, I_{33} = 4A_{11}, 4A_{22}, 4A_{33}$$

$$I_{12}, I_{13}, I_{23} = 8A_{12}, 8A_{13}, 8A_{23}$$

$$\pi, \bar{\alpha} = \frac{\pi}{a}, \frac{\bar{\alpha}}{b}$$

and for the ellipse:

$$F_{11} = \frac{\pi}{a^2} (A_{11} + 1/3\bar{\alpha}^2 A_{33})$$

$$F_{12} = \frac{\pi}{3ab} (A_{12} + A_{33})$$

$$F_{13} = \frac{\pi}{15ab^2} (A_{12} - A_{33})$$

$$F_{14} = \frac{2\pi}{3a^2} (5B_{11} + \bar{\alpha}^2 B_{12} + 2\bar{\alpha}^2 B_{33})$$

$$F_{22} = \frac{\pi}{b^2} (A_{22} + \frac{1}{3}\bar{\alpha}^2 A_{33})$$

$$\begin{aligned}
 F_{23} &= \frac{\pi}{15 a^2 b} (A_{12} - A_{33}) \\
 F_{24} &= \frac{2\pi}{3ab^2} \left(\frac{B_{12}}{a} + 3B_{22}\bar{a} + 2\frac{B_{13}}{a} \right) \\
 F_{33} &= \frac{\pi}{105a^4} (3A_{11} + 2\bar{a}^2 A_{12} + 3\bar{a}^4 A_{22} + 4\bar{a}^2 A_{33}) \\
 F_{34} &= \frac{2\pi}{a^3} (B_{11} + 1/3 \bar{a}^2 B_{12} + 2/3 \bar{a}^2 B_{33}) \\
 G_{13} &= -\frac{\pi}{6a^2} A_{11} - \frac{\pi}{6b^2} A_{21} \\
 H_3 &= \frac{2\pi}{a} (D_{11} + \frac{2}{3} \bar{a}^2 D_{12} + \bar{a}^4 D_{22} + \frac{4}{3} \bar{a}^2 D_{33}) \\
 l_{11}, l_{22}, l_{33} &= \pi A_{11}, \pi A_{22}, \pi A_{33} \\
 l_{12}, l_{13}, l_{23} &= 2\pi A_{12}, 2\pi A_{13}, 2\pi A_{23}
 \end{aligned}$$

7. STRAIN ENERGY MINIMIZATION

For a given unit far field strain field of the plate, the amplitudes: C_1, C_2, f ; are obtained by strain energy minimization.

$$\begin{aligned}
 \frac{\partial}{\partial C_1} \left(\frac{2U}{ab} \right) &= F_{11} C_1 + F_{12} C_2 + F_{13} f^2 + F_{14} f = 0 \\
 \frac{\partial}{\partial C_2} \left(\frac{2U}{ab} \right) &= F_{12} C_1 + F_{22} C_2 + F_{23} f^2 + F_{24} f = 0 \\
 \frac{\partial}{\partial f} \left(\frac{2U}{ab} \right) &= 2F_{13} C_1 f + F_{14} C_1 + 2F_{23} C_2 f + F_{24} C_2 + \\
 &\quad 2F_{33} f^3 + 3F_{34} f^2 + 2(G_{13}\bar{e}_x + G_{23}\bar{e}_y + G_{33}\bar{Y}) ef + 2H_3 f = 0
 \end{aligned}$$

From the first two equations we get:

$$\begin{aligned}
 C_1 &= F_1 f^2 + F_3 f \\
 C_2 &= F_2 f^2 + F_4 f
 \end{aligned} \tag{7}$$

and substituting into the third:

$$\begin{aligned}
 &2(F_{13} F_1 + F_{23} F_2 + F_{33}) f^3 + (2F_{13} F_3 + 2F_{23} F_4 + 3F_{34} + F_{14} F_1 + \\
 &F_{24} F_2) f^2 + [2(G_{13}\bar{e}_x + G_{23}\bar{e}_y + G_{33}\bar{Y}) e + 2H_3 + F_{14} F_3 + \\
 &F_{24} F_4] f = 0
 \end{aligned} \tag{8}$$

where:

$$e_x, e_y, Y = \frac{df}{d\bar{x}}, \bar{e}_x, \bar{e}_y, \bar{Y} = \bar{e}_x, \bar{e}_y, \bar{Y}$$

$$\begin{aligned}
 F_1, F_3 &= -\frac{F_{22} F_{13} - F_{12} F_{23}}{F_{11} F_{22} - F_{12}^2}, \quad -\frac{F_{22} F_{14} - F_{12} F_{24}}{F_{11} F_{22} - F_{12}^2} \\
 F_2, F_4 &= -\frac{F_{11} F_{23} - F_{12} F_{13}}{F_{11} F_{22} - F_{12}^2}, \quad -\frac{F_{11} F_{24} - F_{12} F_{14}}{F_{11} F_{22} - F_{12}^2}
 \end{aligned}$$

Equation (8) governs the deflected shape of the plate. One solution, $f = 0$, represents the stationary position of the plate. A second solution exists iff:

$$e \geq -\frac{2H_3 + F_{14} F_3 + F_{24} F_4}{2(G_{13}\bar{e}_x + G_{23}\bar{e}_y + G_{33}\bar{Y})}$$

Noting that positive strains produce negative stresses; i.e., compressive stress is positive; and defining the equality as critical strain

$$\epsilon_{cr} = -\frac{2H_3 + F_{14}F_3 + F_{24}F_4}{2 \bar{G}_{13}} \quad (9)$$

where

$$\bar{G}_{13} = G_{13}\bar{\epsilon}_x + G_{23}\bar{\epsilon}_y + G_{33}\bar{\gamma}$$

The behavior of the plate is now characterized. In order to characterize the short transverse behavior of the panel, the following quantities:

$$\begin{aligned} Q_x &= M_{xx} + M_{xy}y \\ Q_y &= M_{xy}x + M_{yy}y \\ V_x &= Q_x + M_{xy}y \\ V_y &= Q_y + M_{xy}x \end{aligned} \quad (10)$$

obtained from equilibrium considerations, are evaluated.

8. DISCUSSION OF SOLUTION

The preceding solution only admits symmetric modes. It is reasonable that skewed modes may produce lower buckling strains and, therefore, more realistic behavior (2). The solution presented herein, therefore, only represents the initial approach to the determination of the physics of failure for delaminated regions in advanced composite laminates.

9. SAMPLE SOLUTIONS

In order to demonstrate the utilization of this approach, it was incorporated into a computer program which delineates the progressive failure of a laminate (4,5) given the stress resultants at a point. It also obtains the ultimate strength if the ratios between stress resultants were to remain the same. V_x and V_y represent transverse stress resultants on the boundary. The relationship between the stress resultants and the peeling stress between the panel and supporting structure must still be developed. At the present time, magnitudes may be studied to minimize peeling stresses.

A total of 12 laminate configurations are studied. They are all 4-ply [0/ $\pm 45/90$]c balanced laminates differing only in stacking sequence. Table I shows their flexural/membrane properties for the reference axis at the center of the laminate. Two loading conditions are studied:

$$1. \bar{\epsilon}_x = 1, \bar{\epsilon}_y = 0, \bar{\gamma} = 0.$$

$$2. \bar{\epsilon}_x = 1, \bar{\epsilon}_y = -0.3, \bar{\gamma} = 0.$$

The initial study comprises a survey of the configurations with $a = b = 1$ inch at $n = 2$, where the far field strain

$$\epsilon \stackrel{df}{=} n \cdot \epsilon_{cr}$$

is normalized with respect to the buckling strain. The results are shown on table II. On this table an estimate of the failure strain

$$\hat{\epsilon}_{ult} = n \cdot \epsilon_{cr} (M.S. + 1)$$

is made.

In order to study delaminations, compatibility must be maintained between the "thinner" and remaining portions of the unflawed laminate. Assuming for this study that the remaining portion does not buckle and has relatively insignificant out-of-plane motion, then the relationship between ϵ_y and ϵ_x will be governed by "Poisson's" effect. Therefore, depending on stacking sequence, case 2 represents a realistic case and will be studied further. Table III shows results of a study representing monotonically increase of loading until failure occurs, i.e., M.S. = 0. For the rectangular and elliptical delaminations, the laminate configurations producing the highest and lowest estimates of critical strain were studied.

TABLE I
LAMINATE PROPERTIES

Laminate Configuration	Property	11	12	13	22	23	33
[0/ $\pm 45/90$]	A ~#/IN. B ~#/IN./IN. D ~#/IN ² /IN.	167275. 726. 7.4	52843. 0. .7	0. 121. 0	167245. -726. 7.4	0. 121. 0	57201. 0. .9
[0/ $\mp 45/90$]	A B D			-121.		-121.	
[90/ $\pm 45/0$]	A B D		-726.		121.	726.	121.
[90/ $\mp 45/0$]	A B D			-121.		-121.	
[$\pm 45/0/90$]	A B D		8. 3.6	234. 1.9	121. 1.3	-477. 8.7	121. 1.3
[$\mp 45/0/90$]	A B D			-121. -1.3		-121. -1.3	
[$\pm 45/90/0$]	A B D		-477. 8.7		121. 1.3	8. 3.6	121. 1.3
[$\mp 45/90/0$]	A B D			-121. -1.3		-121. -1.3	
[0/90/ ± 45]	A B D	477.	-234.	121.	-8.	121.	-234.
[0/90/ ∓ 45]	A B D			-121. 1.3		-121. 1.3	
[90/0/ ± 45]	A B D		-8. 3.6	121. -1.3	477. 8.7	121. -1.3	
[90/0/ ∓ 45]	A B D			-121. 1.3		-121. 1.3	

Note: A blank implies no change from data above it.

TABLE II
CONFIGURATION SURVEYS

Type	Laminate Orient.	Case	r_{cr} in./in.	r in.	n	M.S. Min.			Q_{max}			V_{max}			σ_{ult} psi/in.	
						\bar{x}	\bar{y}	\bar{z}	lb/in.	\bar{x}	\bar{y}	lb/in.	\bar{x}	\bar{y}		
Rect.	[0/ $\pm 45/90]$	1	1016.	.0180	2	3.08	0.	0.	-2.397	.5	0.	1.932	0.	1.	8289. 7401.	
		2	1451.	.0180	2	1.55	0.	.5	-2.329	.5	.1	1.924	0.	1.		
	[0/ $\pm 45/90]$	1	1016.	.0180	2	3.08	0.	0.	-2.397	.5	0.	1.932	0.	1.	8289. 7401.	
		2	1451.	.0180	2	1.55	0.	.5	-2.329	.5	.1	1.924	0.	1.		
	[90/ $\pm 45/0]$	1	1016.	.0180	2	3.01	1.	0.	-2.397	.5	0.	2.055	0.	1.	147. 0300.	
		2	1451.	.0180	2	1.06	1.	0.	-2.397	.5	0.	2.055	0.	1.		
	[90/ $\pm 45/0]$	1	1016.	.0180	2	3.01	1.	0.	-2.397	.5	0.	2.055	0.	1.	8147. 8088.	
		2	1451.	.0180	2	1.06	1.	0.	-2.397	.5	0.	2.051	0.	1.		
	[$\pm 45/0/90]$	1	768	.0157	2	4.28	1.	0.	-2.421	.2	.1	2.151	-2	1.	8106. 7874.	
		2	1097	.0157	2	2.59	1.	0.	-2.403	.2	.1	2.148	-2	1.		
Elliptope	[$\pm 45/0/90]$	1	768	.0157	2	4.28	1.	0.	-2.421	.2	.1	2.151	-2	1.	8106. 7874.	
		2	1097	.0157	2	2.59	1.	0.	-2.403	.2	.1	2.148	-2	1.		
	[$\pm 45/90/0]$	1	768	.0157	2	3.66	.2	.2	-3.011	.5	0.	1.600	-4	1.	7155. 6580.	
		2	1097	.0157	2	1.99	.2	.2	-2.998	.5	0.	1.612	-4	1.		
	[$\pm 45/90/0]$	1	768	.0157	2	2.59	.3	.4	3.000	-.5	0.	-1.611	-4	1.	5516. 6580.	
		2	1097	.0157	2	1.99	.3	.4	2.998	-.5	0.	-1.612	-4	1.		
	[0/90/ $\pm 45]$	1	768	.0156	2	2.91	-.9	.1	2.994	-.5	0.	-1.590	-4	1.	6003. 7172.	
		2	1097	.0156	2	2.27	-.1	.0	2.908	-.5	0.	-1.494	-4	1.		
	[0/90/ $\pm 45]$	1	768	.0156	2	3.74	0.	0.	-2.982	.5	0.	1.590	-4	1.	7277. 7172.	
		2	1097	.0156	2	2.27	0.	0.	-2.906	-.5	0.	1.494	-4	1.		
Elliptope	[90/0/ $\pm 45]$	1	768	.0156	2	4.39	0.	0.	-2.424	-.2	.1	2.258	-4	1.	8275. 8288.	
		2	1097	.0156	2	2.87	0.	0.	-2.424	-.2	.1	2.258	-4	1.		
	[90/0/ $\pm 45]$	1	768	.0156	2	4.39	0.	0.	-2.424	-.2	.1	2.258	-4	1.	8275. 8288.	
		2	1097	.0156	2	2.87	0.	0.	-2.407	-.2	.1	2.224	-4	1.		
	[0/ $\pm 45/90]$	1	510	.0383	2	3.88	0.	-.1	4.31	.052	-.999	4.58	.052	-.999	4973. 4415.	
		2	728	.0383	2	2.17	0.	.156	.988	3.96	.156	.988	4.22	.156	.988	
	[0/ $\pm 45/90]$	1	510	.0383	2	3.88	0.	-.1	4.29	.052	-.999	4.56	.052	-.999	4973. 4935.	
		2	728	.0383	2	2.19	0.	.156	.988	3.90	.156	.988	4.17	.156	.988	
	[90/ $\pm 45/0]$	1	510	.0383	2	2.26	1.	.588	4.22	.156	.988	4.48	.156	-.988	3322. 4138.	
		2	728	.0383	2	1.68	1.	.588	.809	4.49	.052	-.999	4.69	.052	-.999	
Elliptope	[90/ $\pm 45/0]$	1	510	.0383	2	2.13	.548	.839	4.27	.156	-.988	4.56	.156	-.988	3190. 3756.	
		2	728	.0383	2	1.58	.548	.839	4.51	.052	-.999	4.71	.052	-.999		
	[$\pm 45/0/90]$	1	851	.0495	2	3.85	0.	-.4	6.34	.052	-.999	-7.36	.358	.934	8854. 8096.	
		2	1216	.0495	2	2.33	0.	-.4	-6.63	.259	.966	-7.72	.358	.934		
	[$\pm 45/0/90]$	1	851	.0495	2	3.85	0.	-.4	6.58	.208	.978	7.65	.309	-.951	8854. 8096.	
		2	1215	.0495	2	2.33	0.	-.4	-6.16	0.	.1	-7.19	0.	1.0		
	[$\pm 45/90/0]$	1	851	.0495	2	1.70	1.	0.	-6.01	.966	.259	-7.10	.934	.358	4598. 5470.	
		2	1216	.0495	2	1.25	1.	0.	-6.01	.966	.259	-7.10	.934	.358		
	[$\pm 45/90/0]$	1	851	.0495	2	1.70	1.	0.	-6.01	.966	.259	-7.10	.934	.358	4598. 5470.	
		2	1216	.0495	2	1.25	1.	0.	-6.01	.966	.259	-7.10	.934	.358		
Elliptope	[0/90/ $\pm 45]$	1	851	.0495	2	2.40	.358	-.934	-5.98	.351	-.309	-7.06	.934	-.358	5787. 6397.	
		2	1216	.0495	2	1.59	.358	0.	-5.85	1.	0.	-6.80	.934	-.358		
	[0/90/ $\pm 45]$	1	851	.0495	2	2.31	.407	-.914	-5.88	.914	-.407	-7.05	.914	-.407	5633. 6397.	
		2	1216	.0495	2	1.01	.407	0.	-5.85	1.	0.	-6.87	.934	-.358		
	[90/0/ $\pm 45]$	1	851	.0495	2	2.48	.707	-.707	-6.65	0.	.9	7.57	.156	-.988	5923. 6807.	
		2	1216	.0495	2	1.45	.707	0.	-6.45	6.91	.156	.988	7.89	.156	-.988	
	[90/0/ $\pm 45]$	1	851	.0495	2	1.73	.669	-.743	-6.57	0.	.9	7.40	.309	-.951	4446. 5489.	
		2	1216	.0495	2	1.34	.669	-.743	-6.49	0.	.9	7.15	.156	-.999		

TABLE III
SELECTED NONLINEARITY CHECKS

Type	Laminate Orientation	Case	ϵ_{cr}	f	n	M. S. min.	$\Omega_{max.}$	$v_{max.}$	$\bar{v}_{max.}$	\bar{x}	\bar{y}	lb./in. ²	lb./in.	\bar{x}	\bar{y}	ϵ_{ult}	u in./in.	
Rect.	[±45/90/0]	2	.1097	.0157	2	1.99	.1	-2.998	.5	0.		1.612	.4	1.		6558.		
			.0221	.0221	3	1.05	.1	-.4,.236	.5	0.		2.278	.4	1.		6744.		
			.0271	.0271	4	.53	.1	-.1,.186	.5	0.		2.799	.4	1.		6712.		
			.0313	.0313	5	.42	.1	-.7	-.5	0.		3.220	.4	1.		7766.		
			.0350	.0350	6	.02	.1	-.1	-.6	0.		3.599	.4	1.		6712.		
			.0363	.0363	7	-.12	.1	-.1	-.7	0.		3.912	.4	1.		6755.		
Ellipse	[90/0/45/0]	2	.1097	.0156	2	2.87	-.2	.4	-2.408	-.15	.1		2.226	-.15	1.		8488.	
			.0221	.0221	3	1.51	.05	.4	-.4,.09	-.15	.1		3.151	-.15	1.		8256.	
			.0270	.0270	4	.87	.0	.3	-.4,.176	-.15	.1		3.861	-.15	1.		8203.	
			.0312	.0312	5	.51	.05	.3	-.4,.823	-.15	.1		4.059	-.15	1.		8280.	
			.0349	.0349	6	.26	0.	.3	-.5	-.394	-.15		4.936	-.15	1.		8291.	
			.0382	.0382	7	0.03	.05	.3	-.5	.919	-.15		5.463	-.15	1.		8367.	
			.0413	.0413	8	-.04	0.	.3	-.6	.383	-.15		5.901	-.15	1.		8422.	
Ellipse	[90/45/0]	2	.723	.0383	2	1.58	.545	.839	4.51	.052	-.999	4.71	-.052	-.999	3756.			
			.0541	.0541	3	0.75	.545	.839	6.40	.052	-.999	6.69	.052	-.999	3822.			
			.0663	.0663	4	0.35	.545	.839	7.88	.052	-.999	8.24	.052	-.999	3931.			
			.0766	.0766	5	0.07	.545	.839	9.19	0	-.9	9.57	.052	-.999	3891.			
			.0856	.0856	6	-.03	.454	.891	-.10	.76	0	-.9	10.76	.052	.995	4237.		
[±45/0/90]	2	1216	.0495	2	2.33	0.	.4	-6.63	.259			-.966	-7.72	.358	.934	8996.		
			.0700	.0700	3	0.86	0.	.5	-.9	.40			-.966	-10.95	.358	.934	6733.	
			.0857	.0857	4	0.28	0.	.5	-.11	.58			-.966	-13.47	.358	.934	6224.	
			.0990	.0990	5	-.02	0.	.5	-.13	.44			-.966	-15.62	.358	.934	5957.	

10. DISCUSSION OF RESULTS

Some anomalies appear in the results. The analytic development for the elliptical plate has been independently checked, whereas the rectangular plate has been checked by the author only. The same is true for the computational portions of the computer program. The complete program has also been checked by the author only and in the case of the progressive failure analysis portion, only the failure analysis for flexural/membrane loading. This must be kept in mind when drawing conclusions from the discussion that follows.

Twelve 4-ply $[0/\pm 45/90]_C$ graphite/epoxy laminate configurations with $a = b =$ one inch were studied for both rectangular and elliptical shapes. Note that since delaminations can and do occur at any point in the laminate, nonsymmetric configurations are studied. Note also that the aspect ratio is one and only symmetric modes are admissible. The initial points of interest are the buckling loads. For the rectangular panels, the buckling strains for all configurations were the same, $\sigma_{cr} = 735, 1050 \mu$ in./in. for cases 1 and 2, respectively, when flexural/membrane coupling, B matrix, was not considered. Therefore, the differences are due to flexural/membrane coupling. The results fall into two categories. When the $\pm 45^\circ$ plies are on one side of the laminate configuration, the elliptical plate fails at a higher strain than the rectangular plate. Conversely, when the $\pm 45^\circ$ plies are on the interior, the reverse is true. This should indicate the equilibrium shape of the delaminated region and correlates with experimental data (1). Further studies are needed in this area. The variation in the buckling strain for the configurations studied was about 70 percent for the ellipse and 30 percent for the rectangle with the highest minimum being for the configuration $[(0/90)_C/(\pm 45)_C]_C$. It should be noted that an admissible deflected shape is a rectangle inscribed in an ellipse or vice-versa.

The ultimate strength due to flexural/membrane loading does not appear to be a function of the buckling load. Variations of up to 50 percent for the rectangle and 150 percent for the ellipse are observed. For case 2, $[90/0/\pm 45]_T$ is the best configuration for the rectangle while the $[\pm 45/0/90]_T$ is the best for the ellipse. Conversely, for case 1, $[\pm 45/90/0]_T$ and $[90/\pm 45/0]_T$ are the worst, respectively. The "peeling" stress causing delamination growth is a function of V_x, M_x or V_y, M_y , on the $x = \pm a$ or $y = \pm b$ boundary of the rectangular plate, respectively, and similarly normal to the boundary for the ellipse. Transformation of boundary stress resultants to stresses must still be performed, however, similarity to adhesive bonded lap joint analyses should render the problem tractable.

11. CONCLUSIONS

A relatively simple model to determine the stress fields which cause delamination has been presented. Utilization of this approach to determine the growth trajectories of delaminations under monotonically increasing loading is quite straightforward. Since these growth trajectories are in an isotropic region and the stress fields are deterministic, application of conventional techniques appears to be feasible to determine growth under spectrum loading.

Of more currency is the relatively simple expression to obtain buckling load under combined loading. The effects of flexural/membrane coupling are included but validity is contingent upon applicability of the selected displacement functions. Obviously, utilization of the method to determine perturbations to solutions obtained by more exact methods is possible.

12. REFERENCES

1. Konishi, D. Y. and Johnston, W. R.: "Fatigue Effects on Delaminations and Strength Degradation in Graphite/Epoxy Laminates," *Composite Materials Testing and Design* (Fifth Conference) ASTM STP 674, S. W. Tsai, ed. 1979.
2. Konishi, D. Y. "On the Postbuckled Strength of Advanced Composites," *Proceedings of Sixth conference of Fibrous Composites in Structural Design*, January 1983, New Orleans, LA.
3. Chai, H. "The Growth of Impact Damage in Compressively Loaded Laminate," *Dissertation, California Institute of Technology*, March 1982.
4. Konishi, D. Y., Lo, K. H., and Wu, E. M., "Progressive Failure Model for Advanced Composite Laminates Containing a Circular Hole," *Composite Structures*, Applied Science Publishers, London, 1981
5. Lo, K. H., Konishi, D. Y., and Wu, E. M., "Failure Strength of Notched Composites," *Journal of Composite Materials*, In press.

REPORT DOCUMENTATION PAGE

REPORT DOCUMENTATION PAGE			
1. Recipient's Reference	2. Originator's Reference	3. Further Reference	4. Security Classification of Document
	AGARD-CP-355	ISBN 92-835-0333-3	UNCLASSIFIED
5. Originator	Advisory Group for Aerospace Research and Development North Atlantic Treaty Organization 7 rue Ancelle, 92200 Neuilly sur Seine, France		
6. Title	CHARACTERIZATION, ANALYSIS AND SIGNIFICANCE OF DEFECTS IN COMPOSITE MATERIALS		
7. Presented at	the 56th Meeting of the Structures and Materials Panel in London, United Kingdom on 12-14 April 1983.		
8. Author(s)/Editor(s)	Various		9. Date July 1983
10. Author's/Editor's Address	Various		11. Pages 320
12. Distribution Statement	This document is distributed in accordance with AGARD policies and regulations, which are outlined on the Outside Back Covers of all AGARD publications.		
13. Keywords/Descriptors	Composite materials Defects Damage Structural analysis Tolerances (mechanics) Quality control		
14. Abstract	<p>Composite materials are not proof against defects in manufacture. The absence hitherto of a covering philosophy has led, in general, to a policy of "when in doubt, scrap". This document records the proceedings of a meeting, the aim of which was to try to specify criteria and tolerances for the acceptance of defective composites from a knowledge of the consequences of damage.</p> <p>An important feature emerging from the papers was the apparent capacity of a damaged or defective composite component to resist further damage in subsequent normal service.</p>		

AGARD Conference Proceedings No.355 Advisory Group for Aerospace Research and Development, NATO CHARACTERIZATION, ANALYSIS AND SIGNIFICANCE OF DEFECTS IN COMPOSITE MATERIALS Published July 1983 320 pages	AGARD-CP-355 Composite materials Defects Damage Structural analysis Tolerances (mechanics) Quality control	AGARD Conference Proceedings No.355 Advisory Group for Aerospace Research and Development, NATO CHARACTERIZATION, ANALYSIS AND SIGNIFICANCE OF DEFECTS IN COMPOSITE MATERIALS Published July 1983 320 pages	AGARD-CP-355 Composite materials Defects Damage Structural analysis Tolerances (mechanics) Quality control
	Composite materials are not proof against defects in manufacture. The absence hitherto of a covering philosophy has led, in general, to a policy of "when in doubt, scrap". This document records the proceedings of a meeting, the aim of which was to try to specify criteria and tolerances for the acceptance of defective composites from a knowledge of the consequences of damage.	P.T.O.	Composite materials are not proof against defects in manufacture. The absence hitherto of a covering philosophy has led, in general, to a policy of "when in doubt, scrap". This document records the proceedings of a meeting, the aim of which was to try to specify criteria and tolerances for the acceptance of defective composites from a knowledge of the consequences of damage.
AGARD Conference Proceedings No.355 Advisory Group for Aerospace Research and Development, NATO CHARACTERIZATION, ANALYSIS AND SIGNIFICANCE OF DEFECTS IN COMPOSITE MATERIALS Published July 1983 320 pages	AGARD-CP-355 Composite materials Defects Damage Structural analysis Tolerances (mechanics) Quality control	AGARD Conference Proceedings No.355 Advisory Group for Aerospace Research and Development, NATO CHARACTERIZATION, ANALYSIS AND SIGNIFICANCE OF DEFECTS IN COMPOSITE MATERIALS Published July 1983 320 pages	AGARD-CP-355 Composite materials Defects Damage Structural analysis Tolerances (mechanics) Quality control
	Composite materials are not proof against defects in manufacture. The absence hitherto of a covering philosophy has led, in general, to a policy of "when in doubt, scrap". This document records the proceedings of a meeting, the aim of which was to try to specify criteria and tolerances for the acceptance of defective composites from a knowledge of the consequences of damage.	P.T.O.	Composite materials are not proof against defects in manufacture. The absence hitherto of a covering philosophy has led, in general, to a policy of "when in doubt, scrap". This document records the proceedings of a meeting, the aim of which was to try to specify criteria and tolerances for the acceptance of defective composites from a knowledge of the consequences of damage.

<p>An important feature emerging from the papers was the apparent capacity of a damaged or defective composite component to resist further damage in subsequent normal service.</p> <p>Papers presented at the 56th Meeting of the Structures and Materials Panel in London, United Kingdom on 12-14 April 1983.</p>	<p>An important feature emerging from the papers was the apparent capacity of a damaged or defective composite component to resist further damage in subsequent normal service.</p> <p>Papers presented at the 56th Meeting of the Structures and Materials Panel in London, United Kingdom on 12-14 April 1983.</p>
<p>ISBN 92-835-0333-3</p>	<p>ISBN 92-835-0333-3</p>
<p>An important feature emerging from the papers was the apparent capacity of a damaged or defective composite component to resist further damage in subsequent normal service.</p> <p>Papers presented at the 56th Meeting of the Structures and Materials Panel in London, United Kingdom on 12-14 April 1983.</p>	<p>ISBN 92-835-0333-3</p>